Faculty of Science and Engineering
Department Physics and Astronomy

Development of a Dynamic Underwater Acoustic Communication Channel Simulator with Configurable Sea Surface Parameters to Explore Time-Varying Wide-Band Signal Distortion

Michael Stephen Caley

This thesis is presented for the Degree of
Doctor of Philosophy
of
Curtin University

March 2016

DECLARATION

To the best of my knowledge and belief this thesis contains no material previously published by any other person except where due acknowledgment has been made.

This thesis contains no material which has been accepted for the award of any other degree or diploma in any university.

Signature:

Date: …13th June 2016……...

ABSTRACT

A wide-band phase-coherent multi-path underwater acoustic channel simulation is developed based on an approximate quantitative model of the acoustic wave response to a time-varying three-dimensional (3D) rough surface. It has been demonstrated over transmission ranges from 100 m to 8 km by experimental channel probing and comparable synthetic replication of the channel probing through the simulated channel, that the simulation is capable of reproducing fine-time-scale Doppler and delay distortions consistent with those generated in real shallow water ocean channels.

The simulation enables improved exploration of over-spread channels, as the channel response can be generated to simultaneously encompass the significant channel Doppler and delay spreads, which cannot be achieved by experimental channel probing or replay of experimentally measured channel responses. The simulation incorporates realistic phase-coherence between rough-surface micro-paths and the underlying multi-path response structure represented by conceptual flat surface eigenpaths.

The channel simulation relies on successive calculation in time of a discrete tangent-plane implementation of the Kirchhoff Approximate (KA) rough-surface responses for bistatic rough surface interactions. The multi-path rough channel response is built combining one or more bistatic responses with the conceptual flat surface eigenpath structure determined from an established ray-tracing model.

The validation of the static and dynamic characteristics of the KA bistatic response model is achieved by comparison with a reliable Helmholtz-Kirchhoff Integral Equation (IE) reference bistatic response for a two-dimensional time-evolving surface profile. Comparative analyses of the Doppler and delay spreading functions for the KA and IE reference models, and the derived Doppler power spectrum and delay power profile, are used to evaluate and justify the dynamic characteristics of the KA model.

Comparative simulations using the KA and IE dynamic models show that when the horizontal discretisation of the ocean surface into planar elements becomes coarse relative to the surface profile an artificial Doppler response in excess of the

true Doppler response of a realistic continuous surface is generated. This artificial response is observable as distinct “shoulders” in the Doppler power spectrum. This insight allows the coarseness of the surface discretisation to be tailored depending on the dynamic range of Doppler fidelity required of the simulation.

The same dynamic KA versus IE model exploration demonstrates that attempts to exclude the KA response of shadowed parts of a rough surface inherently generates an artificially high Doppler response due to abrupt discrete-time switching of surface element contributions. The model comparison is used to demonstrate that the most useful and reliable simulation of Doppler and channel response power is achieved for KA by including the response of all parts of the surface, irrespective of apparent local shadowing, at the expense of modest and explicable positive biasing of the bistatic response power and delay.

Evaluation of the whole multi-path channel simulation is achieved by comparison of simulated and measured channel probe responses and derived Doppler and delay-spreading characteristics for two marine environments over different ranges, depths, and surface roughnesses.

ACKNOWLEDGEMENTS

I would like to particularly thank my principal supervisor Dr Alec Duncan for strategic problem orientation, questioning, patience, encouragement, and substantially through Alec's engaging on-line presentation of marine acoustics courses, the inspiration to pursue further study in this field. Alec's willingness to facilitate a geographically flexible post-graduate experience made my pursuit of studies and project work at Curtin University possible whilst situated in Brisbane and is greatly appreciated.

I would also like to express my thanks to the many other people who were instrumental in supporting the project on which this thesis is based, people who supported the preparation of this thesis, and people being supportive in life beyond the project, including:

- Prof. Sven Nordholm, supported by Prof. Yue Rong, Prof. Defeng Huang, and Dr Alec Duncan, for instigating the project under the Australian Research Council's (ARC) Discovery Projects funding scheme (No. DP110100736);
- Alessandro Ghiotto and Prof. Yue Rong for project associate supervision
- Ann Smith, Curtin Uni. Centre for Marine Science and Technology (CMST), for unwavering administrative support in respect of orientation, finances, conference travel and accommodation, visiting study space, building access and visitor parking, inclusion in CMST communications and social/sporting events;
- Scholarship finance – ARC, L3-Communications Oceania Ltd., Curtin University postgraduate scholarships;
- Alessandro Ghiotto for early L3-Oceania field trial inclusion and support;
- CMST field instrumentation and technical support from Frank Thomas, Dr Tim Gourlay, Malcolm Perry, and Dr Iain Parnum;
- Field support during at-sea testing from Dr Alec Duncan, Frank Thomas, Dr Tim Gourlay, Malcolm Perry, and Prof. Yue Rong;
- Bette Caley (nee Lehrer) & David Caley, Sarah Caley, Dr Miles Parsons & Dr Sylvia Osterrieder for Accommodation & transport assistance in Perth;

- Prof. David Mee, Prof. Peter Knights (St Lucia Campus) and A/Prof. Michael Noad (Gatton Campus) for study space support at the Univ. of Qld;
- Peter Rea & Margaret Caley for the 'life-saving' final year+ family 'scholarship'/loan;
- Thesis editing/review by Dr Alec Duncan, Alessandro Ghiotto, Prof. Yue Rong, Peter Rea, and Dr Peter Caley;
- All fellow post-grad. students and staff at Curtin CMST and the Dept. of Imaging and Applied Physics, that have been constantly welcoming and inclusive during my many (~14) visits to Curtin Uni over 4.5 years of study;
- My immediate family – Kate White, Leo, Miranda, and Vivien;
- My parents Jim & Isabel Caley for encouragement and final year travel assistance; and
- Light-hearted ribbing and encouragement from sailors at Oxley Sailing Club

TABLE OF CONTENTS

NOMENCLATURE AND ABBREVIATIONS

α – plane-wave attenuation coefficient [nepers/m]

α' – plane-wave attenuation coefficient [dB/km]

B_{chan} – communication channel bandwidth [Hz]

c – speed of sound in water [m/s]

$C(\Delta t, \tau_1, \tau_2)$ – channel response coherence in delay band

dF –discrete acoustic frequency step for Fourier synthesis [Hz]

ds –infinitesimal surface element

DWRB – directional wave rider buoy

EMR = electro-magnetic radiation

f – acoustic frequency [Hz]

f_o – acoustic signal centre frequency [Hz]

f_s – signal sample rate [samples/s]

$\mathcal{F}$ – Fourier transform

FIR –finite impulse response filter

Λ – ocean surface wavelength [m]

$h(t, \tau)$ –time-varying channel delay response

$\hat{h}(t, \tau)$ – probed estimate of the time-varying channel delay response

$h(\tau)$ – static channel delay response

$\widetilde{H}_{patch}(\omega)$– complex bistatic frequency response of rough surface patch

H_s – significant wave height [m]

IE –Helmholtz-Kirchhoff integral equation boundary element model

k – acoustic wavenumber [rad/m]

KA – Kirchhoff Approximation

$\widehat{\ }$ – estimate of a function or variable

L_{chan} – communication channel delay spread [s]

LFM – linear frequency modulated sweep

λ – acoustic wavelength in water [m]

λ_{min} – minimum acoustic wavelength of simulation bandwidth [m]

$n(t)$ – noise signal at receiver

N_{top} – number of surface bounces on a ray path

N_{bot} – number of bottom bounces on a ray path

θ_f – rotation of surface element about global y-axis [rad]

γ_f – rotation of surface element about global x-axis [rad]

θ_0 – elevation angle from bistatic source to rough surface discrete element [rad]

θ_r – elevation angle from bistatic receiver to rough surface discrete element [rad]

ϕ_0 – bearing angle about z-axis from bistatic source to surface discrete element [rad]

ϕ_r – bearing angle about z-axis from bistatic receiver to surface discrete element [rad]

ρ_0 – mean density of seawater [kg/m^3]

p – acoustic pressure [Pa]

p_{Tot} – total incident plus scattered field acoustic pressure [Pa]

p_{inc} – bistatic incident acoustic pressure field [Pa]

p_r – bistatic KA surface-scattered acoustic pressure field [Pa]

p_{scat} – bistatic IE surface-scattered acoustic pressure field [Pa]

PRBS – pseudo-random binary sequence

$P(\tau)$ –channel power delay profile

$P(\nu)$ –channel Doppler power spectrum

$\vec{r}$ – bistatic position vector

r – radius from discrete surface element local coordinate origin to receiver point [m]

r' – radius from infinitesimal element dson discrete element to receiver [m]

r_0 – radius from omnidirectional source to discrete rough surface element [m]

r_r – radius from discrete rough surface element to bistatic receiver [m]

R – transmission range [m]

s_o – planar surface element

$S(\nu, \tau)$ –channel spreading function

t – global time [s]

Δt – discrete channel response update period [s]

τ – channel delay time [s]

T – wave period [s]

T_{probe} – probe symbol repeat period [s]

T_{p} –wave period associated with peak of the surface wave spectral density [s]

T_{m} –mean wave period [s]

Δt - channel update time interval [s]

Δt_{symb} – probe symbol length [s]

UAC – underwater acoustic communications

u_o – acoustic surface velocity normal to surface [m/s]

v – velocity [m/s]

V_x – horizontal wave speed [m/s]

v – Doppler frequency shift [Hz], also local x-coordinate on discrete surface element [m]

VLA – vertical line array

$x(t)$ – channel transmit signal

x – discrete transmit symbol vector

R_{xx} – autocorrelation of discrete transmit symbol vector x

$\chi(\nu, \tau)$ – ambiguity function of discrete transmit symbol vector x

$\tilde{x}$ – analytic discrete transmit symbol vector

Δx – horizontal surface discretisation in global x-axis direction

$y(t)$ – channel receive signal

y – distorted receive signal vector

ω – acoustic angular frequency [rad/s]

w –local y-coordinate on discrete surface element [m]

W_{probe} –probe symbol repeat frequency [Hz]

1 INTRODUCTION

1.1 Underwater acoustic communication applications

The knowledge derived from the ocean across diverse areas of human endeavour is supported by the collection and transmission of data within the ocean. Transmission of data through the ocean may be achieved by a range of technologies depending on the application, including cable, wireless transmission, human controlled submersibles, remotely controlled vehicles (ROV's) or autonomous underwater vehicles (AUV's).

Wireless data transmission using electro-magnetic radiation (EMR), via light is one important form of underwater wireless, however visible EMR is only suited to transmission over relatively short distances of the order of tens of meters through water (Potter, Porter, and Preisig 2013). Wireless underwater communication at greater distances must be achieve by the coding and transmission of data in underwater acoustic signals.

Developing uses for underwater acoustic communications include single link applications, such as between a boat and an AUV, such as a marine glider, or multi-link applications involving a network of fixed and/or mobile underwater communication nodes. Multi-link fixed node uses include pipeline process control nodes for marine oil and gas infrastructure (Ribeiro, de Castro Pinto Pedroza, and Costa 2015), networks of passive acoustic monitoring stations for coastal security (Ghiotto, Andronis, and Dragojevic 2012) or spatial monitoring of other marine parameters. Mobile networks under development include acoustically communicating Autonomous Underwater Vehicles (AUVs) for subsea exploration, monitoring and defence applications (Freitag et al. 2001, Caiti et al. 2011).

The miniaturisation and decreasing power usage of digital signal processing technology is bringing down the cost of the hardware needed for underwater communications (Benson, Ryan, and Frater 2012) enabling greater utilisation of acoustic communications in commercial and environmental monitoring contexts.

1.2 Underwater Acoustic Communication Challenges

There are a number of challenges with the underwater acoustic communications (UAC) channel that combine to make wireless UAC relatively slow, or conversely

unreliable, making improvements particularly for shallow horizontal channels the subject of on-going research. These challenges include a hostile marine environment, high channel latency, strong transmission multi-path and refraction, frequency-dependent absorption, and high proportional Doppler.

The marine environment for both UAC trials and operational systems is physically challenging to humans and instrumentation. Accessing the underwater environment is inherently difficult compared to terrestrial communications and is hazardous or prohibitive in rough conditions. Trials in deeper water require substantial vessel time, and increasingly large/expensive vessels as the distance to a UAC site from shore increases. For electronic equipment salt-water immersion requires robust design to prevent leakage and corrosion damage. At all depths, but particularly in shallow environments, marine bio-fouling of transducer radiation/reception elements is a challenge (Alves et al. 2014) which alters transmitter and receiver efficiencies over time.

Compared to terrestrial wireless the two-way time-delay between two communicating nodes, or latency, is long in UAC due to the low speed of sound through water (~1.5 km/s) compared to terrestrial wireless EMR communications (~300,000 km/s). This poses unique challenges coordinating and designing messaging protocols at the network level (Chitre and Soh 2015).

The shallow horizontal UAC channel is characterised by strong multi-path transmission that, particularly with calmer ocean surface conditions, sees a transmitted signal arrive at a receiver as a series of over-laid signal replicas of similar relative strength. Surface paths are further fragmented into micro-paths with difficult to predict time-varying delays and Doppler from boundary interactions and any movement of the transmitter and receiver (Stojanovic and Preisig 2009).

Sound refraction due to variations in sound speed due to temperature, pressure and salinity variations combine to cause curvature of transmitted sound paths (Jensen et al. 2011). In horizontal shallow environments this can lead to loss of the direct transmission path between a transmitter and receiver. The receiver must then recover the signal from the relatively highly distorted surface reflected transmission path(s), and/or a some-what distorted sea-bottom reflected path.

Strong frequency-dependence of sound absorption by sea-water causes high frequencies to be more quickly attenuated with range than low frequencies. Consequently the useful UAC bandwidth is strongly range dependent, varying from hundreds of kHz at distances less than 100m, to approximately 20 kHz at 10 km range, and around 1 kHz bandwidth at 100 km range (Stojanovic 2007).

The relatively high rate of movement of the ocean surface boundary relative to the speed of sound through water leads to a high proportional Doppler of the order of 0.1% for stationary UAC node links. These Doppler shifts fluctuate and the spectrum of the Doppler varies with the roughness of the surface. For mobile UAC links (e.g. involving nodes attached to boats or AUV's) much higher proportional Doppler of the order of 0.5% may occur, but with better information about the Doppler velocity causing the shift. For comparison this proportional Doppler is about 10,000 to 50,000 times higher than a terrestrial base-station radio link to a vehicle gaining distance at 100 km/hr.

1.3 Role of channel simulators

Two key steps to improving the reliability of underwater acoustic communication systems are developing an understanding of how challenging and diverse acoustic communication conditions are physically created in the ocean, and secondly, simulating the acoustic channel for these conditions to enable testing and evaluation of communications software and hardware (van Walree 2013).

Channel simulation provides a tool to enhance understanding of the interaction between physical ocean conditions and poor acoustic communication conditions. Often these conditions are known to some degree through field experience with underwater communication applications, however the high costs of field-trials and the un-predictability of ocean conditions make physical trials to replicate and explore a particular set of ocean circumstances difficult. Channel simulation offers a controllable environment to explore otherwise elusive environmental conditions. It is also the case that the diversity of ocean channels that need to be understood is extensive due to the many factors that contribute to unique underwater acoustic propagation conditions, and therefore practically beyond what may be explored by field trials alone.

For comparative testing of algorithms and hardware, channel simulation enables reliable benchmarking of alternatives. This is very difficult to achieve at sea due

to the many time-varying processes in the ocean that affect sound propagation. These include signal interactions with the constantly changing dynamic sea surface, movement of the transmitter or receiver positions, sound refraction from dynamic horizontal and vertical sound speed gradients, bubble clouds from breaking waves, and varying water depth with tides. The sea-bottom becomes a source of time-variability when relative movement of transmitter and/or receiver results in changing bathymetry for bottom interactions. Good overviews of the range of time-varying effects impacting on underwater acoustic communication include Preisig (2007) and Stojanovic and Preisig (2009).

1.4 Research Aims and Objectives

This simulation research focuses on the variability in the multi-path ocean acoustic channel caused by the time-varying signal scattering off the under-side of the moving rough sea surface, with particular focus on this effect in relatively shallow in-shore waters at depths less than approximately 100 m, over ranges from 100 m to 10 km, at frequencies nominally between 5 kHz and 30 kHz.

The key advance in the field of underwater channel simulators that is sought through this research is the ability to realistically simulate at the signal sampling frequency, the Doppler and delay distortion of wide-band phase-coherent communication signals, in response to an arbitrarily defined realistic time-evolving three-dimensional ocean surface.

This research aims to extend the underwater acoustic channel simulation capability for wide-band phase-coherent communication signals in shallow water environments, with particular focus on the multi-path channel distortions generated by signal interaction with arbitrary surface wave conditions.

The capabilities sought for the channel simulator were initially developed from literature review for PhD Candidacy and reflected in the early project description (Caley and Duncan 2011). These capabilities were further refined following post-processing of the initial channel probing experiments in a 13.5 m deep environment off Cottesloe, Perth (Caley and Duncan 2013a). The capabilities sought include, to:

- enable analysis of directional effects of surface wave fields on propagation;

- simulate the propagation of wide-band phase-coherent communication signals; and
- enable synthetic generation of the received signal by transmission of a transmit signal through the simulated channel.

The objectives of this research are to:

1. develop a quantitative computer simulation of fine time-scale acoustic signal distortion between a source and receiver located within an arbitrary marine environment;
2. measure and characterise the fine time-scale acoustic signal distortion in point-to-point underwater acoustic transmission tests (channel probing experiments) for a range of transmission distances, depths, and surface wave conditions;
3. explore and develop efficient computational algorithms such that the simulation of rapid time-varying channel distortion may be implemented in real-time for future hardware implementation of a channel simulator by others; and
4. use the quantitative computer simulation to replicate the transmission of the experimental transmit signals, and compare standard measures of the dynamic signal distortion for the experimental and simulation channels over a range of experimental propagation distances, water depths and surface wave conditions.

1.5 Original contributions to field

A number of original channel simulation capabilities and understandings have been developed and demonstrated in this project.

The complete channel simulation represents an approximate whole-wave multi-path channel response for an arbitrarily defined time-varying three-dimensional surface, that is capable of simulating realistic response coherence across the underlying eigenpaths of the multi-path response structure and the micro-path variations associated with the rough surface boundary. The simulation enables improved exploration of over-spread channels, as the channel response can be generated to simultaneously encompass the significant channel Doppler and delay spreads, which cannot be achieved by experimental channel probing or replay of experimentally measured channel responses.

The time-circular multi-path channel response is generated from a single time-circular three-dimensional surface realisation. This innovation allows a transmit signal of arbitrary length to be convolved (or 'run through') the synthetic channel without encountering artificial response discontinuities.

The efficient computational re-use of a single time-circular three-dimensional surface realisation and derived time-circular bistatic responses, for the calculation of many horizontally displaced but spatially correlated bistatic rough surface interactions that are modelled for each underlying eigenpath, is an original innovation.

The time-varying analysis of the bistatic rough-surface response calculated by the discrete facetted implementation of the tangent-plane Kirchhoff Approximation (KA) is an original development in improving understanding of the dynamic delay, Doppler, and amplitude response effects of KA applied to the underwater acoustic rough-surface interaction.

By comparison of KA and IE time-varying bistatic responses it has been identified that a sufficiently coarse discretisation of the rough surface generates a readily identifiable additional Doppler response in excess of the true Doppler response of a realistic continuous surface, observable as distinct "shoulders" in the Doppler power spectrum. This approach allows the coarseness of the discretisation to be tailored depending on the dynamic range of Doppler fidelity required of the simulation.

This analysis of time-varying bistatic responses has also demonstrated that attempts to exclude the KA response of shadowed parts of a rough surface inherently generates an artificially high Doppler response due to the discrete-time switching of intermittently shadowed surface elements. The methodology has been used to demonstrate that the most reliable simulation of Doppler spectra and delay power profiles are achieved for KA by including the response of all parts of the surface, irrespective of apparent local shadowing, at the expense of modest and explicable positive biasing of the channel delay response and signal power.

1.6 Overview of thesis

The background material (Chapter 2) presents the established analysis techniques that are used to explore the acoustic transmission through the ocean

experimentally, and the established methods and techniques drawn upon to create and evaluate the developed computer simulation of wide-band acoustic signal distortion through the ocean.

The literature review (Chapter 3) establishes the specific challenges to improved reliability and rate of data transmission in underwater acoustic communication. The current capabilities of underwater simulations are explored, and the needs for improved simulation capability are identified.

Field channel probing trials (Chapter 4) describes the experimental design, fieldwork, and results from at-sea trials conducted to experimentally investigate the time-varying distortion (i.e. channel response) of communication signal transmission through a 13.5 m deep marine environment offshore from Cottesloe, Perth, and a 53 m deep marine environment south-west of Rottnest Island, near Perth.

The simulation development (Chapter 5) describes and justifies the developed methodology for calculation of the time-varying multi-path channel response.

In Chapter 6 the simulation is used to synthetically replicate the time-varying channel response measured experimentally in the Cottesloe and Rottnest channel probing trials.

The conclusions (Chapter 7) outlines the key strengths of the simulation and limitations of the developed simulation methodology.

The recommendations for further work (Chapter 8) outlines suggested avenues for exploration of real channels, improvements in simulation fidelity and work towards real-time simulator implementation.

2 BACKGROUND MATERIAL

2.1 Overview

This chapter presents established channel modelling concepts that are relied upon in the experimental investigations, simulation model development and comparisons of measured and simulated channel responses.

Section 2.2 presents the underlying channel simulation methodology for a static geometry channel with a smooth ocean surface. Section 2.3 explores the inherent assumptions in modelling a time-varying channel as a series of discrete static channels, setting the context for progressing to a time-series of rough static-channel responses to simulate the time-varying rough ocean response.

Section 2.4 presents the development of a discrete tangent plane Kirchhoff-approximate bistatic rough surface response, used to calculate time-sequential rough static-channel responses. The mathematical behaviour of the developed discrete KA element response for self-shadowing is explored to provide background to the simulation results in Chapters 5 and 6 for shadowed surfaces. The calculation implementation of the proven Helmholtz-Kirchhoff integral equation boundary element reference model for the same rough surface bistatic response is presented in Section 2.5.

Section 2.6 summarises the method of correlative channel sounding, or channel probing, used to sample the time-varying experimental and synthetic (or simulated) channels. Alternative metrics for presenting time-varying characteristics of the channel response are presented.

2.2 Static channel modelling

2.2.1 What is a “channel”?

The term “channel” is used as an abbreviation of a “communication channel”. The communication channel is the physical medium that carries a signal between a transmitter and a receiver (Proakis 2000), such as a wire, optical fibre, or the atmosphere. In this thesis the channel is the underwater environment between a transmitter and receiver. The channel changes the transmitted signal during propagation, and may also include noise at the receiver that is not related to the transmitted signal.

Because signal transmission characteristics change depending on many physical and dimensional properties of the underwater environment, many distinctly different channels may be identified. So for example, transmission over a 100 m range in a given water depth is a distinctly different channel to transmission over a 1000 m range in the same water depth. The 100 m transmission range is a distinctly different channel on a day when the ocean surface is flat compared to a day when the surface is rough. Further, the 100 m range transmission represents a different channel when the transmitter and receiver are suspended near the surface, versus mounted on the sea-bed.

Within a given environment, if the nature of the signal distortion and/or additive noise in two instances differ significantly, then the two channels are also distinct.

2.2.2 Linear time-invariant channel model

The time-invariance of a static channel means that every sample of a time-varying input signal $x(t)$ is transformed identically regardless of time (t). However the response can vary depending on the time-delay since it was transmitted (τ), normally referred to as the delay. The experience of multiple acoustic echoes after a clap within an acoustically reflective environment is an example of a response that varies with time-delay. This time-invariant but delay-dependent channel response is designated $h(\tau)$.

The time-varying input signal $x(t)$ and a static channel response $h(\tau)$ combine to produce the time-varying channel output $y(t)$ at a receiver as per Eq.(2-1) (Proakis 2000). The noise term $n(t)$ represents the received noise from the channel that is unrelated to the transmitted signal $x(t)$.

$$y(t) = \int_{-\infty}^{\infty} h(\tau)x(t-\tau)\,d\tau + n(t) \tag{2-1}$$

The 'linear' characteristic indicates that the channel output signal magnitude, excluding the noise term, varies proportionally to the input magnitude. Eq.(2-1) may be expressed in the discrete-time form of Eq.(2-2) (Siderius and Porter 2008) where $\tilde{A}_n$ is the discrete complex amplitude for the n^{th} arrival at delay τ_n and $\tilde{x}(t-\tau_n)$ is the analytic transmit signal delayed by τ_n.

$$y(t) = \mathrm{Re}\left[\sum_{n=1}^{N} \tilde{A}_n \tilde{x}(t-\tau_n)\right] + n(t) \qquad (2\text{-}2)$$

2.2.3 Ray-tracing for smooth-boundary channels

The ray-tracing acoustic propagation method provides an efficient method of calculating the discrete complex amplitude coefficients $\tilde{A}_n$ and associated channel delays τ_n for the static smooth-boundary channel response in Eq.(2-2). The meaning of 'smooth' here is the scale of boundary roughness is much larger than the minimum acoustic wavelength of interest.

The primary advantage of the ray-tracing method is that, with the exception of sea-water absorption, the field solution in a medium with dimensions much larger than the minimum wavelength, free of scatterers and smooth reflective boundaries is independent of acoustic frequency. A comprehensive theoretical development of ray acoustics is presented in Ziomek (1995) for inhomogeneous media, and an abbreviated summary described in Jensen et al. (2011).

Sound absorption through sea-water is characterised by a frequency-dependent plane-wave attenuation coefficient as per Eq.(2-3) with acoustic frequency f in kHz (Jensen et al. 2011),

$$\alpha' = 3.3 \times 10^{-3} + \frac{0.11 f^2}{1+f^2} + \frac{44 f^2}{4100+f^2} + 3.0 \times 10^{-4} f^2 \ [\mathrm{dB/km}] \qquad (2\text{-}3)$$

For the 8 kHz to 16 kHz bandwidth in this study the deviation in actual acoustic absorption with range from that implied by single-frequency ray calculation at the 12 kHz centre frequency is summarised in Table 2-1. It is clear that except at very short ranges of the order of 100 m, the frequency dependence of the sea-water absorption needs to be accounted for.

Table 2-1: Deviation in acoustical absorption at upper and lower band frequencies relative to absorption at 12 kHz centre-frequency

Range	8 kHz (deviation rel.12 kHz)	12 kHz (dB)	16 kHz (deviation rel.12 kHz)
0.1 km	-0.1	0.2	+0.1
1 km	-0.9	1.7	+1.1
10 km	-8.4	16.5	+8.5

The Bellhop (Porter 2011) model implementation of ray-tracing is used in this study to calculate the flat-surface ray-path responses for a range-independent sound speed gradient and a smooth semi-infinite fluid sea-bed (that may be tilted).

Using 'geometric' ray-beams, the Bellhop model calculates the propagation of a fan of rays which trace the wave-path normal to propagating wave-fronts according to the local sound speed gradient and boundary reflections. The amplitude A_n at the receiver for the n^{th} ray-path is calculated. The net phase change from ocean surface or bottom boundary interactions is tracked for each ray-path and incorporated into the complex path amplitude $\tilde{A}_n$. The number of surface (N_{top}) and bottom reflections (N_{bot}), and the total flight-time from source to receiver along the n^{th} ray-path is τ_n, referred to as the path delay.

Whilst a smooth sea surface may be approximated as 100% reflective and frequency independent at all grazing angles, the modelled fluid sea-bottom exhibits some frequency dependence (Jensen et al. 2011). The frequency-dependence of the bottom reflection coefficient for a comparable semi-infinite homogeneous fluid bottom model was previously established by Siderius and Porter (2006). The bottom reflection loss was calculated at 500 Hz and 5 kHz for grazing angles from 0-50 degrees for homogeneous and inhomogeneous semi-infinite fluid sea-beds. The multi-path channel delay spreads were also compared for 100 m water depth at 2 km range. For the homogeneous fluid bottom case the results were coincident for the 500 Hz and 5 kHz results. Any sensitivity to frequency may be expected to decrease further for the higher 8 kHz-16 kHz range considered in this thesis project, as the channel dimensions effectively become larger relative to the acoustic wavelength as the acoustic frequency is increased. Siderius and Porter (2006) note that quite apart from the demonstrated frequency insensitivity of the bottom reflection coefficient between 500 Hz and 5 kHz, the knowledge of the sea-bed strata that would be necessary to correctly predict this frequency-dependence is generally not available. On this basis the calculation of the frequency response of ray-path bottom interactions at the centre frequency of 12 kHz is justified.

2.3 Time-varying channel modelled by series of static channels

The goal of channel simulator is to produce an efficient discrete-time implementation of the signal convolution with a linear time-varying model of the underwater acoustic channel described by Eq.(2-4) (Proakis 2000).

$$y(t) = \int_{-\infty}^{\infty} h(t,\tau)x(t-\tau)\,d\tau + n(t) \tag{2-4}$$

The time-varying underwater acoustic channel response $h(t,\tau)$ is often modelled as a time-series of 'snapshot' linear time-invariant (or static) channels $h_i(\tau)$ (Dol et al. 2013, Siderius and Porter 2008). The validity of this approach is examined by considering a nominal channel response update period Δt of 20 ms, for horizontal propagation ranges of 100 m, 1 km and 10 km relevant to the channel probe experiments described in Chapter 3.

For a sound speed in water c of 1500 m/s, a sound-wave will travel 30 m during the 20 ms time-step between successive channel response updates. Thus, the actual flight-time for 100 m, 1 km and 10 km channels would consist of approximately 3, 33 and 333 such time-steps respectively.

In contrast, approximating $h(t,\tau)$ as a time-series of static channels at 20 ms intervals implies that a 'packet' of sound travels the entire length of the modelled static channel in an instant, regardless of channel length. This approximation has been noted by others (Dol et al. 2013, Siderius and Porter 2008). Dol et al. (2013) addressed the problem for a time-varying 2D surface realisation by making the surface profile a composite of realisations concatenated spatially from sequential realisations at intervals of $c\Delta t$. The composite surface realisation then approximates a time-evolving surface for surface wavelengths longer than 2 x $c\Delta t$, equivalent to 30 m for the 10 ms channel update rate reported.

It would in principle be possible to calculate a more continuous time-warped 'fly-through' surface profile $\mathcal{Z}(\mathrm{x},\theta,\tau)$ representing the shape of the dynamic surface experienced by a wavelet launched at angle θ at time delay τ as it travels the length of the channel. Successive 'snapshot' channel responses calculated using this warped surface profile $\mathcal{Z}$ would maintain the time-invariant assumption implicit in Eq.(2-1), however the surface would need to be recalculated for every transmitter acoustic launch angle. The complexity of the approach would be compounded further for a three-dimensional surface.

The anticipated computational burden of generating multiple instances of the 'fly-through' surface encourages the question of whether a simpler series of approximate 'snapshot' ocean surfaces is sufficient. This question can be examined by considering the maximum positional error of surface waves from their true 'experienced' position implied by the 'snapshot' simplification.

Consider an acoustic wavelet travelling at speed c, and sea surface waves travelling with the horizontal speed V_x dependent on the wave period T. For illustrative purposes surface wavelengths in the range of 1 m to 150 m have been considered as typical of conditions that might be experienced in a shallow 14 m deep environment over 0.1 km, 1 km, and 10 km ranges R. The maximum horizontal error ξ in wave position along the transmission transect, caused by adopting the 'snapshot' channel profile, will occur at the receiver (corresponding to the maximum time-of-flight or range) as per Eq.(2-5) and summarised in Table 2-2.

$$\xi = \frac{R}{c}.V_x \tag{2-5}$$

The 'snapshot' approximation results in a spatial distortion of the surface wavelength spectrum of up to 0.08% for slow 1 m wavelength waves and 0.75% for faster-moving 150 m wavelength waves. These errors translate to phase shifts in the modelled responses off sub-portions of the surface depending on distance from the source, and depending on the surface wavelength. However, other than these phase distortions, the velocity of all parts of the surface response, realised by the change in surface displacement from one realisation to the next, is not altered by the 'snapshot' approximation.

Table 2-2: Maximum wave positional error ξ resulting from 'snapshot' surface profile approximation, measured in surface wavelengths (Λ)

Transmission Range	Wind waves Λ = 1 m , T = 0.8 s V_x = 1.25 m/s	Swell Λ = 150 m, T = 14 s V_x = 10.7 m/s
0.1 km	0.08 Λ = 0.08 m	0.005 Λ = 0.75 m
1 km	0.8 Λ = 0.8 m	0.05 Λ = 7.5 m
10 km	8 Λ = 8 m	0.5 Λ = 75 m

For any of the example transmission ranges, unless one had extensive spatial surface wave monitoring capability, it would be difficult to experimentally record or predict the position of either surface wave crests or swell at the full transmission range more accurately than the maximum positional error associated with the 'snapshot' assumption in Table 2-2. Thus the positional errors are not considered significant in terms of the surface profile shape.

On the basis of the above analysis, the modelling of a time-varying underwater acoustic channel response $h(t,\tau)$ as a time-series of linear time-invariant channels is justified. This approach may be extended to the limiting case where the channel response is updated at the signal sampling rate, since the estimated maximum positional error of wave crests estimated by Eq.(2-5) is independent of the channel response update interval Δt.

2.4 Kirchhoff Approximation of rough-surface response

The Kirchhoff Approximation (KA), also known as the Tangent Plane or Physical Optics assumption (Ogilvy 1991) approximates that the reflected pressure p_r at every point on a reflective boundary with free-space has identical and opposite magnitude to the incident pressure $p_{inc}(x,y,z)$ at the surface as per Eq.(2-6), as if each point was part of an infinite flat surface.

$$p_{Tot}(x,y,0) = p_{inc}(x,y,0) + p_r(x,y,0) = 0 \qquad (2\text{-}6)$$

This implies that the reflected pressure field at a point on the surface is influenced only by the incident pressure field from afar, and not secondary reflections from other surface points. A strict interpretation is that Eq.(2-6) also implies the pressure at a point is not affected by shadowing from other surface points.

The primary advantage of the KA is of a numerical nature, that the scattered surface pressure at points across a rough surface may be determined simply from the incident pressure, independent of the surrounding surface. Numerically this greatly simplifies the method relative to an exact method that includes secondary reflections and shadowing, such as the Kirchhoff-Helmholtz Integral Equation boundary element method (IE). By contrast, the IE method requires inversion of an N^2 matrix to establish the scattered surface pressure over the patch, where N is the number of points that defines the surface patch.

2.4.1 Single rectangular element plane-wave response

The basic building block of the simulation is the expression for the reflected pressure $p(x,y,z)$ remote from a finite rectangular element of sea surface with side dimensions a and b, after making the Kirchhoff Approximation (KA).

An expression for the KA reflected pressure from a rectangular element of ocean surface has been developed similar to the method that Kinsler et al. (1982) used to determine the radiation from a plane circular piston treated as a simple baffled source, but with the motion of the baffle being replaced by the boundary motion induced by a plane-wave at oblique incidence.

Consider the pressure at $p(x,y,z)$ generated by an infinitesimal surface element ds with velocity $u_0(v,w)$ normal to the surface. This point $p(x,y,z)$ is located a distance r from the origin of surface element s_0, and r' from ds as illustrated on Figure 2-1.

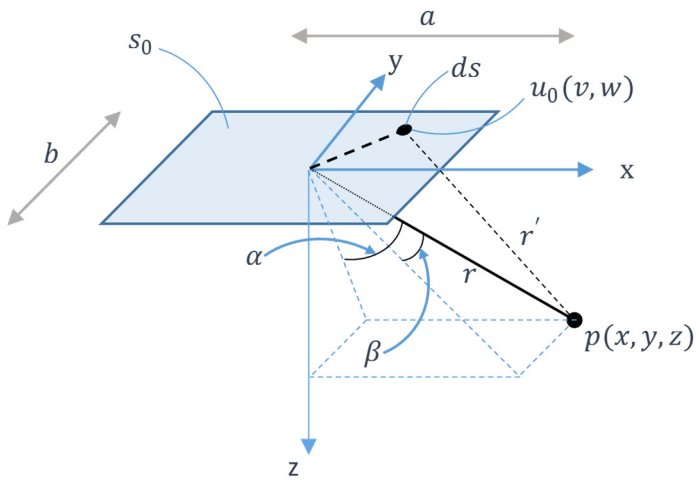

Figure 2-1: Rectangular surface element local coordinates

Treating the element ds as a simple baffled source of strength $dQ = u_0 ds$, and allowing the surface velocity $u_0(v,w)$ perpendicular to element ds to vary across s_0 with local in-plane element coordinates v and w, the pressure from the whole element s_0 may be represented in Eq.(2-7) by an integration of infinitesimal sources dQ each radiating spherically over r' to the receiver point.

$$p(x,y,z,t) = \frac{ik\rho_0 c}{4\pi}\int_{s_0} \frac{u_0(v,w)\, e^{i(kr' - \omega t)}}{r'} ds \qquad (2\text{-}7)$$

If the time dependence is not required, the spatial pressure distribution at an instant in time simplifies to Eq.(2-8).

$$p(x,y,z) = \frac{ik\rho_0 c}{4\pi}\iint_{S_0}\frac{u_0(v,w)\,e^{ikr'}}{r'}dv.dw \tag{2-8}$$

The pressure amplitude is dependent on geometrical spreading via the radius r' in Eq.(2-8). This may be approximated in the denominator by r when r' is large compared to the element dimensions a and b. The phase dependence of r' in the numerator exponent may also be approximated by seeking an approximate equivalent to r' developed from the geometrical approximation below.

$$\begin{aligned} r' &= \sqrt{(x-v)^2+(y-w)^2+z^2} \\ &= r\sqrt{1-\frac{2xv}{r^2}-\frac{2yw}{r^2}+\frac{v^2}{r^2}+\frac{w^2}{r^2}} \end{aligned} \tag{2-9}$$

The $\frac{v^2}{r^2}$ and $\frac{w^2}{r^2}$ terms are negligible when r is large compared to the element dimensions a and b, leading to Eq.(2-10).

$$r' \cong r\left(1-2\left(\frac{xv}{r^2}-\frac{yw}{r^2}\right)\right)^{\frac{1}{2}} \tag{2-10}$$

The requirement that r is large compared to the element dimensions a and b is again invoked such that ϵ may be taken as much smaller than unity in Eq.(2-11), enabling the approximate expansion in Eq.(2-12).

$$\epsilon = \left|-2\left(\frac{xv}{r^2}-\frac{yw}{r^2}\right)\right| \ll 1 \tag{2-11}$$

$$\begin{aligned} r' &\cong r(1+\epsilon)^{\frac{1}{2}} \\ &\cong r(1+1/2\,\epsilon) \\ &\cong r-\frac{xv}{r}-\frac{yw}{r} \end{aligned} \tag{2-12}$$

Observing that $\frac{x}{r}=\sin\alpha$ and $\frac{y}{r}=\sin\beta$, giving $r' \cong r - v\sin\alpha - w\sin\beta$ Eq.(2-8) becomes

$$p(x,y,z) = \frac{ik\rho_0 c}{4\pi}\iint_{S_0}\frac{u_0(v,w)\,e^{ik(r-v\sin\alpha-w\sin\beta)}}{r}dv.dw$$

$$= \frac{ik\rho_0 c}{4\pi}\frac{e^{ikr}}{r}\iint_{S_0} u_0(v,w)\, e^{-ik(\, vsin\alpha + wsin\beta)}\, dv.dw \tag{2-13}$$

$$= \frac{ik\rho_0 c}{4\pi}\frac{e^{ikr}}{r}\iint_{S_0} u_0(v,w)\, e^{-i(\, vk_x + wk_y)}\, dv.dw \tag{2-14}$$

where k is coincident with r on Figure 2-1 such that $k_x = ksin\alpha$ and $k_y = ksin\beta$.

We now wish to develop an expression for the variation of $u_0(v,w)$ over the rectangular element resulting from an incident plane-wave, that will then allow the integrals in Eq.(2-14) to be evaluated.

Consider an infinitesimal particle on surface s_0. The motion of this particle normal to the surface (z direction) will be governed by Newton's Law as expressed in Eq.(2-15).

$$\frac{\partial p_{Tot}}{\partial z} = -\rho_0 \partial^2 z/\partial t^2 \tag{2-15}$$

Assuming a general harmonic plane-wave solution for the particle velocity in the normal z direction $\partial z/\partial t = u(x,y,z) = Ue^{i(kz-\omega t)}$, differentiation once with respect to time gives the relationship $\frac{\partial^2 z}{\partial t^2} = -i\omega\, u(x,y,z)$. Thus on the surface $u_0(v,w)$ may be expressed by Eq.(2-16).

$$u_0(v,w) = \frac{-i}{\rho_0\omega}\partial p_{Tot}/\partial z\Big|_{z=0} \tag{2-16}$$

Making the Kirchhoff Assumption for the reflected wave at the element surface, an incident plane-wave $p_{inc}(x,y,z) = A_{inc}e^{i(k_{0x}x + k_{0y}y - k_{0z}z)}$ will produce a reflected plane-wave $p_r(x,y,z) = -A_{inc}e^{i(k_{0x}x + k_{0y}y + k_{0z}z)}$, giving Eq.(2-17). (Note: the x,y coordinates become v,w on the element surface)

$$\partial p_{Tot}/\partial z|_{z=0} = -2ik_{0z}A_{inc}e^{i(k_{0x}v + k_{0y}w)} \tag{2-17}$$

Combining Eq.(2-16) and Eq.(2-17) we have

$$u_0(v,w) = \frac{-2k_{0z}A_{inc}}{\rho_0\omega}e^{i(k_{0x}v + k_{0y}w)} \tag{2-18}$$

The expression for $u_0(v,w)$ from Eq.(2-18) may then be used within the integration of Eq.(2-14) to give Eq.(2-19).

$$p(x,y,z) = \frac{-ik\rho_0 c}{4\pi}\frac{2k_{0z}A_{inc}}{\rho_0\omega}\frac{e^{ikr}}{r}\iint_{S_0} e^{i(k_{0x}v + k_{0y}w)}e^{-i(k_x v + k_y w)}\,dv.dw$$

$$= \frac{-ik_{0z}A_{inc}}{2\pi}\frac{e^{ikr}}{r}\int_{-a/2}^{a/2} e^{ik_{0x}v}e^{-ik_x v}\,dv \int_{-b/2}^{b/2} e^{ik_{0y}w}e^{-ik_y w}\,dw$$

$$= \frac{-ik_{0z}A_{inc}}{2\pi}\frac{e^{ikr}}{r}\int_{-\infty}^{\infty}\left[\mathrm{rect}\left(\frac{v}{a}\right)e^{ik_{0x}v}\right]e^{-ik_x v}\,dv.\int_{-\infty}^{\infty}\left[\mathrm{rect}\left(\frac{w}{b}\right)e^{ik_{0y}w}\right]e^{-ik_y w}\,dw \quad (2\text{-}19)$$

Each integral in Eq.(2-19) has the form a Fourier-transformed rectangular pulse, with frequency shifts of $-k_{0x}$ and $-k_{0y}$ respectively, giving the product of sinc functions in Eq.(2-20), with the sinc definition $sinc(x) = \frac{\sin(x)}{x}$ for non-zero x, and $sinc(0) = 1$. This result is used to model the KA far-field response of a flat rectangular element of sea surface to an incident plane-wave.

$$p(x,y,z) = \frac{-ik_{0z}A_{inc}}{2\pi}\frac{e^{ikr}}{r}a\mathrm{sinc}\left[\frac{a}{2\pi}(k_x - k_{0x})\right].b\mathrm{sinc}\left[\frac{b}{2\pi}(k_y - k_{0y})\right] \quad (2\text{-}20)$$

Examples of the lobed two-dimensional response represented by Eq.(2-20) in the XZ plane are illustrated on Figure 2-2 at 5° and 50° incident grazing angles for 8 kHz and 16 kHz frequencies, and an element dimension, a, of 0.47 m, representing five wavelengths at 16 kHz. The bottom two plots illustrate that the primary angular lobed response narrows as the acoustic frequency increases, and also as the grazing angle increases. The top two plots illustrate that the secondary lobe responses have opposite then alternating phase relative to the primary lobe response.

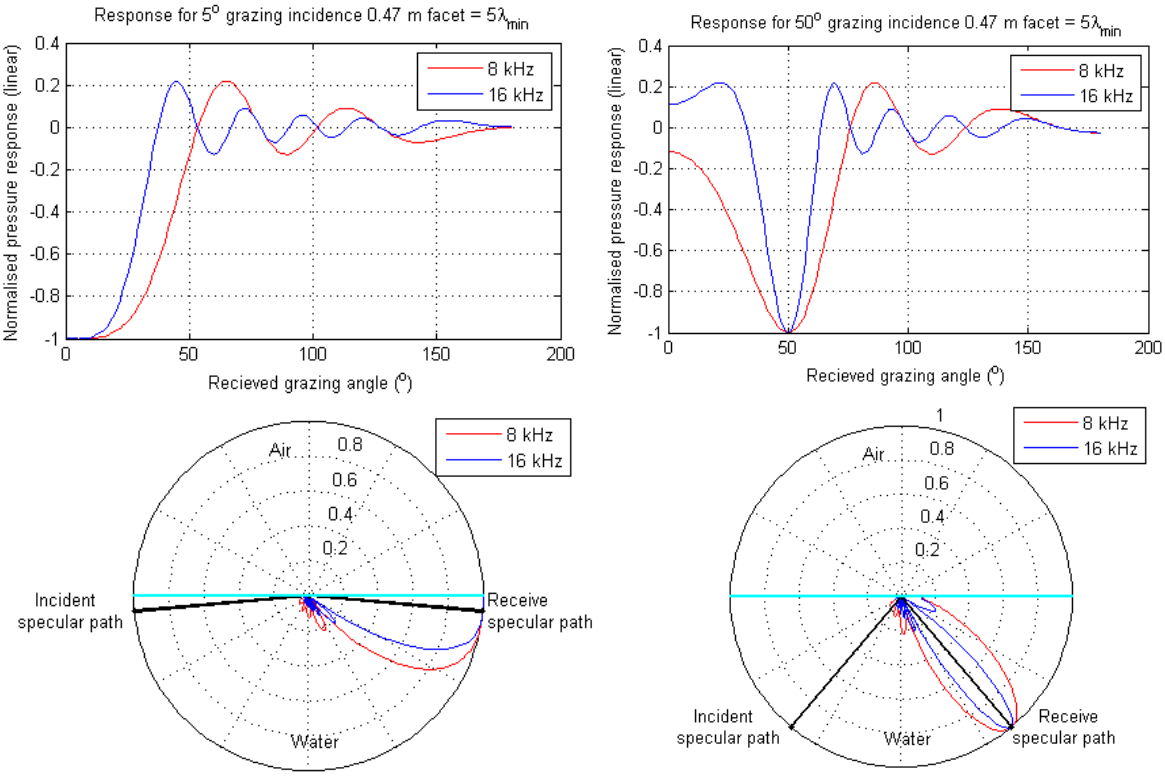

Figure 2-2: Phase response versus grazing angle (top), and angular amplitude response versus grazing angle (bottom) for KA response of a flat 0.47 m long element to a plane-wave at 5° grazing incidence (left plots) and 50° grazing incidence (right plots)

2.4.2 Element size effect on element response directivity

The angular spread of the calculated pressure response from each element depends on element size as per Eq.(2-20). In Figure 2-3 the angular response of an element to a plane-wave at 20° grazing incidence is presented for element lengths of $\lambda_{min}/4$ and $5\lambda_{min}$calculated by Eq.(2-20). As the length of discretised surface elements increases the directivity of the element response increases, or alternatively the angular spread of the primary response lobe narrows.

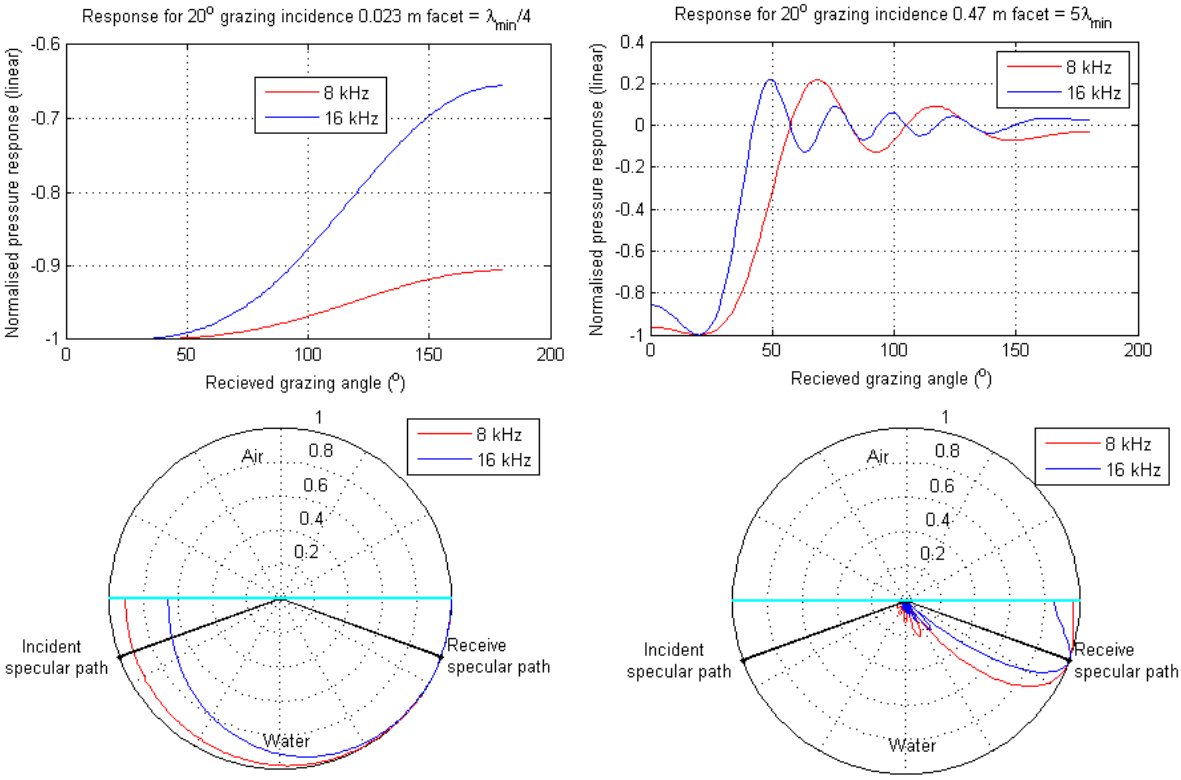

Figure 2-3: Phase response versus grazing angle (top), and angular amplitude response versus grazing angle (bottom) for KA response of a flat element to a plane-wave at 20° grazing incidence, for $\lambda_{\min}/4$ long element (left) and $5\lambda_{\min}$ long element (right)

2.4.3 Equation behaviour for element self-shadowing

For sufficiently rough surfaces, elements may be self-shadowed with respect to either the transmitter or the receiver in a bistatic geometry. Eq.(2-20) was developed to describe scattering from an element with positive incident and scattered grazing angles. For completeness the effect of self-shadowing on the behaviour of this equation is also described. Later in Section 5.4.2 this behaviour proves to be useful in modelling the dynamic response of significantly shadowed surfaces.

The inclusion of shadowed elements in a KA rough surface response is consistent with a strict application of Eq.(2-6) and the numerical implementation of the KA method reported by (Siderius and Porter 2008), which implicitly includes self-shadowed parts of the rough surface by allowing the surface pressure gradient to change sign depending on the incident field direction relative to the local surface normal.

When the incident field geometrically impinges on the back or air-side of the developed model of a KA a surface element, such as illustrated by the red element

in the top image on Figure 2-4, Eq.(2-20) calculates the radiation angular response as if the incident field was an out-of-phase image source. In the converse situation where the incident grazing angle is positive but the scattered field corresponds to the back or 'air' side of a surface element, such as in the bottom image on Figure 2-4, Eq.(2-20) calculates the response as if it were for an image receiver. Figure 2-5 illustrates the angular amplitude response behaviour of Eq.(2-20) for a KA element self-shadowed with respect to the source (left image) and self-shadowed with respect to the receiver (right image).

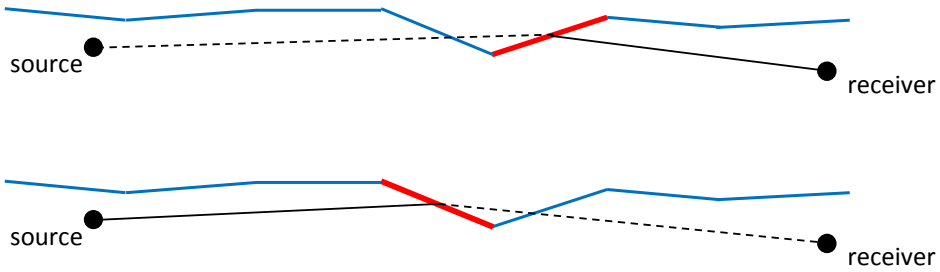

Figure 2-4: Illustration of element shadowing relative to transmitter (top) and relative to receiver (bottom)

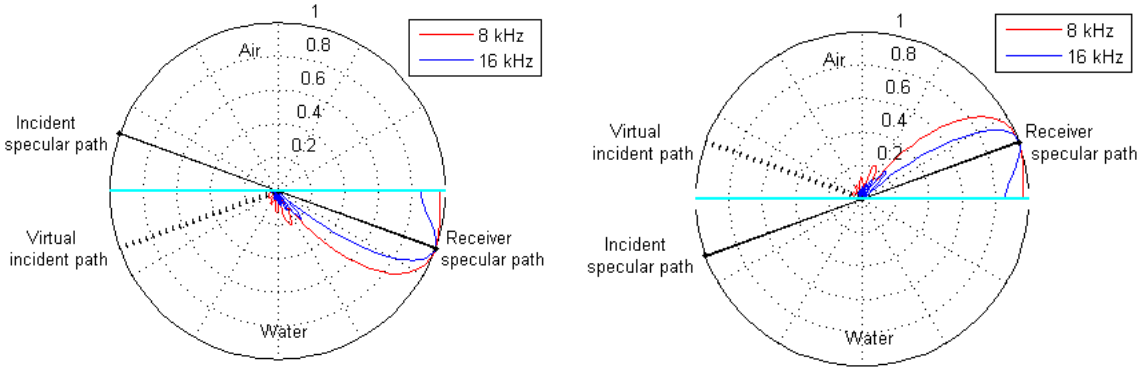

Figure 2-5: Modelled angular amplitude response for self-shadowed KA element with respect to transmitter (left image) and receiver (right image)

Equation (2-20) has the interesting property of producing net zero pressure at a receiver when two elements form an infinitesimal width peak or trough, as illustrated schematically on Figure 2-6, because the modelled radiation pattern from each element is identical but opposite in phase with respect to the receiver.

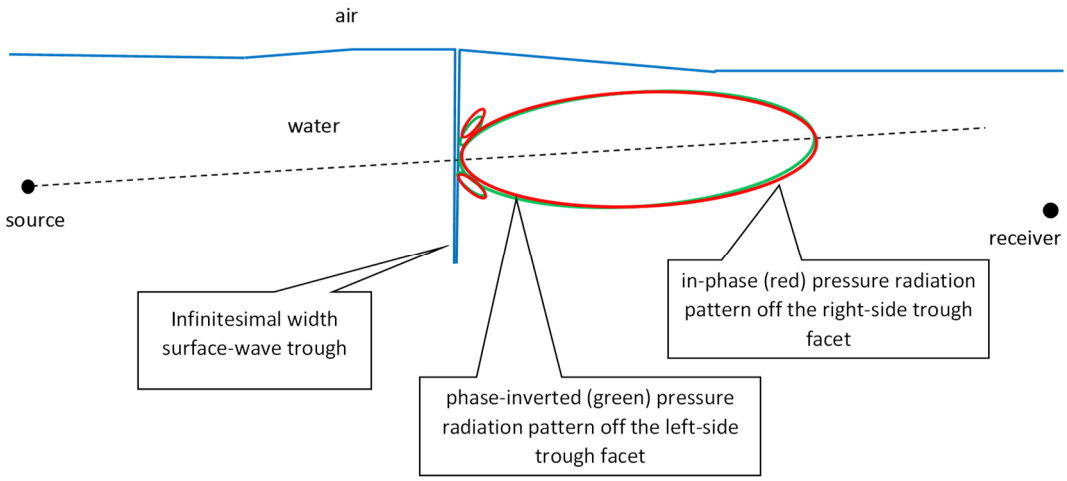

Figure 2-6: Schematic illustration of KA response illustrating response cancellation from a pair of elements forming an infinitesimal-width surface-wave peak or trough

At more realistic adjacent element angles, pairs of self-shadowed elements produce asymmetric radiation patterns, as shown schematically superimposed on Figure 2-7. It may be observed by considering the sum of the opposite phase angular distributions (green plus red lobe on Figure 2-7) that the net effect of self-shadowed elements produces increasingly uneven phase cancellation as the receiver (or source) grazing-angle increases.

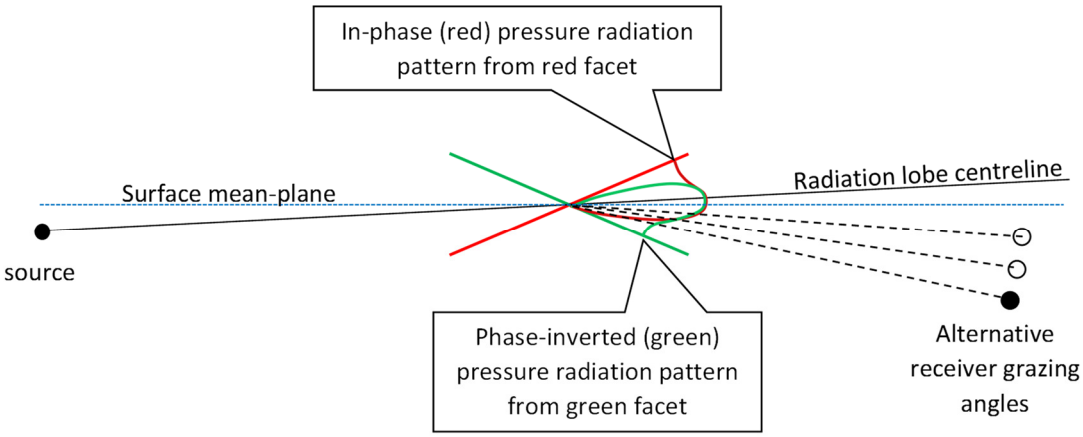

Figure 2-7: Schematic illustration of partial angular-response phase-cancellation from a pair of superimposed symmetrical self-shadowed KA elements

2.4.4 Aggregate coherent response of a rough patch

The step is now taken to use the single-element response of Eq.(2-20) which was developed for plane-wave incidence, to calculate the aggregate response of a rough surface comprised of many elements for a bistatic source and receiver geometry such as illustrated on Figure 2-8. This step assumes that the actual spherical

radiation from the source is a reasonable approximation to a plane-wave when it interacts with the surface. This approximation is consistent with the inexact nature of the discrete tangent plane implementation of KA, providing the element size is small compared to the radius from the transmitter, because the local curvature of each surface element is being approximated as flat in this KA implementation.

The local coordinate response of Eq.(2-20) oriented around the element axes must be transformed to global coordinates of a source and receiver, to enable the aggregate response of a discretised rough surface to be calculated. The spatial parameters used to relate the local element response to the global coordinate system are shown on Figure 2-8.

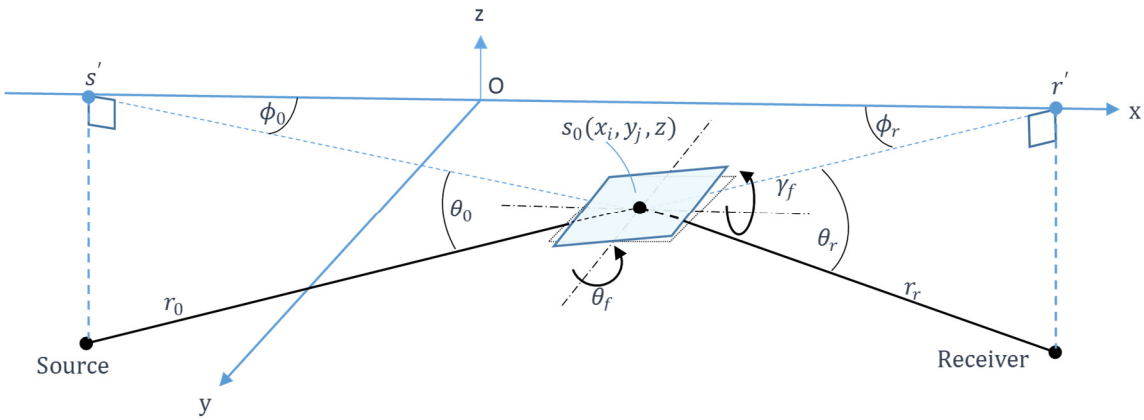

Figure 2-8: Local-to-global coordinate relationship for discrete planar surface element in a bistatic source-receiver geometry

It is now approximated that the incident plane-wave amplitude A_{inc} at each element is the result of a source producing a spherical wave of unit amplitude at unit distance, at slant radius r_0 as per Eq.(2-21).

$$A_{inc} = \frac{e^{ikr_0}}{r_0} \tag{2-21}$$

The resultant pressure at the receiver may now be expressed as a summation of individual element contributions as per Eq.(2-22), with element dimensions and wavenumber components related to the local coordinate system of each element as per Eq.(2-23).

$$\tilde{p}_r(\omega) = \frac{-i}{2\pi} \sum \frac{k'_{0z} e^{ik(r_0 + r_r)}}{r_0 r_r} a' \mathrm{sinc}\left[\frac{a'}{2\pi}(k'_{rx} - k'_{0x})\right] b' \mathrm{sinc}\left[\frac{b'}{2\pi}(k'_{ry} - k'_{0y})\right] \tag{2-22}$$

$$a' \cong a\ /\cos\theta_f$$

$$b' \cong b\ /\cos\gamma_f$$

$$k'_{0x} = k_0(\cos\phi_0 \cos\theta_0 \cos\theta_f - \sin\theta_f \sin\gamma_f \sin\phi_0 \cos\theta_0 + \sin\theta_f \cos\gamma_f \sin\theta_0)$$

$$k'_{0y} = k_0(\cos\gamma_f \sin\phi_0 \cos\theta_0 + \sin\gamma_f \sin\theta_0)$$

$$k'_{0z} = k_0(-\sin\theta_f \cos\phi_0 \cos\theta_0 - \cos\theta_f \sin\gamma_f \sin\phi_0 \cos\theta_0 + \cos\theta_f \cos\gamma_f \sin\theta_0)$$

$$k'_{rx} = k_0(\cos\theta_r \cos\phi_r \cos\theta_f + \cos\theta_r \sin\phi_r \sin\theta_f \sin\gamma_f - \sin\theta_r \sin\theta_f \cos\gamma_f)$$

$$k'_{ry} = k_0(-\cos\gamma_f \cos\theta_r \sin\phi_r - \sin\gamma_f \sin\theta_r) \qquad (2\text{-}23)$$

The final expressions in Eq.(2-22) and Eq.(2-23) for the reflected pressure accord with established expressions for the KA response from a rough surface (Ogilvy 1991, Ishimaru 1978).

2.5 Exact calculation of rough-surface response

An 'exact' two dimensional Helmholtz-Kirchhoff integral equation (IE) boundary element model as described by Thorsos (1988) and Siderius and Porter (2008) was implemented to provide a reference model calculation for the KA bistatic rough patch response $\widetilde{H}_{patch}(\omega)$ within the 8 kHz to 16 kHz simulation bandwidth of interest.

The implementation and nomenclature follows that described by Siderius and Porter (2008) as the required output of the bistatic response is the pressure at a point, rather than the rough surface scattering cross-section calculated by Thorsos (1988). The IE model was initially used to calculate the distributed pressure field from a point source at a single frequency for a flat surface to verify the calculation methodology. Subsequently the model was used to calculate the field at just a single point for multiple time-sequential surface realisations and at multiple frequencies.

The IE model is 'exact' on the proviso that the surface discretisation is fine-enough relative to the shortest signal wavelength of interest, in this case corresponding to an acoustic frequency of 16 kHz. It is noted however that when the IE model is used to model the bistatic response off a spatially limited patch of surface in order to achieve a manageable problem size the surface delay-response is cropped by the spatial limitation, and in this sense the bistatic response is not exact even if

calculated by the IE model. This is the case for the IE model bistatic model comparisons, but has been circumvented by running the Kirchhoff Approximate (KA) model for exactly the same constrained surface patch dimensions. In this way the verification of the KA method may be examined, even with the limited realism of the truncated bistatic simulation of a realistic rough ocean surface.

2.5.1 Integral equation (IE) boundary element model

The starting point of the IE method is the statement of Eq.(2-23) that the total pressure as a function of spatial position vector $p(\vec{r})$, is the sum of the direct incident field $p_{inc}(\vec{r})$, and the field scattered off the surface $p_{scat}(\vec{r})$. The term of interest in modelling the rough surface response is $p_{scat}(\vec{r})$.

The Helmholtz-Kirchhoff integral equation of Eq.(2-25) may be used to describe the time-harmonic scattered pressure response in a semi-infinite medium with a two-dimensional free surface boundary (often described as a 1D surface profile). $H_0^{(1)}$ is the first-order Hankel function of the first kind, $k = \omega/c$ is the acoustic wavenumber, and $\vec{r}'$ a position vector describing a point on the scattering surface. The term $\frac{\partial p(\vec{r})}{\partial n'}$ represents the total pressure field gradient normal to the scattering surface at the position of surface area element *ds'*. Vector quantities are illustrated on Figure 2-9.

$$p(\vec{r}) = p_{inc}(\vec{r}) + p_{scat}(\vec{r}) \tag{2-24}$$

$$p(\vec{r}) = p_{inc}(\vec{r}) - \frac{1}{4i}\int_s H_0^{(1)}(k|\vec{r} - \vec{r}'|)\frac{\partial p(\vec{r})}{\partial \hat{n}'}ds' \tag{2-25}$$

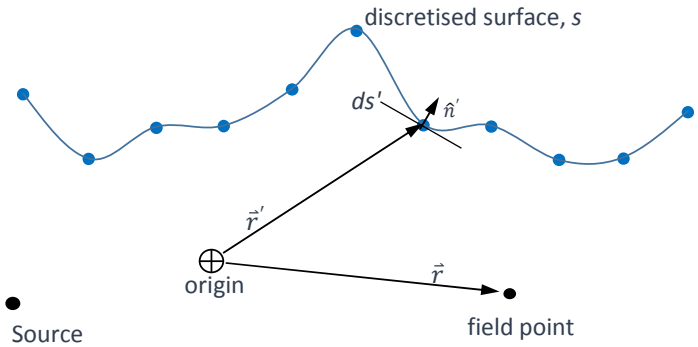

Figure 2-9: Vector notation for Helmholtz-Kirchhoff integral equation

Observing that the total pressure field at the free surface of the ocean must be zero leads to Eq.(2-26) applicable at the surface.

$$p_{inc}(\vec{r}) = \frac{1}{4i}\int_s H_0^{(1)}(k|\vec{r} - \vec{r}'|)\frac{\partial p(\vec{r})}{\partial \hat{n}'}ds' \tag{2-26}$$

The incident pressure a_m at each discrete point may then be equated to a summation of surface contributions from each of N surface points by Eq.(2-27) which represents the discretised form of Eq.(2-26).

$$a_m = \sum_{n=1}^{N} A_{mn}b_n\,, m = 1, \dots, N \tag{2-27}$$

The incident pressure a_m at the surface is known by Eq.(2-28). The unknown total pressure gradient $\frac{\partial p(\vec{r})}{\partial \hat{n}'}$ at each surface point is included in a term b_n defined by Eq.(2-29). The Hankel functions that relate the pressure contribution from every surface point to the incident pressure a_m are defined by Eq.(2-30) to avoid singularities by self-contribution for $m = n$ in the summation of contributions.

$$a_m = p_{inc}(\vec{r}_m) \tag{2-28}$$

$$b_n = \frac{\Delta x}{4i}\gamma_n \frac{\partial p(\vec{r})}{\partial \hat{n}'}\bigg|_{\vec{r}_n} \tag{2-29}$$

$$A_{mn} = \begin{cases} H_0^{(1)}(k|\vec{r}_m - \vec{r}'_n|), & m \neq n \\ H_0^{(1)}[(k\Delta x/2e)\gamma_n], & m = n \end{cases} \tag{2-30}$$

For a discrete surface height function $f(x')$, the tilted surface element length per unit horizontal distance γ_n is defined by Eq.(2-31) so that $ds' = \gamma_n \Delta x$ is the length of the surface element.

$$\gamma_n = \sqrt{1 + (f(x')/dx')^2} \tag{2-31}$$

All surface point pressure gradients may be expressed simultaneously by writing Eq.(2-27) in matrix notation of Eq.(2-32) then solved by Eq.(2-33) after matrix inversion of **A**.

$$\mathbf{a} = \mathbf{A}\mathbf{b} \tag{2-32}$$

$$\mathbf{b} = \mathbf{A}^{-1}\mathbf{a} \tag{2-33}$$

The scattered field at the receiver point $p_{scat}(\vec{r})$ can then be calculated for a single acoustic frequency by Eq.(2-34), noting that $p_{inc}(\vec{r}) = -p_{scat}(\vec{r})$ at the surface from Eq.(2-24). Considered in three dimensions Eq.(2-34) represents a cylindrical wave

solution to a line source oriented perpendicular to the page for each surface point on Figure 2-9.

$$p_{scat}(\vec{r}) = -\sum_{n=1}^{N} H_0^{(1)}(k|\vec{r}_m - \vec{r}'_n|)\, b_n \tag{2-34}$$

2.5.2 Conversion of 2D IE response to 3D for a corrugated surface

The Helmholtz-Kirchhoff integral equation cylindrical wave solution to a two-dimensional (2D) surface profile can be converted to an equivalent centre-line spherical wave response solution to an equivalent corrugated 3D surface as detailed by Siderius and Porter (2008). The equivalent 3D surface is simply the 2D profile extended infinitely in the third dimension transverse to the propagation path (perpendicular to the page for Figure 2-9).

First the similarities of the free-space field from a line source given by Eq.(2-35) and for a point source given by Eq.(2-36) are compared. By inspection the point source field may be obtained from the line source field after multiplication by the factor $\sqrt{k/i2\pi R}$.

$$p_{\text{line}}(R) = \frac{i}{4} H_0^{(1)}(kR) \cong \sqrt{\frac{i}{8\pi kR}}\, e^{ikR} \tag{2-35}$$

$$p_{\text{point}}(R) = \frac{e^{ikR}}{4\pi R} \tag{2-36}$$

Thus the field from a line-source may be converted to the equivalent field from a point source by Eq.(2-37) where R is the distance between the source and a receive point.

$$p_{\text{point}}(R) = \sqrt{\frac{k}{i2\pi R}}\, p_{\text{line}}(R) \tag{2-37}$$

To calculate the equivalent point-source response off a flat surface, the correction of Eq.(2-37) is applied with R set to the mean-plane specular path length, consistent with the method of images for a flat reflecting boundary. For a corrugated 3D surface equivalent to a 2D profile, the 3D surface is flat in the transverse direction and rough in the longitudinal direction. In this case the

correction of Eq.(2-37) needs to be applied utilising the unique total source-receiver path-length for each point on the 2D surface profile.

For the comparative IE versus KA bistatic calculations presented in Section 5.4 of this study the 2D rough surface IE response to the line-source was re-scaled to an equivalent 3D point source solution using the mean-plane specular path distance as per Eq.(2-38). This approximate correction becomes exact for a flat surface, but will slightly over-state the pressure response from portions of the rough surface with longer path-length by a factor equal to the square root of the exact to mean path-length ratio, $\sqrt{R_{exact}/R_{mean-path}}$. For an example relatively large bistatic delay variation of 2 ms (or 3 m) over a rough patch at 100 m range this factor is approximately 1.015, or 0.13 dB. For the same 2 ms delay variation over a rough patch at 500 m range the over-estimation factor reduces to 1.003, or 0.03 dB. It is thus concluded that use of the mean-plane bistatic path-length for the IE line-source to point-source correction as per Eq.(2-38) is reasonable. It should be noted that, but for the slight amplitude errors introduced by Eq.(2-38), the correct phase relationships from contributions across the rough surface are maintained by the use of the exact bistatic path lengths in the original 2D rough surface calculation.

$$p_{scat}(\vec{r})_{\text{point}} \cong \sqrt{\frac{k}{i2\pi R_{mean-path}}}\, p_{scat}(\vec{r})_{\text{line}} \tag{2-38}$$

By calculating Eq.(2-38) for discrete frequencies across the acoustic bandwidth of interest, the frequency dependent pressure response vector $\tilde{p}_{scat}(\omega)$ is formed, which can then be compared to the equivalent KA term $\tilde{p}_r(\omega)$ from Eq.(2-22) in Section 2.4.4 derived by the discrete tangent-plane implementation of the Kirchhoff Approximation.

2.6 Experimental channel probing methods

2.6.1 Calculation of experimental channel response estimate

The aim of channel probing (or channel sounding) is to uncover the time and delay dependencies of the real time-varying channel response $h(t,\tau)$, so that the transmission of various trial signals through the channel may be simulated by the convolution process of Eq.(2-4) reproduced as Eq.(2-39).

$$y(t) = \int_{-\infty}^{\infty} h(t,\tau)x(t-\tau)\,d\tau + n(t) \tag{2-39}$$

A channel is probed by the repeated physical transmission of a probe symbol x, representing a distinctive acoustic signal of finite length, and recorded as a distorted receive signal y.

In idealised impulse channel probing the symbol x is infinitesimally short in duration and infinitely high in amplitude with integrated area of one (i.e. a Dirac delta function δ_x), and repeated at interval $T_{probe} = 1/W_{probe} > L$, where L is the length of the channel response $h(t,\tau)$ and W_{probe} is the probe repeat frequency, the receive signal $y(t_i,\tau)$ resulting from the impulse δ_x at t_i is given by Eq.(2-40), where $n(t)$ is the unrelated noise at the receiver .

$$y(t_i,\tau) = \int_{-\infty}^{+\infty} [h(t_i,\tau)\,\delta_x(t-t_i)\,]\,d\tau \; + n(t_i+\tau) = \; h(t_i,\tau) + n(t_i+\tau) \tag{2-40}$$

For compactness in the following section the symbol '⊗' will be used to represent correlation and the asterisk symbol '∗' to represent convolution. The tilde '~' indicates analytic quantities and the raised asterisk '*' denotes the complex conjugate.

If the noise is negligible the receive signal $y(t_i,\tau)$ is then a copy of the channel response $h(t_i,\tau)$ for transmission instant t_i since the convolution of $\delta_x(t-t_i)$ with the channel response leaves the response unchanged apart from the time shift as per Eq.(2-41).

$$h(t_i,\tau) = \; h(t,\tau) * \delta_x(t-t_i) \tag{2-41}$$

For probing of shallow horizontal channels where discrimination of the probe signal from noise is important the transmit symbol x must be of finite length and amplitude using the process of correlative channel probing (or sounding) (Molisch 2011). The receive signal $y = h(t_i,\tau) * x$ is different to $h(t_i,\tau)$ and is also overlaid with noise. The channel response estimate $\hat{h}(t_i,\tau)$ resulting from the transmission commencing at instant t_i must then be recovered by cross-correlation of x and y.

To obtain the channel response estimate $\hat{h}(t_i,\tau)$, the transmit and receive symbols are cross-correlated by Eq.(2-42). Substituting $\tilde{y} = h(t_i,\tau) * \tilde{x} + \tilde{n}$ into Eq.(2-42) gives Eq.(2-43), since correlation is a linearly additive process.

$$\hat{h}(t_i,\tau) = \tilde{x} \otimes \tilde{y} \tag{2-42}$$

$$\hat{h}(t_i,\tau) = \tilde{x} \otimes [h(t_i,\tau) * \tilde{x}] + \tilde{x} \otimes \tilde{n} \tag{2-43}$$

The correlation-to-convolution identity $\tilde{f} \otimes \tilde{g} = \tilde{f}(-t)^* * \tilde{g}(t)$ (Burdic 1984a) is then used to rearrange Eq.(2-43) to Eq.(2-44). The associative and commutative properties of convolutions may be used to obtain Eq.(2-45) (Burdic 1984b).

$$\hat{h}(t_i,\tau) = \tilde{x}^*(-\tau) * [h(t_i,\tau) * \tilde{x}(\tau)] + \tilde{x} \otimes \tilde{n} \tag{2-44}$$

$$\hat{h}(t_i,\tau) = [\tilde{x}^*(-\tau) * \tilde{x}(\tau)] * h(t_i,\tau) + \tilde{x} \otimes \tilde{n} \tag{2-45}$$

After applying the reverse correlation-to-convolution identity, the first term of Eq.(2-45) in square brackets is the autocorrelation of the transmit symbol x, denoted $R_{xx}(\tau)$, giving Eq.(2-46).

$$\hat{h}(t_i,\tau) = R_{xx}(\tau) * h(t_i,\tau) + \tilde{x} \otimes \tilde{n} \tag{2-46}$$

If x is chosen such that it has a very high autocorrelation at zero lag, and very low correlation at all non-zero lags, then $R_{xx}(\tau)$ behaves as a noisy band-limited approximation to the delta-function $\delta_x(t - t_i)$, and Eq.(2-46) bears a noisy similarity to Eq.(2-41). In this manner the delay resolution of the response estimate can be much shorter than the symbol duration. Importantly, x can be chosen such that the result of cross-correlation with the unrelated noise is low.

If the symbol x correlation with the non-signal noise is negligible, there is still noise in $\hat{h}(t_i,\tau)$ from non-zero $R_{xx}(\tau)$ for $\tau \neq 0$, which behave like small random Dirac delta functions. Another estimate of $h(t_i,\tau)$ could be deconvolved from $R_{xx}(\tau) * h(t_i,\tau)$ however this process generates additional noise (Molisch 2011).

With negligible symbol-noise correlation, the decibel separation ΔN between the true response power and the noise within the estimate $\hat{h}(t_i,\tau)$ is determined by the ratio of the zero-lag autocorrelation peak to the maximum non-zero autocorrelation (Eq.(2-47)), or the "peak to off-peak ratio" (Molisch 2011).

$$\Delta N = 20.\log\left[\frac{R_{xx}(0)}{\max\limits_{\tau \neq 0}[R_{xx}(\tau)]}\right] \tag{2-47}$$

The noise separation ΔN increases with longer symbol repeat period T_{probe}, but with corresponding loss of information in the real time dimension (t) due to the associated lower probe rate W_{probe}.

An implicit assumption in the derivation of Eq.(2-46) is that $h(t_i,\tau) \cong h(t_i + T_{probe},\tau)$ (Molisch 2011). That is, the channel response has not changed appreciably over the transmission time T_{probe} of the symbol x. This assumption breaks down for long enough symbols.

2.6.2 Probe symbol length and over-spread channels

Ideally, a repeated probe symbol x would enable the structure of the time-varying channel response $h(t,\tau)$ to be simultaneously explored at arbitrarily fine resolution in time and delay dimension.

However, a symbol repeated at frequency $W_{probe} = 1/T_{probe}$, chosen to ensure the transmit-receive correlation delay window length T_{probe} is larger than the channel delay-spread L_{chan}, automatically limits (by the Nyquist sampling theorem) the detectable channel frequency shifts to $\pm W_{probe}/2$. Any actual time-varying effects within the channel response at higher frequencies become aliased in the channel frequency response $\mathcal{F}\{\hat{h}(t,\tau)\}$ along the time dimension. Thus, to extract fine time-domain response detail from a probe there is motivation to select a high symbol rate W_{probe}.

Conversely if the symbol repeat frequency W_{probe} is chosen to exceed the (two-sided spectrum) channel response bandwidth B_{chan}, the repeat interval T_{probe} may inadvertently be shorter than the channel delay-spread L_{chan}, resulting in delay aliasing of the response within $\hat{h}(t,\tau)$.

When the condition exists that $T_{probe} < L_{chan}$ leading to time-aliasing of the probe response the channel is described as over-spread in delay, and if $W_{probe} < B_{chan}$ leading to frequency aliasing of the probe response the channel is described as over-spread in Doppler, and doubly spread if both conditions exist (Baggeroer 2012).

If the significant channel response bandwidth-delay-spread product is greater than one (i.e. $B_{chan}L_{chan} > 1$) then it is not possible for a probe symbol x to simultaneously reveal the full channel delay and Doppler spread (without aliasing in Doppler or delay) since for the probe the product $W_{probe}T_{probe} = {T_{probe}}^{-1}T_{probe} = 1$ by definition.

In practice, the channel Doppler and delay spreads are not known a priori and consequently two or more probes with significantly different repeat intervals T_{probe} are used in quick succession to ensure that the full extent channel delay and Doppler spreads may be determined (van Walree 2011).

2.6.3 Probe symbol ambiguity function

The ambiguity function $\chi(\mathrm{v},\tau)$ of the complex baseband probe symbol $\tilde{x}$ is a two-dimensional autocorrelation function in the dimensions of velocity shift v and delay shift τ defined by Eq.(2-48) (Collins and Atkins 1998) where f_o is the centre frequency of the signal, ν is the base-band frequency shift and c is the speed of sound in water.

$$\chi(\mathrm{v},\tau) = \int_{-\infty}^{+\infty} \tilde{x}(t)\tilde{x}^*(t+\tau)e^{i2\pi c(\nu/f_o)t}\,dt \qquad (2\text{-}48)$$

The ambiguity function of a pseudo random binary sequence (PRBS) (Figure 2-10) has the property that the correlation maximum delay is not distorted if the received signal is Doppler shifted (Collins and Atkins 1998).

In contrast, the ambiguity function of a linear frequency modulated sweep (LFM) with the same bandwidth (Figure 2-11) produces an apparent (i.e. false) shift in delay when the symbol is Doppler-shifted during transmission. The LFM is useful for extracting the delay response of a channel by cross-correlation due to the lower off-peak ambiguity noise, providing the potential delay error is acceptable.

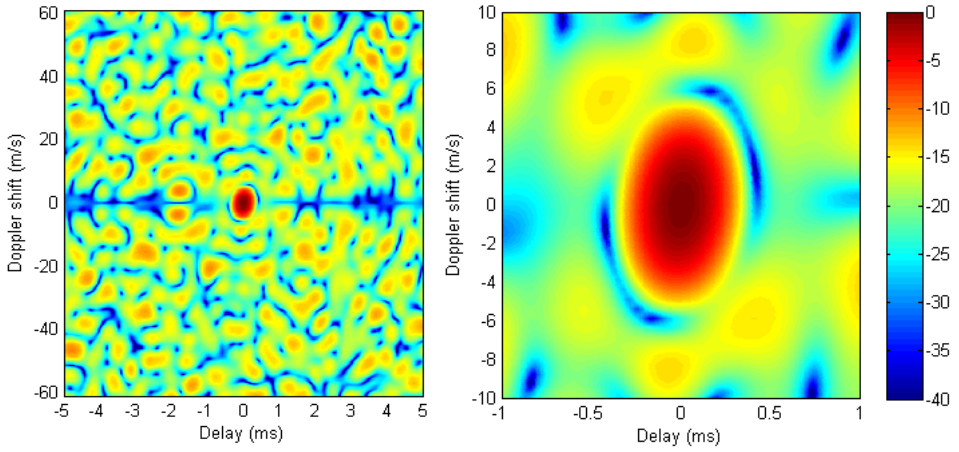

Figure 2-10: Ambiguity function surface $|\chi(\nu,\tau)|^2$ (dB) of measured experimental PRBS probe @1m, 21ms 63 bit, 3kHz bit-rate modulation of 12kHz carrier – (left) large Doppler scale, (right) magnified axes

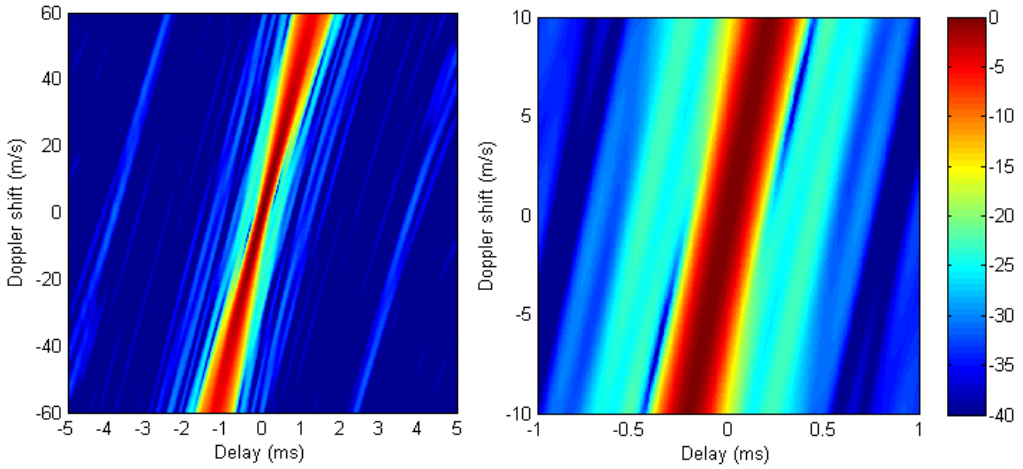

Figure 2-11: Ambiguity function surface $|\chi(\nu,\tau)|^2$ (dB) of measured experimental LFM probe @1m, 16ms 8-16kHz LFM – (left) large Doppler scale, (right) magnified axes

The ambiguity function has much the same sense in channel probing as in active radar and sonar studies, where uncertainty in the velocity and range of the target are of interest. In channel probing the full channel multi-path response is effectively the 'target'.

2.6.4 Probe symbol delay and Doppler resolution

The probe delay resolution (δ_τ) and time Doppler velocity resolution (δ_v) are defined by the -3dB contour of the probe ambiguity function relative to the delay and Doppler axes respectively (Collins and Atkins 1998), expressed by Eq.(2-49) and Eq.(2-50) respectively, where B is the probe symbol bandwidth and T is the probe symbol duration.

$$\delta_\tau = \frac{1}{B} \tag{2-49}$$

$$\delta_\mathrm{v} = \frac{1}{T}.\frac{c}{f_o} \tag{2-50}$$

The cross-correlation delay resolution δ_τ of a probe signal is important for interpretation of the experimental channel response history $\hat{h}(t,\tau)$ because it establishes the minimum delay between closely delay-spaced multi-path responses that will be resolvable.

For a spread-spectrum PRBS probe symbol, such as the bottom image Figure 2-12, the probe bandwidth, and therefore the delay resolution δ_τ is determined by the chipping interval t_{chip} of the binary sequence shown on the top image Figure 2-12 as per Eq.(2-51) (Colin and Beerens 2011). For a linear frequency sweep δ_τ is the inverse of the sweep frequency range ($f_{max} - f_{min}$) as per Eq.(2-52).

$$\delta_{\tau(\mathrm{PRBS})} = \frac{\mathrm{t}_{chip}}{2} \tag{2-51}$$

$$\delta_{\tau(\mathrm{LFM})} = \frac{1}{(f_{max} - f_{min})} \tag{2-52}$$

The Doppler resolution δ_{v} of a probe signal determines whether the expected scale of Doppler will be detectable by time-domain Doppler search (Section 2.6.6), in which case T is the length of the probe symbol, or detectable within the resolution of frequency-domain Doppler spectrum (Section 2.6.8), in which case T the duration of the channel response.

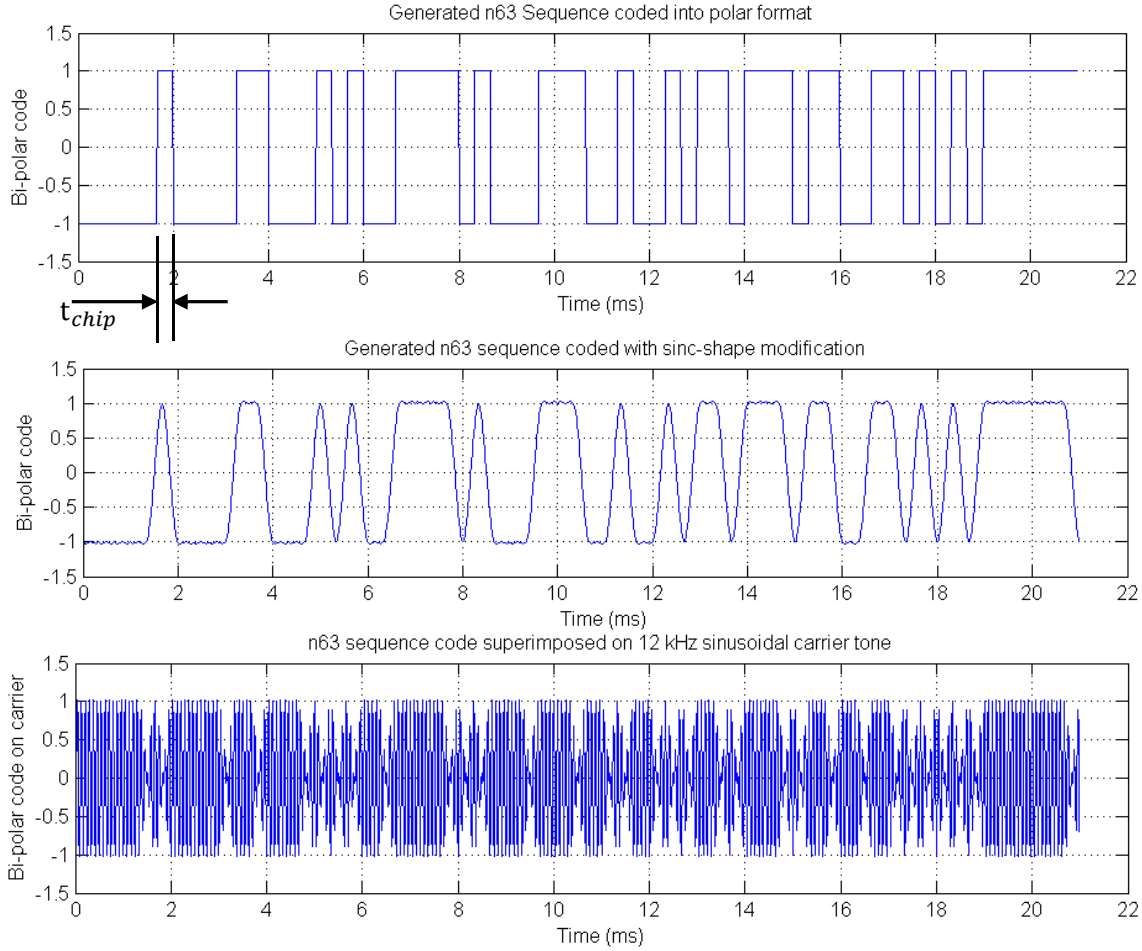

Figure 2-12: Illustrative derivation of a spread 21 ms PRBS probe signal by phase modulation of a 12 kHz sinusoidal carrier by a 63 bit PRBS sequence

2.6.5 Time-varying channel response presentation

The most readily observable time-varying channel properties of interest for this study are the channel response dependence on time (t) and delay (τ), which may be observed by two-dimensional plots of $\hat{h}(t,\tau)$, most conveniently displayed as the decibel response power $10log_{10}\left|\hat{h}(t,\tau)\right|^2$ such as in Figure 2-13.

The example measured channel response in Figure 2-13 has been formed from 1500 successive channel response estimates $\hat{h}_i(t_i,\tau)$ calculated at discrete time intervals by Eq.(2-46), then normalised by the average response power over the 30 s response history. For convenience the delay axis has been shifted ~330 ms relative to the first-arriving direct transmission path, to avoid plotting the first ~330 ms of blank delay response that represents the minimum flight-time from source to receiver via the direct path.

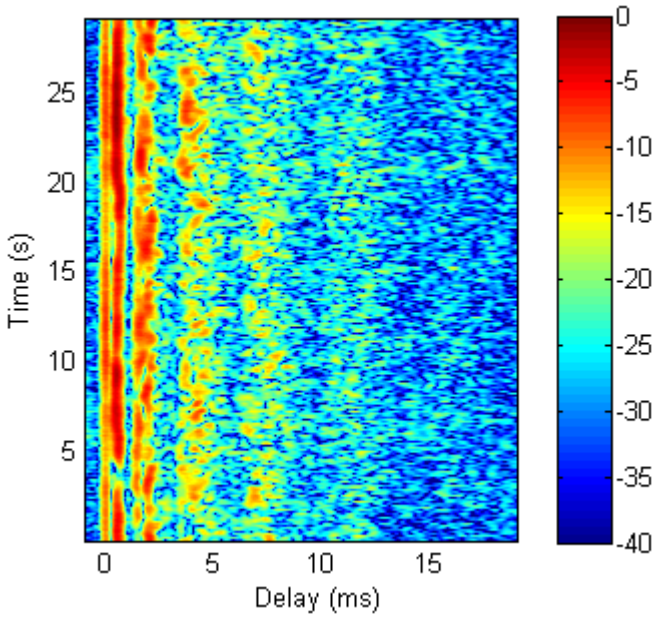

Figure 2-13: Example normalised measured channel response history$10log_{10}|\hat{h}(t,\tau)|^2$(dB)– 500 m range, 13.5 m channel depth, low sea-state

Increasingly rapid response fluctuations in the time dimension can be noted at increasing delay relative to the first signal arrival band. The increasing fragmentation of $\hat{h}(t,\tau)$ with delay may also be observed.

The less obvious time-varying property of the channel response $\hat{h}(t,\tau)$ is the instantaneous Doppler frequency shift (v) imparted to the signal by the time-varying elongation/compression of the transmission micro-paths that comprise the full channel response. This effect causes modulation of the response phase in both time and delay but is not fully apparent on Figure 2-13 because the response is plotted as a power quantity.

If the same data is plotted on a linear scale the underlying phase information may be noted, but with limited insights into the response dynamic range. The left image of Figure 2-14 represents the same data from Figure 2-13 but plotted with linear scale. The response phase oscillations in time are clearly visible, with

effects of 'bunching' and 'stretching' of phases due to both drift and cyclic swell effects on the relative transmitter-receiver ranges evident particularly in the earlier path arrivals. The right image of Figure 2-14 has been post-processed to exclude as far as practical the Doppler shifts due to motion of the transmitter. It can be observed by the slow phase-modulation of the first arrival that represents the direct and bottom-reflected path that the Doppler compensation is imperfect. Both the left and right images of Figure 2-14 would be indistinguishable if the data had been plotted as a decibel power such as in Figure 2-13.

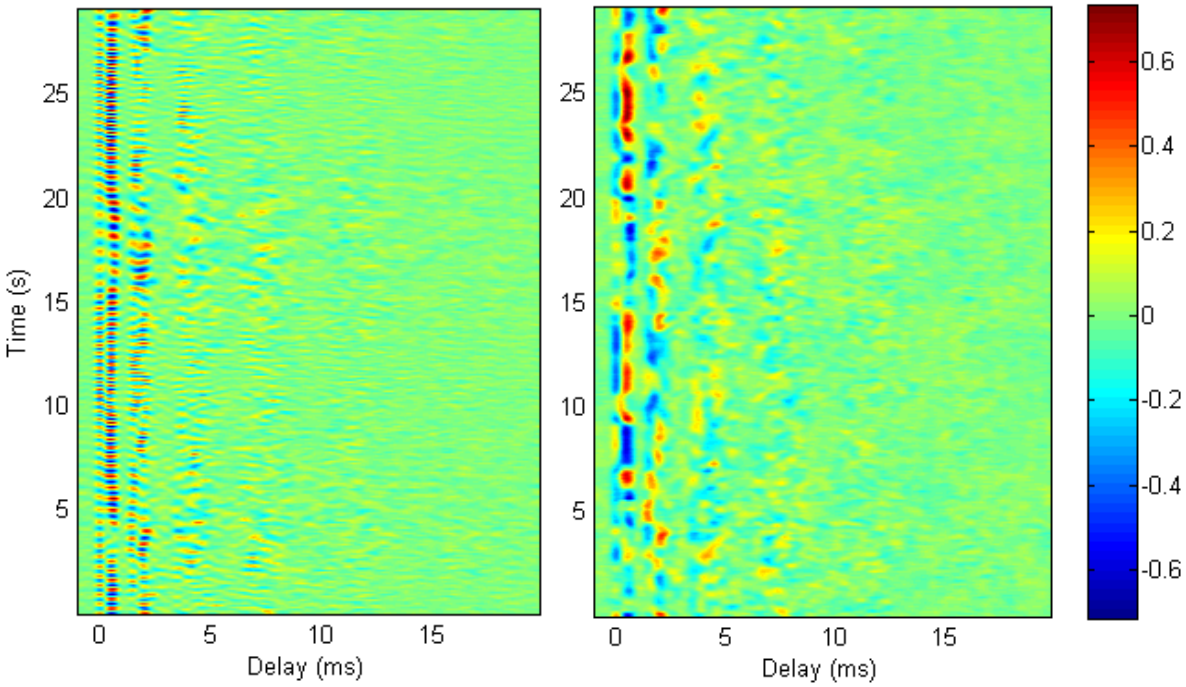

Figure 2-14: Example normalised measured channel response history $\hat{h}(t,\tau)$(linear)– 500 m range, 13.5 m channel depth, low sea-state, (left) including 17 cm/s average on-axis drift, and (right) with relative on-axis drift approximately excluded by post-processing

The time-varying Doppler evident in Figure 2-14 may be inspected by Doppler search using correlative matched-filtering on successive received probe-signal blocks (Section 2.6.6), or alternatively by inspection of the Doppler spectrum obtained by frequency analysis of $\hat{h}(t,\tau)$ along the time dimension (Section 2.6.7).

2.6.6 Time-domain channel Doppler response

The example experimental response versus time and Doppler velocity plot $\hat{h}(t,\mathrm{v})$ presented on the right-hand side of Figure 2-15 is generated from block-by-block Doppler search on the first arrival of the delay response history $\hat{h}(t,\tau)$ presented for context on the left-hand side of Figure 2-15.

The $\hat{h}(t,\mathrm{v})$ presentation of time-varying channel response is uncommon in underwater channel sounding but is included here for completeness, representing an early aspect of the experimental channel response analysis that provided important insight into the origin and magnitude of Doppler created by transmitter drift and oscillatory movement induced by swell.

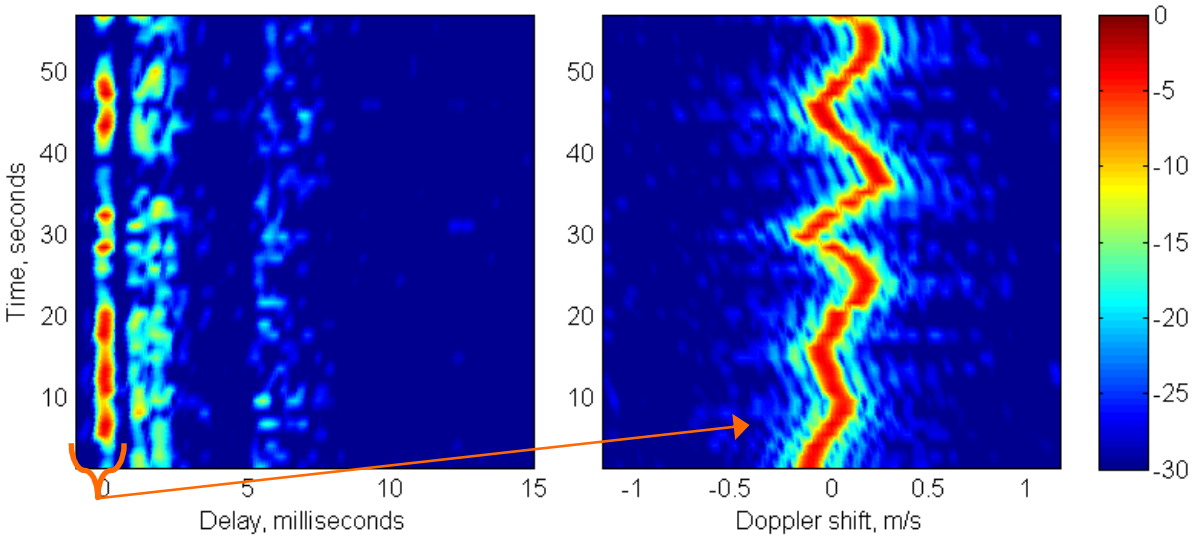

Figure 2-15: (left) Experimental channel response versus time and delay, $20\log\left|\hat{h}(t,\tau)\right|$(dB), and (right) Channel response versus time and Doppler velocity, $20\log\left|\hat{h}(t,\mathrm{v})\right|$ (dB) – calculated from 43 repeats of 1.365 s PRBS probe symbol

The first step in the Doppler search process is to create an array of Doppler-shifted replicas of the repeated probe symbol x. A vector of Doppler-shifted resampling rates F is calculated centred on the transmit signal sample rate F_s, using a vector of positive and negative Doppler velocities v according to Eq.(2-53). The resampling rates F define a corresponding array of Doppler perturbed discrete-time vectors $[t]$ by Eq.(2-54). An array of time vectors is used in Eq.(2-55) to resample the Hilbert-transformed probe symbol $\tilde{x}$, generating an array of Doppler-shifted analytic transmit symbols $[\tilde{x}]$ which are shifted to base-band frequency in Eq.(2-56) using the signal centre-frequency f_o.

$$F = F_s/\left(1 - \frac{\mathrm{v}}{c}\right) \tag{2-53}$$

$$[t] = \frac{t}{F} \tag{2-54}$$

$$[\tilde{x}] = \text{resample}\{\tilde{x}, [t]\} \tag{2-55}$$

$$[\tilde{x}]_{base} = [\tilde{x}].e^{-i2\pi f_o t} \tag{2-56}$$

The circular cross-correlation is formed between each successive base-band receive signal block $\tilde{y}_{base}$ and the probe symbol replicas $[\tilde{x}]_{base}$ to form the correlation matrix $[R]$ by Eq.(2-57).

$$[R] = \mathcal{F}^{-1}[\{\mathcal{F}([\tilde{x}]_{base})\}^{*}.\mathcal{F}(\tilde{y}_{base})] \tag{2-57}$$

The matrix $[R]$ represents the channel Doppler-delay ambiguity function, varying with Doppler on the first dimension, and with delay-shift on the second dimension. An example plot of matrix $[R]$ is presented in Figure 2-16, capturing a 21 ms long 'instant' during which a surface reflected response at around 1.7 ms arrival delay and 1 m/s equivalent path Doppler exceeds the strength of the direct path response at 0 ms.

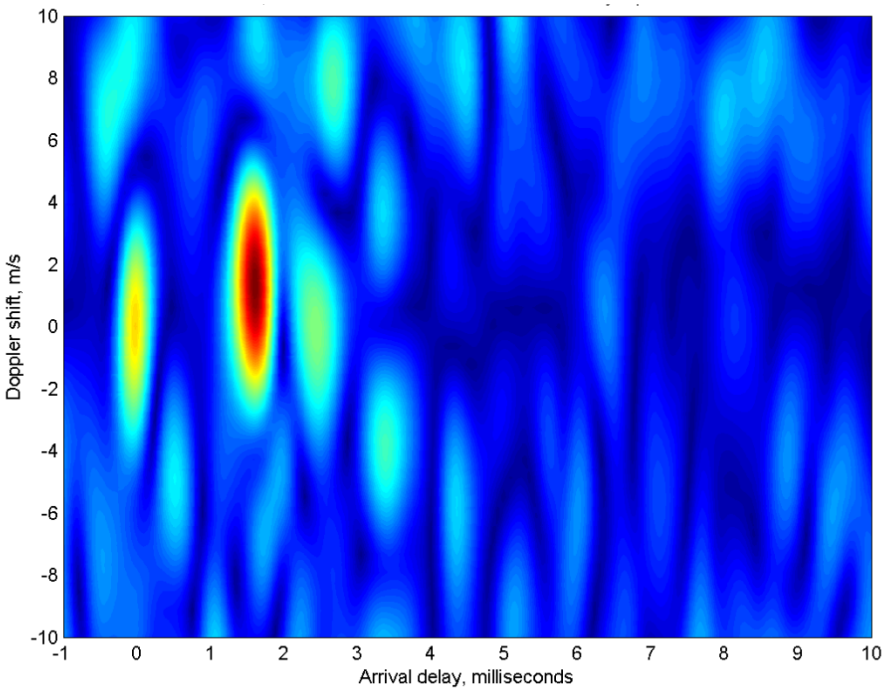

Figure 2-16: Example Doppler-delay ambiguity function surface, 20log|[R]| – block 1400 of 21 ms repeated PRBS probe at 113 m transmission range

The Doppler response estimate at each successive time interval t_i is then obtained by searching for the maximum of $[R]$at every Doppler within the chosen delay-range $[\tau_1, \tau_2]$ as per Eq.(2-58).

$$\hat{h}(t_i, \mathrm{v}) = \left[\max_{\tau_1 \le \tau \le \tau_2} [R]\right]^{T} \tag{2-58}$$

For the example $\hat{h}(t, \mathrm{v})$ shown on the right-hand side of Figure 2-15 the maximum of $[R]$ was sought on delay indexes corresponding to the delay interval [-0.5 ms,0.5 ms] corresponding to the combination of the direct and bottom-

reflected paths. The process is repeated for successive time intervals, with the time increment determined by the length of the repeated probe signal block x.

The time-domain Doppler search enables some cyclic response dynamics to be recognised, however the time-domain Doppler velocity resolution δ_v is generally poor due to the relative short length of a probe symbol. In the example of Figure 2-15 the cyclic nature of the Doppler at approximately 15s period is generated by shallow-water swell motion coupling to the drifting transmitter.

2.6.7 Time-domain channel delay response

The experimental channel response versus time and delay $\hat{h}(t,\tau)$ is calculated by circular cross-correlation using Eq.(2-59). This is simpler than the Doppler search method of Eq.(2-57) as only the unperturbed (i.e. zero-Doppler shifted) Hilbert-transformed base-band transmit signal block $\tilde{x}_{base}$ is required for the circular correlation response. Successive $\hat{h}(t_i,\tau)$ form the time-varying response history $\hat{h}(t,\tau)$.

$$\hat{h}(t_i,\tau) = R = \mathcal{F}^{-1}[\{\mathcal{F}(\tilde{x}_{base})\}^*.\mathcal{F}(\tilde{y}_{base})] \tag{2-59}$$

If the relative positions of the transmitter and receiver are fixed, and the sample rate of the transmitter and receiver devices are identical, then Eq.(2-59) will produce a response history with vertical alignment having the appearance of the right-hand plot of Figure 2-15 representing constant relative delay of the gross path structure. However, if there is a combination of drift and cyclical relative motion of the transmitter and receiver, then Eq.(2-59) will produce a response where the delay of the first arrival is increasing (or decreasing) with time such as is illustrated by the left-hand plot of Figure 2-17. Where the focus on the channel response is the dynamic effect of the ocean surface, this delay drift precludes further meaningful frequency-domain analysis along the time dimension. The centre image of Figure 2-17 represents the case where there is cyclical relative motion of transmitter and receiver but no drift.

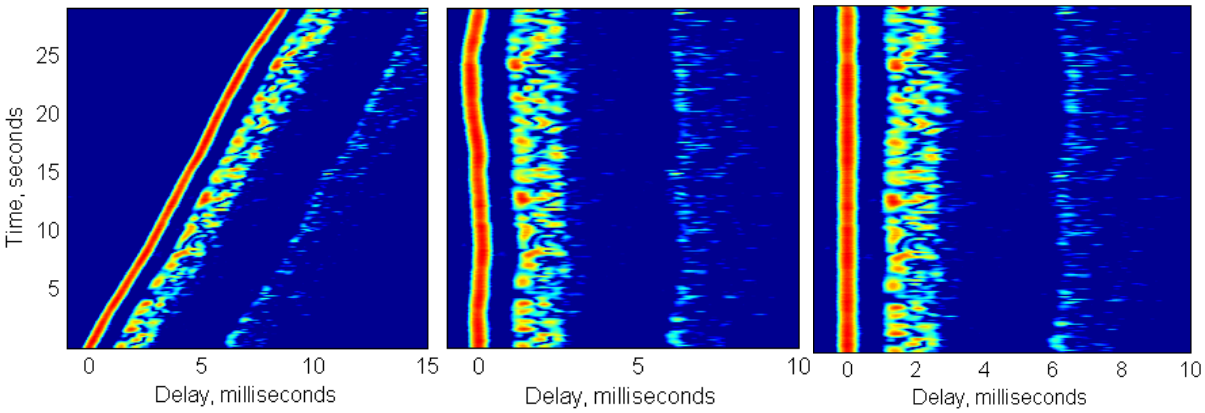

Figure 2-17: Measured channel response, $20\log|\hat{h}(t,\tau)|$, using 21 ms PRBS probe at 110 m range showing (left) received response inclusive of irregular transmitter drift, (centre) response after resampling to compensate average drift, and (right) with additional alignment on direct-path arrival to compensate cyclical relative transmitter-receiver motion

To enable further analysis of dynamic characteristics of the channel that are attributable exclusively to the sea-surface it is necessary to exclude the effects of transmitter-receiver relative movement. This is not possible in an exact sense with an omni-directional source and receiver because the transmitter motion resolves differently into the continuum of signal launch angles. Despite this the dominant Doppler contribution of transmitter motion along the direct transmitter-receiver direction can be approximately and usefully compensated for the whole channel by using Eq.(2-60) to define the Doppler-distorted transmit-time vector $t_{Doppler}$, which is then used with (2-55) to resample the transmit signal prior to the correlation process of Eq.(2-59), where $\vec{v}(t)$ is the time varying transmitter velocity vector, and $\hat{p}$ is the unit vector in the direct path direction.

$$\boldsymbol{t}_{Doppler} = \int (1 + \vec{v}(t).\hat{p}/c)dt \qquad (2\text{-}60)$$

For response contributions associated with surface-interacting path angles that differ from the direct path direction $\hat{p}$, Eq.(2-60) has the effect of over-compensating for the relative transmit/receive motion, which results in a time-varying Doppler error $v(t)_{error} \approx \vec{v}(t)(1 - cos\theta_{grazing})$ on these paths. For paths with grazing angle less than 60° this approximate compensation does not increase the total Doppler from surface effects and relative motion effects, but does mean that there is some retained coherence in response between paths that has its origins in the relative transmitter/receiver movement. For drifting velocities associated with channel probing experiments the Doppler error $v(t)_{error}$

introduced by approximate motion compensation typically remains small relative to Doppler from surface interactions, which increase more rapidly with grazing angle than $\mathrm{v}(t)_{error}$ does.

Further quantification and analysis of the relative significance of surface-related and transmitter-motion Doppler contributions are presented in Section 4.3.3, illustrating graphically the relative constancy of Doppler from transmitter motion across relevant paths for a low amplitude experimental surface.

The centre image of Figure 2-17 was generated from a transmit signal that was Doppler compensated using the average drift velocity in Eq(2-60) only. The right image of Figure 2-17 is a modified version of the centre-image, with resampling to compensate for both drift and cyclic motion on the direct path.

A further source of apparent delay drift that can occur for a fixed transmitter/receiver probe arrangement is sampling-rate offsets of transmitter and receiver instrumentation that have nominally identical sample rates. This type of discrepancy is compensated by transmit signal resampling in the same manner as for a steady drift in range (van Walree 2011).

2.6.8 Frequency-domain Doppler from spreading function

The Doppler on a channel transmission path may be expressed either as a path velocity shift $\Delta\mathrm{v}$ or as an equivalent base-band signal Doppler frequency ν as linked by Eq.(2-61), where positive v represents a velocity that contracts the propagation path length, c is the speed of sound in water, and f_0 is the signal centre-frequency.

$$\nu/f_0 = \mathrm{v}/c \tag{2-61}$$

A useful simultaneous representation of the arrival delay spreading and the Doppler spreading of the underwater acoustic channel response is the two-dimensional spreading function, as described in van Walree, Jenserud, and Smedsrud (2008). A spreading function over the delay-Doppler-frequency plane is obtained by discrete Fourier transform of a Hilbert-transformed response history $\tilde{h}(t,\tau)$ with respect to the real-time (t) dimension as per Eq.(2-62). The Hilbert-transform of the response is necessary to correctly detect the diversity of positive and negative frequency shifts in the response history.

$$\tilde{S}(\nu,\tau) = \mathcal{F}\left(\tilde{h}(t,\tau)\right) = \int_{-\infty}^{+\infty} \tilde{h}(t,\tau)e^{-i2\pi\nu t}\,dt \qquad (2\text{-}62)$$

Implementing Eq.(2-62) as a discrete Fourier transform requires that the response history is first windowed in the time dimension. This is achieved by using half a Hanning window for the first and last 10% of the history in the time direction.

For the spreading function to produce results that are indicative of channel Doppler and delay spreading attributable to the sea surface, it is necessary that Doppler and delay spreading associated with relative transmitter-receiver motion has first been removed. Illustrative examples of the influence of transmitter motion on the experimental spreading functions are presented in Section 4.3.2. An example spreading function corresponding to the right-hand frame of Figure 2-17 is presented in Figure 2-18.

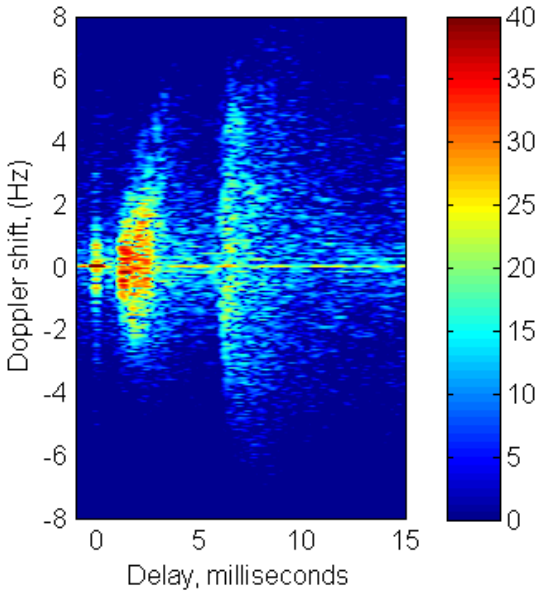

Figure 2-18: Example measured channel spreading function $20\log\left|\hat{S}(\nu,\tau)\right|$ (dB), for 21 ms spread-spectrum PRBS probe, with approximate transmit-signal resampling to negate transmitter drift Doppler, f_0 = 12 kHz, 110 m range

The total channel delay power profile $P(\tau)$ may be obtained by summation of the spreading function over all M Doppler frequency shifts (Eq.(2-63)).

$$P(\tau) = \sum_{m=1}^{M-1} \left|\tilde{S}(\nu_m,\tau)\right|^2 \qquad (2\text{-}63)$$

Similarly, the total channel response Doppler power spectrum $P(\nu)$ may be obtained by summation of the spreading function over all N delays by Eq.(2-64).

A useful variant is to limit the summation to specific delay ranges to allow closer inspection of the Doppler power spectrum associated with specific groups of multi-path channel arrivals.

$$P(\nu) = \sum_{n=1}^{N-1} \left|\tilde{S}(\nu, \tau_n)\right|^2 \tag{2-64}$$

2.6.9 Channel coherence

The coherence of the channel response is not constant across the spread of response arrivals in delay. Thus it is of interest to calculate the normalised coherence $C(\Delta t)$ within a specific delay range $[\tau_1, \tau_2]$ that may encompass a specific path response (or group path response) of interest.

The normalised coherence $C(\Delta t, \tau_1, \tau_2)$ of a channel response $h(t, \tau)$ in the response delay interval $[\tau_1, \tau_2]$ have been calculated by Eq.(2-65) (Huang, Yang, and Huang 2013).

$$C(\Delta t, \tau_1, \tau_2) = \frac{\langle \left[\tilde{h}(t, \tau)^* \tilde{h}(t + \Delta t, \tau)\right]_{\tau_2}^{\tau_1} \rangle}{\sqrt{\langle \left[\left|\tilde{h}(t, \tau)\right|^2\right]_{\tau_2}^{\tau_1} \rangle \langle \left[\left|\tilde{h}(t + \Delta t, \tau)\right|^2\right]_{\tau_2}^{\tau_1} \rangle}} \tag{2-65}$$

3 LITERATURE REVIEW

3.1 Introduction

This literature review is focused on simulation and measurement of underwater acoustic channel transmission responses in relatively shallow waters, typically 100 m or less, at mid-frequencies, nominally between 5 kHz and 30 kHz, over ranges between 100 m and 10 km. The frequency band is influenced by the conflicting needs of maximising signal bandwidth for data throughput, and limiting the effect of increasing signal absorption losses as frequency increases in ocean water (Stojanovic and Preisig 2009). The frequency band is also influenced by industry experience in the optimal combination of transmission range and transmitter bandwidth reflected in the specifications of underwater acoustic modems (Kilfoyle and Baggeroer 2000, Benson, Ryan, and Frater 2012). The bandwidth of interest is also influenced by the transmitter and signal data acquisition hardware available for this study. Within these parameter ranges signal interaction with the ocean surface represents the most problematic driver of shallow channel variability owing to the relative difficulty in realistically simulating the rapid variations in amplitude, Doppler, delay and phase of signal arrivals at a receiver modem.

The review is also focused on what is described as single-input, single-output (SISO) systems, consisting of an omnidirectional transmitter and omnidirectional receiver. This reflects the instrumentation capabilities available for experimental investigations in this study, and the view that understanding the surface interactions for a SISO system is a necessary step towards understanding surface interactions for a multiple-input multiple output (MIMO) system. There are however many valuable channel probing investigations using multiple inputs and outputs (line arrays), and these studies are included where they help to understand the time-varying channel with surface interactions.

The necessary capabilities of an underwater acoustic channel simulation have evolved as the type of acoustic coding has evolved. The earliest underwater acoustic modem systems were developed primarily for control purposes where reliability was a higher design priority than data transmission rates. These systems used phase-incoherent (i.e. energy) signal modulation such as Frequency Shift Keying (FSK or MFSK for >2 multiple frequencies) (Eggen, Baggeroer, and

Preisig 2000, Porter, Hursky, and Siderius 2002). The frequency and temporal characteristics of the FSK signal are used to encode data by successive parallel combinations of multiple tones. FSK utilises sufficient pauses between tone-pulses to avoid overlap of successive symbols arriving via delay-spread multiple reflected paths, and utilises sufficient frequency separation between the tone pulses to achieve insensitivity to channel Doppler. However FSK coding is susceptible to time-variable loss of transmission frequencies due to variable destructive interference, such as results from tide height variation (Badiey et al. 2000) and as the range between a source and receiver changes.

The quest for higher data transmission rates has led to the development of phase-coherent signal modulation methods, using the third property of a wave, its phase, to distinguish successive fundamental bits of information in an acoustic signal, known as Phase Shift Keying (PSK). Together with methods to compensate for the delay-spread arrival of transmit signal replicas, this enables shorter acoustic signal 'chips'. Example PSK methods include Binary Phase Shift Keying (BPSK – two phases) and Quadrature Phase Shift Keying (QPSK – four phases) (Eggen, Baggeroer, and Preisig 2000, Porter, Hursky, and Siderius 2002). Data rates being sought are typically an order of magnitude higher than for phase-incoherent approaches, with reliable rates in the tens of kilo-bits/second being achieved over distances of the order of one kilometre (Li et al. 2009).

Phase-switched chips in a signal-stream may also be combined to comprise longer 'symbols' based on Pseudo Random Binary Sequences (PRBS's) that can be more robustly recognised by correlation methods at a receiver, such as in Direct Spread Spectrum Signalling (DSSS) to provide a more distortion-resistant signal. The correlation properties of the longer symbols enable each symbol to be recognised at lower signal level amongst both noise and a reverberant cluster of multi-path Doppler and delay-shifted surface-reflected signal replicas. This is advantageous where covert communication is required (Ghiotto, Andronis, and Dragojevic 2012). Reliable data transmission at a kilo-bit/second has been demonstrated for distances up to 10 km by a variant of DSSS using parallel symbol transmission (Ghiotto, Andronis, and Dragojevic 2012).

An example of a reliable in-service DSSS communication system from the early 2000's is the L3 communications (formerly Nautronix) Hydro-Acoustic

Information Link (HAIL) developed for the Royal Australian Navy, used between moving submarines in shallow channels (Nautronix 2011).

3.2 What simulation capabilities are needed?

In the early 1980's commercial acoustic telemetry systems were being developed using phase-coherent signalling, that were beginning to outperform FSK systems in throughput and reliability for the relatively vertical paths between the surface and sea-bottom related to oil and gas well-head operation and maintenance (Baggeroer 1984). The signal-surface interaction was recognised as a significant source of Doppler, and the initial design response was to try to minimise the surface path by beam-forming with transmitter arrays. However the complications of additional power draw and the problems of off-targeting of the beam from mobile transmitter platforms returned interest to simpler omnidirectional transmitters. For the mostly vertical communication applications at that time the primary focus of Doppler compensation effects was relative transmitter-receiver movement. The choice and evolution of modulation schemes up to the early 1980's was closely connected to the signal processing electrical power required. The appearance of low power semiconductor technology increasingly enabled methods that had previously been too computationally intensive for practicable underwater power supply.

A decade-and-a-half on in a similar review (Kilfoyle and Baggeroer 2000) it was concluded that "A primary thesis of this paper is that increased integration of high-fidelity channel models into ongoing underwater telemetry research is needed if the performance envelope, defined in terms of range, rate, and channel complexity of underwater modems is to expand". The improved understanding of temporal and spatial coherence of horizontal shallow channels was seen as critical to achieving communication success comparable to that achieved in short-range vertical channels. The focus of high-resolution 3D ray-path modelling was seen as appropriate for improved channel simulation, but concerns were expressed about the methods (or absence of) realistic correlations between closely spaced ray-path responses.

Eggen, Baggeroer, and Preisig (2000) found by experiment using spread-spectrum signalling with 15 kHz and 20 kHz centre frequencies, that the time-variability of shallow channels generated by signal interaction with the sea surface was a

limiting factor in the performance of the receiver demodulator. Similar conclusions were drawn by Freitag et al. (2001) and Preisig (2007).

Pelekanakis and Baggeroer (2011) note that shallow water channels demonstrate time-varying fading of the channel response in the delay and Doppler dimensions, and propose receiver demodulation strategies that are better able to contend with and exploit this variability. It is noted that existing statistical channel models of transmission fading that are built on constant fading statistics are unable to replicate the transient focusing identified by Preisig and Deane (2004) in the shallow water surf zone.

In his third review of the state-of-play of underwater communications Baggeroer (2012) continues to identify the modelling of signal variability on propagation paths as a current challenge to channel simulation. The accurate short time-scale modelling of Doppler spreading is identified as particularly significant for the development of Orthogonal Frequency Division Multiplexing (OFDM) coding methods (Baggeroer 2012, Chitre et al. 2008). OFDM divides the transmission band-width into sub-bands for parallel coding of data. Accurate modelling of Doppler spreading is important to decisions about the frequency width and guard-band width between sub-bands.

The experimental work of van Walree and Otnes (2013) has clearly illustrated that in many channels, the response on a specific path is "smeared" over both delay and Doppler, with correlation between response at different delays and Doppler shifts. Together with Baggeroer (2012) this is noted as contrary to the assumption of Wide-Sense Stationarity Uncorrelated Scattering (WSSUS) that under-pins existing statistical channel models of Doppler and delay spreading.

The realistic correlation between the channel response at different arrival delays and Doppler shifts is identified (Baggeroer 2012) as an important capability that is achieved in simulators that use stochastic replay of measured wide-band channel responses, but which is not achieved by current statistical channel models. This realistic correlation in delay and Doppler spreading is identified as an important capability for future simulators.

3.3 Underwater acoustic channel simulation

3.3.1 Introduction

A number of research teams affiliated to navies around the world have developed high fidelity dynamic channel simulators with dynamic surface-wave effects. Examples include the European Underwater Covert Acoustic Communications (UCAC) "Mime" simulator (van Walree, Jenserud, and Smedsrud 2008), the NARCISSUS-2005 simulator developed by Thales Underwater Systems (Cristol 2005), the COMLAB simulator developed for the European Underwater Acoustic Network (UAN) (Abrahamsson and Ivansson 2010), the high fidelity Acoustic Communications Simulator (ACS) developed by the UK Ministry of Defence (Goddard and Launder 2009), and simulators developed for the SEAWEB program by the US Office of Naval Research (Rice and Green 2008). Not surprisingly, such simulators are not available for public use, however considerable helpful insights into the modelling methodologies have been published.

Publically available simulators or simulation code include the Time-Variable Acoustic Propagation Model (TV-APM) simulator (Rodriguez, Silva, Zabel, et al. 2010), the "Virtual Time-series Experiment" code (VirTEX) (Peterson and Porter 2013), and the Acoustic Channel Simulator (Qarabaqi and Stojanovic 2013).

Literature on channel probing experiments and channel simulations are generally found together as channel simulations rely on experiments for validation, so there are many studies in this section that could equally be included in Section 3.4 on channel experiments. Channel simulations have been grouped according to whether the simulated dynamic surface response has been calculated using statistical models, by direct replay of an experimentally measured time-varying channel response, or by a deterministic physical model. In the case of the statistical models the time-invariant path delay and amplitude structure is usually calculated by ray-tracing.

3.3.2 Simulations with statistical surface scattering

An early high frequency channel simulation by Bjerrum-Niese et al. (1996) describes a statistical modulation of the flat-surface reflection coefficient to simulate the time-varying effects of the surface-interacting path. Transfer

functions describing static and dynamic aspects of the channel response are combined in the frequency domain. The rough surface response is calculated by a static path response multiplied by a randomly time-varying reflectivity function, which has a power spectral density determined by a monochromatic surface reflection model. The reflectivity function is calculated from second-order moments of the rough surface height, representing fluctuations around the mean response. The second-order moments are calculated using the wind-speed dependent temporal coherence function numerically derived by Dowling and Jackson (1993) for a non-shadowed Pierson-Moskowitz surface using the Kirchhoff approximation. The carrier frequency is adaptive depending on range and throughput demand, ranging from 40 kHz to 300 kHz, with the surface reflectivity modulated at the carrier frequency. To achieve computational tractability, the authors chose not to pursue spatial coherence in the rough surface response, but note "Surface scattering has often been interpreted as being caused by the surface acting as a number of tilted mirrors". The authors identify a complete spatial-temporal-spectral coherence function as key to improvement of the simulation.

Chitre (2007) describes a shallow water simulation validated with experimental probe data at ranges up to 1 km in 15 m average depth using a spread-spectrum probe centred on 40 kHz. The simulation utilises deterministic methods to establish the large-scale ray-path delay structure, upon which statistical variations are superimposed to address delay scattering from surface waves. Many fitting parameters are used to tune the statistical model to the experimental data. Measurements of experimental Doppler spread are key to modelling the statistical time-correlation. Correlation between responses at different delays was not considered.

For evaluation of alternative modems Goddard and Launder (2009) describe a simulator that uses repeated ray-traces with interpolation to address the effects of transmitter and receiver movements. The surface is modelled either by applying uncorrelated time and frequency spreading by a complex Gaussian random time-shift, or alternatively using a flat surface moving sinusoidally vertically, with surface reflection losses modelled by scattering theory.

The stochastic channel simulation described by Isukapalli, Song, and Hodgkiss (2011) uses a statistical model of Doppler spreading that achieves correlation

between spread ray-path responses that are grouped in delay using the experimental KAM08 channel (Kang et al. 2010) as a reference. The simulation assigns a common statistical Doppler spread to arrivals within the group which enables the response to be cross-correlated within the group by "by Cholesky decomposition of the cross-correlation matrix in each subgroup". The groups they identify with reference to the experimental spreading function appear to relate to ray-path permutations with the same number of surface interactions. It is reported that the simulation and experimental cross-correlation matrices match.

A comprehensive account of the structure of a statistical channel simulation is presented by Qarabaqi and Stojanovic (2013). The flat-surface amplitude-delay ray-path structure is determined by ray-tracing. Statistical models are used to describe large scale channel motions induced by effects such as swell and platform motions, and small scale effects such as surface motions of the scale of an acoustic wavelength. The methodology requires mean and variance statistics to describe small scaled delay and Doppler associated with each surface interacting path. These are either obtained experimentally, or analytically based on tractable surface and bottom profiles such as Gaussian height distributions.

3.3.3 Channel replay simulations

van Walree, Jenserud, and Smedsrud (2008) developed a simulator with a channel replay mode that interpolates experimental channel probe responses $\hat{h}(t,\tau)$ in time. The simulator also has a mode where the dynamic response is generated by ray-paths with superimposed delay and Doppler scattering functions determined from experimental channels. An updated account of this simulation (referred to as the "MIME" simulator) is given in Dol et al. (2013). This work uses a wide range of channel responses, examples of which are documented (van Walree 2011) to provide a range of standard simulation test environments. The channel replay simulation is used to leverage development of a deterministic simulator described in Dol et al. (2013).

Socheleau, Laot, and Passerieux (2011) describe a stochastic replay simulation that begins with the complex-valued experimental estimate of the channel impulse response history $\hat{h}(t,\tau)$. This is treated as an instance of the underlying channel scattering function, from which dynamic channel realisations are synthesised. The spreading function response is first classified into stochastic and

deterministic components by a process described as "empirical mode decomposition" (EMD). The expression "*trend* stationary" is used to describe a channel observation that is not strictly stationary in the sense of Wide-Sense-Stationary (WSS), because the statistical mean changes with time, but for which the trend is essentially deterministic due to slow changing well understood processes, such as path-length changes due to slow platform movements or swell. With the deterministic part of the response separated by a low-pass filtering process, the stochastic part of the response is then treated as a WSS-Uncorrelated Scattering channel (WSSUS).

3.3.4 Simulations with deterministic surface response

Most channel simulators with deterministic surface response have addressed the rough surface by computing the channel impulse response $h(t,\tau)$ at discrete intervals by ray-tracing on a frozen realisation of the ocean surface between the source and receiver. At each interval t_i, the amplitude and delay of found rays are ordered by the delay τ to create a vector of amplitudes at monotonically increasing delays that comprises $h(t_i,\tau)$. Notable examples include the "IRsim" simulator (Dol et al. 2013), the "VirTEX lite" simulator options (Peterson and Porter 2013), and the "RAYLAB" simulator (Abrahamsson and Ivansson 2010).

Ray-tracing can simulate short-range focusing effects if conducted with a fine-enough fan of rays (Dol et al. 2013). The method can simulate the emergence and disappearance of micro-paths, however this is contingent on the ray-trace repeat interval being rapid enough and the angular definition of the initial ray fan being fine enough to adequately sample the surface. An inherent difficulty in ray-tracing is the non-linear relationship between the density of ray-path interactions with the surface profile and range from the receiver, which limits the ability to simulate the channel response effects of fine rough surface detail. This potentially leads to under-sampling of the surface at increasing range.

A number of authors address rough-surface response by 2D full-wave models, including Preisig and Deane (2004), Siderius and Porter (2008), Senne et al. (2012), and Badiey, Song, and Smith (2012). Choi and Dahl (2006) address surface scattering by developing a physics based incoherent forward scattering coefficient for surface interactions on nominal flat-surface eigenpaths determined by ray-tracing.

Preisig and Deane (2004) modelled short-range (40 m) shallow water (~6 m) channel responses in a surf zone with particular attention given to the transient acoustic-focussing effect of the wave profile. The time varying channel impulse response was modelled using a 2D Wavefront Model described in Tindle (2002). At this short-range the focusing events were concluded to be caused by the underside of the smooth wave crests.

Choi and Dahl (2006) describe an incoherent sound intensity channel simulation that accounts for rough-surface multi-path by combining ray-modelling for the large-scale delay structure, and surface physics to model the rough surface response. The authors reported the sound intensity channel response rather than pressure response due to their focus on linear array transmitter and receiver arrangements. Comparative channel probing results are presented using 3 ms tones at 8 kHz and 16 kHz, and 20 ms long 8-16 kHz LFM pulses at ranges from 500 m to 1000 m in 105 m water depth. Directional surface-wave statistics were measured at the site. The simulation models the bistatic rough surface response using the Rayleigh parameter to calculate an incoherent reflection coefficient for forward scattering based on the small-slope approximation, which is also modified for the presence of near-surface bubbles. The bistatic response is summed over an elliptical shaped surface patch defined by a constant-delay boundary. A similar incoherent rough-bottom reflection coefficient is used in addition to a layered bottom-loss function. The response for a multiple-surface bounce path is achieved by time-domain convolution of successive bistatic impulse responses using the image source and receiver depths pertaining to each boundary interaction. Convincing agreement between simulated and measured matched-filtered responses were achieved for channel responses corresponding to the first 6 ray-paths. The authors noted "no significant improvement in model-data comparisons (was achieved) upon incorporating directional wave properties" into the surface bistatic cross-section.

Siderius and Porter (2008) describe the algorithms behind two time-domain channel simulations for broad-band signals interacting with a rough sea surface. The first simulation describes two variant ray-trace field interpolation algorithms behind "VirTEX for Platform Motion" (although not yet given this name in 2008) and presents an exact model for verification using a superposition of the flat-surface reflected fields from an equivalent set of virtual image sources. In the

second simulation example a 2D Helmholtz-Kirchhoff integral-equation reference model of the surface-scattered field is computed at 200 Hz to benchmark the 40 m deep x 0-750 m range field calculated by a Kirchhoff Approximate (KA) method. Having validated the KA field in two dimensions the KA field can then be extended to a three-dimensional rough surface, although this is not explicitly mentioned. Using the concept of image sources, six such computationally efficient KA approximate pressure fields (for image-source geometries nominally equivalent to the first six ray-paths in the flat-surface case – D, S, B, SB, BS, BSB) are then coherently added to create the rough surface field response. A second efficient computational feature is used to adapt the single frequency rough-surface field response to a broadband transmit signal. Instead of recalculating the surface response at regular frequency intervals across the band-width, the wide-band response is achieved by multiplying the frequency domain transmit signal $S(\omega)$ by the $\sqrt{k}$ vector for the acoustic wavenumber k, then returning $S(\omega)$ to $S(t)$ before signal convolution with the response. The combination of this rough-surface response field, computed at successive intervals together with the field interpolation algorithms in the first part of the paper are understood from Peterson and Porter (2013) to represent the "full VirTEX" simulation incorporating both transmitter-receiver motions and a dynamic rough sea surface. The authors note that whilst the method models the response relating to only the first 6 ray-paths, these path responses normally account for the bulk of phase-coherent signal demodulation of mid-frequency communication signals in shallow channels.

Silva et al. (2010) use ray-tracing at time intervals ranging from 2 ms to 300 ms to simulate a time-varying channel, with the channel response up-sampled by interpolation to the signal sampling rate. It is unclear how the dynamic surface is described. The absence of fine-scale spreading in the appearance of the reported spreading functions suggests that the dynamic effects for the simulations were focused on dynamic transmitter, receiver, bathymetry, and sound speed gradient effects.

Abrahamsson and Ivansson (2010) describe a methodology for adapting RAYLAB and REV3D ray-path models to incorporate Doppler from platform movement similar to that described in (Siderius and Porter 2008), with results compared

with a wavenumber-integration model for 10 kHz shallow-water (100m) propagation over 1 km (Karasalo 2011).

Rodriguez, Silva, Gomes, et al. (2010) use ray-tracing at 500 Hz, repeated at 10 ms intervals, on 2D sections of a directional 3D time-evolving surface-swell realisation to simulate the channel response for fixed transmission and reception points. The effect of different propagation directions is explored in the simulated channel response and spreading function.

Karjadi et al. (2012) simulated high-frequency forward scattering from surface waves in shallow water by experimental investigation of a 15 m deep by 387 m long channel. Channel probing with 1-18 kHz signals was followed by ray-tracing on 2D sections of a realistic dynamic 3D surface wave realisation. Channel probing used fixed transmitter and receiver vertical line arrays, with a 0.345 s broadband chirp probe symbol repeated at intervals over a week. The data and simulation results were used to correlate the statistical arrival time variation (and therefore indirectly the overall Doppler spread) with wind speed.

Senne et al. (2012) used a 2D parabolic equation (PE) model at 512 frequencies between 12.5 kHz and 17.5 kHz to model by Fourier synthesis the time-varying received intensity at 100 m depth over 650 m range, to simulate the KAM08 experiment (Kang et al. 2010). The channel response was updated at 12.5 ms intervals. The rough surface paths corresponded nominally to the first four ray-traced paths, including two single surface-bounce path variants. The surface profile for simulation was synthesised from a low-amplitude (0.17 m RMS) experimentally measured surface power-spectral density. Good agreement between the simulated and experimental responses was demonstrated for the surface-interacting and direct path responses. Further details of this modelling work, including the modelled inclusion of an evolving bubble-field are described in Senne's PhD dissertation (Senne 2012).

Badiey, Song, and Smith (2012) described similar PE modelling work to that of Senne et al. (2012) but for the subsequent KAM11 trial in the same locality at 100 m depth and at 500 m and 1000 m ranges, using fixed transmitter and receiver positions. In this trial the transmission direction was switched within a short space of time (2 minutes) to enable the effect of reversal of the surface-wave direction to be examined. Both the experimental and simulated channel response

histories feature time evolved response "striation" patterns, illustrating responses off travelling waves that increase in delay with time for one transmission direction, and decrease in delay with time when the transmission direction is reversed relative to the same prevailing surface swell direction.

Deane et al. (2012) measured the short-term (25 ms probe repeats) and long-term (12 days) time-varying channel response over short ranges (64 m to 1000 m) in a 15 m deep environment. A full-wave 2D section model using the Kirchhoff Approximation was used to simulate channel responses from single surface-bounce paths at each range on a wave-by-wave basis. Both experimental and simulated channel responses illustrated significant time-varying focusing.

The work of Dol et al. (2013) is significant for its focus on integrating both the effects of realistic sea-surface motion and surface bubble plumes in their consideration of surface scattering. The "IRsim" channel response simulation utilises repeated ray-traces for 2D cross-sections of an evolving 3D surface realisation to determine the impulse response of successive surface realisations. The described example uses a dynamic sea-surface realisation defined at 1 m horizontal intervals for a 6 kHz signal (which corresponds to a spacing of 4λ, where λ is the acoustic wavelength). An interesting approximate approach is used to account for the evolution of the ocean surface shape during the flight-time of sound-waves at longer ranges. The 2D cross-section used for the ray-trace is made piece-wise, of a composite of sections each of length $c\Delta t$, where c is the sound speed in water and Δt is the channel update interval, which would approximately correspond to the horizontal position of a travelling sound-wave as it progressed beneath the surface realisation. The simulation does not include out-of-plane surface responses. The impulse responses at 10 ms are then up-sampled to the signal rate using the "MIME" channel simulator. Successive ray-traces utilise 5001 rays at 6 kHz. Simulation results for a specified Pierson Moskowitz surface are presented for 300 m, 600 m and 1800 m ranges for 30 m and 60 m water depths.

Peterson and Porter (2013) report two useful variants developed from the original algorithms described in (Siderius and Porter 2008) that substantially reduce computational intensity. In the case of "VirTEX for Platform Motion" a single ray-trace is performed for a flat ocean on a field of receiver positions that bound the proposed relative motion of a source and receiver. A spatial interpolation scheme

is then used to calculate the amplitude, delay and phase shift of the underlying flat-surface ray-paths at intermediate points in the receiver space. The model is able to simulate the emergence and disappearance of ray-paths as the transmission range changes in a realistic way, in addition to correctly modelling the in-path Doppler. The other variant "VirTEX for sea surface dynamics" begins with a single flat-surface ray-trace. Essentially, time-varying perturbations to the flat-channel delays are included which relate to vertical movement of the real surface at positions corresponding to the mean-plane-specular points of the flat-surface ray paths. In doing so the authors note that the simulation is not able to represent emergent/vanishing micro-paths. The simulation is tested for an example of surface swell for which the algorithm works well. Equivalently the simulation is not able to model focusing, or rough surface effects associated with finer-detail wind driven waves. However, the computational simplification achieved enables real-time deployment in on-board settings that would otherwise not be possible (Peterson and Porter 2013). The simulation is illustrated to enable extensive multiple runs to explore the effectiveness of transmitter and receiver positions throughout an extensive environmental spatial domain (i.e. 0-5000 m depth x 0-100 km range).

On a large scale, the need to integrate acoustic communication simulations with a global time-dependent 3D oceanographic model has been identified by Porter (2013). The extraction of channel responses within this global oceanographic model in relatively deep water is being addressed by computationally efficient adaptations of the BELLHOP 3D ray-tracing simulation.

3.3.5 Simulator validation

Otnes et al. (2009) argue the need for standardisation of simulators and channel test cases to achieve consistent benchmarking of coding schemes and hardware, and interoperability between hardware systems.

Otnes, Jenserud, and Van Walree (2013) identify multi-dimensional and parameter measures of channel response that could be used to standardise the simulated description of a channel response. These include 2D plots of the time-varying channel response $h(t,\tau)$, the spreading function $S(\nu,\tau)$, the Doppler power spectrum and delay power profile, and the temporal coherence. The standardised measures are then compared between an experimental channel probe result that

has been collected with sufficient supporting environmental parameters to enable simulation, and the simulation of the experimental channel response using the same probe signal. For rapid-changing channel effects the description of the environment should include measurement of the surface-wave spectrum either directly and/or indirectly by wind-speed observations.

The suggested simulator fidelity measures for transmission of actual coded data include the Bit Error Rate (BER) and output Signal-to-Interference-plus-Noise Ratio SINR. The SINR accounts for the fact that in some channels, incoherently dispersed signal reverberation effectively contributes to noise to the point that increasing the signal power does not improve the SINR. The difficulty of direct BER evaluation is interpretation of lower BER results. Does the lower BER indicate loss of simulator fidelity, or decreased SINR?

One important function of a channel simulator is to enable exploration of alternative coding strategies. Field BER validation data will almost by definition not be available for developing coding strategies, and less so in a specific channel environment. Thus, it is argued that evaluation of channel simulator fidelity should be based on transmit-receive correlation properties of probe signals that are selected to maximise the validated Doppler bandwidth and delay spread of the channel.

The suggestions of Otnes, Jenserud, and Van Walree (2013) are clearly focused on single-input, single-output (SISO) communication systems that are not explicitly concerned with the simulation of spatial coherence. This is consistent with the current study focus. Multiple-input, multiple-output (MIMO) communication simulation would require extra dimensions and complexity to adequately test simulator fidelity.

3.4 Channel probing experiments

The shallow-channel mid-frequency probing experiments in this section complement the experiments briefly discussed in Section 3.3 that are reported concurrently with channel simulations. Channel probing experiments have been sought to illustrate how the dynamic response of channels, characterised by arrival delay spreading and Doppler spreading, is related to channel geometry and surface conditions. And in some instances, such as Huang, Yang, and Huang

(2013), to examine directly the strength of correlations between surface-scattered paths at different delays.

Badiey et al. (2000) explored a 15 m deep by 387 m long channel at sub-second and diurnal time scales using fixed transmitter and receiver positions. The aim was to relate acoustic fluctuations to concurrently sampled environmental conditions, including wind-speed and direction, tide height, surface wave spectra, current and sound speed profiles. Short time-scale channel effects were probed with a 0.6-18 kHz chirp at 0.345 s repeat intervals in 5 s clusters repeated each 10 minutes, and 40 s clusters repeated at hourly intervals, over several days. The results clearly illustrate the correlation between wind-speed and the degradation of the multi-path response for multiple-surface-bounce transmission paths. Spectral transmission coherence estimates over the 40 s clusters clearly illustrate the changing frequency selectivity of the channel at different times of the day over the 0.6 kHz to 18 kHz bandwidth, a problematic reality for Frequency Shift Keying (FSK).

Dahl (2001) experimentally investigated single-bounce forward scattering under controlled conditions at ranges of 70 m to 100 m in 26 m deep water, and over ranges of 500 m to 1000 m in 4000 m deep water, spanning grazing angles from 4.5^{o} to 20^{o}, with probe frequencies greater than 20 kHz. The experiment was used to determine characteristic length-scales 'L' for time spreading, and characteristic angular scales σ_{θ_h},σ_{θ_v} for horizontal and vertical angular spreading from the bistatic rough surface response. The inverse of the delay spreading parameter L (which is weighted from the arrival intensity delay response) defines the frequency coherence width for the bistatic response. It was found that whilst near-surface bubbles caused signal attenuation, their presence "had little effect" on delay or angular spreading.

Preisig and Deane (2004) report the channel response at short-range (38 m) in a shallow (~6 m) surf zone, transmitting towards shore perpendicular to the shoreline. Broad-band probe signals were used with centre-frequencies ranging from 12-26 kHz. The response history captured direct, bottom-bounce and four distinct single-surface bounce path variants, with notable time-varying amplitude enhancement determined from modelling to result from focusing by the surface wave profile.

Beaujean and Strutt (2005) used an omnidirectional source and vertical line array (VLA) receiver at ranges of 51 m and 166 m in 20 m deep water to illustrate the multi-path response as a function of delay and array steering angle. This presentation of the channel response history tends to obscure the reading of the channel SISO delay response.

Song et al. (2008) describe time-varying ocean effects recorded in the Kauai experiment in 100 m deep water over 3 km and 27 hours using 8 kHz to 50 kHz BPSK probe signals. The omnidirectional transmitter was placed 5m above the bottom, and the 16 element VLA receiver spaced over the full depth. A wave-rider buoy recorded the surface wave spectra, reported at hourly intervals. A thermistor chain recorded the temperature profile at what appear to be 1 minute intervals and 5 m depth increments. The channel impulse response was post-processed at 40 Hz sampling rate (each 25 ms), using overlapping 100 ms long (400 symbol) sections of the BPSK transmissions. Example 10 s sections of response for the 36.5 m deep array hydrophone were illustrated. The primary focus was examining the VLA output SNR in response to environmental change over the 27-hour probing period. Siderius et al. (2007) provide additional interpretation of the effect of the changing thermocline on the receiver performance as a function of depth.

Tomasi et al. (2010) present channel probe histories for up to 9 hours for 60 m, 70 m and 80 m water depths over ranges of 700 m, 1500 m and 2200 m respectively. The trial was repeated in the months of May, June and September to capture different sound speed profiles and surface wave conditions. The probe signal for channel response sampling was a 9-14 kHz hyperbolic frequency modulated (HFM) sweep. The results appear to show some intermittency of the direct and bottom bounce paths that has made it difficult to align successive impulse responses in the data presentation. Significant changes to the delay-spread of single-surface bounce path permutations are observed over a period of hours.

Socheleau, Laot, and Passerieux (2011) report channel responses from the Mediterranean Sea probed at 8 Hz with spread-spectrum signals (6 kHz centre frequency), for 0.5 –10 km ranges over 60-120 m depths, and from the Atlantic Ocean probed with continuous bit streams of spread-spectrum signals (11.2 and 17.5 kHz centre frequencies), for 0.5–3 km ranges over 10-40 m depths. The

illustrated responses include examples where all path responses are intermittent, and examples with stable direct path.

van Walree (2011) explains the methods and challenges of channel-sounding, and presents a diverse range of experimental channel responses. Channel experimental impulse response histories, frequency spreading functions and channel correlation functions are presented for 15 experimental data sets, mostly sampled with fixed geometry, but with some examples of moving transmitters. The normalised coherence times are compared for the different channels. In more detailed analysis of two of the channels in a previous study, van Walree, Jenserud, and Otnes (2010) use simultaneous 10, 12, 14, 16, and 18 kHz tones to explore time-averaged Doppler power spectra of shallow channel responses over ranges of 750 m and 1500 m. The probing with multi-tones was alternated with 16 ms and 32 ms PRBS probe signals to enable calculation of the Doppler power spectra for the same channels as a function of arrival delay, and to explore the effect of aliasing of the response from delays beyond the length of the probe signal block. This work is notable for its presentation of the experimental Doppler-delay spreading function.

Yang (2012) presents analyses of the experimental temporal coherence of various shallow channel responses at ranges of 3 km to 42 km for the purpose of improving channel equaliser functions. Channels with rough and smooth surfaces are investigated, as well as downward refracting environments where negligible surface interaction occurs, and channels where response intermittency is generated by medium inhomogeneities. A range of probe frequencies are used from 200 Hz to 22 kHz.

Huang, Yang, and Huang (2013) calculate and plot the normalised cross-path coherence matrix for smooth and rough shallow channels, which gives insight into whether there is reasonable prospect of phase-coherent recombination of signal from different scattered surface paths, and within a single-scattered surface path. The experimental data was obtained with fixed transmitter and receiver positions to ensure that any cross-path coherence was not unintentionally caused by platform Doppler, which automatically induces coherence across paths. The study concludes “multi-path arrivals are highly cross-correlated when the channel is temporally coherent, and are uncorrelated when the channel is temporally

incoherent". A cross path coherence is described qualitatively as "mostly correlated" if the cross-path coherence is greater than 0.8.

van Walree (2013) provides additional analyses of channels previously presented in van Walree (2011) and provides a comprehensive overview of available channel sounding literature by others. The opening comments on the diversity of channel responses and absence of a 'typical' response underlines the challenge to improve channel simulation to the point that the diversity of responses become explicable and to some degree predictable.

3.5 Approximate model of surface scattering

Central to the goal of a high-resolution phase-coherent modelling of the channel response is the achievement of realistic micro-path Doppler and delay shifts for a spatially coherent acoustic interaction with the rough surface. Accordingly, an approximate calculation method was sought for the wide-band forward-scattered acoustic response from a limited patch of the three-dimensional rough ocean surface. The method would need to work with significant shadowing at low grazing angles, and allow deterministic time-coherence of micro-path responses.

Shaped by early time-varying-channel simulation using successive 2D ray-traces for ocean swell (Caley and Duncan 2013b), the initial scattering conceptualisation was around a two-scale model, as depicted on Figure 3-1, that would enable ray-tracing for successive swell realisations to be enhanced with an un-specified scattering model for finer deterministic surface detail.

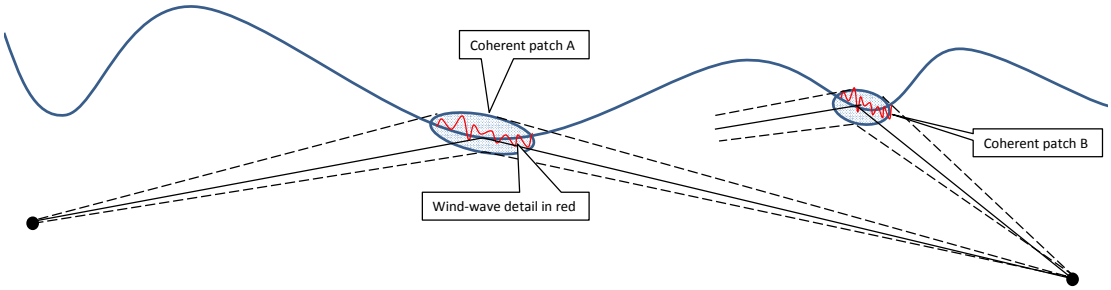

Figure 3-1: Initial two-scale conceptualisation of the surface scattering problem

However this two-scale approach was discarded as unsuitable because realistic ocean surface spectra represent a continuum of length scales, which appeared difficult to reconcile with a ray-trace response to surface swell.

A second objective was to develop a suitable reference model of surface scattering that could be used to check the validity of the approximate scattering method for limited cases.

The consideration of surface scattering models was weighted towards implementation of the Kirchhoff Approximation (KA) of the scattered field on the scattering surface due to the simplicity of the method numerically, and the significant attention that has been given to understanding the strengths and weaknesses of this model, and, not-withstanding issues with shadowing, the absence of limits on surface amplitude and surface gradients to which the Kirchhoff Approximation can be applied (Ogilvy 1991).

For rough surfaces with varying degrees of shadowing, clarification was sought about how the KA approximation affects the delay-dependent reflected response and Doppler response in the context of underwater communication signal simulation, and for what parameter choices a reliable response may be calculated using the KA method.

Elfouhaily and Guérin (2004) present a comprehensive review of approximate scattering theories for random rough surfaces, including many scattering models that are reportedly suitable for modelling "whole-wave" scattering including a wide spectrum of surface frequencies. With regard to the Tangent Plane Approximation (TPA) version of the Kirchhoff Approximation (KA), the authors note that the calculation kernel is non-reciprocal (a point that is relevant later when considering bistatic calculation geometries), dependent on the local slope. TPA is described as a "local" scattering model, because the response on the tangent plane is independent of the response elsewhere on the scattering surface. It is also described as a "single scatter" model because multiple scattering within the rough surface structure is not modelled.

Ziomek (1982) notes that previous models of bistatic rough surface scattering for acoustic communication have relied on the assumption of plane-wave incidence on the surface, and plane-wave reception, when realistically the relevant insonified surface-patch in shallow channels is bounded by significantly divergent incident geometrical boundary-rays, and the reception is bounded by significantly convergent received rays, the geometry of which may alter the response from previous plane-wave conceptions. A random time-varying frequency response

function for the bistatic ocean surface response is developed directly from the Kirchhoff Approximation on the scatterer surface, but developed for geometries that do not include surface shadowing.

McCammon and McDaniel (1986) explored the realism of the Kirchhoff approximation when applied to a sinusoidal rough surface, by examining the exact surface velocity distribution compared to that implied by the Kirchhoff approximation for grazing angles between 1° and 20°. It was concluded that "no correction (for shadowing) should be applied to the specular reflection coefficient, and the simple percentage of the illuminated area provides the best fit to the exact coefficient for off-specular reflection". The contribution of multiple scattering within the sinusoidal structure was found to be negligible. An interesting aspect of the work was exploration of the "Born" surface shape that would produce the correct response when KA is applied. This resulted in sinusoidal surfaces that were increasingly flattened as the grazing angle decreased from 20° to 1°.

Thorsos (1988) examines the validity of the Kirchhoff approximation for bistatic surface scattering by comparing the KA response with an exact Integral Equation (IE) response averaged over 50 random realisations of a 2D surface, at acoustic frequencies of the order of "a few hundred Hz". For a source grazing angle of 45° the KA response was found to be a close match to IE around the specular forward-scattered direction +/-10°. At a lower grazing angle of 20° with shadowing KA was found to significantly under-predict (-5dB) compared to IE. The shadowing corrections of Wagner (1967) were explored. The Wagner correction is based on the RMS surface slope s. At low grazing angles it is suggested that correction for the proportion of shadowing does not match the response-enhancing effects of diffractive multiple scattering for short surface correlation lengths, such that shadowing correction degrades rather than improves agreement between KA and IE. For the purpose of calculating the shadowing correction Thorsos suggests that an adjusted (reduced) effective surface slope $s' = \sqrt{kl}$, where l is the roughness length scale, produced a better match to IE when shadowing is present. Qualitatively this aligns with the computed trend of equivalent "Born" surfaces reported by McCammon and McDaniel (1986). Thorsos notes that "further work is required to fully understand the applicability of the Kirchhoff approximation to forward scattering with low incident grazing angles".

The work of Ogilvy (1988) adopts an investigative philosophy similar to McCammon and McDaniel (1986) and considers that comparison of approximate and exact responses for individual surface realisations is instructive, in addition to the more conventional examination of responses averaged over a number of surface realisations. Ogilvy notes that valuable information about phase response is lost by averaging, and that phase is useful in predicting the time-dependent scattering off rough surfaces (or defects) by Fourier synthesis, or alternatively the frequency spreading caused by scattering. The KA response is benchmarked against an exact Helmholtz-Kirchhoff integral equation solution to rough-surface scattering. Problems with the KA model are noted for significant shadowing of the surface profile.

McDaniel (1992) examined forward scattering for the Kirchhoff approximation for rough surfaces with varying degrees of shadowing overlying a refractive sound channel, to seek scattering coefficients that could apply to multiple surface-reflected transmission paths. Upward refraction was found to interfere with the generation of meaningful analytical results.

In the context of electro-magnetic radiation (EMR) scatter from above the rough ocean surface Toporkov and Brown (2002) present a Doppler analysis on a time-series of modelled bistatic responses from a dynamic rough surface, to evaluate the dynamic fidelity of approximate rough-surface response models at low grazing angle (LGA) compared to an exact integral equation (IE) model. The EMR wavelengths in that study were 10cm and 23cm, which translate to underwater acoustic frequencies of 6.5 kHz and 15 kHz having the same respective wavelengths. Results of bistatic cross-section analysis are also presented for the full 180^{o} range of scattered angles (i.e. including forward scatter) in response to 10^{o} grazing incidence. Linear and non-linear 2D ocean-like surfaces (with sharp peaks) were studied using an IE model and approximate models, including Small Slope Approximation (SSA), and Extended Kirchhoff Approximation (EKA). Whilst for non-linear peaked surfaces the approximate methods were not able to reproduce Doppler spectra well at close to grazing, the Doppler spectra generated by both methods for linear surfaces, which do not have sharp peaks "were successful in predicting the change in the shape of the Doppler spectrum from normal incidence to LGA (low grazing angle)". The view is expressed that

"Doppler analysis proves to be a much more precise and sensitive tool in assessing the scattering model's validity than the usual comparison of cross sections".

Siderius and Porter (2008) also use an exact 2D IE model to validate the approximate 2D KA acoustic field response of a rough sea surface (described in Section 2.5). The rough surface appears to include a degree of surface shadowing at incident grazing angles of the order of 4^o to 5^o. The validation is presented for the static field response to a frozen surface realisation. No mention is made of problems with KA due to shadowing of rough surfaces. The description of the implementation notes that the response from each discretised surface point responds locally to the incident field, without reference to the surrounding surface profile. It is understood that the implementation therefore ignores shadowing of the surface in calculating the incident field distribution on the surface.

3.6 Gaps in current knowledge of channel simulation

The need to improve the simulation of fine-scale channel Doppler in response to surface waves, and to improve the simulation of cross-path coherence and micro-path coherence when it exists, are consistently expressed by researchers seeking to increase the data rate and reliability of underwater acoustic communication channels.

Until relatively recently (~2010) few experimental channel probing experiments reported estimates of Doppler attributed to sea-surface dynamics because Doppler associated with movement of the transmitter and/or receiver usually dominated the receiver signal-processing task. Even fewer underwater acoustic channel simulation studies report channel Doppler spreading functions associated with realistic sea surfaces. Accordingly, the scale of Doppler spreading associated with surface interacting transmission paths, and how and where the Doppler shifts are generated by the acoustic-ocean-surface interaction are poorly understood.

Whilst ray-tracing has proven effective in establishing the detailed response delay history $h(t,\tau)$ for relatively smooth ocean surfaces including paths with any number of surface interactions, this method is seen as unreliable for significantly shadowed rough surfaces. Ray-tracing is also regarded as limited in the extent to which cross-path coherence associated with micro-paths can be reliably modelled.

Given unlimited computational capacity, an ideal channel simulation might utilise rapid repetitions of a full-wave three-dimensional model that is able to model fine-scale Doppler and cross-path coherence effects for the multi-path response including multiple surface interacting paths for a shallow rough channel. However this is not presently viewed as realistic (Potter, Porter, and Preisig 2013).

With the exception of ray-trace modelling, the deterministic phase-coherent modelling of surface-interacting paths has been limited to paths with just one rough surface interaction and two-dimensional surface profiles (Senne et al. 2012, Badiey, Song, and Smith 2012, Deane et al. 2012, Siderius and Porter 2008). The approximate incoherent modelling of multiple surface-interaction paths for a three-dimensional rough surface has been reported (Choi and Dahl 2006) by decomposition of a path into multiple bi-static surface interactions, to enable the bistatic rough surface response to be convolved in the time domain. However this has not yet been demonstrated for a coherent signal simulation, or for a complete shallow channel multi-path response including paths with two or more surface interactions.

In summary, the deterministic modelling of the coherent multi-path acoustic channel response relevant to mid-frequency underwater communication signals, including realistic coherence within and between paths with multiple surface interactions has not yet been reported in literature and is key to the development of improved underwater acoustic communication signalling strategies and hardware for shallow channels.

4 FIELD CHANNEL PROBING TRIALS

4.1 Experimental sites

The primary objective of channel probing trials was to gain a diverse range of experimental channel response histories, $h(t,\tau)$, varying with wave height, water depth, propagation direction relative to the prevailing wave direction, and transmission range. Diverse channel geometries and conditions were sought to provide a variety of experimental data for later comparison to channel response simulations.

A preliminary channel probing trial was conducted courtesy of L3-Oceania in 85 metres of water north-west of Rottnest Island, 25 nautical miles north-west Fremantle. This site is marked in the upper left corner of Figure 4-1. Instrumentation deployment and trials occurred on 7th and 8th March 2012, with instrumentation retrieval on 14th March. The communication signals sampled during this trial were not designed for channel probing, but provided an opportunity to explore the channel response with minimal outlay by Curtin CMST. The trial allowed observation and testing of instrumentation deployment and recovery procedures, and provided data for testing and development of processing algorithms that informed the design of subsequent dedicated channel probing experiments.

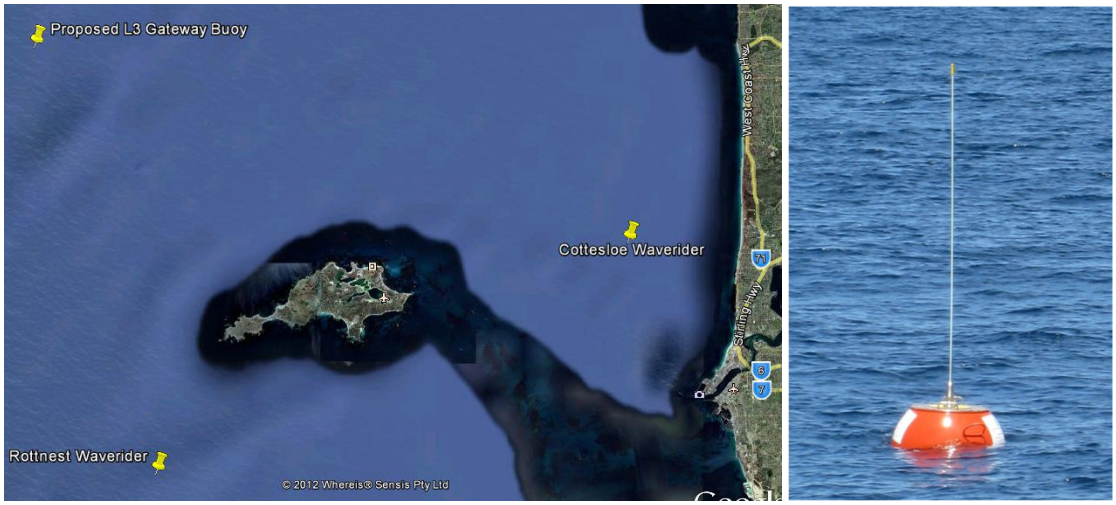

Figure 4-1: Test sites (left) (image from Google Earth) and Direction Waverider Buoy (right)

The experimental data-sets presented in this thesis were obtained from two subsequent channel probing trials. These sites were selected to achieve relatively

constant water depth between transmission and reception points and close proximity to a Directional Wave Rider Buoy (DWRB) shown on the right of Figure 4-1. A DWRB provides a sampling record of the surface-wave spectrum and direction in the test locality. This led to experimental sites in the vicinity of each of the Cottesloe and Rottnest 'Waverider' sites indicated on Figure 4-1.

4.2 Cottesloe trial description

4.2.1 Cottesloe trial site

The Cottesloe DWRB is approximately 6 km (3.3 nm) off-shore from Cottesloe Beach as illustrated on Figure 4-2. Probing trials were conducted on 28th April 2012. The test site needed to be clear of shipping near the Fremantle Port shipping channel. Permission to install a sea-bed recorder with surface retrieval float during daylight was obtained from the Fremantle Port Authority. The Royal Australian Navy was notified of the proposed position and timing of acoustic channel probing tests.

Bathymetry data for the site from aerial LiDAR (Light Detection and Ranging) confirmed a water depth range of 13 m to 14 m relative to mean sea level. Water depth profiles extracted from the LiDAR data are illustrated on Figure 4-3 and Figure 4-4. The centre receiver location was selected to provide the opportunity for directional soundings to be aligned with, and transverse to, the prevailing swell and sea directions, whilst maintaining relatively constant bathymetry. Transmission ranges of 50 m, 100 m, 500 m and 1 km were planned.

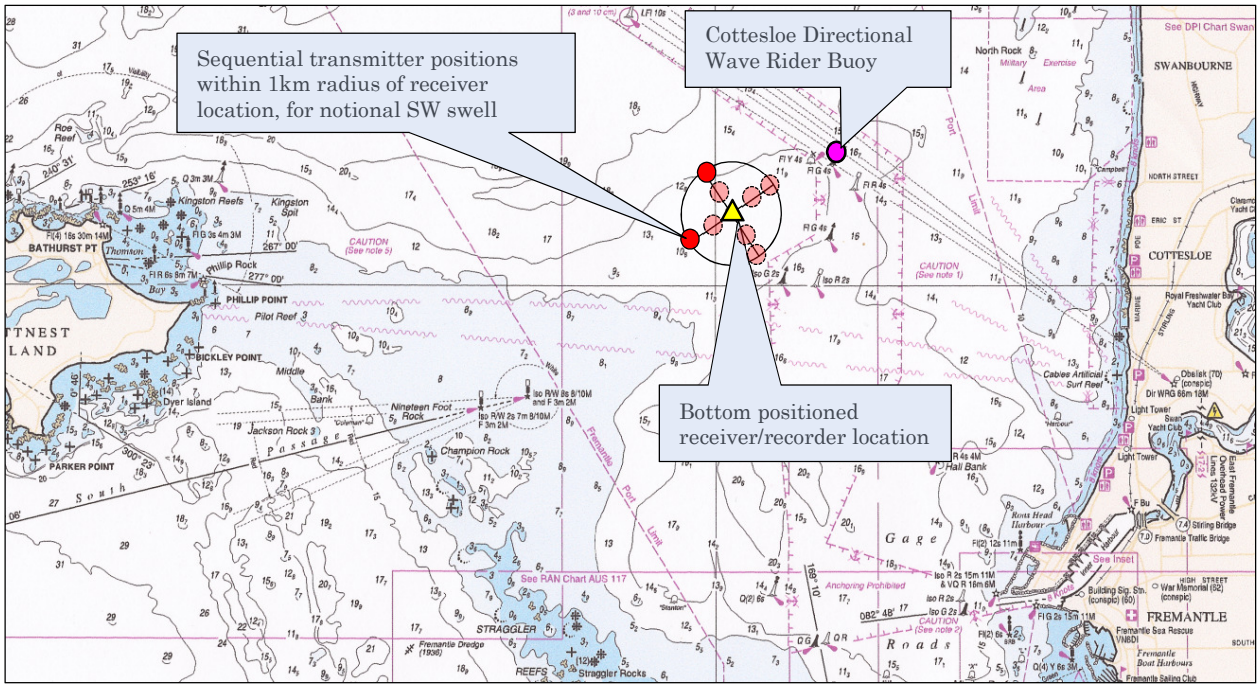

Figure 4-2: Planned Test locations relative to Cottesloe Directional Wave Rider Buoy (DWRB) (base map source DPI Map WA001)

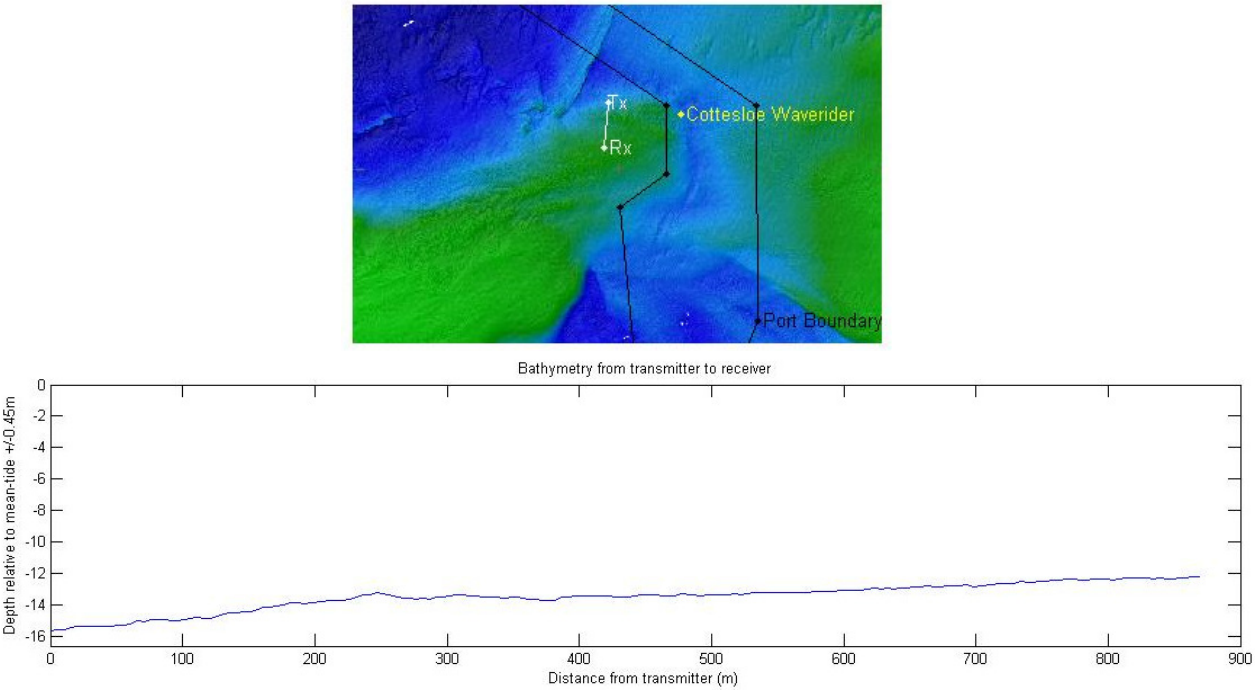

Figure 4-3: Exploration of site LiDAR bathymetry north (Tx) to south (Rx) of proposed Cottesloe site (see upper image)

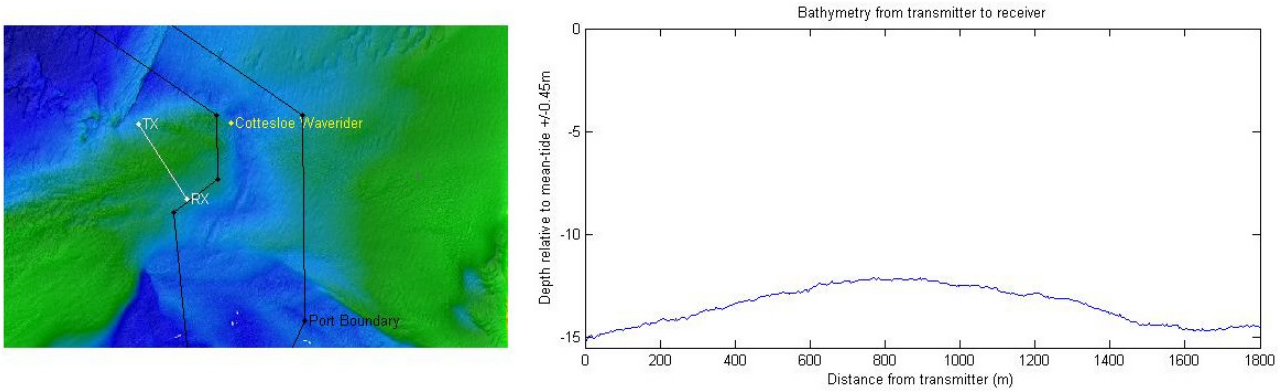

Figure 4-4: Exploration of site LiDAR bathymetry north-west (Tx) to south-east (Rx) across proposed Cottesloe site (see left image)

4.2.2 Trial vessel

The Cottesloe trial was conducted on board the 11 m long "Kharisma" vessel, previously a cray-fishing boat (Figure 4-5). The capstan winch from this former use was a necessary feature for retrieving the sea-bed acoustic recorder. A temporary davit (not pictured) was fabricated and fitted to the vessel by Mal Perry of CMST to enable lowering and raising of the sea-bed recorder and associated ballast.

Figure 4-5: "Kharisma" Cottesloe trial vessel

4.2.3 Experimental arrangement

The channel probing experiment consisted of a drifting transmitter illustrated on Figure 4-6 and an acoustic recorder positioned on the sea-bed illustrated on Figure 4-7. The dunking transmitter was inverted vertically to maximise the signal transmission via the sea-surface.

The recorder, complete with sufficient adhesive tape to retain excess hydrophone cabling and to prevent rattles and squeaks in shackles while deployed, is

illustrated on Figure 4-8. The retrieve line system prior to deployment is shown on Figure 4-9.

Consideration was given to the merits of a fixed versus drifting transmitter. Fixed transmitter and receiver positions enable the Doppler of the ocean surface movement to be experimentally isolated from Doppler due to relative transmitter-receiver motion (van Walree 2011), however the desired flexibility to explore different ranges and transmit angles relative to prevailing surface swell direction, and the much simpler deployment logistics led to the choice of a drifting transmitter.

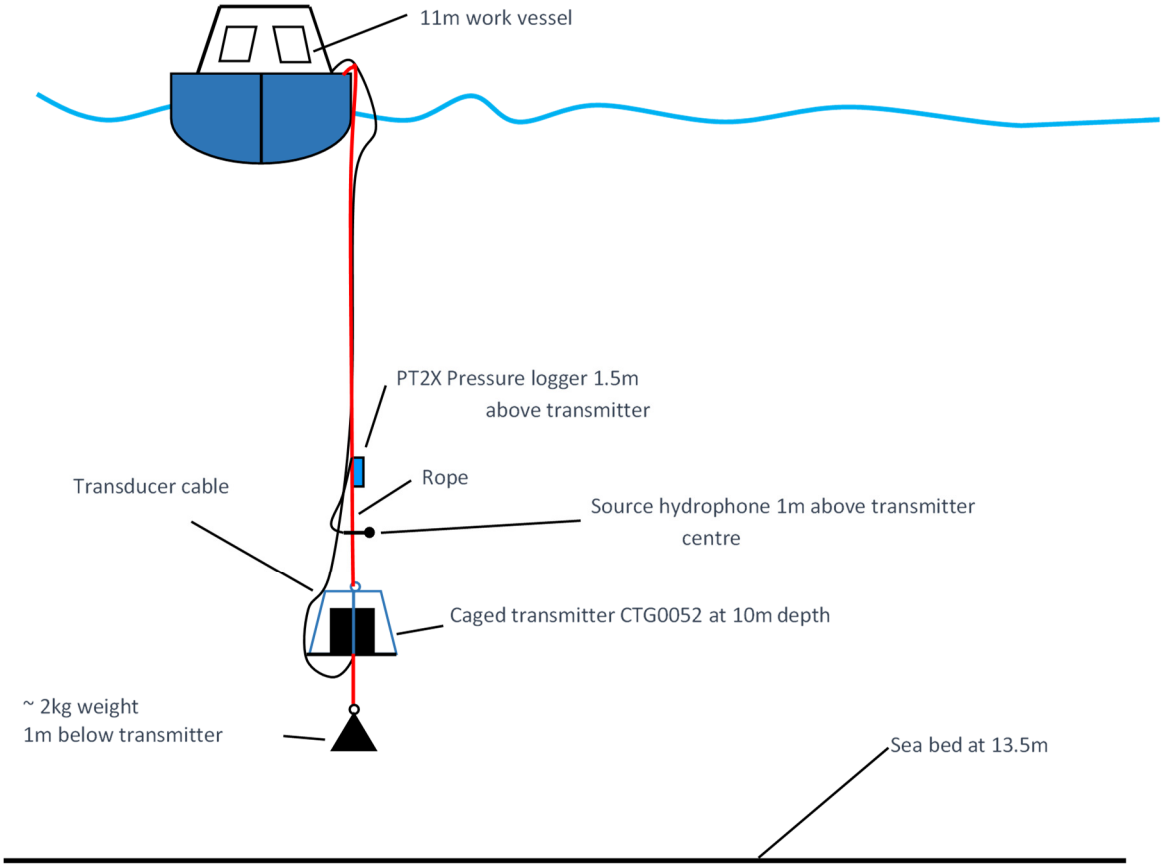

Figure 4-6: Cottesloe trial transmitter arrangement

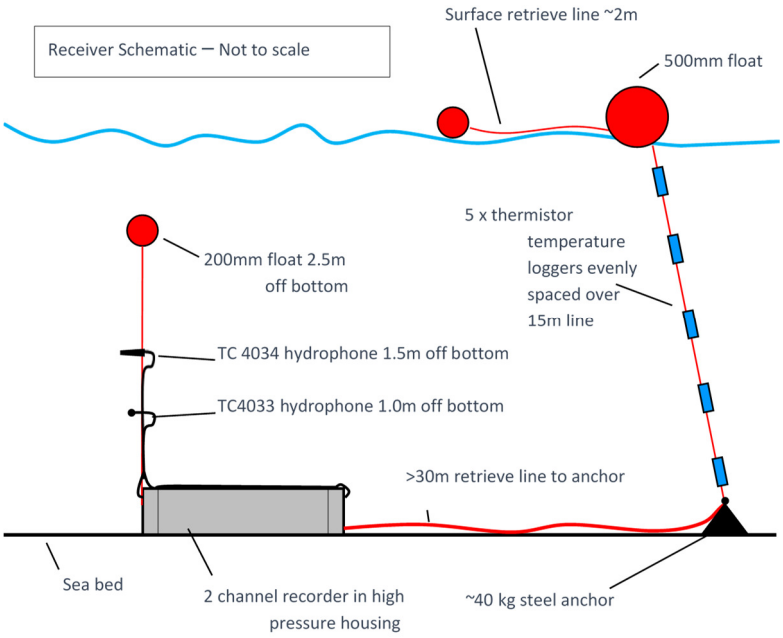

Figure 4-7: Cottesloe trial receiver arrangement

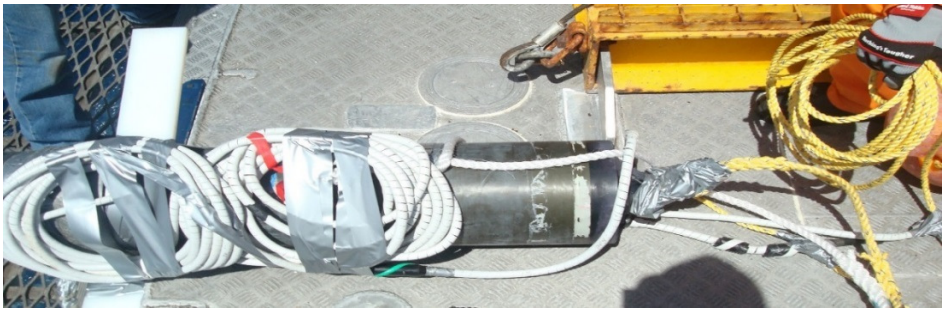

Figure 4-8: Receiver high pressure housing with excess cable (image from deck of L3 trial)

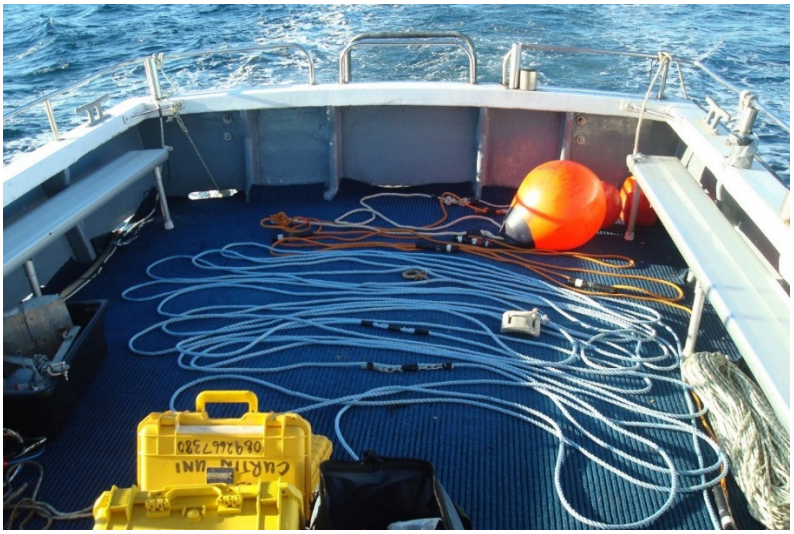

Figure 4-9: Retrieve float and line prior to deployment

The acoustic receiver consisted of a Sound Devices SD722 digital audio recorder, 40 dB pre-amplifiers, and batteries within a high-pressure underwater housing, recording two channels at 96 kS/s and 24-bit depth. The two receiver hydrophones were separated vertically by 0.5 m (Reson TC4033 at 1 m off bottom, and Reson TC4034 1.5 m off bottom). The second hydrophone was included to enable future exploration of the benefit of spatial diversity at the receiver. The hydrophone vertical separation was selected based on simulation of the fine spatial resolution transmission loss calculated by the Bellhop model (Porter 2011) at the 9 kHz and 15 kHz band-limit frequencies of the proposed experimental probe signal.

The receiver system is summarised in Table 4-1, with its considerable 77 kg total mass accounted in Table 4-2. Due to the significant weight of this item it was both assembled and disassembled on the trial vessel to avoid transfer of the total weight between the vessel and dock.

Table 4-1: Receiver system summary

Item	Details
Digital recorder & housing	CMST high-pressure housing with No.37 endcap incorporating, Sound Devices 722, with CMST 40 dB pre-amp gain on each channel, +3 dB ch1 recorder gain, +18 dB ch.2 recorder gain 96 kS/s sampling rate, 24 bit, .wav mono, 2 s pre-record time, mic inputs limiter enabled, mic low-cut disabled, 1.8 GB max file size
Ch. 1 hydrophone	Reson TC4033 at 1 m off bottom, sensitivity -203 dB re: 1 µPa/V @1 m, +40 dB preamp gain, +3 dB SD722 ch.1 recorder gain, overall system sensitivity -160 dB re: 1 µPa/V @1 m
Ch. 2 hydrophone	Reson TC4034 1.5 m off bottom, sensitivity -218 dB re: 1 µPa/V @ 1 m, +40 dB preamp gain, +18 dB SD722 ch.2 recorder gain, overall system sensitivity -160 dB re: 1 µPa/V @1 m
Float line temperature loggers	All loggers sampling at 1 minute intervals • top - Aqualogger 520PT Pressure & Temperature 23-892 • 2nd top - Aqualogger 520PT Pressure & Temperature 23-889 • 3rd - Aqualogger 520T Temperature 23-860 • 4th top - Aqualogger 520T Temperature 23-931 • bottom - Aqualogger 520T Temperature 23-869

Table 4-2: Receiver system mass

Component	Mass
battery	15 kg
Casing & slings	43 kg
End-caps and recorder No. 037	19 kg
total	77 kg

The acoustic transmitter was a Chelsea Technologies CTG0052 transmitter shown on Figure 4-10 with vertical directivity shown on Figure 4-11 and transmit sensitivity shown on Figure 4-12. The transmitter was driven by a battery-powered 200 W audio amplifier with a custom-built output transformer to match the input impedance of the CTG0052 transducer. The input signal to the amplifier was provided by a HR05 digital audio recorder at 24 bit, 96 kS/s (or as it turned out, only approximately 96 kS/s). The in-water output signal at 1 m from the transmitter centre was measured (shown schematically on Figure 4-6) with a Reson TC4033 hydrophone, Reson VP2000 preamplifier, and Sound Devices SD744T digital audio recorder. This provided a simple method to determine/record the transmit signal spectrum, inclusive of transducer and amplifier characteristics. The transmitter system is summarised in Table 4-3.

Table 4-3: Transmitter system details

Item	Details
Transmitter	Chelsea Technologies CTG0052 dunking transducer S/N11-8287-001 in inverted orientation
Transmitter amplifier	35 Ah battery-powered 200 W audio power amplifier with custom matching output transformer and chain earth to the water
Transmit signal source	HR05 digital audio player – at least 0.72 s delay between pressing 'start' and replay commencing.
Hydrophone	Reson TC4033 at 1 m above transmitter centre with Reson VP2000 preamplifier
Transmitter signal recorder	Sound Devices 744T, 96kHz sampling rate, 24 bit
Transmitter pressure transducer	Unispan PT2x, S/N 2949003 sampling at 10 Hz

Directional surface wave data was obtained courtesy of Fremantle Ports for the Cottesloe Directional Wave Rider Buoy (DWRB). The sound speed profile at a number of transmission positions was sampled with a Seabird SBE 19Plus Conductivity Temperature Depth (CTD) probe (Figure 4-13).

Figure 4-10: Chelsea Technologies CTG0052 transmitter

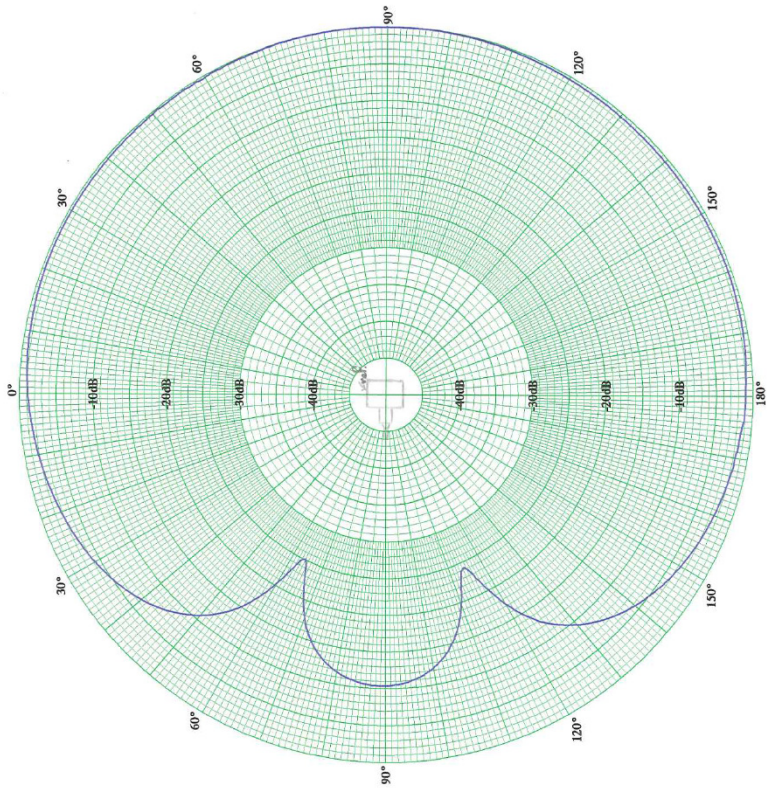

Figure 4-11: CTG0052 vertical directivity at 10 kHz (oriented on page as per in-field use, with top of graph directed towards sea surface)

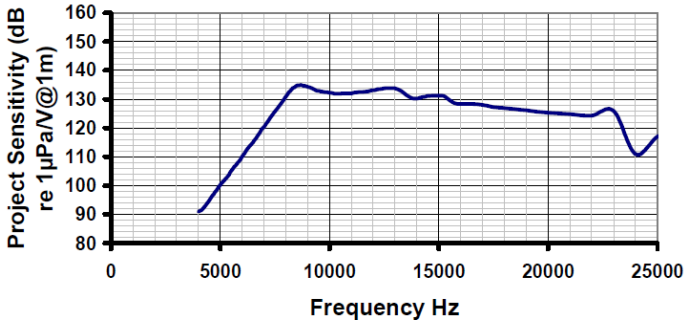

Figure 4-12: CTG0052 transmit sensitivity

Figure 4-13: Seabird SBE 19 Plus Conductivity, Temperature, Depth Probe

The vessel GPS position was logged at 1 s intervals using a Velocitek Speedpuck GPS. The vessel was fitted with pitch, heave and roll data acquisition sampling at 100 Hz by Dr Tim Gourlay, enabling the vertical motion time-history of the suspended transmitter to be calculated. This proved to be a more effective method of characterising the vertical movement of the transmitter than the pressure sampling at 8 Hz recorded by the P2Tx pressure logger positioned 1.5 m above the transmitter.

Five temperature loggers sampling at 60 second intervals were suspended from the surface float line. From inspection of the relative temperature records of these transducers it was concluded that the CTD vertical temperature profiles provided a more reliable method of determining the vertical sound speed gradient in shallow water over a relatively short period of time.

Grab samples of the bottom material were collected at some test locations using a grab sampler borrowed from the Curtin University Geology Department courtesy of Prof. Lindsay Collins. Samples from this grab indicated a consistently fine sandy silt bottom throughout the test area (Figure 4-14). Miscellaneous test equipment is summarised in Table 4-4.

Table 4-4: Miscellaneous test equipment

Item	Details
Conductivity-temperature-depth probe	Sea-Bird SBE19plus S/N. 5231 (Figure 4-13)
Bottom grab	Curtin Geology Dept. Peterson Grab (Figure 4-14)
Pitch-heave-roll monitoring system	100 Hz sampling rate (Appendix A.1)
GPS1	Humminbird CX 898 SI
GPS2	Velocitek Speedpuck S/N VT000038_20120426_062859 sampling at 1 s intervals
Fremantle Ports Directional Waverider Buoy	Datawell DWR-Mk3

Figure 4-14: Bottom grab sampling

4.2.4 Calibration and Synchronisation

Instrumentation was manually synchronised within 1 second of the clock on a laptop computer on the day prior to testing.

The planned method of space-time synchronisation was by manual marking of the GPS position coincident with starting the transmit signal recording. However this method did not consistently work as intended as the modal method for marking position with the Humminbird GPS was inadvertently used in an inconsistent manner, such that most marks proved to be time-stamped to one-minute resolution only. It was later found during post-processing that a 0.72 second lag occurred between pressing start on the HR05 digital audio player and the output signal commencing. The actual signal start time positions in the digital files were then confirmed by inspection of the waveform.

The eventual method of time-synchronising the transmitter position and transmit signal start time was approximate but reliable. This was done by relating the inspected signal start and stop times in the continuous receiver audio recordings to the Speedpuck GPS position history that was time-stamped at one second intervals. Two records of the logger touch-down position were available. One by manual GPS mark when the logger was perceived to have touched bottom as the lowering rope went slack, and secondly by inspecting the time in the receive recording when the audible impact of the logger landing on the sea-bed was recorded. These two times agreed within one second. The bottom contact time was then cross-referenced to the Speedpuck GPS record to provide an estimate of the logger position.

A relatively small estimated positional error in the GPS-inferred transmitter position of up to 0.3 m was incurred as a consequence of ignoring the signal flight-time when relating the received signal time to the transmitter GPS time. This range error is the product of the received signal time-lag (i.e. 0.66 s at maximum 1000 m range) multiplied by the maximum transmitter drift speed of 0.5 m/s. The error in positioning the logger was comprised of:

a) marking the logger resting position in 14 m water depth by GPS from the surface, estimated as 10% of the depth (+/-1.4 m);

b) the uncertain position of the receiver hydrophone depending on the unknown orientation of the logger casing (+/-0.5 m);

c) the fixed displacement, but of uncertain orientation between the canopy Speedpuck and the receiver lowering rope (+/-2.7 m, also applicable to uncertainty in the position of the transmitter at the same location); and

d) the inherent GPS relative position error (+/-10 m).

Including all factors it is estimated that the error bounds on calculated transmission ranges are approximately +/- 17.6 m [(1.4+2.7+0.5) + (0.3+10+2.7)], or 10.8 m RMS uncertainty as these factors may reasonably be considered independent.

4.2.5 Transmit signals

Determining the likely spread of signal arrival delays in advance of a field trial is uncertain, as it depends on the strength of successive multiple surface-reflected propagation paths. A flatter sea-surface will enable paths with a higher number of surface-bottom reflections to be detectable at the receiver, and vice versa.

The Bellhop model was run at a number of ranges to check the delay spread in 14m water depth representing the Cottesloe test site. The delay between the direct and single-surface-reflected paths was determined as shown in Table 4-5. In the event that the signal was too degraded after two surface bounces to enable detection, it was reasoned that the probe signal should at least be longer than the single-bounce-path delays in Table 4-5 to enable exploration of the single-surface-interacting channel delay structure.

Table 4-5: Bellhop delay in 14 m depth – single surface-reflected paths relative to direct path

Transmission Range	Surface path delay relative to direct path
50 m	15 ms
100 m	8 ms
200 m	4 ms
500 m	2 ms
1000 m	1.5 ms

Guided by this consideration, the shortest probe symbol, a 63 element spread-spectrum Pseudo-Random Binary Sequence design (PRBS), was chosen having 21 ms length. This would enable the channel response to be updated at a rate of 1/21 ms = 47.6 Hz. A binary switching frequency of 3 kHz, commonly referred to as the 'chipping' frequency, was used to achieve a 6 kHz bandwidth. The sinusoidal carrier centre-frequency was chosen at 12 kHz to enable the bandwidth to fall within the relatively even power plateau in the CTG0052 transmit characteristic (Figure 4-12). The next shortest PRBS sequence with 31 elements would have been 10.3 ms long, which was considered too short with respect to potential time-aliasing at short-range.

The signal power outside of the desired nominal 9 kHz to 15 kHz band-width was minimised by sinc-shaping the bi-polar modulated sequence (Schanze 1995), as shown in the middle graph on Figure 4-15 for the shortest 21 ms PRBS.

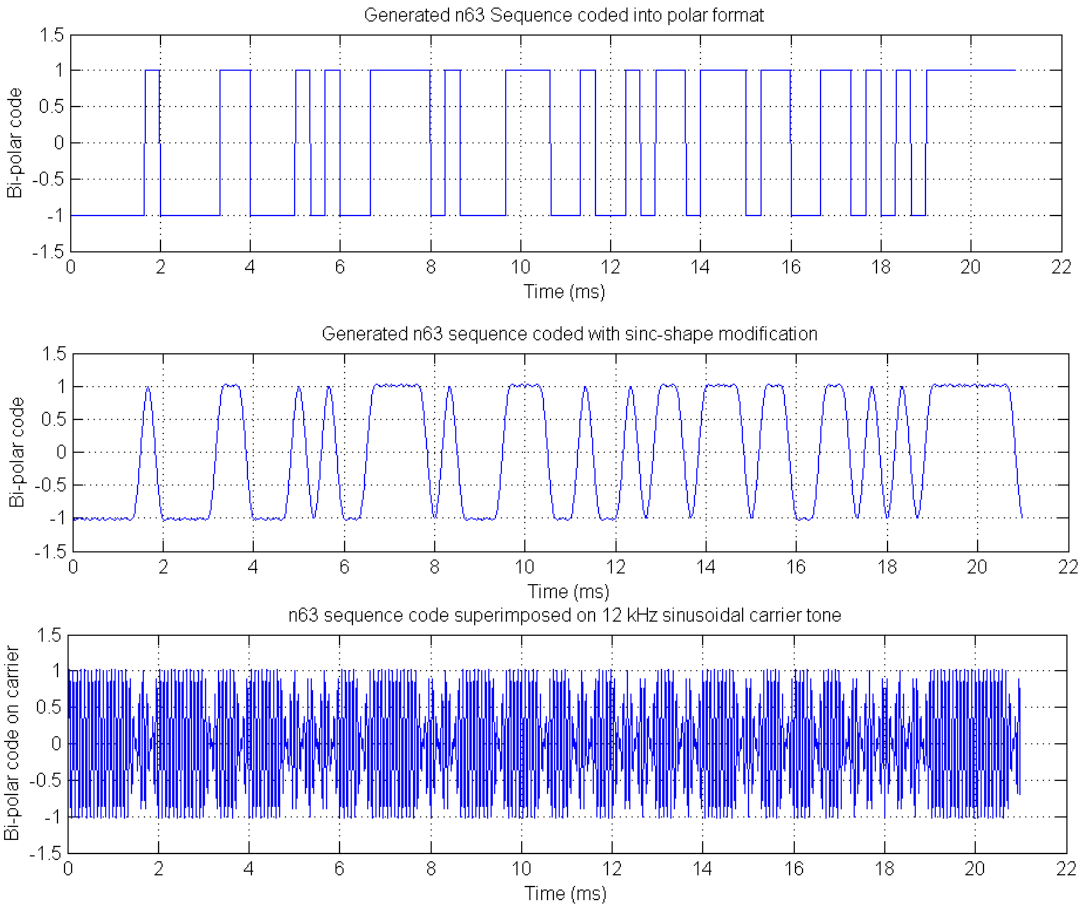

Figure 4-15: Example generation of 21 ms PRBS probe signal

In the event that the detectable delay-spread of multiple-surface interacting paths was as much as 100 ms, a much longer 511 element PRBS of 170 ms length was included in the line-up of experimental probe symbols. However this longer probe would only allow the channel response to be updated at a rate of 1/170 ms = 5.9 Hz.

The original concept for exploring the time-varying Doppler in the received signal was by time-domain Doppler search on successive received signal blocks as described in Section 2.6.6. This Doppler search objective led to the inclusion of a 4095 element PRBS symbol of 1.365 s duration in the composite experimental probe signal.

A 8-16 kHz LFM sweep of 16 ms duration was included in the composite signal due to the superior 0.125 ms delay resolution of this symbol. However in a bid to

cover all possible imagined delay spreads, the repeat interval was set at a very large 1 s. In retrospect, because post-processing indicated that the maximum detectable delay spread was of the order of 20 ms, this LFM symbol could have been repeated at a much greater frequency (e.g. 50 Hz).

A multi-tone signal comprising simultaneous 8, 10, 12, 14 and 16 kHz tones was included to enable direct indication of the Doppler frequency shifts on the whole channel response. However the desire to explore channel Doppler on specific paths or groups of paths meant this data was of lesser usefulness than PRBS and LFM symbols for which the multi-path response could be resolved in delay.

Considering the multiple objectives of rapid channel sampling with short sequences, maximizing the Doppler resolution, and spanning the possible multi-path delay spread, a composite channel probing signal was assembled comprising n63, n511 and n4095 spread PRBS and LFM symbols, and continuous multi-tones as summarised in The composition of the Cottesloe transmit signal is summarised in Table 4-7 and illustrated in the spectrogram on Figure 4-16. Pauses were added to enable the power amplifier time to cool when operating at maximum capacity.

Table 4-6. For each type of probe the number of symbol repetitions was chosen to achieve a total duration of at least 30 seconds, sufficient to robustly span the longest swell period of around 15 seconds anticipated in the 14 m deep test conditions.

The composition of the Cottesloe transmit signal is summarised in Table 4-7 and illustrated in the spectrogram on Figure 4-16. Pauses were added to enable the power amplifier time to cool when operating at maximum capacity.

Table 4-6: Cottesloe trial test signal components

Signal descriptor	Carrier frequency f_o (kHz)	Repeat period T (s)	Bandwidth B (Hz)	Delay resolution δ_τ (ms)	Doppler resolution δ_v (m/s)
n4095 PRBS	12	1.365	6000	0.16	0.094
n511 PRBS	12	0.170	6000	0.16	0.75
n63 PRBS	12	0.021	6000	0.16	6.1
CW	8, 10, 12, 14, 16	60	-	-	0.0031 to 0.00156
16 ms LFM sweep	8-16	1.0	8000	0.125	-

Table 4-7: Composition of Cottesloe probe signal (96 kHz and signed 24 bit)

Element	Sequence Duration	Repeats	Section Duration
n4095 PRBS 'M12sequence'	1.365 s	44	60.06 s
pause			30 s
n511 PRBS 'M9seqpol'	0.170 s	180	30.60 s
pause			15 s
n63 PRBS 'M6seqpol'	0.021 s	1500	31.50 s
pause			15 s
simultaneous multi-tone (8,10,12, 14,16kHz)	60 s	1	60 s
pause			30 s
8kHz to 16kHz linear sweep in 16 ms, repeated each second	1 s	30	30 s
Total			302.16 s

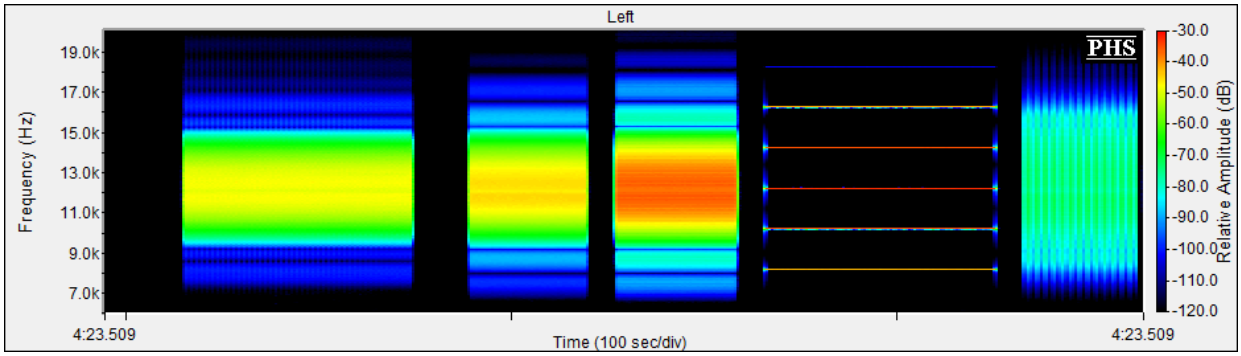

Figure 4-16: Spectrogram of composite Cottesloe probe signal

4.2.6 Summary of acoustic recordings

A summary of the transmitter and receiver recordings, and the correspondence of the start and end times for each type of probe signal to the position and movement of the transmitter and receiver are included in Appendix A.1. A visual summary of the relatively large (1.8 GB) receiver audio recordings is included in Appendix A.2. The spectrogram summary of the first such receiver recordings is shown in Figure 4-17, which represents the channel 1 TC4033 hydrophone positioned 1 m off the bottom.

The first partial transmission evident on the far left of Figure 4-17 was preliminary, such that the noise evident from a passing ship was of no consequence. The remainder of the received signal transmissions indicate an

absence of noise at levels that would interfere with cross-correlation of transmit and receive signals in the frequency band of interest. The fourth transmission sequence on Figure 4-17 shows the spectral replication effect of signal overload at the receiver at short range.

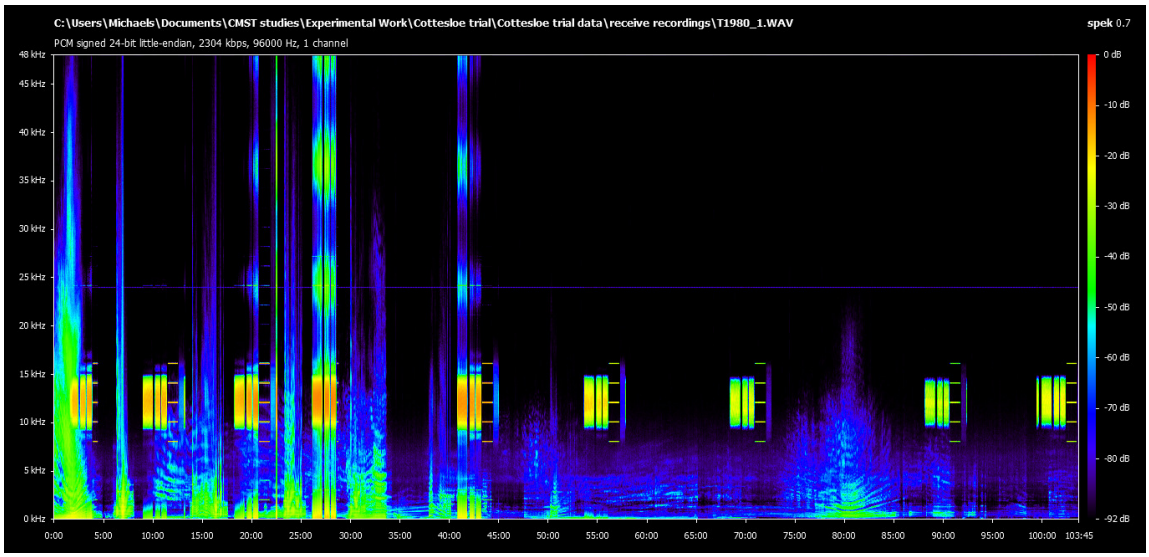

Figure 4-17: Summary 104 minute long 0-48 kHz spectrogram for receiver channel-1file T1980_1.wav

An example spectrogram for the second channel of the receiver is included in Appendix A.2 (Figure A-4), corresponding to the TC4034 hydrophone positioned 1.5 m off the bottom. This spectrogram shows approximately 10 dB higher noise floor across the spectrum.

4.2.7 Sound speed profile

The measured sound speed profiles indicated slight warming of the surface waters over the period of the experiment, leading to a maximum downward refracting sound speed differential within the profile of approximately 2.4 m/s by 1:35 pm.

The correspondence between the sound speed profiles and the signal transmissions is included in the data summary in Appendix A.1, with the sound speed profiles included in Appendix A.3.

Whilst the degree of speed stratification was initially thought to be of little consequence, it was found during flat-surface ray-path modelling at 500 m transmission range (using the profile from CTD cast 3 at 10:33 am as illustrated on Figure 4-18) that refraction was sufficient for the direct path from the 10 m deep transmitter to 12.5 m deep receiver to be precluded. This cast was done

approximately 1 km distant from the receiver. Modelling was done in the context of simulating the experimental transmission of transmit signal T08 n63 PRBS at 10:47 am. This conclusion remained even when the launch angle resolution was made much finer (the number of launch rays between +/- 80^{o} increased from 1601 to 16001). When ray-modelling was replicated using the next CTD cast, Cast 4, 43 minutes later as shown on Figure 4-19, the direct path existed in ray-modelling. Cast 4 was made within 100 m of the receiver. The uncertainty about the direct path from modelling is mirrored to some extent in the channel probe response for the same range (Figure 4-24), where the first arrival representing the direct and bottom reflection paths appears somewhat weakened.

Considering the short time interval of 43 minutes between Cast 3 and Cast 4, and the approximate 1 km separation between these casts, it is apparent that there was significant spatial variation in the sound speed profile. Given the relatively shallow sea-bed plateau of the test site (Figure 4-4) in proximity to the deeper shipping channel and other deeper waters nearby, it is perhaps not surprising that there would be significant spatial variation in temperature profile.

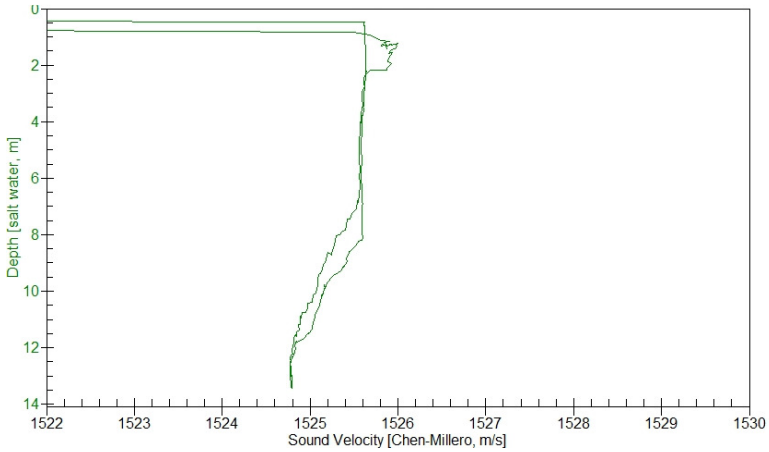

Figure 4-18: Sound Speed Profile CTD Cast 3– 10:33 am

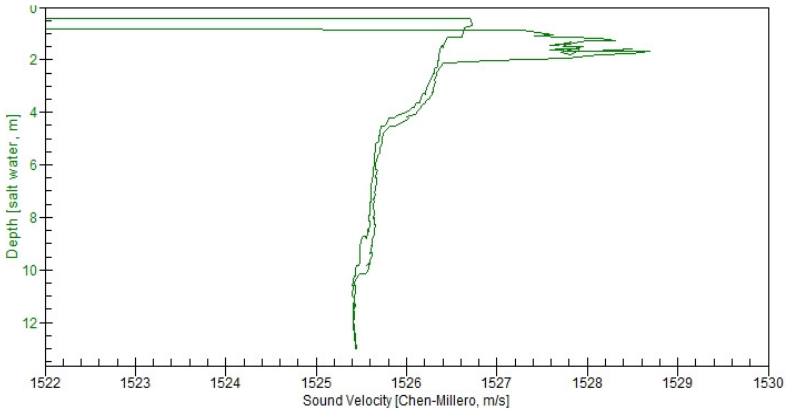

Figure 4-19: Sound Speed Profile CTD Cast 4 – 11:16 am

4.2.8 Surface wave records

The experimental ocean surface consisted of low swell and sea in the morning accompanied by light breezes, with the sea diminishing further by early afternoon accompanied by still air. The conditions were favourable for experimentally observing multiple-surface reflected path arrivals.

The sea surface at 9:32 am, approximately 15 minutes after the commencement of signal transmissions is illustrated in the top image of Figure 4-20. The centre image at 12:40 pm illustrates the surface during still-air conditions approximately 80 minutes before the last transmission. The bottom image shows slightly increased high-frequency waves approximately one hour later after arrival of a light afternoon breeze.

Figure 4-20: Experimental sea surfaces - morning (top) at 9:52 am and afternoon (middle) at 12:40 pm with Dr Alec Duncan taking CTD profiles, and 1:41 pm (bottom)

The Cottesloe DWRB samples the buoy motions each 0.78 s and produces a spectral density from a buffer of 2048 samples (25 minute span) each 15 minutes. The derived surface spectral densities in Figure 4-21 have been averaged from 8 such spectra over successive 2 hour periods, (or the equivalent of approximately 480 x 15 s swell periods) to observe the trend in the surface spectrum over the experimental hours between 9 am and 2 pm.

The dynamic cut-off frequency of the DWRB at approximately 3.7 radians/s, is notable on Figure 4-21 just below the 4.03 radian/s Nyquist frequency. The top graph shows some progressive reduction in the high-frequency sea spectrum with time, however much of the surface texture contrast in the photographic record is of too high a frequency to be measurable by the DWRB.

The swell spectrum in the 13 m-14 m deep test area would differ slightly from that at the DWRB which is nominally located in 17 m water depth.

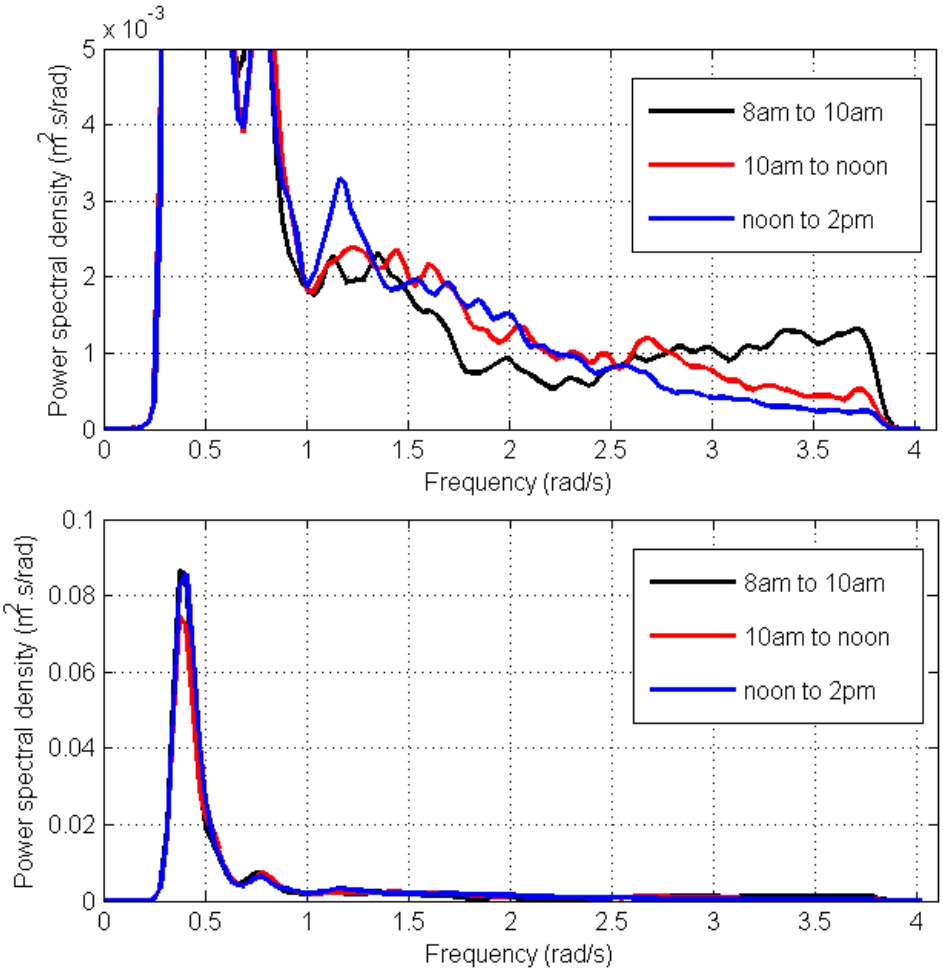

Figure 4-21: Experimental surface wave spectra for Cottesloe DWRB illustrating the sea spectrum (top, with x 20 amplitude scale magnification), and swell spectrum detail (bottom)

The quarter-hourly data summary supplied by Fremantle Ports that show wave height and direction statistics spanning the test period are shown on Figure 4-22. The split between swell and sea in the supplied DWRB data is defined by a wave period of 8 s. The changes in high-frequency surface wave texture observable on Figure 4-20 are not observable as a change in the significant wave height of the sea (red) in the top graph of Figure 4-22.

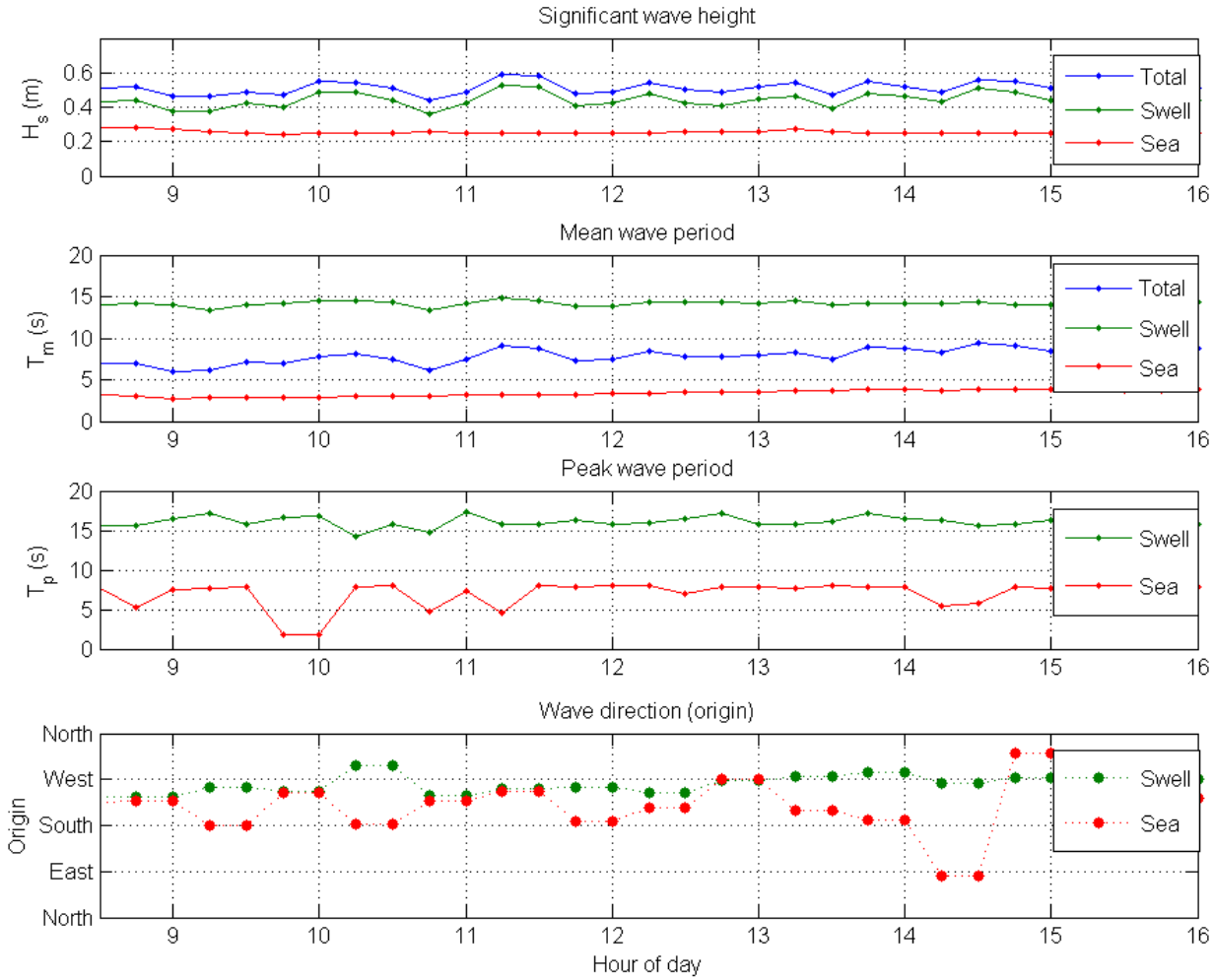

Figure 4-22: Quarter-hourly surface wave summary data for duration of trial from Cottesloe DWRB (data source: Fremantle Ports)

4.2.9 Wind conditions

The nearest meteorological station relevant to the test location is Station 009193 on Rottnest Island at elevation of 43.1 m above sea level. The wind speed and direction records for the experimental period are shown on Figure 4-23. The estimated equivalent wind speed at 2 m height was calculated from the measured data at 43 m height using the over-sea correction of Eq.(4-1) (Hsu, Meindl, and Gilhousen 1994).

$$u = u_r \left(\frac{z}{z_r}\right)^{0.11} \tag{4-1}$$

Dr Tim Gourlay made notes "wind initially 10-12 knots ENE (5-6 m/s), died out by 1100". After almost two hours of still air conditions the commencement of a light breeze was noted at 12:55 pm, estimated an hour later at 4-5 knots (2-3 m/s).

The observed conditions are similar to the estimated levels at 2 m height based on the elevated Rottnest Island weather station, which also showed a wind-speed minima occurring at 11 am.

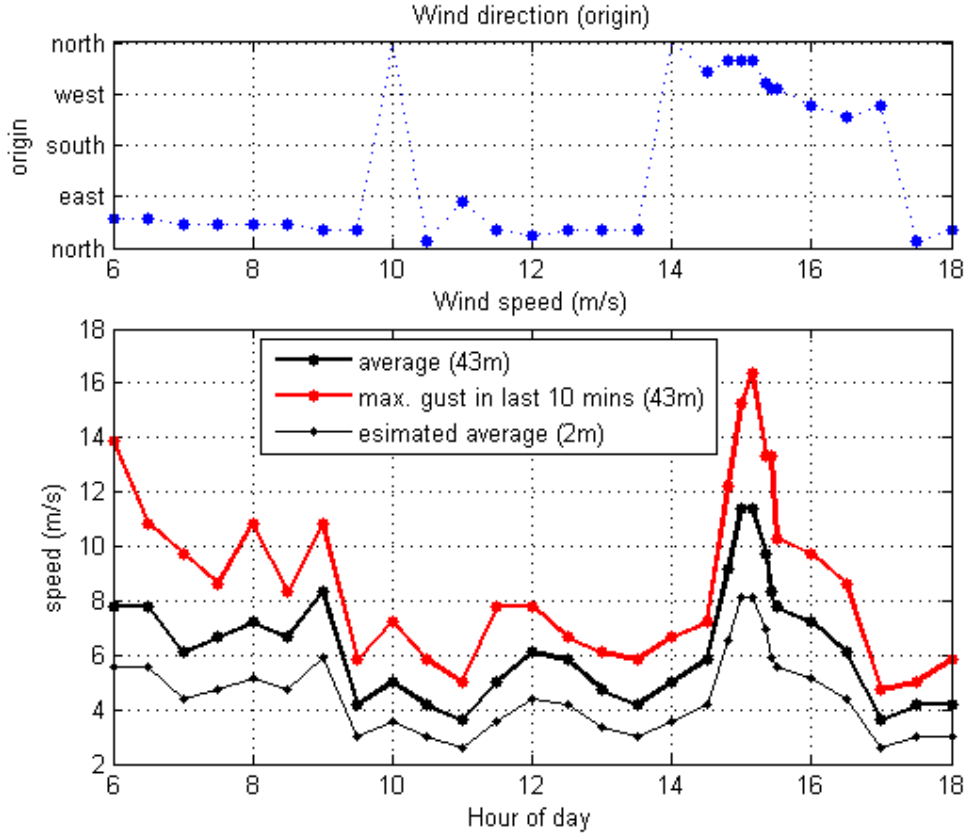

Figure 4-23: Wind data for Rottnest Is. met. station 43 m above sea level – 28/4/2012

4.3 Cottesloe channel probing results

4.3.1 Introduction

The experimental channel response was calculated by post-processing the recorded transmit and receive signals by correlative channel probing as described in Section 2.6.

The channel Doppler response was investigated both by a time-domain resampling Doppler search method on successive received PRBS blocks, and also

by Fourier transform of the channel impulse response $h(t,\tau)$with respect to time t, to generate an experimental estimate of the frequency-domain Doppler-delay spreading function. The former method was helpful in correctly detecting the relatively slow-changing Doppler due to aspects of the transmitter movement, whereas the latter method is needed to explore rapidly changing Doppler associated with the moving sea surface.

4.3.2 Channel probing results

The shortest 21 ms PRBS probe symbol was the most useful for generating an estimate of the channel response. The results presented therefore almost exclusively relate to this probe signal.

Figure 4-24 shows the experimental probe response at ranges of 110 m, 500 m and 1010 m, with alignment of responses on the earliest path arrival. The spreading functions corresponding to Figure 4-24 and inclusive of the effects of drift are presented in Figure 4-25. The corresponding delay power profiles are presented on Figure 4-26.

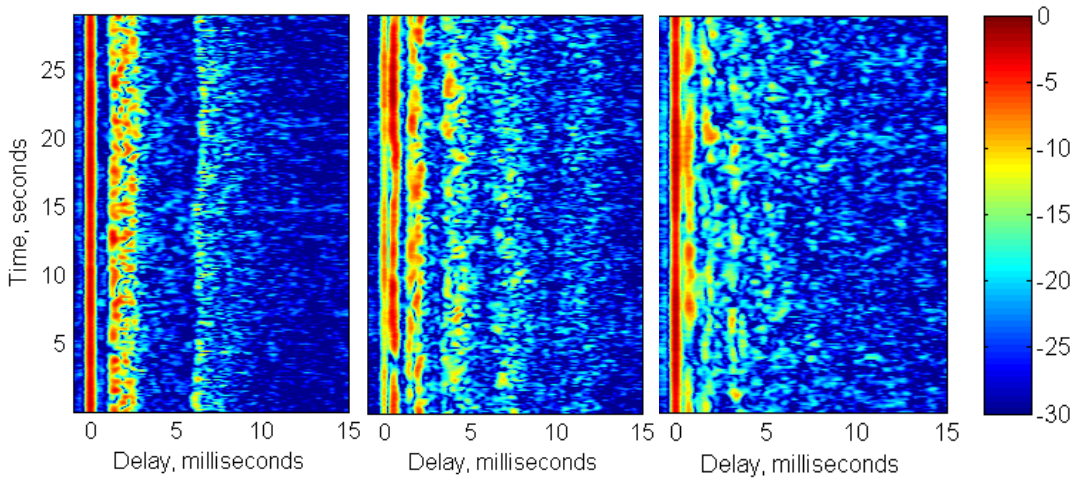

Figure 4-24: Measured channel response, $20\log\left|\hat{h}(t,\tau)\right|$, (dB) using 21 ms PRBS probe at 110 m range (left), 500 m range (centre), and 1010 m range (right)

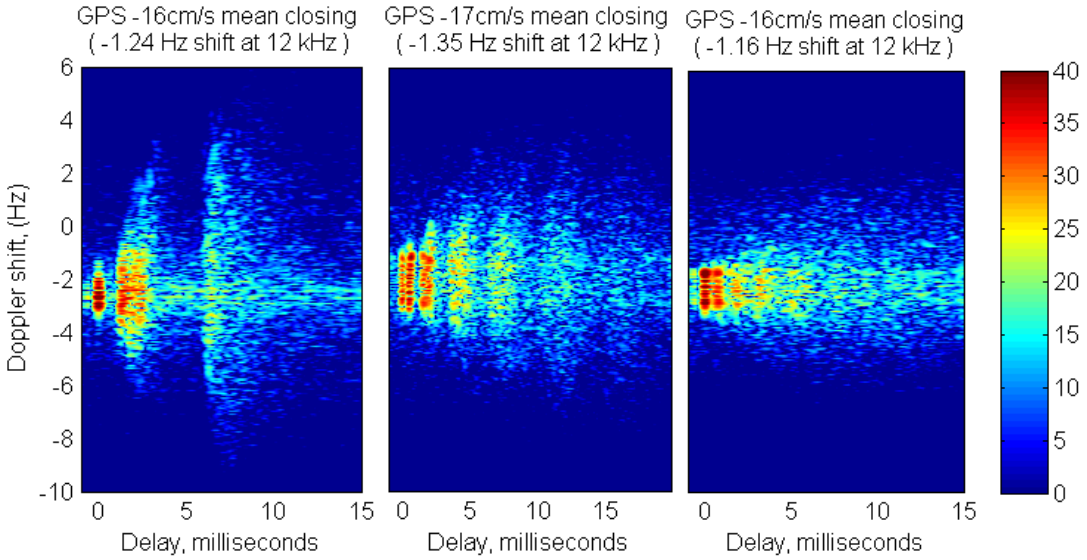

Figure 4-25: Measured channel spreading function, $20\log\left|\hat{S}(\nu,\tau)\right|$ (dB), $f_0 = 12$ kHz, 110 m range (left), 500 m range (centre), and 1010 m range (right)

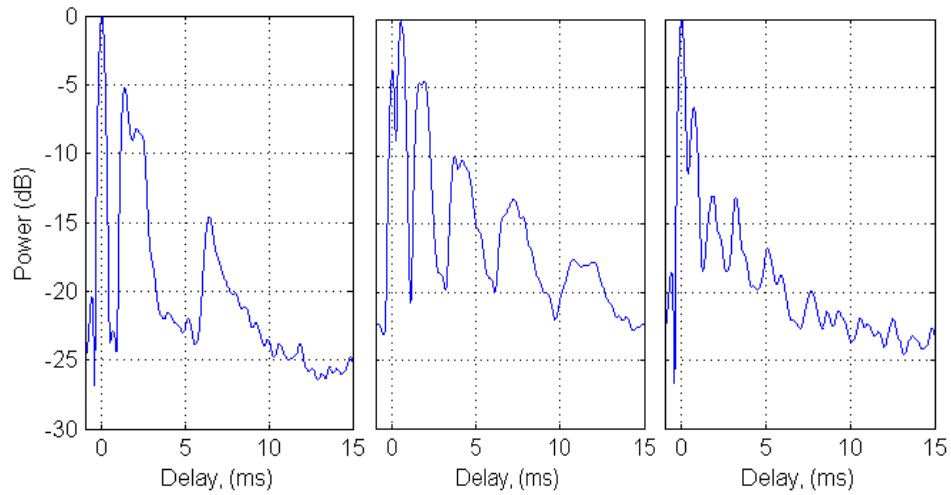

Figure 4-26: Measured channel response power versus delay, $10\log\left|\hat{P}(\tau)\right|$ (dB) using 21 ms PRBS probe over 30 s, 110 m range (left), 500 m range (centre), and 1010 m range (right)

The apparent average Doppler indicated by the spreading function has contributions from both the small sampling rate deviation between the transmitter and receiver, and the average closing rate. For this experiment the autocorrelation of the recorded transmit signal showed that the n63 PRBS signal appeared to be 2000 samples long to the nearest sample, when it was actually constructed in Matlab as 2016 samples long. The difference can be accounted by an approximate 0.8% higher actual sample replay rate of the HR05 transmitter audio player relative to the SD722 recorder. The 0.5 sample uncertainty in the length of the 2000 sample n63 PRBS block translates to a 'phantom' average drift velocity uncertainty of +/-38 cm/s (or +/-3 Hz). However without a test trial over a fixed range it is not possible to exactly establish the exact relative signal rate, and therefore the exact average relative motion from Doppler analysis.

In data analysis it was found that the 'phantom' average drift Doppler caused by differential sampling rates was typically as large, or larger, than the average drift velocities (and corresponding frequency shifts) determined from GPS records.

It is worth noting that in the subsequent Rottnest trial, where all digital audio players and recorders were of the same make and higher quality, the large discrepancy between the design and actual transmit probe sample length vanished.

The channel response approximating that which would be obtained with fixed transmitter and receiver positions has been calculated by post-processing the experimental results with a drifting transmitter for each range as described in Section 2.6.7, so that the Doppler spreading due to surface waves only can be more clearly indicated. The approximate fixed channel responses are presented in Figure 4-27.

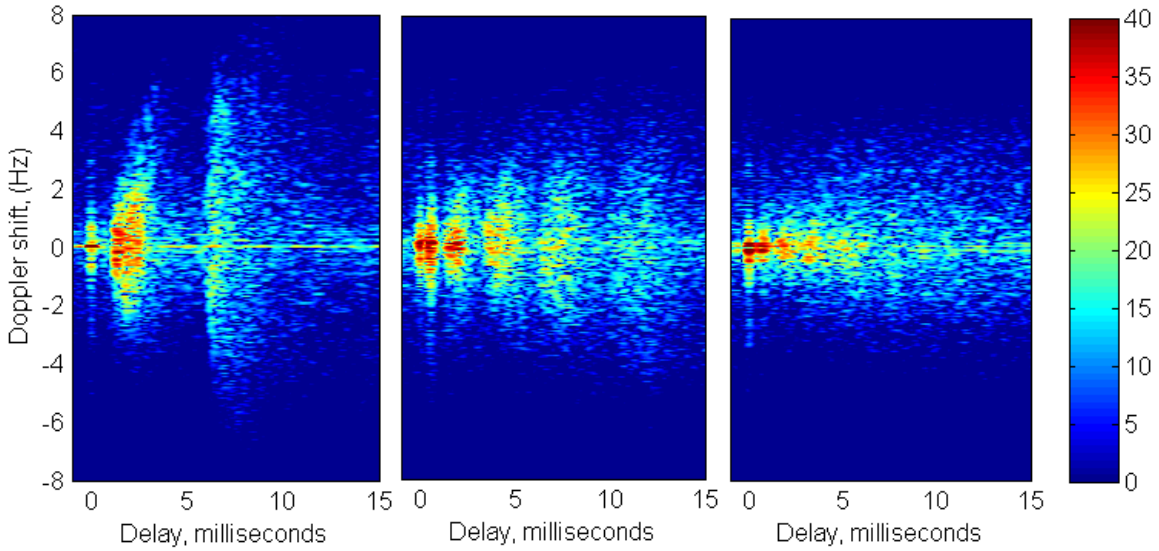

Figure 4-27: Measured channel spreading function with approximate resampling to negate transmitter drift Doppler, $20\log\left|\hat{S}(\nu,\tau)\right|$ (dB), $f_0 = 12$ kHz,110 m range (left), 500 m range (centre), and 1010 m range (right)

The results of the time-domain Doppler search on the 1.4 s long PRBS symbol are shown in the bottom frames of Figure 4-28. This plot of the response as a function of time and Doppler, $\hat{h}(t,\mathrm{v})$, was helpful in confirming the oscillatory relative transmitter-receiver movement related to swell action. The same time-varying Doppler information, but with much finer time resolution is obtainable indirectly from the block correlation alignment record obtained in the previous results with the short 21 ms PRBS probe.

The top frame of Figure 4-28 shows the response $\hat{h}(t,\tau)$at 117 m range for the same long PRBS probe. Comparing the left image of Figure 4-24, probed by a much shorter 21 ms PRBS, and the right image of Figure 4-28 probed with a much longer1.4 s PRBS it may be observed that the longer PRBS probe is more susceptible to Doppler distortion, causing lower correlation output.

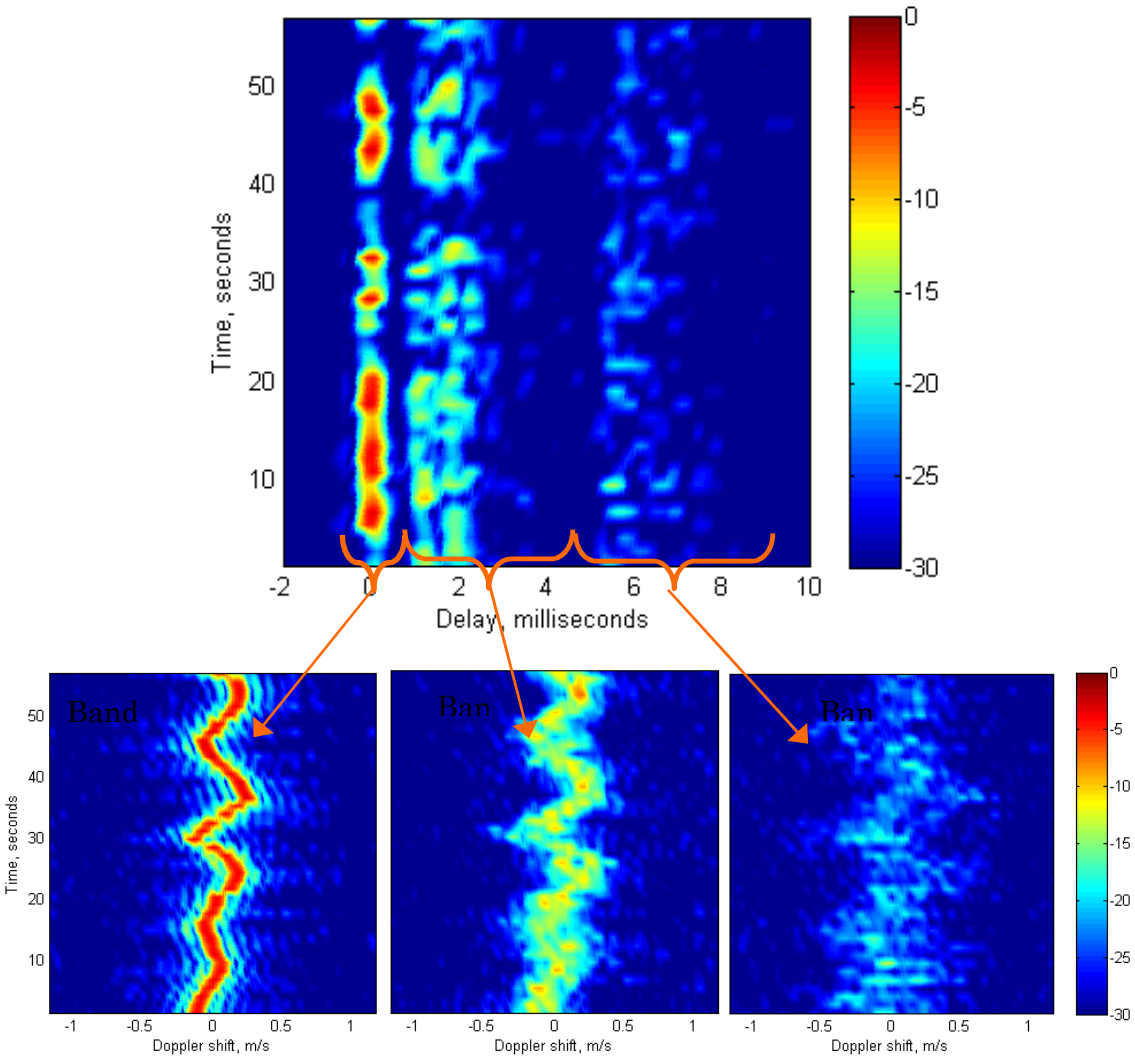

Figure 4-28: (top) Experimental channel response versus time and delay, $20\log|\hat{h}(t,\tau)|$ (dB), (bottom left) Experimental channel response versus time and Doppler, $20\log|\hat{h}(t,\nu)|$, (dB), for 1st arrival group, (centre-bottom) 2nd arrival group of 4 single-surface-bounce paths, and (bottom-right) 3rd arrival group of 4 double-surface-bounce paths– calculated from 43 sequential correlations of 1.4 s PRBS probe

4.3.3 Preliminary analysis of Cottesloe probe results

In this section the experimental results have been analysed to gain insight and explain the observed delay response and Doppler spreading. This work was informative at commencement of channel simulation development.

The conceptual origins of the time-varying delay and Doppler frequency spreading of the received signal imparted by the moving sea-surface are shown schematically in Figure 4-29.

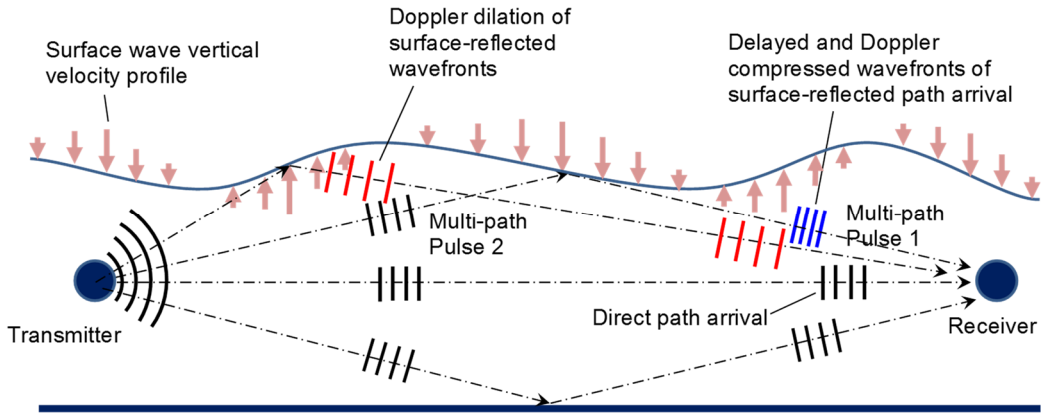

Figure 4-29: Conceptual signal Doppler and path delay

The other experimental sources of Doppler associated with transmitter motions are shown on Figure 4-30. It may be seen that these motions resolve differently into transmission paths depending on the path grazing angle.

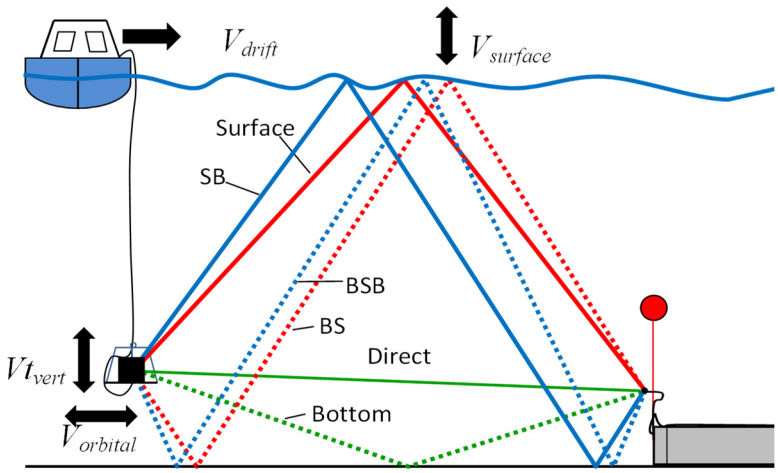

Figure 4-30: Sources of Doppler in Cottesloe experiment

The experimental sea surface parameters for this analysis are summarised in Table 4-8, and the sea surface appearance for the results presented was as for the top image of Figure 4-20.

Table 4-8: Surface wave summary for Cottesloe probe results

Wave type	Significant height H_s	Mean period T_m	Mean frequency
Swell	0.4 m	13-14 s	0.074 Hz
Sea	0.25 m	3 s	0.33 Hz

The experimental Doppler includes contributions from sea-surface motion, wave orbital motion coupling to the suspended transmitter and also possibly the float-

elevated receiver hydrophone, and transmitter movement generated by vessel rolling and drift. These components were resolved into the idealised flat-surface acoustic transmission paths, then combined to provide a Doppler-velocity interpretation of the Doppler indicated by the experimental spreading functions $\hat{S}(\nu, \tau)$.

In combining the Doppler velocity components to create a net Doppler estimate the slow-changing contributions (drift and swell orbital motion) were treated as constant values, whereas the rapidly changing Doppler contributions from sea-surface reflections and vertical transmitter oscillation were quantified as 3σ estimates where σ is the standard deviation. Successive surface reflections on multiple-surface-bounce paths, and vertical transmitter oscillations were treated as independent processes. Transmission path length elongation and contraction from vertical variation of surface reflections is quantified. The potential variable in-path Doppler component for paths with a horizontally travelling reflection point (associated with swell) are discussed later, but not included in the total Doppler estimate.

The average closing speed V_{drift} was calculated from GPS data. This speed ranged from 0.11 m/s to 0.19 m/s. This relative motion contributes almost the same Doppler to all transmission paths as per Eq.(4-2), where θ is the path launch angle from horizontal.

$$V_d = V_{drift} cos\theta \tag{4-2}$$

At the depth of the transmitter the horizontal component of swell orbital motion was significant, however the contribution from wind-waves did not extend below mid-depth. If it is conservatively assumed that the transmitter is completely compliant horizontally, the relative horizontal orbital motion $V_{orbital}$was calculated at up to 0.17 m/s for the Table 4-8 data. This relative motion contributes almost the same Doppler to all transmission paths as per Eq.(4-3).

$$V_o = V_{orbital} cos\theta \tag{4-3}$$

The maximum vertical surface velocity $V_{surface}$ at the point of surface reflections was estimated based on the 3σ wave height for swell and sea by Eq.(4-4), providing estimates of 0.39 m/s for the H_s = 0.25m sea-waves, and 0.13 m/s for the H_s = 0.4 m swell. The higher estimate obtained from the wind-waves was used as an upper

bound estimate for $V_{surface}$. The vertical surface motion from a single surface reflection can be resolved in the direction of an idealised surface-reflected path as per Eq.(4-5) assuming a sinusoidal vertical motion.

$$V_{surface} = 3\pi H_s/2T_m \tag{4-4}$$

$$V_s = 2V_{surface} sin\theta \tag{4-5}$$

The vertical velocity spectral density of the transmitter in Figure 4-31 was calculated from the combined vessel pitch, heave and roll data by averaging 18 x 160 s blocks of data with Hanning windowing. This data shows a peak at 0.07 Hz that corresponded approximately to the DWRB swell data, and peaks at frequencies similar to the DWRB data for wind-driven surface waves. The vertical root-mean-square (RMS) velocity from the data in the 0-2 Hz range was 0.13 m/s, providing a 3σ estimate of 0.39 m/s RMS for the vertical transmitter motion. The vertical transmitter velocity $V_{t,vert}$ can be resolved in the direction of all surface and/or bottom reflected transmission paths as per Eq.(4-6).

$$V_t = V_{t,vert} sin\theta \tag{4-6}$$

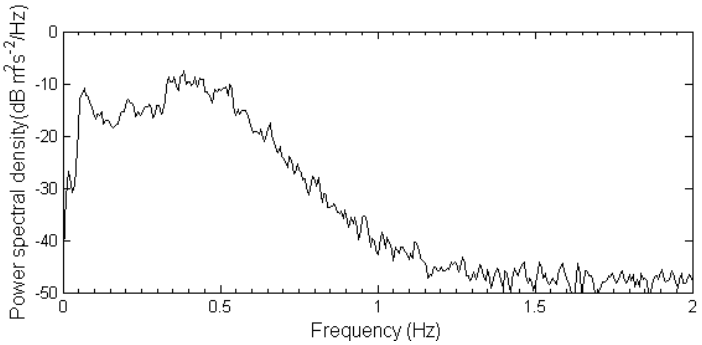

Figure 4-31: Transmitter vertical velocity power spectrum

An estimate of the 3σ total Doppler for a path involving n_b surface bounces was calculated from components assuming independence of stochastic processes as per Eq.(4-7).

$$V_{total} = V_d + V_o + \sqrt{{V_t}^2 + n_b {V_s}^2} \tag{4-7}$$

The estimated Doppler components are compared in Figure 4-32 for ray paths within 10 ms delay relative to the direct path, for the example test distances of 110 m, 500 m, and 1007 m. The experimental drift rate varied at each distance. This analysis indicates that the potential maximum in-path Doppler increases significantly with the number of surface bounces, and with decreasing range.

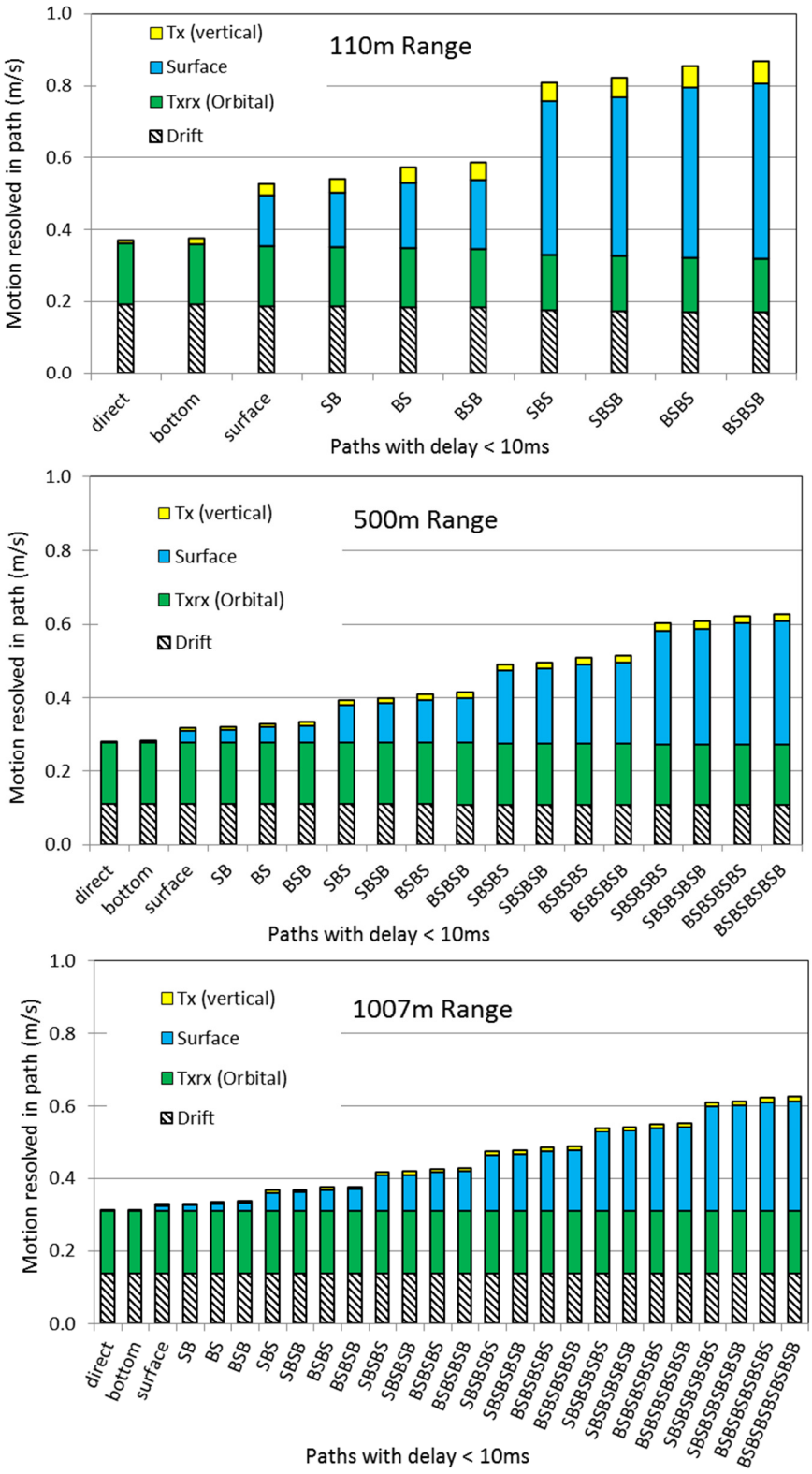

Figure 4-32: 3σ estimates of maximum in-path Doppler velocity shifts for path delays < 10 ms

The channel Doppler may be quantified either as a velocity shift v or equivalent carrier-dependent frequency shift ν as linked by Eq.(4-8), where positive ν represents an equivalent velocity shift that contracts the propagation path length.

$$\nu/f_0 = \mathrm{v}/c \tag{4-8}$$

The experimental spreading functions corresponding to the 110 m, 500 m and 1007 m ranges are presented in Figure 4-33. These are over-plotted with white markers representing the 3σ Doppler estimates from geometrical consideration as per Figure 4-32, making use of the correspondence between Doppler frequency shift and velocity shift in Eq.(4-8) to present a secondary Doppler axis on the right side of each graph in the units of m/s. The corresponding delays of the white markers relate to an idealised iso-speed waveguide with parallel flat boundaries. In reality the delays will vary with the path elongation and contraction associated with vertical surface movement, and transverse movement of reflection points linked to travelling surface waves. The variation in actual delay of surface-interacting paths is indicated by the notable delay-spreading (x-axis) evident in the spreading function compared to the idealised discrete delay points.

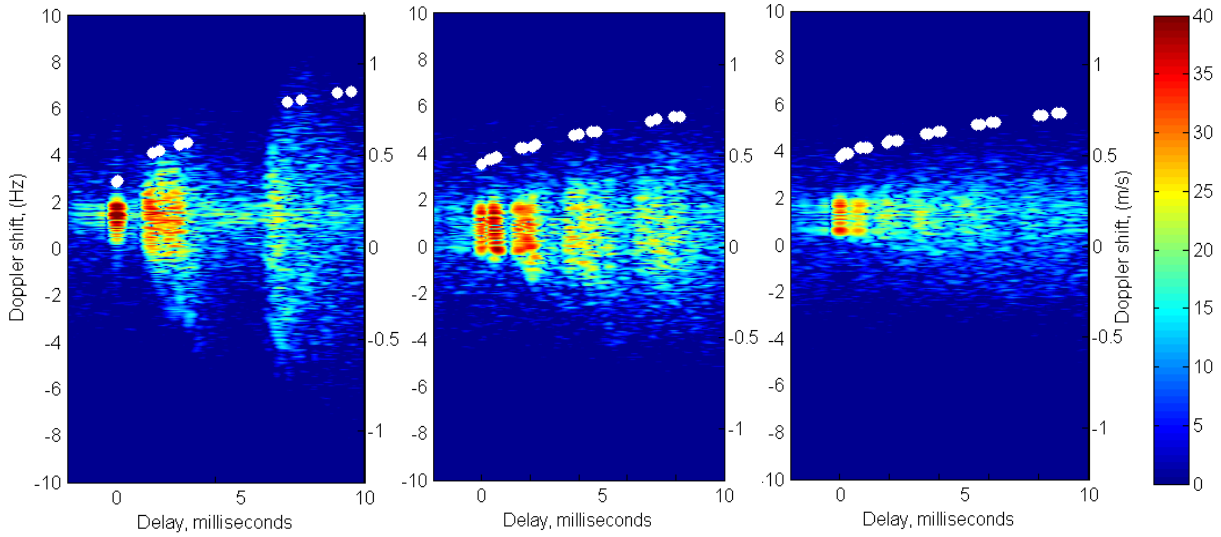

Figure 4-33: Experimental spreading functions, $20\log\left|\hat{S}(\nu,\tau)\right|$ (dB), over-plotted with 3σ estimates of maximum in-path Doppler frequency and velocity shifts, $f_0 = 12$ kHz, 110 m range (left), 500 m range (centre), and 1007 m range (right)

Notwithstanding the uncertainty in the mean Doppler indicated by the experimental spreading function the 3σ estimates of total Doppler velocity shift from the above simple treatment of surface wave movement readily account for the scale of Doppler shifted arrivals within 25 dB - 30 dB of the strongest arrival at all delays. Thus the interchangeable interpretation of Doppler as both a velocity shift and frequency shift is considered helpful to interpretation of the spreading function Doppler.

The Doppler caused by a horizontally travelling reflection point varies considerably depending on the horizontal position of the moving reflection point relative to the transmitter and receiver. Consider the two single-reflected paths indicated on Figure 2-10. The path shown in black has reflection point 'A' travelling to the right at v_{swell}. At position 'A' the two chords of the path are equal length, and the instantaneous rate of elongation of this path is zero. The red path is sketched to represent the black path at a later time when the reflection point has shifted to position 'B' directly above the receiver. At position 'B' the rate of path elongation is $v_{swell}\cos\theta$, or approximately v_{swell} for the shallow experimental channels. If the reflection point continued to the right of 'B' into backscatter, in the limit the rate of path elongation could approach $2v_{swell}$.

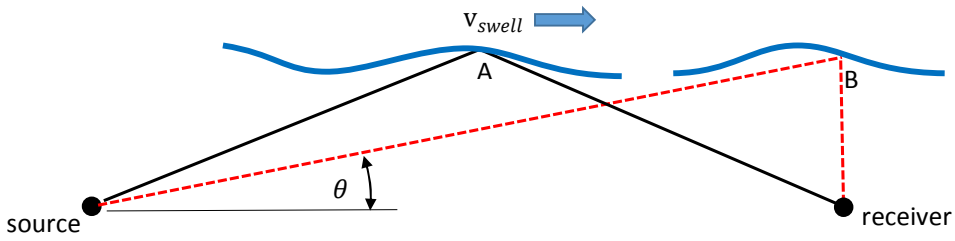

Figure 4-34: Consideration of in-path Doppler from travelling reflection point

In the shallow water of the experiment the swell speed was of the order of 10 m/s. Thus it may be seen that subject to the existence of a surface shape supporting a coherent reflected path at 'B', the time-varying Doppler on micro-paths having a travelling reflection point could conceivably approach an order of magnitude higher than other geometric sources of experimental Doppler. This Doppler may vary from a positive maximum of the order of 10 m/s through zero to a negative maximum of the same order, depending on the swell direction relative to the transmission alignment.

The coherence of the experimental response was explored for the repeated 21 ms PRBS probe sequence to investigate the effect of range and multiple surface bounces on path coherence. Results corresponding to the 110 m, 500 m and 1007 m channels are presented in Figure 4-35. Markers on the figures indicate the calculated coherence at 21 ms intervals. The results for each channel represent the average of ten three-second sub-blocks of the full 30 s sample. The normalised coherence $\hat{C}(\Delta t)$ of each sub-block is calculated by Eq.(2-65) then averaged.

The results demonstrate high coherence for the first arrival group (combined direct and bottom path) at all ranges. The coherence of subsequent path arrivals degrades as would be expected after additional rough boundary interactions. However the coherence of later arrivals generally improves with range, consistent with the geometrical trend greater phase coherence and reduced in-path Doppler from surface movement as range increases and the grazing angles reduce.

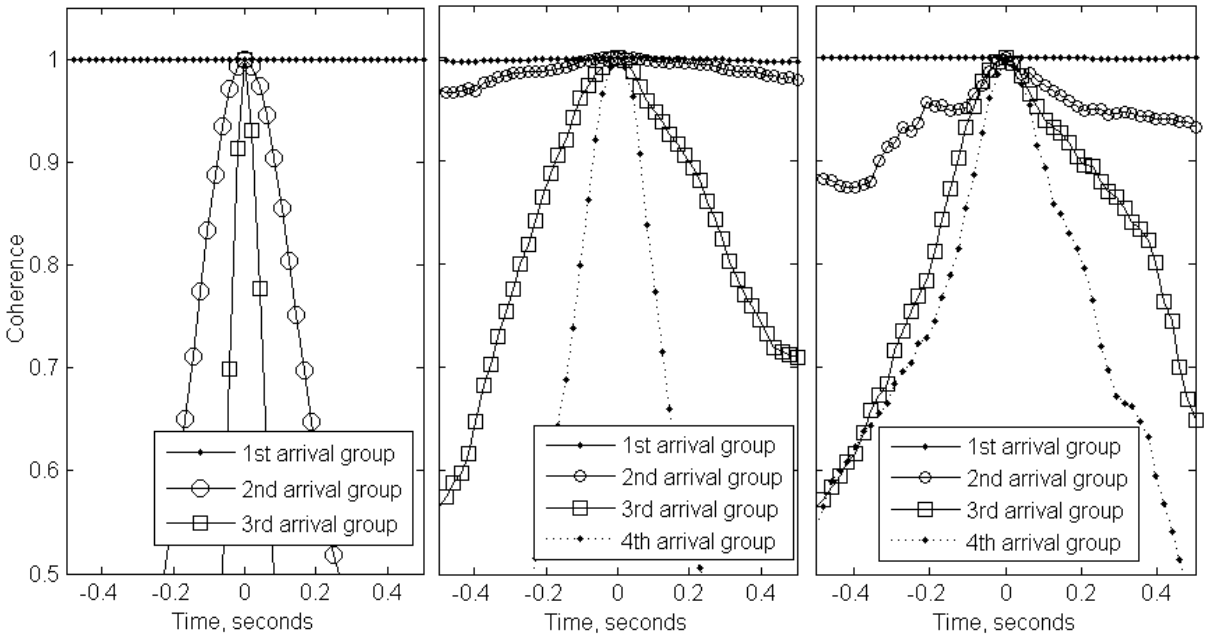

Figure 4-35: Experimental channel coherence, $\hat{C}(\Delta t)$, 110 m range (left), 500 m range (centre), and 1007 m range (right)

4.3.4 Summary of results from Cottesloe trial

This preliminary analysis was conducted to ascertain the significant sources and scale of channel Doppler spreading and delay spreading that needed to be incorporated into a dynamic channel simulation. The analysis showed that the estimation of maximum channel Doppler in the units of equivalent velocity, from simplified consideration of surface movement and relative motion is a useful approach to explaining the trends in experimental Doppler indicated by the spreading function.

Whilst the Doppler resolution achieved by direct Doppler search in the time domain was relatively low compared to that achievable by frequency-domain analysis of the response history, the coarse Doppler time history provided by this approach was complementary to the spreading function in that it clarified the origins of Doppler associated with strong channel responses.

Coherence analysis indicated that coherence of later path arrivals improves with increased transmission range, consistent with the geometrical trend of diminished in-path scattering and Doppler contributions from the moving surface as range increases.

4.4 Rottnest trial description

4.4.1 Rottnest trial site

The second channel probing site was selected south-west of Rottnest Island, along the 50 metre depth contour in the vicinity of the Rottnest Island DWRB (Figure 4-36). Trials at this site were conducted on 1st December 2012. Nominal transmission ranges were 125 m, 250 m, 500 m, 1 km, 2 km, 4 km, 6 km, 8 km and 10 km.

Permission to install a sea-bed recorder with surface retrieval float at this site during daylight hours was obtained from the WA Department of Transport. The Royal Australian Navy was notified of proposed date and timing of acoustic channel probing tests.

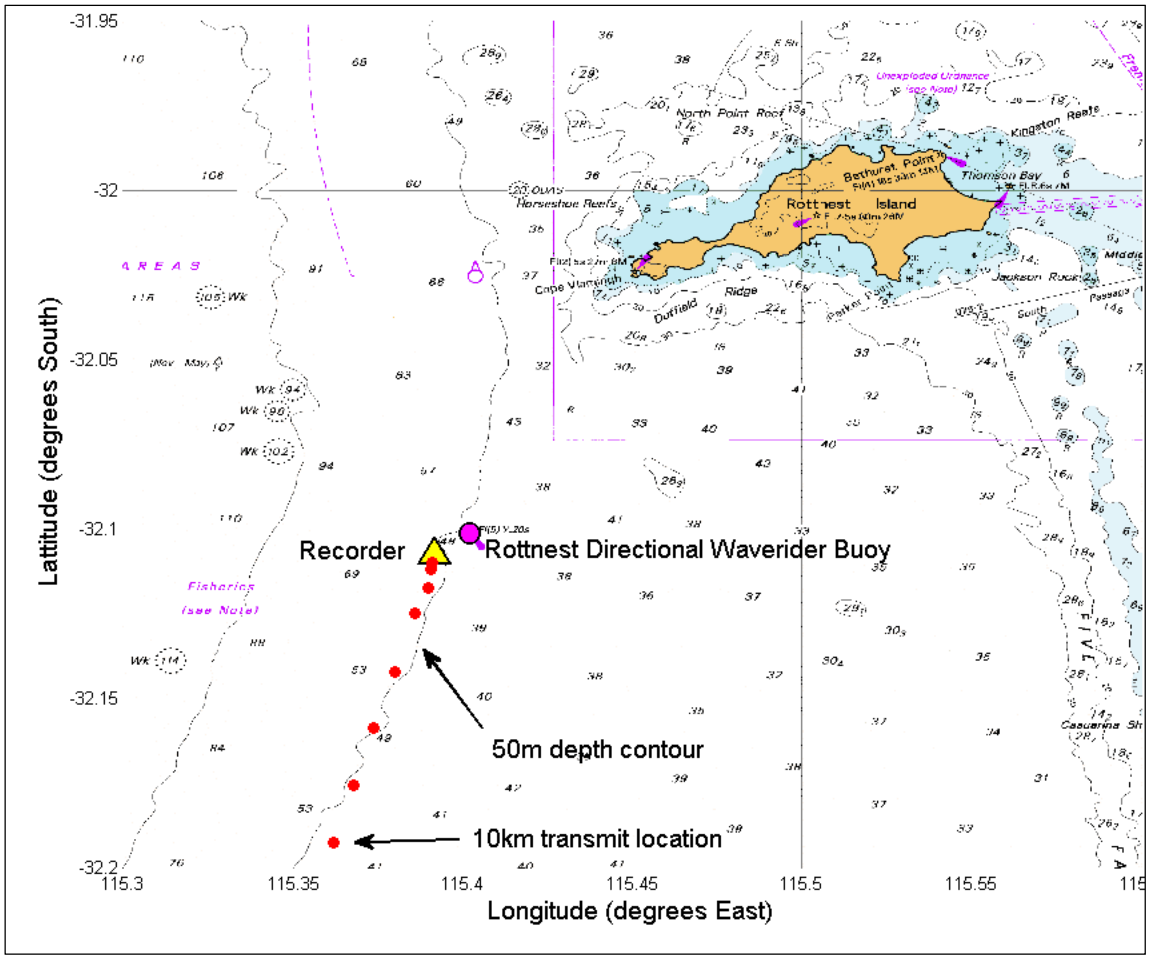

Figure 4-36: Planned transmit and record locations relative to Rottnest Island (DWRB) (base map source- Lancelin to Cape Peron 1:150 000 Aus00754)

A unique consideration in choosing the site for the sea-bed recorder was avoidance of known and unknown wrecks in the Rottnest Deepwater Graveyard (Green

2011). The proximity of the sea-bed recorder to this area is illustrated on Figure 4-37.

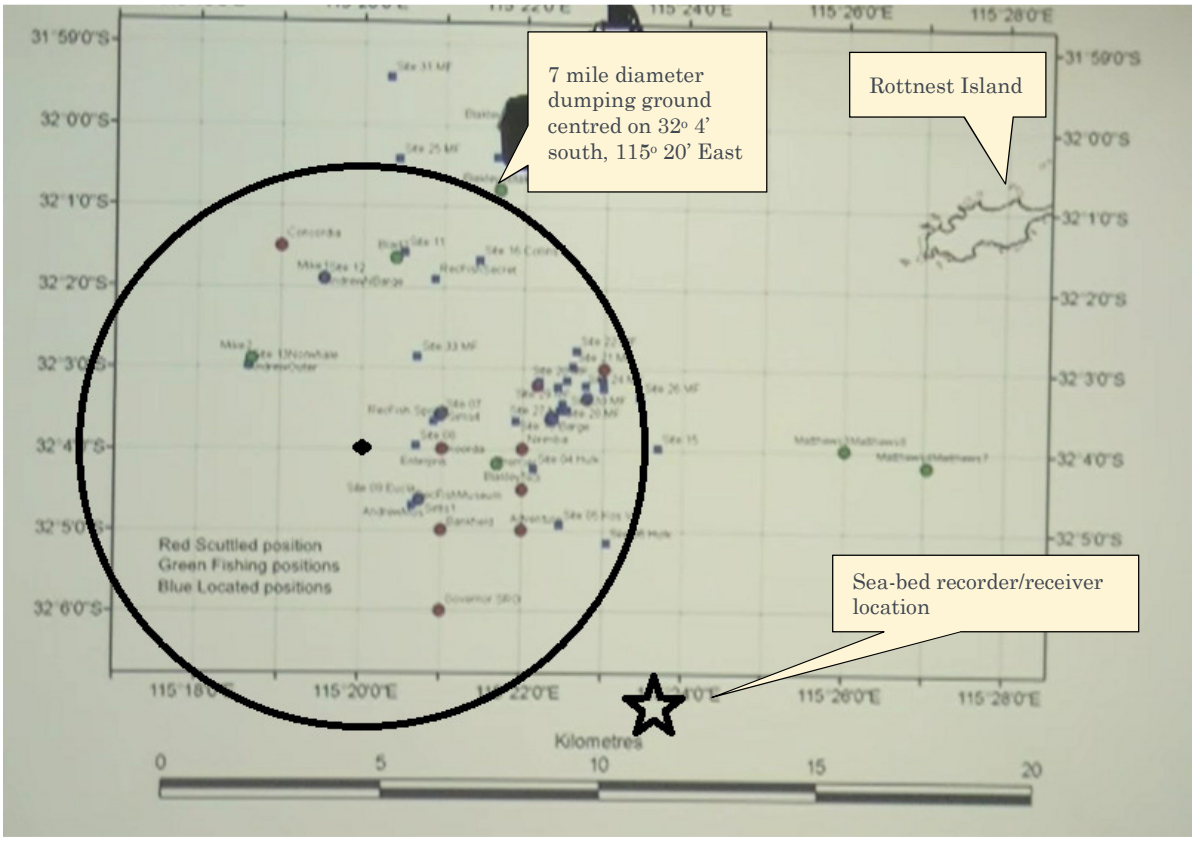

Figure 4-37: Receiver position relative to the Rottnest Deepwater Graveyard and known wreck positions (base image source:- WA Museum video presentation (Green 2011))

4.4.2 Trial vessel

The Rottnest trial was conducted on board the 16.5 m long "Simone K" marine work vessel illustrated on Figure 4-38. This vessel also began life as a cray-fishing boat featuring a capstan winch (that failed when needed to retrieve the sea-bed logger) and sturdy davit visible in the right-hand image. The open transom of this vessel suited the deployment of the heavy anchor-weight for the retrieval system float (~120 kg). The existing davit was ideal for raising and lowering the heavy (77 kg total mass) audio recorder and batteries in high pressure housing.

Figure 4-38: “Simone K“ Rottnest trial vessel

4.4.3 Experimental arrangement

The transmitter system was the same as previously summarised in Table 4-3, but with the exceptions that the transmitter depth was increased to 20 m, and the transmitter digital audio player was upgraded to a Sound Devices 744T unit with a more accurate 96 kS/s sampling rate match to the 96 kS/s receiver logger incorporating a Sound Devices 722 unit. The independent hydrophone recording of the transmitted signal 1m above the transmitter used a Sound Devices 702 unit.

The receiver hydrophones, digital audio recorder and housing were also the same unit as used in the Cottesloe trial and summarised previously in Table 4-1. More substantial ballast weight and surface floats were used for the deeper more open water environment as illustrated on Figure 4-39. Temperature loggers were deployed on the surface float line as illustrated on Figure 4-39 however the much longer than anticipated riser line (~100 m) meant that the depths of the temperature loggers were ambiguous. In data analysis the CTD casts proved more useful.

Figure 4-40 shows the recorder complete with sufficient adhesive tape to retain excess hydrophone cabling and to prevent rattles and squeaks in shackles while deployed, and the retrieve line and floats ready for deployment.

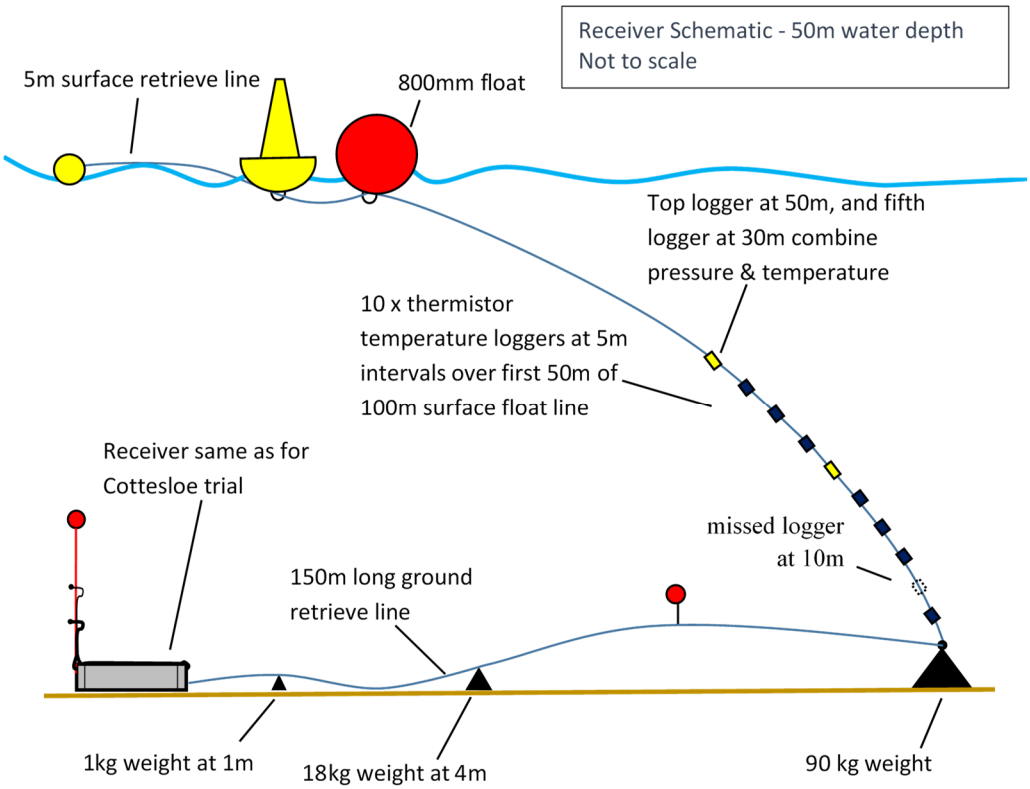

Figure 4-39: Rottnest trial receiver system

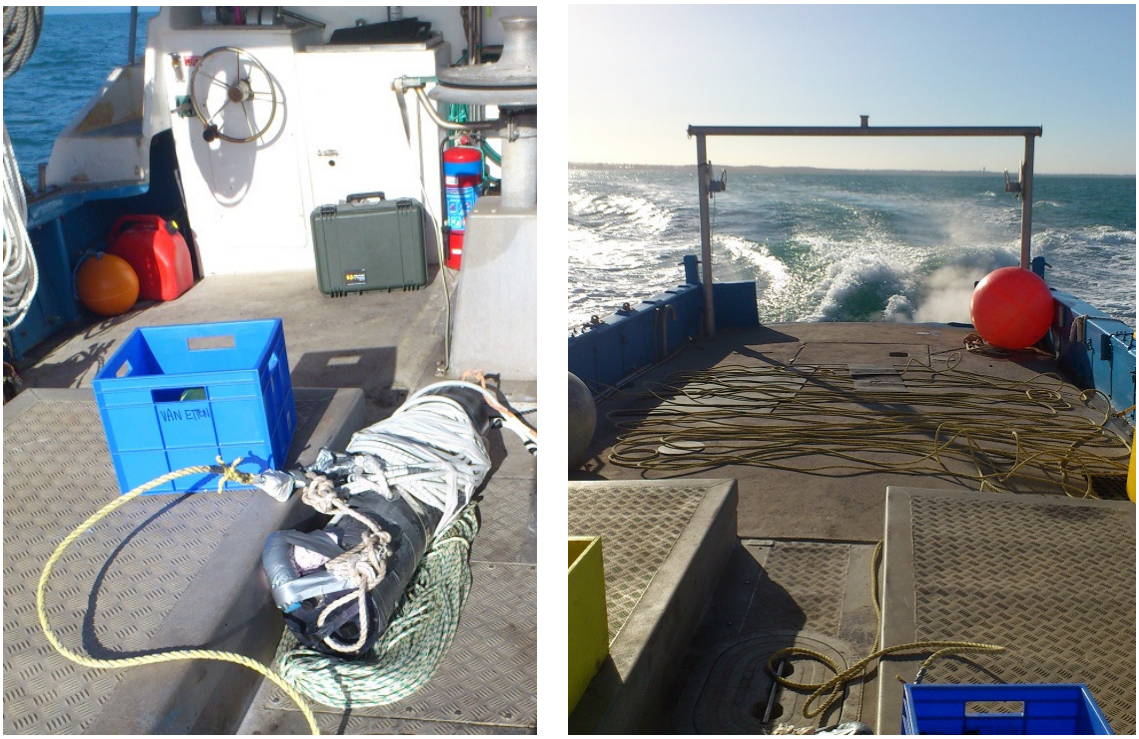

Figure 4-40: Recorder (left) and retrieve line and buoys (right) ready for deployment

Directional surface wave data was obtained courtesy of the WA Dept. of Transport for the Rottnest Datawell DWR-Mk3 Directional Wave Rider Buoy (DWRB). The

sound speed profile at a number of transmission positions was sampled with a Seabird SBE 19Plus Conductivity Temperature Depth (CTD) probe as per the Cottesloe trial (Figure 4-13).

The vessel was fitted with pitch, heave and roll data acquisition sampling at 100 Hz by Dr Tim Gourlay, enabling the vertical motion time-history of the suspended transmitter to be calculated.

It was intended that the vessel GPS position be logged at 1s intervals using a Velocitek Speedpuck, with backup from the vessel chart plotter. However the Speedpuck failed due to flat batteries, and the vessel chart plotter records were lost, possibly due to the failure of the auxiliary vessel generator whilst returning to port. Fortunately Dr Alec Duncan had enabled GPS tracking on his mobile phone for the duration of the trial. The tracking algorithm was set to a hybrid of maximum 1 s sampling and a position tolerance, such that the log data is at variable time intervals.

Bottom grab samples were not planned due to the considerable depth and the relatively constrained time schedule.

4.4.4 Calibration and Synchronisation

Synchronisation of the transmitter and receiver recorders was achieved on-deck prior to and after completion of channel probing, by contacting all hydrophones to the transmitter whilst transmitting three groups of ten chirps (each chirp a16 ms long 8 kHz-16 kHz LFM sweep). The relative clock times showed that the drift between the transmitter and receiver recorders was no greater than 1 second over the 8 hours between these two timing events.

In spite of this, because the transmitter recorder was not run continuously (i.e. paused at times) the start time of the transmit recordings was incomplete in the recorded transmit file data, which has the file end-time and overall run-time. The eventual method of time-synchronising the vessel (transmitter) position and transmit signal start time was as used for the Cottesloe trial, by interpolating the GPS position history according to the signal start and stop times determined from the continuous receiver audio recordings.

The logger position was determined by noting the time in the receive recording of audible impact of the logger landing on the sea-bed. The bottom contact time was

then cross-referenced to the GPS record to provide an estimate of the logger position.

A range error in the GPS-inferred transmitter position was incurred as a consequence of ignoring the signal flight-time when relating the received signal time to the transmitter GPS time. This range error, conservatively estimated at up to 5 m, is the product of the received signal time-lag (up to 6.6 s at 10 km range) multiplied by the maximum transmitter average closing speed of 0.77 m/s. This error is in addition to range uncertainty comprised of:

a) marking the logger resting position in 53 m water depth by GPS from the surface, estimated as 10% of the depth (+/-5.3 m);

b) the uncertain position of the hydrophone depending on orientation of the logger casing (+/-0.5 m);

c) the fixed displacement, but of uncertain position of the GPS in Dr Alec Duncan's pocket relative to the lowering rope (+/-1 m);

d) the similar pocket-GPS on-deck position uncertainty during transmissions (+/-3 m); and

e) the inherent GPS relative position error (+/-10 m).

It is estimated that the error bounds on transmission range estimates are approximately +/- 24.8 m [(5.3+1+0.5) +(5+10+3)], or 12.8 m RMS uncertainty as these factors may be reasonably considered independent.

4.4.5 Transmit signals

The potential arrival delay-spread was explored by spreadsheet for a uniform sound speed environment guided by the Cottesloe channel probing experience. The maximum anticipated delay-spread of 150 ms was established for the nominal minimum range of 125 m for a path with three surface bounces.

The goal of the probe signal design was then to achieve a 21 ms channel update rate in an environment with a potential arrival delay spread of up to 150 ms, depending on range. In an attempt to achieve this, a set of 8 x 21 ms orthogonal PRBS probe sequences was constructed, having the high autocorrelation property

of PRBS sequences, and as low as possible cross-correlation property within the set.

There is a well-developed theory of PRBS sequences to create sets of related sequences that maximise the autocorrelation of each PRBS and minimise the cross-correlation of variants within the set that is commonly used for radio-frequency coding of data (Proakis 2000). In essence, the longer the binary length of the PRBS sequence the lower the cross-correlation, or cross-interference between the sequences within the code set. A type of PRBS code-set know as a Gold code was used for this purpose.

A combination of the small dynamic range available for the relatively short 21 ms Gold code set and problems with their implementation meant that useful channel responses were measured using proven 21 ms PRBS, 1.4 s PRBS and 16 ms 8-16 kHz LFM sweep probe symbols. The LFM sweep repeat interval was altered with range to maximise the channel sampling rate. The trial also included coded data sequences provided by Prof. Yue Rong's communications research group within the Curtin Dept. Electrical and Computer Engineering.

Doppler and delay resolutions for the different signal types are summarised in Table 4-9. A summary of the anticipated channel delay-spread with range, and the series of sequences planned to measure the channel response is shown in Table 4-10. Each full transmit signal totalled close to 11 minutes and 8 seconds. The spectral shape of the 21 ms PRBS, 1.36 s PRBS, 8psk, and qpsk signals are illustrated in Appendix B.1.

Table 4-9: Rottnest trial probe symbols

Signal descriptor	Carrier frequency f_o (kHz)	Symbol repeat period T (s)	Bandwidth B (Hz)	Delay resolution δ_τ (ms)	Doppler resolution δ_v (m/s)
n4095 PRBS	12	1.365	6000	0.16	0.094
n63 PRBS Gold code set	12	0.021	6000	0.16	6.1
n63PRBS	12	0.021	6000	0.16	6.1
16 ms LFM sweep	8-16	50 ms to 200 ms	8000	0.125	-

Table 4-10: Probe signal summary

<table>
<tr><th>Range</th><th>Surface bounces</th><th>Est. delay spread</th><th>21 ms PRBS</th><th>1.36 s PRBS</th><th>16 ms 8 kHz-16 kHz linear sweep</th><th>21 ms M6 Gold code cycle</th><th>Computer Eng. Signal</th></tr>
<tr><td>125 m</td><td>3</td><td>150 ms</td><td rowspan="9">60 s of repeats</td><td rowspan="9">60 s of repeats</td><td rowspan="3">60 s at 200 ms repeat interval</td><td rowspan="3">60 s of 8x21 ms cycle</td><td rowspan="5">4 minutes qpsk + 3 minutes 8psk</td></tr>
<tr><td>250 m</td><td>3</td><td>106 ms</td></tr>
<tr><td>500 m</td><td>4</td><td>104 ms</td></tr>
<tr><td>1 km</td><td>4</td><td>58 ms</td><td rowspan="2">60 s at 100 ms repeat interval</td><td rowspan="2">60 s of 4x21 ms cycle</td></tr>
<tr><td>2 km</td><td>5</td><td>45 ms</td></tr>
<tr><td>4 km</td><td>5</td><td>23 ms</td><td rowspan="4">60 s at 50 ms repeat interval</td><td rowspan="4">60 s of 2x21 ms cycle</td><td>4 minutes bpsk + 3 minutes qpsk</td></tr>
<tr><td>6 km</td><td>6</td><td>21 ms</td></tr>
<tr><td>8 km</td><td>6</td><td>16 ms</td></tr>
<tr><td>10 km</td><td>6</td><td>13 ms</td><td>7 minutes bpsk</td></tr>
</table>

4.4.6 Summary of acoustic recordings

A summary of the transmitter and receiver audio recordings, and the correspondence of the start and end times for each type of probe signal to the position and movement of the transmitter are included in Appendix B.2. A summary of the recorder and amplifier settings is included in Appendix B.3. A visual summary of the receiver audio recordings at each transmission range is included in Appendix B.4.

The spectrogram summary of the receiver recording of the T52 transmission at 125 m is shown in Figure 4-41 for the channel 1 TC4033 hydrophone located 1 m off the bottom.

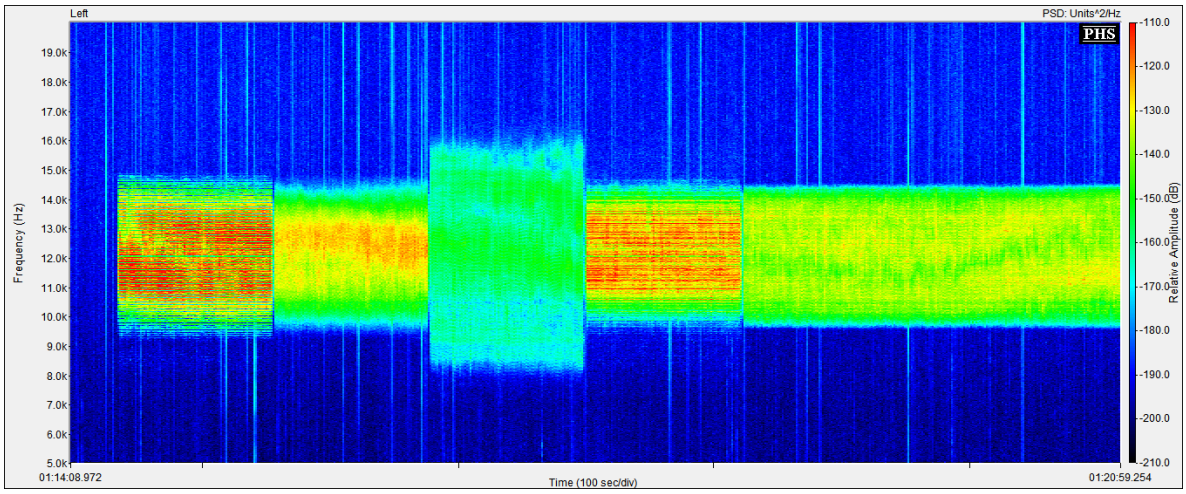

Figure 4-41: T52 transmission Rx T1995 at 125 m range -40 dB Tx output

The T53 transmission was terminated before completion due to concern about the degree of heating of the amplifier.

An example spectrogram for the second channel of the receiver (Figure B-10) is included in Appendix B.4, corresponding to the TC4034 hydrophone positioned 1.5 m off the bottom. This spectrogram shows approximately 10 dB higher noise floor across the spectrum than the TC4033 hydrophone.

The very last transmission T67 starting at a range of 500 m (Figure B-18) was conducted with the transmitter inverted (in the normal orientation for the device). The starting position for this transmission was the same as transmission T65 (Figure B-16). The depth of the transmitter differed slightly after inversion, being 18 cm closer to the surface, and 18 cm closer to the transmitter recording hydrophone.

The final series of 3 x 10 chirp repetitions on deck with all hydrophones contacting the transmitter was conducted back at the Fremantle marina. The first series of chirps was conducted while engines were idling, and then repeated with the engines switched off to ensure the signal-to-noise was adequate. (Figure B-19).

4.4.7 Sound speed profile

The correspondence between the sound speed profiles sampled by CTD and the signal transmissions is included in the data summary in Appendix B.2, with all sound speed profiles included in Appendix B.5.

The sound speed profiles indicated warming of the surface waters over the period of the experiment to the extent of approximately 0.5 m/s sound speed differential

(Figure 4-42 and Figure 4-44). However the progression of profiles as the CTD sampling position was shifted out to 10 km then back to near the receiver, indicates that the further south the sampling position (

Figure 4-36) the greater the upward refracting sound speed profile of the character illustrated on Figure 4-43. It is speculated that the tidal dynamics created by the constriction between Rottnest Island and Garden Island results in greater mixing closer to the receiver location.

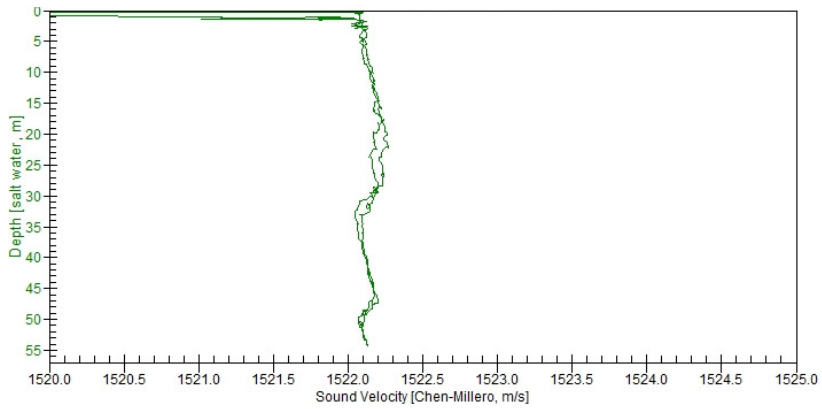

Figure 4-42: Sound speed profile CTD Cast 1 – 9:38 am, 125 m Tx-Rx range

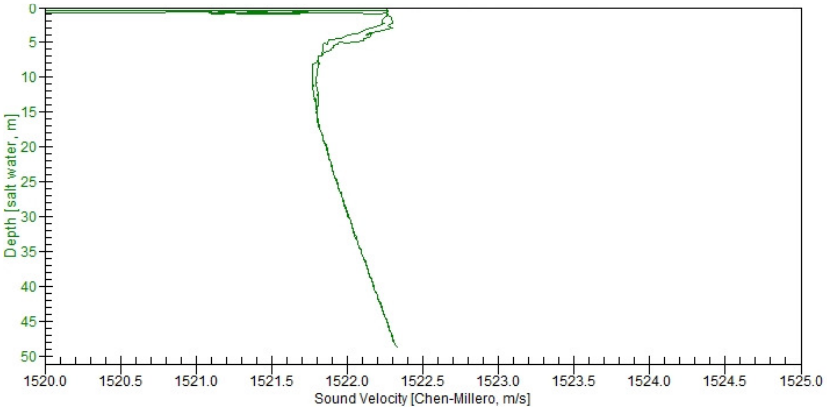

Figure 4-43: Sound speed profile CTD Cast 6 –12:40 pm – 10 km Tx-Rx range

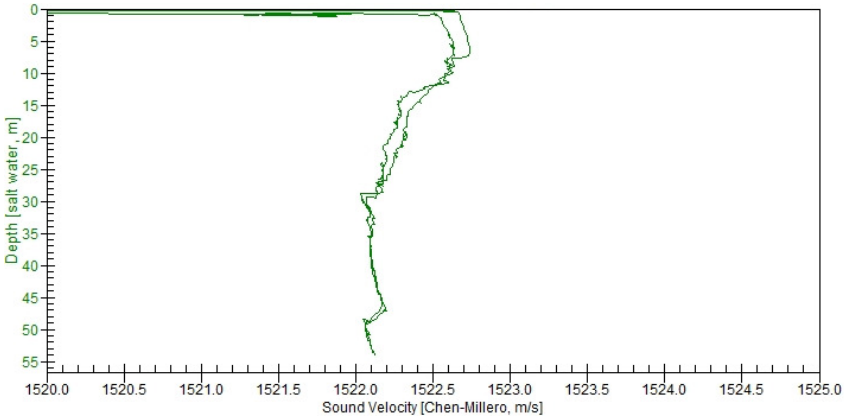

Figure 4-44: Sound speed profile CTD Cast 11 – 2:46 pm, 500 m Tx-Rx range

Referring to the progression of profiles in Appendix B.5, it is surmised that the warming of the surface waters down to 15m depth may have been reasonably range independent over the duration of the experiment. However the deeper water (>15 m depth) profile appears range-dependent, transitioning between the upward refracting Cast 6 profile at 10 km and the roughly neutral Cast 1 profile at 125 m.

4.4.8 Surface wave records

The surface wave trend was gradual decline of a moderate swell over the 6 hour period of testing, with sea declining until 1:30 pm, then increasing afterwards, accompanied by the formation of minor white-caps within the last hour of testing. The sea surface at 9:03 am at the commencement of signal transmissions is illustrated in the top image of Figure 4-45. The centre image shows the surface at 12:16 pm and the bottom image shows the surface at 2:57 pm just after the last signal transmission.

Figure 4-45: Experimental sea surfaces - morning (top) at 9:03 am mid-trial (middle) at 12:16 pm, and at end of last transmission at 2:57 pm (bottom)

WA Transport advised that the Rottnest DWRB was located 36o 6'4.3"S, 115o24'8.0"E in 50m water depth at the time of the trial. The relative position of the DWRB, the fixed recorder and the transmit locations are shown on

Figure 4-36.

The DWRB samples the buoy motions each 0.78 s and produces a spectral amplitude summary from a buffer of 2048 samples (25 minute span) each 15 minutes. The derived surface spectral densities in Figure 4-46 have been averaged from 8 such spectra in 2 hour blocks.

The dynamic cut-off frequency of the DWRB at approximately 3.7 radians/s is notable on Figure 4-46 just below the 4.03 radian/s Nyquist frequency.

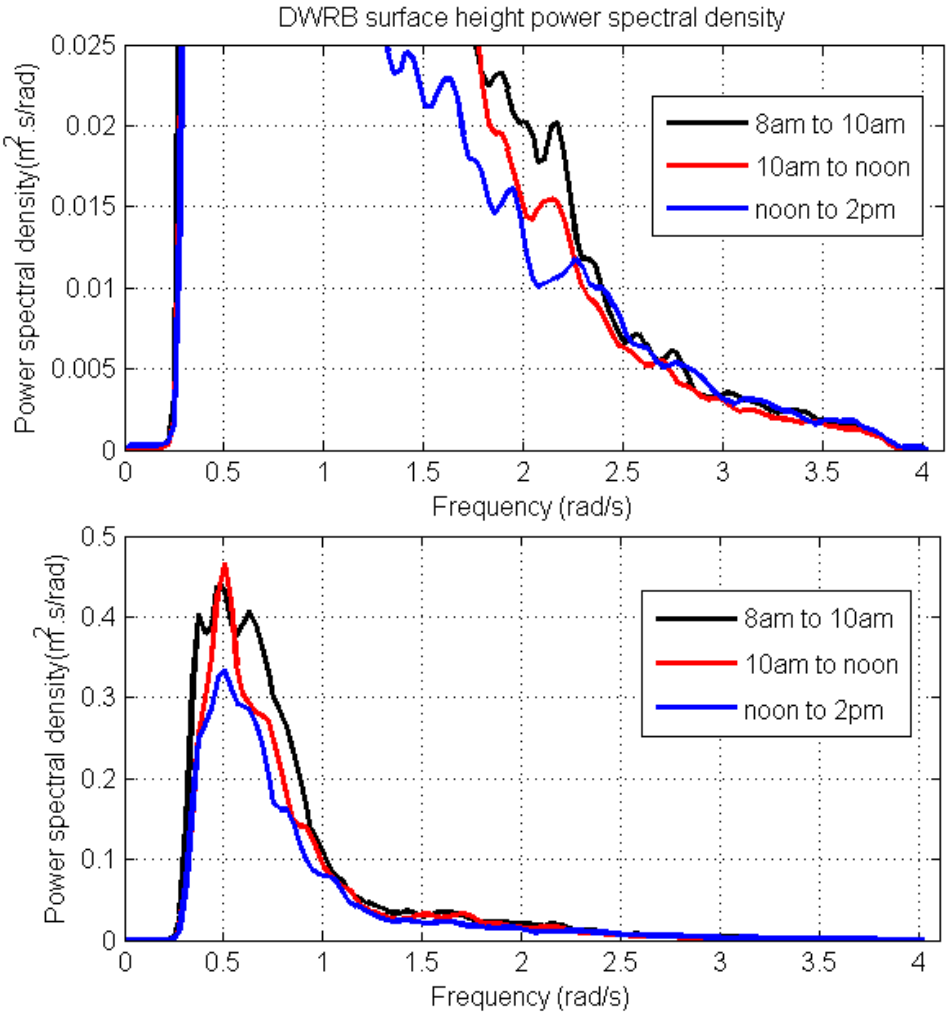

Figure 4-46: Experimental surface wave spectra for Rottnest Is. DWRB illustrating the sea spectrum (top, with x20 magnification), and swell spectrum detail (bottom)

The half-hourly summary wave height and direction statistics spanning the test period supplied by WA Transport are shown on Figure 4-47. The 12:45 pm record

was absent from the data set. The split between swell and sea in the supplied DWRB data was defined by a wave period of 8 seconds.

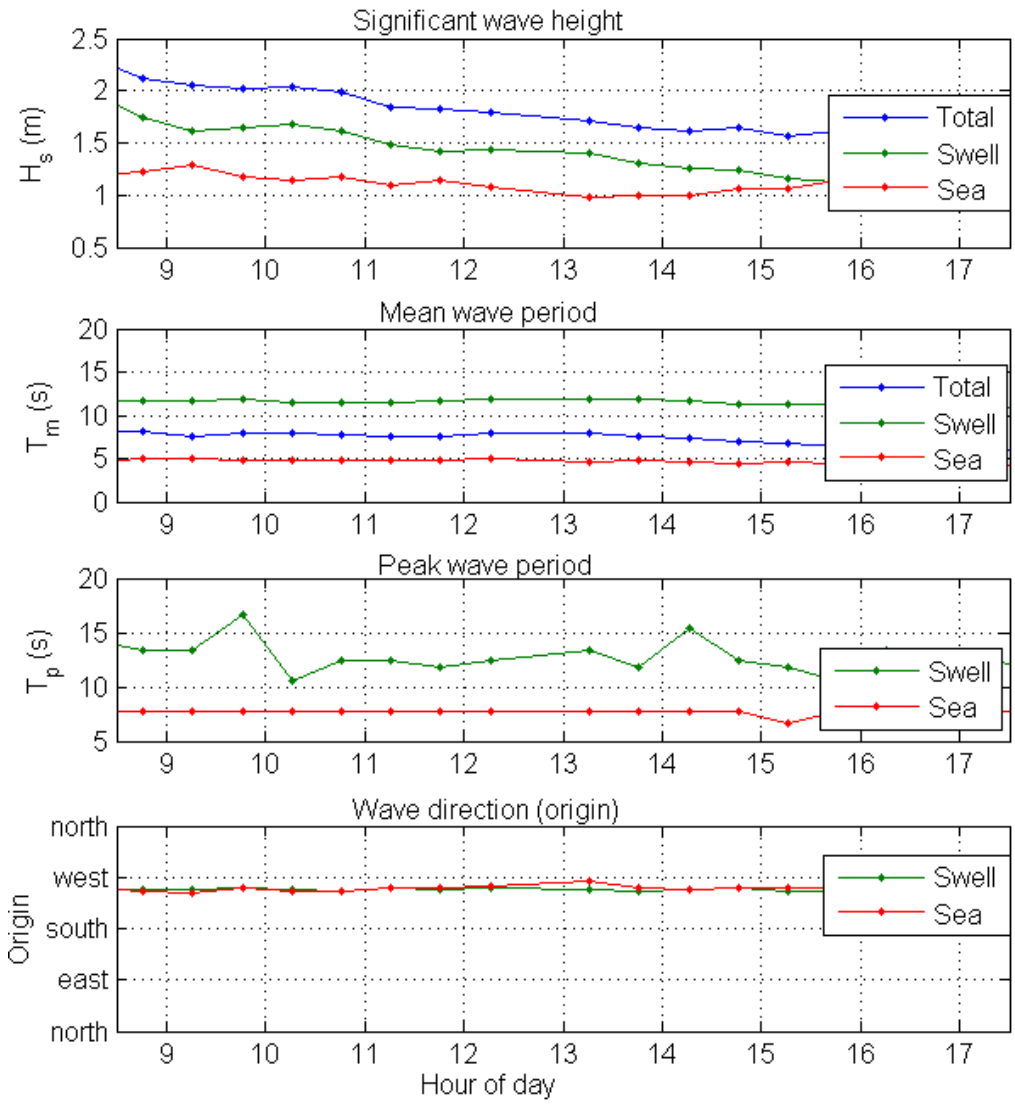

Figure 4-47: Half-hourly surface wave summary data for trial duration from Rottnest DWRB (data source: WA Dept. Transport)

4.4.9 Wind conditions

The nearest meteorological station relevant to the test location is Station 009193 on Rottnest Island at an elevation of 43.1m above sea level. The wind speed and direction records for the experimental period are shown on Figure 4-48. The estimated equivalent wind speed at 2m height was calculated from the measured data at 43 m height using Eq.(4-1).

Dr Tim Gourlay made notes "Wind SE 10 kn (~5 m/s) at 0900, SE 5 kn (~2.5 m/s) at 1100, sea breeze arrived 1230, SW 12 kn (~6m/s) at 1300, SW 20 kn (~10m/s) at 1500".

The observed trends in direction and timing are very similar to records from the Rottnest Island meteorological station. The estimated speeds are generally similar to what the meteorological station gust speeds would be translated to 2 m height.

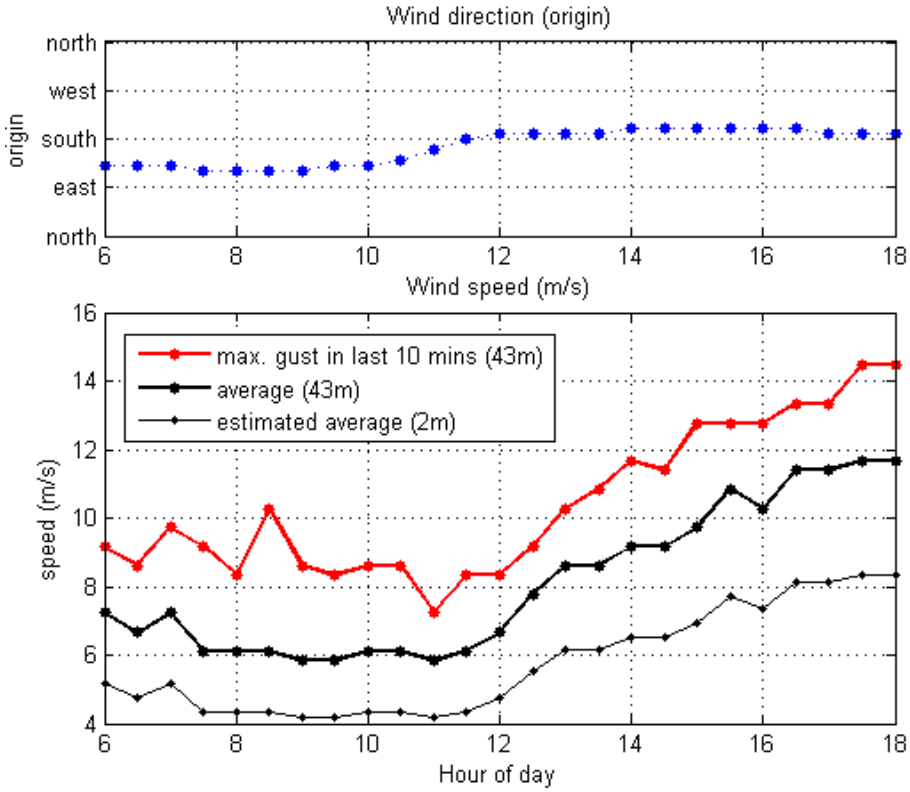

Figure 4-48: Wind data for Rottnest Is. met. station 43 m above sea level – 1/12/2012

4.5 Rottnest trial channel probing results

4.5.1 Introduction

At short-range the early part of the channel delay response has been elucidated by the 21 ms PRBS with the remainder examined from the LFM sweep repeated at 200 ms intervals. At longer ranges the 21 ms PRBS probe was capable of determining the majority of the channel response, as was the LFM sweep repeated at 50 ms intervals. The results from the 21 ms PRBS and LFM sweeps were sufficiently comprehensive that the data for the long 1.4 s PRBS probe signals was not analysed. All of the channel probe results were obtained with a slowly drifting transmitter, and are presented aligned on the first arrival after resampling of the transmit signal to compensate for range drift between the transmitter and receiver. Results

Figure 4-49 shows the experimental 21 ms PRBS probe channel response at ranges of 137 m, 1112 m and 7864 m, generated by stacking 2880 successive transmit-receive correlation results. The horizontal lines in the right image at 7864 m range are caused by impulsive shrimp 'snaps' close to the receiver hydrophone.

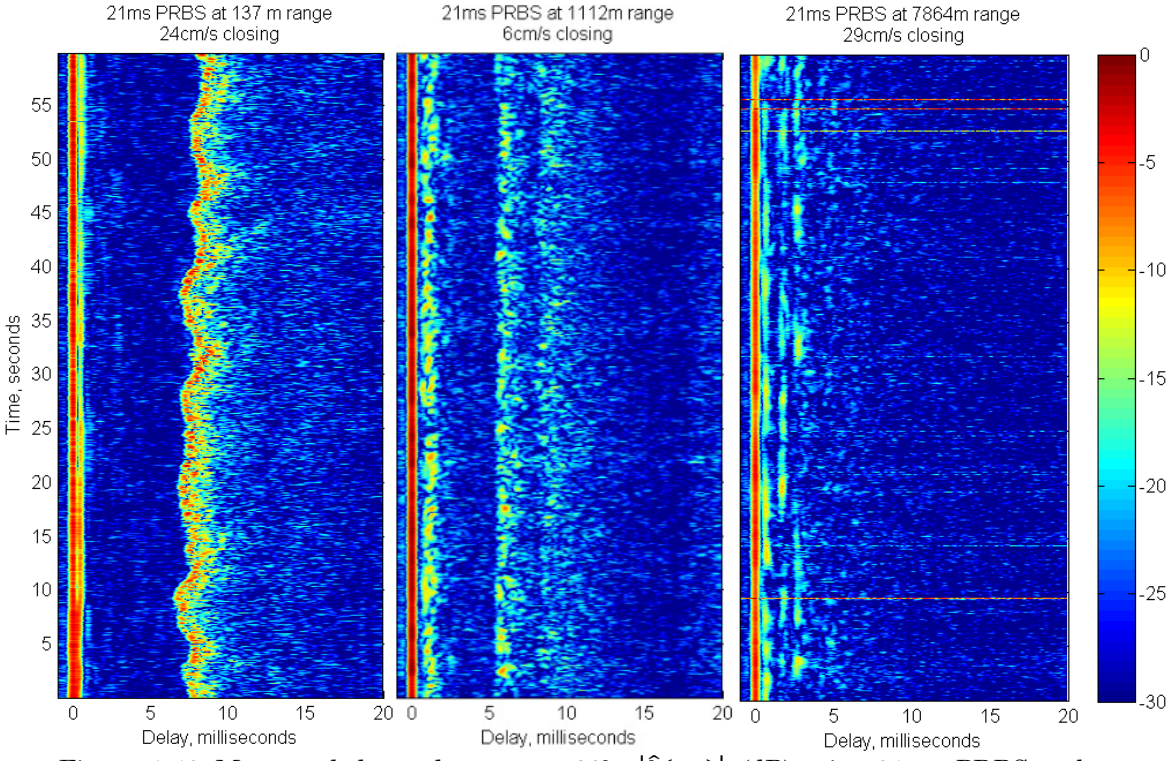

Figure 4-49: Measured channel response, $20\log\left|\hat{h}(t,\tau)\right|$, (dB) using 21 ms PRBS probe at ranges of 137 m (left), 1112 m (centre), and 7864 m (right)

It was attempted as far as possible to limit the influence of snapping shrimp noise on the correlation by using zero phase-shift band-pass filtering (Matlab 'filtfilt') on the receive signal prior to correlation, however the remaining signal spikes from shrimp snaps were still sufficient to 'swamp' the channel response.

The algorithm used to display $\hat{h}(t,\tau)$ normalises the correlator output by the power of the transmit-receive signal product, averaged over the 60 second probing period. An alternative algorithm was originally used, that normalised the correlator output for the transmit-receive signal product power for each block. This avoided the spikes in the correlator output, but led to the blocks containing shrimp 'snaps' to display as uncertain 'holes' in the response, in addition to masking changes in the response amplitude with time. It was considered better that the shrimp effects on the correlator response be explicit, and that dynamic changes in path amplitude response be accurate.

The alternative response histories generated by the linear sweep probe 2 minutes later at each range are shown on Figure 4-50. The light horizontal lines of about 12 ms length represent the correlation of a shrimp 'snap' with the 16 ms linear sweep signal.

The delay power profiles for the Rottnest trial channels are best illustrated from the LFM sweep probes, which give better delay resolution over a wider delay range than the 21 ms PRBS. These are obtained by averaging the Figure 4-50 responses over the time dimension, generating the corresponding delay power spectra in Figure 4-51.

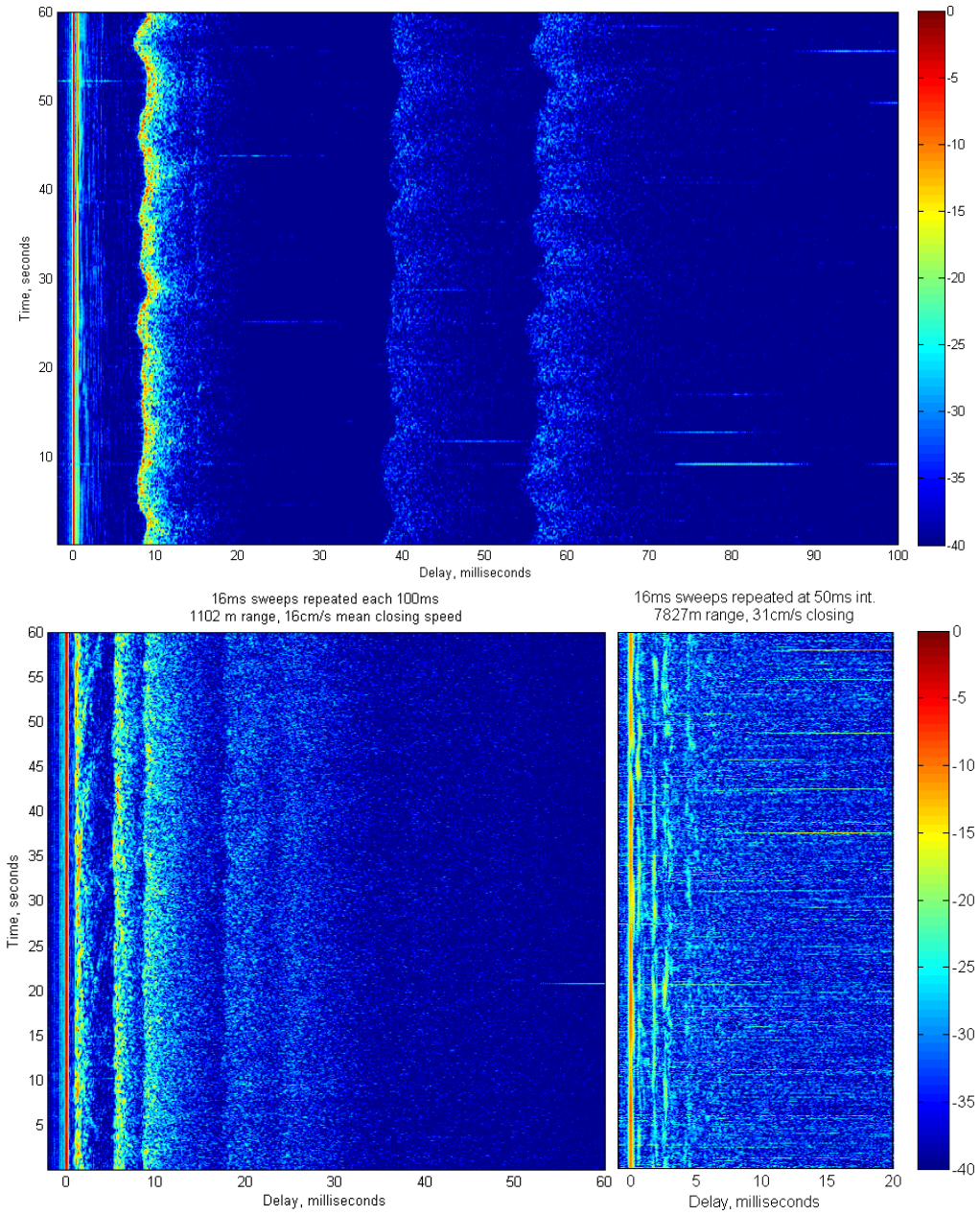

Figure 4-50: Measured channel response, $20\log|\hat{h}(t,\tau)|$, (dB) using 16 ms 8 -16 kHz LFM sweep at ranges of 121 m (top), 1102 m (lower left), and 7827 m (lower right)

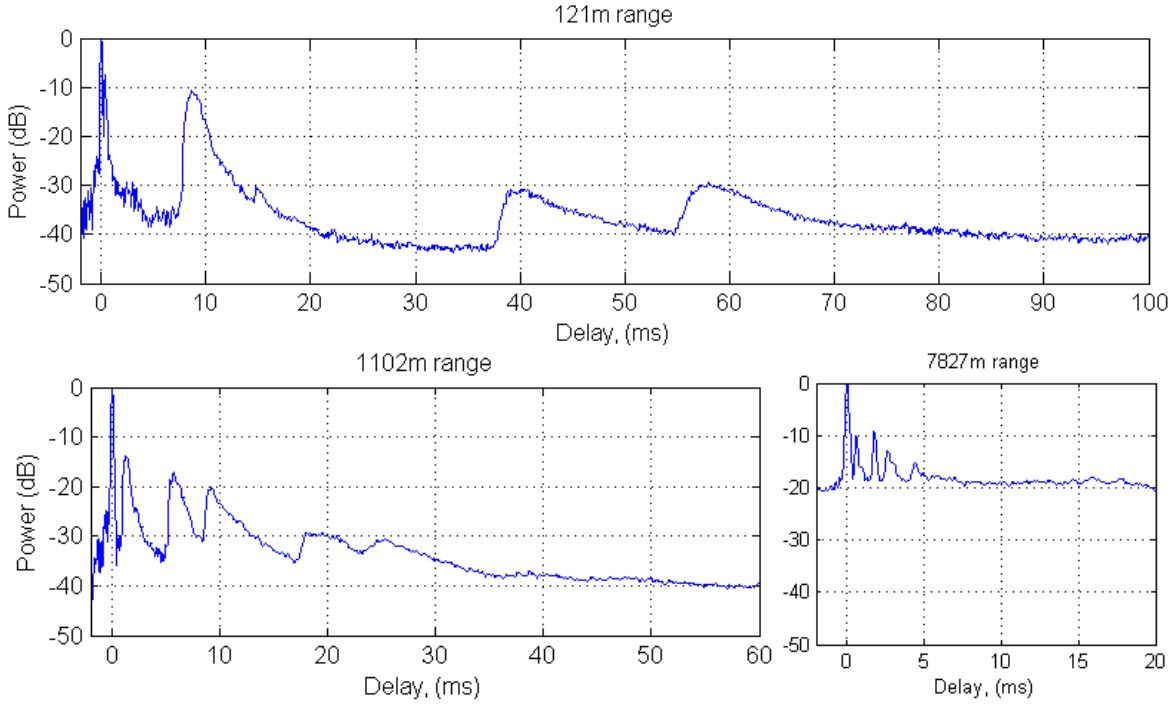

Figure 4-51: Measured response power versus delay, $10\log\left|\hat{P}(\tau)\right|$ (dB) using 16 ms 8 - 16 kHz LFM sweep at ranges of 121 m (top), 1102 m (lower left), and 7827 m (lower right)

The comparative, (albeit truncated with time aliasing) delay power profiles for the 21 ms PRBS probe are presented in Figure 4-52.

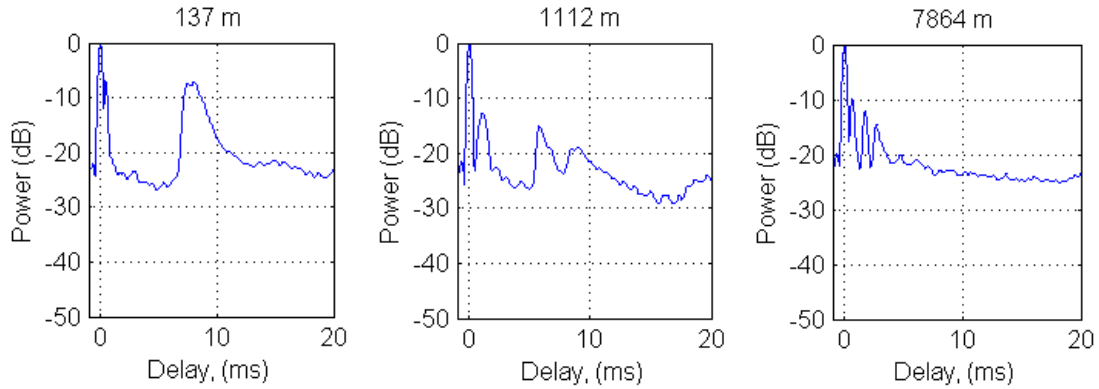

Figure 4-52: Measured response power versus delay, $10\log\left|\hat{P}(\tau)\right|$ (dB) using 21 ms PRBS probe at ranges of 137 m (left), 1112 m (centre), and 7864 m (right)

Whilst the linear sweeps are ideal for exploring the full delay structure, the slow repetition rate limits the ability to capture the frequency spreading. For example, the 16ms LFM sweeps repeated at 200 ms intervals (5 Hz) that are ideal to illustrate the delay power structure at short range cannot also show the frequency spreading. The resulting spreading function at 121 m range shown on Figure 4-53 (that hardly looks like one) has a Nyquist frequency of 2.5 Hz in the Doppler dimension. Clearly a more rapid probe is needed.

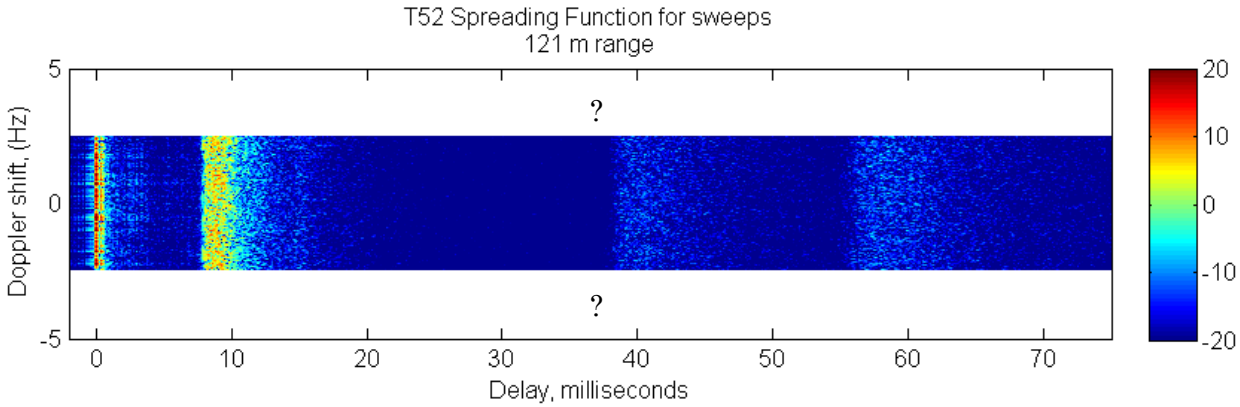

Figure 4-53: Illustrative deficient spreading function at 121 m range, $20\log\left|\hat{S}(\nu,\tau)\right|$ (dB), LFM sweep probe repeat at 5 Hz

The short PRBS with its 48 Hz repetition rate is better suited to explore frequency spreading. The spreading functions from the 21 ms PRBS probe corresponding to Figure 4-49 inclusive of the effects of drift and swell effects on the transmitter motion are presented in Figure 4-52.

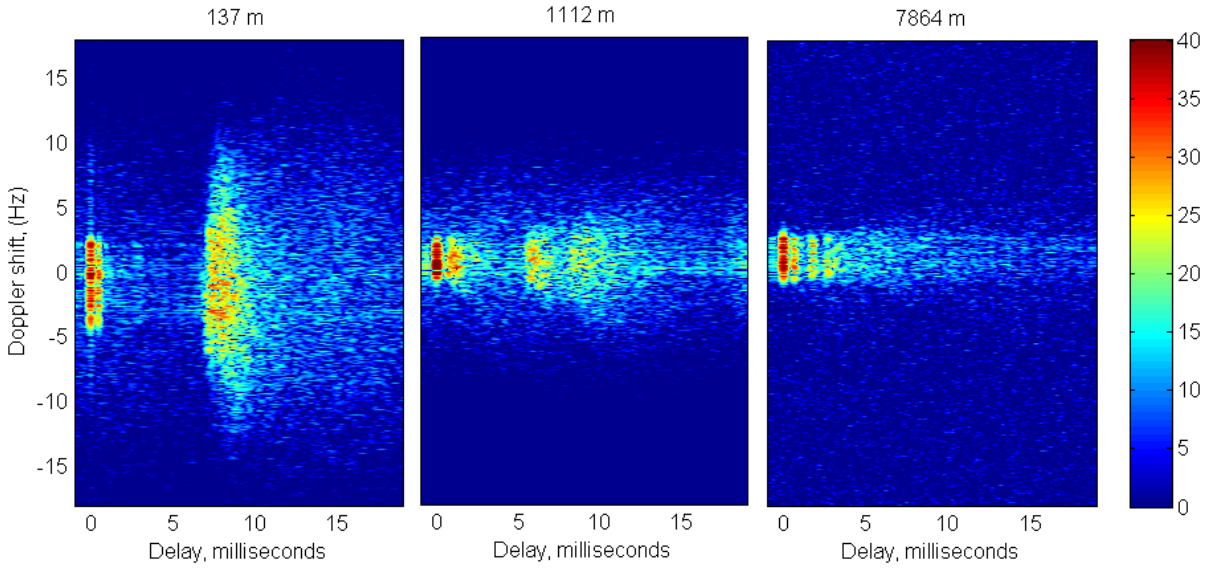

Figure 4-54: Measured channel spreading functions for 21 ms PRBS probe including transmitter drift, $20\log\left|\hat{S}(\nu,\tau)\right|$ (dB), f_0 = 12 kHz, 137 m range (left), 1112 m range (centre), and 7864 m range (right)

Approximation to the fixed transmitter-receiver spreading functions, calculated after resampling of the transmit signal to exclude direct path relative motion of the transmitter and receiver are presented in Figure 4-55.

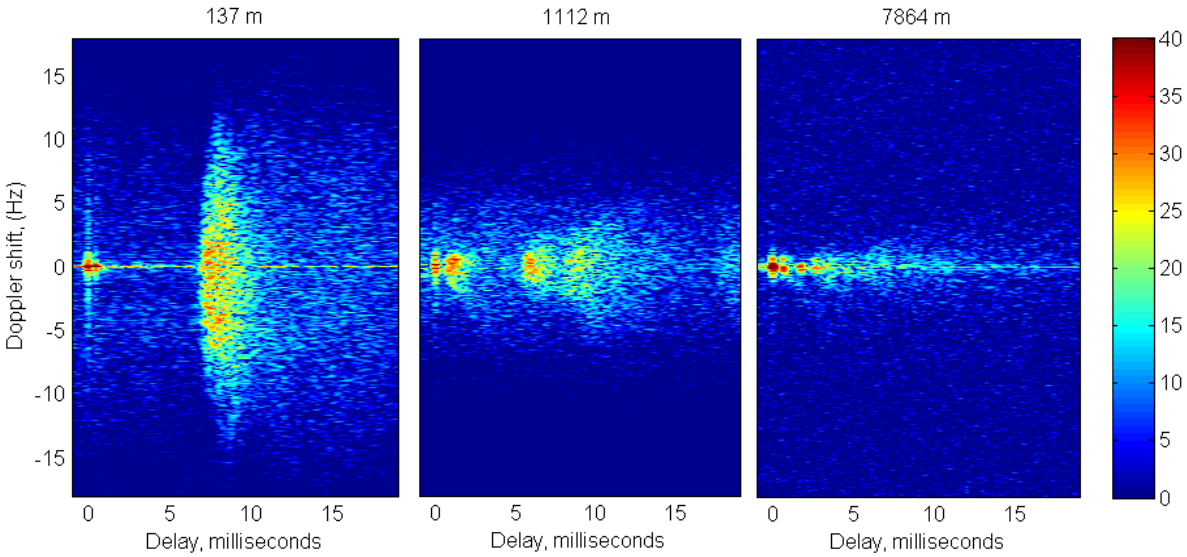

Figure 4-55: Measured spreading function with approximate resampling to exclude direct path drifting an cyclical motion , $20\log\left|\hat{S}(\nu,\tau)\right|$ (dB),$f_0$12 kHz, 137 m range (left), 1112 m range (centre), and 7864 m range (right)

4.5.2 Summary

The Rottnest trial successfully obtained channel responses over a wide range of distances for constant depth. The CTD probes showed some range-dependence of the sound speed profile and gradual heating of the surface-layer over the 6 hours of channel probing. The propagation direction was, with one relatively short-range exception, more-or-less constant NNE heading relative to the prevailing ENE swell and sea heading. There was some variation in surface wave amplitude during the trial but not sufficient to present responses for contrasting surface conditions.

The Rottnest channel probe results clearly illustrate the problematic nature of simultaneously obtaining a detailed record of both Doppler and delay spreading in the channel response. At 8 km range both the Doppler and delay spreading can be simultaneously explored with either a short 21 ms PRBS probe or a similarly short sweep, whereas at 1 km or 125 m range this is not possible. This situation is described as an 'over-spread' channel with respect to delay or Doppler, depending on whether a short or long probe signal is used respectively.

The question arises, how does one determine whether a channel is being probed frequently enough to establish the full extent of the Doppler spreading? The answer relates to the idea of Nyquist sampling frequency. The channel must be probed frequently enough such that the surface-reflected transmission paths do

not change more than a half wavelength in each interval, else the phase-shift in that interval becomes ambiguous, and consequently the frequency of the Doppler is aliased. If the response in a channel probe spreading function extends beyond the Doppler axis Nyquist limits (such as on Figure 4-53), then the channel can quickly be identified as over-spread in frequency with respect to the probe symbol rate.

5 SIMULATION DEVELOPMENT

5.1 Chapter overview

The description of the simulation development in this chapter includes a combination of straight-forward descriptive material on how components of the simulation work, and more detailed explorations of the simulation behaviour and justification of specific modelling choices.

The overall scope and capability of the channel simulation in outlined in Section 5.2.

The calculation structure in Section 5.3 treats the rough-surface response for surface interactions along eigenpaths as a given, and seeks to illustrate how the time-varying rough surface response is combined with the channel eigenpath amplitude-delay response for the more familiar case of a static flat surface channel.

Section 5.4 addresses in more detail how the rough surface bistatic response is approximated and justified for a limited selection of bistatic geometries using a spatially limited portion of the ocean surface. The general thrust of the approximations made is to economise on the computational storage and calculations necessary.

Section 5.5 addresses the discrete time and space generation of the time-varying surface realisations, with modelling selections and features similarly motivated by efficiency of array storage and calculation intensity whilst achieving time-varying channel characterisation consistent with the signal bandwidth of interest.

The overall synthesis of the multipath channel response is described in Section 5.6 followed by summary of the important findings made in the process of simulation model development in Sections 5.7 and 5.8.

5.2 Simulation overview

The scope of the simulation described here is illustrated schematically on Figure 5-1. The 'Channel response builder' computes a sequence of channel responses at specified regular intervals (e.g. 20ms) for a defined transmission geometry, sound speed profile and surface-wave conditions (the 'Environment Definition'). This is

carried out over a period of 30-60 seconds which is sufficient to capture the time-varying effects of sea and swell. The time-varying channel response is pre-calculated for later convolution with signals of interest.

The 'Channel/signal convolution' then convolves an arbitrary length transmit signal $x(t)$ with the time-varying channel response $h(t,\tau)$ to produce a synthetic received signal $y(t)$. This simulation is implemented using the Matlab™ programming language.

In the current implementation the receive signal is not computed in real-time, however this would be possible with suitable parallel computing architecture and time-efficient machine-level digital signal processing code.

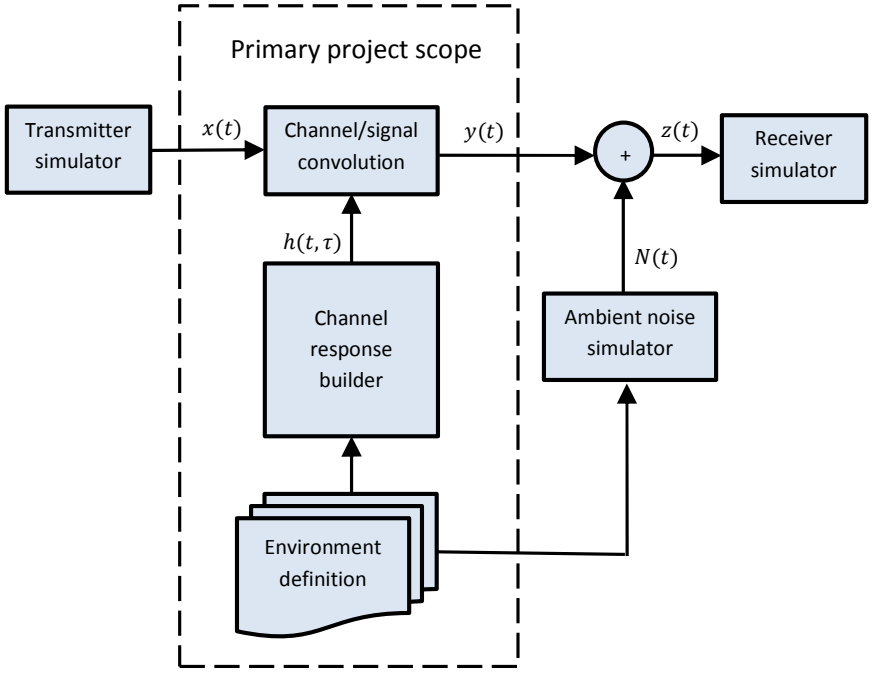

Figure 5-1: Schematic channel simulation structure

Whilst the inclusion of ambient noise is important to realistic channel simulation, the 'Ambient noise simulator' indicated in Figure 5-1 was not developed for this project. It was decided that the simulation of ambient noise as a research focus was of secondary importance, as there are ample available ambient noise recordings to provide a wide selection of realistic ambient noise conditions.

The simulation is configured to address channels where the relative vertical and horizontal displacements of the transmitter over the duration of the simulation are small compared to the channel depth and transmission range respectively.

The implementation described relates to a channel band from 8 kHz to 16 kHz, with the input and output signals sampled at 96 kS/s. These parameters relate to the experimental trial data, obtained using a transmitter operated at 12 kHz centre frequency and 9 kHz to 15 kHz transmit signal band. Simulations can be carried out for any high-frequency bandwidth for which the acoustic propagation with smooth boundaries can be adequately described by ray acoustics as discussed in Section 2.2.3.

5.3 Calculation structure

5.3.1 Simulation of ideal flat-surface ocean channel

For the flat-surface condition, the received signal can be understood as the sum of delayed, amplitude-scaled and phase-shifted replicas of the original transmit signal $x(t)$ along ray eigenpaths as shown schematically on Figure 5-2, and calculated by Eq.(5-1).

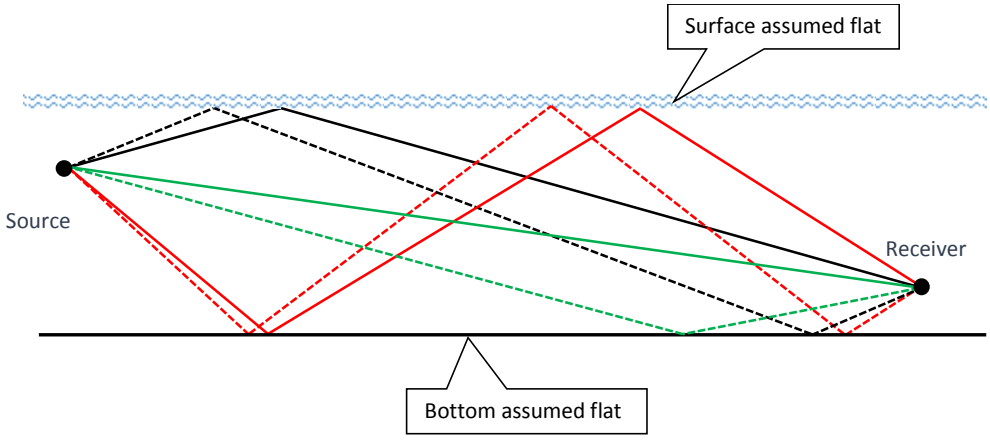

Figure 5-2: First-arriving six flat-surface eigenpaths for an iso-sound-speed channel

The channel response along each path may be characterised by complex amplitude $\tilde{A}_n$ that includes the path phase shift, and an arrival delay time τ_n. The delay relates to the transmission path-length, and the amplitude is scaled by geometrical spreading, sea-water attenuation (at the communication band centre-frequency) and the calculated bottom reflection loss. Ray-path transmission parameters have been calculated using the Bellhop (Porter 2011) ray propagation model.

$$y(t) = \sum_{n=1}^{N} \tilde{A}_n x(t - \tau_n) \tag{5-1}$$

5.3.2 Addition of time-varying rough-surface interactions

With the addition of a time-varying surface two time dimensions are required to describe the channel response. The real or global time t is defined at the transmitter. Both the input signal and the moving sea-surface change in real time. The delay time τ is the elapsed transmission time relative to each signal transmission instant, for representing the 'instant' or impulse time-varying response at the receiver.

The simulation is implemented as a time-domain convolution of the transmit signal with a pre-calculated set of Finite Impulse Response (FIR) filter cascades, with one cascade representing each modelled eigenpath with rough surface interactions.

Calculation of the FIR cascades begins in the frequency domain with respect to delay time τ. For the n^{th} ray eigenpath, the response for a frozen 'snapshot' of the rough surface channel at time t_i, is calculated first in the frequency domain, as the product of the flat-surface eigenpath amplitude,$\tilde{A}_{n,flat}$, and a Fourier-synthesised approximation to the bistatic rough-surface pressure response, $\widetilde{H}_{n,patch}(t_i, \omega)$, as per Eq.(5-2). In the case of multiple surface interactions, $\widetilde{H}_{n,patch}(t_i, \omega)$ is obtained from frequency-domain multiplication of successive bistatic responses as conceptualised in Section 5.4.9.

$$\widetilde{H}_{n,path,}(t_i, \omega) = \tilde{A}_{n,flat}\widetilde{H}_{n,patch}(t_i, \omega) \tag{5-2}$$

Figure 5-3 illustrates the concept of the real-time progression of the successive frequency-domain channel responses for a bistatic rough surface interaction corresponding to the real-time progression of surface realisations. The surface realisations are described as being 'time-circular' on Figure 5-3, referring to the harmonic method of surface realisation synthesis as described in Section 5.5.3. In this manner the last surface realisation may be 'seamlessly' followed by the first. By association the same real-time circularity is inherited by the bistatic frequency responses,

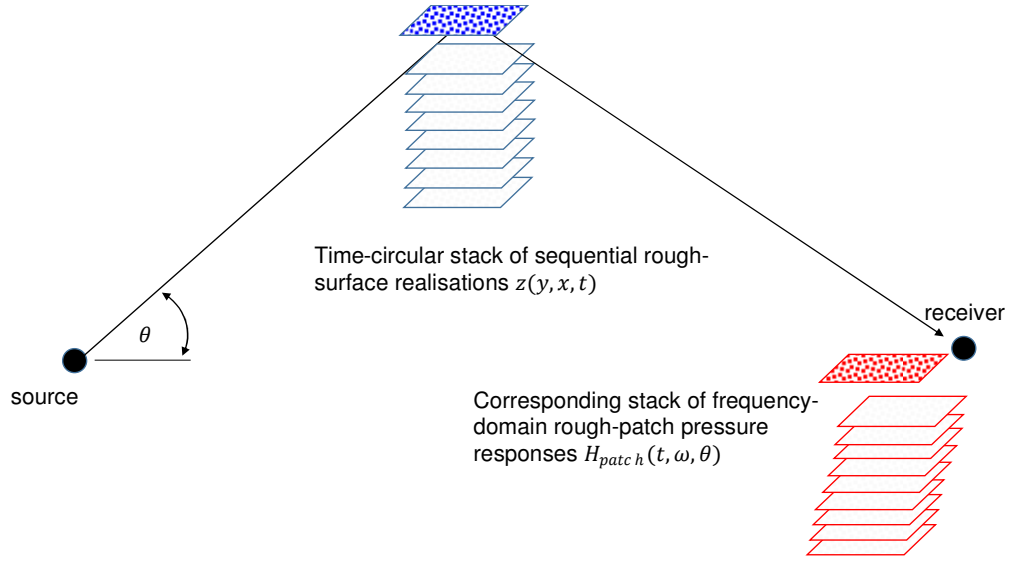

Figure 5-3: Schematic calculation of time-sequential frequency-domain bistatic responses from time-sequential sea-surface realisations

The path response is inverse transformed by Eq.(5-3) with respect to angular frequency (ω) to obtain $h_{n,path}(t_i,\tau)$ on the n$^{\text{th}}$ ray-path for the frozen rough surface snapshot at time t_i. (The term $e^{-(\alpha(\omega)-\alpha_{\text{centre}})c\tau_n}$ introduces the frequency-dependent sea-water absorption $\alpha(\omega)$ across the simulation bandwidth relative to the centre-frequency absorption coefficient (α_{centre}) implicit in Bellhop model path amplitude $\tilde{A}_{n,flat}$). The frequency-response vector $\tilde{H}_{n,rough}(t_i,\omega)$ is zero-padded to achieve a delay-time interval matching the input signal.

$$h_{n,path}(t_i,\tau) = \mathcal{F}^{-1}\left\{\tilde{A}_{n,flat}\tilde{H}_{n,rough}(t_i,\omega)e^{-(\alpha(\omega)-\alpha_{\text{centre}})c\tau_n}\right\} \qquad (5\text{-}3)$$

Each response vector on a path $h_{n,path}(t_i,\tau)$ has the form of an FIR.

5.3.3 Simulating spatial coherence between surface interactions

The spatial coherence between surface interactions along an eigenpath could be implicitly simulated by calculating successive surface responses from subsections of a sufficiently large spatially continuous 3D surface realisation. However many of these surface interactions that have similar bistatic geometry (i.e. grazing angle and virtual source/receiver depths) will yield similar time-varying responses (excepting a time-shift) owing to the time and space-harmonic nature of an idealised linear harmonic ocean surface.

The calculation of unique surface interactions has been minimised by taking a calculated time-varying response for a single surface interaction and re-using it

to represent similar horizontally displaced surface interactions. Judgements have been made about the bistatic geometry variants that may be considered 'similar'. The rationale and justification for these judgements of similarity are addressed in Sections 5.4.6 and 5.4.9.

For the case of a multiple-surface-bounce eigenpath it has been assumed that successive surface interactions are sufficiently similar that they are modelled with time-shifted versions of the same time-varying bistatic response. The frequency-domain response to a single surface realisation at real-time instant t_i is approximated as the product of N_{top} bistatic rough patch responses $\breve{H}_{n,patch}(t_i, \omega)$ as per Eq.(5-4), where N_{top} is the number of surface interactions along the eigenpath. The q_j represent non-sequentially selected instances from a common time-circular stack of Q bistatic rough-patch responses.

$$\tilde{H}_{n,path}(t_i, \omega) = \tilde{A}_{n,flat} \prod_{j=1}^{N_{top}} \tilde{H}_{n,patch}(t_{q_j}, \omega) \tag{5-4}$$

A new time-sequential instance of $\tilde{H}_{n,path}(t_i, \omega)$ is calculated from Eq.(5-4) by indexing each $q_j$by one. This idea is shown schematically for a double-surface-bounce path in Figure 5-4.

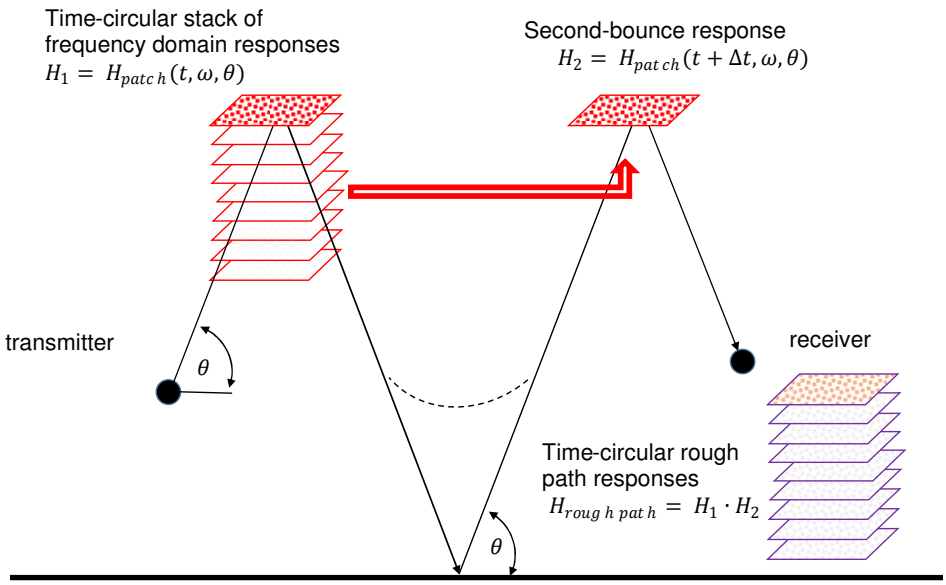

Figure 5-4: Conceptual frequency-domain calculation of double-surface bounce path response, by recycling the bistatic response stack using a different starting instance

Depending on channel range, the manner in which the initial N_{top}instances of $\tilde{H}_{n,patch}$ are selected to give the first rough-path response $\tilde{H}_{n,path}(t_i, \omega)$ at $t = 0$ by

Eq.(5-4) affects the realism of the spatial coherence achieved. At short range when all surface interactions are horizontally displaced at distances comparable to the surface swell wavelength the initial draw of bistatic response instances in time needs to emulate the equivalent spatial displacement with respect to the dominant swell wavelength. This comment relates not only to multiple surface responses along an eigenpath but also to surface interactions on different eigenpaths.

For shorter channels, approximate spatial coherence is achieved by relating the on-axis spatial off-set distance $\Delta x_{n,p}$ of the p^{th}surface interaction along the n^{th}eigenpath to the equivalent discrete-time starting index positions $q_{n,p}$ in the time-circular response stack by Eq.(5-5). The time and spatial offsets are scaled by the peak swell-speed on the transmission axis $\mathrm{v}_{swell(pk)}$ obtained from the angularly spread surface-wave spectrum.

$$t = 0, \qquad q_{n,p} = \mathrm{round}\left[\left(\frac{\Delta x_{n,p}}{\mathrm{v}_{swell(pk)}}\right) f_s\right] \tag{5-5}$$

For longer range simulations where surface interactions span multiple swell wave-lengths, and there is consequently no discernible correlation between rough eigenpath responses in experimental channel response histories, the random-draw of starting bistatic responses is adequate. For this option the discrete starting index positions $q_{n,p}$ for surface interactions $p = 1 \,..\, N_{top}$ along the n^{th} eigenpath are chosen by Eq.(5-6) using the Matlab™ *Randi* function, indicating the random generation of N_{top} integers each from the interval [1:Q].

$$t = 0, \qquad q_{n,p} = \mathrm{Randi}\left[N_{top}, Q\right] \tag{5-6}$$

The first rough path response is then calculated by Eq.(5-7) with q_p determined by Eq.(5-5) for shorter ranges comparable to the swell wavelength, to achieve approximate spatial correlation of surface interactions across eigenpaths and between interactions along a path, or at longer ranges by Eq.(5-6) when the relative swell phase at different surface interactions may be approximated as random.

$$\mathrm{t} = 0,\ \widetilde{H}_{n,path}(t_i, \omega) = \tilde{A}_{n,flat} \prod_{p=1}^{N_{top}} \widetilde{H}_{n,patch}\left(t_{q_{n,p}}, \omega\right) \tag{5-7}$$

The subsequent instances of $\widetilde{H}_{n,patch}$ that are multiplied to form $\widetilde{H}_{n,rough}(t_i,\omega)$ are then drawn sequentially and circularly from the same time-sequential array $\widetilde{H}_{n,patch}(t,\omega)$ as per Eq.(5-8) and illustrated schematically in Figure 5-4. In this manner realistic time-coherence is achieved in every surface interaction.

$$t>0, \qquad \widetilde{H}_{n,path}(t_i,\omega)=\tilde{A}_{n,flat}\prod_{p=1}^{N_{top}}\widetilde{H}_{n,patch}\left(t_{q_{n,p}},\omega\right),$$

$$q_{n,p}=\ Q, if\ \mathrm{rem}\left[\frac{q_{n,p}+\ i-1}{Q}\right]=0, else, q_{n,p}=\ \mathrm{rem}\left[\frac{q_{n,p}+\ i-1}{Q}\right] \qquad (5\text{-}8)$$

5.3.4 Surface-path response up-sampling

The size of the $h_{n,path}(t,\tau)$ FIR response arrays is manageable for storage and re-use at a later time. However, a time interval Δt of 20 ms between successive $h_{n,path}(t_i,\tau)$ FIR responses is too coarse for the purpose of convolution with a communication signal sampled at 96 kHz.

The channel response in the real-time (t) dimension is therefore up-sampled to the input signal sampling rate. This has been done by linear interpolation in the time dimension of the real and complex components of the frequency domain response $\widetilde{H}_{n,path}(t,\omega)$, followed by inverse transform of $\widetilde{H}_{n,path}(t,\omega)$ to $h_{n,path}(t,\tau)$ just prior to signal convolution.

Linear interpolation in time of $\widetilde{H}_{n,path}(t,\omega)$ was chosen over time domain interpolation of $h_{n,path}(t,\tau)$, as frequency-domain linear-interpolation is physically meaningful, implying a linear change in the coherently summed rough-patch pressure response (at a specific wave frequency) over the interval as the surface changes. For most of the surface elements from which the aggregate pressure response is calculated this will correspond to a near linear change in element elevation and/or tilt angle.

5.3.5 Signal convolution with surface-path responses

The total signal output $y(t)$ is calculated as the sum of N_{path} eigenpath FIR responses $h_{n,path,}(t,\tau)$, with each FIR having M delays. The sum of the eigenpath FIR responses is given by Eq.(5-9) which represents the discrete-time

implementation of the continuous signal-time-varying channel convolution expressed by Eq.(2-4). In the case of relative transmitter movement each eigenpath response is convolved with the corresponding Doppler shifted copy of the input signal $x_n(t)$. The gross delay for the n^{th} eigenpath $\bar{\tau}_n$ is obtained from the Bellhop ray model. This is shown with a bar to distinguish it from the discrete variable delay τ_m within the surface response FIR.

The real-time subscript 'j' is used to indicate discretisation at the signal sampling rate (1/96 kHz), whereas the subscript 'i' indicates discretisation at the channel sampling rate (20 ms). The indexes 'm' and 'j' have the same time resolution.

$$y(t_j) = \sum_{n=1}^{N} \left\{ \sum_{m=1}^{M} h_{n,path}(t_{(i+m-1)}, \tau_{(M-m+1)}) x_n(t_{(i+m-1)} - \bar{\tau}_n) \right\} \qquad (5\text{-}9)$$

On each of the eigenpaths, the response interpolation at the signal sampling rate enables each input signal sample $x_n(t\ )$ to be convolved with a unique interpolated path FIR response $h_{n,path,}(t\ \ ,\tau)$ over a period of M FIR delays. At any instant in time, the output value from a single eigenpath is the summation of M sequential micro-path FIR outputs, each representing successive 'frozen' rough channel response as shown schematically on Figure 5-5.

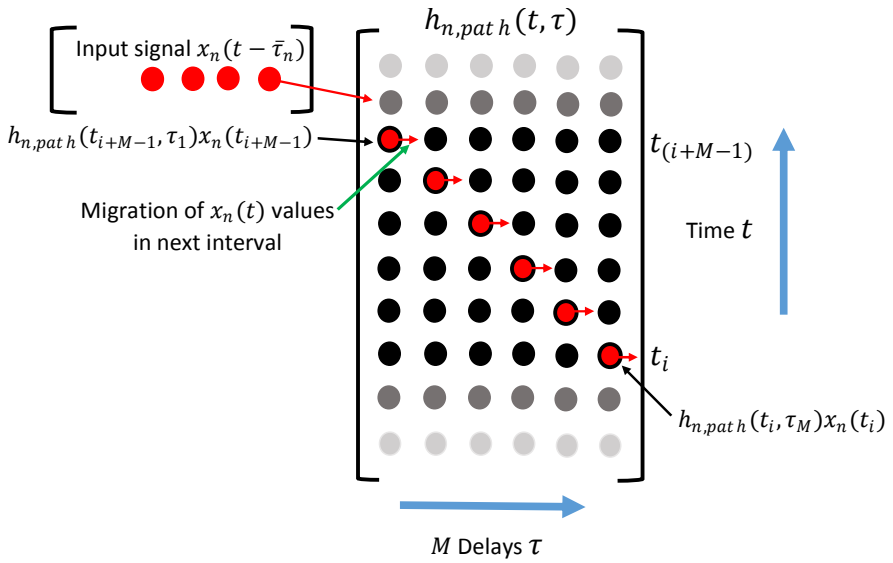

Figure 5-5: Schematic convolution of transmit signal (discrete stream of red dots) with path FIR cascade (black dots). An individual input value x_i is convolved with a complete unique path response $h(t,\tau)$ over M successive time intervals. At any instant the output is the summation of M successive x values (in red) convolved with M unique successive $h(t,\tau)$ (black values coincident with the red values)

5.3.6 Doppler compensation of transmit signal

Doppler time compression/expansion from transmitter motion resolved into the mean path grazing angle is accounted for by calculating a unique Doppler-shifted input signal copy $x_n(t)$ for each eigenpath. This signal copy is calculated in two steps. The first is to calculate the Doppler-shifted discrete time vector $t_{Doppler}$ as per Eq.(5-10), where $\vec{v}(t)$ is the time varying transmitter velocity vector, and $\hat{p}$ is the unit vector in the path launch angle direction. Complex-plane interpolation (by A. Duncan) is then used to interpolate a Hilbert-transformed copy of the input signal using $t_{Doppler}$ to define the interpolated points.

$$t_{Doppler} = \int (1 + \vec{v}(t).\hat{p}/c)dt \tag{5-10}$$

The separate convolution of the signal with each eigenpath response enables Doppler effects from transmitter motions to be uniquely resolved into each eigenpath grazing angle. This still represents an approximation however, as Doppler applied to the path grazing angle is also implicitly applied, without adjustment, to the continuous fan of incident and reflected angles that comprise the bistatic response geometry of surface interactions as described in the next section.

5.4 Calculation of bistatic rough surface response

5.4.1 Introduction

The frequency domain rough-surface pressure response $\widetilde{H}_{patch}(\omega)$ for a single surface interaction with a 'snapshot' of the real moving surface (such as Figure 5-6), is calculated for the discretised surface as described in Section 2.4, making the Kirchhoff Approximation on the scattering surface that the scattered pressure at the surface is equal and opposite to the incident pressure (Ogilvy 1991).

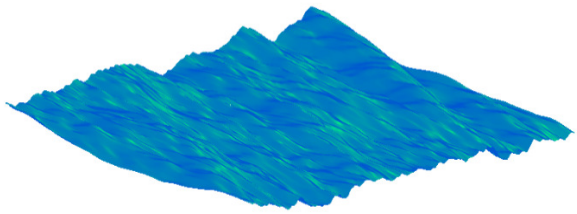

Figure 5-6: Surface realisation using WAFO Toolbox (WAFO 2011)

The complex-valued net pressure response $\tilde{p}_r(\omega)$ at a receiver for the aggregation of surface elements is calculated by coherent addition of individual element pressure responses as in Eq.(2-22), based on the geometry in Figure 2-8. In the next step the terminology is altered from $\tilde{p}$ for pressure to $\widetilde{H}$ for a general frequency-domain response function. The bistatic-range-normalised frequency-domain rough patch pressure response $\widetilde{H}_{patch}(\omega)$ is then represented by Eq.(5-11).

The terms $(R_0 + R_r)(-1)e^{-ik(R_0 + R_r)}$ normalise the patch response by the flat-surface specular bistatic path range, and removes the phase-change associated with the surface reflection and path-range. This enables the result to be combined with the flat-surface ray-path response $\tilde{A}_{n,flat}$ without duplicating geometric spreading and phase changes already included in the flat-surface eigenpath-model.

$$\widetilde{H}_{patch}(\omega) = \tilde{p}_r(\omega)(R_0 + R_r)(-1)e^{-ik(R_0 + R_r)} \qquad (5\text{-}11)$$

By evaluating Eq.(5-11) for successive surface realisations in time t, a time-series array of bistatic surface responses $\widetilde{H}_{patch}(t,\omega)$ is generated, then discrete inverse transformed by Eq.(5-12) to obtain $h_{patch}(t,\tau)$, which is a real-valued array.

$$h_{patch}(t,\tau) = \mathcal{F}^{-1}\left(\widetilde{H}_{patch}(t,\omega)\right) = \frac{1}{M}\sum_{m=1}^{M-1} \widetilde{H}_{patch}(t,\omega_m)\mathrm{e}^{i2\pi m\tau} \qquad (5\text{-}12)$$

Figure 5-7 schematically illustrates the discretised calculation geometry, and the optional exclusion of pressure contributions from elements that are shadowed with respect to either the source or receiver. The green rays represent the element incident field centreline at radius r_0 and the red rays the element-receiver centreline at radius r_r. The dashed black line represents the mean-plane specular path radii R_0 and R_r . The model does not include secondary reflections within the surface structure or diffraction into shadowed portions of the surface structure (if the shadowing option is selected). Thus the surface response model may be described as a 'local single reflection' model (Elfouhaily and Guérin 2004).

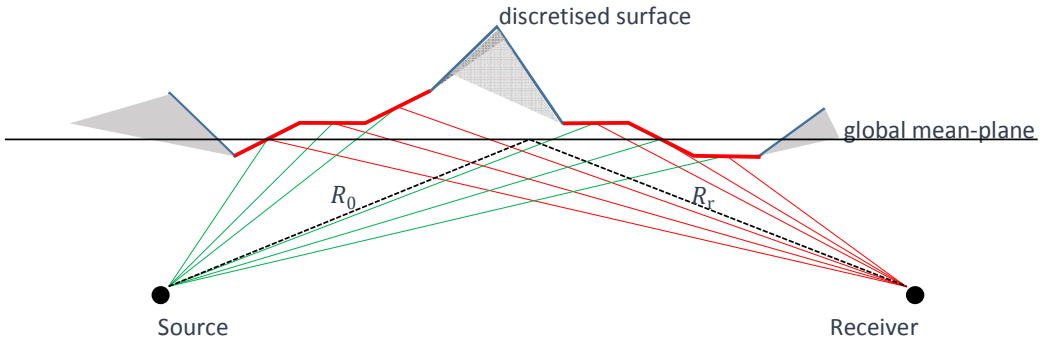

Figure 5-7: Geometry for summation of bistatically illuminated surface element contributions, showing elements shadowed by either the source or receiver. Mean-plane geometry shown superimposed (black)

5.4.2 Exploration of KA dynamic response for shadowed surfaces

Literature on the Kirchhoff approximation rough surface response notes the uncertainty of the KA response fidelity at low grazing angles when a high proportion of the surface profile is shadowed (Ziomek 1982, McCammon and McDaniel 1986, Ogilvy 1988, Thorsos 1988).

In this section the time-varying bistatic response $h(t,\tau)$ of a shadowed rough surface is modelled for 500m range with a 10m deep source and receiver, using the KA implementation described in Section 2.4. The model is explored for three alternative methods of addressing surface-shadowing. Results for the KA model are compared with the 2D Integral Equation (IE) boundary element reference model described in Section 2.5. The dynamic comparison of KA and IE response characteristics for a bistatic rough surface response is similar to that presented by Toporkov and Brown (2002) in the context of EMR bistatic scattering from the top-side of the ocean surface. All comparisons use Fourier synthesis in the 8 kHz to 16 kHz bandwidth to generate the delay-time-domain response.

The IE versus KA comparison would ideally be calculated for a 2D surface patch with length comparable to the 500 m bistatic range. This comparison has been achieved with a smaller 34 m long 2D patch, with the smaller patch length determined by available computational resources for the IE model, by running three comparative simulations representing the near-source, centre, and near-receiver parts of a 500 m range as depicted in Figure 5-8. This is justified on the basis that the wave responses from portions of the surface may be expected to be

coherently additive, such that IE versus KA comparisons for representative patches provide accurate insights to a comparison of the surface response with dimension comparable to the whole range.

The centred patch corresponds to a symmetrical 2.3° mean grazing angle, whilst the biased-position patches offset 50 m from the ends produce uneven 1.3° and 11.3° grazing angles. The combination of geometry and wave-direction combine to produce 95% shadowing averaged over time for the near-source patch, 99% for the centre patch and 96% for the near-receiver patch. The end patch positions have a mean-path delay 0.47 ms longer than the centrally positioned patch.

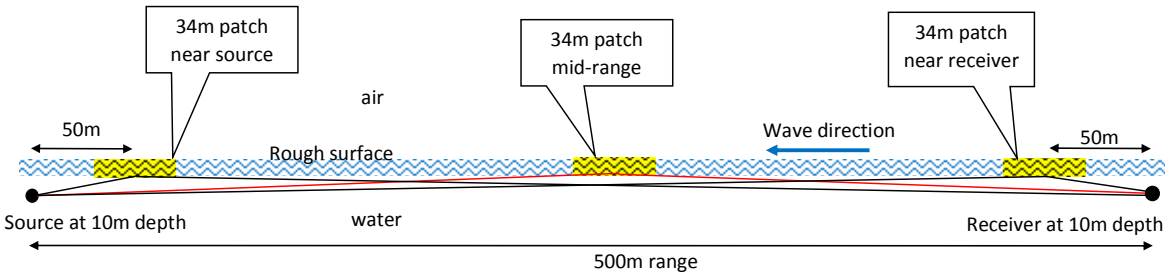

Figure 5-8: Three small rough-patches used to explore the IE/KA comparative response for a much longer 500 m rough surface patch

5.4.2.1 Problem size constraints

A 2D IE reference model was used rather than a three-dimensional (3D) model because the computational problem is too large in three dimensions for the 16 kHz maximum frequency of interest. For example, the modelled 34 m long 2D patch was discretised at a quarter-wavelength for the maximum frequency of 16 kHz, or $\lambda_{min}/4 =$ 2.34 cm. For the IE methodology this requires inversion of a 1500 x 1500 = 2.25 x 10^6 element matrix for each frequency, of each surface realisation. This inversion was replicated for 1500 surface realisations at 20 ms intervals to achieve a 30 s response history, multiplied by 81 frequencies at $dF = 100$Hz between 8 kHz and 16 kHz to achieve $1/dF = 10$ ms delay window. The computational time for 64-bit processing at 10 GHz in Matlab was approximately 20 hours.

If this IE computation was extended to 3D by including rough patch variation in the transverse direction, the computational time would be increased by a factor of ${n_y}^2$, where n_y would be the number of points at $\lambda_{min}/4$ spacing in the transverse y direction. An inadequate 1 m wide section of a 3D 34 m long patch would require

4 years of continuous processing at 10 GHz to generate 30 seconds of bistatic bounce response history (by a standard matrix inversion implementation). Thus, the use of the IE reference model is pragmatically limited to the consideration of 2D rough patch calculations only.

In comparison, the KA model using the Kirchhoff Approximation required approximately 2 minutes to run the same 1500 realisations for the same bandwidth and frequency resolution, and in doing so actually represented a 34 m x 7 m 3-dimensional surface patch using 12 cm longitudinal and transverse patch discretisation. For the IE model to include comparable 3-dimensional surface functionality would have required almost three-hundred-fold increase in the number of boundary points to represent the transverse dimension, with computation then requiring 198 years for the same 30 s simulation task to manage the very large matrix inversions. The point of this comparison is to highlight the enabling benefit of the Kirchhoff approximation for studying the bistatic response of three-dimensional surfaces.

5.4.2.2 Simulated rough surface

The 2D surface realisations were generated using the WAFO sea-surface simulation routines (WAFO 2011). The 2D profile was extended into a 7 m wide 3D corrugated surface for the KA model. The IE model response was computed in 2D using cylindrical coordinates, then converted to an equivalent 3D response as described in Section 2.5.2 to enable comparison with the KA model.

A fine horizontal increment of 2.34 cm was used for both IE and KA models (corresponding to $\lambda_{min}/4$ at 16 kHz). The amplitudes for a simulated rough surface with a high degree of shadowing were chosen to be four times greater than the Cottesloe experimental surface. Two Pierson-Moskowitz surface wave spectra were generated and combined to achieve an empirical fit to the Cottesloe experimental surface, then the significant wave height was increased four-fold. A lower frequency spectrum was generated for H_s = 1.6 m significant height swell at T_p =13.5 s peak wave period. This was added to a higher frequency Pierson-Moskowitz spectrum generated for H_s = 1 m sea and T_p = 3 s peak period (left-hand Figure 5-9). Both spectra were then dispersed for a 13.5 m water depth using assumed 'Poisson' angular spreading (right-hand Figure 5-9 and Figure 5-10).

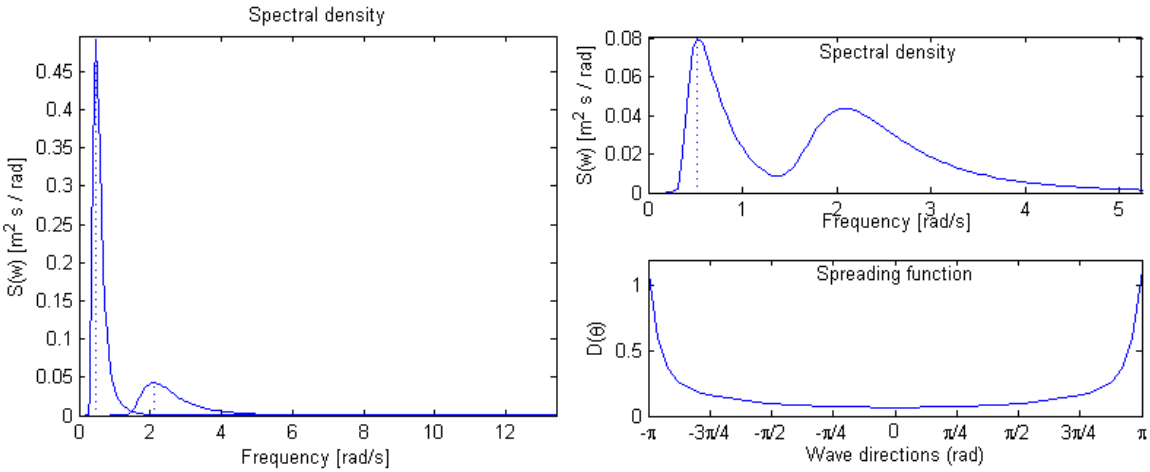

Figure 5-9: Swell and Sea Pierson-Moskowitz spectra for shadowed rough surface before depth/directional dispersion (left), and after 3D dispersion (right)

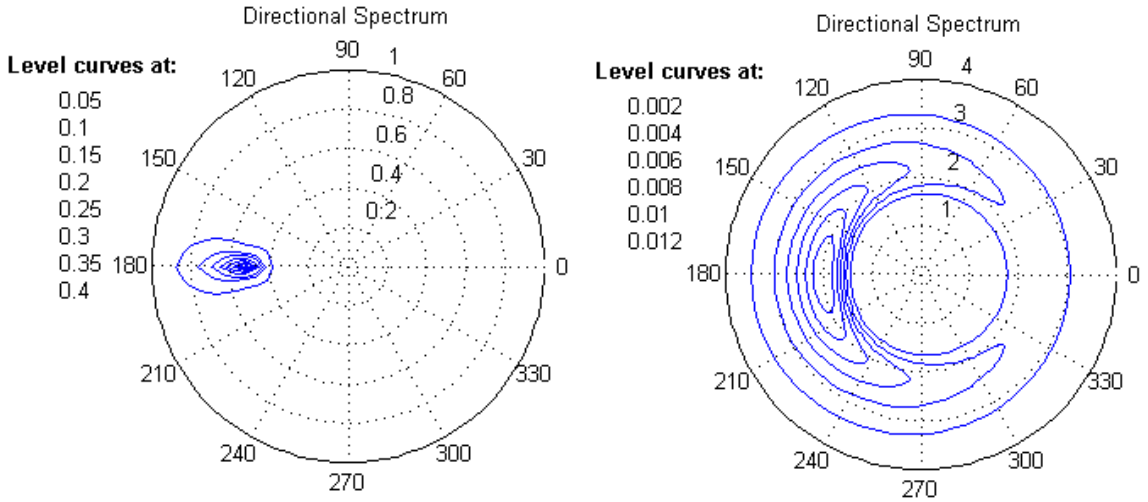

Figure 5-10: Directional spectra for swell (left) and sea (right) of shadowed rough surface

Example surface profiles plotted at 5 s intervals over the 30 s simulation duration, and the time evolution of the 2D profile are illustrated on Figure 5-11.

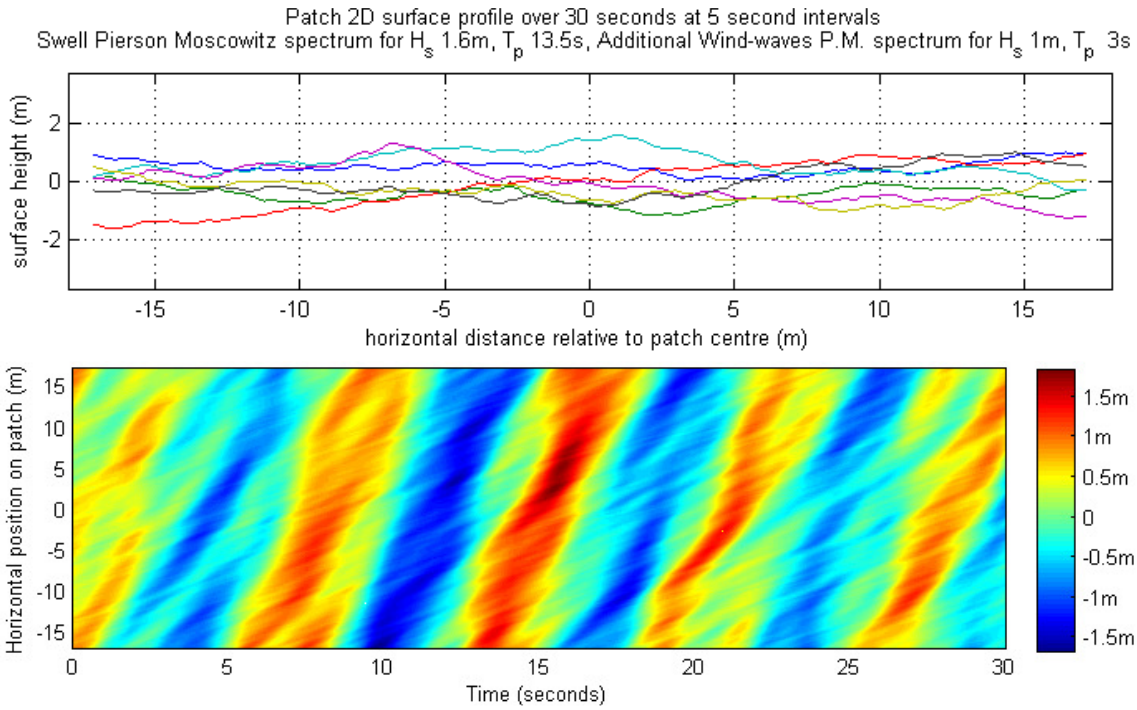

Figure 5-11: Patch 2D surface realisations over 30 s interval – shown as correct aspect-ratio profiles (top), and showing time-evolution of the source-receiver profile (bottom)

5.4.2.3 Simulation results

The IE and KA model bistatic response histories $h(\tau, t)$ for the 34 m long rough surface patch located centrally at 500 m range are presented in Figure 5-12. Both the IE and KA methods show side-band oscillations due to the 8 kHz -16 kHz band-limited Fourier synthesis of the response. The zero reference time corresponds to the mean path delay for a flat surface.

The left-most image is the IE model result. The high degree of surface shadowing (99%) is such that exclusion of all shadowed elements in the KA model (centre-left image) generates a response approximately 25 dB lower than the IE reference model. It is clear from this result that more of the surface is involved in creating the IE response than the 1% of bistatically illuminated wave troughs.

For the centre-right KA simulation result on Figure 5-12 the responses from elements that were self-shadowed with respect to either the source or receiver were excluded, on the basis that these situations fell outside the scope of the KA element response derivation. The responses from elements over-shadowed by others, but otherwise having incident and reflected paths both on the water side of the element, were retained on the basis that they could conceivably contribute via an unspecified secondary diffraction/multiple-reflection mechanism (not

included in the model). This result also bears a poor resemblance in magnitude and temporal characteristics to the IE result.

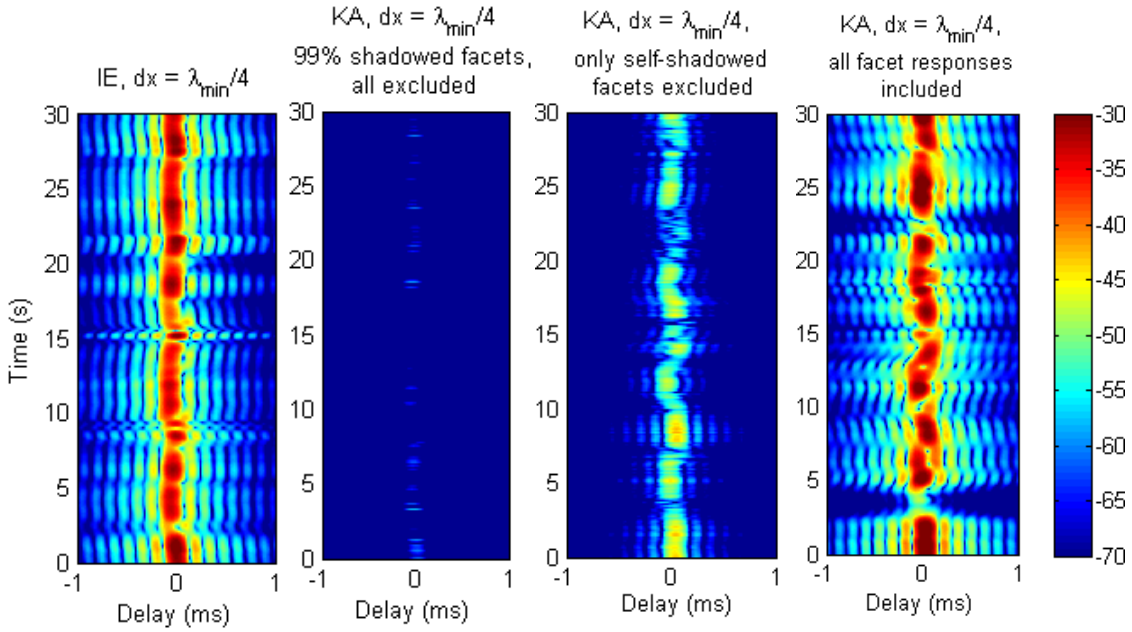

Figure 5-12: Bistatic response history $|h(t,\tau)|^2$(dB) for 99% shadowed 34 m long rough surface patch at 2.3° mean grazing angle located midway on 500 m range. IE (far left), KA with all shadowed elements excluded (centre left), KA with only self-shadowed elements excluded (centre right), KA with contributions from all elements included (far right)

The far right image on Figure 5-12 is the KA result including responses from all elements, regardless of shadowing. This produces element contributions that are modulated in phase along the surface profile by self-shadowing with respect to the source as described in Section 2.4. Whilst the response detail is not a close match to the IE model, the scale of temporal variations and magnitude is realistic from a simulation perspective.

The comparative mid-range delay power profiles and Doppler power spectra corresponding to the first, second and fourth images of Figure 5-12 are shown on Figure 5-13 and Figure 5-14 respectively. These are derived as described in Section 2.5 from summation of the spreading function over the vertical time (t) dimension and horizontal delay (τ) dimension respectively. On the delay power profile, the inclusion of all shadowed elements in the KA response predictably biases the profile to the right, due to inclusion of responses off the underside of wave peaks at greater path delay than responses off wave troughs.

On the Doppler power spectrum, the inclusion of responses from shadowed elements results in a more dynamically continuous response. The exclusion of

shadowed elements results in elevated noise generated by the discontinuous exclusion of shadowed elements.

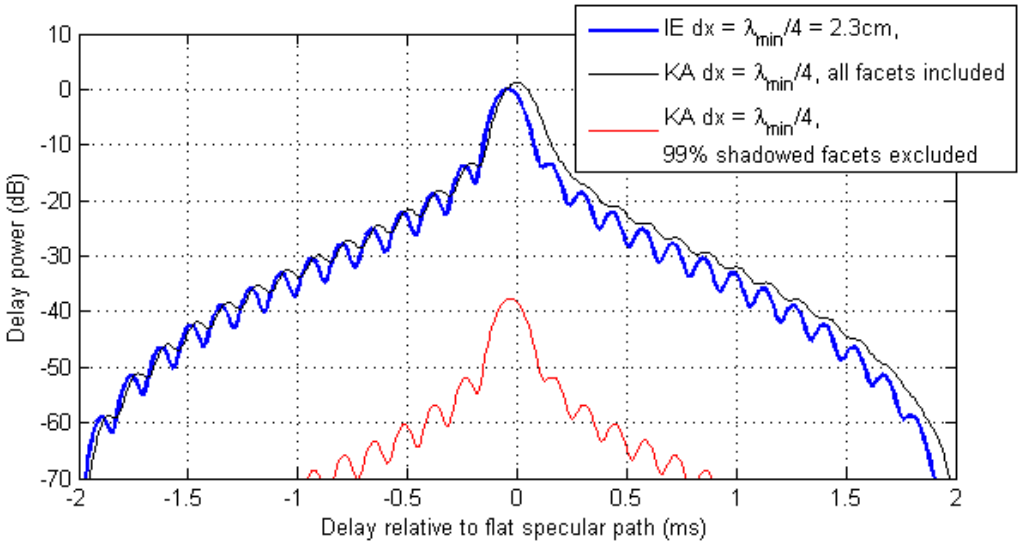

Figure 5-13: Bistatic IE versus KA delay power profiles $P(\tau)$ (dB), for 34 m long shadowed rough patch located mid-way at 500 m range illustrating KA response with and without inclusion of shadowed elements

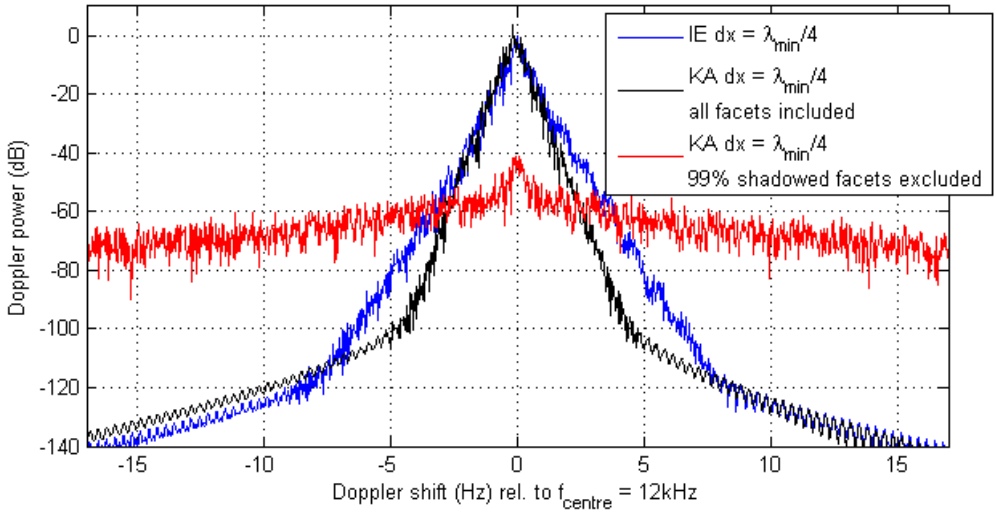

Figure 5-14: Bistatic IE versus KA Doppler power spectra $P(\nu)$ (dB), for 34 m long shadowed rough patch located mid-way at 500 m range illustrating KA response with and without inclusion of shadowed elements

The comparative IE/KA histories for the 34 m rough surface patch located 50 m from the source with uneven mean grazing angles (as depicted in Figure 5-8) are presented in Figure 5-15. The similar results with the patch located 50 m from the receiver are presented in Figure 5-16. The left images are the IE model, centre images KA with shadowed element responses excluded, and the right images are the KA model inclusive of all element responses.

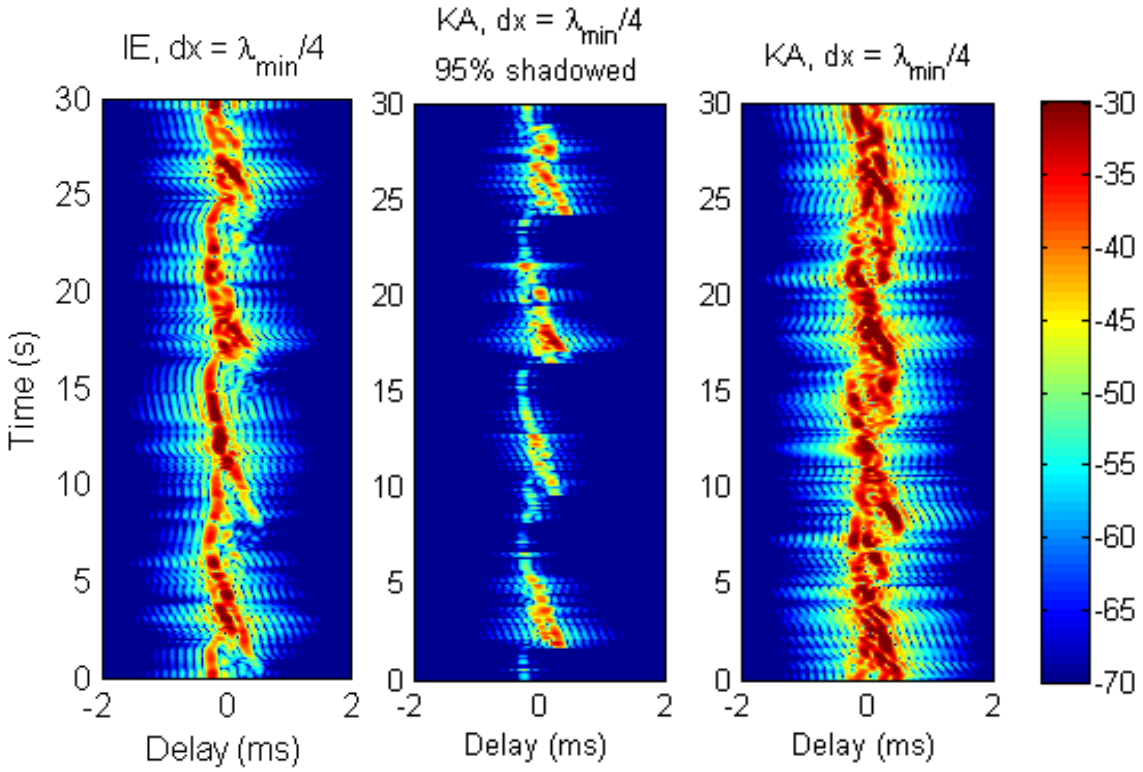

Figure 5-15: Bistatic response history $|h(t,\tau)|^2$(dB) for 95% shadowed 34 m long rough surface patch close to transmitter at 500 m range. IE (left), KA with shadowed elements excluded (centre), KA with all elements included (right)

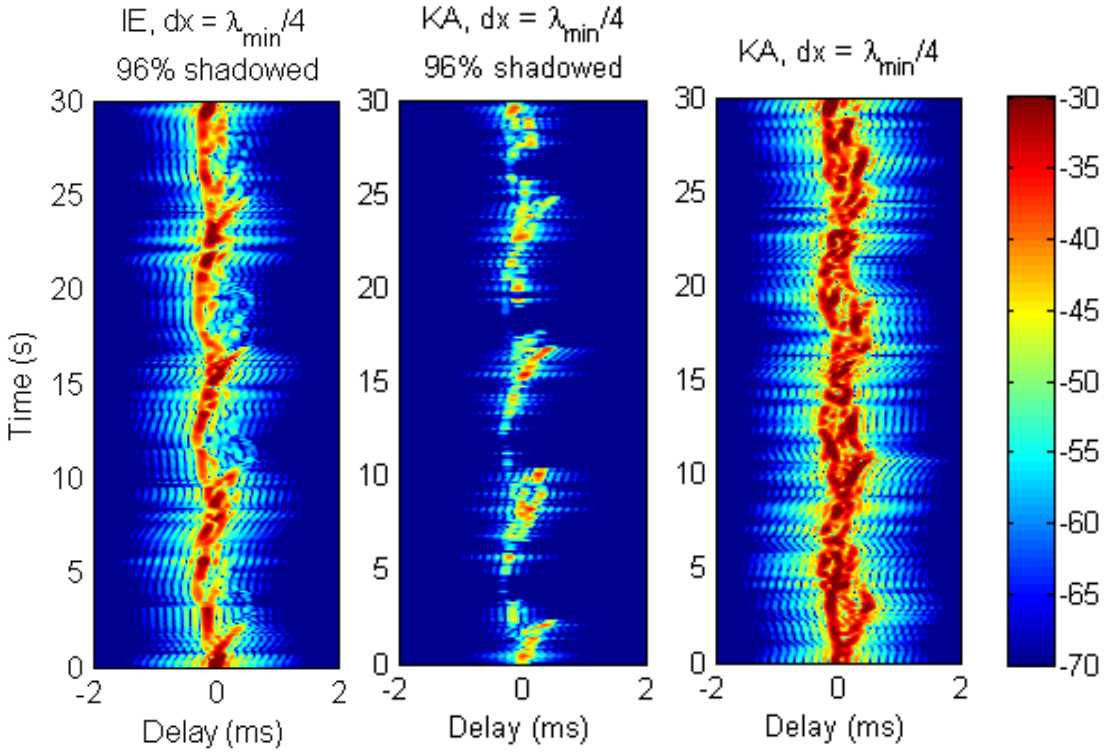

Figure 5-16: Bistatic response history $|h(t,\tau)|^2$(dB) for 96% shadowed 34 m long rough surface patch close to receiver at 500 m range. IE (left), KA with shadowed elements excluded (centre), KA with all elements included (right)

The comparative delay and Doppler characteristics corresponding to Figure 5-15 are shown on Figure 5-17 and Figure 5-18 respectively. On the delay power profile, the inclusion of all shadowed elements in the KA response delay-biases the delay power profile as was the case for the centre-range patch. By comparison of Figure 5-14 and Figure 5-18 it may be observed that the Doppler spreading is wider from surface portions closer to the source or receiver than from the range centre.

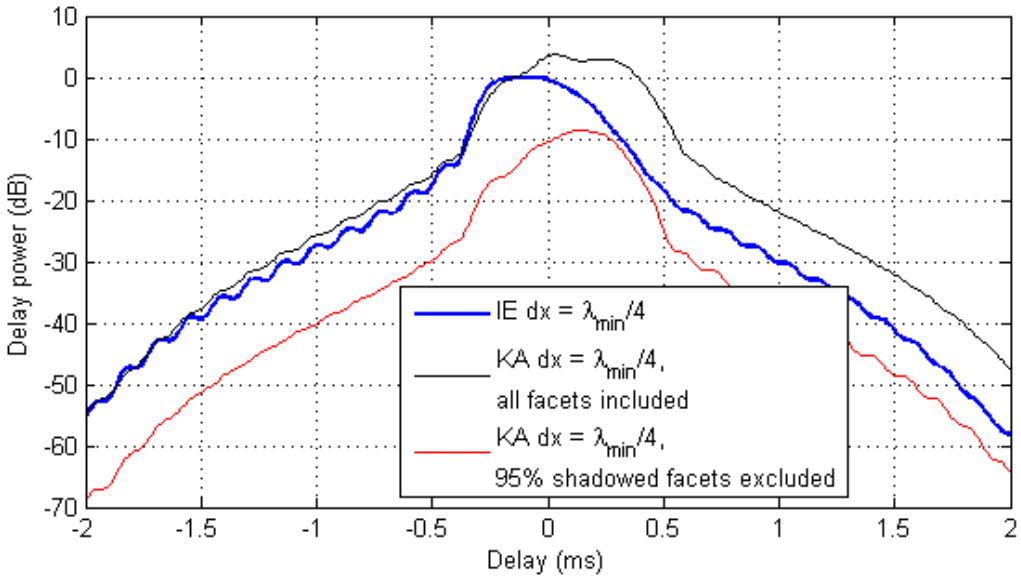

Figure 5-17: Bistatic IE versus KA delay power profiles $P(\tau)$ (dB), for 34 m long shadowed rough patch located near source at 500 m range illustrating KA response with and without inclusion of shadowed elements

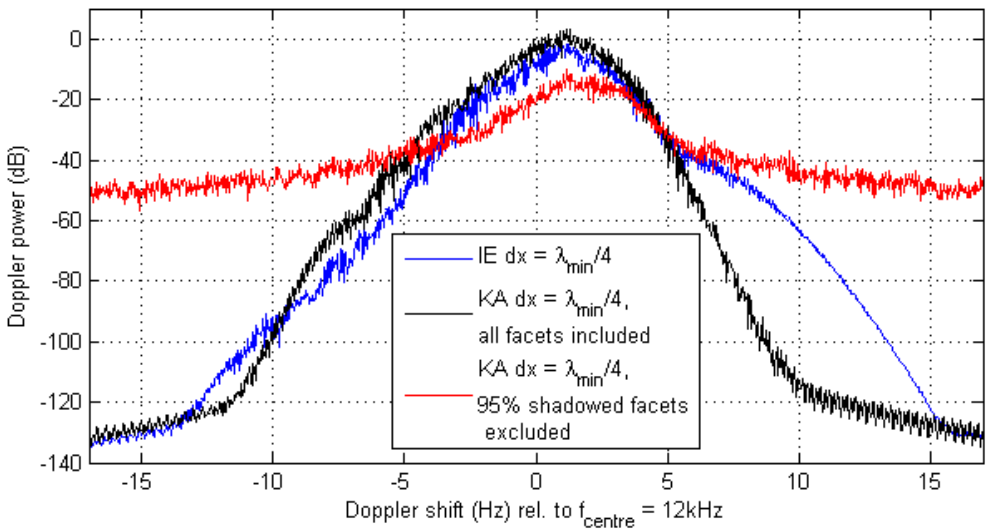

Figure 5-18: Bistatic IE versus KA Doppler power spectra $P(\nu)$ (dB), for 34 m long shadowed rough patch located near source at 500 m range illustrating KA response with and without inclusion of shadowed elements

The above results indicate that KA implementation for the full 500 m rough surface, without consideration of surface shadowing, will be most accurate for the centre part of the surface from which the highest response coherence will originate. The response towards the extremities will increasingly be overestimated, however because the portions equidistant from the range centre contribute at the same delay (~ 0.47ms), there will be a tendency for the contributions from the end portions (i.e. Figure 5-15 and Figure 5-16) to combine incoherently. The over-estimation of these end responses by the unshadowed KA method is therefore of lesser significance when the surface is considered in entirety.

To check the above assertions and to provide insight into how the KA response from a large surface patch compares to the small comparative patches, the KA response has been calculated for the full 466 m long surface incorporating the end patches depicted on Figure 5-8, with the results illustrated on Figure 5-19. This calculation used a larger horizontal discretisation of $1.25\lambda_{\min}$ to assist computations, based on the justification in Section 5.4.3. The calculation with shadowed elements excluded (left image) is clearly deficient in the primary mid-range response which generates the first part of the surface arrival in the delay.

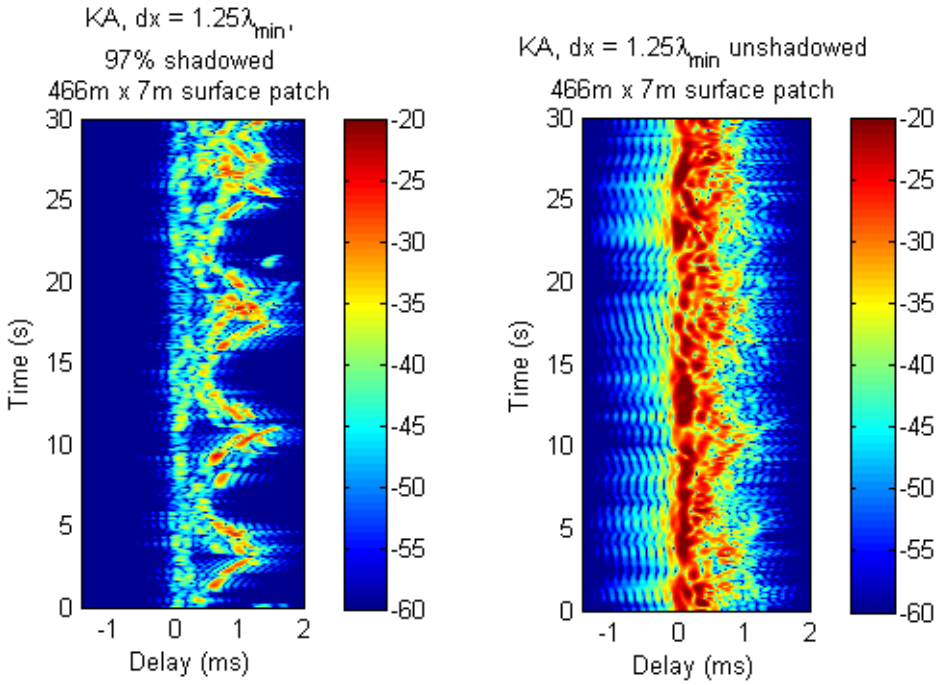

Figure 5-19: Bistatic response history $|h(t,\tau)|^2$(dB) for 97% shadowed 466 m long x 7 m wide corrugated 97% shadowed rough surface patch at 500 m range. KA with shadowed elements excluded (left), KA with contributions from all elements included (right)

In summary, the delay lag-bias and magnitude errors caused by inclusion of responses off all shadowed elements in the KA implementation are considered benign in comparison to the elevated Doppler power noise, and under-prediction of average response magnitude that result if shadowed element responses are included. On this basis inclusion of all elements is recommended for the KA method.

5.4.3 Exploration of KA dynamic dependence on element size

In this section the effect of the KA surface element discretisation size is explored, using the IE model as a reference. For the substantially shadowed rough surface simulation the KA model is run with and without inclusion of shadowed elements to provide additional evidence supporting the inclusion of shadowed elements in the KA model.

5.4.3.1 Exact effect of coarse surface discretisation

The exact effect of increasing the horizontal discretisation interval is investigated for the same shadowed rough surface as was used in Section 5.4.2 for 100m bistatic range. This has been achieved by running the IE model for both the fine reference surface discretisation ($dx = \lambda_{min}/4$), and an equivalently fine discretisation of the coarser discretised surface (i.e. $dx = \lambda_{min}/4$ on $dx = 5\lambda_{min}/4$ elements) as illustrated on Figure 5-20.

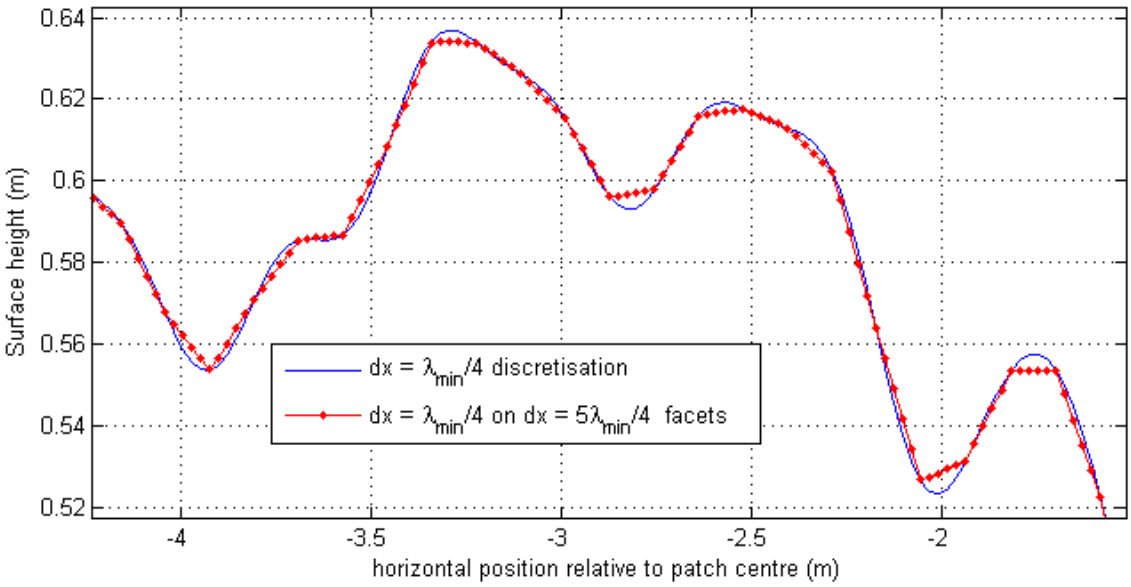

Figure 5-20: Relationship of discretised surface to reference surface for investigation of exact response to increased horizontal surface discretisation

The bistatic Doppler power spectra calculated by IE and KA for these two surfaces are compared on Figure 5-21. This comparison shows that the effect of the coarser discretisation is qualitatively similar for both IE and KA models at negative Doppler shifts, although larger for the KA model. At positive Doppler the effect on the IE response is more gradual. It is concluded that the change in the Doppler power spectrum for the KA model as element size is increased (notably the appearance of 'shoulders' in the KA spectrum) is partly attributable to the Kirchhoff approximation, and partly attributable to the changed surface profile associated with the coarser surface definition.

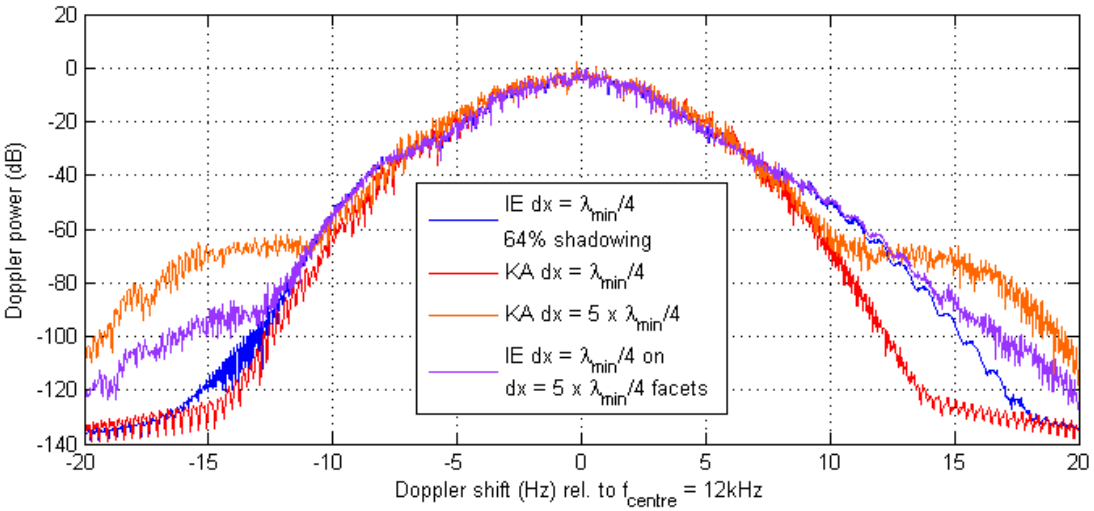

Figure 5-21: IE versus KA effect on bistatic Doppler power spectrum $P(\nu)$ (dB), of discretised approximation to reference surface– highly shadowed 34m long surface patch simulation located midrange at 100m

The delay power profiles for the same comparison (Figure 5-22) shows no trend between the fine and coarsely defined surface for either the IE or KA model. This is consistent with expectation as larger elements will not change the average path length. The higher KA response is consistent with inclusion of shadowed elements.

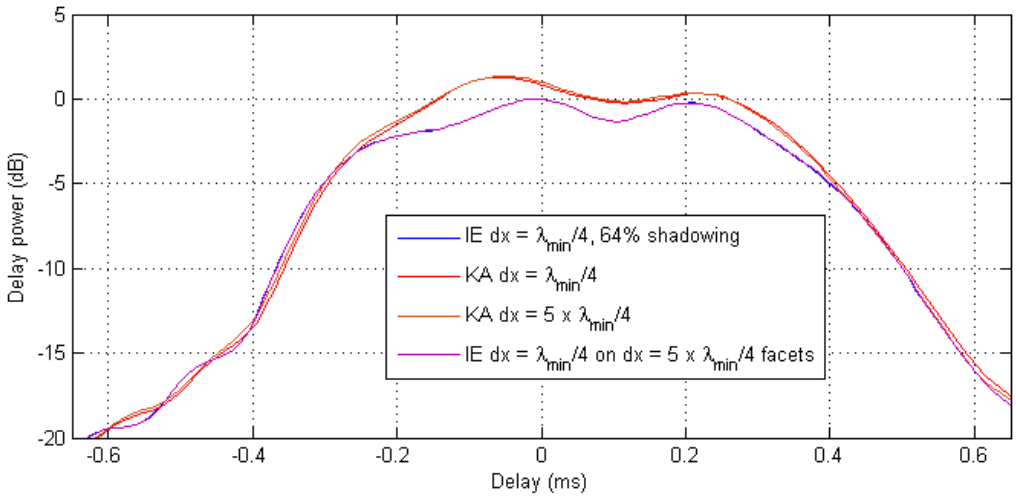

Figure 5-22: Bistatic delay power profile $P(\tau)$ (dB), of discretised approximation to reference surface – 64% shadowed 34 m long surface patch simulation located midrange at 100 m

The sign of the asymmetric Doppler spectrum of Figure 5-21 was verified by increasing the surface profile height at rates of 50 mm/s and 200 mm/s over the 30 s simulation, which should create a negative Doppler trend, and increasing delay with time. The resulting KA response history (Figure 5-23), spreading function (Figure 5-24) and Doppler power spectrum (Figure 5-25) show correct trends. The associated increase in positive Doppler in Figure 5-25 is explicable by the increased grazing angle and associated increase in in-path Doppler as the mean height of the surface increases.

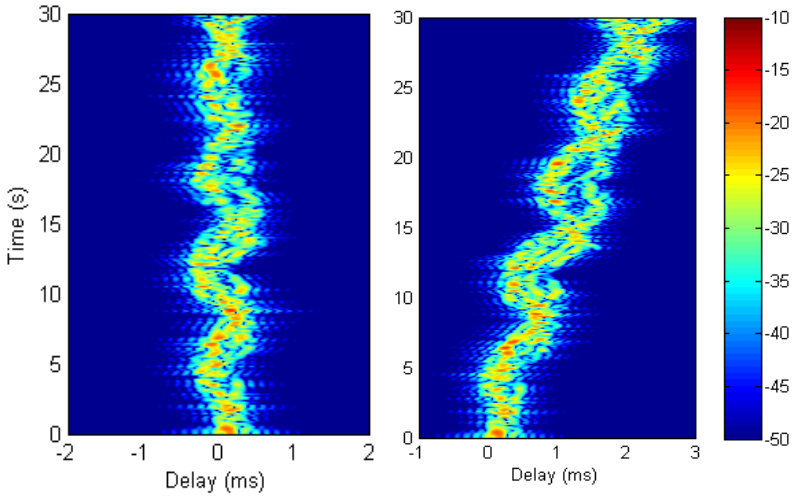

Figure 5-23: Bistatic response history $|h(t,\tau)|^2$(dB) for 64% shadowed 34 m long rough surface patch located midway on 100 m range. KA with zero-mean surface (left), KA with 200 mm/s increase in mean surface height over 30 s simulation interval (right)

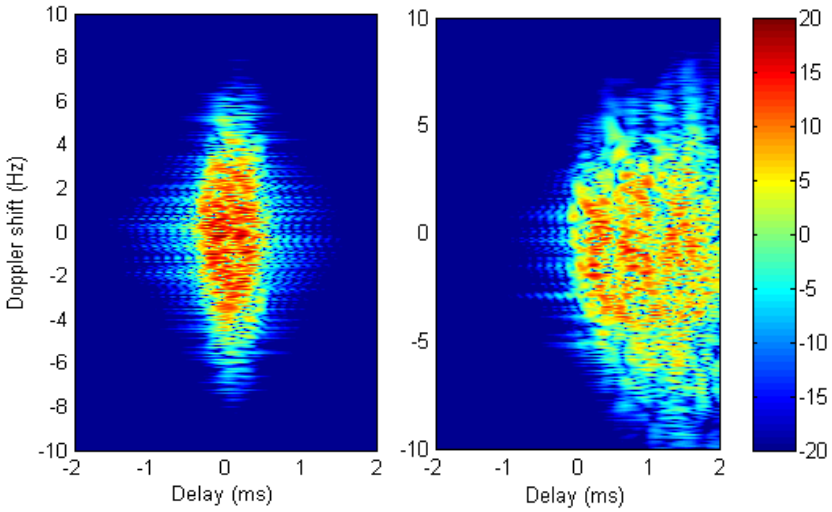

Figure 5-24: Bistatic spreading function $|S(\nu,\tau)|^2$(dB) for 64% shadowed 34 m long rough surface patch located midway on 100 m range. KA with zero-mean surface (left), KA with 200 mm/s increase in mean surface height over 30 s simulation interval (right)

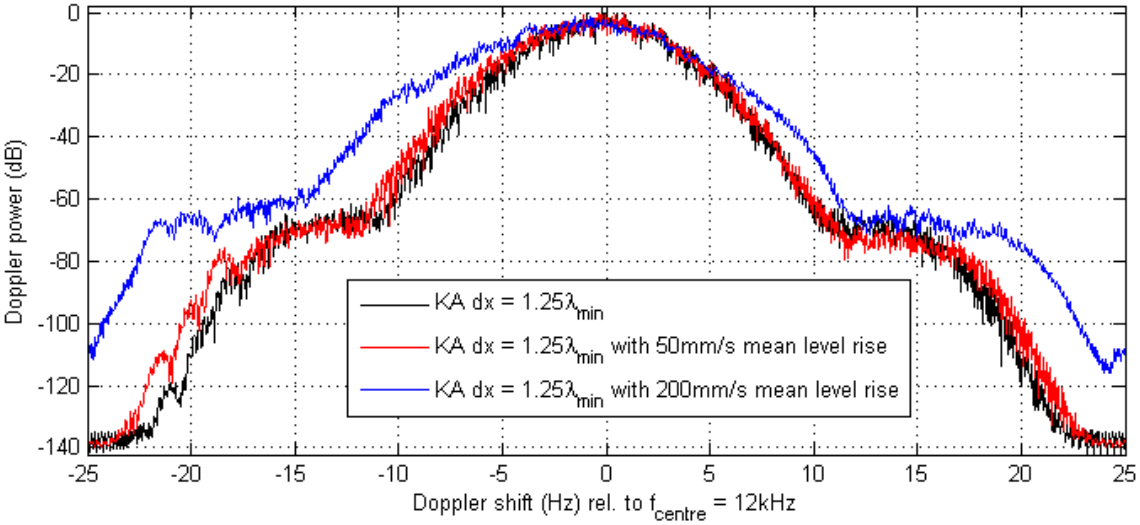

Figure 5-25: Bistatic KA Doppler power spectrum $P(\nu)$(dB) for 64% shadowed 34 m long rough surface patch located midway on 100 m range – 0 mm/s, 50 mm/s and 200 mm/s mean surface height increase over 30 s simulation interval

5.4.3.2 Derivation of surfaces with increased discretisation interval

To exclude high-frequency aliasing noise from down-sampling at coarser discretisation intervals $N_{\text{gridfactor}}\,\lambda_{min}/4$, the surface height vector was first zero-phase low-pass filtered with a Nyquist-normalised stopband frequency of $1/N_{\text{gridfactor}}$, before linear interpolation at the new horizontal interval $N_{\text{gridfactor}}\,\lambda_{min}/4$.

5.4.3.3 KA model with minimally shadowed surface

Comparisons of the KA and IE responses are presented below for a low sea-state surface with approximately 99.8% bistatic illumination, similar to the

experimental surface for the Cottesloe channel probe trial. bistatic geometry consisting of a 34 m long rough patch of surface centred at 100 m range with 10 m deep source and receiver, producing a 11.3° specular grazing angle. The experimental surface was generated as described in Section 5.4.2.2.

Example surface realisations are presented on Figure 5-26, plotted at 5 s intervals over the 30 s simulation duration at correct aspect ratio (top plot), with zoomed vertical scale (centre plot), and showing the time evolution of the profile (bottom plot). The correct-aspect figure gives a qualitative sense of the low amplitude and slopes of this surface.

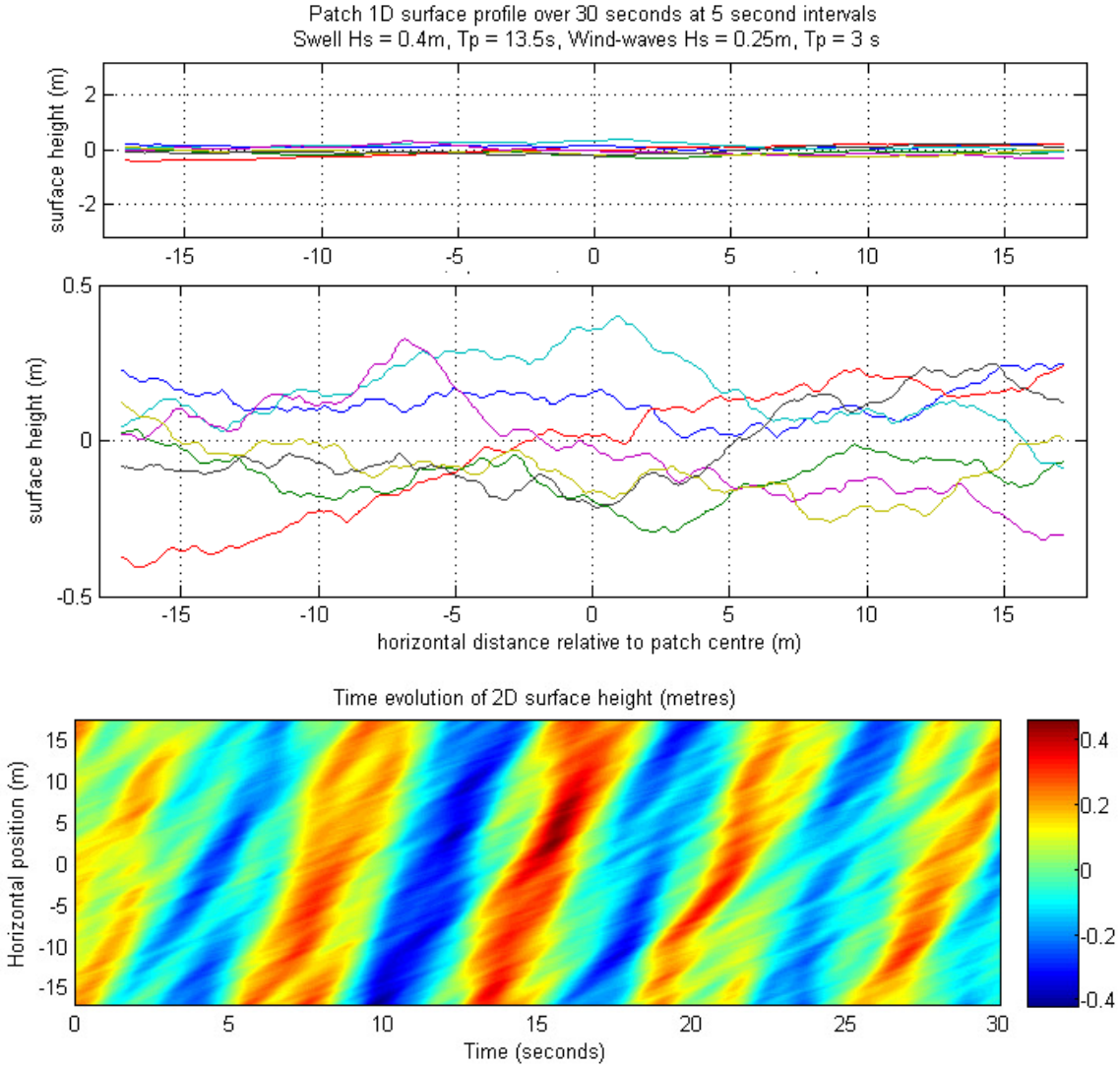

Figure 5-26: Patch 2D surface realisations over 30 s interval for negligibly shadowed surface – shown in-proportion (top) and with expanded vertical axis (centre), and showing time-evolution (bottom)

Figure 5-27 presents comparisons of the bistatic response histories $h(\tau, t)$ for the IE and KA models. The top plot shows the IE result for a 2.4 cm horizontal surface

discretisation. The bottom figures show the KA results for 2.4 cm, 12 cm, and 48 cm surface discretisation intervals Δx, corresponding to 1x, 5x, and 20x the IE model surface discretisation interval. The reference surface profile was low-pass filtered to exclude surface wavelengths shorter than $2\Delta x$ prior to definition at coarser intervals.

The KA calculation was conducted both including and excluding the small proportion (0.2%) of shadowed elements, with the response histories found to be very similar. The results presented relate to the inclusion of shadowed elements. The IE and KA response histories demonstrate similar temporal and delay spreading patterns for all KA discretisation variants.

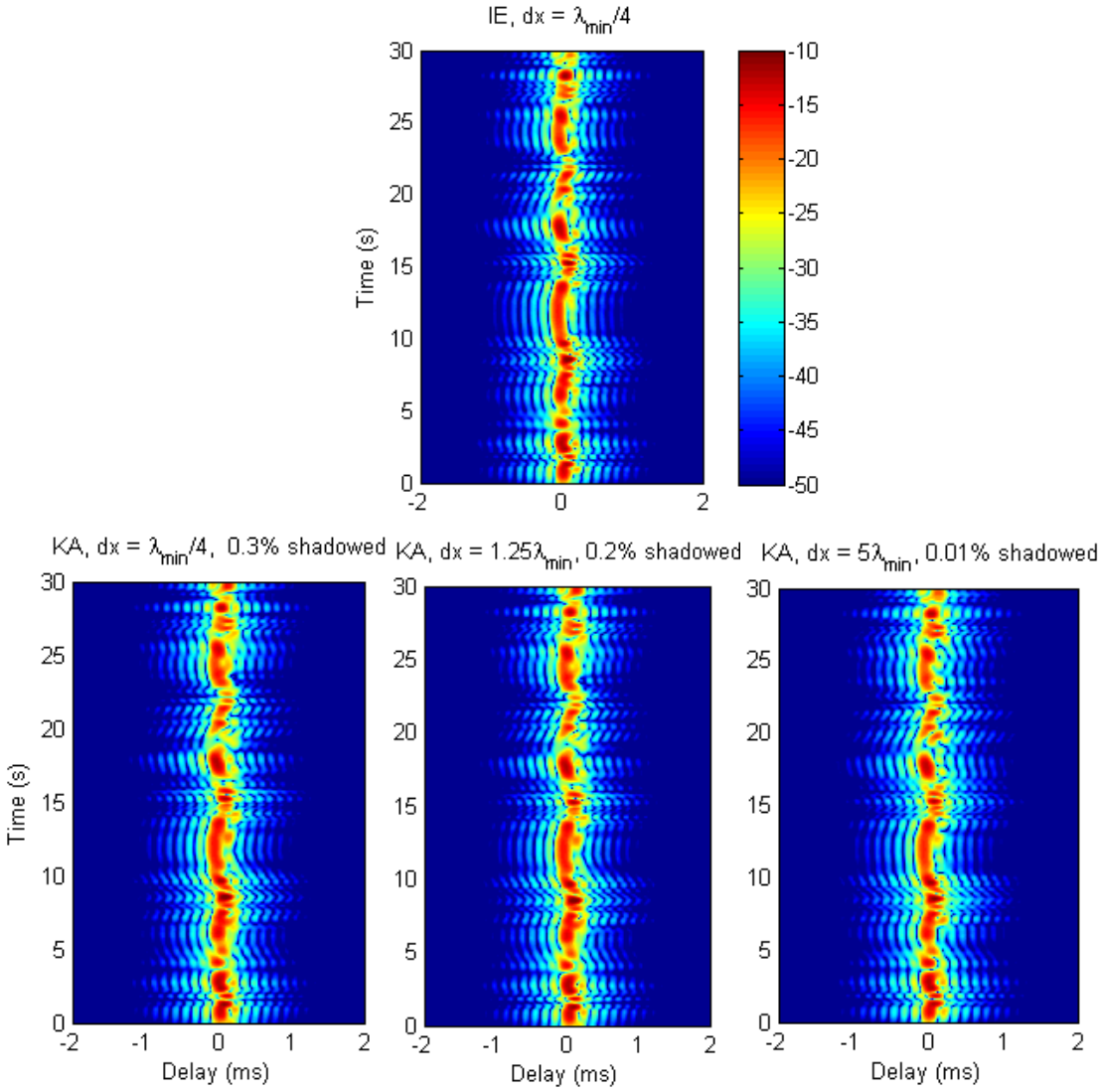

Figure 5-27: Bistatic response history $|h(t,\tau)|^2$(dB) - IE (top), KA model horizontal discretisation variants (bottom)– 34 m low-roughness patch centred at 100 m range and 11.3° grazing angle

The comparative IE and KA spreading functions are plotted on Figure 5-28. The KA spreading function is only shown for the largest discretisation (dx = $5\lambda_{min}$) as there was little appreciable difference for the other KA results.

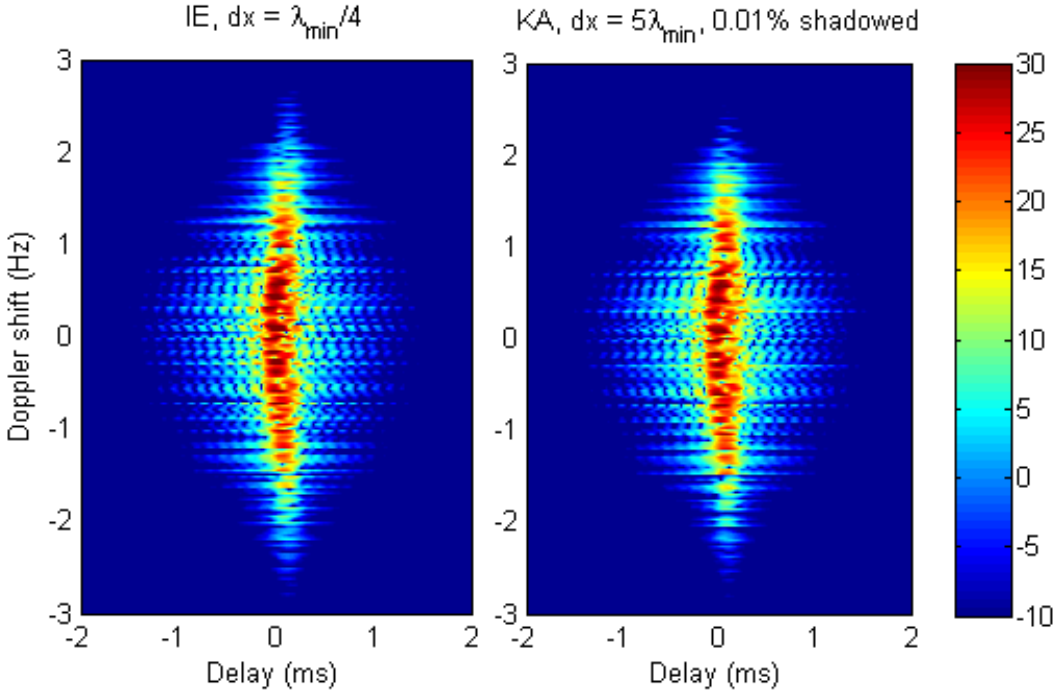

Figure 5-28: Spreading function $|S(\tau,\nu)|^2$(dB), IE (left), KA (right) – 34 m low-roughness patch centred at 100 m range and 11.3° grazing angle

The comparative IE and KA Doppler power spectra are illustrated on Figure 5-29. It is desirable that the envelope of the KA Doppler spectrum does not exceed that of the IE model, as to do so implies the existence of rapid transients that are absent from the IE reference model. It may be seen that as surface discretisation interval is increased to $5\lambda_{min}$, the KA model begins to over-predict at large Doppler. The qualitative appearance of "shoulders" in the KA Doppler power spectrum was determined in Section 5.4.3.1 to be attributable to the discretised shape of the surface profile as the discretisation interval grows larger. Thus, the appearance of Doppler "shoulders" is indicative of dynamically significant alteration of the surface by the surface discretisation process.

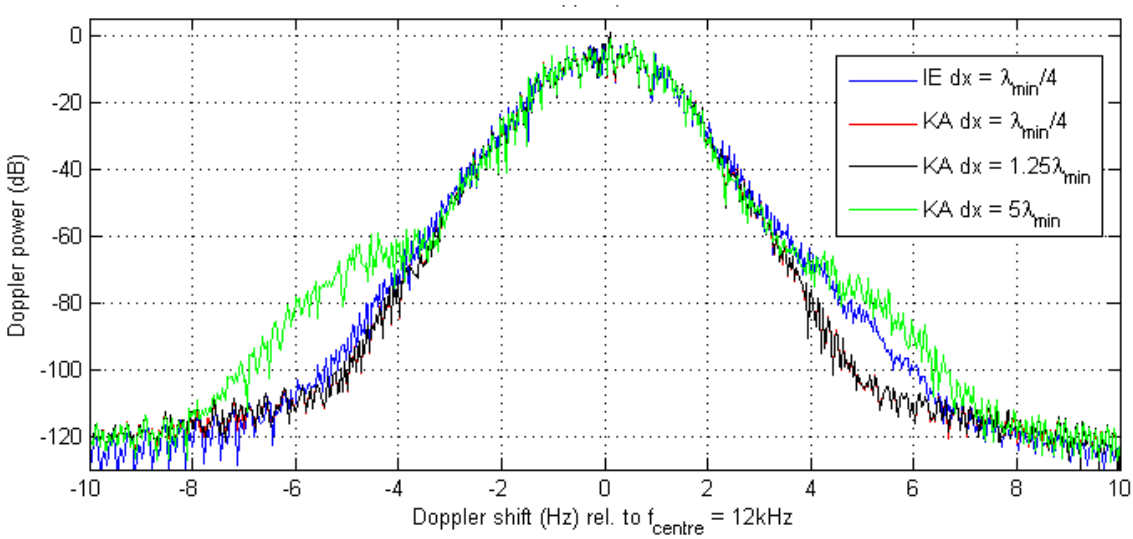

Figure 5-29: Doppler power spectrum $P(\nu)$ (dB), for bistatic response off low-amplitude surface – 34 m low-roughness patch centred at 100 m range. KA element size sensitivity with IE reference. KA model inclusive of shadowed elements

The comparative IE an KA delay power profiles are shown on Figure 5-30, indicating agreement in average power within 1 dB for the largest discretisation interval (green).

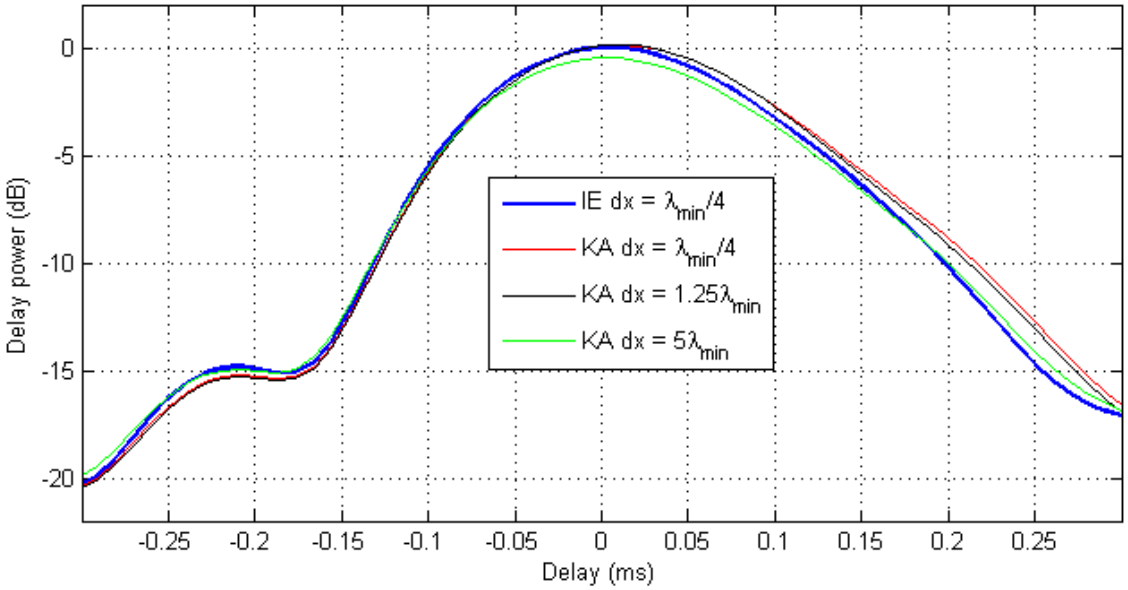

Figure 5-30: Delay power profile $P(\tau)$ (dB), for bistatic response off low-amplitude surface – 34 m low-roughness patch centred at 100 m range. KA element size sensitivity with IE reference. KA model inclusive of shadowed elements

The comparative IE and KA coherence plots are presented on Figure 5-31, calculated as described in Section 2.6.9. The line markers show the coherence progression in 20 ms steps either side of the zero reference time. The results show high coherence (0.99) for both IE and KA models at the 20 ms simulation interval.

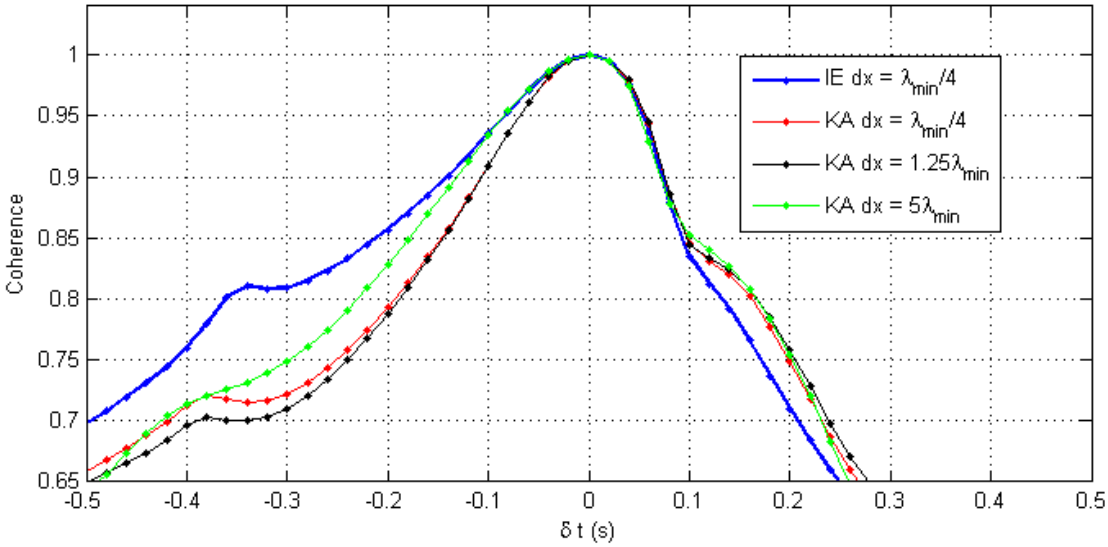

Figure 5-31: Coherence for bistatic response off low-amplitude surface $C(\Delta t)$ – 34 m low-roughness patch centred at 100 m range. KA element size sensitivity with IE reference. KA model inclusive of shadowed elements

5.4.3.4 KA model with highly shadowed surface

The effect of KA discretised element size is explored here for a rough surface with substantial surface shadowing. The rough surface simulation used here is the same as described in Section 5.4.2.

The IE/KA model comparison was explored at 100 m and 500 m ranges for this rougher shadowed surface. The bistatic geometry consisted of a 34 m long rough patch positioned mid-range with 10m deep source and receiver. At 100 m range this resulted in 64% shadowing at 11.3° specular grazing angle, and at 500 m range 99% shadowing at 2.3° specular grazing angle.

The IE and KA response histories are presented on Figure 5-32, with the IE reference model shown at the top of the figure. The KA results are presented for 2.4 cm, 12 cm and 48 cm surface discretisation intervals, corresponding to 1x, 5x, and 20x multiples of the IE model surface discretisation interval. The contributions of all KA surface elements are included irrespective of shadowing.

For this range, with a large proportion of shadowed elements, the time-delay structure of the response history is not greatly influenced by the element size.

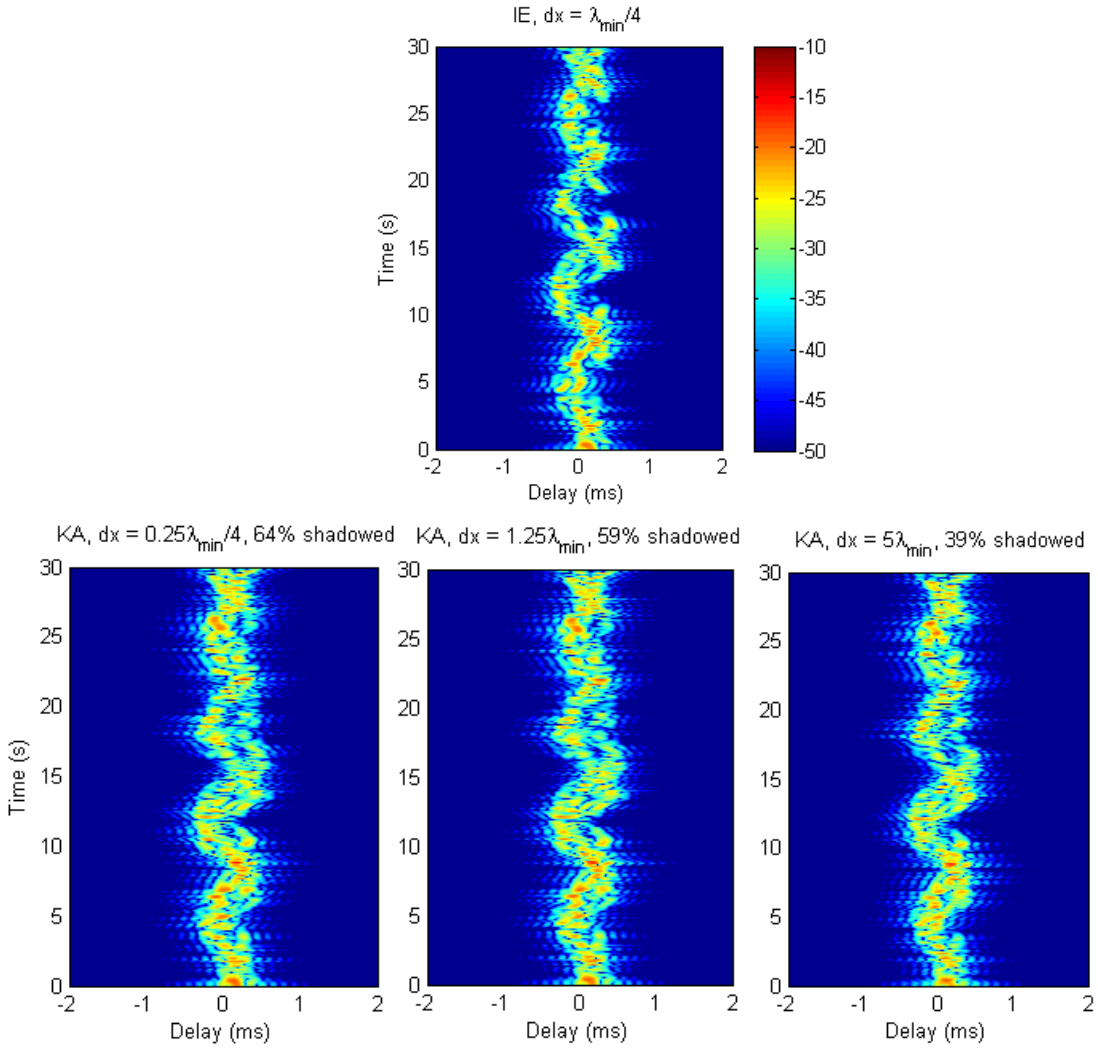

Figure 5-32: Effect of KA element size on bistatic response history $|h(t,\tau)|^2$(dB), IE reference model (top) versus KA model variants including all elements (bottom) – 34 m high-roughness patch centred at 100 m range and 11.3° grazing angle

The comparative Doppler power spectra for the shadowed and unshadowed KA model variants are shown on Figure 5-33. It may be seen that the larger discretisation interval tends to over-estimate the response magnitude at larger Doppler frequency shifts. Exclusion of shadowed elements results in high Doppler noise due to the discontinuity introduced to the response by discrete-time exclusion of elements. An element size of $1.25\lambda_{\min}$ for the KA model achieves a response within the IE envelope within 60 dB dynamic range.

The comparative delay power profiles for the shadowed and unshadowed KA model variants are shown on Figure 5-34. The unshadowed KA model slightly over-estimates the average response power. The shadowed KA model appears to be sensitive to element size, however this is a direct result of the proportion of shadowed elements reducing as the surface is rediscretised.

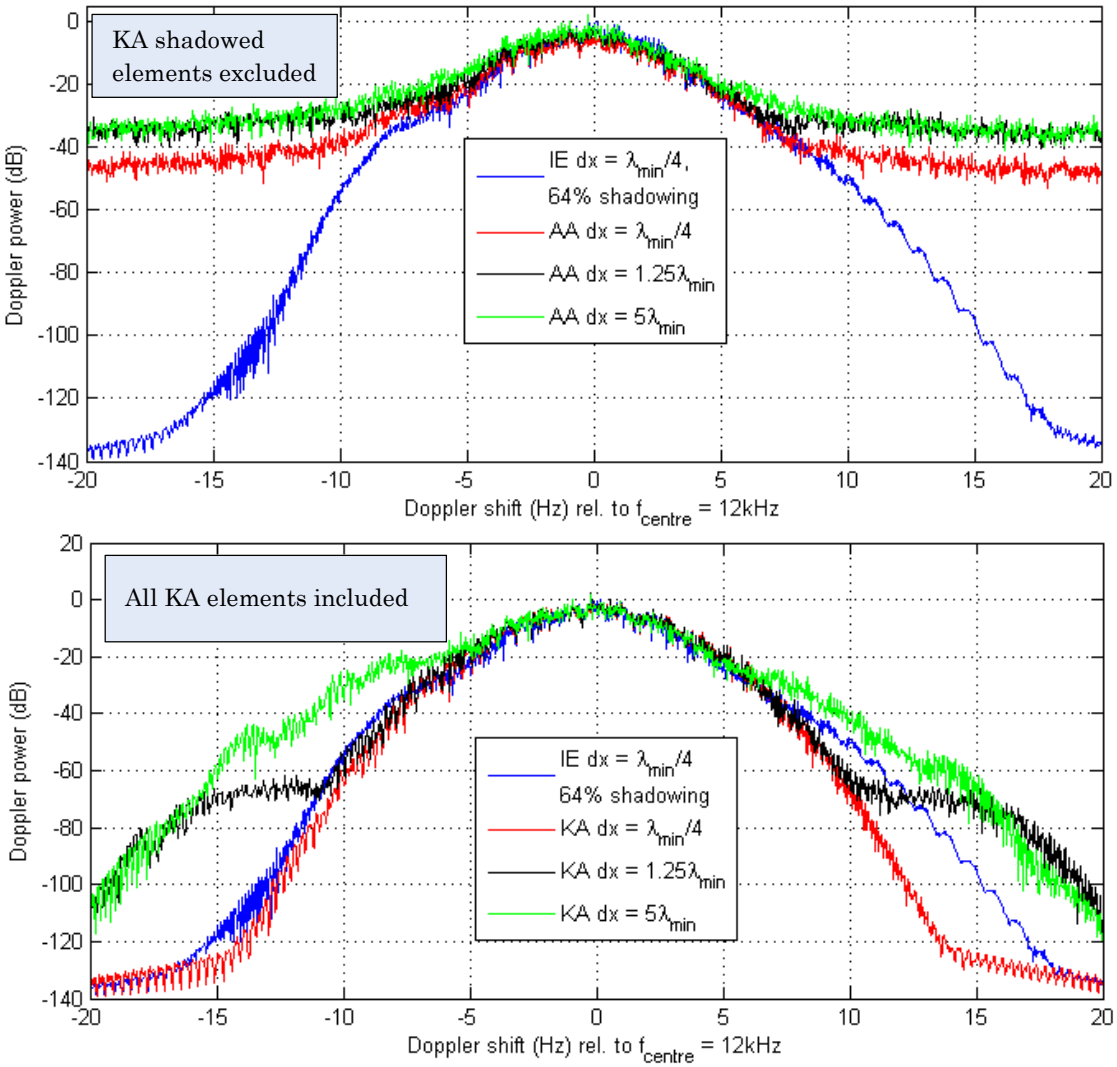

Figure 5-33: Effect of KA element size on bistatic Doppler power spectra relative to IE reference model $P(v)$ (dB), – 34 m high-roughness patch centred at 100 m range, 11.3° grazing angle – KA with shadowed elements excluded (top), KA including shadowed elements (bottom)

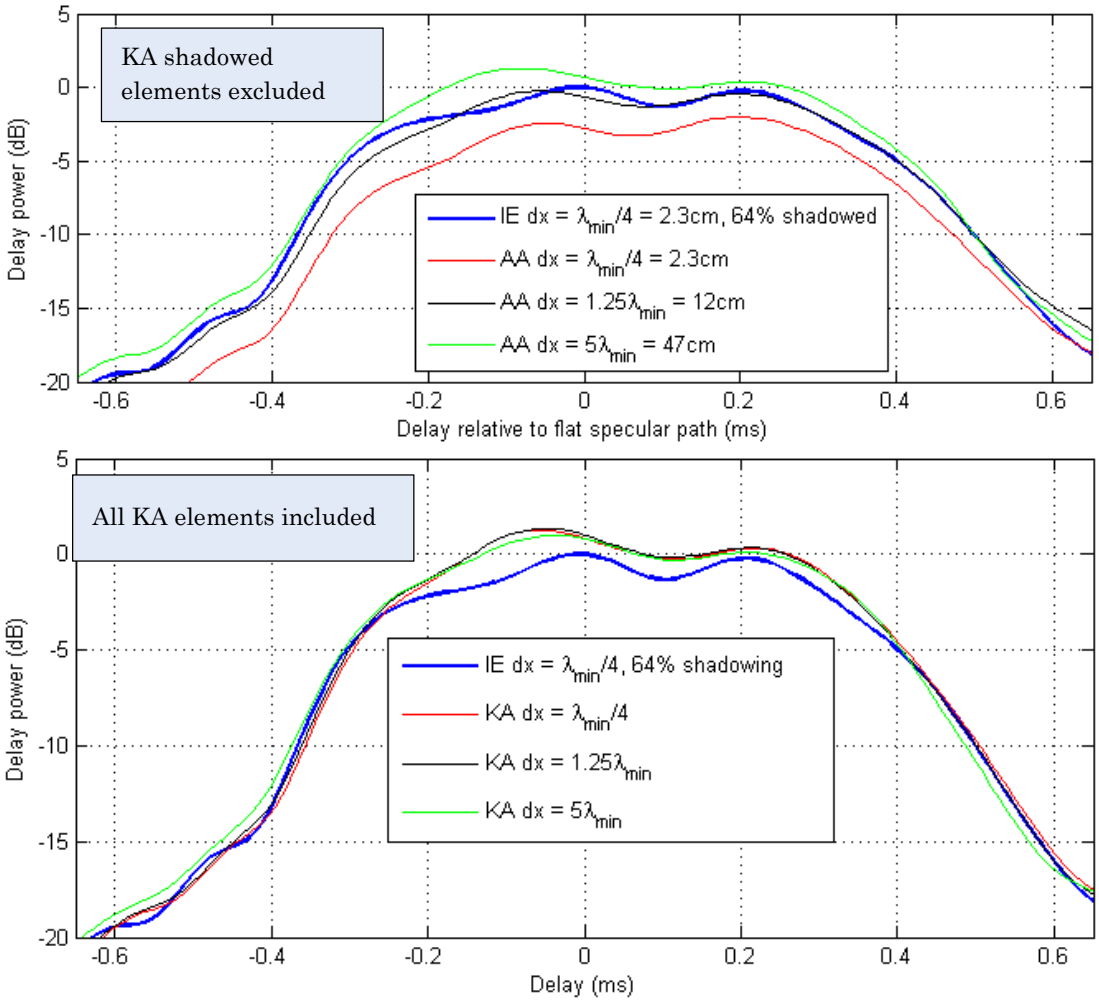

Figure 5-34: Effect of KA element size on bistatic delay power relative to IE reference model $P(\tau)$ (dB), – 34 m high-roughness patch centred at 100 m range, 11.3° grazing angle – KA with shadowed elements excluded (top), KA including shadowed elements (bottom)

Similar trends in delay power, Doppler power, and response history are found at 500 m range with 2.3° grazing as illustrated in Figure 5-35, Figure 5-36, and Figure 5-37. The high proportion of shadowed points in the fine structure of the wave troughs leads to significant under-prediction of signal power at any element size if shadowed elements are excluded. In contrast, inclusion of all elements in the KA model results in a consistent minor over-prediction of delay power, and minor biasing in the delay (when considered relative to the overall delay structure of the whole channel multi-path response).

An element size of $2.5\lambda_{\min}$ for the unshadowed KA model achieves a Doppler power spectrum response within the IE envelope within 60 dB dynamic range.

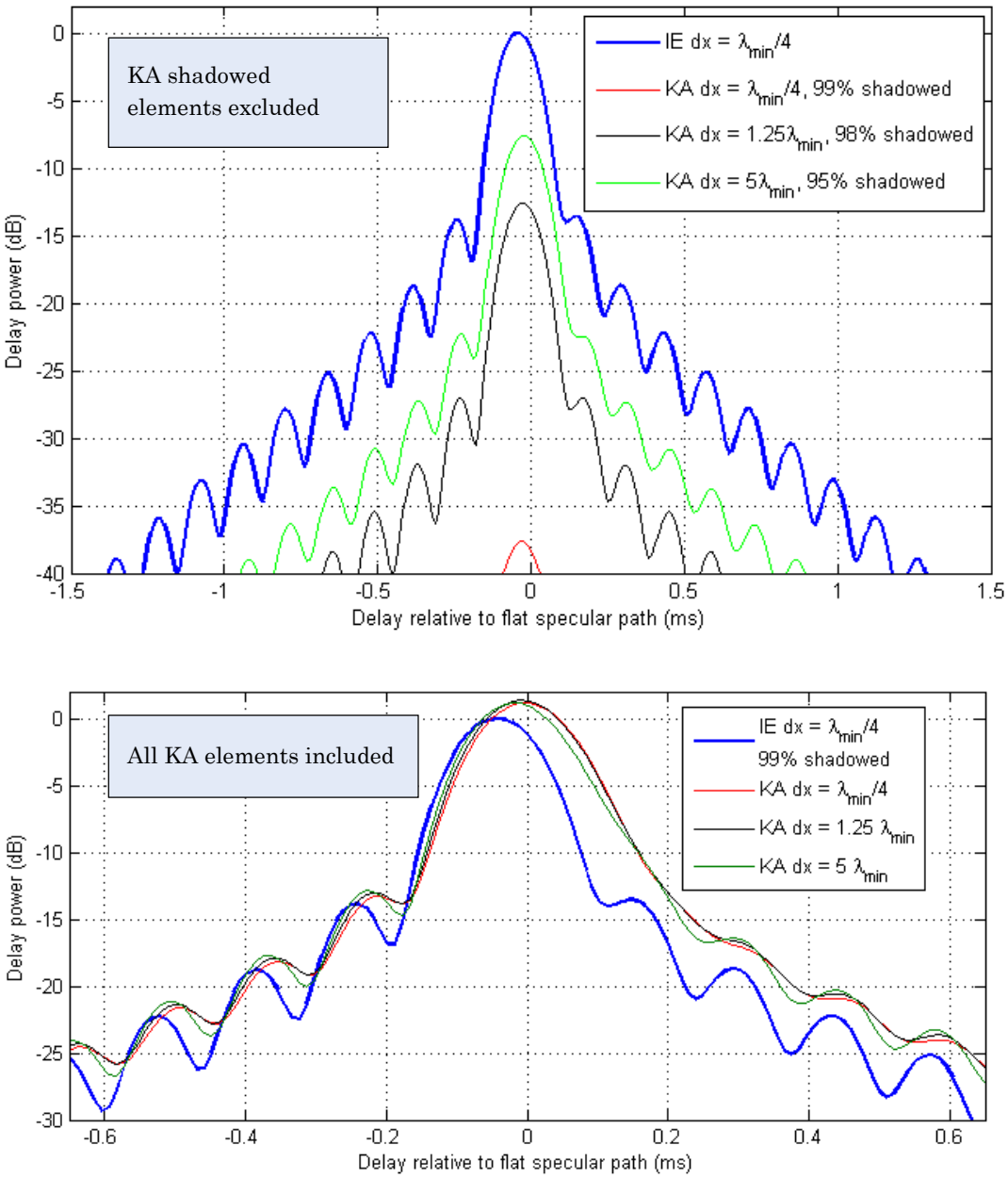

Figure 5-35: Effect of KA element size on bistatic delay power relative to IE reference model $P(\tau)$ (dB), – 34 m high-roughness patch centred at 500 m range,2.3° grazing angle – KA with shadowed elements excluded (top), KA including shadowed elements (bottom)

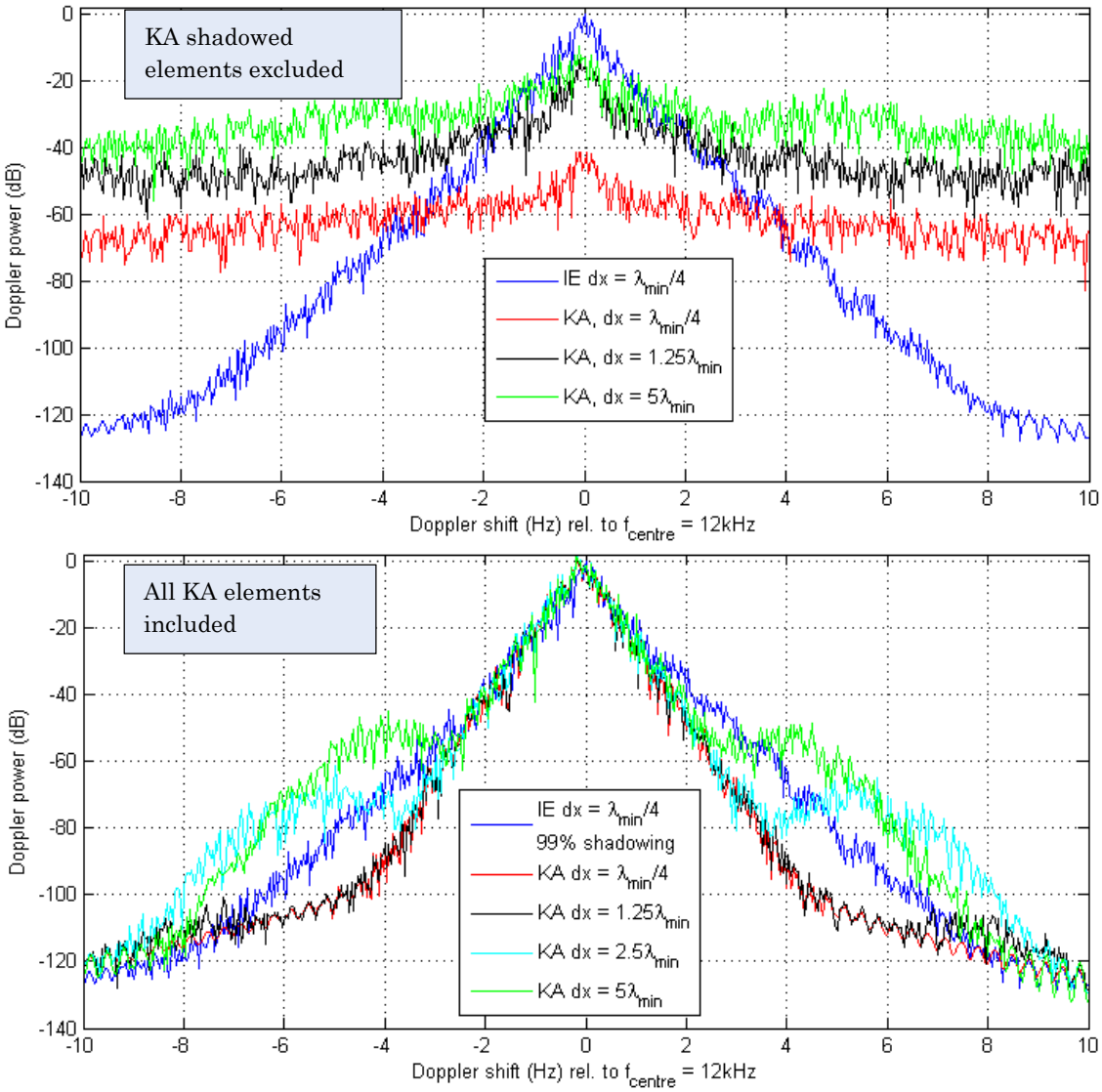

Figure 5-36: Effect of KA element size on bistatic Doppler power relative to IE reference model $P(v)$ (dB), – 34 m high roughness patch centred at 500 m range,2.3° grazing angle – KA with shadowed elements excluded (top), KA including shadowed elements (bottom)

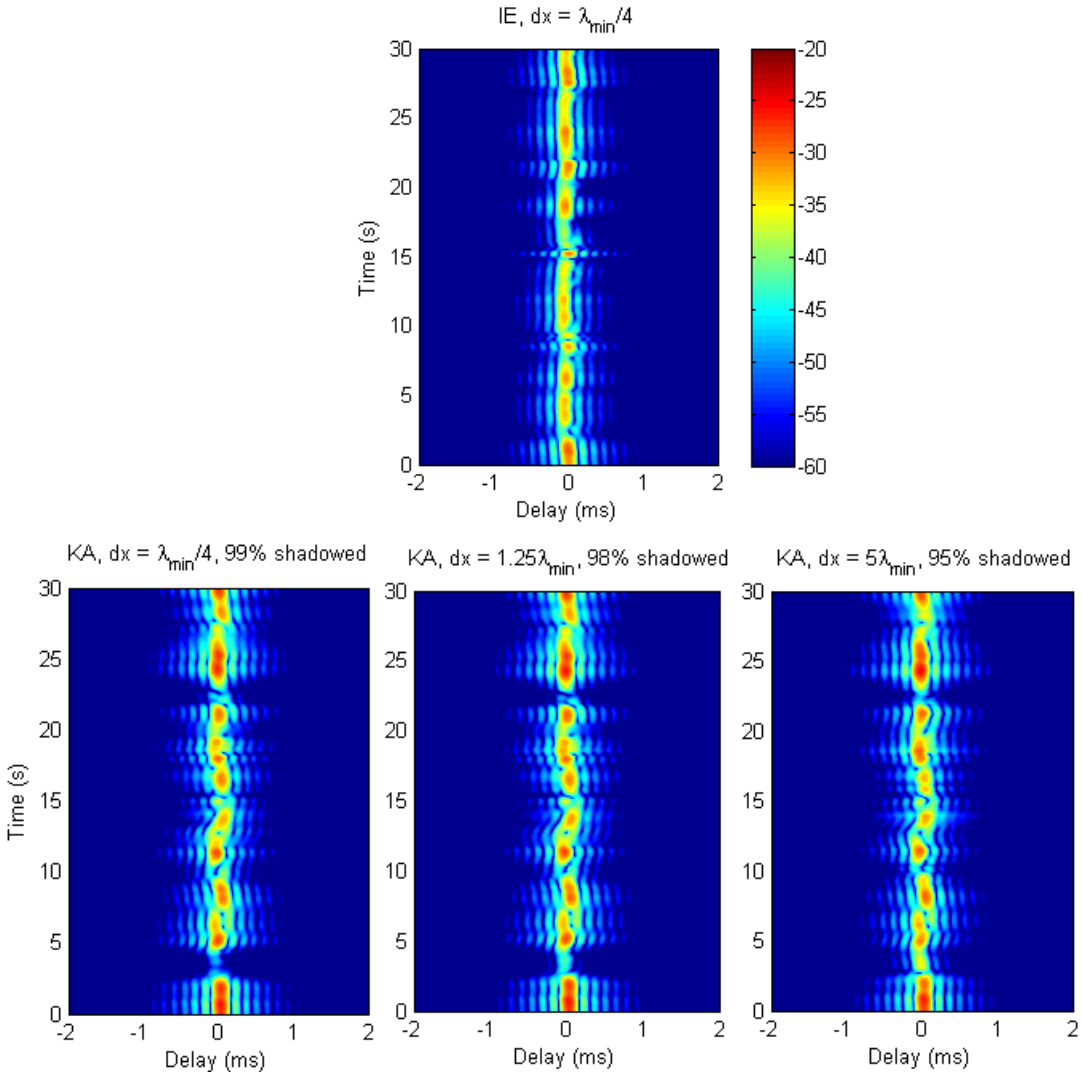

Figure 5-37: Effect of KA element size on bistatic response history $|h(t,\tau)|^2$(dB), IE reference model (top) versus KA model variants (bottom) – 34 m high-roughness patch centred at 500 m range, 2.3° grazing angle

5.4.3.5 Summary

At 100 m range, a horizontal discretisation of $1.25\lambda_{\min}$, (or 11.5 cm at 16 kHz) for the unshadowed KA model achieves a Doppler power spectrum response within the IE envelope, and within 60 dB dynamic range, for both highly shadowed and unshadowed surfaces. At 500 m range this discretisation may be increased to $2.5\lambda_{\min}$ (or 23 cm at 16 kHz). These relaxations are useful for application of KA to a three-dimensional surface, representing a 25-fold reduction ($1.25\lambda_{\min}$ at 100 m) and 100-fold reduction ($2.5\lambda_{\min}$ at 500 m) in the number of points needed to represent the surface relative to the $\lambda_{\min}/4$ reference surface discretisation.

5.4.4 Spatial windowing of the surface reflection coefficient

The rectangular surface patch that is used to calculate the bistatic surface response is elliptically windowed, with the edge 10% tapered using a raised cosine taper function. This tapers the reflection coefficient from an otherwise abrupt change to minimise the step in the spatial response being translated into side-lobes in the delay (τ) dimension of the bistatic impulse response $h_{\text{patch}}(t,\tau)$. The windowing is illustrated on Figure 5-38 and calculated by Eq.(5-13), where Δs is the variable width 10% edge margin. The surface reflection coefficient is tapered from 1 to zero.

$$C_{taper} = [1 + \cos(\pi\Delta s)]/2 \qquad (5\text{-}13)$$

The effect of the elliptic patch windowing on the bistatic delay power profile is illustrated on Figure 5-39.

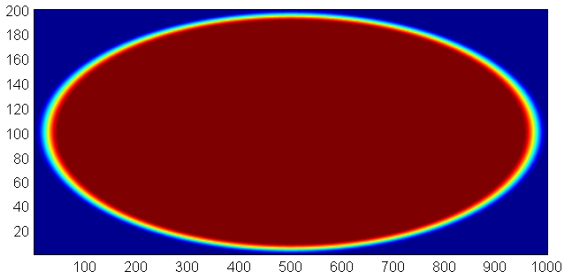

Figure 5-38: Elliptical spatial windowing function for the surface reflection coefficient across the discretised surface patch

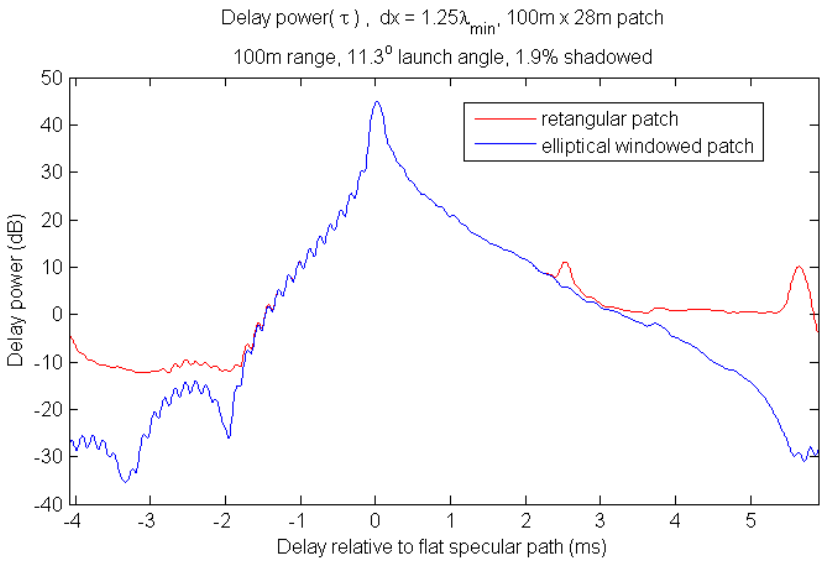

Figure 5-39: Effect of elliptic spatial windowing on delay power profile $P(\tau)$ (dB), for 30 second low amplitude surface simulation with negligible shadowing

5.4.5 Selecting the rough surface patch bounds

The task of estimating the minimum relevant patch dimensions is difficult as it depends on the diffuse scattering potential of the sea surface. For very diffuse surfaces the significant delay response (say within 30 dB of the peak in the bistatic delay power spectrum) may be calculated from very wide surface extents, extending into back-scatter with respect to the source and receiver locations. Conversely, for relatively smooth surfaces that produce a strong coherent near-specular response the significant surface patch length may be limited to a minor fraction of the transmission range, with conveniently small time window.

The initial patch size estimation algorithm was based on the delay variation associated with vertical movement of the mean-plane specular point, illustrated schematically on Figure 5-40. The transverse and longitudinal extents of the estimated 'relevant' patch were defined by the geometrical condition that the bistatic path-length deviation via horizontally displaced wave-troughs at nominal $3\sigma_{surface}$depression relative to the mean-plane, was within the path-length deviation associated with a $3\sigma_{surface}$ elevation of the mean-plane specular.

This algorithm was satisfactory until realistic surfaces with diffusive high-frequency surface spectra were explored, at which point it was apparent that the delay power profile for a diffusive surface tapers off slowly with delay. The adequacy of the patch dimensions was then assessed retrospectively on a case-by-case simulation basis, by inspection of the delay power profile derived from the response history $h(t,\tau)$.

The qualitative dependence of the patch-dimensions on surface grazing angle is illustrated in plan-view on Figure 54-41.

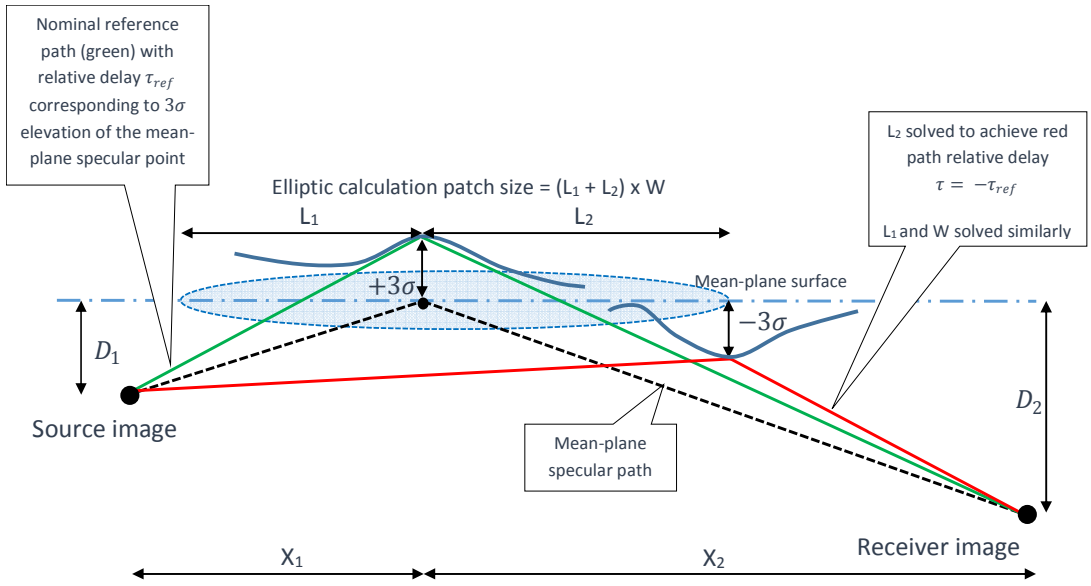

Figure 5-40: Early heuristic concept for estimating the relevant patch dimensions – patch dimensions were defined by the relative delay (τ_{ref}) associated with a notional upward movement of the mean-plane specular point by 3σ

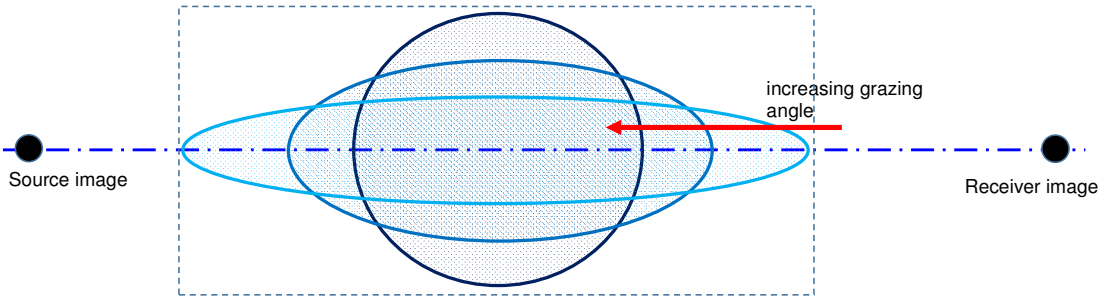

Figure 54-41: Qualitative dependence of bistatic surface patch extents on grazing angle in plan view

5.4.6 Selection of rough surface response calculation angles

For a given rough surface the bistatic response changes with horizontal range, transmitter and receiver depths. Ideally a bistatic response history would be calculated for each unique combination of ray-path grazing angle, image-source depth and image-receiver depth, for the bistatic surface-bounces that may be conceptualised as comprising the ray eigenpaths.

However, because there is significant computational investment in the calculation of the surface response history for a single instance of bistatic geometry, it is desirable to minimise the number of combinations of grazing angle, image-source depth and image-receiver depth for which a response history is calculated. The method of rationalizing the path bistatic calculation angles (distinct from the related calculation depths) is discussed here.

Depending on the transmitter and receiver depths, which may be different, there will be a spread of surface grazing angles for flat-surface surface-interacting ray-paths. The spread of launch angles may be even, or clustered depending on the relative transmitter and receiver depths. In the Cottesloe experiment with both transmitter and receiver near the bottom the surface grazing angle of eigenpaths having the same number of surface (or bottom) bounces tend to cluster together. This is shown on Figure 5-42, with the eigenpath grazing angle plotted on the left y-axis, and proportional increase relative to the first angle in a cluster plotted on the secondary y-axis.

Over some increment of grazing angle it is desirable for computational efficiency to represent a range of surface-grazing angles by a single angle. The computational approximation that was settled on was to represent a cluster of path grazing angles within 20% of the minimum angle by the average angle for that cluster of angles. This results in a simulation in which the first eight surface-interacting path arrivals are typically represented by just three bistatic calculation angles.

When simulation exploration was at the stage of trying to achieve more realistic (i.e. increased) delay-spreading, the cluster-angle tolerance was explored to see whether over-simplification of the bistatic calculation angles was limiting delay-spreading. This was found not to be the case.

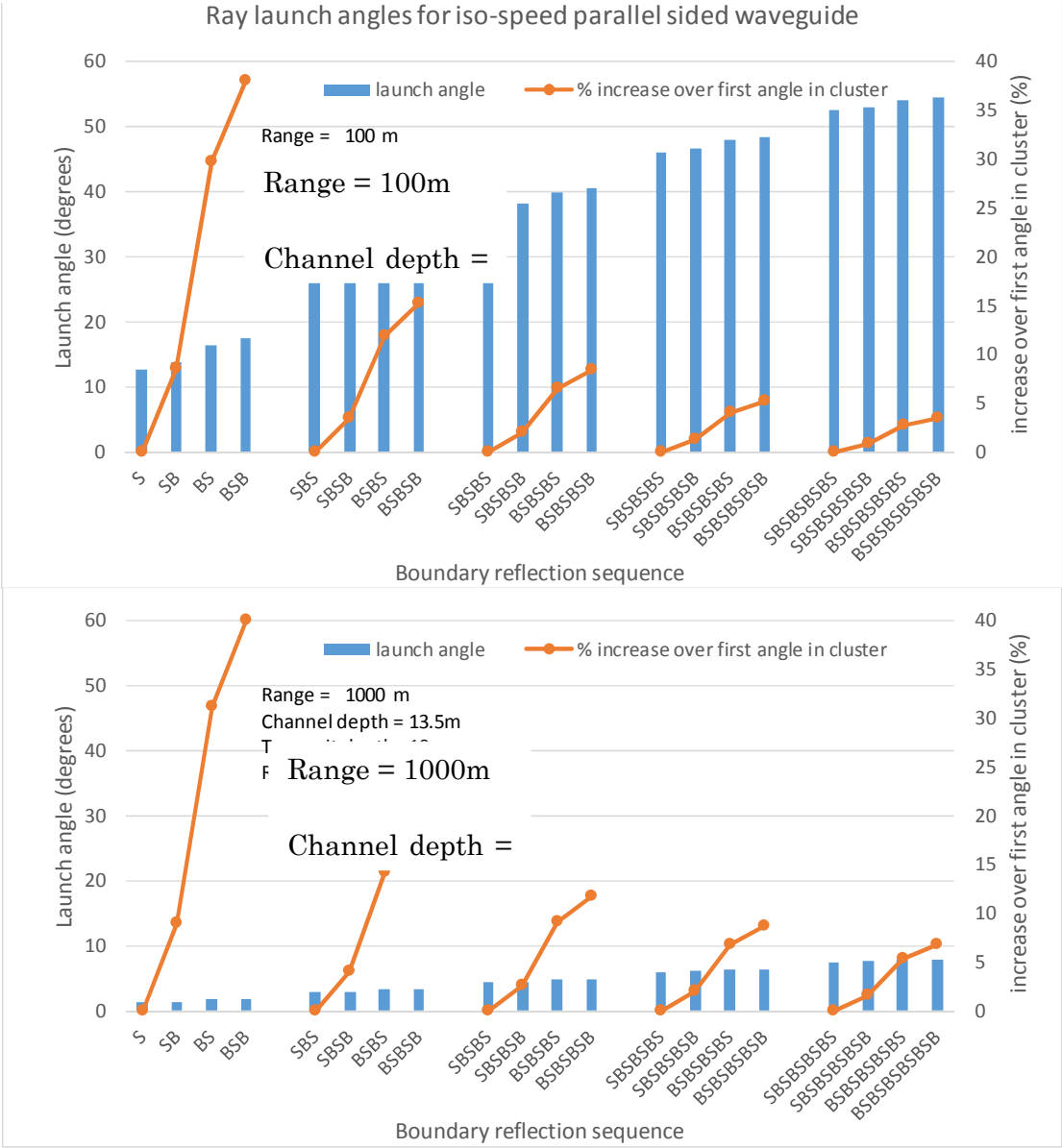

Figure 5-42: Ray eigenpath surface grazing angles, and proportional increase in angle for monotonically increasing clusters of path grazing angles - iso-speed channel approximating the Cottesloe trial – 100 m range (top), 1000 m range (bottom)

The comparative experimental and synthetic channel spreading function and delay power profiles for this exploration are presented below in Figure 5-43. The results compare the channel response encompassing the first 10 ray-path arrivals, comprising direct, bottom, 4 single surface-bounce permutations, and 4 double surface-bounce permutations. Figure 5-43 illustrates the experimental result (top), the synthetically probed channel, with 20% cluster-angle tolerance for which 8 surface path grazing angles were rationalised into 3 (middle), and the model channel with a 1% cluster-angle tolerance (bottom) which led to calculation of a bistatic response at every eigenpath angle.

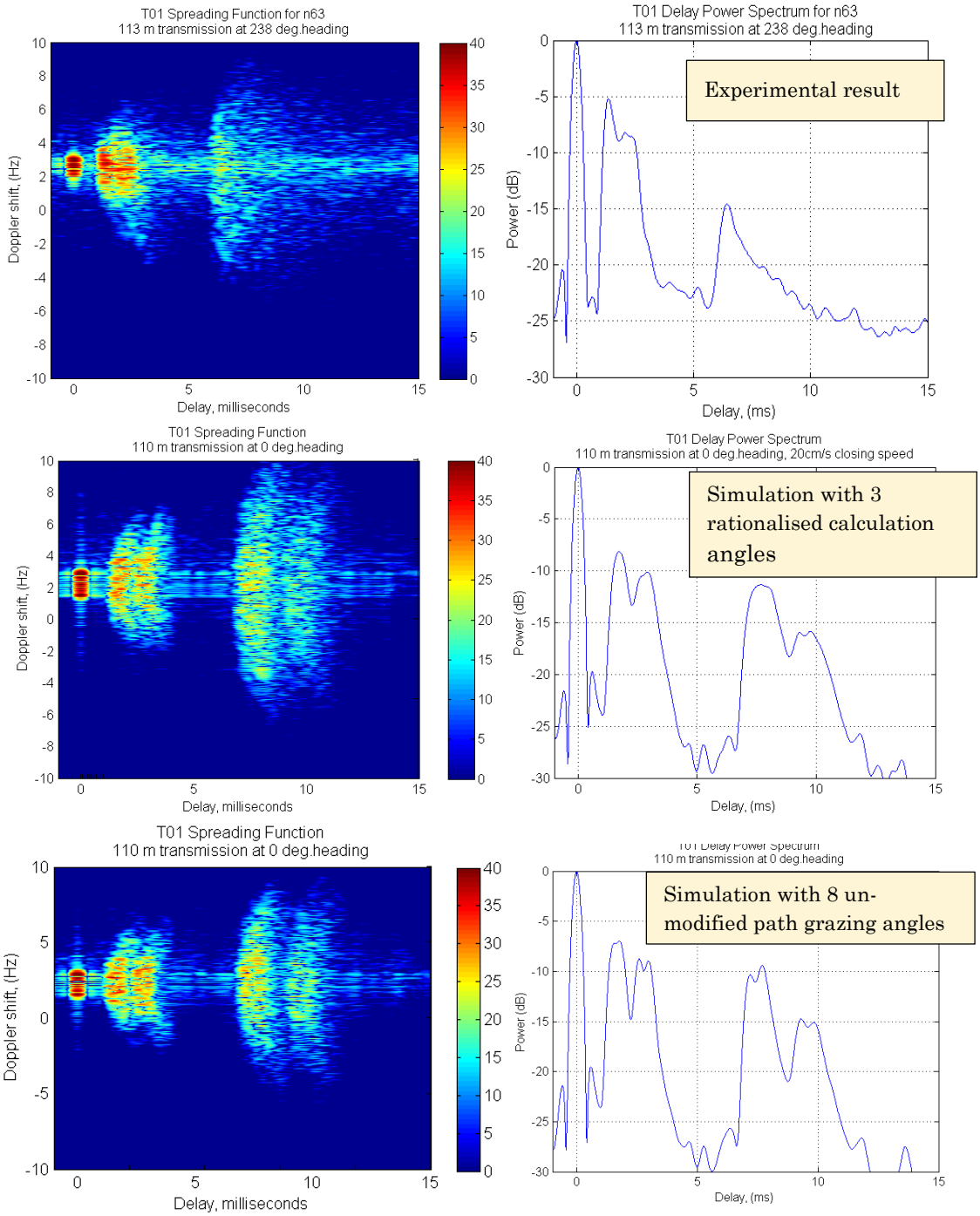

Figure 5-43: Effect of bistatic calculation angle rationalisation on channel probe response – (top) Experimental 113m channel probe response, (middle) Synthetic with simplified 12°, 15.5°, and 26.1° bistatic calculation angles, (bottom)11.5°, 12.5°, 15°, 16°, 24.2°, 25.1°,27.3°, 28.1° bistatic calculation angles

Whilst there were other simulation factors at play which have since been altered (i.e. the bistatic calculation depth now utilises asymmetric Tx and Rx depths) the results presented illustrate that, for a short-range case where grazing angle changes are most pronounced the spreading function is not greatly sensitive to exact replication of minor differences in path grazing angle.

Additional views of the effect of the eigenpath grazing angle on the calculated bistatic delay power profile and Doppler power spectrum are presented in Figure 5-44 and Figure 5-45 respectively. These plots relate to the same simulation as the bottom plots on Figure 5-43, with no simplification of the calculation angles, and relate to the modelled low-amplitude Cottesloe experimental surface. Both the delay and Doppler power spectra illustrate that whilst there are significant differences in spectrum shape between path angles relating to differing number of surface bounces, the differences between path angles relating to the same number of surface bounces are relatively minor. (Note:- whilst the grazing angles on Figure 5-44 and Figure 5-45 'relate' to single and double surface reflected paths as per the figure legends, all results are for a bistatic response calculation)

It is concluded that the rationalisation of the bistatic calculation angles, using an angle-cluster tolerance of 20% is a reasonable and useful approximation to make.

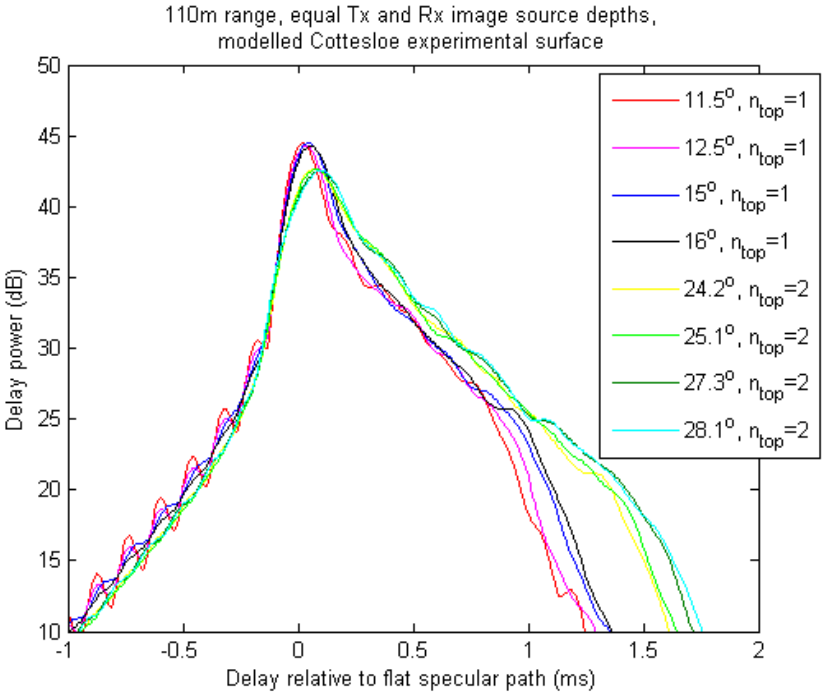

Figure 5-44: KA model bistatic delay power profile versus mean-path grazing angle $P(\tau)$ (dB), – low-amplitude surface similar to Cottesloe experimental surface

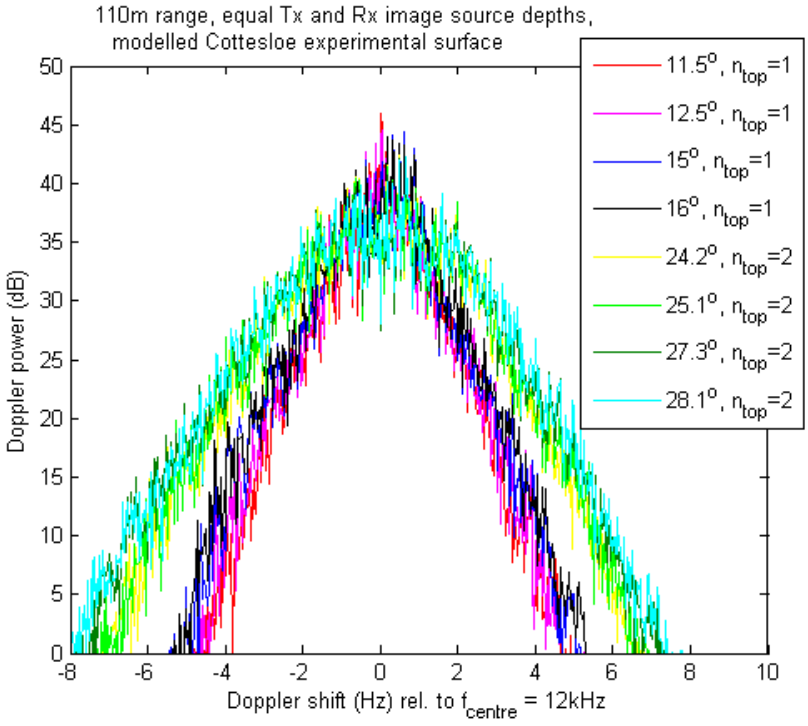

Figure 5-45: KA model bistatic Cottesloe surface Doppler power versus mean-path grazing angle $P(v)$ (dB), – low-amplitude surface similar to Cottesloe experimental surface

5.4.7 Surface path grazing angle adjustment for sound speed

The grazing angle that the mean-plane specular eigenpath makes with the surface is calculated from the launch grazing angle θ_{source} and the sound speeds at the source depth and the surface as per Eq.(5-14).

$$\theta_{surface} = \cos^{-1}\left[c_{surface}/c_{source}\cos(\theta_{source})\right] \qquad (5\text{-}14)$$

This modified surface grazing angle is then used to infer an approximate modified source and receiver depth for the path, so that the bistatic surface response calculation proceeds as if the micro-paths connecting the source image, surface elements and receiver image were straight rays. This aspect of the model has been coded sufficiently to address the slightly refracting sound speed profiles encountered experimentally that still result in alternating surface and bottom reflections on a ray-path.

It may be possible to adapt the methodology to address a surface duct path by assigning a virtual image-source and image receiver depth associated with each surface interaction. The bistatic decomposition would differ in that no bottom boundary would be involved. This is an area for future development that would

benefit from an example surface-duct probe response for model evaluation purposes.

5.4.8 Fourier synthesis frequencies

The Fourier synthesis frequency spacing dF ($= d\omega/2\pi$) for calculation of the bistatic response $H_{patch}(\omega)$ is determined by the delay bounds for the rough-patch response as per Eq.(5-15). This avoids time-aliasing of the time-domain pressure response $H_{patch}(t,\tau)$ after inverse-transforming,

$$dF \leq 1/(\tau_{max} - \tau_{min}) \tag{5-15}$$

The bistatic frequency response vector $H_{patch}(\omega)$ is zero-padded outside of the channel bandwidth F_{min}= 8kHz to F_{max}= 16kHz, from zero up to $F_{sampling}/2$, where $F_{sampling}$ is the signal sampling rate (96 kS/s in this study). This achieves a response $h_{patch}(t,\tau)$ with resolution in the delay τ dimension to match the input signal.

5.4.9 Bistatic decomposition of multiple-reflected paths

Each mean-plane eigenpath has been decomposed into a series of bistatic boundary interactions using the image-source and image-receiver depths. This idea is illustrated for an example Surface-Bottom-Surface (SBS) hybrid wave/ray-path with reference to Figure 5-46.

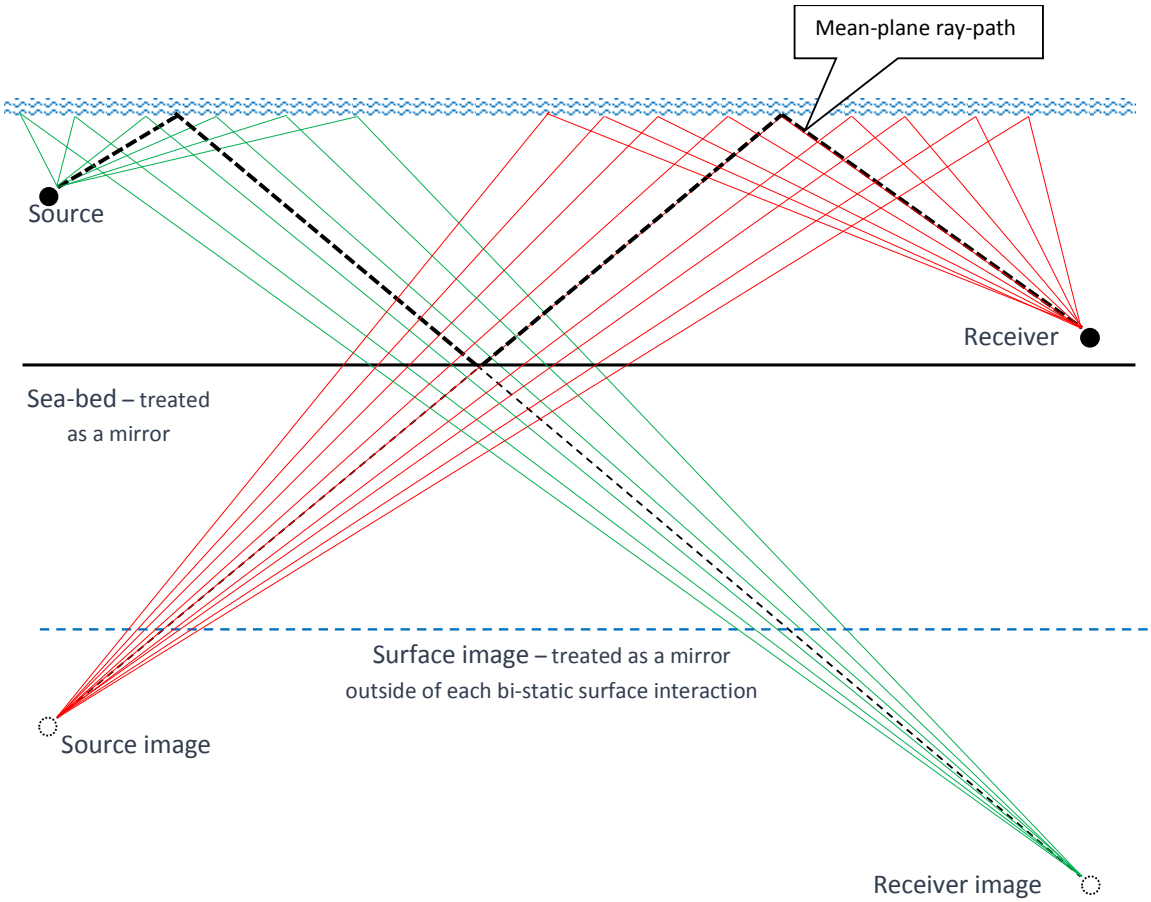

Figure 5-46: Rough-surface eigenpath response modelled by consecutive bistatic responses – first bounce bistatic geometry shown green – second bounce bistatic geometry shown red

The first bistatic surface-interaction is represented by the green-. The formation of the image-receiver for this bistatic geometry makes the assumption that other boundary interactions are as for a flat-boundary with no phase change. This idea has been partially described previously (Choi and Dahl 2006) where for a double-bounce path the surface impulse responses derived from a bistatic rough-surface scattering coefficient were convolved in the time domain. This idea was alluded to by (Siderius and Porter 2008) in the context of modelling the time-domain rough-surface response for the first 6 ray-paths "*…paths with multiple surface bounces could be included in an approximate way by modifying the amplitude of the first surface bounce by taking only the specular path and then include the scattering in the second interaction with the surface.*" The second bistatic sea-surface interaction is represented by the red-rays, with the same flat-boundary assumptions in forming the source image depth.

This concept cannot be exact because there is no sequential deterministic interaction of wavelets from one surface interaction to the next. However the

sequential sense of the calculation is still retained in the frequency domain because each bistatic response is range-normalised, to enable multiplication with the base eigenpath amplitude response, without introducing additional geometric attenuation. The method provides a plausible way for each rough surface-interaction to modify the overall response independent of the field distortions introduced by other 'upstream' or 'downstream' rough-boundary interactions in a geometrically approximate but relevant manner.

The conceptualisation is approximate in that real scattering at each boundary that occurs in directions contrary to the sketched fan of modelled wavelet directions is ignored.

By extending the idea of Figure 5-46 to the modelling of the other three $N_{top} = 2$ eigenpaths (i.e. SBSB, BSBS, BSBSB) as shown on Figure 5-47, and then considering similar permutations for paths with other numbers of surface bounces, it may be seen that introducing uneven image source/receiver depths introduces additional permutations to the bistatic geometry, potentially growing the channel response calculation effort further.

As an example, if a channel was modelled with the first eight surface-interacting eigenpaths (i.e. up to two surface bounces), in general there would then be 4 bistatic geometries representing the single-surface-bounce eigenpath permutations, and 8 bistatic geometries representing the four double-surface-bounce eigenpath permutations. The 8 bistatic surface-interaction geometries relating to the four double-surface-bounce ($N_{top} = 2$) eigenpath permutations are illustrated in the bistatic geometry decomposition on Figure 5-47.

Even with the eight ray-path grazing angles reduced to three as described in Section 5.4.6, introduction of unique image-source and receiver depth combinations would potentially expand the number of bistatic permutations requiring calculation from three to twelve.

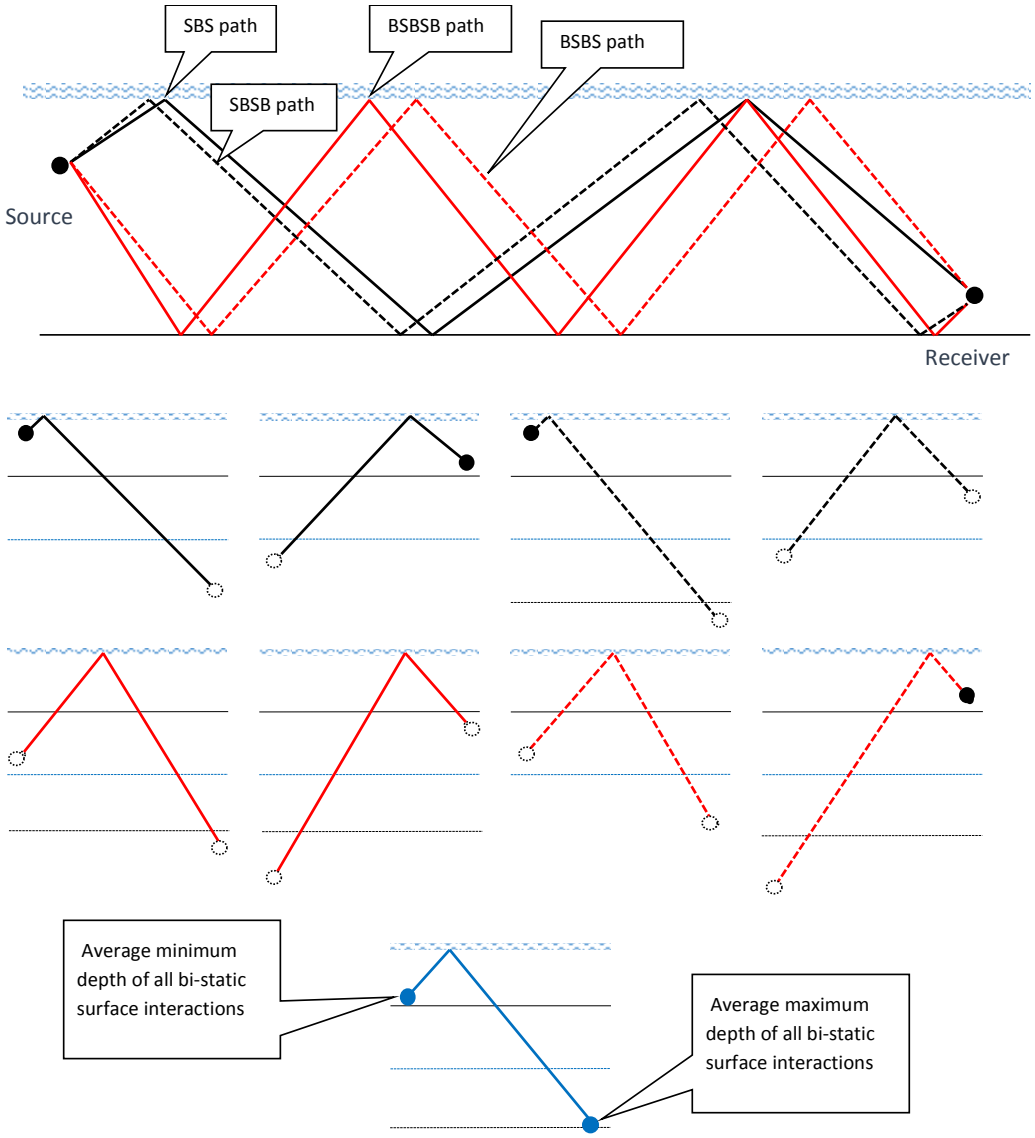

Figure 5-47: Bistatic decomposition of four double-surface-bounce eigenpaths

The initial modelling response to this new complexity was to make the bistatic source and receiver depths equal. However it was apparent that this approach would reduce surface interaction diversity associated with asymmetric source and receiver depths.

The many component bistatic geometries in Figure 5-47 were then rationalised by averaging the minimum and maximum depths of the various bistatic geometries that correspond to clustered grazing angles (see Section). For the example of the double-surface-bounce (N_{top}=2) paths illustrated on Figure 5-47, the rationalised 'average' bistatic geometry is illustrated in blue at the bottom of the figure. In a double-surface-bounce path different instances of the bistatic response calculated this way are then multiplied in the frequency domain.

When attempting to economise on the number of bistatic variants, the question arises about the degree of bistatic response reciprocity if asymmetric source/receiver depths are interchanged. Referring to Eq.(2-20), on the specular axis of each element the source and receiver may be interchanged, achieving an identical response. However for off-specular directions the element response is not reciprocal because of the errors in element edge response introduced by the Kirchhoff assumption on the surface.

The effect of interchanging the source-receiver depths was tested by calculating the bistatic response first with 5 m source depth and 12 m receiver depth at 110 m, and then with the depths switched, using the same sequence of 100 m x 20 m low-amplitude surface realisations with the primary swell direction opposed to the transmission direction. The results of this simulation are presented in Figure 5-48 and Figure 5-49.

Whilst at low Doppler the strongest response is similar for both cases, consistent with expectation, the Doppler trend in the fainter spreading function detail appears to be reversed when the source and receiver depths are interchanged. This may be explained for a simplified two-dimensional representation with reference to Figure 5-50.

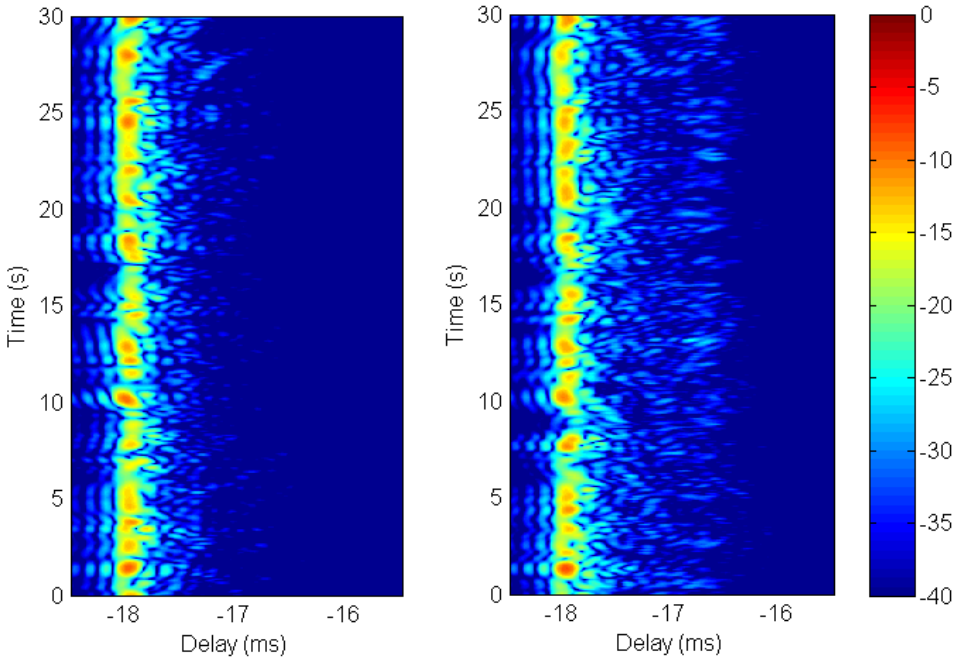

Figure 5-48: Bistatic response history for asymmetric source and receiver depths$|h(t,\tau)|^2$(dB), 5 m deep source and 12 m deep receiver (left), switched 12 m deep source and 5 m deep receiver (right)

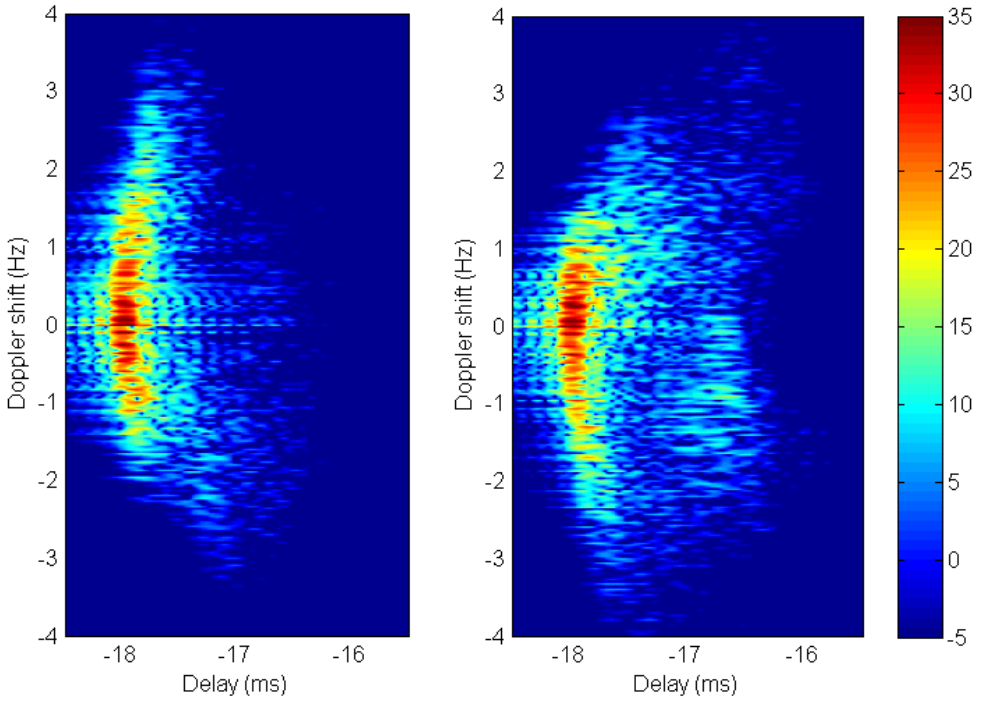

Figure 5-49: Bistatic spreading functions for asymmetric source and receiver depths $|S(t,\nu)|^2$(dB), 5 m deep source and 12 m deep receiver (left), 12 m deep source and 5 m deep receiver (right)

The top section of Figure 5-50 schematically represents travelling reflection responses off travelling waves. The blue paths are becoming shorter and the red paths longer. The black paths represent the momentary path-length minima when the Doppler is zero. The varying Doppler of responses off travelling waves produce striations in both experimental and simulated channel response histories for single-surface interacting paths, similar (in trend a least) to the sketches in the middle of Figure 5-50. The middle section of Figure 5-50 shows schematically how these striations may relate to both the bistatic geometry, and the resultant bistatic spreading functions. There are other aspects of response frequency and delay spreading not included in these diagrams, in particular the effect of more diffuse incoherent surface responses.

For asymmetric source and receiver depths, the Doppler on the transmission path via travelling waves may produce a biasing of the Doppler frequency shift. Depending on the geometrical reflective properties of the sea-surface, the response may be dominated by either surface reflection off travelling waves that are approaching the mean-specular geometry (Variant (a) of Figure 5-50), or by responses off travelling waves receding from the mean-specular geometry (Variant (b)). This has been demonstrated experimentally by others (Badiey,

Song, and Smith 2012). The centre sketches of Figure 5-50 shows responses of similar strength off both approaching and receding travelling waves.

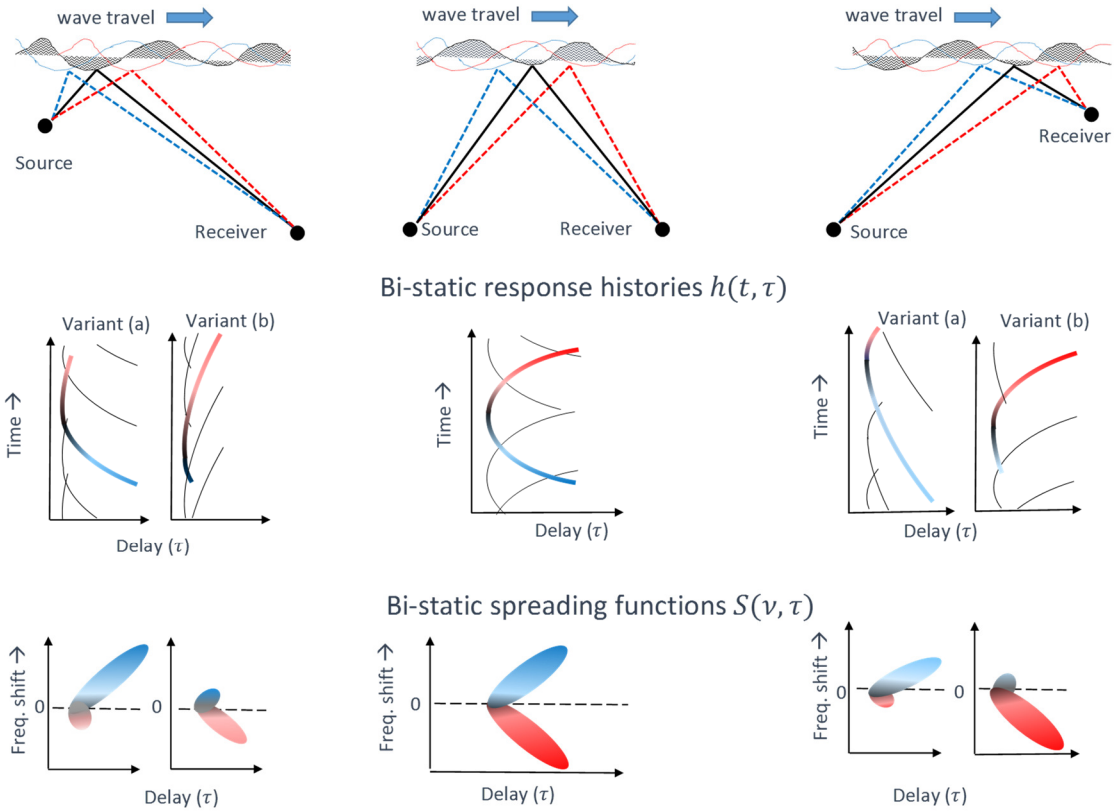

Figure 5-50: Schematic interaction between (top line) bistatic geometry and continuous reflected paths off travelling waves, (middle line) bistatic response histories $h(t,\tau)$, and (bottom line) with spreading function Doppler $S(\nu,\tau)$.

An additional asymmetry not included in Figure 5-50 is the left-right profile asymmetry of real surfaces with travelling waves.

It is concluded that ideally the bistatic response history should be calculated for every bistatic geometry of each surface-bounce on every path, at least for paths including up to two surface bounces. For more complex paths with a higher number of surface paths the response becomes of marginal or irrelevant significance to the coherent transmission, but still relevant to the incoherent channel response. For such paths it is arguable that a simplified approach can adequately model the incoherent response.

If the calculated bistatic geometries must be limited for computational efficiency, it is suggested that at least for the single-surface-bounce path variants, the bistatic responses should be calculated for actual asymmetric source/receiver depths so that the prominent response history structure can be qualitatively

reproduced. In the coherent modelling work of Siderius and Porter (2008), the authors concluded that for coherent phase communications, it is principally the direct and single-surface bounce paths that are relevant to receiver demodulation algorithms.

5.4.10 Summary of rationalised bistatic calculation geometries

The final implemented method of rationalizing the source and receiver depths and angles for bistatic response calculation is summarised in Figure 5-51. The rationalisation of calculation angles usually splits the first two pairs of single-surface-bounce paths, making it advantageous to calculate these pairs with corresponding average source and receiver depths.

For higher-order paths (i.e. paths with two or more surface bounces) the bistatic calculation utilises a single calculation angle per N_{top} bounce-path order, and equal average source and receiver depths.

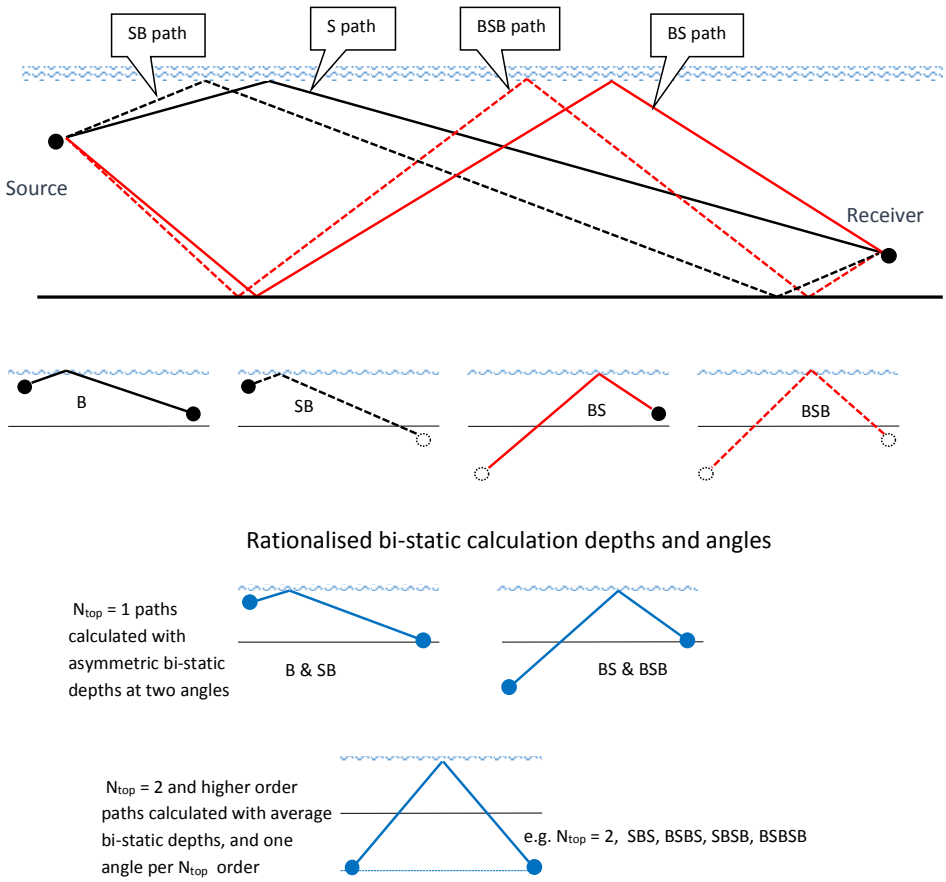

Figure 5-51: Rationalised bistatic calculation geometries (shown in blue) for single and multiple-surface-bounce paths

5.5 Rough surface realisation methodology

5.5.1 Introduction

The three-dimensional time-varying simulation of the ocean surface has been generated by Fourier synthesis using the Wave Analysis for Fatigue and Oceanography (WAFO) Toolbox routines published on-line by Lund University (WAFO 2011).

The WAFO surface is generated by linear summation of sinusoidal harmonic surface profiles. The resulting summation is inherently symmetrical in the distribution of positive and negative slopes along any cross-section, unlike some realistic wind-driven surfaces that are inherently asymmetric.

The simulation includes dispersion of the surface wavenumber spectrum for water depth, and provides a range of simulation options for the angular dispersion of waves. The primary direction of swell and wind-waves may be specified independently.

In principle, the channel response simulation described in this chapter could equally well be applied to a time evolving three-dimensional non-linear surface simulation that includes solitary waves and trains of steeper non-linear or *cnoidal* waves (Holthuijsen 2007), however the problem of 3D time-varying surface synthesis would likely dwarf the channel-response calculation for useful rough surface patches involving of the order of tens or hundreds of 3D wave crests.

5.5.2 Selecting rough patch dimensions

To economise array storage, surface responses at different path grazing angles, and for different surface-bounces along a multiple surface-bounce path, are computed from the same array of three-dimensional surface 'snapshots' representing the moving sea surface.

Referring to Figure 5-52, the sea and swell surface realisations for each 'snapshot' surface are independently calculated for a square portion of sea surface with side-length equal to the longest surface wavelength represented in the sea or swell spectrum. Most of the calculated sea and swell realisation is then discarded, with only the central portion that encompasses the estimated patch areas necessary for bistatic calculations retained (black dashed rectangle). This methodology

retains the surface tilt and displacement effects associated with long-wavelength swell.

Figure 5-52 is not drawn to realistic scale. In general, the area of the sea realisation is much smaller than that relating to ocean swell, with the horizontal discretisation for swell realisation synthesis chosen five-times larger than that used for the sea realisation synthesis. When the common central portion of the sea and swell realisations are added, the swell realisation is linearly interpolated on to the finer sea-realisation grid. Example realisations of swell and sea are illustrated on Figure 5-53 and Figure 5-54.

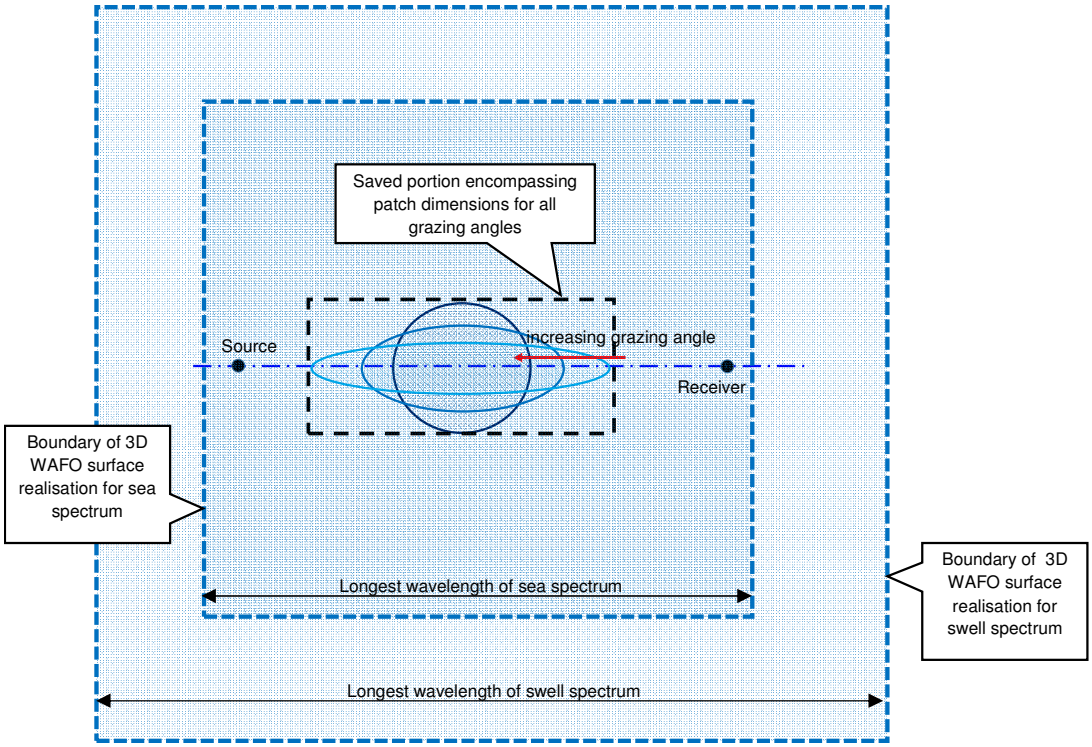

Figure 5-52: Schematic plan-view showing the relationship between the extent of the swell and sea surface-realisations (blue dashed outlines) and the central portion of the combined realisation that is stored and used for calculation of bistatic surface responses

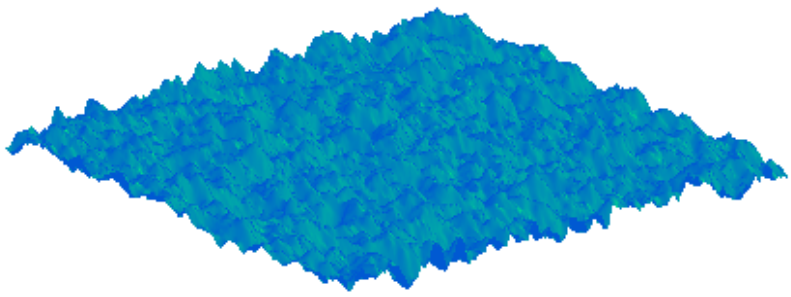

Figure 5-53: Example realisation of surface sea waves

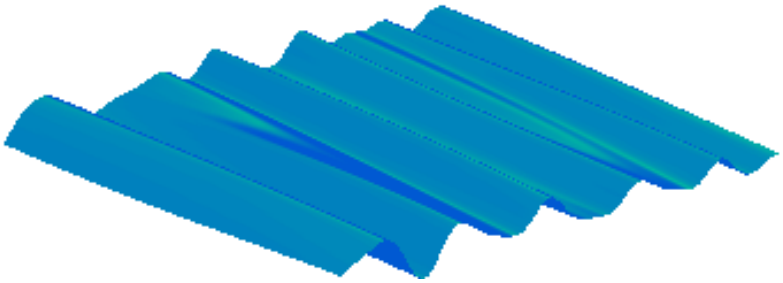

Figure 5-54: Example realisation of surface swell waves

5.5.3 Achieving a time-circular channel response

The simulation is designed to ensure that surface realisations are circular in time, to achieve a derived channel response that is also circular in time. This allows a transmit signal of arbitrary length (longer that the period of surface realisations) to be transmitted through the synthetic channel without risk of spurious discontinuity.

This is achieved by discretising the two-dimensional surface angular frequency array at an angular frequency increment, $d\omega = 2\pi/T$, to achieve circularity of surface realisations in T seconds. For $T = 60\,s$ (for example) the time-varying surface is represented by 3000 x 20 ms surface realisations. The peakedness of the one-dimensional surface spectral density affects how small $d\omega$ needs to be to ensure the spectrum is adequately reproduced after discretised angular spreading. For simulation of the Cottesloe experimental surface, a longer circular period of 120 s was used.

5.5.4 Approximate discretisation of the surface

The surface has been modelled on a rectangular grid which produces surface elements that are not planar. These portions have been treated as planar elements, so that they may be modelled using the rectangular element response developed in Section 2.4 without need for a triangular tessellation of elements.

For the purpose of applying the Kirchhoff approximation, the key characterisation of the element is the element height relative to the mean-plane, and the element tilt around the longitudinal and transverse axes. The element elevation is modelled as the average of the four corner elevations. The element tilts have been calculated as the average gradients of the pairs of opposite sides.

5.5.5 Avoiding spatial Doppler aliasing in the bistatic response

If the bistatic path-length of any surface element changes in the simulation time increment Δt by more than a half wavelength at the signal bandwidth upper frequency ($i.e. \lambda_{\min}/2$), the frequency response will be ambiguous. The excess path-length change will be 'wrapped' in the frequency domain. Thus the maximum valid simulated bistatic Doppler velocity shift v_{max} that is possible via any part of the wave is given by Eq.(5-16).

$$v_{max} = \lambda_{\min}/(2\Delta t) \tag{5-16}$$

For $\Delta t = 20$ ms and $\lambda_{\min} = 9.4$ cm at 16kHz, the maximum possible simulated bistatic Doppler is 2.3 m/s, or 18 Hz relative to the 12 kHz centre frequency. This Doppler is of the same order as that generated by the natural ocean surface or even a drifting transmitter.

Thus for high-amplitude surfaces at short range it can be necessary to generate surface realisations at smaller Δt (10ms has been used) to ensure that bistatic Doppler is not aliased. When aliasing does occur, it is apparent in the bistatic spreading function when a portion of the response falls outside of the channel sampling Nyquist frequency, such as illustrated in Figure 5-55 where the Nyquist frequency is 25 Hz.

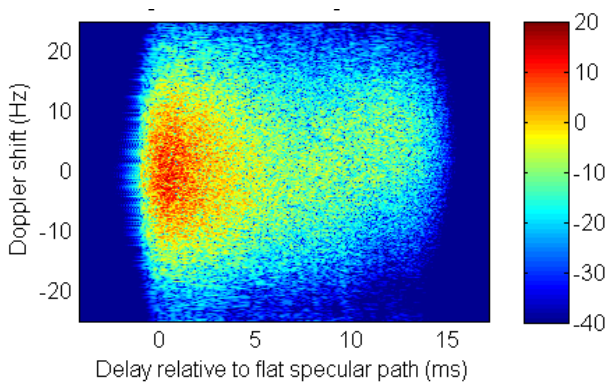

Figure 5-55: Bistatic spreading function $|S(\tau,\nu)|^2$(dB) illustrating Doppler aliasing beyond ±25 Hz, Significant wave height H_s = 1.9 m, 120m range, 64° eigenpath grazing angle

5.5.6 Simulated surface wave spectra

The experimental DWRB spectra for both the Cottesloe (Figure 5-56) and Rottnest trials (Figure 5-57) are limited by the high-frequency cut-off of the DWRB at 4 rad/s. For modelling, the experimental spectra have been enhanced by addition of a high-frequency Pierson-Moskowitz spectrum taper from around 4 rad/s up to

2π rad/s, to simulate high-frequency waves relevant to the signal frequencies but not detectable by the DWRB's.

The portion of the experimental spectrum shown in red below 1 rad/s has been utilised to represent the swell in the simulation. The sea spectrum has been modelled using the experimental spectrum portion in the range 1 to π rad/s, merged with the empirical high frequency Pierson-Moskowitz wind-wave spectrum as shown in green on Figure 5-56 up to 2π rad/s.

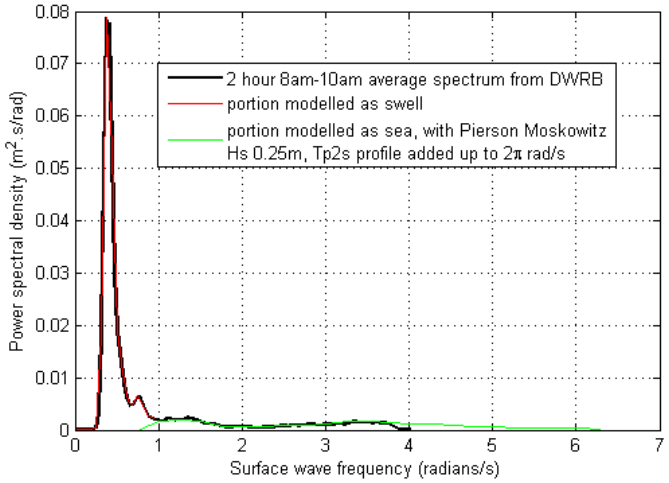

Figure 5-56: Experimental and simulated Cottesloe surface wave spectrum

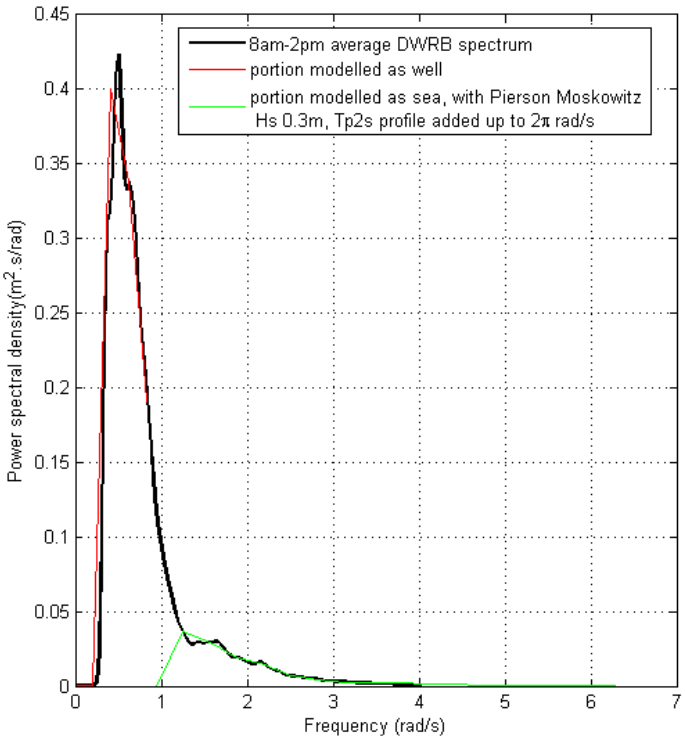

Figure 5-57: Experimental and simulated Rottnest surface wave spectrum

The significance of the surface spectrum at frequencies above 1 rad/s is illustrated by calculating the channel response with and without the modelled high frequency surface waves. This comparison for the simulated Cottesloe 110 m channel response (prior to convolution with a transmit signal) is illustrated on Figure 5-58.

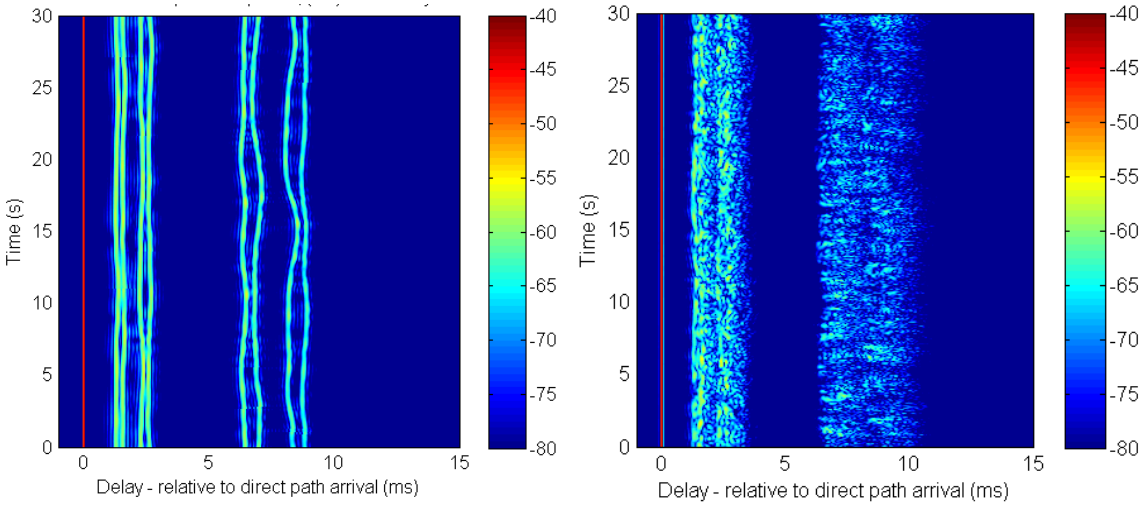

Figure 5-58: Simulation Cottesloe 110 m response history $|h(\tau,t)^2|$ (dB), with swell only (left), and with swell and sea (right)

After convolution with a repeated 21 ms probe signal, the respective matched-filtered channel responses, delay power spectra, and spreading functions are illustrated in Figure 5-59 for the swell-only channel (left figures) and swell-and-sea channel (right-figures). This figure illustrates the role of higher frequency surface waves in spreading the channel delay and frequency response for a relatively flat ocean.

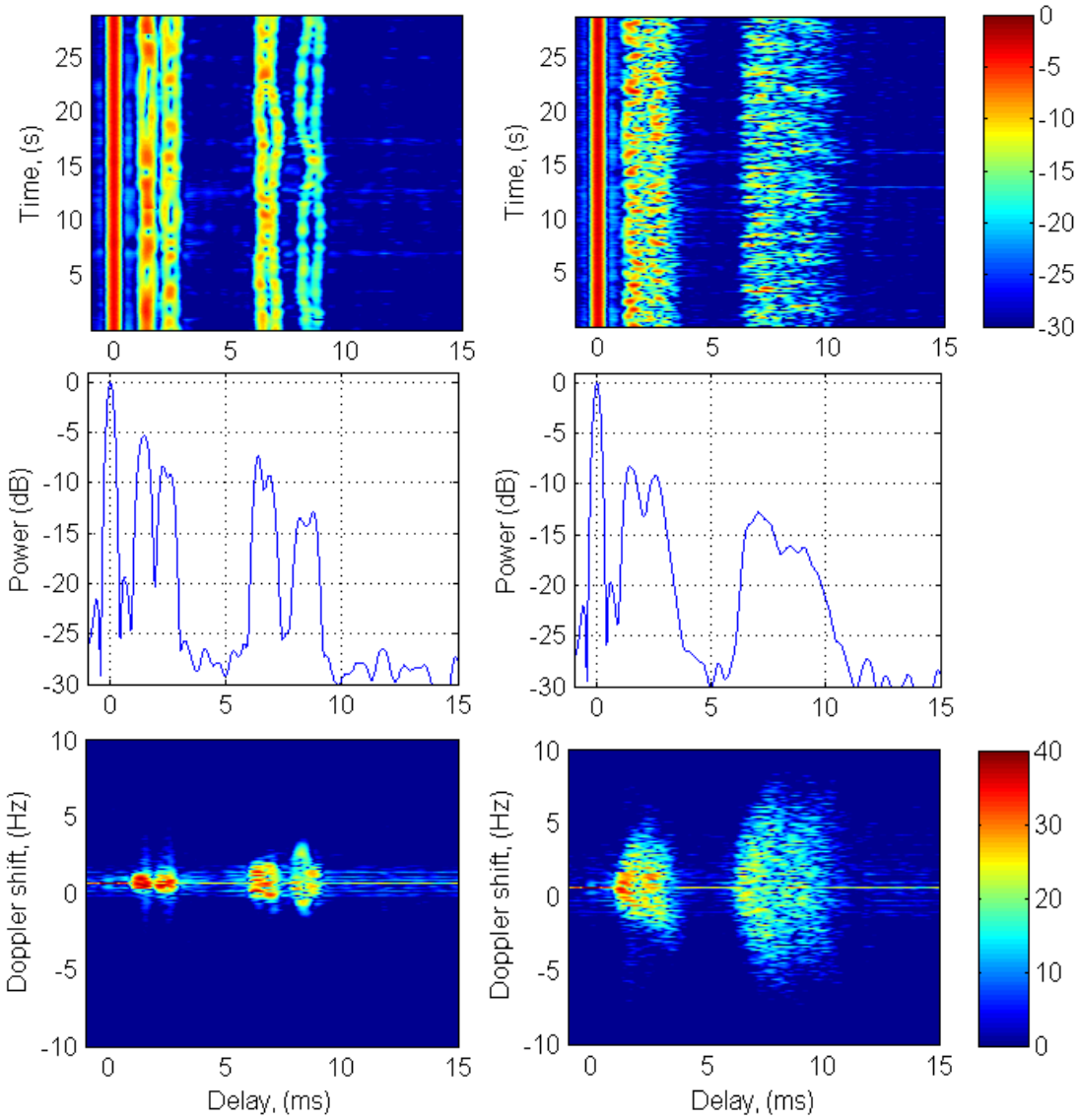

Figure 5-59: Synthetic channel probe response $|h(\tau,t)^2|$ (dB) (top), delay power profile $|P(\tau)|$ (dB) (middle) and spreading function $|S(\tau,\nu)^2|$ (dB) (bottom), for swell only (left), and swell plus sea (right)

5.6 Whole (multi-path) channel impulse response history

Figure 5-60 shows an example 8-16 kHz synthetic multipath channel response history for the low-amplitude Cottesloe surface based on the first 10 ray-paths (direct, bottom, 4 x single-surface-bounce variants, 4 x single-surface-bounce variants) for a 110 m range, 13.5 m deep environment.

The response for the 8 surface-interacting paths has been calculated using the rationalised set of 3 grazing angles, 12° (2 paths),15.5° (2 paths), and 26° (4 paths). The bistatic response histories from which these path responses are drawn are illustrated in Figure 5-61. For the double-bounce paths, two instances of the bistatic response at 26° are multiplied in the frequency domain then returned to

the time domain. The closely spaced direct and bottom paths have a band-limited FIR representation that results from the frequency-dependent absorption (see Eq.(5-3)) giving the appearance of single arrival.

To check whether the resultant relative path amplitudes are realistic, the simulation response generated for the experimental environment must be convolved with the experimental probe signal to generate a synthetic channel probe response. The dynamic characteristics of this synthetic probed response can then be compared with the experimental results. These comparisons are made in Chapter 6.

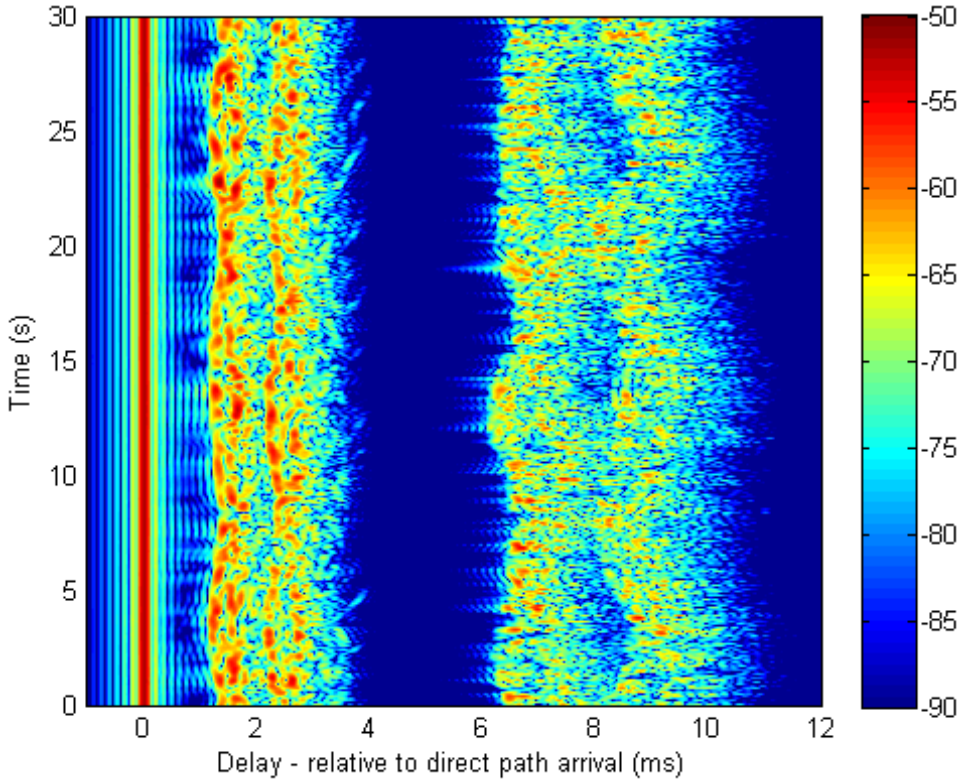

Figure 5-60: KA model 8 kHz – 16 kHz multi-path response history $|h(t,\tau)|^2$ (dB) based on coherent responses for the first 10 flat-surface ray-paths, 120 m range, 13.5 m channel depth.

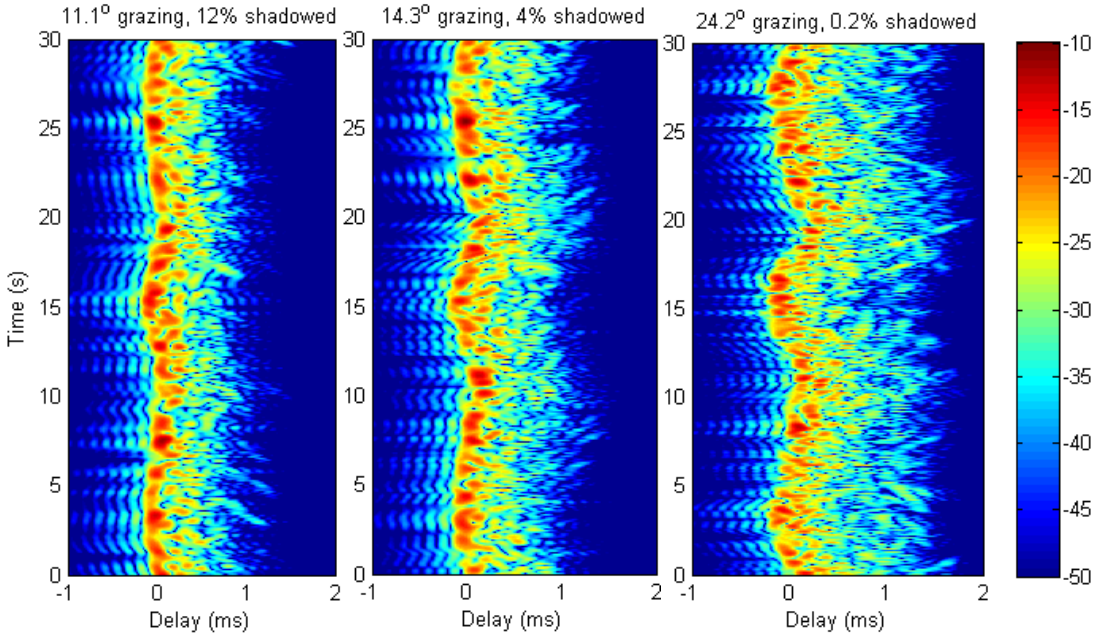

Figure 5-61: Component range-normalised bistatic path responses $|h(t,\tau)|^2$ (dB) used to generate Figure 5-60, representing the pre-cursor responses for synthesis of the first two single-bounce paths (left), second two single-bounce paths (centre), and the four double-bounce paths prior to frequency-domain 'doubling' (right)

5.7 Discussion on KA for rough surface response simulation

5.7.1 Treatment of shadowing

Initially the dynamic simulation of bistatic shadowing was thought to be important to the realistic modelling of the Doppler and delay spreading. However it was observed that use of a discrete-time shadowing algorithm for the planar-discretised surface inherently introduced artificially abrupt changes in net pressure response that translated to artificially high Doppler responses. This is observable as elevation of the noise floor at the sides of the simulated Doppler power spectra (e.g. Figure 5-33 and Figure 5-36).

The shadowing algorithm also caused the well-known problem (Thorsos 1988, Ogilvy 1988) of decimation of the Kirchhoff amplitude response as the proportion of bistatically 'illuminated' surface elements approached zero at low grazing (Figure 5-35 top frame). The solution discussed in Section 5.4.2 was to model all surface elements as permanently irradiated in the manner previously described in the KA implementation by Siderius and Porter (2008), with modulation of each element response according to tilt only.

Inclusion of KA responses of all elements results in over-estimation of the response power to an acceptable degree (Figure 5-35 bottom frame), due to the

inclusion of responses from the shadowed underside of wave crests, that in reality do not contribute. Inclusion also tends to obscure the simulated reproduction of response history striation effects (Figure 5-15, Figure 5-16).

However the slight over-prediction of response, which will always be no greater than 3dB from consideration of simulated wave peak/trough symmetry, is less problematic than the very large under-prediction caused by shadowing when the proportion of directly illuminated elements is small. Consistent with the inclusion of artificial responses from the shadowed underside of wave crests, response delay power profiles are slightly positive-biased in delay commensurate with the weighting towards longer transmission path lengths. Importantly however, the Doppler response no longer demonstrates artificial discontinuities from discrete-time shadowing (Figure 5-33, Figure 5-36).

5.7.2 Optimisation of rough surface discretisation

It is desirable to maximise the horizontal surface discretisation interval to minimise array storage and calculation load, whilst at the same time ensuring that the KA Doppler spectrum does not exceed that of the IE model, as to do so would imply the existence of rapid transients that are absent from reality.

The qualitative appearance of "shoulders" in the KA Doppler power spectrum was determined in Section 5.4.3.1 to be attributable partly to the facetted shape of the surface profile as the discretisation interval grows larger, evidenced by the same characteristic appearing in the IE model response to increasingly coarse facetted surface shape, and partly due to the KA approximation. Thus, the appearance of Doppler spectrum "shoulders" is indicative of alteration of the surface by the surface discretisation process, which is acceptable so long as the Doppler power associated with this surface alteration remains insignificant. The practical judgment as to what level of significance is appropriate for this artificial Doppler has not been considered in this study, and has arbitrarily been set to -60 dB in the preparation of illustrative examples.

Simulation parameters found to be critical to the attainment of a dynamically realistic KA surface response include the horizontal surface discretisation interval used to define the surface elements, the grazing angle and transmission range. The inclusion of all KA element responses as if fully exposed to the incident field, regardless of the actual shadowing by the surface profile was found to be

essential. The significance of these parameters for the realistic reproduction of Doppler by the rough surface can be understood by considering the coherent addition of the individual lobed KA angular pressure responses of discrete tangent-plane elements described in Section 2.4 that comprise the modelled rough surface.

The IE response by its mathematical nature is continuous as the rough surface-realisation evolves in time. The goal of simulation is to ensure that the simplified KA response avoids unrealistic transient Doppler that is implied by artificially rapid surface response changes from one realisation to the next. The KA finite tangent-plane model attempts to replace the real spatially and temporally continuous field response with enough modelled discrete over-lapping beam-like lobed pressure responses from surface elements, in space and time, to achieve the same degree of continuity within the bandwidth defined by the channel sampling Nyquist frequency $f_{Nyquist} = 1/2\Delta t$, where Δt is the interval between successive modelled surface realisations.

Broad angular central lobes in the discretised KA element responses, and smaller Δt, support continuity of the net coherent response at the bistatic receiver as the surface elements change tilt with time. The central radiation pattern beam-width of the KA element increases with bistatic range, increases with reduced grazing angle, and increases with reduced element size. As the range and grazing angle for each of the rough-surface eigenpaths are properties of the channel, the horizontal surface element size, and the channel sampling interval Δt, become the key controllable parameters to maintain simulation continuity depending on the combination of path range and grazing angle.

5.8 Discussion on computational capacity considerations

Generation of the multi-path channel response within computer memory and processing-time constraints requires optimisation of problem discretisation parameters in two time dimensions (t and τ) and the two horizontal spatial dimensions (dx and dy).

The overall size of the discretised rough surface patch should be large enough to capture the significant dynamic range of single-surface bounce bistatic responses. The Fourier synthesis frequency increment dF across the signal bandwidth must then be small enough such that the time window $1/dF$ captures the bistatic delay-

spread $\Delta\tau$ associated with the bistatic responses. A flat-surface ray-model of the multi-path delay-spread is a useful starting point for considering the time-window that may be of interest for bistatic responses.

The surface discretisation interval dx must be short enough to represent the highest surface wavenumber of interest, and at shorter ranges, dx must also be small enough to ensure that the discretised surface does not generate significant artificial Doppler in the dynamic surface response. The total number of surface realisations necessary is determined by the circular time interval T_{circ} divided by the channel calculation interval Δt. In general, the sharper the peak in the surface-wave spectral density, the longer T_{circ} needs to be to produce sufficiently fine surface frequency discretisation $d\omega = 2\pi/T_{circ}$ to adequately represent the surface spectral density. Finally, the problem size is proportional to the number of underlying ray eigenpaths that are modelled.

With unlimited computer resources a bistatic response history could be calculated for every bistatic geometry of each surface-interaction comprising every underlying eigenpath in the multi-path FIR cascade model, to retain as much geometrical diversity of modelled micro-paths as possible. However, the calculation of bistatic response histories is computationally intensive, such that there is incentive to re-use bistatic responses for geometrically similar surface interactions.

It is recommended that the bistatic surface response of single surface-interacting paths be modelled with unique bistatic geometry, with correct relative depth of source and receiver, to simulate as accurately as possible the net coherent response of these paths. For paths with two or more surface interactions the response becomes of marginal or irrelevant significance to the coherent transmission, but still relevant to the incoherent channel response. For such paths it is recommended for computational economy that simplified average bistatic geometries be used for all surface interactions (or 'bounces') on a path, and for paths with similar grazing angle.

The size of the signal-channel convolution problem is proportional to the signal sampling rate, the FIR length on each path (proportional to the modelled path delay-spread) and the number of paths.

6 COMPARISON OF MEASURED AND SIMULATED CHANNELS

6.1 Introduction

In Chapter 5 the KA model implementation for a bistatic time-varying rough surface-response was justified using the IE model as a verification reference. However this justification did not extend to the consideration of channel responses via paths with two or more surface plus bottom interactions, or for a three-dimensional time-varying rough surface.

In this chapter the experimentally measured channel probe responses are compared with the simulated channel probe responses (using identical probe sequences and matched-filtering), to provide evidence supporting the proposed methodology for simulation of full-scale and full-dimensional geometries extending to multiple-surface interacting response paths (Sections 5.3.2, 5.4.9). These comparisons are presented for a selection of experimental channels representing the diversity of experimental transmission ranges, (and therefore surface grazing angles), 13.5 m and 53 m depth environments, and two experimental sea-surfaces (0.5 m and 2 m significant wave heights).

The simulated channel probe responses were calculated using the experimental probe signals, samples of sound speed profile, surface wave records, and records of transmitter motion and drift as simulation inputs. A smooth, sandy sea-bed was modelled consistent with the fine sand experimental grab samples for the Cottesloe trial (Section 4.2.3), and assumed the same for the Rottnest trial environment. The bathymetry was assumed constant for simplicity because the gross flat-surface eigenpath delay structure was not the focus of this study, however the actual bathymetry was tilted on each transmission transect, varying by ±5% of the nominal depth over the longest transmission ranges at each site. The scale of roughness of the sea bottom was not measured for either experimental trial.

The KA bistatic model which is the basic building block of the whole channel response includes the contributions of all shadowed and unshadowed discretised surface elements (Section 5.4.2). The simulated path responses are synthesised from time-circular arrays of KA bistatic surface responses (Section 5.5.3), which are calculated from a time-circular three-dimensional surface realisation.

The experimental transmitter arrangement (Figure 4-6) permitted a combination of relatively steady horizontal transmitter drift and oscillatory movement, and more irregular vertical transmitter oscillations due to motion of the boat transferred to the transmitter via the transmitter cable. For simulation/experimental comparative purposes, a partially motion-compensated experimental response has been generated by post-processing, to remove Doppler associated with relatively slow-changing horizontal transmitter movement that is largely common to all paths except at very short range.

The vertical transmitter motion history, indirectly measured by the vessel pitch-roll-heave instrumentation at a sampling rate of 100 Hz, was used to deterministically apply in-path Doppler distortions from this motion as a function of eigenpath launch angle (Section 5.3.6). In this manner comparable experimental and simulated channel probe responses that include the minor path-dependent Doppler contribution of vertical transmitter motion are obtained.

The channel responses are graphically presented at the full dynamic range of the experimental and simulated probe responses to provide insight into the useable dynamic range of both experimental and simulated data sets.

In appraising the temporal similarity between measured and simulated channel responses, it should be noted that there is no basis (or expectation) for the response histories to be in phase in the time (vertical) dimension at any delay. The simulated surface realisations are based on the estimated surface wave power spectrum during the experiment and there has been no attempt to match the phases of the spectral components to those occurring during experimental transmissions.

A discussion is presented in Section 6.2.1 on the causes of common and contrasting response 'speckle' in the experimental and simulation response histories, using the 120m Cottesloe example as the discussion point. This discussion is applicable in varying degrees to all of the comparisons presented for both the Cottesloe and Rottnest experimental sites.

6.2 Cottesloe site comparisons – spread PRBS probe

Comparisons between simulated and measured channel probe responses are presented for 120 m, 500 m and 1000 m ranges. The simulated channels were

calculated using a 120 s duration time-circular 3D surface simulation at 20 ms intervals. Table 6-1 presents more complete list of parameters relating to the three channel ranges.

The simulated channel responses and derived spreading and delay/Doppler power functions for 120 m, 500 m and 1000 m ranges prior to convolution with a probe signal are presented respectively in Appendices C.1, C.2, and C.3. These appendices also contain response histories, spreading functions and delay/Doppler power functions for the grazing-angle dependent bistatic responses from which the multi-path channel responses are built.

Table 6-1: Parameters for Cottesloe channel simulations

Range	120 m	496 m	1007 m
Bellhop flat-surface amplitude-delay simulation parameters			
calculation frequency	12 kHz		
ray description	geometric rays, 1601 rays, with launch angles from -80° to +80°		
source depth	10 m		
receiver depth	12.5 m		
environment depth	13.5 m		
mean seawater sound speed	1525 m/s		
seawater density	1024 kg/m^3		
seawater sound absorption	0.00021 dB/wavelength		
surface and bottom profiles	flat		
bottom description	sand, single semi-infinite fluid layer		
Assumed bottom compressional absorption for silt (Jensen et al. 2011)	1 dB/wavelength		
Assumed bottom density	1941 kg/m^3		
Assumed bottom compressional sound speed	1749 m/s		
sound speed profile corresponding to experimental range transmit position	Cottesloe CTD cast 1 (Figure A-5)	Cottesloe CTD cast 4 (Figure A-8)	Cottesloe CTD cast 3 (Figure A-7)
number of base eigenpaths	10	22	26
KA response bistatic geometry parameters			
rationalised bistatic calculation angles	11.1°, 14.3°, 24.2°	2.7°, 3.5°, 6.0°, 6.7°, 9.3°, 12.3°, 15.2°	1.3°, 1.7°, 3.3°, 4.6°, 6.1°, 7.6°, 9.1°
rationalised bistatic source (Tx) and receiver (Rx) calculation depths	11.1°, Tx 10m, Rx 13.5m 14.3°, Tx 17m, Rx 17m 24.2°, Tx27m, Rx 27m	2.7°, Tx 10m, Rx 13.5m 3.5°, Tx 17m, Rx 13.5m 6.0°, Tx 26m, Rx 26.7m 6.7°, Tx 30.5m, Rx 28m 9.3°, Tx 40.5m, Rx 40.5m 12.3°, Tx 54m, Rx 54m 15.2°, Tx 67.5m, Rx 67.5m	1.3°, Tx 10m, Rx 13.5m 1.7°, Tx 17m, Rx 13.5m 3.3°, Tx 30.5m, Rx 28.4m 4.6°, Tx 40.5m, Rx 40.5m 6.1°, Tx 54m, Rx 54m 7.6°, Tx 67.5m, Rx 67.5m 9.1°, Tx 81m, Rx 81m

Range	120 m	496 m	1007 m
surface patch dimensions	11.1°, 82m L x 16m W 14.3°,73m L x 18m W 24.2° 60m L x 25m W	2.7°, 339m L x 16.5m W 3.5°, 302m L x 19m W 6.0°, 235m L x 25m W 6.7°, 223m L x 26m W 9.3°, 191m L x 21m W 12.3°, 168m L x 36m W 15.2°, 152m L x 40m W	1.3°, 689m L x 16.6m W 1.7°, 611m L x 19m W 3.3°, 449m L x 26.4m W 4.6°, 384m L x 31.1m W 6.1°, 334m L x 35.9m W 7.6°, 300m L x 40.1m W 9.1°, 276m L x 44m W
method of including spatial coherence between starting instances of bistatic responses on a ray-path and across ray-paths	random	random	random
Surface response simulation parameters			
surface simulation duration	120 seconds = 6000 realisations x 20 ms interval		
sea dx, dy	12 cm	24 cm	48 cm
surface response band width	8 kHz – 16 kHz, (zero padding 0 – 48 kHz to achieve 96 kS/s delay resolution)		
Fourier synthesis increment, dF, and resultant bistatic delay window (1/ dF)	100 Hz (10 ms)		
surface wave spectral density	Figure 5-56		
surface angular frequency increment	$2\pi/T$, T = 120 s		
sea significant wave height (H_s)	0.25 m		
sea peak period (T_p)	1.9 seconds		
sea angular frequency	$1 - 2\pi$ rad/s		
swell significant wave height (H_s)	0.4 m		
swell peak period (T_p)	16.7 seconds		
swell dx, dy	= 5 times sea dx, dy, $dx = dy$		
swell maximum angular frequency	1 rad/s		
TxRx heading	240°	240°	240°
sea heading	3°	65°	65°
swell heading	118°	65°	65°
WAFO swell and sea spreading model	Poisson		
transmitter vertical motion history	"r4_pitch_roll_heave.txt"	"r6_pitch_roll_heave.txt"	"r6_pitch_roll_heave.txt"
channel computation time (per 60 s)	2.5 hours	3 hours	2 hours
channel signal convolution computation time (per 60 s of signal)	38 minutes	84 minutes	100 minutes

Example realisations of the simulation sea and swell for the Cottesloe environment are illustrated on Figure 6-1.

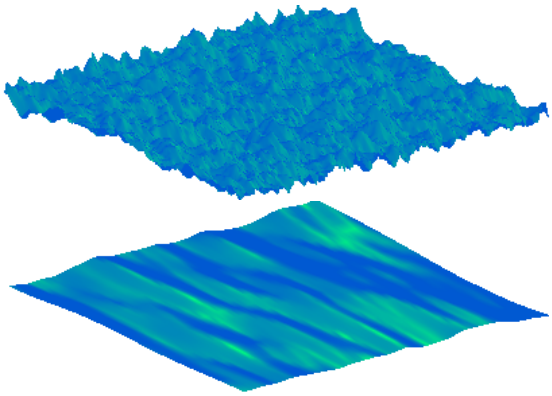

Figure 6-1: Surface patch realisations of sea (left) and swell (right)

6.2.1 13.5 m deep 120 m range low sea-state environment

The 120 m channel response was modelled using a horizontal discretisation interval $1.25\lambda_{min}$ = 12 cm as justified in Section 5.4.3, with model parameters and surface wave characteristics as summarised in Table 6-1. The rough channel response was calculated around 10 flat surface eigenpaths. A 30 s duration transmit signal consisting of a repeated 21 ms spread-spectrum PRBS probe was convolved with the time-circular synthetic channel response to generate a simulated receive signal. The probe signal and simulated receive signal were then matched-filtered to generate the simulated channel probe response.

The single-surface bounce paths exhibit similar temporal-delay patterns (Figure 6-2), frequency spreading (Figure 6-3) and average signal power (Figure 6-4) between measurement and simulation. To achieve comparability of the delay power profiles (Figure 6-4) both profiles were normalised by the maximum correlation power at any delay of the measured response.

The double-surface-bounce paths show similar temporal characteristics (Figure 6-2), but the simulated power is typically 5 dB higher as shown on the delay power profile (Figure 6-4). There are many factors that either individually or in combination could account for this difference. Possibilities include the simple modelled bottom reflection loss based on assumed sea-bed parameters, and discrepancies in the simulated surface realisation, particularly for the high-frequency component of the surface-wave spectrum above the DWRB cut-off frequency. The insignificant shadowing of the double-surface-bounce paths at this short range would indicate that the KA choice of ignoring shadowing (which in

shadowed rough surfaces may lead to 3 dB over-prediction) is not significant in this instance.

The Doppler power spectrum (Figure 6-5) shows comparable measured and simulated profiles for non-surface interacting paths (black) and single surface-bounce paths (green). The simulated Doppler power for the double surface-bounce paths (red) is higher for the same reasons as for the delay power profile discrepancy. For small Doppler shifts up to 2 Hz this figure shows the dominant signal power originating from single-surface reflected paths. For greater Doppler the dominant signal arrives via double-surface reflected paths.

The coherence functions (Figure 6-7) show the simulated results slightly under-estimate coherence on surface-interacting paths. The slightly greater coherence for the simulated non-surface paths might be attributable to the imperfect post-processing to remove horizontal Doppler from the measured result. The dots on the measured results represent the data at 21 ms intervals. The simulated data is calculated at the same 21 ms interval, however the markers are omitted for clarity. (For clarification, the underlying simulated channel response is calculated at 20 ms intervals for this range then interpolated to interval $1/F_S$ for $F_S = 96$ kS/s before convolution with the repeated 21 ms probe signal) The coherence profiles have been calculated from the channel responses (Figure 6-2) using the same delay ranges as used in calculating the Doppler power spectra.

The measured and simulated channel probe responses at 120 m (Figure 6-2) show a background of diffuse response that will be referred to as 'speckle'. The background speckle that is common to the measurement and simulation can be the result of correlation noise inherent in the probe autocorrelation function away from the PRBS correlation peak (Section 2.6.3). The experimental response can also include 'speckle' that represents time-aliasing of diffuse real received signal responses at delays beyond the 21 ms PRBS probe signal correlation window. In this particular example (120 m range) the simulated response is limited to the first 10 eigenpaths such that the potential for aliasing into the probe response window exists in the experimental probe response, but is excluded for the simulated probe response.

A third type of noise that could conceivably contribute to background 'speckle' is the ambient noise at the receiver. However the experimental signal-to-noise was

high at the receiver, such that even impulsive shrimp snaps were not evident in time-expanded inspection of the receiver spectral histories (Section A.2). Significant correlation of the probe with background noise is considered unlikely at 120m range, but is considered to be a factor for the long-range experimental channels.

Any artificial response that is due to correlation noise or time-aliasing of diffuse response associated with the channel probing methodology carries through to the derived spreading function estimate (Figure 6-3), the delay power profile (Figure 6-4), and Doppler power spectrum (Figure 6-5). The alterations to the spreading function and Doppler spectrum attributable to the channel probing methodology may be observed by considering the synthetic channel response (Figure C-1), spreading function (Figure C-2) and Doppler power spectrum (Figure C-3) plotted prior to channel convolution with the probe signal.

The hat symbol '^' that indicates an estimated channel result (e.g. $\hat{h}(\tau, t)$) has been used in figures to indicate both the measured and simulated probe responses, on the basis that the same numerical processing problems and limitations for over-spread channels that constrain the usefulness of measured estimates apply to both results. The comparable simulated results from Appendix C that relate to the channel before convolution with a signal are indicated without the hat (i.e. $h(\tau, t)$).

Some portion of the diffuse-like experimental response that is not replicated by the simulation logically represents real multiple reflected paths with irregular and changing (along the micro-path) grazing angle between successive boundary interactions, that are not encompassed by the modelled bistatic decomposition of eigenpaths (Figure 5-46). This would occur because the real bottom exhibits roughness (undulations) on some unknown scale that produces non-plane-wave angular scattering off the bottom, enabling greater geometrical diversity of micro-paths (and therefore path lengths) than the micro-paths embodied by the model. The greater diversity of paths that is enabled by angular scattering off the bottom enables diffuse micro-path responses at delays that are greater than modelled, but with time-domain Doppler that will necessarily be similar to those modelled.

Comparison of Figure 6-5 with Figure 6-6 (Figure 6-6 is reproduced with compatible axes from the same data on Figure C-3) shows that the experimentally

measureable portion of the Doppler power spectrum on Figure 6-5 that is free of processing noise associated with probing is limited to ±10Hz. The lower Doppler power at the sides of the simulated Doppler power spectrum (on RHS of Figure 6-5) compared to the experimental Doppler spectrum (on LHS of Figure 6-5) is understood, at least in part, to be attributable to the lesser simulated micro-path diversity.

Combining the ideas from the above, it may be concluded that whilst the simulation likely under-represents the micro-path diversity at higher greater than ±10Hz, for this channel, this under-response occurs at a power level that is sufficiently low to be less significant than artificial Doppler associated with the probing methodology.

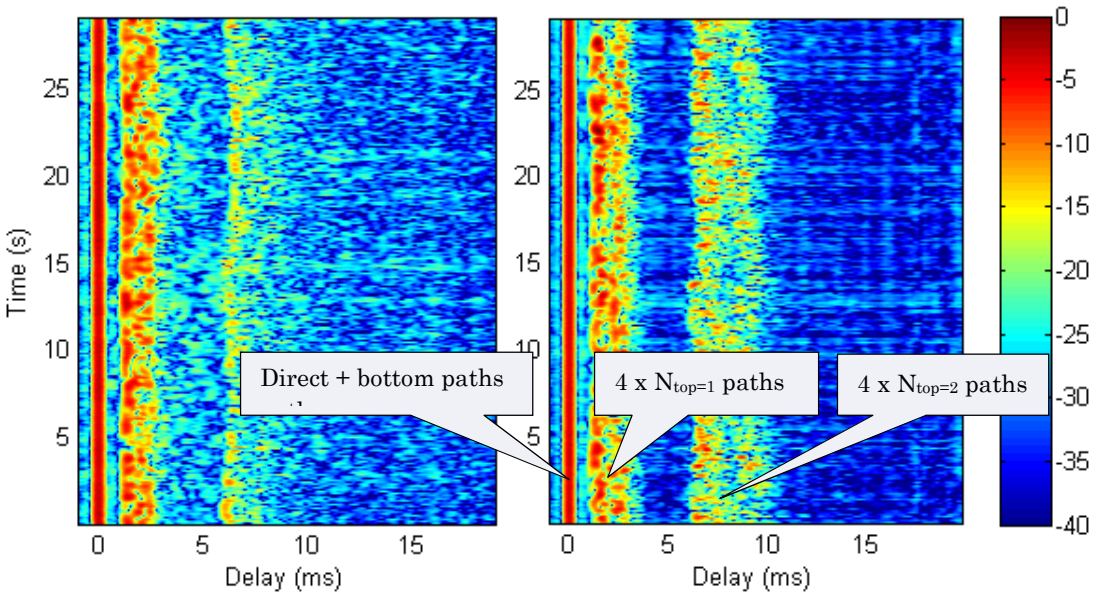

Figure 6-2: Measured (left) and simulated (right) response history $\left|\hat{h}(\tau,t)\right|^2$(dB)– 21 ms PRBS probe in 120 m range 13.5 m depth, surface H_s = 0.5 m

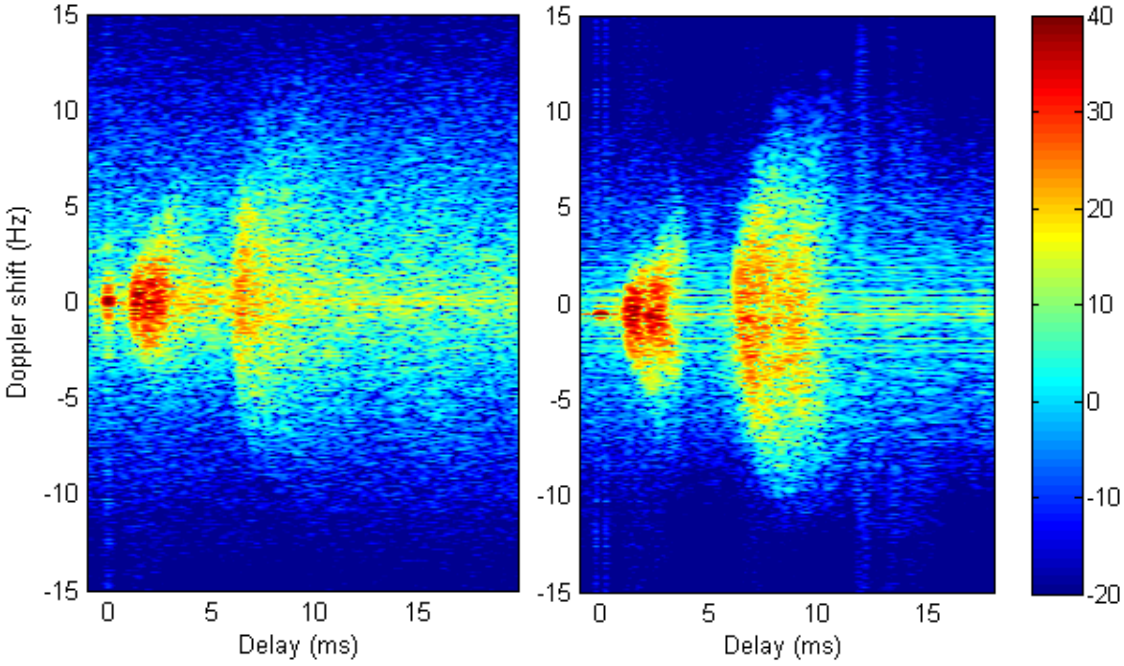

Figure 6-3: Measured (left) and simulated (right) spreading function $|\hat{S}(\nu,\tau)|^2$ (dB) rel. to 12 kHz – 21 ms PRBS probe at 120 m range 13.5 m depth, surface $H_s = 0.5$ m

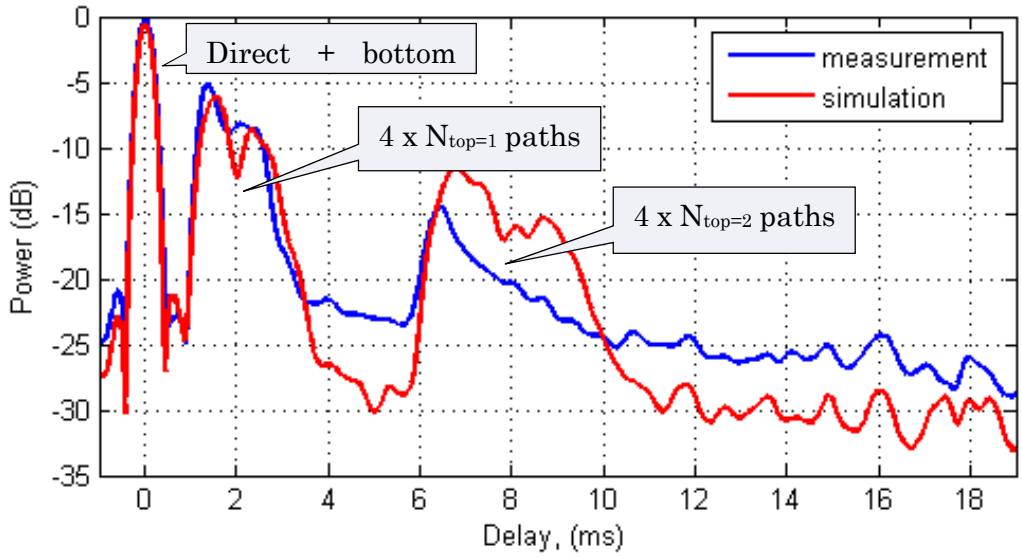

Figure 6-4: Measured and simulated delay power profile $|\hat{P}(\tau)|$ (dB) – 21 ms PRBS probe at 120 m range 13.5 m depth, surface $H_s = 0.5$ m

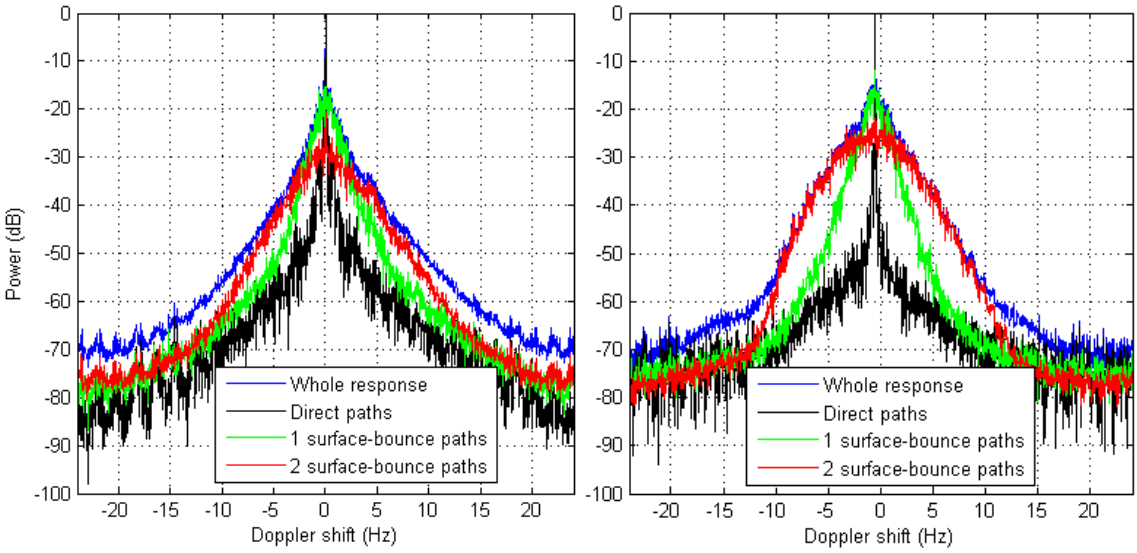

Figure 6-5: Measured (left), simulated (right) Doppler power spectrum $|\hat{P}(\nu)|$ (dB) rel. to 12 kHz – 21 ms PRBS probe at 120 m range 13.5 m depth, surface $H_s = 0.5$ m

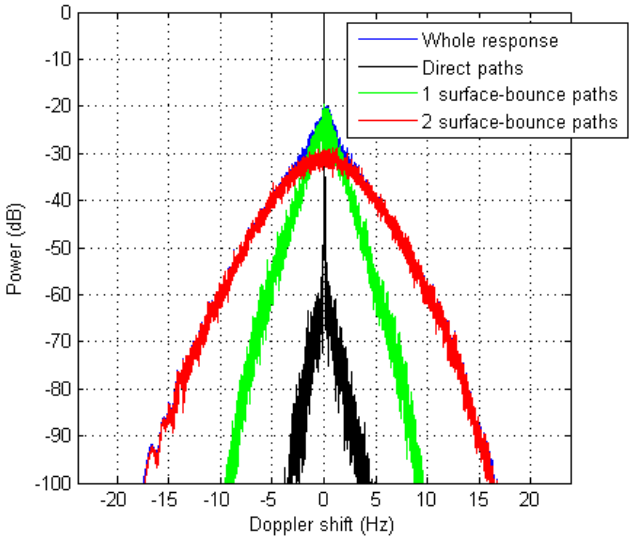

Figure 6-6: Synthetic Doppler power spectrum, fixed Tx and Rx, $|P(\nu)|$ (dB) relative to 12 kHz –20 ms channel interval at 120 m range 13.5 m depth, surface $H_s = 0.5$ m

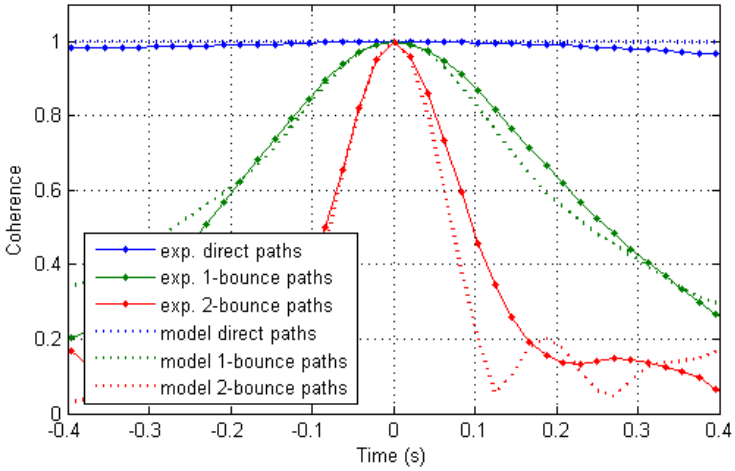

Figure 6-7: Measured and simulated channel coherence in delay bands $\hat{C}(\Delta t, \tau_1, \tau_2)$ - 21 ms PRBS probe at 120 m range 13.5 m depth, surface $H_s = 0.5$ m

6.2.2 13.5 m deep 500 m range low sea-state

The 500m channel response was simulated using a horizontal discretisation interval $2.5\lambda_{min}$ = 24 cm as justified in Section 5.4.3, with simulation parameters and surface wave characteristics as summarised in Table 6-1. The rough channel response was calculated around 22 flat surface eigenpaths.

The experimental response history (left side of Figure 6-8) shows some destructive interference in the pair of first-arriving non-surface paths, compared to the next band of four single surface-bounce paths coincident at around 0.8 ms delay. This feature was partially replicated in the simulation, which illustrates modulation of the magnitude of the first arrival band on a similar 10-15 s period. The Bellhop ray-path simulation for this channel was conducted twice, using the sound speed profile (SSP) measured prior to experimental probing (Cottesloe CTD 3 Figure A-7) and after the experimental probing (Cottesloe CTD 4 Figure A-8). The ray-path simulation with the downward-refracting experimental SSP CTD 3 prior to the experimental probe sequence did not return a direct path, whereas the subsequent CTD 4 profile did. There was also evidence (Section 4.2.7) of spatial variation in SSP, whereas the simulation utilised a constant SSP with range. It is concluded that the drift of the experimental transmitter combined with the spatially variable SSP may have generated the measured variable strength of the combined direct and bottom-bounce paths by a combined process of variable destructive interference and refraction effects.

The spreading functions (Figure 6-9) indicate similar measured and simulated delay and frequency spreading, however the background speckle in the experimental result (left-hand figure) tends to obscure the visual similarity. This discrepancy in background speckle is understood to partly represent the greater real micro-path diversity of the experimental channel.

The comparable delay power profiles (Figure 6-10) show agreement in the average correlation magnitude for the double, triple and quadruple surface bounce paths. The simulation over-estimates the average power of the fifth-order surface-bounce paths (10-16ms delay), however the discrepancy of 5 -7 dB may be considered unexpectedly favourable considering the paths have interacted five times with a partially-assumed rough surface specification, and typically five times with an assumed model of the sea bed. The increased discrepancy in delay, at increasing

delay, is attributed to differences in actual depth over the transmission transect from the modelled 13.5 m depth. No geometrical adjustments were made to try and achieve a better match of the path delay structure.

The contribution of processing noise to the experimental power versus Doppler spectrum (Figure 6-11) distorts the overall Doppler spectrum (shown blue), giving the impression of seemingly unbounded Doppler at low power. However, examination of the Doppler power spectrum prior to probe signal convolution (Figure 6-12, cropped from the same data on Figure C-10) indicates that a significant portion of both the experimental and simulated Doppler power spectrum beyond approximately ±5 Hz is attributable to probe correlation processing noise. The lower overall power of the synthetic Doppler power spectrum (Figure 6-12) is partly attributable to the fact that the synthetic channel response does not include the in-path Doppler from vertical oscillation of the transmitter, which is included in both the experimental and simulation probe Doppler power spectra (Figure 6-11).

The response coherence calculated at different delay-bands show consistently high and similar coherence values between measurement and simulation, particularly at the 20 ms interval position relevant to the underlying channel simulation (Figure 6-13).

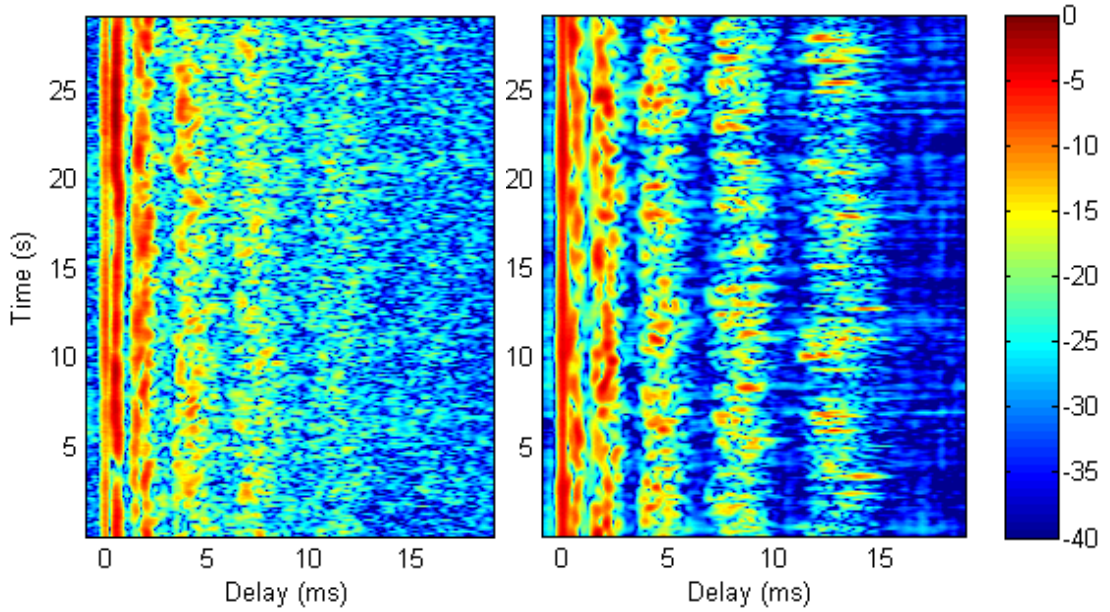

Figure 6-8: Measured (left) and simulated (right) response history $|\hat{h}(\tau,t)|^2$(dB) – 21 ms PRBS probe in 500 m range 13.5 m depth, surface H_s = 0.5 m

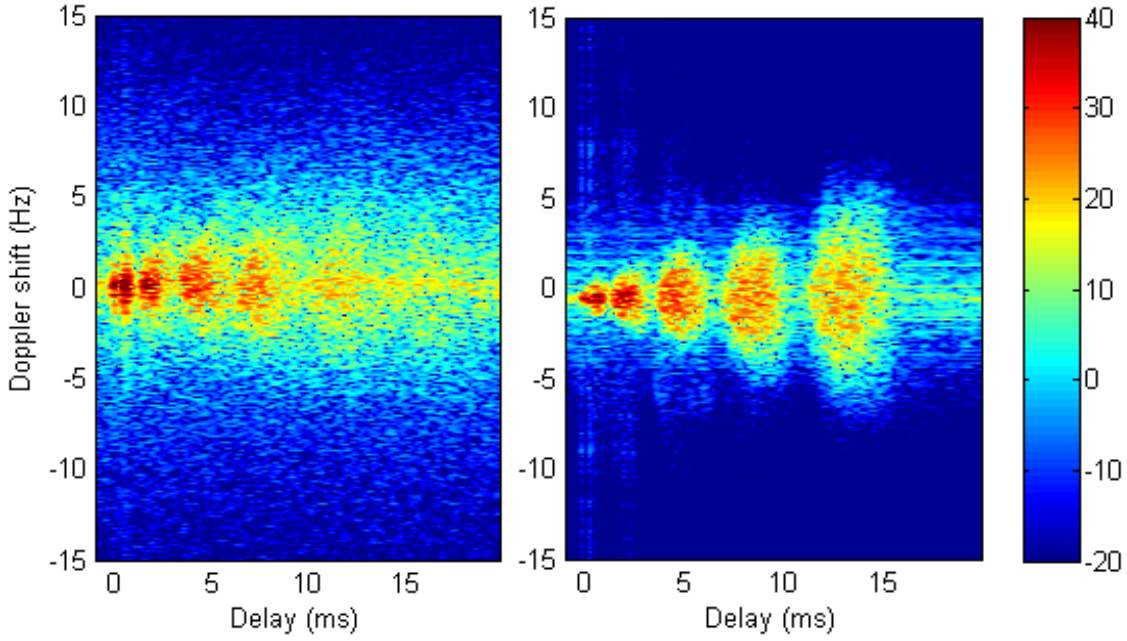

Figure 6-9: Measured (left) and simulated (right) spreading function $\left|\hat{S}(\nu,\tau)\right|^2$(dB) rel. to 12 kHz – 21 ms PRBS probe at 500 m range 13.5 m depth, surface H_s = 0.5 m

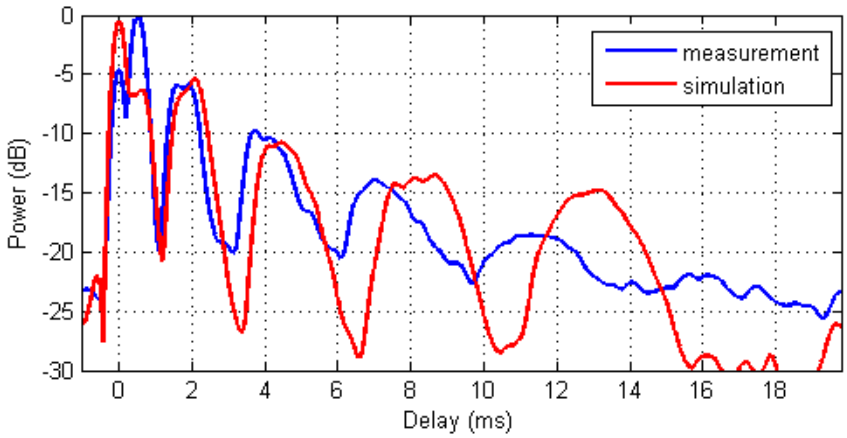

Figure 6-10: Measured and simulated delay power profile $|\hat{P}(\tau)|$ (dB) – 21 ms PRBS probe at 500 m range 13.5 m depth, surface $H_s = 0.5$ m

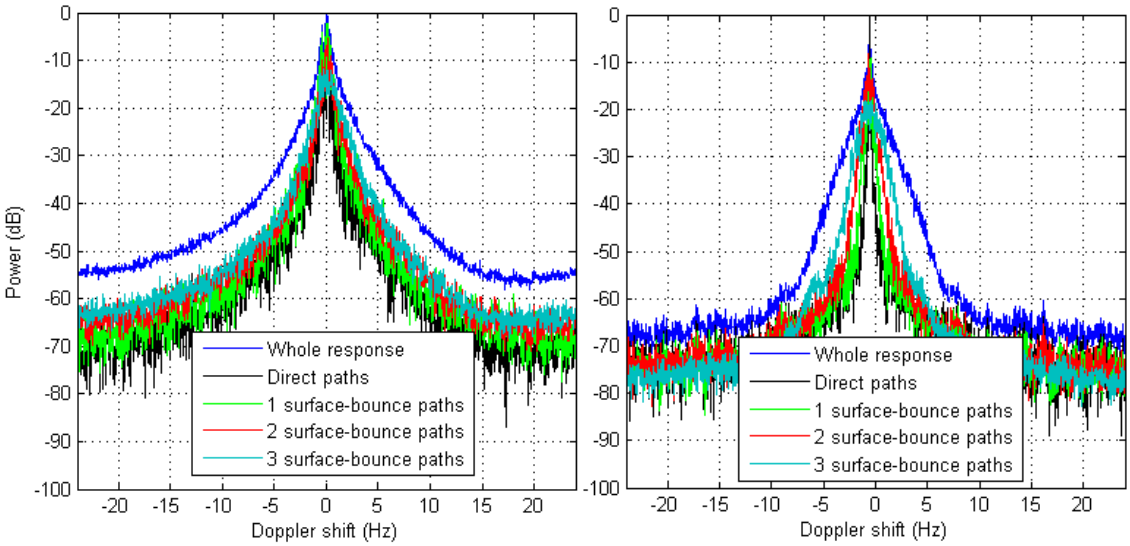

Figure 6-11: Measured (left) and simulated (right) Doppler power spectrum $|\hat{P}(\nu)|$ (dB) rel. to 12 kHz – 21 ms PRBS probe at 500 m range 13.5 m depth, surface $H_s = 0.5$m

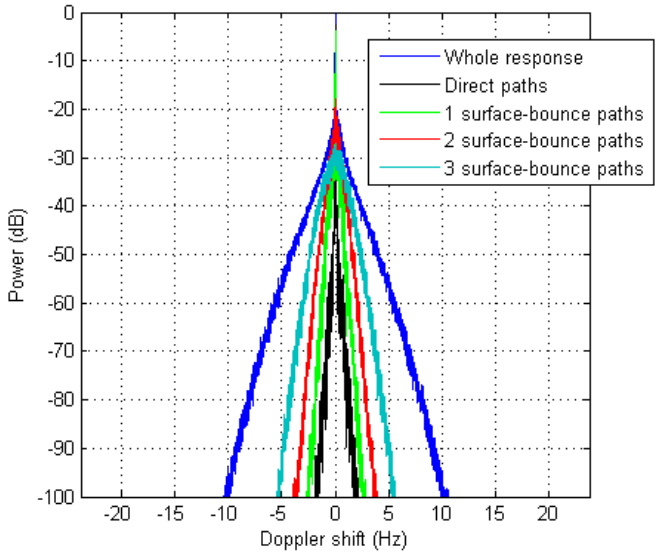

Figure 6-12: Synthetic Doppler power spectrum, fixed Tx and Rx,$|P(\nu)|$ (dB) relative to 12 kHz –20 ms channel interval at 500 m range 13.5 m depth, surface $H_s = 0.5$ m

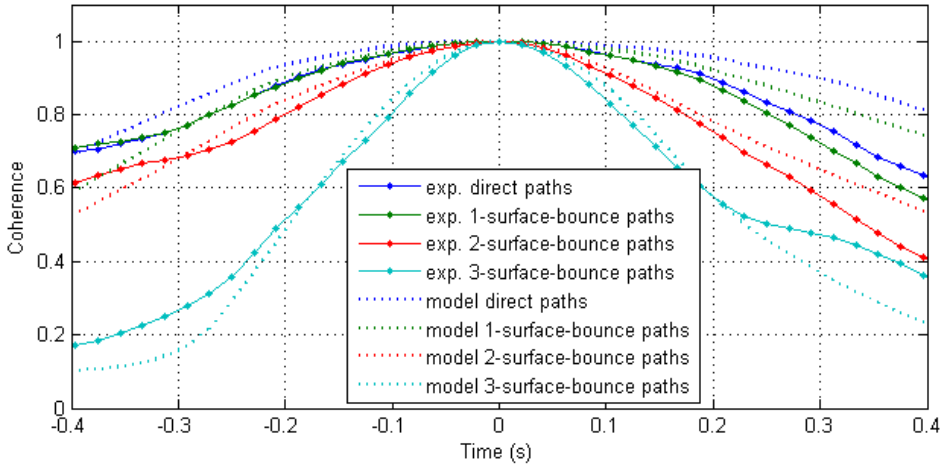

Figure 6-13: Measured and simulated channel coherence in delay bands $\hat{C}(\Delta t, \tau_1, \tau_2)$ – 21 ms PRBS probe at 500 m range 13.5 m depth, surface $H_s = 0.5$ m

6.2.3 13.5 m deep 1000 m range low sea-state

The 1000 m channel response was modelled using a horizontal discretisation interval $5\lambda_{min}$ = 48 cm as justified in Section 5.4.3 for a much rougher surface at 500 m, with simulation parameters and surface wave characteristics as summarised in Table 6-1. The rough channel response was calculated around 26 flat surface eigenpaths.

The simulated probe response history at 1000 m (right side of Figure 6-14) illustrates some of the persistence of the early arriving surface path responses that is observed experimentally. The simulation ray-path structure of the first arrivals consists of five single-surface interacting paths, but no direct or bottom paths. This may partially account for the steadier experimental first arrival-band response. The spatial differences in the SSP and effects of drift potentially complicate the phase-constructive/destructive multi-paths at 1000 m as was the case at 500 m.

The delay power profiles (Figure 6-16) do not appear greatly similar at first, partly because the overall delay structure of the measurement and simulation differ, which obscures the correspondence in delay between the measurement and simulation traces. However the power of arrival groups is generally within 5 dB of the measurement. The loss of the direct path in the simulation likely accounts for the relatively low power of the first arrivals in the simulation.

The Doppler power spectra calculated in path delay bands (Figure 6-17) suggest that the underlying simulated path responses tend to under-estimate the

experimental Doppler. The much lower experimental Doppler power at large Doppler on Figure 6-17 is understood to be partly indicative of lower micro-path diversity in the simulation, and partly the result of increased ambient noise at the receiver.

The synthetic Doppler power spectrum prior to probe signal convolution (Figure 6-18, cropped from Figure C-17) indicates that the probe processing noise is relatively large for Doppler outside of approximately ± 2 Hz.

The comparative coherence results, differentiated by response delay range are presented on Figure 6-19.

There exist notable side lobes of the synthetic channel Doppler power spectrum of Figure C-17, that are also expressed in the bistatic Doppler power spectrum of Figure C-19. These lobes are understood from the analysis using the IE reference and KA models presented in Section 5.4.3.1 to be both a consequence of the planar discretisation of the surface, and exacerbated by Kirchhoff approximated response to the planar discretised surface. If such Doppler side-lobes were high enough to compromise the channel simulation, they can be reduced by decreasing the horizontal surface discretisation interval, at increased computational effort.

It is also possible that these side lobes are indicative of the most energetic interaction of the probe with surface-wave spectral density as reported by Roderick and Deavenport (1993). However, this is difficult to establish since the power level is well below the Doppler noise on the equivalent experimental result.

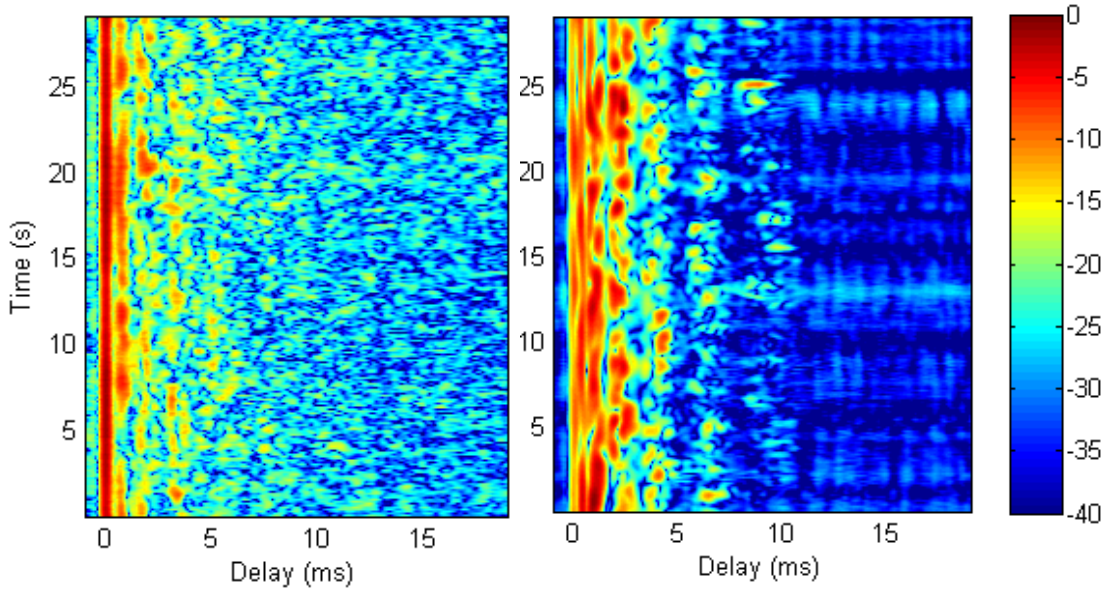

Figure 6-14: Measured (left) and simulated (right) response history $|\hat{h}(\tau,t)|^2$(dB) –21 ms PRBS probe at 1000 m range 13.5 m depth, surface $H_s = 0.5$ m

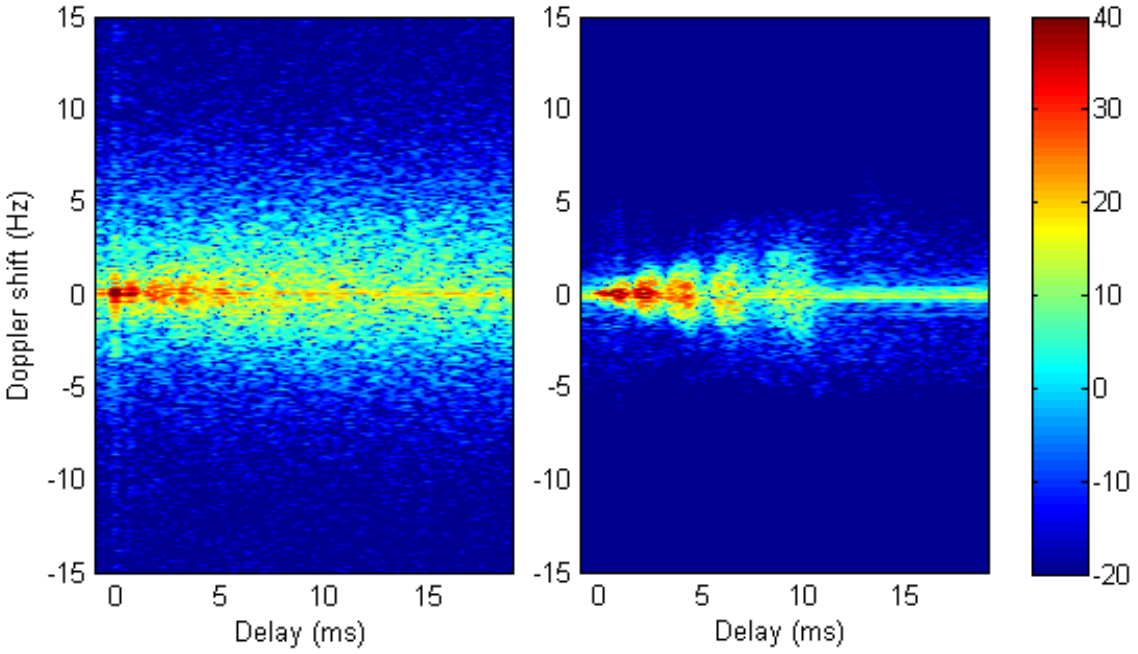

Figure 6-15: Measured (left) and simulated (right) spreading function $\left|\hat{S}(\nu,\tau)\right|^2$(dB) rel. to 12 kHz – 21 ms PRBS probe at 1000 m range 13.5 m depth, surface $H_s = 0.5$m

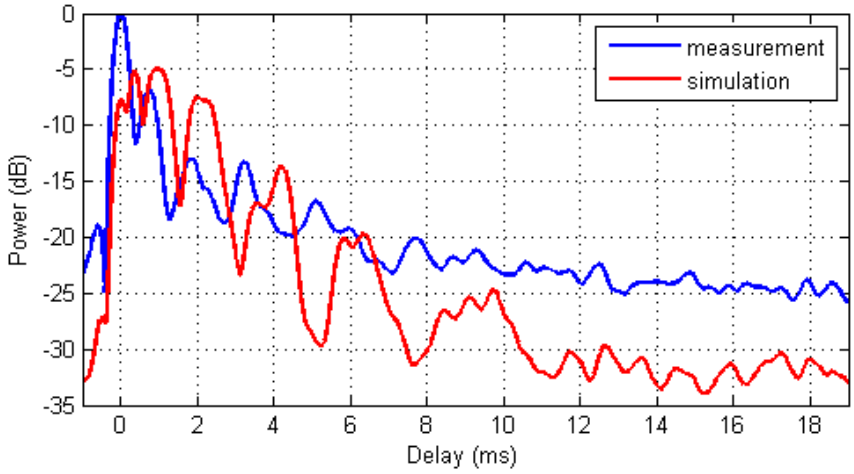

Figure 6-16: Measured and simulated delay power profile $|\hat{P}(\tau)|$ (dB) – 21 ms PRBS probe at 1000 m range 13.5 m depth, surface $H_s = 0.5$ m

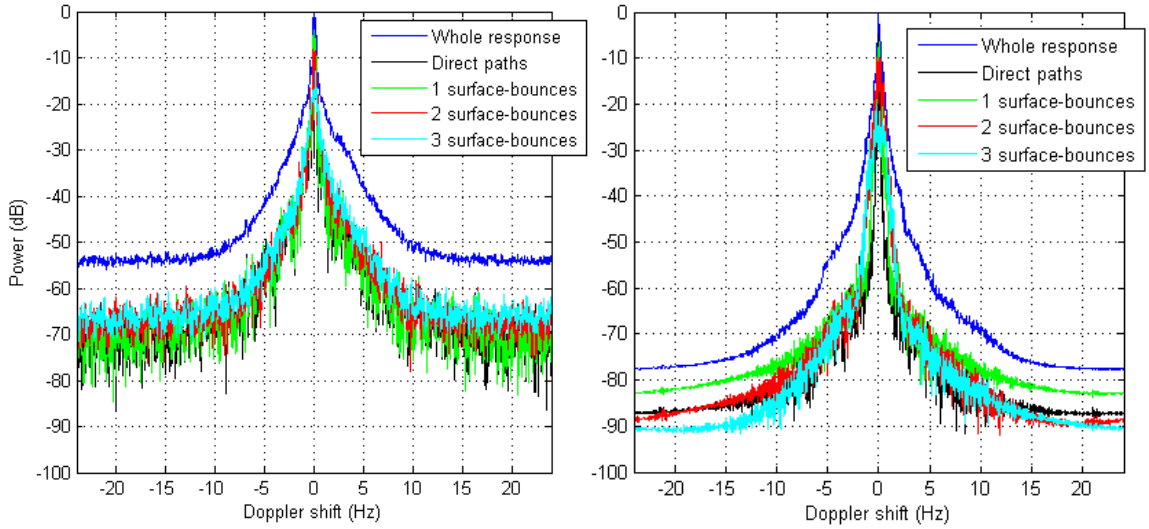

Figure 6-17: Measured (left) and simulated (right) Doppler power spectrum $|\hat{P}(v)|$ (dB) rel. to 12 kHz – 21 ms PRBS probe at 1000 m range 13.5 m depth, surface Hs = 0.5 m

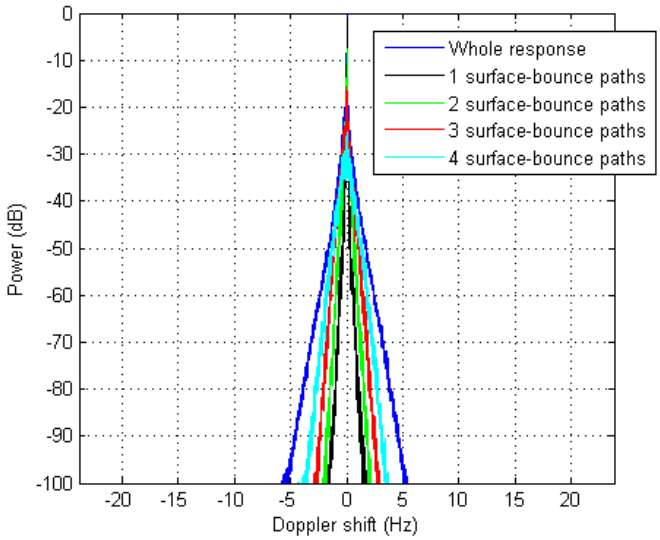

Figure 6-18: Synthetic Doppler power spectrum, fixed Tx and Rx, $|P(v)|$ (dB) relative to 12 kHz –20 ms channel interval at 1000 m range 13.5 m depth, surface $H_s = 0.5$ m

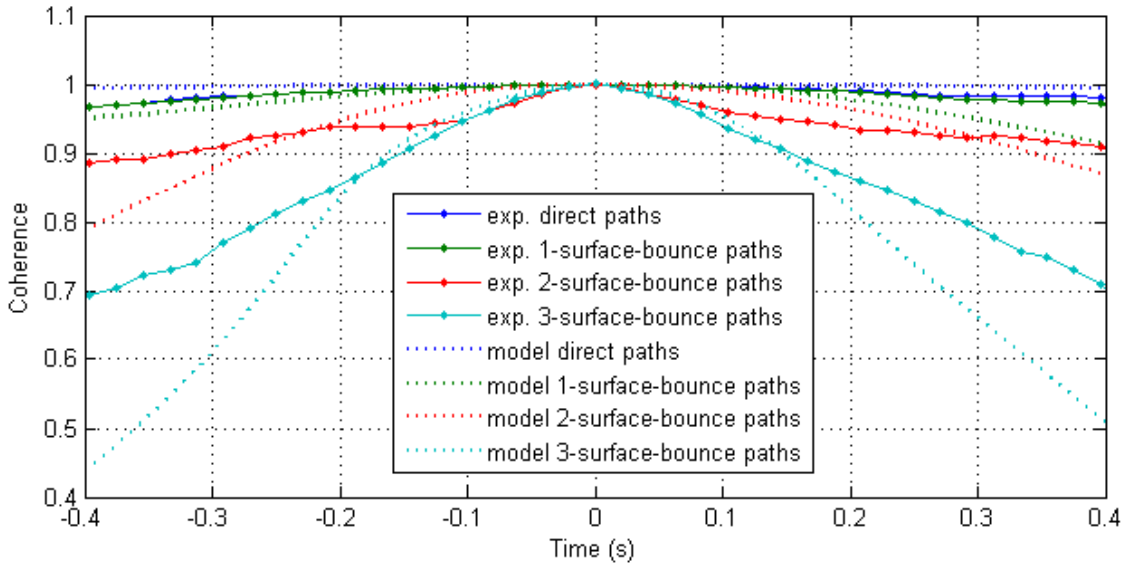

Figure 6-19: Measured and simulated channel coherence in delay bands $\hat{C}(\Delta t, \tau_1, \tau_2)$ – 21 ms PRBS probe at 1000 m range 13.5 m depth, surface $H_s = 0.5$ m

6.3 Rottnest site comparisons – spread PRBS probe

Comparative simulated and measured channel probe responses are presented for ranges of 120 m, 1100 m and 8727 m. Simulation results were calculated for a shorter 30 s duration time-circular 3D surface simulation. The shorter circular time compared to 120 s used for the Cottesloe simulations was necessitated by computer memory constraints relating to the combination of the larger sea-surface areas relevant to the Rottnest environment, and at the finer frequency spacing for Fourier synthesis necessitated by the longer delay responses. This resulted in minor loss of fidelity in the reproduction of the swell part of the experimental surface-wave spectrum (Figure 5-57). Simulation parameters relating to the three channel ranges are summarised in Table 6-2. For the 120 m and 1100 m Rottnest simulations approximate spatial coherence of surface interactions was included as described in Section 5.3.2.

The completely synthetic whole channel responses and derived spreading and delay/Doppler power functions for 120 m, 1100 m and 8727 m ranges prior to convolution with a probe signal are presented respectively in Appendices C.4, C.5, and C.6. These appendices also contain response histories and derived spreading and delay/Doppler power functions for the grazing-angle dependent bistatic responses upon which the whole channel responses are built.

Table 6-2: Parameters for Rottnest channel simulations

Range	120 m & 137 m	1100 m	8727 m
Bellhop flat-surface amplitude-delay model parameters			
calculation frequency	12 kHz		
ray description	geometric rays, 1601 rays, with launch angles from -80° to +80°		
source depth	20 m		
receiver depth	52 m		
environment depth	53 m		
mean seawater sound speed	1525 m/s		
seawater density	1024 kg/m^3		
seawater sound absorption	0.00021 dB/wavelength		
surface and bottom profiles	flat		
bottom description	sand, single semi-infinite fluid layer		
Assumed bottom compressional absorption for silt (Jensen et al. 2011)	1 dB/wavelength		
Assumed bottom density	1941 kg/m^3		
Assumed bottom compressional sound speed	1749 m/s		

Range	120 m & 137 m	1100 m	8727 m
sound speed profile corresponding to experimental range transmit position	Rottnest CTD cast 1 (Figure B-20)	Rottnest CTD cast 3 (Figure B-22)	Rottnest CTD cast 5 (Figure B-24)
number of base eigenpaths	8	14	20
KA response bistatic geometry parameters			
rationalised bistatic calculation angles	31°,53° (120m)	3.8°, 7.2°, 9.2°, 13.5°, 17.7°	1.0°, 1.3°, 1.9°, 2.6°, 3.4°
rationalised bistatic source (Tx) and receiver (Rx) calculation depths	(120 m) 31°, Tx 20m, Rx 53m 53°, Tx, 79.5m, Rx 79.5m	3.8°, Tx 20m, Rx 53m 7.2°, Tx 86m, Rx 53m 9.2°, Tx 73m, Rx 106m 13.5°, Tx 132.5m, Rx 132.5m 17.7°, Tx 192m, Rx 159m	1.0°, Tx 80m, Rx 59m 1.3°, Tx 71m, Rx 103m 1.9°, Tx 127.5m, Rx 127.5m 2.6°, Tx 178.5m, Rx 178.5m 3.4°, Tx 229.5m, Rx 229.5m
surface patch dimensions	(120 m) 31°, 153m L x 117m W 53°, 160m L x 139m W	3.8°, 931m L x 125m W 7.2°, 733m L x 125m W 9.2°, 633m L x 125m W 13.5°, 483m L x 125m W 17.7°, 385m L x 124m W	1.0°, 4264m L x 93m W 1.3°, 3575m L x 91m W 1.9°, 2574m L x 90m W 2.6°, 1830m L x 86m W 3.4°, 1387m L x 83m W
method of including spatial coherence between starting instances of bistatic responses on a ray-path and across ray-paths	bounce point space-time approximation	bounce point space-time approximation	random
Surface response simulation parameters			
surface simulation duration	30 s	30 s	30 s
number of channel realisations	3000	1500	1500
channel calculation interval	10 ms	20 ms	20 ms
sea dx, dy	24 cm	48 cm	95 cm
surface response band width	8 kHz – 16 kHz, (zero padding 0 – 48 kHz to achieve 96 kS/s delay resolution)		
Fourier synthesis increment, dF, and resultant bistatic delay window (1/ dF)	25 Hz (40ms)	50 Hz (20ms)	100 Hz (10 ms)
surface wave spectral density	Figure 5-57		
sea significant wave height (H_s)	0.3 m		
surface angular frequency increment	$2\pi/T$, T = 30 s		
sea peak period (T_p)	2 seconds		
sea angular frequency	$1 - 2\pi$ rad/s		
swell significant wave height (H_s)	1.9 m		
swell peak period (T_p)	12.5 seconds		
swell dx, dy	= 5 times sea dx, dy, $dx = dy$		
swell maximum angular frequency	1 rad/s		
TxRx heading	52°	13°	17°
sea heading	70°	66°	70°
swell heading	70°	66°	70°
WAFO swell and sea spreading model	Poisson		
transmitter vertical motion history	"dep01_pitch_roll_heaveCG_heaveDL.txt"	"dep04_pitch_roll_heaveCG_heaveDL.txt"	"dep08_pitch_roll_heaveCG_heaveDL.txt"
channel computation time (per 60s)	16 hours	16 hours	4.5 hours
Channel signal convolution computation time (per 60s of signal)	100 minutes	75 minutes	50 minutes

Example simulated sea and swell realisations for the Rottnest environment that give a sense of the number of swell wavelengths in the calculation patch are illustrated on Figure 6-20. The transmission direction is from the front-left edge towards the rear right-hand edge. These images illustrate why approximate inclusion of spatial coherence between rough-surface interactions is important at 120 m range (top right) but unimportant at ~8 km range (bottom right).

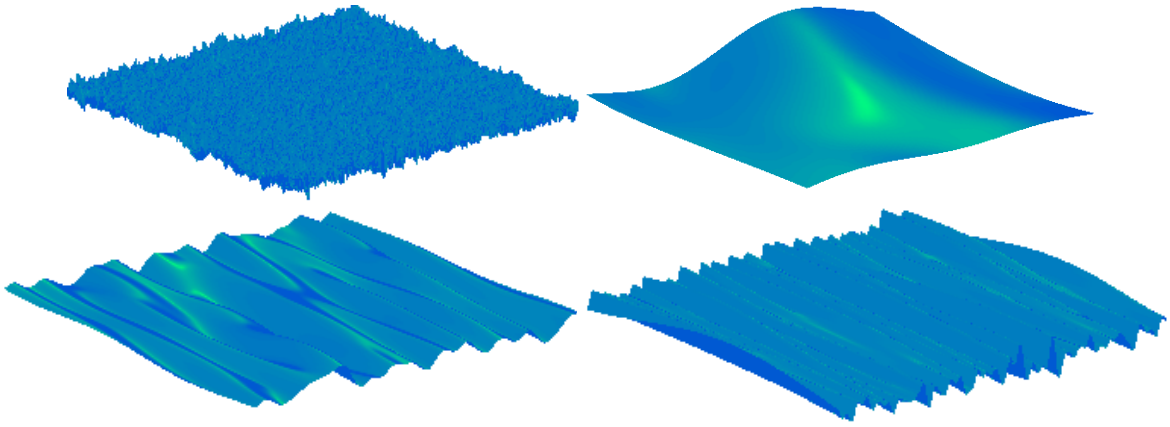

Figure 6-20: Surface patch realisations of 1100 m range sea (top left) 120 m swell (top right), 1100 m swell (bottom left), 7827 m swell (bottom right)

6.3.1 53 m deep 137 m range medium sea-state

The 120 m channel response was modelled using a horizontal discretisation interval $2.5\lambda_{min}$ = 24 cm. The channel response was calculated at shorter 10 ms intervals to avoid spatial-frequency aliasing of the channel Doppler on the relatively steep short-range propagation paths. Other simulation parameters and surface wave characteristics are detailed in Table 6-2. The rough channel response was calculated around 8 flat surface eigenpaths, sufficient to reproduce the banded delay structure experimentally observed by sweep probe signals repeated at 200 ms interval (Figure 4-50-top).

The simulation channel probe response (right of Figure 6-21) shows some striations (circled) that represent responses from the first two single-surface-bounce paths, aliased in advance of the main surface response. The absence of comparable aliased striations in the measured response indicates that these late arrivals from the single-surface-bounce rough responses (clearly evident in the synthetic channel response to the simulated surface (Figure C-20)) were not evident experimentally. The causes of this are further discussed in Section 6.4. The experimental direct and bottom-bounce paths diverge due to transmitter drift (closing) that is not reproduced in the simulation.

This channel typifies an 'over-spread' channel (refer Section 2.6.2) that cannot be fully characterised in Doppler and delay spreading using a repeated probe, but can be successfully explored by simulation. Both the experimental and simulation channel probe spreading functions (Figure 6-22) illustrate considerable speckle originating from correlation processing noise and time-aliasing of responses beyond the 21 ms probe window.

The comparative delay power profiles (Figure 6-23) illustrate a close match in average response power, but with misalignment in the first arrival band due to the sloping sea bottom that was not included in the simulation.

The synthetic Doppler power spectrum (Figure 6-25, cropped from Figure C-22) shows that the simulation surface patch dimensions have slightly truncated the single-bounce Doppler spectrum (green). Due to the strong response at relatively large Doppler in this short channel, the Doppler spectrum measureable by channel probing for single surface-bounce paths, including aliasing (Figure 6-24) is similar to the synthetic spectrum.

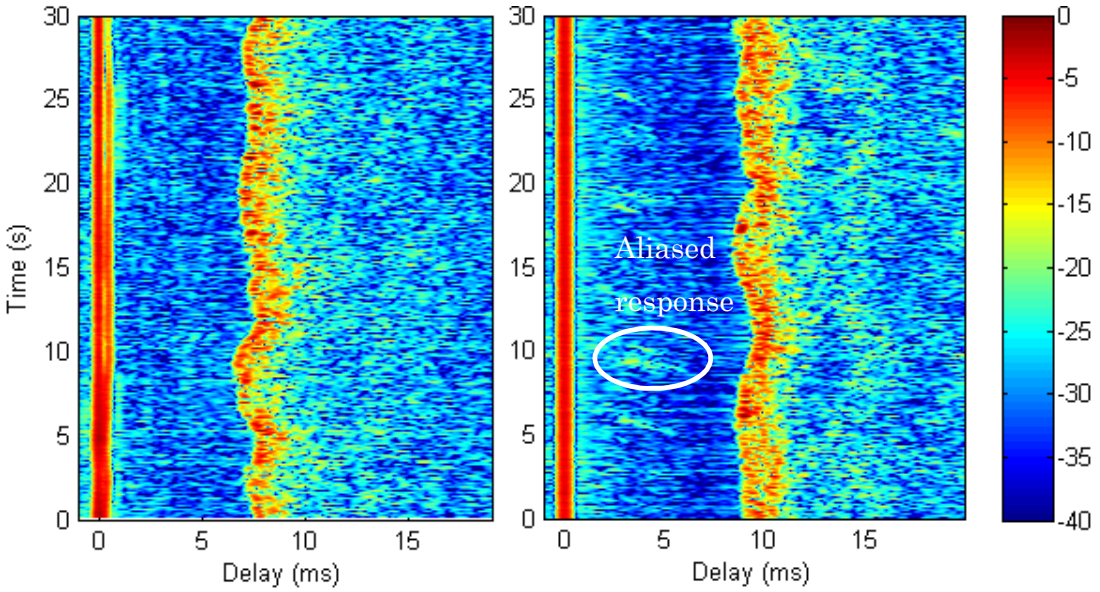

Figure 6-21: Measured (left) and simulated (right) response history $|\hat{h}(\tau,t)|^2$(dB) –21 ms PRBS probe in 137 m range 53 m depth, surface H_s = 2 m

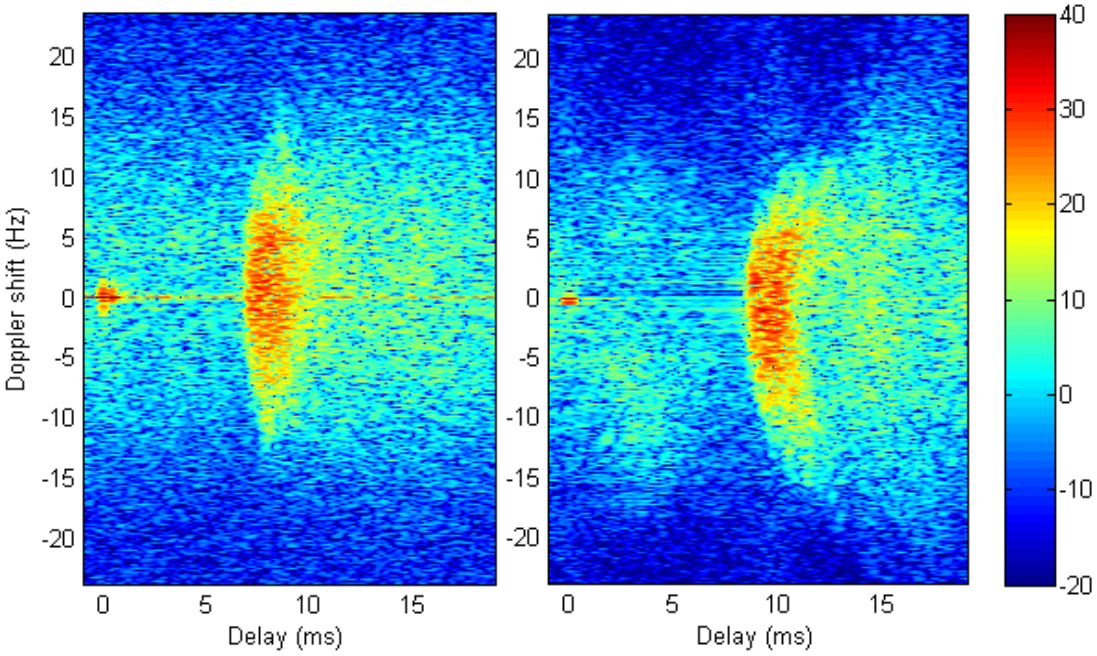

Figure 6-22: Measured (left) and simulated (right) spreading function $\left|\hat{S}(\nu,\tau)\right|^2$ (dB) rel. to 12 kHz – 21 ms PRBS probe at 137 m range 53 m depth, surface $H_s = 2$ m

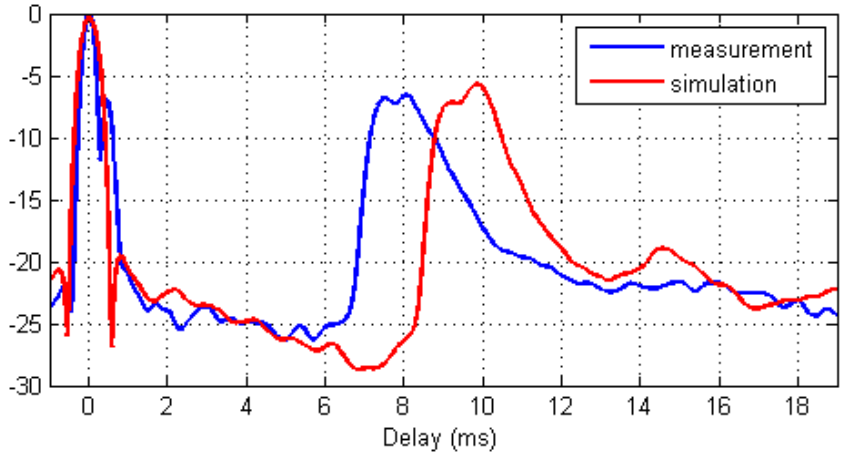

Figure 6-23: Measured and simulated delay power profile $\left|\hat{P}(\tau)\right|$ (dB) – 21 ms PRBS probe at 137 m range 53 m depth, surface $H_s = 2$ m

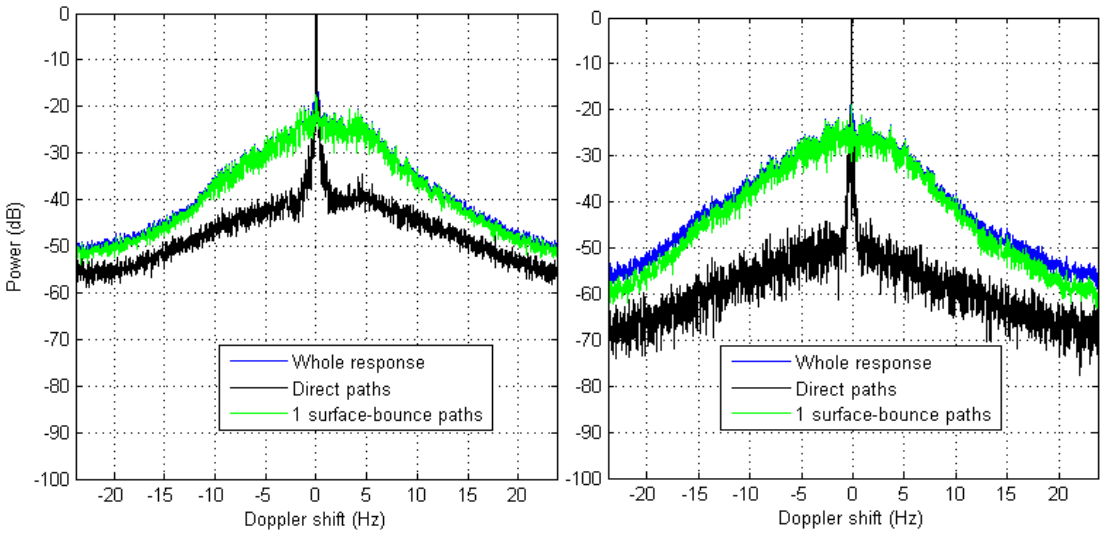

Figure 6-24: Measured (left) and simulated (right) Doppler power spectrum $|\hat{P}(\nu)|$ (dB) relative to 12 kHz – 21 ms PRBS probe at 137 m range 53 m depth, surface $H_s = 2$ m

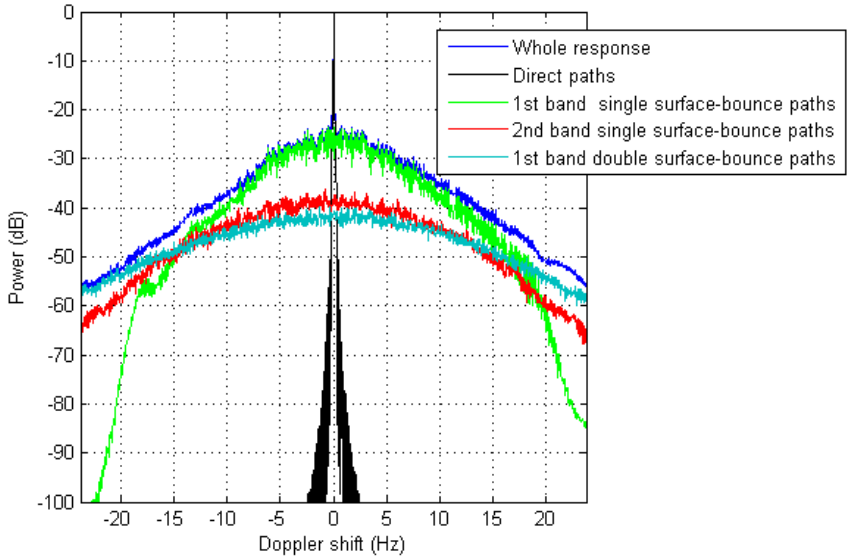

Figure 6-25: Synthetic Doppler power spectrum, fixed Tx and Rx, $|P(\nu)|$ (dB) relative to 12 kHz – 10 ms channel interval at 1000 m range 53 m depth, surface $H_s = 2$ m

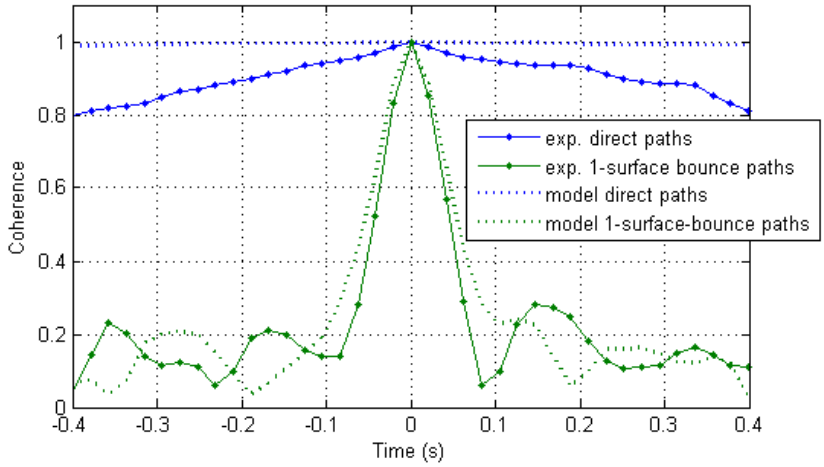

Figure 6-26: Measured and simulated channel coherence in delay bands $\hat{C}(\Delta t, \tau_1, \tau_2)$ – 21 ms PRBS probe at 137 m range 53 m depth, surface $H_s = 2$ m

6.3.2 53 m deep 1100 m range medium sea-state

The 1100 m channel response was modelled using a horizontal discretisation interval $5\lambda_{min}$ = 48 cm, and 20 ms channel update interval. Other simulation parameters and surface wave characteristics are summarised in Table 6-2. The rough channel response was calculated around 14 flat surface eigenpaths, sufficient to reproduce the banded delay structure experimentally observed by sweep probe signals repeated at 100 ms interval (Figure 4-50 lower left).

The simulation probe response shows similar delay and temporal patterns to the measurement (Figure 6-27), but with the response power of surface-reflected paths up to 5 dB higher than measurement (Figure 6-28, Figure 6-29). There is some misalignment of the gross delay structure due to the unmodelled seabed slope.

Comparison of the synthetic Doppler power spectrum prior to probing (Figure 6-31, cropped from Figure C-29) and the simulated probed Doppler spectrum (right image of Figure 6-30) indicates that only the central ±7-8 Hz portion of the response is not modified by the probing procedure, and therefore reliably indicate the surface Doppler. The remainder can be attributed to the processing noise associated with probing as discussed in Section 6.2.1. By implication, the measured Doppler response (LHS Figure 6-30) beyond ±7-8 Hz is increasingly indicative of the probe processing noise. It may be concluded that at larger Doppler the synthetic response provides a more reliable indication of coherent Doppler due to the absence of spurious response associated with probe processing.

Results show similar coherence functions for the simulation and experimental probes for the first three bands of surface interacting paths (Figure 6-32).

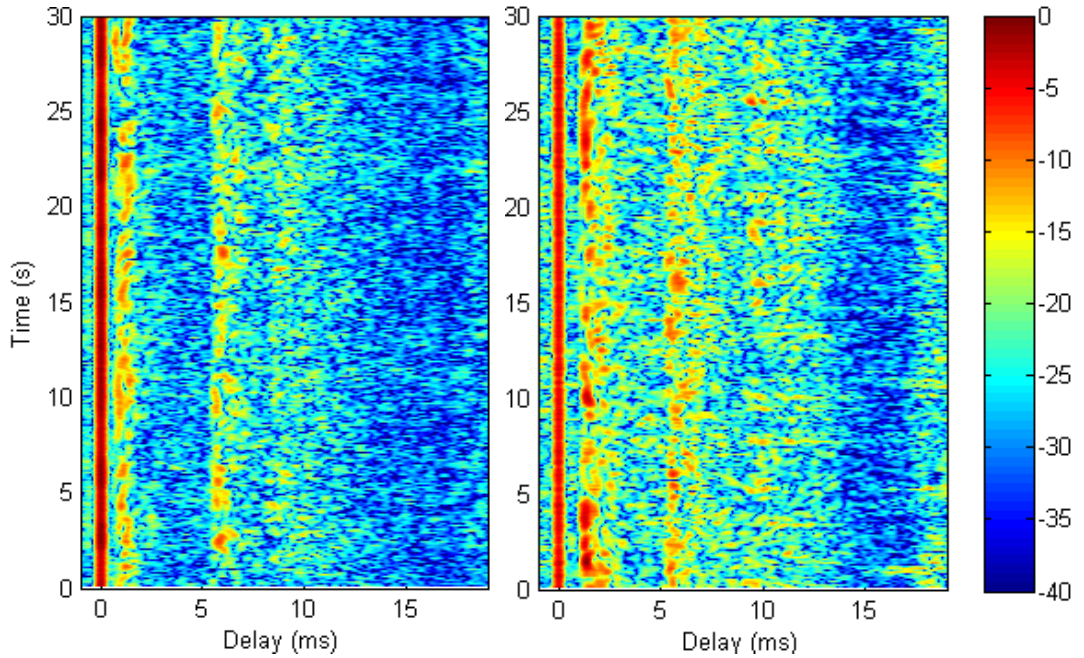

Figure 6-27: Measured (left) and simulated (right) response history $|\hat{h}(\tau,t)|^2$(dB) –21 ms PRBS probe in 1100 m range 53 m depth, surface $H_s = 2$ m

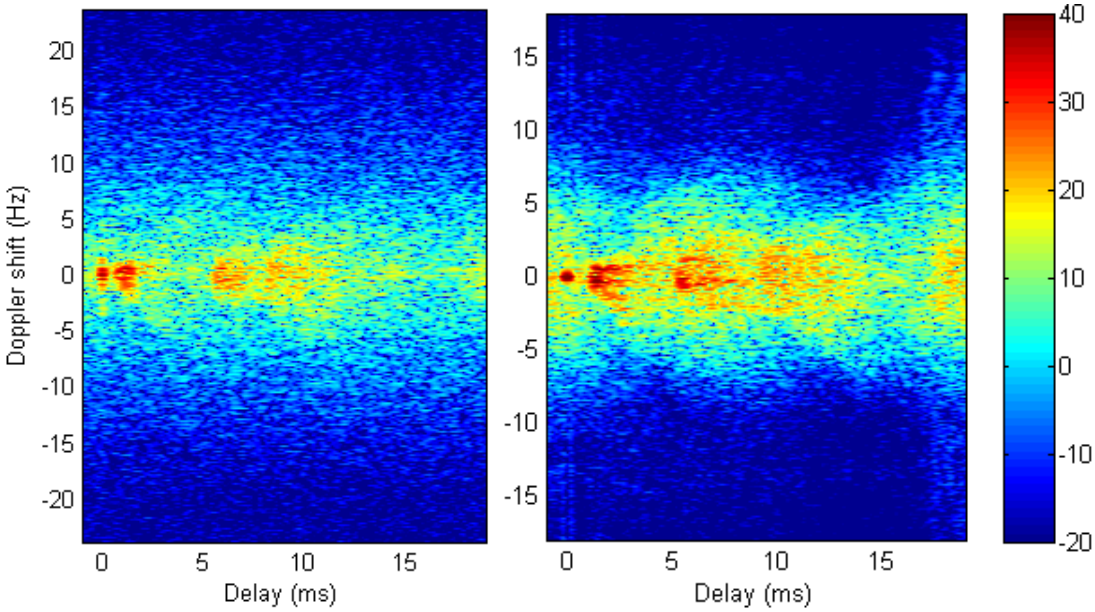

Figure 6-28: Measured (left) and simulated (right) spreading function $\left|\hat{S}(\nu,\tau)\right|^2$(dB) rel. to 12 kHz – 21 ms PRBS probe at 1100 m range 53 m depth, surface $H_s = 2$ m

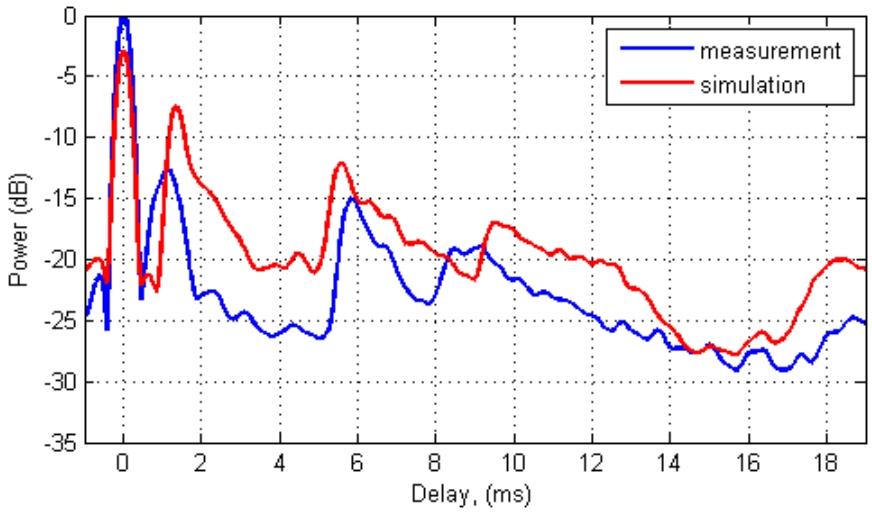

Figure 6-29: Measured and simulated delay power profile $|\hat{P}(\tau)|$ (dB) – 21 ms PRBS probe at 1100 m range 53 m depth, surface $H_s = 2$ m

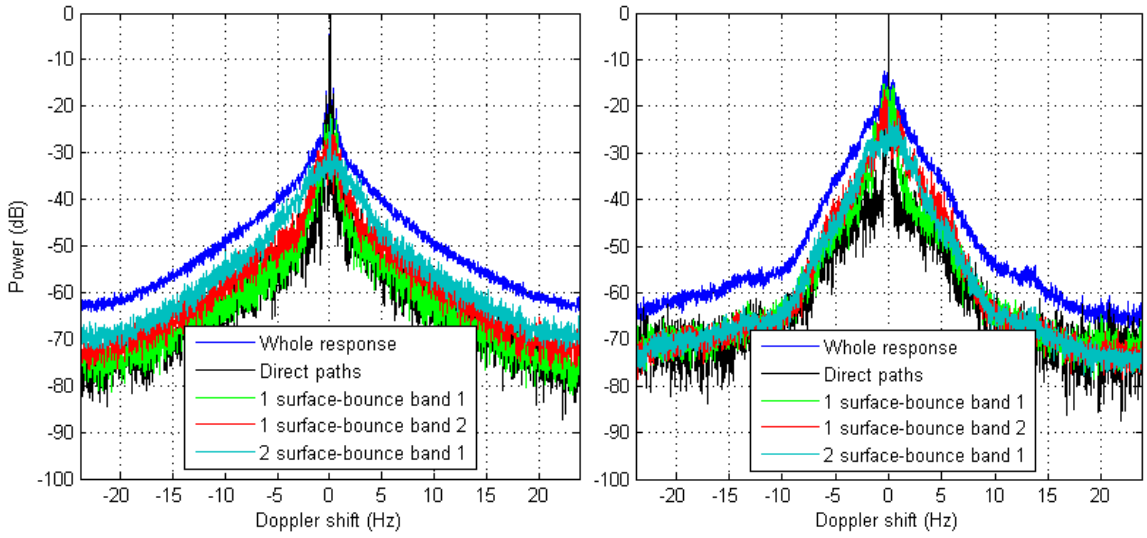

Figure 6-30: Measured (left) and simulated (right) Doppler power spectrum $|\hat{P}(\nu)|$ (dB) rel. to 12 kHz –21 ms PRBS probe at 1100 m range 53 m depth, surface $H_s = 2$ m

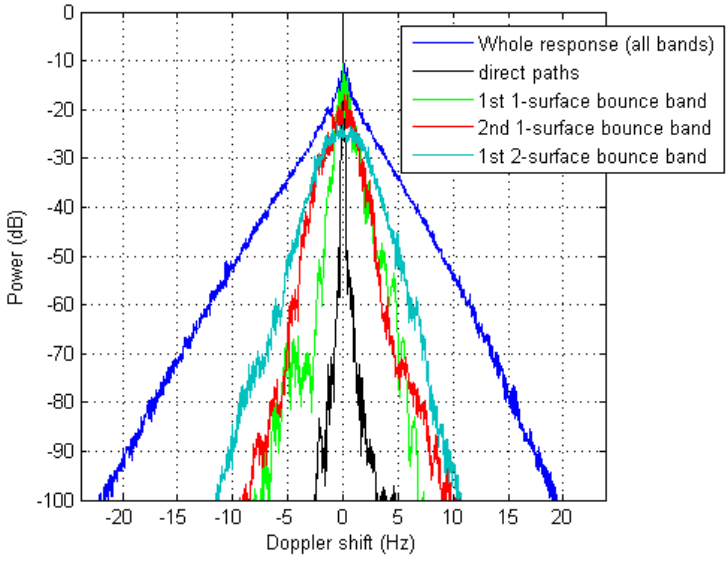

Figure 6-31: Synthetic Doppler power spectrum, fixed Tx and Rx, $|P(\nu)|$ (dB) relative to 12 kHz – 20 ms channel interval at 1100 m range 53 m depth, surface $H_s = 0.5$ m

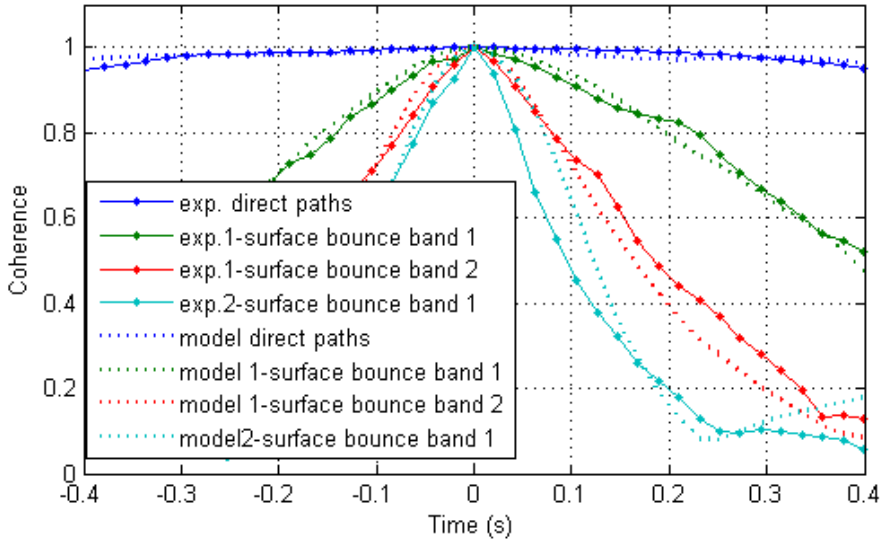

Figure 6-32: Measured and simulated channel coherence in delay bands $\hat{C}(\Delta t, \tau_1, \tau_2)$ – 21 ms PRBS probe at 1100 m range 53 m depth, surface $H_s = 2$ m

6.3.3 53 m deep 7827 m range medium sea-state

The 7827 m channel response was modelled using a horizontal discretisation interval of $10\lambda_{min} = 95$ cm, with a 20 ms channel calculation interval. The simulation methodology at this range is a computationally intensive method to generate a relatively slow-changing channel response. Nevertheless, the result shows that even at long range with a high degree of surface shadowing the simulation produces credible temporal response patterns (Figure 6-33) and small Doppler at all delays (Figure 6-34).

The delay power profile (Figure 6-35) shows close measurement/simulation agreement of the first band consisting of single surface-bounce path variants, 5 dB simulation over-prediction of double-bounce paths and similar power of triple and quadruple surface-bounce paths.

The effects of a relatively low received signal-to-noise ratio compared to other transmission ranges (Figure B-11) is understood to have been partly responsible for the significantly higher noise floor in the experimental Doppler power spectrum (left of Figure 6-36) compared to the simulated probed Doppler response (right of Figure 6-36). However real fluctuations through the medium, and greater real micro-path diversity may also contribute significantly.

Comparison of the measured Doppler power spectrum with the synthetic profile (Figure 6-37) demonstrates that the simulated channel is unaffected by the side-lobes, as these features, at more than -70 dB relative magnitude are well below what was experimentally detectable.

The qualitative discrepancy between the relatively smooth and higher simulated probe coherence functions compared to the experimental curves (Figure 6-38) suggests that at this longer range there may be other time-varying channel response influences in the experimental response. This could include medium inhomogeneities, more complex bottom scattering, and the effect of additive snapping shrimp noise at the experimental receiver.

Snapping shrimp noise was audibly confirmed from receive signal playback and is evident in the spectrogram summary of the receive signal at this range (Figure B-11). Two prominent shrimp impulses are captured in the channel response (horizontal lines towards bottom of RHS of Figure 6-36)

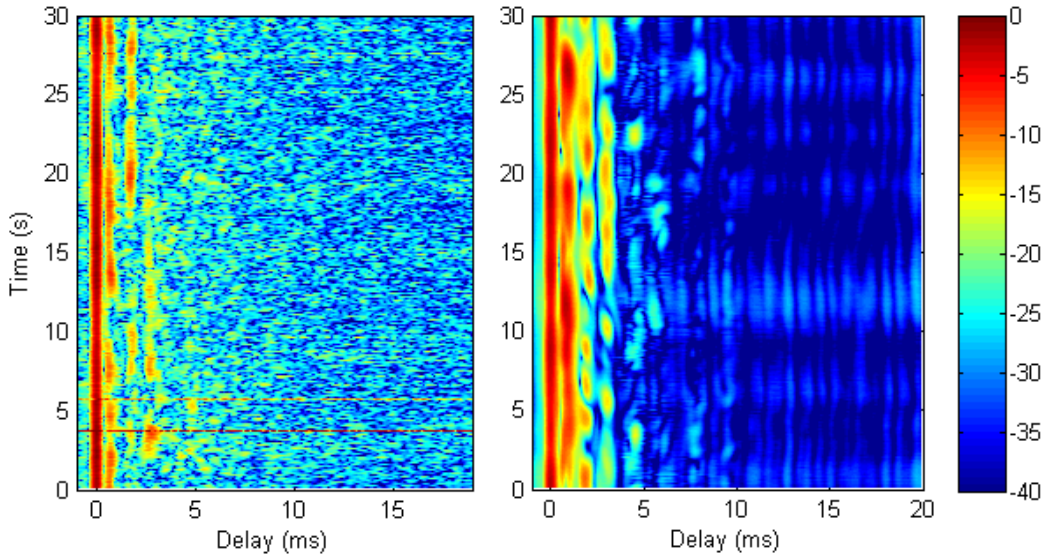

Figure 6-33: Measured (left) and simulated (right) response history $|\hat{h}(\tau,t)|^2$(dB) –21 ms PRBS probe in 7827 m range 53 m depth, surface $H_s = 2$ m

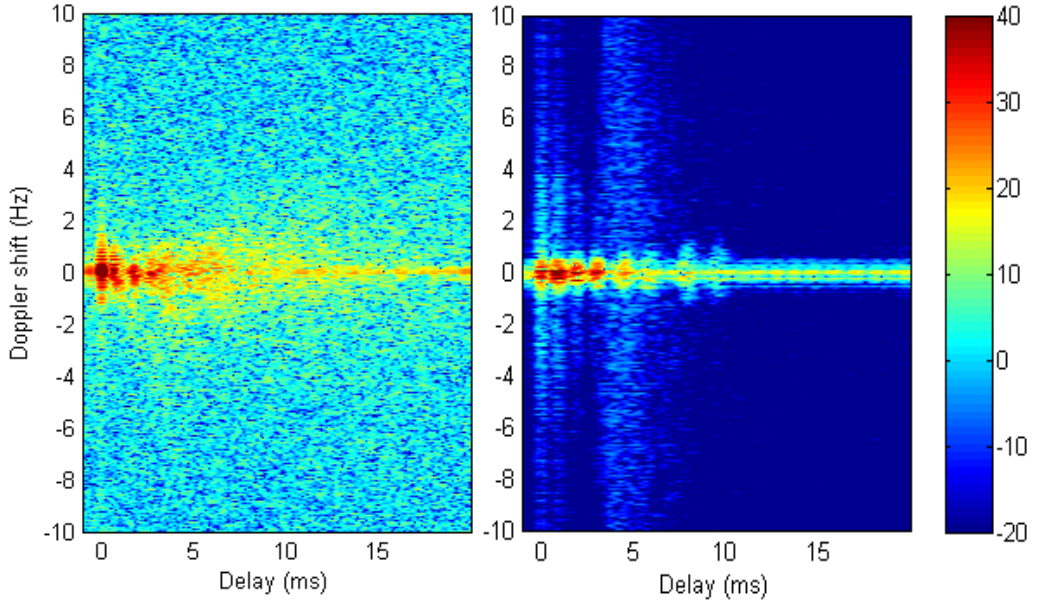

Figure 6-34: Measured (left) and simulated (right) spreading function $\left|\hat{S}(\nu,\tau)\right|^2$(dB) relative to 12 kHz – 21 ms PRBS probe at 7827 m range 53 m depth, surface $H_s = 2$ m

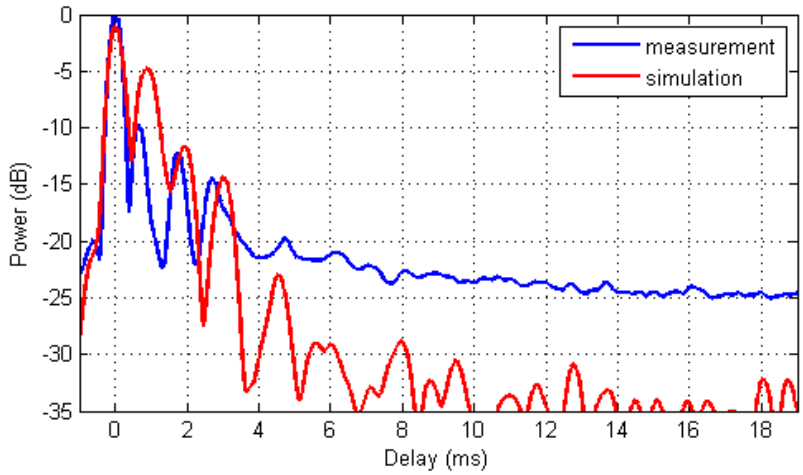

Figure 6-35: Measured and simulated delay power profile $|\hat{P}(\tau)|$ (dB) – 21 ms PRBS probe at 7827 m range 53 m depth, surface $H_s = 2$ m

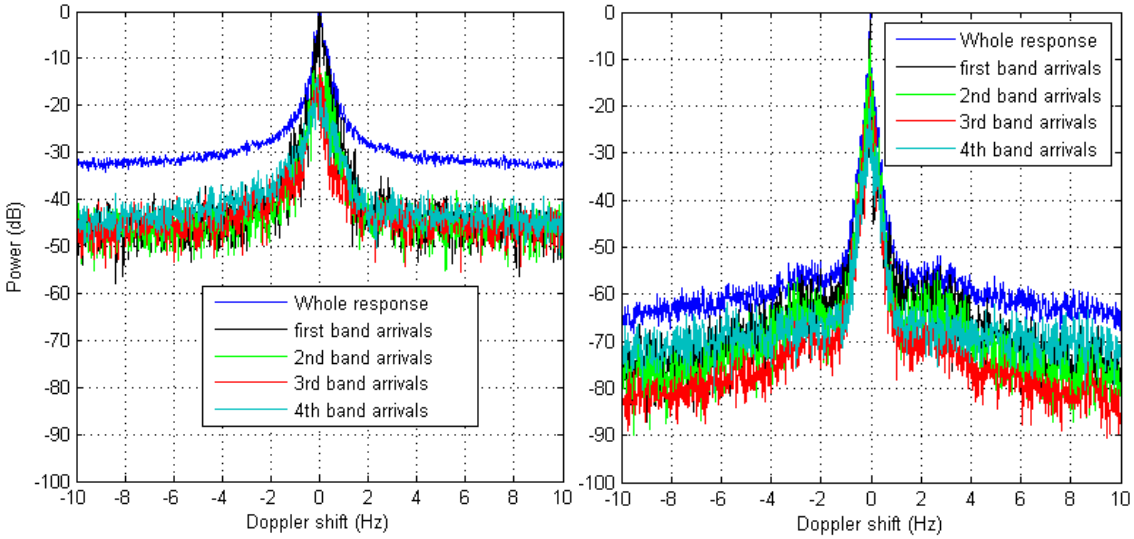

Figure 6-36: Measured (left) and simulated (right) Doppler power spectrum $|\hat{P}(\nu)|$ (dB) relative to 12 kHz – 21 ms PRBS probe at 7827 m range 53 m depth, surface $H_s = 2$ m

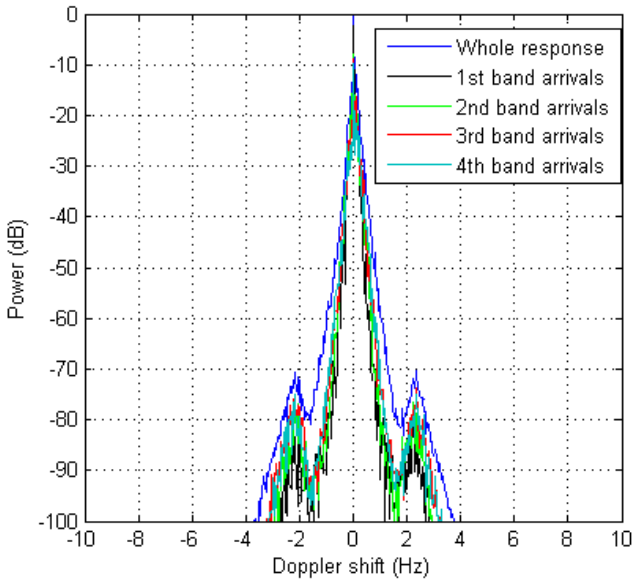

Figure 6-37: Synthetic Doppler power spectrum, fixed Tx and Rx, $|P(\nu)|$ (dB) relative to 12 kHz – 20 ms channel interval at 8727 m range 53 m depth, surface $H_s = 2$ m

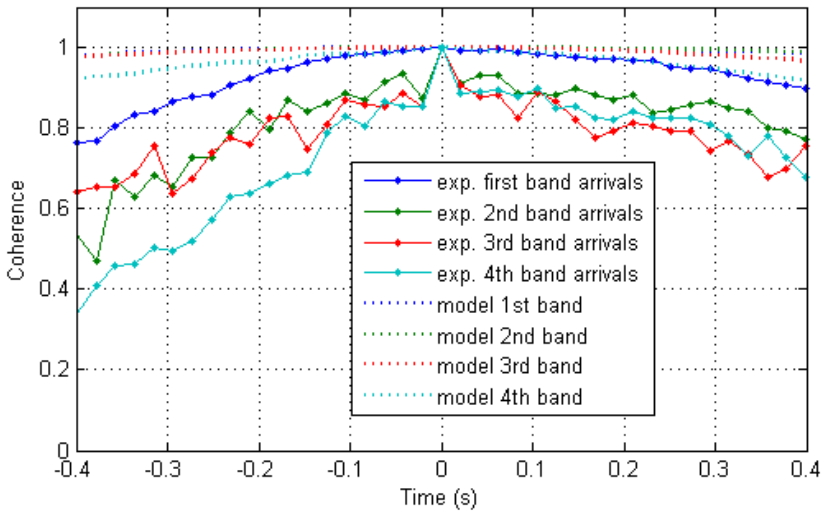

Figure 6-38: Measured and simulated channel coherence in delay bands $\hat{C}(\Delta t, \tau_1, \tau_2)$ – 21 ms PRBS probe at 7827 m range 53 m depth, surface $H_s = 2$ m

6.4 Rottnest site comparisons – LFM sweep probe

The channel response to 16 ms LFM sweeps repeated at relatively long intervals enables inspection of a greater span of the delay response, but with the loss of a useful spreading function.

The experimental channel responses to repeated LFM sweeps that were presented earlier in Section 0 over 121 m, 1102 m and 8727 m ranges are reproduced below (Figure 6-39), followed by the simulated sweep probe responses for the same ranges (Figure 6-40).

The measured and simulated delay power profiles for both measurements and simulations are then presented overlaid on Figure 6-41.

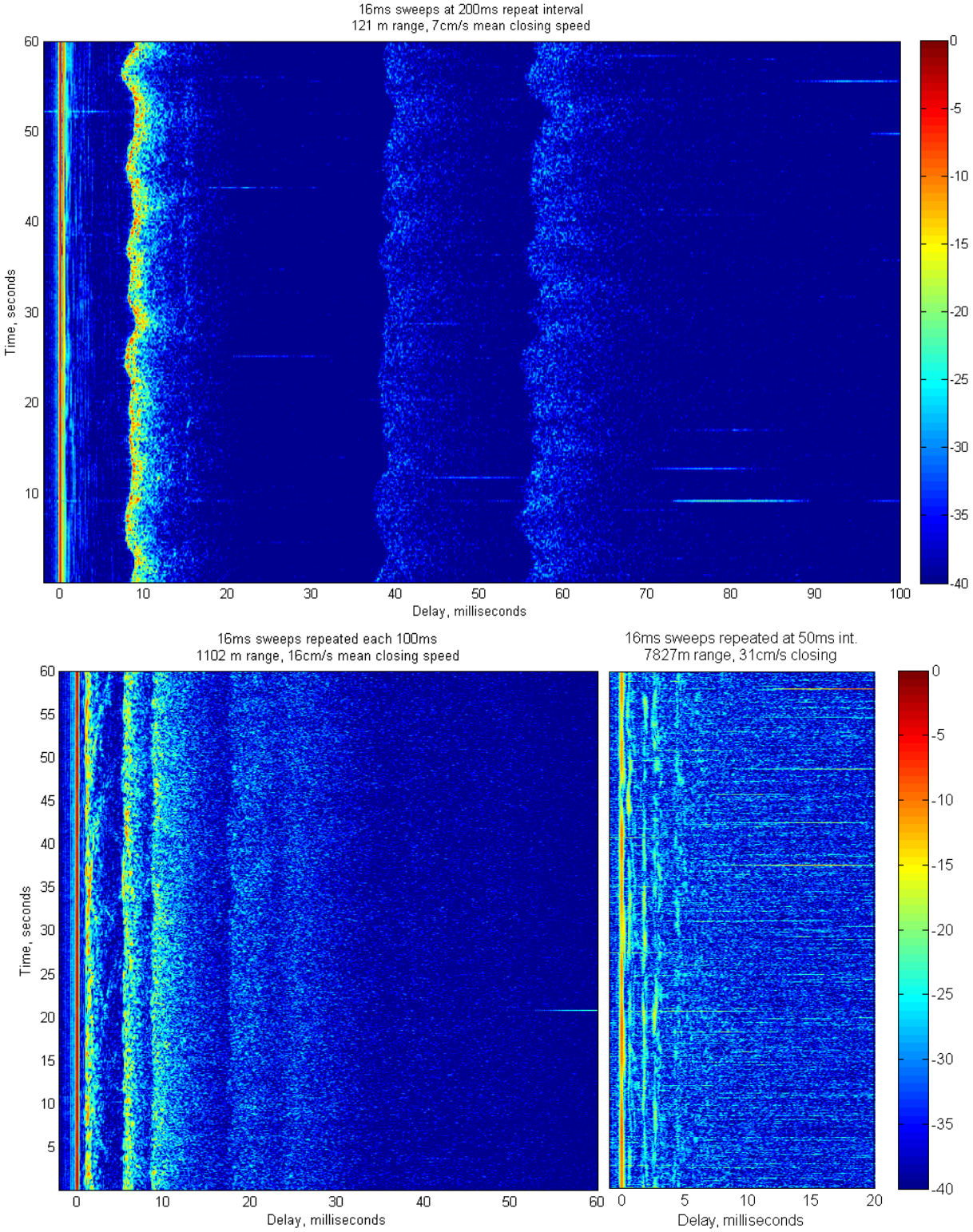

Figure 6-39: Measured response history, $\left|\hat{h}(t,\tau)\right|^2$, (dB) using 16 ms 8 – 16 kHz LFM sweep probe at 121 m range (top), 1102 m (lower left), and 7827 m (lower right)

(reproduced Figure 4-50)

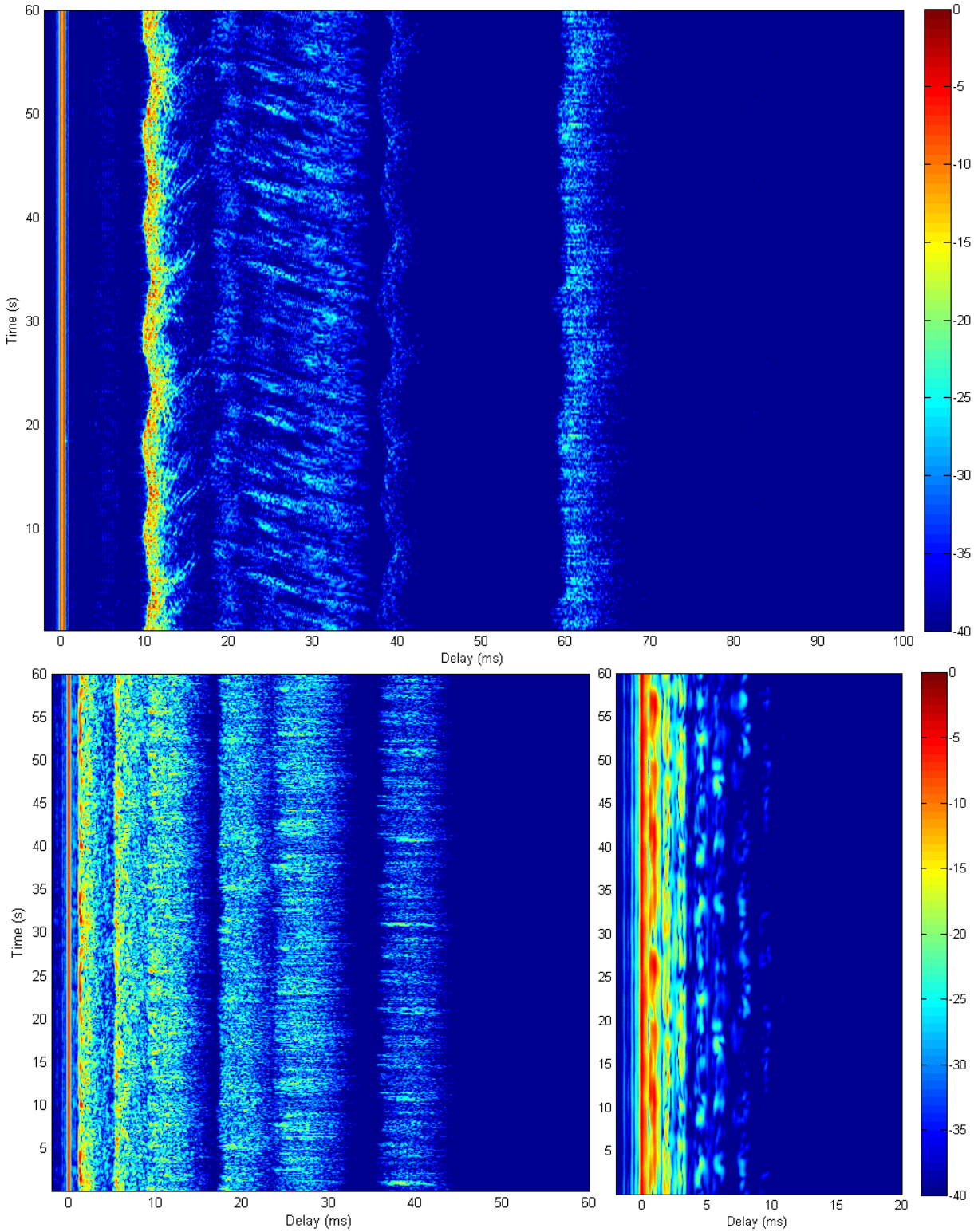

Figure 6-40: Simulated response history, $\left|\hat{h}(t,\tau)\right|^2$, (dB) using 16 ms 8 - 16 kHz LFM sweep probe at 120 m range (top), 1100 m (lower left), and 7827 m (lower right)

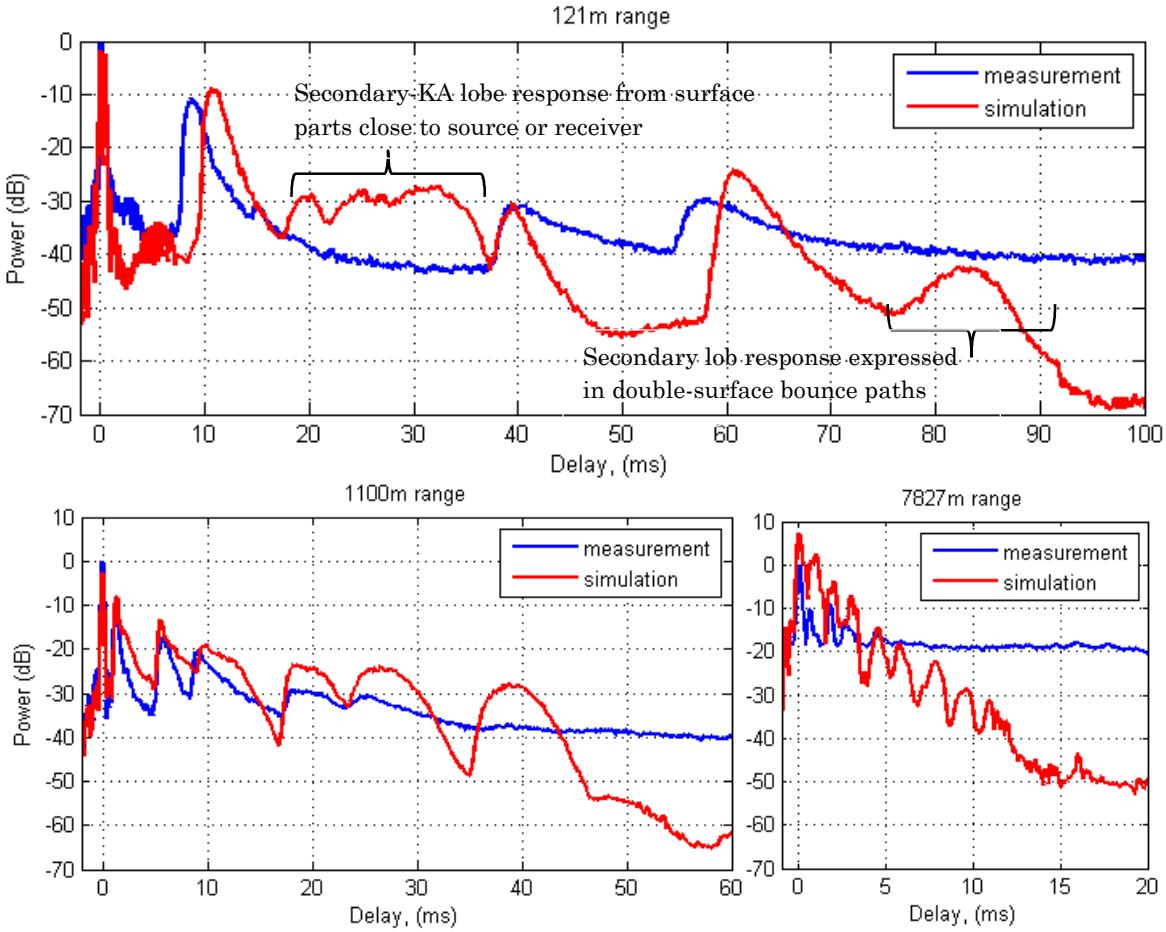

Figure 6-41: Measured and simulated delay power profiles, $\hat{P}(\tau)$ (dB) using 16 ms 8 – 16 kHz LFM sweep probe at 120 m range (top), 1100 m (lower left), and 7827 m (lower right)

At 120 m range the simulation response history (Figure 6-40 top) features striations at delays ranging from 18 - 38 ms that are not evident in the measurements. This delay-range corresponds to single surface-bounce responses off surface elements that are close to the source or receiver, and where the difference between the incident and receiver grazing angle is greatest.

The cause of the discrepancy was identified as the secondary radiation lobes of the discrete tangent-plane approximated element response, which is valid for a discrete tangent-plane in isolation, but not valid for the real surface, for which the KA approximation includes errors at the discrete angular surface-element boundaries.

Figure 6-42 illustrates the two-dimensional KA radiation magnitude pattern for a horizontal surface element with 100° incident grazing angle and 25° receive grazing angle. This geometry typifies, for the Rottnest 120 m surface simulation, the source/receiver surface grazing angles for parts of the surface near the source.

This discrepancy appears in short-range simulations only, where the angular span of incident/transmitted grazing angles is sufficient to engage the secondary radiation lobes.

This problem could be avoided by reducing the surface discretisation interval to broaden the primary radiation lobe and ensure the secondary lobes are beyond the relevant grazing angle range. Alternatively, the problem might be avoided by designing a surface response function for elements that minimises the amplitude of the lobed radiation pattern. This would need to be explored across a wide range of incident grazing angles.

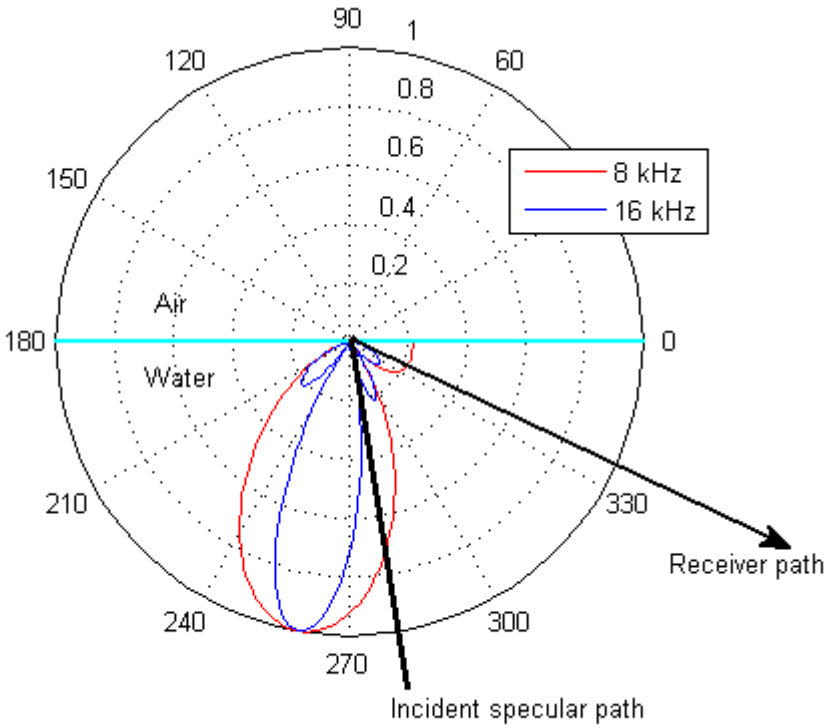

Figure 6-42: Radiation magnitude pattern for 24 cm discretised two-dimensional KA surface element -100° source grazing incidence with 25° receiver grazing path shown in angular proximity to secondary radiation lobes – linear radial pressure amplitude scale

At 1100 m range the striation patterns at 2 - 5 ms delay in the measurements (Figure 6-39 lower left image) are not clearly evident in the simulation result. This may indicate that the assumed high-frequency simulated surface waves produced too much diffusion of the single-surface interacting paths. This could also result from the inclusion of all element responses, shadowed or otherwise, which tends to obscure striation patterns in the KA response (refer Section 5.4.2).

6.5 Summary

A range of metrics have been used to present comparisons between the experimental and simulated channels as recommended by Otnes, Jenserud, and Van Walree (2013), highlighting both realistic aspects and discrepancies in the simulated channel responses.

The range of experimental/simulation comparisons clearly demonstrate the capability of the simulation to produce realistic channel Doppler and delay spreading characteristics.

The delay power profiles in some instances show remarkable agreement between model and experiment, and in other instances highlight that the modelling of the boundary interactions is approximate at best.

For some channels it is apparent from the spreading function comparisons that the geometric micro-path diversity encompassed by the bistatic decomposition of rough-boundary eigenpaths (described in Section 5.4.9) is incomplete, however the spreading functions also suggest that this path diversity characterisation is adequate to model the significant part (i.e. power) of the experimental response. The comparisons pose interesting questions about additional micro-path diversity that may arise out of actual roughness of the sea bottom.

The unexpected but explicable evidence of artificial secondary KA element lobe responses identified and discussed in Section 6.4 underline the benefit of experimental channel probing using alternative probe symbols. The comparisons based on the short 21 ms PRBS symbol alone did not enable this discrepancy to be identified, which was only possible with the benefit of the extended delay response of experimental probing by LFM sweeps. In retrospect the influence of the KA secondary lobe was evident in developmental bistatic simulations, however the whole channel comparisons provided the clarity necessary to highlight this issue.

7 CONCLUSIONS

7.1 Whole (multi-path) channel simulation

A wide-band phase-coherent multi-path underwater acoustic channel simulation has been developed based on an approximate quantitative model of the acoustic wave response to a time-varying three-dimensional rough surface. It has been demonstrated over transmission ranges from 100 m to 8 km by experimental channel probing and synthetic replication of the channel probing through the simulated channel, that the simulation is capable of reproducing fine time-scale Doppler and delay distortions consistent with those generated in real shallow water ocean channels.

Realistic phase-coherence between conceptual micro-paths within a rough-surface path response is achieved by the approximate KA acoustic wave response built around the flat surface eigenpath responses. Spatial correlation between surface interactions associated with different nominal eigenpath reflection points is approximately included by relating the spatial separation of nominal reflection points to an equivalent time lag/advance in the time-circular rough-path response arrays (Section 5.3.2).

7.2 Kirchhoff approximation to rough surface response

The bistatic rough surface response has been calculated by a discrete tangent-plane implementation of the Kirchhoff Approximation (KA). An integral equation (IE) boundary element model has been used to calculate a reliable reference response for the simplified case of a two-dimensional time-varying rough surface. The fidelity of the Doppler and delay response calculated by the KA method for a range of simulation parameters has been explored (Sections 5.4.2, 5.4.3).

7.2.1 Response to shadowed surfaces

The relative merits of attempting to exclude shadowed parts of the rough surface in the time-varying simulation of the bistatic response are discussed in Section 5.7.

It is concluded that the positive lag-bias in the KA bistatic response delay power profile, and relatively minor magnitude errors caused by inclusion of responses from all shadowed elements in the KA implementation are preferable to the

elevated Doppler response noise, and significant under-prediction of average response magnitude that result if shadowed element responses are excluded. On this basis the inclusion of all elements is recommended for the demonstrated tangent-plane implementation of KA for both highly shadowed and unshadowed bistatic rough surface interactions.

7.2.2 Horizontal surface discretisation interval

In Section 5.4.3 the effect of surface discretisation interval on the fidelity of the KA model Doppler response was explored with further discussion in Section 5.7.2.

It is concluded that the qualitative appearance of "shoulders" in the KA Doppler power spectrum is indicative of alteration of the surface by the surface discretisation process, which is acceptable so long as the Doppler power associated with discretisation remains insignificant. The surface discretisation interval may be selected to ensure this artificial Doppler contribution is acceptably low.

At 100m range, a horizontal surface discretisation of $1.25\lambda_{\min}$, (or 11.5 cm at 16 kHz) was justified by demonstrating that the KA model Doppler power spectrum was within the comparable IE envelope over 60 dB dynamic range for both highly shadowed and unshadowed surfaces. At 500 m range a discretisation of $2.5\lambda_{\min}$ (or 23 cm at 16 kHz) was similarly justified.

For longer ranges up to 10 km, the use of larger 48 cm ($20\lambda_{\min}$,) and 95 cm ($40\lambda_{\min}$,) intervals was justified without reference to a comparative IE model, on the basis that the characteristic shoulders on the Doppler power spectrum, that represent the effect of increasingly coarse discretisation, remain below the nominal threshold of -60 dB used for this study.

7.2.3 Limitations of KA implementation

At short range (or equivalently for high depth/length aspect ratio channels) there is a wide spread of surface grazing angles that contribute to the delay-response for the surface-only transmission path. For portions of surface close to the source or receiver, where the difference between the source and receiver grazing angle is greatest, the secondary-lobe response of the KA discrete tangent-plane element may cause the appearance in the simulation of a false delayed 'backscatter-like' response as discussed in Section 6.4.

The secondary radiation lobes could be avoided by reducing the surface discretisation interval to broaden the primary radiation lobe and ensure the secondary lobes are beyond the relevant grazing angle range. Alternatively, the problem might be avoided by designing a discrete-element window function that minimises the amplitude of the lobed radiation pattern across a wide range of element local grazing angles.

7.3 Computational capacity considerations

Generation of the multi-path channel response within computer memory and processing-time constraints requires optimisation of problem discretisation parameters in two time dimensions (t and τ) and the two horizontal spatial dimensions (dx and dy) as discussed in Section 5.8.

It is recommended that the bistatic surface response of single surface-interacting paths be modelled with unique bistatic geometry, with correct relative depth of source and receiver, to simulate as accurately as possible the coherent response of these paths. For paths with two or more surface interactions the response becomes of marginal or irrelevant significance to the coherent transmission, but still relevant to the incoherent channel response. For such paths it is recommended that simplified average bistatic geometries be used for all surface interactions along a path.

7.4 Channel probing

Comparison of the synthetically probed channel response with the simulated channel response prior to probing indicates that the probing methodology itself artificially elevates the Doppler power spectrum for larger Doppler, contributing to 'tails' in the Doppler power spectrum. The synthetic channel provides a method of exploring the channel Doppler response without incurring the artificial Doppler elevation that is inherent in the channel probing methodology, or alternatively, to improve understanding of the reliable Doppler bounds for coherent channel responses.

The simulation enables improved exploration of over-spread channels, as the channel response can be explored for a larger delay/Doppler window (subject to computational capacity) than the Doppler/delay response window limitations inherent in channel probing.

Channel simulation subsequent to channel probing experiments has illustrated that it would be advantageous to sample the spectrum of high-frequency surface waves during channel probing to improve the verification of simulated surface scattering. This could be achieved by near-surface meteorological monitoring, an electromagnetic method (e.g. radar), or a direct surface-height recording system. The surface wave spectra recording system would ideally detect surface wavelengths approaching the shortest acoustic wavelength.

7.5 Original contributions to channel modelling and simulation

The work of others on key channel simulation building blocks, including channel probing and dynamic channel characterisation techniques, surface simulation, Integral Equation boundary element method, ocean acoustic ray-tracing, Kirchhoff approximate rough surface scattering, Fourier synthesis and modern powerful signal acquisition equipment and personal computing, have allowed the candidate the opportunity to focus on channel simulation. By combining these methods a number of channel simulation and analysis capabilities have been demonstrated that have not previously been described in underwater acoustic channel simulation literature.

The complete channel simulation represents an approximate whole-wave multi-path channel response for an arbitrarily defined time-varying three-dimensional surface, that is capable of simulating realistic response coherence across the underlying eigenpaths of the multi-path response structure and the micro-path variations associated with the rough surface boundary. The simulation enables improved exploration of over-spread channels, as the channel response can be generated to simultaneously encompass the significant channel Doppler and delay spreads, which cannot be achieved by experimental channel probing or replay of experimentally measured channel responses.

By discretising the directional surface-wave spectrum by the circular time period during surface synthesis, the whole channel response is generated from a single time-circular three-dimensional surface realisation. This innovation allows a transmit signal of arbitrary length to be convolved (or 'run through') the synthetic channel without encountering artificial response discontinuities. This is important when using a simulator to evaluate Bit Error Rates (BER), which requires transmission of relatively long-duration coded signals.

The efficient computational re-use of a single time-circular three-dimensional surface realisation and derived time-circular bistatic responses, for the calculation of many horizontally displaced but spatially correlated bistatic rough surface interactions that are modelled for each underlying eigenpath, is an original innovation.

The time-varying analysis of the bistatic rough-surface response calculated by the discrete facetted implementation of the tangent-plane Kirchhoff Approximation (KA) is an original development in improving understanding of the dynamic delay, Doppler, and amplitude response effects of KA applied to the underwater acoustic rough-surface interaction.

By comparison of KA and IE dynamic bistatic responses it has been identified that a sufficiently coarse discretisation of the rough surface generates a readily identifiable additional Doppler response in excess of the true Doppler response of a realistic continuous surface, observable as distinct “shoulders” in the Doppler power spectrum. This approach allows the coarseness of the discretisation to be tailored depending on the dynamic range of Doppler fidelity required of the simulation.

This analysis of time-varying bistatic responses has also demonstrated that attempts to exclude the KA response of shadowed parts of a rough surface inherently generates an artificially high Doppler response due to the discrete-time switching of intermittently shadowed surface elements. The methodology has been used to demonstrate that the most reliable simulation of the Doppler spectrum and delay power profile are achieved for KA by including the response of all parts of the surface, irrespective of apparent local shadowing, at the expense of modest and explicable positive biasing of the channel delay response and signal power.

8 RECOMMENDATIONS FOR FURTHER WORK

There are significant opportunities for further exploration and development of the simulation from three perspectives - exploration of specific real-world channels; improvements in model fidelity; and implementation of hardware interconnectivity of the simulator.

8.1 Exploration of real-world channels

The exploration of synthetic channel responses for geometries and circumstances that have been identified as problematic for coherent communications is of immediate interest. The most challenging circumstance is understood to be instances where coherent direct paths are lost due to refraction but surface-path dispersion is high. For this condition coherent channel simulation enables the prospect of coherent recombination of surface-dispersed transmission paths to be evaluated or improved. The simulation may also be utilised to evaluate the relative merits of coherent versus incoherent signalling strategies, and gain insight into the relative performance of strategies.

Exploration of signalling strategies with and without the simple addition of ubiquitous sources of noise that are problematic to underwater communications is an important task. Such noise sources include snapping shrimp, rain and transient vessel/cavitation noise is important to the realism of simulation.

8.2 Improvements in simulation fidelity

There is scope to further explore the multi-path channel response for a range of experimental high-frequency surface-wave spectra above approximately 4 radians/s, the upper frequency recording limit of common wave height recording buoys (DWRB's). For coherent communications, the coincidence between wind bursts and loss of coherent communications has been experimentally noted (van Walree 2013), with entrained bubble screening of the surface proposed as the mechanism for signal interruption. The same observed phenomenon could be explored for an alternative hypothesis, that increased surface roughness may account for the loss of signal coherence, associated with localised high-frequency surface waves that may occur at frequencies above 4 radians/s.

It is of practical interest to verify the simulation for sound speed profiles that cause surface ducting in ray-path modelling. An experimental channel-probe result would assist with simulation evaluation for this case.

The inclusion of the dynamic effects of entrained surface-bubbles is of significant importance for the modelling of a wide range of experimentally encountered channels (Dol et al. 2013). This would be achieved by modification to the sound speed profile and frequency dependent absorption function that can be applied uniquely within the simulation structure to the rough-response around each ray eigenpath.

In the discrete tangent-plane KA implementation it would be desirable to explore favourable assumed scattered pressure distributions across the discrete surface elements that minimise secondary radiation lobes, thereby minimising the appearance of spurious modelled secondary-lobe responses for short/deep channels.

8.3 Implementation of simulator hardware interconnectivity

The simulation operates by pre-calculating a time-circular channel response, which is later convolved with a signal of arbitrary length. The channel response calculation need not be calculated in real-time, and once calculated can be re-used for any alternative signal.

The maximum value of the signal convolution part of the simulation is realised when the simulation can be substituted for the real ocean in a hardware-implemented transmit-receive arrangement. For bi-directional communication this requires better than real-time rate of convolution of a transmit signal with the synthetic channel. The current channel-signal convolution implemented in the high-level Matlab programming language on 4 cores of a personal computer is achieved 30 to 100 times slower than real-time, depending on the length and number of FIR filters (for each eigenpath) used to represent the channel. However there is scope numerically to trim the convolution process as currently implemented by discarding insignificant portions of the channel response, and to achieve much faster implementation of the essential computations using a low-level language, utilising more processing cores, and/or hardware acceleration through a suitable Digital Signal Processor (DSP) architecture. Minor

modification of the manner in which the circular responses are accessed would enable simulation of transmission on the reverse path.

The described channel synthesis method becomes more computationally intensive for higher signal frequencies as the overall problem size in general increases with the fourth power of the upper signal band-width frequency. The static channel 'freeze-frame' rate must be increased proportional to the upper frequency to prevent spatial/frequency aliasing, the three-dimensional surface storage needs to be increased as the square of the upper frequency to address smaller surface-waves that become significant at shorter acoustic wavelength, and the number of rough surface Fourier synthesis frequencies increases proportional to the upper bandwidth frequency (assuming constant proportional bandwidth).

An alternative avenue to achieve real-time simulation may be to use this computationally intensive coherent channel simulation to leverage development of a simpler semi-deterministic coherent channel simulation that can be extended to higher frequencies but with reduced computational load, whilst adequately simulating phase coherence in the micro-path and macro-path structure.

9 REFERENCES

Abrahamsson, L., and S. Ivansson. 2010. Ray modelling including Doppler effects for underwater acoustic communications. In *10th European Conference on Underwater Acoustics*. Instanbul, Turkey.

Alves, J., J. Potter, P. Guerrini, G. Zappa, and K. LePage. 2014. The LOON in 2014: Test bed description. In *Underwater Communications and Networking (UComms), 2014*.

Badiey, M., Y. Mu, J. A. Simmen, and S. E. Forsythe. 2000. "Signal variability in shallow-water sound channels." *IEEE Journal of Oceanic Engineering* no. 25 (4):492-500.

Badiey, M., A. Song, and K. B. Smith. 2012. "Coherent reflection from surface gravity water waves during reciprocal acoustic transmissions." *The Journal of the Acoustical Society of America* no. 132:EL290. doi: 10.1121/1.4747815.

Baggeroer, A. B. 1984. "Acoustic telemetry - An overview." *IEEE Journal of Oceanic Engineering* no. 9 (4):229-235. doi: 10.1109/JOE.1984.1145629.

Baggeroer, A. B. 2012. An Overview of Acoustic Communications from 2000 - 2012. In *Underwater Communications: Channel Modelling & Validation*. Sestri Levante, Italy.

Beaujean, P., and G. T. Strutt. 2005. "Measurement of the Doppler shift in forward-scattered waves caused by moderate sea surface motion in shallow waters." *Acoustics Research Letters Online* no. 6 (4):250-256. doi: DOI: 10.1121/1.1989747.

Benson, C. R., M. J. Ryan, and M. R. Frater. 2012. A tipping point for undersea networks. In *Military Communications and Information Systems Conference*. Canberra, Australia.

Bjerrum-Niese, C., L. Bjorno, M. A. Pinto, and B. Quellec. 1996. "A simulation tool for high data-rate acoustic communication in a shallow-water, time-varying channel." *IEEE Journal of Oceanic Engineering* no. 21 (2):143-149.

Burdic, W. S. 1984a. "Correlation and Correlation Functions." In *Underwater Acoustic System Analysis*, 204-231. Englewood Cliffs, NJ: Prentice-Hall.

Burdic, W. S. 1984b. "Fourier Methods." In *Underwater Acoustic System Analysis*, 149-191. Englewood Cliffs, NJ: Prentice-Hall.

Caiti, A., P. Felisberto, T. Husoy, S. M. Jesus, Iikka Karasalo, R. Massimelli, T.A. Reinen, and A Silva. 2011. UAN - Underwater Acoustic Network. In *Oceans 2011*. Santander, Spain.

Caley, M. S., and A. J. Duncan. 2011. Conceptual development of a dynamic underwater acoustic channel simulator. In *Acoustics 2011, Annual Conference of the Australian Acoustical Society*. Gold Coast, Australia.

Caley, M. S., and A. J. Duncan. 2013a. "Investigation of underwater acoustic multi-path Doppler and delay spreading in a shallow marine environment." *Acoustics Australia* no. 41 (1):20-28.

Caley, M. S., and A. J. Duncan. 2013b. Transient Underwater Acoustic Channel Simulator Development. In *Acoustics 2013, Annual Conference of the Australian Acoustical Society*. Victor Harbor, Australia.

Chitre, M. 2007. "A high-frequency warm shallow water acoustic communications channel model and measurements." *Journal of the Acoustical Society of America* no. 122 (5):2580-2586. doi: DOI: 10.1121/1.2782884.

Chitre, M., S. Shahabudeen, L. Freitag, and M. Stojanovic. 2008. Recent advances in underwater acoustic communications and networking. In *OCEANS 2008*. Quebec City, Canada.

Chitre, M., and Ws Soh. 2015. "Reliable Point-to-Point Underwater Acoustic Data Transfer: To Juggle or Not to Juggle?" *IEEE Journal of Oceanic Engineering* no. 40 (1):93-103. doi: 10.1109/JOE.2014.2311692.

Choi, J. W., and P. H. Dahl. 2006. "Measurement and simulation of the channel intensity impulse response for a site in the East China Sea." *Journal of the Acoustical Society of America* no. 119 (5):2677-2685. doi: 10.1121/1.2189449.

Colin, M. E. G. D., and S. P. Beerens. 2011. "False-Alarm Reduction for Low-Frequency Active Sonar With BPSK Pulses: Experimental Results." *IEEE Journal of Oceanic Engineering* no. 36 (1):52-59.

Collins, T., and P. Atkins. 1998. "Doppler-sensitive active sonar pulse designs for reverberation processing." *Radar, Sonar and Navigation, IEE Proceedings* - no. 145 (6):347-353. doi: 10.1049/ip-rsn:19982434.

Cristol, X. 2005. NARCISSUS-2005: A Global Model of Fading Channel for Application to Acoustic Communication in Marine Environment. In *Oceans - Europe 2005*. Brest, France.

Dahl, P. H. 2001. "High-frequency forward scattering from the sea surface: the characteristic scales of time and angle spreading." *IEEE Journal of Oceanic Engineering* no. 26 (1):141-151.

Deane, G. B., J. C. Preisig, C. T. Tindle, A. Lavery, and M. D. Stokes. 2012. "Deterministic forward scatter from surface gravity waves." *Journal of the Acoustical Society of America* no. 132 (6):3673-3686. doi: 10.1121/1.4763996.

Dol, H. S., M. E. G. D. Colin, M. A. Ainslie, P. A. van Walree, and J. Janmaat. 2013. "Simulation of an Underwater Acoustic Communication Channel Characterized by Wind-Generated Surface Waves and Bubbles." *IEEE Journal of Oceanic Engineering* no. 38 (4):642-654. doi: 10.1109/JOE.2013.2278931.

Dowling, D. R., and D. R. Jackson. 1993. "Coherence of acoustic scattering from a dynamic rough surface." *Journal of the Acoustical Society of America* no. 93 (6):3149-3157.

Eggen, T. H., A. B. Baggeroer, and J. C. Preisig. 2000. "Communication over Doppler spread channels - Part I: Channel and receiver presentation." *IEEE Journal of Oceanic Engineering* no. 25 (1):62-71.

Elfouhaily, T. M., and C. Guérin. 2004. "A critical survey of approximate scattering wave theories from random rough surfaces." *Waves in Random Media* no. 14 (4):R1-R40. doi: 10.1088/0959-7174/14/4/r01.

Freitag, L., M. Stojanovic, S. Singh, and M. Johnson. 2001. "Analysis of channel effects on direct-sequence and frequency-hopped spread-spectrum acoustic communication." *IEEE Journal of Oceanic Engineering* no. 26 (4):586-593.

Ghiotto, A., N. Andronis, and M. Dragojevic. 2012. Reliability in Underwater Acoustic Networks. In *Acoustics 2012, Annual Conference of the Australian Acoustical Society*. Fremantle, Perth.

Goddard, N., and M. Launder. 2009. Standardised Testing of Acoustic Communications Modems using a High Fidelity Simulator. In *3rd International Conference and Exhibition on Underwater Acoustic Measurements: Technologies & Results*. Greece.

Green, J. 2011. *The Rottnest Deepwater Graveyard*. Perth, Australia: Western Australian Museum http://museum.wa.gov.au/explore/videos/rottnest-deepwater-graveyard.

Holthuijsen, L. H. 2007. "Linear wave theory (oceanic waters)." In *Waves in Oceanic and Coastal Waters*. Cambridge: Cambridge University Press.

Hsu, S. A., E. A. Meindl, and D. B. Gilhousen. 1994. "Determining the Power-Law Wind-Profile Exponent under Near-Neutral Stability Conditions at Sea." *Journal of Applied Meteorology* no. 33 (6):757-772.

Huang, S. H., T.C. Yang, and C. Huang. 2013. "Multipath correlations in underwater acoustic communication channels." *Journal of the Acoustical Society of America* no. 133 (4):2180-2190.

Ishimaru, A. 1978. *Wave propagation and scattering in random media*. New York: New York : Academic Press.

Isukapalli, Y., H. C. Song, and W. S. Hodgkiss. 2011. "Stochastic channel simulator based on local scattering functions." *Journal of the Acoustical Society of America* no. 130 (4):EL200-EL205. doi: 10.1121/1.3633688.

Jensen, F. B., W. A. Kuperman, M. B. Porter, and H. Schmidt. 2011. *Computational Ocean Acoustics* 2nd ed. New York: Springer.

Kang, T., H. C. Song, W. S. Hodgkiss, and J. S. Kim. 2010. "Long-range multi-carrier acoustic communications in shallow water based on iterative sparse channel estimation." *Journal of the Acoustical Society of America* no. 128 (6):EL372-EL377. doi: 10.1121/1.3514157.

Karasalo, I. 2011. Time-domain modelling of turbo-coded underwater communication. In *OCEANS, 2011 IEEE - Spain*.

Karjadi, E. A., M. Badiey, J. T. Kirby, and C. Bayindir. 2012. "The Effects of Surface Gravity Waves on High-Frequency Acoustic Propagation in

Shallow Water." *IEEE Journal of Oceanic Engineering* no. 37 (1):112-121. doi: 10.1109/JOE.2011.2168670.

Kilfoyle, D. B., and A. B. Baggeroer. 2000. "The state of the art in underwater acoustic telemetry." *IEEE Journal of Oceanic Engineering* no. 25 (1):4-27. doi: 10.1109/48.820733.

Kinsler, L. E., A. R. Frey, A. B. Coppens, and J. V. Sanders. 1982. *Fundamentals of Acoustics*. Edited by John Wiley & Sons. Third ed.

Li, B., J. Huang, S. Zhou, K. Ball, M. Stojanovic, L. Freitag, and P. Willett. 2009. "MIMO-OFDM for High-Rate Underwater Acoustic Communications." *IEEE Journal of Oceanic Engineering* no. 34 (4):634-644.

McCammon, D. F., and S. T. McDaniel. 1986. "Surface velocity, shadowing, multiple scattering, and curvature on a sinusoid." *Journal of the Acoustical Society of America* no. 79 (6):1778-1785. doi: 10.1121/1.393239.

McDaniel, S. T. 1992. "High-frequency forward scattering in a refracting ocean." *Journal of the Acoustical Society of America* no. 92 (1):324-331. doi: 10.1121/1.404297.

Molisch, A. 2011. "Channel Sounding." In *Wireless Communications*, 145-164. Wiley-IEEE Press.

Nautronix. *Subsea acoustics on the upgrade*. ROVworld.com 2011. Available from http://www.rovworld.com/article-printpdf-5716.html.

Ogilvy, J. A. 1988. "Computer simulation of acoustic wave scattering from rough surfaces." *Journal of Physics D: Applied Physics* no. 21 (2):260-277. doi: 10.1088/0022-3727/21/2/006.

Ogilvy, J. A. 1991. *Theory of Wave Scattering from Random Rough Surfaces*. Bristol, Great Brittain: Adam Hilger.

Otnes, R., T. Jenserud, and P. A. Van Walree. 2013. "Validation of replay-based underwater acoustic communication channel simulation." *IEEE Journal of Oceanic Engineering* no. 38 (4):689-700. doi: 10.1109/JOE.2013.2262743.

Otnes, R., T. Jenserud, J. E. Voldhaug, and C. Solberg. 2009. A roadmap to Ubiquitous Underwater Acoustic Communications and Networking. In *3rd International Conference and Exhibition on Underwater Acoustic Measurements: Technologies & Results*. Greece.

Pelekanakis, K., and A. B. Baggeroer. 2011. "Exploiting Space-Time-Frequency Diversity With MIMO-OFDM for Underwater Acoustic Communications." *IEEE Journal of Oceanic Engineering* no. 36 (4):502-513. doi: 10.1109/JOE.2011.2165758.

Peterson, J. C., and M. B. Porter. 2013. "Ray/Beam Tracing for Modeling the Effects of Ocean and Platform Dynamics." *IEEE Journal of Oceanic Engineering* no. 38 (4):655-665. doi: 10.1109/JOE.2013.2278914.

Porter, M. B. 2011. The BELLHOP Manual and Users Guide - *preliminary draft*. HLS Research Inc, La Jolla, CA, USA: http://oalib.hlsresearch.com/Rays/HLS-2010-1.pdf.

Porter, M. B. 2013. Out-of-Plane Effects in Ocean Acoustics. HLS Research Inc, La Jolla, CA, USA: http://www.onr.navy.mil/reports/FY13/oaporter.pdf.

Porter, M. B., P. Hursky, and M. Siderius. 2002. "High-frequency propagation for acoustic communications." In *Impact of Littoral Environmental Variability on Acoustic Predictions and Sonar Performance*, edited by N. G. Pace and F. B. Jensen. Kluwer.

Potter, J. R., M. B. Porter, and J. C. Preisig. 2013. "UComms: A Conference and Workshop on Underwater Communications, Channel Modeling, and Validation." *IEEE Journal of Oceanic Engineering* no. 38 (4):603-613. doi: 10.1109/JOE.2013.2283094.

Preisig, J. C. 2007. "Acoustic propagation considerations for underwater acoustic communications network development." *Mobile computing and communications review* no. 11 (4):2-10.

Preisig, J. C., and G. B. Deane. 2004. "Surface wave focusing and acoustic communications in the surf zone." *Journal of the Acoustical Society of America* no. 116 (4):2067-2080.

Proakis, J. G. 2000. *Digital Communications*. Fourth Edition ed. New York: McGraw Hill.

Qarabaqi, P., and M. Stojanovic. 2013. "Statistical characterization and computationally efficient modeling of a class of underwater acoustic communication channels." *IEEE Journal of Oceanic Engineering* no. 38 (4):701-717. doi: 10.1109/JOE.2013.2278787.

Ribeiro, Fabrício, Aloysio de Castro Pinto Pedroza, and Luís Costa. 2015. "Underwater monitoring system for oil exploration using acoustic sensor networks." *Telecommunication Systems* no. 58 (1):91-106. doi: 10.1007/s11235-014-9948-6.

Rice, J., and D. Green. 2008. Underwater Acoustic Communications and Networks for the US Navy's Seaweb Program. In *The Second International Conference on Sensor Technologies and Applications*. Cap Esterel, France.

Roderick, W. I., and R. L. Deavenport. 1993. Doppler Characteristics of Sea Surface Reflected and Scattered Acoustic Signals Induced by Surface Wave Motion. In *Oceans 1993*. Victoria, BC.

Rodriguez, O. C., A. J. Silva, J. P. Gomes, and S. M. Jesus. 2010. Modeling arrival scattering due to surface roughness. In *10th European Conference on Underwater Acoustics*. Instanbul, Turkey.

Rodriguez, O. C., A. J. Silva, F. Zabel, and S. M. Jesus. 2010. The TV-APM interface: a web service for collaborative modeling. In *10th European Conference on Underwater Acoustics*. Instanbul, Turkey.

Schanze, T. 1995. "Sinc interpolation of discrete periodic signals." *IEEE Transactions on Signal Processing* no. 43 (6):1502-1503. doi: 10.1109/78.388863.

Senne, J. 2012. *High frequency acoustic propagation under variable sea surfaces*. Dissertation, Ocean Engineering, University of Delaware, Ann Arbor, United States.

Senne, J., A. Song, M. Badiey, and K. B. Smith. 2012. "Parabolic equation modeling of high frequency acoustic transmission with an evolving sea surface." *Journal of the Acoustical Society of America* no. 132 (3):1311-1318. doi: 10.1121/1.4742720.

Siderius, M., and M. B. Porter. 2006. "Modeling techniques for marine-mammal risk assessment." *IEEE Journal of Oceanic Engineering* no. 31 (1):49-60.

Siderius, M., and M. B. Porter. 2008. "Modeling broadband ocean acoustic transmissions with time-varying sea surfaces." *Journal of the Acoustical Society of America* no. 124 (1):137-150.

Siderius, M., M. B. Porter, P. Hursky, and V. McDonald. 2007. "Effects of ocean thermocline variability on noncoherent underwater acoustic communications." *Journal of the Acoustical Society of America* no. 121 (4):1895-1908.

Silva, A. J., O. C. Rodriguez, F. Zabel, J. Huilery, and S. M. Jesus. 2010. Underwater acoustic simulations with a time variable acoustic propagation model. In *10th European Conference on Underwater Acoustics*. Instanbul, Turkey.

Socheleau, F., C. Laot, and J. Passerieux. 2011. "Stochastic Replay of Non-WSSUS Underwater Acoustic Communication Channels Recorded at Sea." *IEEE Transactions on Signal Processing* no. 59 (10):4838-4849. doi: 10.1109/TSP.2011.2160057.

Song, A., M. Badiey, H. C. Song, W. S. Hodgkiss, M. B. Porter, and the KauaiEx Group. 2008. "Impact of ocean variability on coherent underwater acoustic communications during the Kauai experiment (KauaiEx)." *Journal of the Acoustical Society of America* no. 123 (2):856-865. doi: DOI: 10.1121/1.2828055.

Stojanovic, M., and J. C. Preisig. 2009. "Underwater acoustic communication channels: propagation models and statistical characterization." *IEEE Communications Magazine* no. 47 (1):84-89.

Stojanovic, Milica. 2007. "On the relationship between capacity and distance in an underwater acoustic communication channel." *Mobile computing and communications review* no. 11 (4):34-43.

Thorsos, E. I. . 1988. "The validity of the Kirchhoff approximation for rough surface scattering using a Gaussian roughness spectrum." *Journal of the Acoustical Society of America* no. 83 (1):78-92. doi: 10.1121/1.396188.

Tindle, C. T. 2002. "Wavefronts and waveforms in deep-water sound propagation." *Journal of the Acoustical Society of America* no. 112 (2):464-475. doi: 10.1121/1.1489437.

Tomasi, B., G. Zappa, K. McCoy, P. Casari, and M. Zorzi. 2010. Experimental Study of the Space-Time Properties of Acoustic Channels for Underwater

Communications. In *Proceedings of IEEE Oceans 2010 Conference* Sydney, Australia.

Toporkov, J. V., and G. S. Brown. 2002. "Numerical study of the extended Kirchhoff approach and the lowest order small slope approximation for scattering from ocean-like surfaces: Doppler analysis." *IEEE Transactions on Antennas and Propagation* no. 50 (4):417-425. doi: 10.1109/tap.2002.1003376.

van Walree, P. A. 2011. Channel sounding for acoustic communications: techniques and shallow-water examples, FFI report 2011/00007. Norwegian Defence Research Establishment.

van Walree, P. A, T. Jenserud, and R. Otnes. 2010. "Stretched-exponential Doppler spectra in underwater acoustic communication channels." *Journal of the Acoustical Society of America* no. 128 (5):EL329-EL334.

van Walree, P. A. 2013. "Propagation and Scattering Effects in Underwater Acoustic Communication Channels." *IEEE Journal of Oceanic Engineering* no. 38 (4):614-631. doi: 10.1109/JOE.2013.2278913.

van Walree, P. A., T. Jenserud, and M. Smedsrud. 2008. "A Discrete-Time Channel Simulator Driven by Measured Scattering Functions." *IEEE Journal on Selected Areas in Communications* no. 26 (9):1628-1637.

van Walree, P. A., and R. Otnes. 2013. "Ultrawideband Underwater Acoustic Communication Channels." *IEEE Journal of Oceanic Engineering* no. 38 (4):678-688. doi: 10.1109/JOE.2013.2253391.

WAFO. 2011. (Wave Analysis for Fatigue and Oceanography)- A Matlab toolbox for analysis of random waves and loads- Version 2.5 Lund University, Sweden http://www.maths.lth.se/matstat/wafo.

Wagner, R. J. 1967. "Shadowing of Randomly Rough Surfaces." *Journal of the Acoustical Society of America* no. 41 (1):138-147. doi: 10.1121/1.1910308.

Yang, T. C. 2012. "Properties of underwater acoustic communication channels in shallow water." *Journal of the Acoustical Society of America* no. 131 (1):129-145. doi: 10.1121/1.3664053.

Ziomek, L. J. 1982. "Generalized Kirchhoff Approach to the Ocean Surface-Scatter Communication Channel - 1. Transfer Function of the Ocean Surface " *Journal of the Acoustical Society of America* no. 71 (1):116-126.

Ziomek, L. J. 1995. "Ray Acoustics." In *Fundamentals of acoustic field theory and space-time signal processing*. Florida, USA: CRC Press, Inc.

Appendix A Cottesloe channel probe trial data

A.1 Transmit and receive recording summary

Humminbird data		comment	CTD/ Pitch-roll-heave file/sediment sample	Transmit logger data			N4095 sequence start	N511 sequence start	N63 sequence start	Multitones start	Sweeps start
					duration						
mark	clock			File	seconds	end	elapsed	elapsed	elapsed	elapsed	elapsed
s28	8:46:23	logger touchdown									
s31	9:15:08		r4	t01	301.303	9:19:26	40.6304	114.356	152.2112	190.8997	257.8606
s33	9:24:17		r4	t02	304.198	9:28:42	38.6024	112.3505	150.2057	188.8943	255.8551
s35	9:32:03		r4	t03	205.701	9:34:46	45.9892	119.738	157.5932	196.2817	missing
168			CTD cast 1 /r5	t04	313.315	9:51:14	36.0944	109.8426	147.6979	186.3864	253.3475
			CTD cast 2 /r5	t05	267.471	10:03:38	8.5925	82.3415	120.1969	158.8855	225.8466
170			r5	t06	331.553	10:18:34	54.477	128.2262	166.0815	204.7701	271.7313
171			CTD cast 3 /r6	t07	271.235	10:37:52	8.0748	81.8231	119.6784	158.3669	225.3279
172			r6	t08	360.719	10:50:06	64.5202	138.2684	176.1237	214.8121	281.7732
173			r6	t09	272.217	10:59:08	9.6095	83.3577	121.213	159.9015	226.8625
174		delay start tx record	r6	t11	279.563	11:06:48	17.5933	91.3422	129.1975	167.886	234.8471
			CTD cast 4 /r6	t12	319.806	11:19:02	48.0098	121.7588	159.6141	198.3027	265.2638
176			r7	t13	284.999	11:37:08	9.4604	83.2095	121.0649	159.7535	226.7147
177		delay start tx record	r7	t14	289.454	11:47:02	10.9299	84.6791	122.5346	161.2232	228.1846
179			r7	t15	288.605	12:04:38	31.2759	105.025	142.8805	181.5693	248.5306
s38	12:23:10	delay start tx record	r7	t16	463.109	12:30:12	204.9417	278.691	316.5464	355.235	422.1963
s40	12:37:15		CTD cast 5/r8	t17	351.997	12:42:44	22.9685	96.7176	134.5729	173.2616	240.2228
s42	12:55:40	breeze just starting	r8	t18	355.039	13:00:08	86.3156	160.0648	197.9201	236.6089	303.5701
s44	13:02:48		r8	t19	298.495	13:07:30	16.7873	90.5365	128.3919	167.0806	234.0418
s46	13:10:52		CTD cast 6 /r8	t20	288.865	13:15:24	15.861	89.6101	127.4655	166.1541	233.1153
s48	13:19:55		r9	t21	2620.194	14:02:04	91.3032	165.0516	202.907	241.5955	308.5567
s56	13:57:31		r9	t21 restart	2620.194	14:02:04	2348.0139	2421.7485	2459.604	2498.2927	2565.2534
s58	14:05:05		Grab 1, S31^o 59.121', E115^o 40.666'								
s59	14:11:00		Grab 2, S31^o 59.027', E115^o 40.390'								
s60	14:20:00		Grab 3, S31^o 59.092', E115^o 40.545'								
s61	14:27:00		Grab 4, S31^o 59.206', E115^o 40.480'								

Transmit file	Receive logger data receiver file	Start	duration seconds	end	N4095 sequence start elapsed	clock	Approx. Flight time	N511 sequence start elapsed	clock	N63 sequence start elapsed	clock	Multitones start elapsed	clock	Sweeps start elapsed	clock
	t1979	8:46:22	1194.091	9:06:16			c (m/s)								
		touchdown					1536								
t01	t1980	9:06:17	6225.393	10:50:02	533.6814	9:15:10	0.081	607.4268	9:16:24	645.2799	9:17:02	683.9661	9:17:41	750.9225	9:18:48
t02	t1980	9:06:17	6225.393	10:50:02	1084.367	9:24:21	0.042	1158.1079	9:25:35	1195.961	9:26:13	1234.6478	9:26:51	1301.6092	9:27:58
t03	t1980	9:06:17	6225.393	10:50:02	1552.2363	9:32:09	0.036	1625.9852	9:33:23	1663.8457	9:34:00	1702.5397	9:34:39	missing	#VALUE!
t04	t1980	9:06:17	6225.393	10:50:02	2424.769	9:46:41	0.065	2498.5283	9:47:55	2536.3908	9:48:33	2575.0876	9:49:12	2642.0615	9:50:19
t05	t1980	9:06:17	6225.393	10:50:02	3186.6413	9:59:23	0.278	3260.4057	10:00:37	3298.2673	10:01:15	3336.9636	10:01:54	3403.9396	10:03:01
t06	t1980	9:06:17	6225.393	10:50:02	4065.2775	10:14:02	0.591	4139.0439	10:15:16	4176.9077	10:15:54	4215.6044	10:16:32	4282.5805	10:17:39
t07	t1980	9:06:17	6225.393	10:50:02	5237.184	10:33:34	0.668	5310.9287	10:34:48	5348.7817	10:35:25	5387.4687	10:36:04	5454.4248	10:37:11
t08	t1980	9:06:17	6225.393	10:50:02	5937.9882	10:45:15	0.336	6011.7299	10:46:28	6049.5835	10:47:06	6088.2724	10:47:45	6155.2324	10:48:52
t09	t1981	10:50:01	6225.391	12:33:46	288.0807	10:54:49	0.148	361.8297	10:56:02	399.6841	10:56:40	438.3715	10:57:19	505.3315	10:58:26
t11	t1981	10:50:01	6225.391	12:33:46	747.49	11:02:28	0.092	821.2394	11:03:42	859.0944	11:04:20	897.7822	11:04:58	964.7418	11:06:05
t12	t1981	10:50:01	6225.391	12:33:46	1472.1848	11:14:33	0.070	1545.9312	11:15:47	1583.7861	11:16:24	1622.4743	11:17:03	1689.4331	11:18:10
t13	t1981	10:50:01	6225.391	12:33:46	2554.6225	11:32:35	0.036	2628.3649	11:33:49	2666.2192	11:34:27	2704.9072	11:35:06	2771.8679	11:36:12
t14	t1981	10:50:01	6225.391	12:33:46	3147.3483	11:42:28	0.041	3221.0949	11:43:42	3258.9499	11:44:20	3297.6389	11:44:58	3364.6015	11:46:05
t15	t1981	10:50:01	6225.391	12:33:46	4222.7646	12:00:23	0.093	4296.5102	12:01:37	4334.3652	12:02:15	4373.0527	12:02:54	4440.0136	12:04:01
t16	t1981	10:50:01	6225.391	12:33:46	5757.3696	12:25:58	0.295	5831.124	12:27:12	5868.9819	12:27:50	5907.6723	12:28:28	5974.6381	12:29:35
t17	t1982	12:33:45	6225.391	14:17:30	213.0045	12:37:18	0.605	286.7575	12:38:31	324.6133	12:39:09	363.3026	12:39:48	430.2648	12:40:55
t18	t1982	12:33:45	6225.391	14:17:30	1317.2318	12:55:42	0.090	1390.9871	12:56:56	1428.8458	12:57:33	1467.5375	12:58:12	1534.5046	12:59:19
t19	t1982	12:33:45	6225.391	14:17:30	1745.9306	13:02:51	0.074	1819.6821	13:04:04	1857.5396	13:04:42	1896.2313	13:05:21	1963.1975	13:06:28
t20	t1982	12:33:45	6225.391	14:17:30	2229.0488	13:10:54	0.036	2302.7993	13:12:07	2340.6577	13:12:45	2379.3503	13:13:24	2446.3195	13:14:31
t21	t1982	12:33:45	6225.391	14:17:30	2771.5327	13:19:56	0.041	2845.2829	13:21:10	2883.1396	13:21:48	2921.8308	13:22:26	2988.7966	13:23:33
t21 restart	t1982	12:33:45	6225.391	14:17:30	5028.5439	13:57:33	0.211	5102.2915	13:58:47	5140.1533	13:59:25	5178.8481	14:00:03	5245.8203	14:01:10

Transmit file	tx start northing	tx start easting	tx end northing	tx end easting	tx start radians		tx end radians		tx midpoint radians		N4095 sequence start txrx distance	end txrx distance	(m/s) txrx closing speed	(m) translation distance	(m/s) ave trans speed	ave txrx heading (deg of N)	ave boat heading (deg of N)
	logger touchdown - canopy speedpuck										sequence length(s)=	60					
	-31.9861221	115.6736679			-0.56	2.02											
t01	-31.9854031	115.6746902	-31.9853096	115.6743164	-0.56	2.02	-0.56	2.02	-0.56	2.02	125.0	108.9	0.27	42.8	0.71	223	286
t02	-31.985714	115.6741562	-31.98573685	115.6742706	-0.56	2.02	-0.56	2.02	-0.56	2.02	64.5	71.0	-0.11	13.0	0.22	229	103
t03	-31.986124	115.674263	-31.98618317	115.674408	-0.56	2.02	-0.56	2.02	-0.56	2.02	56.0	70.0	-0.23	17.4	0.29	273	116
t04	-31.9867058	115.6744766	-31.9868145	115.6744156	-0.56	2.02	-0.56	2.02	-0.56	2.02	100.0	104.2	-0.07	13.8	0.23	314	205
t05	-31.989542	115.6757431	-31.98925591	115.6754913	-0.56	2.02	-0.56	2.02	-0.56	2.02	426.9	387.8	0.65	42.3	0.70	333	323
t06	-31.9936085	115.6775589	-31.9934597	115.6771622	-0.56	2.02	-0.56	2.02	-0.56	2.02	908.0	878.2	0.50	47.0	0.78	337	294
t07	-31.9823322	115.683609	-31.98224831	115.6836548	-0.56	2.02	-0.56	2.02	-0.56	2.02	1026.0	1033.7	-0.13	10.6	0.18	246	25
t08	-31.9840603	115.6785812	-31.98395538	115.6788177	-0.56	2.02	-0.56	2.02	-0.56	2.02	516.0	541.1	-0.42	28.7	0.48	244	62
t09	-31.9848366	115.6755447	-31.98487854	115.6756668	-0.56	2.02	-0.56	2.02	-0.56	2.02	227.1	233.3	-0.10	14.3	0.24	232	112
t11	-31.98522	115.674736	-31.98518562	115.6748428	-0.56	2.02	-0.56	2.02	-0.56	2.02	141.9	151.8	-0.16	12.5	0.21	226	69
t12	-31.9852886	115.674263	-31.98525238	115.6743927	-0.56	2.02	-0.56	2.02	-0.56	2.02	108.1	118.2	-0.17	14.9	0.25	213	72
t13	-31.9856281	115.6736069	-31.98557854	115.6731873	-0.56	2.02	-0.56	2.02	-0.56	2.02	55.1	75.4	-0.34	46.9	0.78	156	278
t14	-31.985836	115.6730957	-31.98570442	115.6731949	-0.56	2.02	-0.56	2.02	-0.56	2.02	62.5	64.3	-0.03	18.3	0.30	128	33
t15	-31.98596	115.6721573	-31.98618126	115.6720505	-0.56	2.02	-0.56	2.02	-0.56	2.02	143.3	152.4	-0.15	27.3	0.45	92	202
t16	-31.9871521	115.6690063	-31.98708534	115.6689835	-0.56	2.02	-0.56	2.02	-0.56	2.02	453.4	453.7	0.00	7.8	0.13	76	344
t17	-31.9884663	115.6641846	-31.9883709	115.6642303	-0.56	2.02	-0.56	2.02	-0.56	2.02	929.8	922.8	0.12	11.7	0.20	74	22
t18	-31.9849987	115.6742859	-31.98496437	115.6741257	-0.56	2.02	-0.56	2.02	-0.56	2.02	137.6	135.5	0.03	18.2	0.30	202	284
t19	-31.9852867	115.6743546	-31.98530579	115.6745071	-0.56	2.02	-0.56	2.02	-0.56	2.02	113.0	120.2	-0.12	17.1	0.28	218	98
t20	-31.9857635	115.6740723	-31.98569298	115.6741714	-0.56	2.02	-0.56	2.02	-0.56	2.02	55.1	67.2	-0.20	13.5	0.23	224	50
t21	-31.9855595	115.6736603	-31.98553276	115.6735992	-0.56	2.02	-0.56	2.02	-0.56	2.02	62.4	65.7	-0.05	7.4	0.12	177	297
t21 restart	-31.9856224	115.677063	-31.98562622	115.6769562	-0.56	2.02	-0.56	2.02	-0.56	2.02	324.4	314.4	0.17	11.9	0.20	260	268
	equatorial radius a(m)		6378137														
	polar radius b(m)		6356752.3														
	lat (degrees)		-31.198														
	radius (m)		6358742.13														
	mean earth radius(m)		6371009														

Transmit file	**N511 sequence** start txrx distance	end txrx distance	(m/s) txrx closing speed	(m) translation distance	(m/s) ave trans speed	ave txrx heading (deg of N)	ave boat heading (deg of N)	**N63 sequence** start txrx distance	end txrx distance	(m/s) txrx closing speed	(m) translation distance	(m/s) ave trans speed	ave txrx heading (deg of N)	ave boat heading (deg of N)
	sequence length(s)=	30						sequence length(s)=	30					
t01	116.4	118.6	-0.08	4.0	0.13	236	0	110.8	115.6	-0.16	6.1	0.20	238	21
t02	48.9	54.8	-0.20	8.4	0.28	235	10	44.4	48.3	-0.13	7.9	0.26	245	5
t03	54.2	52.7	0.05	8.5	0.28	285	5	59.9	55.1	0.16	9.4	0.31	297	356
t04	112.1	106.8	0.18	7.4	0.25	316	0	120.1	113.5	0.22	8.7	0.29	319	0
t05	438.1	435.0	0.11	4.6	0.15	334	19	444.6	438.9	0.19	7.2	0.24	334	12
t06	927.1	919.6	0.25	7.9	0.26	336	355	937.0	929.3	0.26	8.1	0.27	337	355
t07	1014.0	1018.9	-0.16	7.8	0.26	246	16	1008.3	1012.7	-0.15	6.6	0.22	247	19
t08	503.0	507.1	-0.14	4.9	0.16	244	39	496.7	501.9	-0.17	6.8	0.23	245	26
t09	221.5	223.7	-0.07	4.5	0.15	232	351	217.2	220.9	-0.12	6.1	0.20	233	0
t11	136.0	138.1	-0.07	3.2	0.11	227	0	130.5	135.9	-0.18	6.8	0.23	229	12
t12	96.4	101.0	-0.16	5.2	0.17	212	8	90.2	95.1	-0.16	5.9	0.20	214	0
t13	39.4	43.6	-0.14	6.8	0.23	183	316	33.3	37.7	-0.15	6.1	0.20	192	331
t14	51.3	56.4	-0.17	6.3	0.21	112	322	48.9	51.2	-0.08	7.0	0.23	104	354
t15	133.0	137.5	-0.15	5.4	0.18	97	294	129.1	132.9	-0.13	4.9	0.16	96	305
t16	455.4	455.3	0.00	3.1	0.10	75	346	454.7	455.6	-0.03	2.5	0.08	74	323
t17	927.9	930.3	-0.08	5.6	0.19	73	315	924.8	926.8	-0.06	4.4	0.15	73	314
t18	140.1	139.2	0.03	7.2	0.24	210	292	141.3	140.1	0.04	8.1	0.27	213	293
t19	110.9	111.5	-0.02	4.5	0.15	218	316	110.8	110.3	0.02	4.8	0.16	221	303
t20	52.6	51.6	0.03	3.9	0.13	231	304	53.1	52.6	0.02	3.3	0.11	235	314
t21	59.6	60.8	-0.04	4.6	0.15	187	295	59.0	59.1	0.00	4.3	0.14	192	283
t21 restart	337.3	331.8	0.19	6.9	0.23	260	234	343.7	338.2	0.19	6.8	0.23	259	236

Transmit file	**Multitones** start txrx distance	end txrx distance	(m/s) txrx closing speed	(m) translation distance	(m/s) ave trans speed	ave txrx heading (deg of N)	ave boat heading (deg of N)	**Sweeps** start txrx distance	end txrx distance	(m/s) txrx closing speed	(m) translation distance	(m/s) ave trans speed	ave txrx heading (deg of N)
	sequence length(s)=	60						sequence length(s)=	30				
t01	104.2	114.3	-0.17	14.6	0.24	240	14	90.7	97.0	-0.21	9.5	0.32	250
t02	40.5	46.6	-0.10	16.4	0.27	253	5	37.1	37.7	-0.02	7.2	0.24	283
t03	64.2	57.1	0.12	17.9	0.30	303	9	#VALUE!	#VALUE!	#VALUE!	#VALUE!	#VALUE!	#VALUE!
t04	127.8	115.9	0.20	17.1	0.29	322	7	142.1	135.0	0.24	9.9	0.33	329
t05	452.5	440.2	0.21	14.8	0.25	335	8	470.6	463.7	0.23	8.8	0.29	337
t06	945.8	931.1	0.24	16.3	0.27	337	3	960.8	954.8	0.20	7.8	0.26	337
t07	1001.8	1011.3	-0.16	13.8	0.23	247	22	989.9	996.4	-0.22	8.3	0.28	248
t08	492.4	499.8	-0.12	11.7	0.20	245	14	485.8	488.6	-0.09	7.0	0.23	247
t09	212.4	219.5	-0.12	11.3	0.19	234	4	204.2	207.3	-0.10	7.2	0.24	239
t11	125.7	135.1	-0.16	13.0	0.22	230	6	119.4	122.9	-0.12	7.7	0.26	238
t12	85.9	93.8	-0.13	10.4	0.17	217	356	79.1	81.2	-0.07	5.7	0.19	225
t13	27.9	36.8	-0.15	13.7	0.23	198	331	20.1	23.6	-0.12	7.0	0.23	227
t14	45.2	50.7	-0.09	13.6	0.23	99	344	43.0	43.6	-0.02	6.8	0.23	77
t15	126.6	131.4	-0.08	8.3	0.14	95	327	119.9	122.8	-0.10	5.1	0.17	90
t16	455.4	455.0	0.01	6.6	0.11	74	347	456.7	457.3	-0.02	3.2	0.11	73
t17	922.3	927.1	-0.08	8.9	0.15	73	306	917.1	919.1	-0.07	4.0	0.13	72
t18	143.4	140.6	0.05	13.4	0.22	215	291	146.1	144.5	0.05	6.4	0.21	221
t19	111.8	110.2	0.03	10.7	0.18	223	304	114.0	113.8	0.01	4.6	0.15	230
t20	55.6	52.8	0.05	7.8	0.13	238	304	61.5	58.7	0.09	4.4	0.15	246
t21	59.3	59.0	0.01	9.5	0.16	194	282	61.4	60.2	0.04	3.4	0.11	204
t21 restart	349.7	340.5	0.15	10.8	0.18	259	247	361.4	357.1	0.14	5.1	0.17	259

A.2 **Visual summary of receiver recordings**

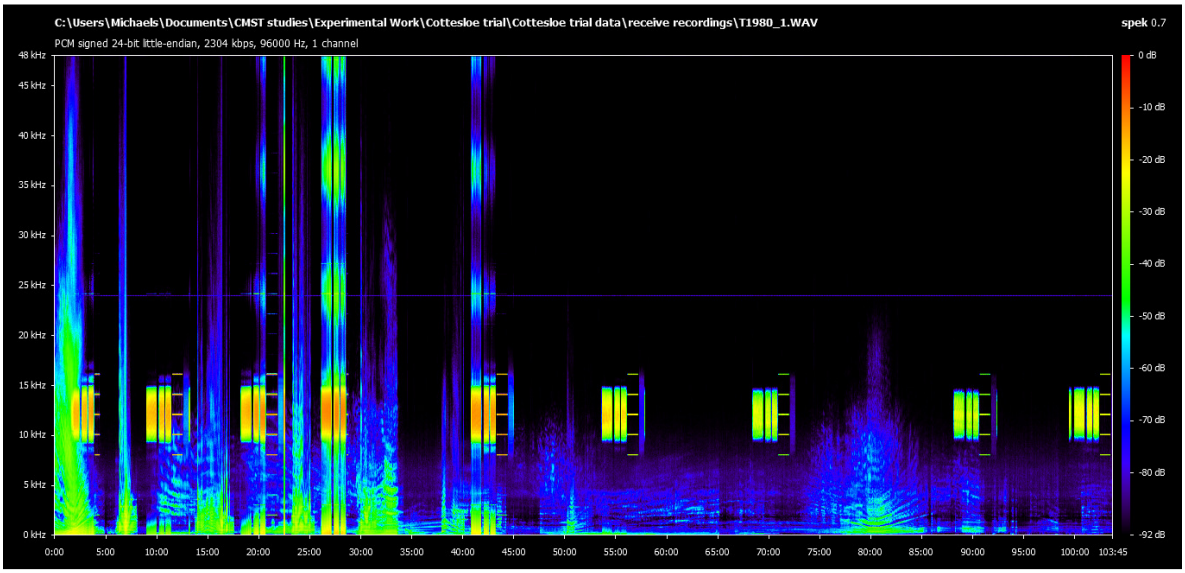

Figure A-1: Spectrogram for receiver channel-1 file T1980_1.wav

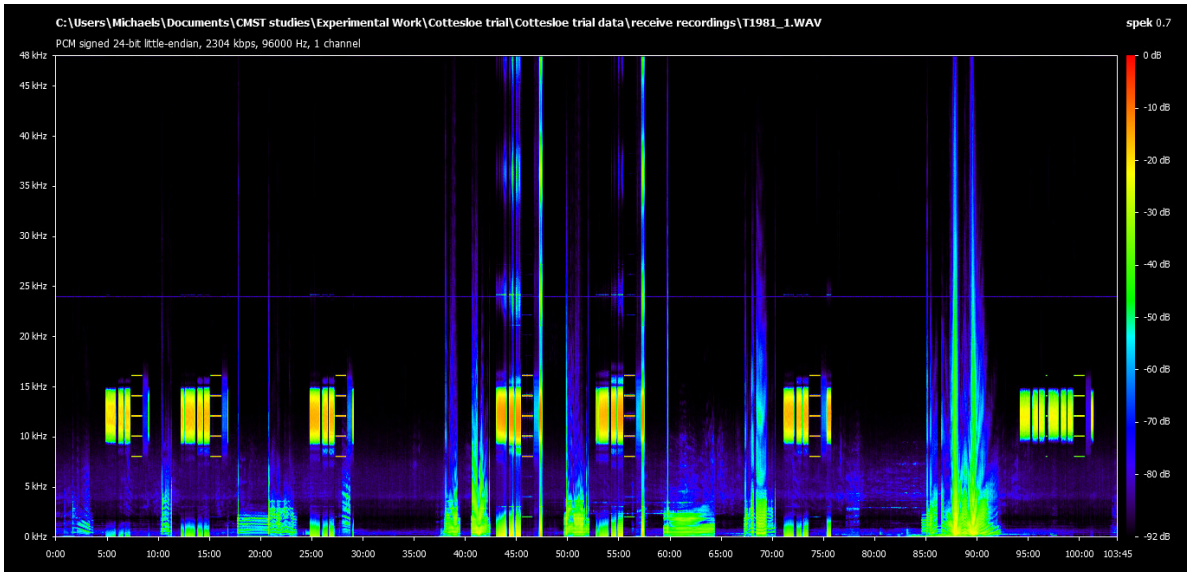

Figure A-2: Spectrogram for receiver channel-1 file T1981_1.wav

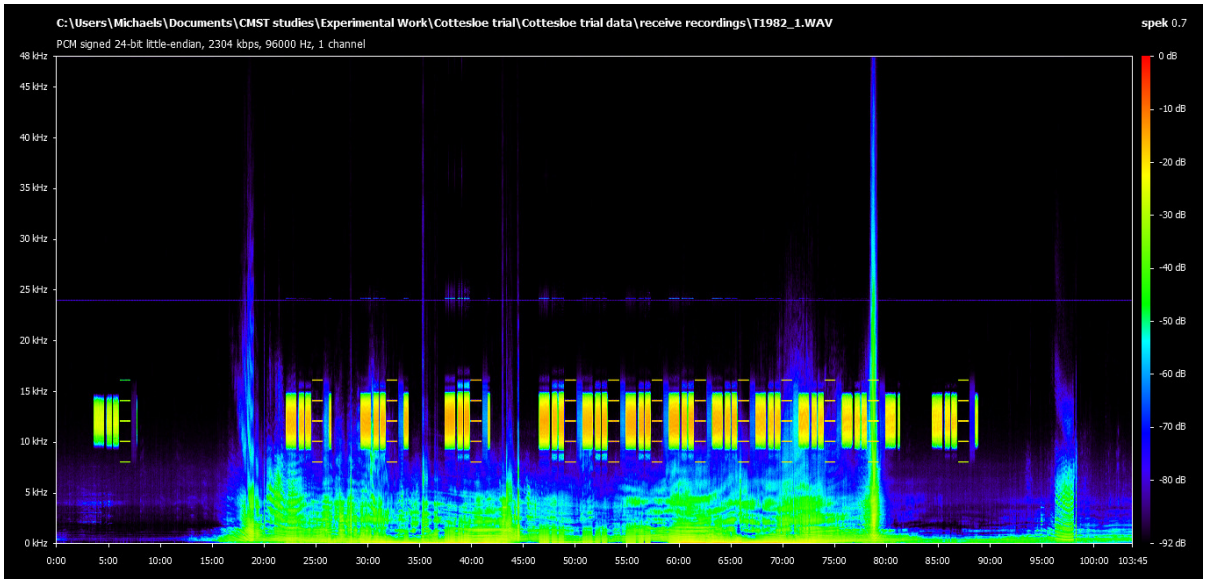

Figure A-3: Spectrogram for receiver channel-1 file T1982_1.wav

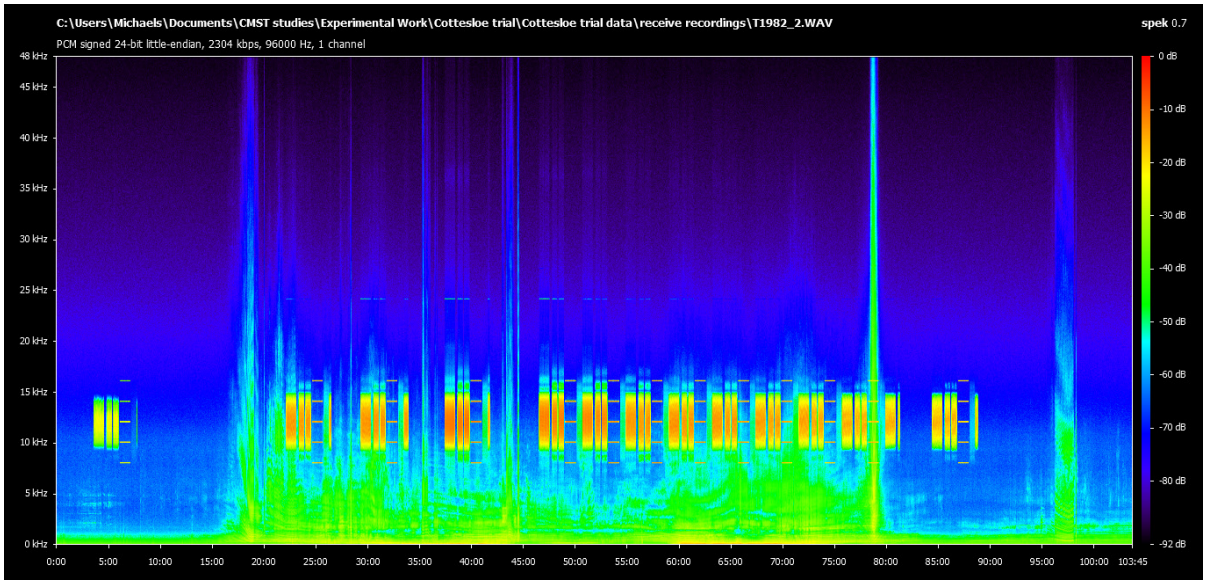

Figure A-4: Spectrogram for receiver channel-2 file T1982_2.wav

A.3 **CTD probe sound speed profiles**

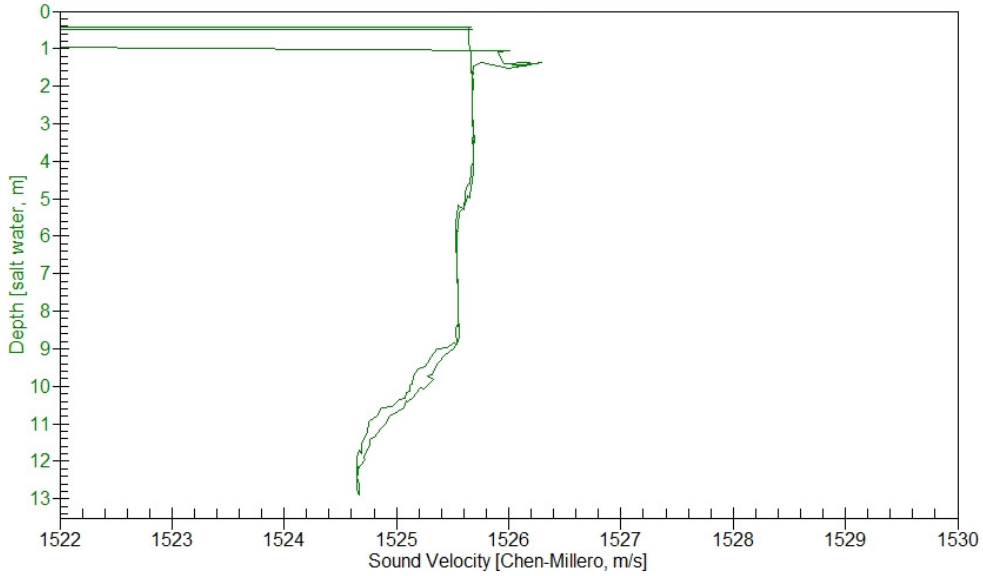

Figure A-5: Sound Speed Profile CTD Cast 1 – 9:47 am

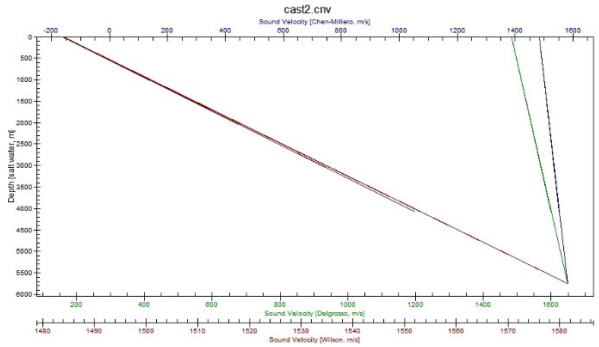

Figure A-6: Sound Speed Profile CTD Cast 2 (malfunction)

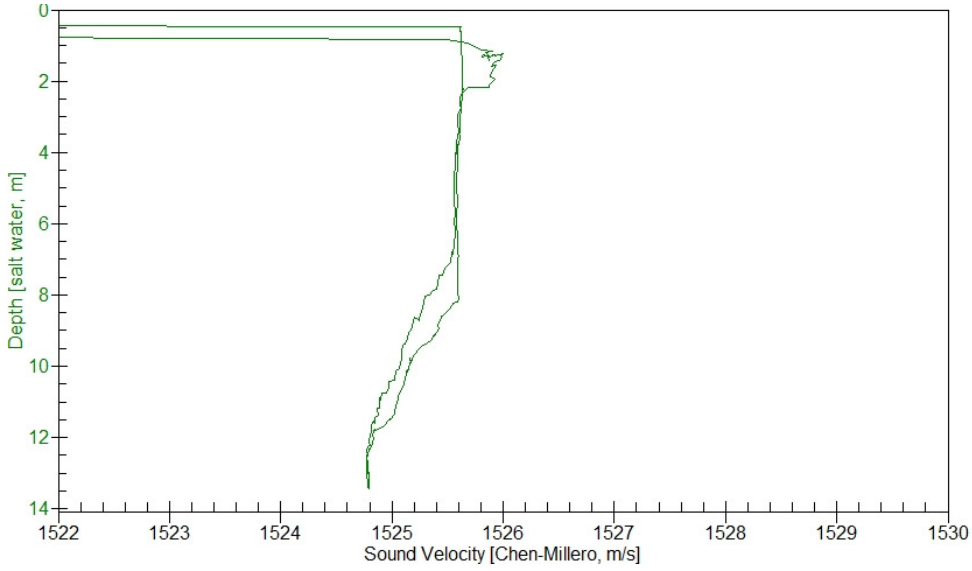

Figure A-7: Sound Speed Profile CTD Cast 3–10:33 am

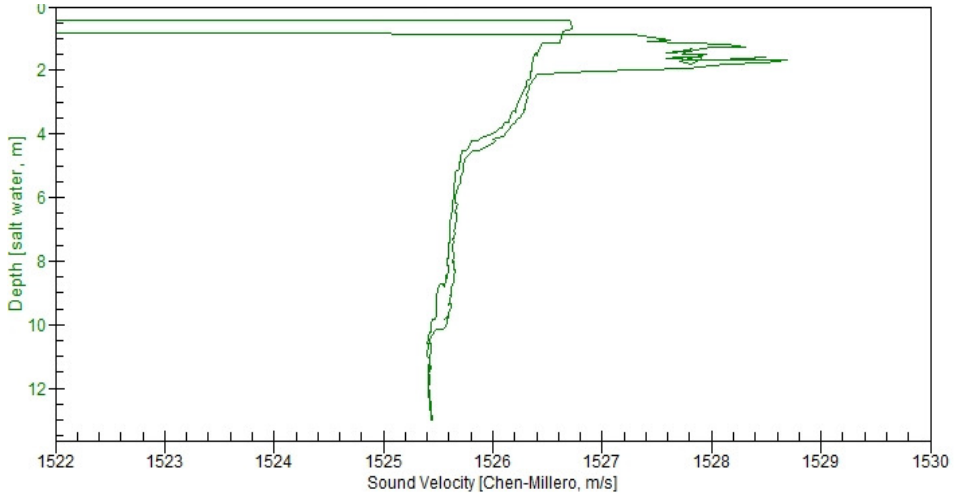

Figure A-8: Sound Speed Profile CTD Cast 4–11:16 am

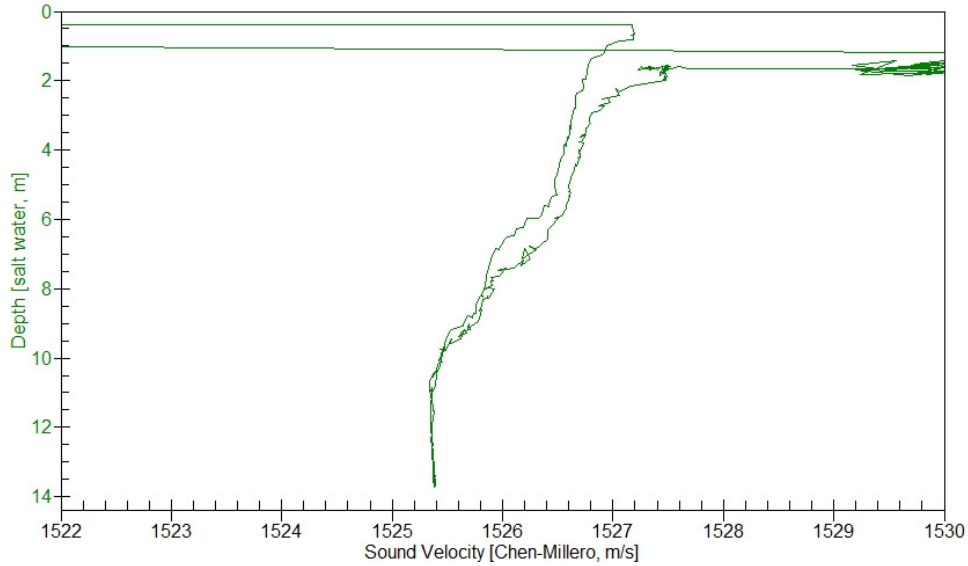

Figure A-9: Sound Speed Profile CTD Cast 5–12:37 pm

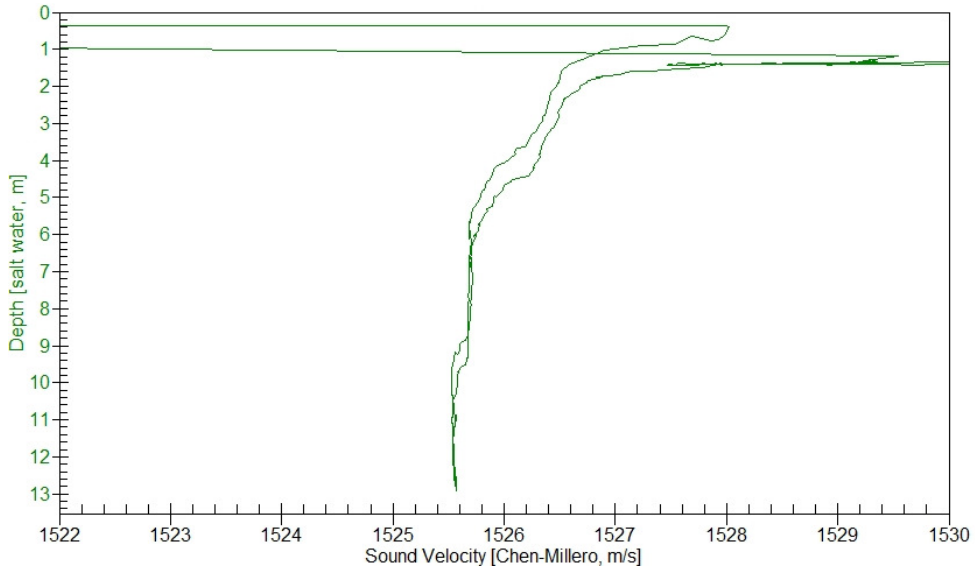

Figure A-10: Sound Speed Profile CTD Cast 6 – 1:35 pm

A.4 **Vessel pitch roll and heave notes**

(notes courtesy Dr Tim Gourlay)

COORDINATE SYSTEM

TSS 0.33m fwd of bulkhead, 0.70m to stbd of centreline

RTK GPS centre 0.5m aft of bulkhead

See also "equipment positions diagram.jpg"

Bulkhead 7.21m fwd of transom

"Midshsips" (based on length overall) 6.32m fwd of transom

See hull drawings

CG position unknown

TSS data files:

3 columns: pitch, roll, heave

pitch in degrees, positive bow-down

roll in degrees, positive to starboard

heave in metres, positive upwards

All synchronized and measured at 100Hz

RUN TIMES

all times WST

r1 0815 - 0820 approx, heading out to ship channel

r2 0851 - 0856 approx, drifting

following times within 1 second of GPS time, from TG watch, set against internet clock beforehand and checked against hummingbird GPS after.

r3 0907.03 - 0915.13 drifting stbd-to

r4 0916.10 - 0940.40

r5 0942.57 - 1029.43

r6 1033.09 - 1126.48

r7 1131.43 - 1231.11

r8 1236.57 - 1316.45

r9 1319.54 - 1402.23

r10 1419.50 - 1445.00 note large roll angles

wind initially 10-12kn ENE, died out by 1100

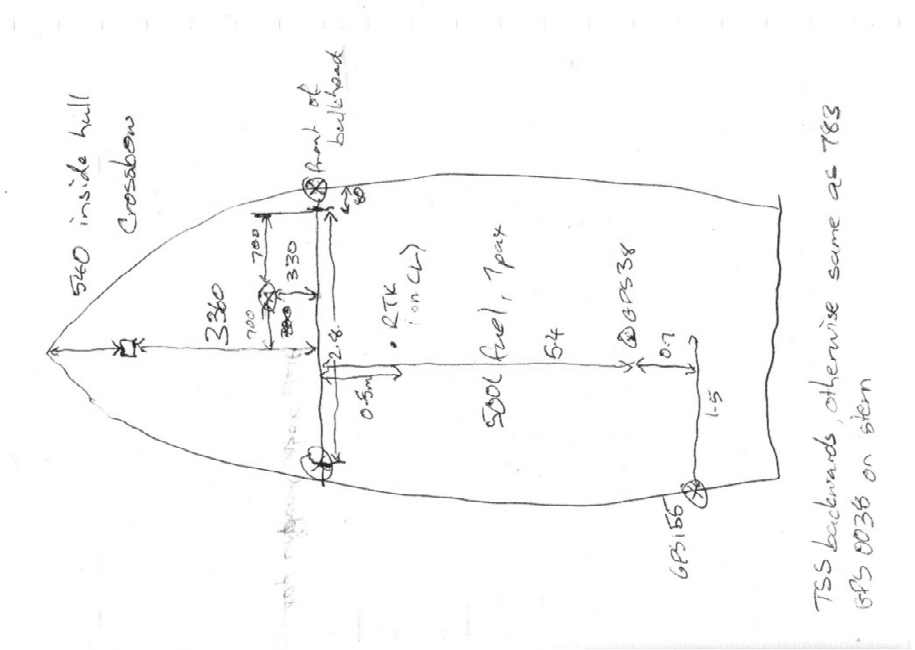

Appendix B **Rottnest channel probe trial data**

B.1 **Spectral shape of probe signals**

n4095 1.4 s sequence spectrum

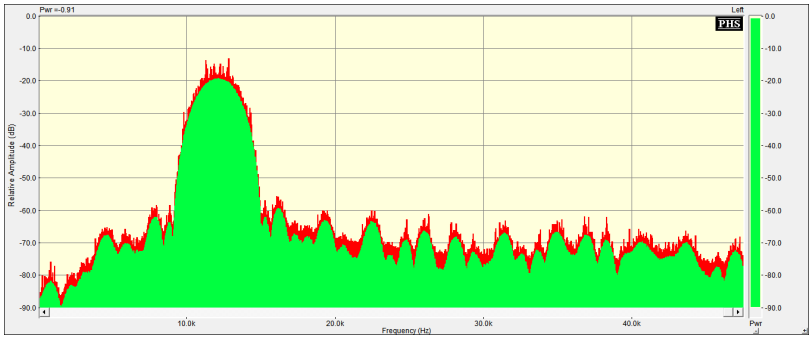

n63 21 ms sequence spectrum

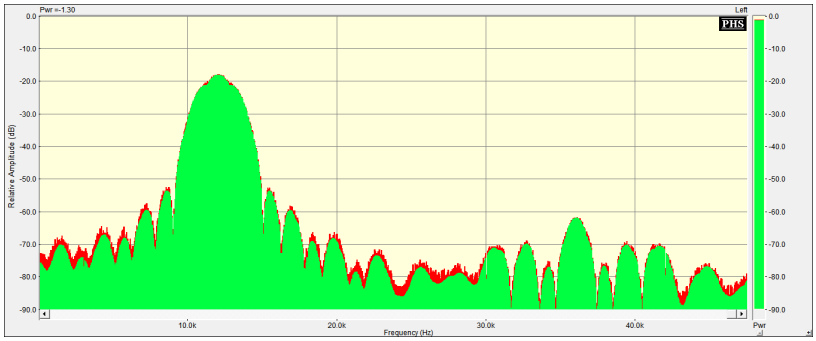

3min_8psk spectrum

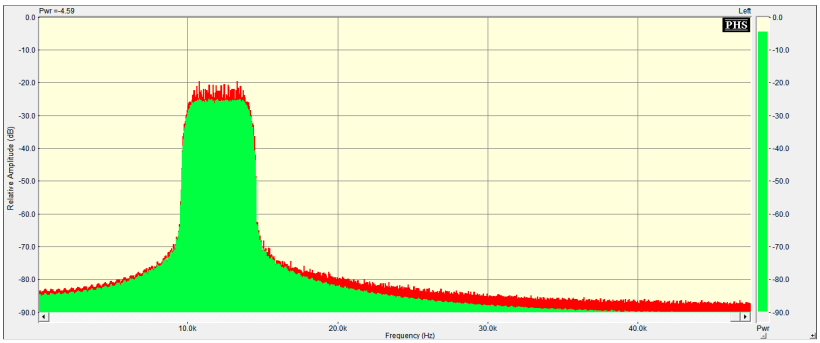

4min_qpsk spectrum

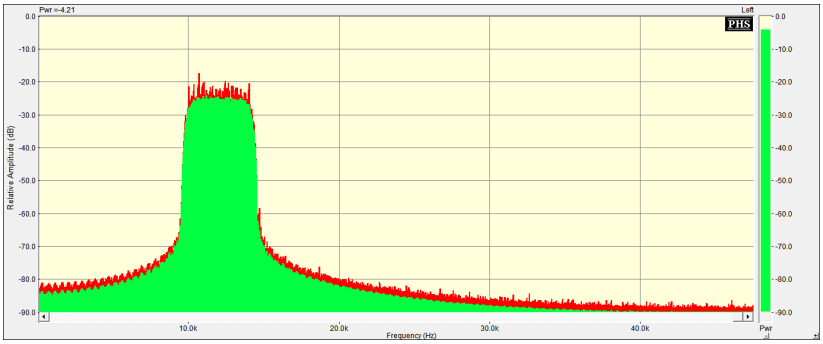

B.2 **Transmit and receive recording summary**

comment	transmit amplifier output attenuation	Transmit signal file name	**Transmit logger data** record File ID	CTD probe / Vessel PitchRollHeave reference	file length start	seconds	end	**Timing sweeps start** elapsed	start	day	**N63 start** elapsed	**N4095 start** elapsed	**Sweeps start** elapsed	**Goldcodes start** elapsed
			t--			sss.sss	hh:mm:ss	ss.ssss			ss.ssss	ss.ssss		ss.ssss
receive logger touchdown							time file modified							
on deck prior to deployment		10_sweeps_for_sync.wav	T51		8:44:41	37.239	8:45:18	8.4477	8:44:49	0.36446				
125m SSW of logger, 51m depth	(-40dB output)	125m_500m_rottnest.wav	T52	CTD1/TSS Dep01	9:34:34	667.927	9:45:42				4.7916	65.8508	126.91	187.9089
second cycle from 125m (too loud for receiver)	(-10dB output)	125m_500m_rottnest.wav	T53 (aborted)		9:34:34	667.927	9:45:42				757.422	818.4825	879.5427	940.5432
250m SSW of logger	(-15dB output)	125m_500m_rottnest.wav	T54	CTD2/TSS Dep02	9:57:32	667.927	10:08:40				9.1654	70.2252	131.285	192.2849
500m SSW of logger	(-15dB output)	125m_500m_rottnest.wav	T55	TSS Dep03	10:17:40	667.927	10:28:48				18.3128	79.3726	140.4323	201.4322
1km SSW of logger	(-15dB output)	1km_2km_rottnest.wav	T56	CTD3/TSS Dep04	10:37:08	667.927	10:48:16				56.3515	117.4113	178.471	239.4709
2km SSW of logger	(-15dB output)	1km_2km_rottnest.wav	T57	TSS Dep05	10:59:14	667.927	11:10:22				15.9601	77.02	138.0797	199.0795
4km SSW of logger	(-15dB output)	4km_rottnest.wav	T58	CTD4/TSS Dep06	11:25:00	667.927	11:36:08				10.531	71.5908	132.6505	193.6503
6km SSW of logger	(-15dB output)	6km_8km_rottnest.wav	T59	TSS Dep07	11:50:37	668.599	12:01:46				8.1002	69.16	130.2195	191.2194
8km SSW of logger	(-10dB output)	6km_8km_rottnest.wav	T60	CTD5/TSS Dep08	12:15:37	668.599	12:26:46				8.6226	69.6823	130.7419	191.7417
10km SSW of logger, 48m depth	(-10dB output)	10km_rottnest.wav	T61	CTD6/TSS Dep09	12:39:54	667.927	12:51:02				16.4703	77.1435	138.203	199.2029
6km SSW of logger, 51m depth	(-10dB output) amp switch late n63	6km_8km_rottnest.wav	T62	CTD7/TSS Dep10	13:08:43	668.599	13:19:52				17.266	77.4931	138.5527	199.5524
4km SSW of logger, 50.5m depth	(-10dB output)	4km_rottnest.wav	T63	CTD8/TSS Dep11	13:30:08	667.927	13:41:16				9.8708	70.9305	131.99	192.9898
1km SSW of logger, 52m depth	(-10dB output)	1km_2km_rottnest.wav	T64	CTD9/TSS Dep12	13:52:48	667.927	14:03:56				59.1126	120.1722	181.2318	242.2316
500m SSW of logger	(-10dB output)	125m_500m_rottnest.wav	T65	CTD10/TSS Dep13	14:11:30	667.927	14:22:38				10.8688	71.9285	132.988	193.9878
200m ESE of logger, drift from previous 51m to 50m depth	(-10dB output)	125m_500m_rottnest.wav	T66	TSS Dep14	14:23:54	667.927	14:35:02				9.9317	70.9914	132.051	193.0507
500m SSW of logger (returned to same point to be comparable to T65 but with transmitter inverted)	(-10dB output - invert transmitter)	125m_500m_rottnest.wav	T67	CTD11	15:00:02	667.927	15:11:10				26.4442	87.504	148.5635	209.5634
on deck after logger retrieval - completed ~4:28pm	(-10dB output)	10_sweeps_for_sync.wav	T71		16:28:01	82.591	16:29:24	65.2386	16:29:07	0.68688				

transmitter	Receive logger data				Timing sweeps start			starting	tx-rx clock	N63 sequence start		N4095 sequence start		sweeps start		Goldcodes start	
record File ID	file	Start	file length seconds	file end time	elapsed	clock	day	Flight time	deviation	elapsed	clock	elapsed	clock	elapsed	clock	elapsed	clock
t--	T----		ss.ssss	hh:mm:ss	ss.ssss			c (m/s)		ss.ssss		ss.ssss		ss.ssss		ss.ssss	
								1525									
	T1995	8:05:31	6225.366	9:49:16	2762.1	8:51:33	0.3691289 logger touchdown										
T51	T1995	8:05:31	6225.366	9:49:16	2348.103	8:44:39	0.3643372	0.000	-10.5								
T52	T1995	8:05:31	6225.366	9:49:16				0.094		4467.519	9:19:58	4528.572	9:20:59	4589.628	9:22:00	4650.63	9:23:01
	T1995	8:05:31	6225.366	9:49:16				0.127		5220.224	9:32:31	5281.3	9:33:32	5342.4	9:34:33	5403.39	9:35:34
T54	T1996	9:49:15	6225.352	11:33:00				0.176		477.738	9:57:12	538.794	9:58:13	599.85	9:59:14	660.845	10:00:15
T55	T1996	9:49:15	6225.352	11:33:00				0.323		1670.786	10:17:05	1731.845	10:18:06	1792.9034	10:19:08	1853.898	10:20:09
T56	T1996	9:49:15	6225.352	11:33:00				0.730		2854.544	10:36:49	2915.605	10:37:50	2976.667	10:38:51	3037.665	10:39:52
T57	T1996	9:49:15	6225.352	11:33:00				1.315		4156.799	10:58:31	4217.863	10:59:33	4278.921	11:00:34	4339.922	11:01:35
T58	T1996	9:49:15	6225.352	11:33:00				2.616		5733.425	11:24:48	5794.481	11:25:49	5855.555	11:26:50	5916.551	11:27:51
T59	T1997	11:33:01	6225.413	13:16:46				3.883		1044.556	11:50:25	1105.604	11:51:26	1166.648	11:52:27	1227.654	11:53:28
T60	T1997	11:33:01	6225.413	13:16:46				5.162		2533.223	12:15:14	2594.278	12:16:15	2655.343	12:17:16	2716.322	12:18:17
T61	T1997	11:33:01	6225.413	13:16:46				6.456		4006.723	12:39:47	4067.379	12:40:48	4128.425	12:41:49	4189.424	12:42:50
T62	T1997	11:33:01	6225.413	13:16:46				3.882		5727.171	13:08:28	5788.225	13:09:29	5849.267	13:10:30	5910.258	13:11:31
T63	T1998	13:16:45	6225.408	15:00:30				2.616		760.629	13:29:25	821.681	13:30:26	882.732	13:31:27	943.713	13:32:28
T64	T1998	13:16:45	6225.408	15:00:30				0.623		2148.833	13:52:33	2209.874	13:53:34	2270.917	13:54:36	2331.909	13:55:37
T65	T1998	13:16:45	6225.408	15:00:30				0.319		3262.629	14:11:07	3323.675	14:12:08	3384.724	14:13:09	3445.706	14:14:10
T66	T1998	13:16:45	6225.408	15:00:30				0.129		4015.265	14:23:40	4076.326	14:24:41	4137.387	14:25:42	4198.395	14:26:43
T67	T1998	13:16:45	6225.408	15:00:30				0.305		5345.412	14:45:50	5406.459	14:46:51	5467.501	14:47:52	5528.486	14:48:53
T71	T1999	15:00:31	6225.352	16:44:16	5304.864	16:28:56	0.6867536	0.000	-11.1								

transmitter record File ID	tx start northing	tx start easting	tx end northing	tx end easting	tx start radians	tx start radians	tx end radians	tx end radians	tx midpoint radians	tx midpoint radians	**N63 sequence** start txrx distance	end txrx distance	ave txrx distance	(m/s) txrx closing speed	(m) translation distance	(m/s) ave trans speed	ave txrx heading (deg of N)	ave boat heading (deg of N)
t--	logger touchdown										sequence length(s)=	60						
	-32.107605	115.39198			-0.56	2.01												
T51	-32.1076167	115.3919333	TG alt coords															
T52	-32.108685	115.39113	-32.108482	115.39107	-0.56	2.01	-0.56	2.01	-0.56	2.01	144.1	129.6	136.8	0.24	23.5	0.39	37	346
	-32.106537	115.39035	-32.106293	115.39025	-0.56	2.01	-0.56	2.01	-0.56	2.01	193.7	218.3	206.0	-0.41	29.3	0.49	130	341
T54	-32.10995	115.39125	-32.10981	115.39115	-0.56	2.01	-0.56	2.01	-0.56	2.01	269.1	256.9	263.0	0.20	19.1	0.32	16	329
T55	-32.11191	115.390724	-32.111816	115.39067	-0.56	2.01	-0.56	2.01	-0.56	2.01	492.1	483.3	487.7	0.15	12.0	0.20	14	334
T56	-32.117455	115.38973	-32.117382	115.3895	-0.56	2.01	-0.56	2.01	-0.56	2.01	1113.4	1109.8	1111.6	0.06	26.8	0.45	12	291
T57	-32.12494	115.38597	-32.12485	115.385864	-0.56	2.01	-0.56	2.01	-0.56	2.01	2005.1	1998.4	2001.7	0.11	15.4	0.26	17	315
T58	-32.142128	115.380165	-32.142	115.38002	-0.56	2.01	-0.56	2.01	-0.56	2.01	3989.1	3979.3	3984.2	0.16	21.5	0.36	16	316
T59	-32.15868	115.37375	-32.158558	115.37366	-0.56	2.01	-0.56	2.01	-0.56	2.01	5921.8	5911.3	5916.5	0.17	16.8	0.28	17	328
T60	-32.17555	115.36792	-32.17538	115.36789	-0.56	2.01	-0.56	2.01	-0.56	2.01	7872.5	7855.3	7863.9	0.29	19.2	0.32	17	352
T61	-32.19254	115.36177	-32.192337	115.36178	-0.56	2.01	-0.56	2.01	-0.56	2.01	9844.7	9822.8	9833.8	0.36	22.6	0.38	17	2
T62	-32.158943	115.37487	-32.15876	115.37488	-0.56	2.01	-0.56	2.01	-0.56	2.01	5920.2	5900.4	5910.3	0.33	20.3	0.34	16	3
T63	-32.14225	115.38068	-32.142017	115.3806	-0.56	2.01	-0.56	2.01	-0.56	2.01	3989.0	3966.1	3977.5	0.38	27.3	0.46	16	344
T64	-32.11594	115.3897	-32.1156	115.389786	-0.56	2.01	-0.56	2.01	-0.56	2.01	949.5	910.9	930.2	0.64	38.9	0.65	13	12
T65	-32.111958	115.39138	-32.111813	115.39132	-0.56	2.01	-0.56	2.01	-0.56	2.01	486.4	471.1	478.7	0.25	17.4	0.29	7	341
T66	-32.1088	115.39352	-32.1086	115.39362	-0.56	2.01	-0.56	2.01	-0.56	2.01	196.3	189.6	193.0	0.11	24.8	0.41	309	23
T67	-32.111763	115.3913	-32.11153	115.39133	-0.56	2.01	-0.56	2.01	-0.56	2.01	465.9	439.9	452.9	0.43	26.1	0.43	8	6
T71																		
	equatorial radius a(m)		6378137															
	polar radius b(m)		6356752.3															
	lat (degrees)		-31.198															
	radius (m)		6358742.13															
	mean earth radius(m)		6371009															

Note: due to pauses in the Tx record file, the time of transmission starts can not be pin-pointed from the Tx logger files. The GPS position of the boat at the start and end of each transmission is assumed to be much the same as the time of the Rx record (i.e. ignoring the flight time difference, which causes a maximum additional positional error of ~6.5s x 0.5m/s = 3.25m)

transmitter record File ID	**N4095 sequence** start txrx distance	end txrx distance	ave txrx distance	(m/s) txrx closing speed	(m) translation distance	(m/s) ave trans speed	ave txrx heading (deg of N)	ave boat heading (deg of N)	**Sweeps** start txrx distance	end txrx distance	ave txrx distance	(m/s) txrx closing speed	(m) translation distance	(m/s) ave trans speed	ave txrx heading (deg of N)	ave boat heading (deg of N)
t--	sequence length(s)= 60								sequence length(s)= 60							
T51																
T52	129.6	122.5	126.1	0.12	12.9	0.21	44	347	122.5	118.5	120.5	0.07	25.5	0.43	52	331
	218.3	235.9	227.1	-0.29	22.8	0.38	134	353	235.9	261.7	248.8	-0.43	29.2	0.49	137	343
T54	256.9	243.9	250.4	0.22	19.4	0.32	19	333	243.9	230.4	237.1	0.23	19.9	0.33	22	337
T55	483.3	472.4	477.8	0.18	14.5	0.24	15	336	472.4	452.3	462.3	0.33	22.0	0.37	16	353
T56	1109.8	1106.8	1108.3	0.05	14.4	0.24	12	296	1106.8	1097.3	1102.1	0.16	15.4	0.26	13	324
T57	1998.4	1994.1	1996.2	0.07	13.7	0.23	17	307	1994.1	1985.8	1989.9	0.14	15.5	0.26	17	322
T58	3979.3	3970.7	3975.0	0.14	20.2	0.34	17	314	3970.7	3956.2	3963.4	0.24	20.4	0.34	17	335
T59	5911.3	5892.5	5901.9	0.31	27.4	0.46	17	332	5892.5	5874.3	5883.4	0.30	24.6	0.41	17	337
T60	7855.3	7836.7	7846.0	0.31	22.1	0.37	17	345	7836.7	7818.2	7827.5	0.31	21.5	0.36	17	347
T61	9822.8	9798.1	9810.5	0.41	25.9	0.43	17	0	9798.1	9790.9	9794.5	0.12	17.3	0.29	17	314
T62	5900.4	5885.8	5893.1	0.24	17.7	0.30	16	343	5885.8	5848.6	5867.2	0.62	39.8	0.66	16	355
T63	3966.1	3956.5	3961.3	0.16	9.7	0.16	16	6	3956.5	3942.7	3949.6	0.23	16.7	0.28	16	42
T64	910.9	873.6	892.3	0.62	42.2	0.70	13	33	873.6	856.1	864.9	0.29	22.7	0.38	12	44
T65	471.1	430.8	451.0	0.67	48.5	0.81	6	34	430.8	397.4	414.1	0.56	36.3	0.61	4	23
T66	189.6	194.7	192.2	-0.08	41.5	0.69	300	37	194.7	207.8	201.2	-0.22	35.9	0.60	290	43
T67	439.9	409.2	424.5	0.51	38.1	0.64	7	37	409.2	365.6	387.4	0.73	46.9	0.78	5	22
T71																

transmitter record File ID	**Goldcodes** start txrx distance	end txrx distance	ave txrx distance	(m/s) txrx closing speed	(m) translation distance	(m/s) ave trans speed	ave txrx heading (deg of N)	ave boat heading (deg of N)
t--	sequence length(s)=	60						
T51								
T52	118.5	115.5	117.0	0.05	19.6	0.33	62	341
	261.7	274.7	268.2	-0.22	13.9	0.23	139	325
T54	230.4	216.3	223.3	0.24	20.4	0.34	26	341
T55	454.0	448.5	451.3	0.09	15.3	0.25	18	312
T56	1097.3	1083.1	1090.2	0.24	19.0	0.32	14	334
T57	1985.8	1980.9	1983.4	0.08	23.2	0.39	18	301
T58	3956.2	3951.0	3953.6	0.09	14.9	0.25	17	310
T59	5874.3	5858.5	5866.4	0.26	19.2	0.32	17	344
T60	7818.2	7805.4	7811.8	0.21	15.0	0.25	17	347
T61	9790.9	9771.5	9781.2	0.32	22.3	0.37	17	348
T62	5848.6	5810.1	5829.4	0.64	39.9	0.66	16	1
T63	3942.7	3896.6	3919.7	0.77	46.9	0.78	16	6
T64	856.1	816.0	836.1	0.67	40.7	0.68	12	2
T65	397.4	362.5	379.9	0.58	37.3	0.62	2	20
T66	207.8	221.3	214.5	-0.23	25.6	0.43	283	49
T67	365.6	332.5	349.0	0.55	36.5	0.61	3	23
T71								

B.3 **Rottnest Trial Field Notes**

- All recorders 96ks/s at 24bit depth •
- Seabed logger SD722 channel 1 connected to TC4033 hydrophone 1m above seabed, with sensitivity -203dB re: 1µPa/V @ 1m, +40dB preamp gain, +3dB SD722 ch1 recorder gain, overall system sensitivity -160dB re: 1µPa/V @ 1m
- Seabed logger SD722 channel 2 connected to TC4034 hydrophone 1.5m above seabed, with sensitivity -218dB re: 1µPa/V @ 1m, +40dB preamp gain, +18dB SD722 ch2 recorder gain, overall system sensitivity -160dB re: 1µPa/V @ 1m
- Loggers synchronised to the second with GPS time
- Transmitter record hydrophone positioned 1m above centre of CTG transmitter element, with transmitter primary axis directed towards surface
- Nominal transmitter depth indicated by cable markings = 20m. Variable drift caused non-vertical transmitter suspension. More accurate transmitter depth (and depth to bottom) can be determined from sequence and chirp surface and bottom returns.
- Chirp spatial ambiguity ~0.1m, sequence spatial ambiguity ~0.25m.

Approx. Start Position	Transmit player Wav file (SD744T, before amplifier)	SD744T output atten.	Transmit signal description	Transmit Recording File (hydrophone 1m above transmitter centre)	Tx recorder input gain - dB (SD702)	Tx recording sensitivity (SD702)	Comment
on deck prior to deployment	10_sweeps_for_sync.wav	-40dB	3 groups of 10 x 8-16kHz 16ms chirps	T50	0	-206dB re: 1µPa/V @ 1m	all 3 hydrophones simultaneously touched to CTG transmitter - but signal too faint for recorder
on deck prior to deployment	10_sweeps_for_sync.wav	-40dB	3 groups of 10 x 8-16kHz 16ms chirps	T51	50	-156dB re: 1µPa/V @ 1m	as above - signal OK
125m SSW of logger, 51m depth	125m_500m_rottnest.wav	-40dB for first transmit cycle, -10dB for second transmit cycle	60s (2860 repeats) of 63bit 21ms M-sequence x 12kHz CW carrier, 2s gap, 60s (44 repeats) of 4095bit 1.36s M-sequence x 12kHz CW carrier, 2s gap, 60s of 16ms 8-16kHz sweep at **200ms** intervals, 2s gap 60s (**360** repeats) of 168ms **8** x 63bit gold code set x 12kHz CW carrier, 2s gap 4 minutes 'v4qpsk.wav', 3 minutes 'v38psk.wav'	T52	30	-176dB re: 1µPa/V @ 1m	CTD scan 9:38am to 9:46am , Tx stopped end of v4qpsk as amp was getting V hot and smelling for first time
250m SSW of logger	125m_500m_rottnest.wav	-15dB	as above	T54	30	-176dB re: 1µPa/V @ 1m	CTD scan 9:58am to 10:07am
500m SSW of logger	125m_500m_rottnest.wav	-15dB	as above	T55	30	-176dB re: 1µPa/V @ 1m	
1km SSW of logger	1km_2km_rottnest.wav	-15dB	60s (2860 repeats) of 63bit 21ms M-sequence x 12kHz CW carrier, 2s gap, 60s (44 repeats) of 4095bit 1.36s M-sequence x 12kHz CW carrier, 2s gap , 60s of 16ms 8-	T56	30	-176dB re: 1µPa/V @ 1m	CTD scan 10:38am to 10:46am

Approx. Start Position	Transmit player Wav file (SD744T, before amplifier)	SD744T output atten.	Transmit signal description	Transmit Recording File (hydrophone 1m above transmitter centre)	Tx recorder input gain - dB (SD702)	Tx recording sensitivity (SD702)	Comment
			16kHz sweep at **100ms** intervals, 2s gap, 60s (**720** repeats) of 84ms **4** x 63bit gold code set x 12kHz CW carrier, 2s gap, 4 minutes 'v4qpsk.wav', 3 minutes 'v38psk.wav'				
2km SSW of logger	1km_2km_rottnest.wav	-15dB	as above	T57	30	-176dB re: 1µPa/V @ 1m	
4km SSW of logger	4km_rottnest.wav	-15dB	60s (2860 repeats) of 63bit 21ms M-sequence x 12kHz CW carrier, 2s gap, 60s (44 repeats) of 4095bit 1.36s M-sequence x 12kHz CW carrier, 2s gap, 60s of 16ms 8-16kHz sweep at **50ms** intervals, 2s gap, 60s (**1440** repeats) of 168ms **2** x 63bit gold code set x 12kHz CW carrier, 2s gap, 4 minutes 'v4qpsk.wav', 3 minutes 'v38psk.wav'	T58	30	-176dB re: 1µPa/V @ 1m	CTD scan ??? to 11:34am
6km SSW of logger	6km_8km_rottnest.wav	-15dB (amplifier RMS output voltage = 16.75V for first sequence)	60s (2860 repeats) of 63bit 21ms M-sequence x 12kHz CW carrier, 2s gap, 60s (44 repeats) of 4095bit 1.36s M-sequence x 12kHz CW carrier, 2s gap , 60s of 16ms 8-16kHz sweep at **50ms** intervals, 2s gap, 60s (**1440** repeats) of 168ms **2** x 63bit gold code set x 12kHz CW carrier, 2s gap, 4 minutes 'v7bpsk.wav', 3 minutes 'v4qpsk.wav'	T59	30	-176dB re: 1µPa/V @ 1m	

Approx. Start Position	Transmit player Wav file (SD744T, before amplifier)	SD744T output atten.	Transmit signal description	Transmit Recording File (hydrophone 1m above transmitter centre)	Tx recorder input gain - dB (SD702)	Tx recording sensitivity (SD702)	Comment
8km SSW of logger	6km_8km_rottnest.wav	-10dB (but little change to amplifier RMS output voltage = 17.9V for first sequence)	as above	T60	30	-176dB re: 1µPa/V @ 1m	CTD scan 12:15pm to 12:24pm
10km SSW of logger, 48m depth	10km_rottnest.wav	-10dB	60s (2860 repeats) of 63bit 21ms M-sequence x 12kHz CW carrier, 2s gap, 60s (44 repeats) of 4095bit 1.36s M-sequence x 12kHz CW carrier, 2s gap, 60s of 16ms 8-16kHz sweep at **50ms** intervals, 2s gap, 60s (**1440** repeats) of 42ms **2** x 63bit gold code set x 12kHz CW carrier, 2s gap, 7 minutes 'v7bpsk.wav'	T61	30	-176dB re: 1µPa/V @ 1m	CTD scan 12:40pm to 12:49pm
6km SSW of logger, 51m depth	6km_8km_rottnest.wav	-10dB	60s (2860 repeats) of 63bit 21ms M-sequence x 12kHz CW carrier, 2s gap, 60s (44 repeats) of 4095bit 1.36s M-sequence x 12kHz CW carrier, 2s gap, 60s of 16ms 8-16kHz sweep at **50ms** intervals, 2s gap, 60s (**1440** repeats) of 42ms **2** x 63bit gold code set x 12kHz CW carrier, 2s gap, 4	T62	30	-176dB re: 1µPa/V @ 1m	CTD scan ??? To 1:16pm

Approx. Start Position	Transmit player Wav file (SD744T, before amplifier)	SD744T output atten.	Transmit signal description	Transmit Recording File (hydrophone 1m above transmitter centre)	Tx recorder input gain - dB (SD702)	Tx recording sensitivity (SD702)	Comment
			minutes 'v7bpsk.wav', 3 minutes 'v4qpsk.wav',				
4km SSW of logger, 50.5m depth	4km_rottnest.wav	-10dB	60s (2860 repeats) of 63bit 21ms M-sequence x 12kHz CW carrier, 2s gap, 60s (44 repeats) of 4095bit 1.36s M-sequence x 12kHz CW carrier, 2s gap, 60s of 16ms 8-16kHz sweep at **50ms** intervals, 2s gap, 60s (**1440** repeats) of 42ms **2** x 63bit gold code set x 12kHz CW carrier, 2s gap, 4 minutes 'v4qpsk.wav', 3 minutes 'v38psk.wav'	T63	30	-176dB re: 1µPa/V @ 1m	CTD done
1km SSW of logger, 52m depth	1km_2km_rottnest.wav	-10dB	60s (2860 repeats) of 63bit 21ms M-sequence x 12kHz CW carrier, 2s gap, 60s (44 repeats) of 4095bit 1.36s M-sequence x 12kHz CW carrier, 2s gap, 60s of 16ms 8-16kHz sweep at **100ms** intervals, 2s gap, 60s (**720** repeats) of 84ms **4** x 63bit gold code set x 12kHz CW carrier, 2s gap, 4 minutes 'v4qpsk.wav', 3 minutes 'v38psk.wav'	T64	30	-176dB re: 1µPa/V @ 1m	CTD scan ??? to 2pm

Approx. Start Position	Transmit player Wav file (SD744T, before amplifier)	SD744T output atten.	Transmit signal description	Transmit Recording File (hydrophone 1m above transmitter centre)	Tx recorder input gain - dB (SD702)	Tx recording sensitivity (SD702)	Comment
500m SSW of logger	125m_500m_rottnest.wav	-10dB	60s (2860 repeats) of 63bit 21ms M-sequence x 12kHz CW carrier, 2s gap, 60s (44 repeats) of 4095bit 1.36s M-sequence x 12kHz CW carrier, 2s gap, 60s of 16ms 8-16kHz sweep at **200ms** intervals, 2s gap, 60s (**360** repeats) of 168ms **8** x 63bit gold code set x 12kHz CW carrier, 2s gap, 4 minutes 'v4qpsk.wav', 3 minutes 'v38psk.wav'	T65	30	-176dB re: 1µPa/V @ 1m	CTD scan 2:10pm to 2:20pm
continued drift from previous 51m to 50m depth	125m_500m_rottnest.wav	-10dB	as above - ~2:23pm start	T66	30		
500m SSW of logger (returned to same point to be comparable to T65 but with transmitter inverted)	125m_500m_rottnest.wav	-10dB	as above	T67	30	-176dB re: 1µPa/V @ 1m	CTD scan ??? to 2:37pm , NB. transmitter inverted, 18cm shorter depth below water, & 18cm shorter distance between hydrphone and centre of transmitter recorded level ~ 2dB lower due to tx directivity

Approx. Start Position	Transmit player Wav file (SD744T, before amplifier)	SD744T output atten.	Transmit signal description	Transmit Recording File (hydrophone 1m above transmitter centre)	Tx recorder input gain - dB (SD702)	Tx recording sensitivity (SD702)	Comment
on deck after logger retrieval	10_sweeps_for_sync.wav	-10dB	3 groups of 10 x 8-16kHz 16ms chirps	T67 (as above)	30	-176dB re: 1µPa/V @ 1m	all 3 hydrophones simultaneously touched to CTG transmitter - hard to hear chirps above the engine noise
on deck after logger retrieval - completed ~4:28pm	10_sweeps_for_sync.wav	-10dB	3 groups of 10 x 8-16kHz 16ms chirps	T67 (as above)	50	-156dB re: 1µPa/V @ 1m	as above with engine backed off

B.4 **Visual summary of receiver recordings**

- All spectrograms 131072 sample (1.36s) FFT, 5-20 kHz range, uncalibrated dB psd units
- NB: the full extent of 7minute communication signal stream (5th part of transmission signal) is not included in plots.

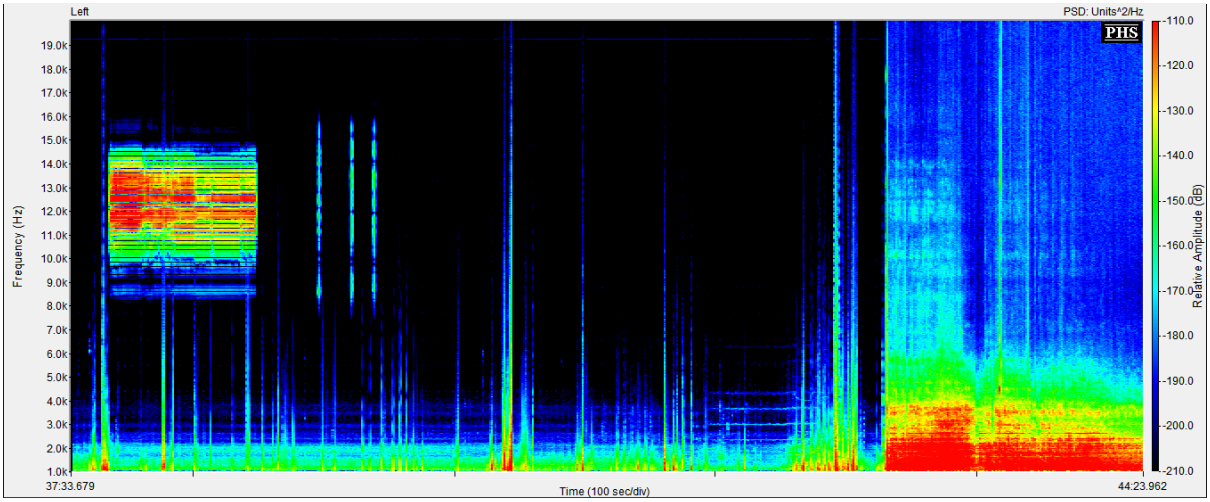

Figure B-1: T51 start sync chirps on deck T1995 ~39 mins – Logger touchdown 46 mins, 2.1 s

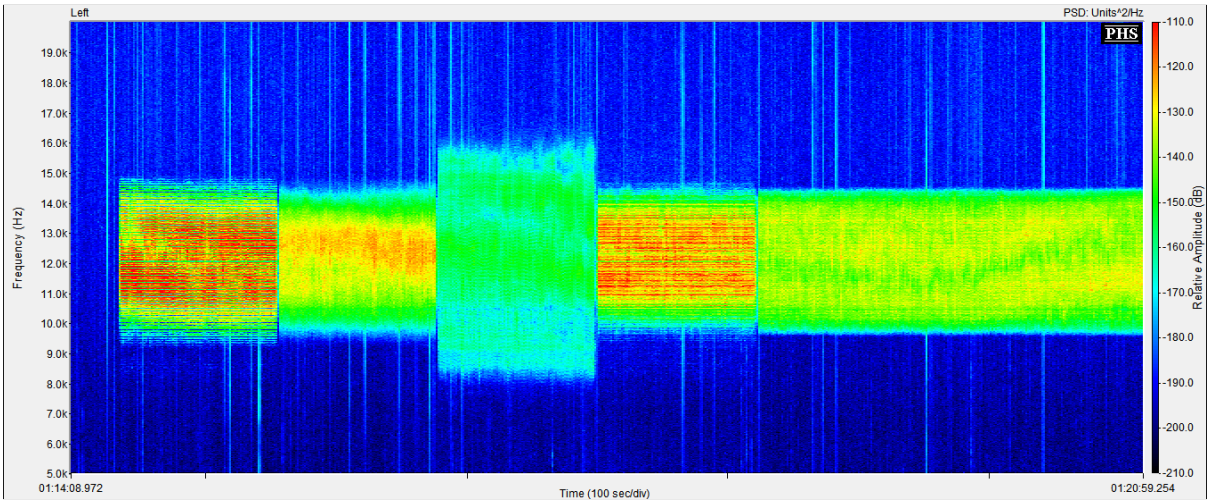

Figure B-2: T52 125 m Rx T1995, -40 dB tx output – trans. start ~1:14 mins, 43 dB SNR

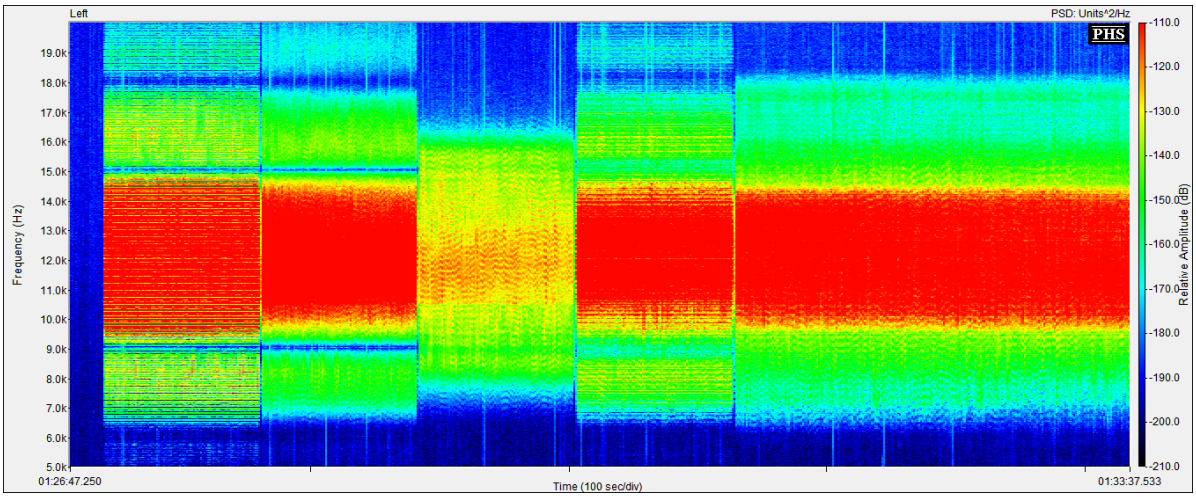

Figure B-3: T52 2nd cycle of 125 m Rx T1995, -10 dB tx output –start ~1:27 mins, 78 dB SNR

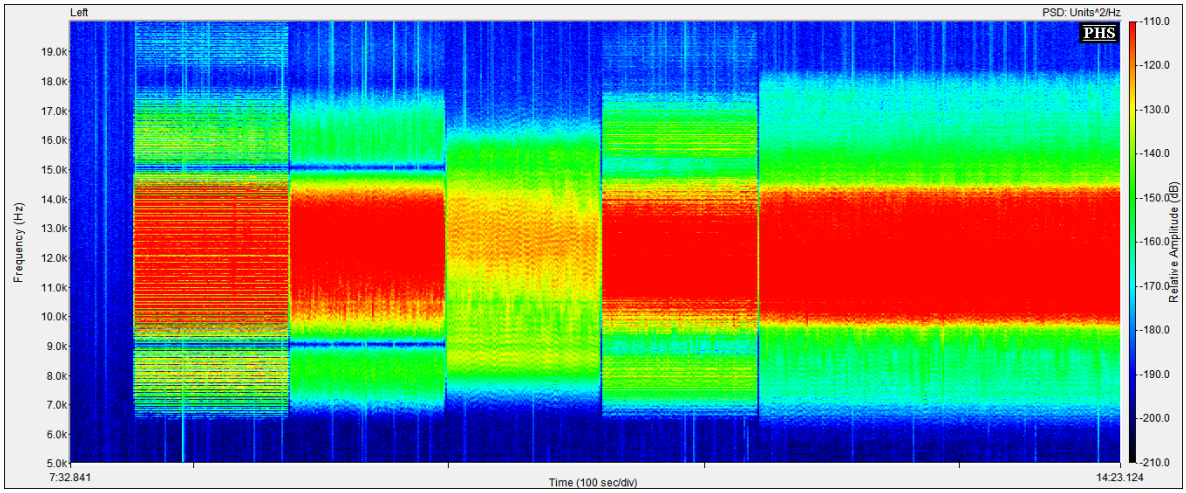

Figure B-4: T54 250 m Rx T1996, -15 dB tx output –start ~7 mins 56 s, 81 dB SNR

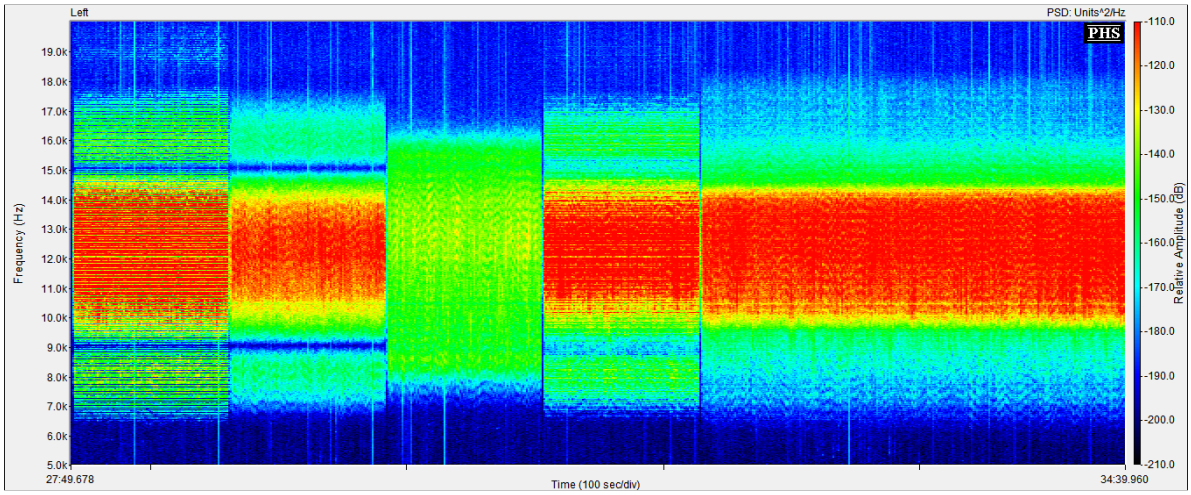

Figure B-5: T55 500 m Rx T1996, -15 dB tx output –start ~27 mins 49 s, 68 dB SNR

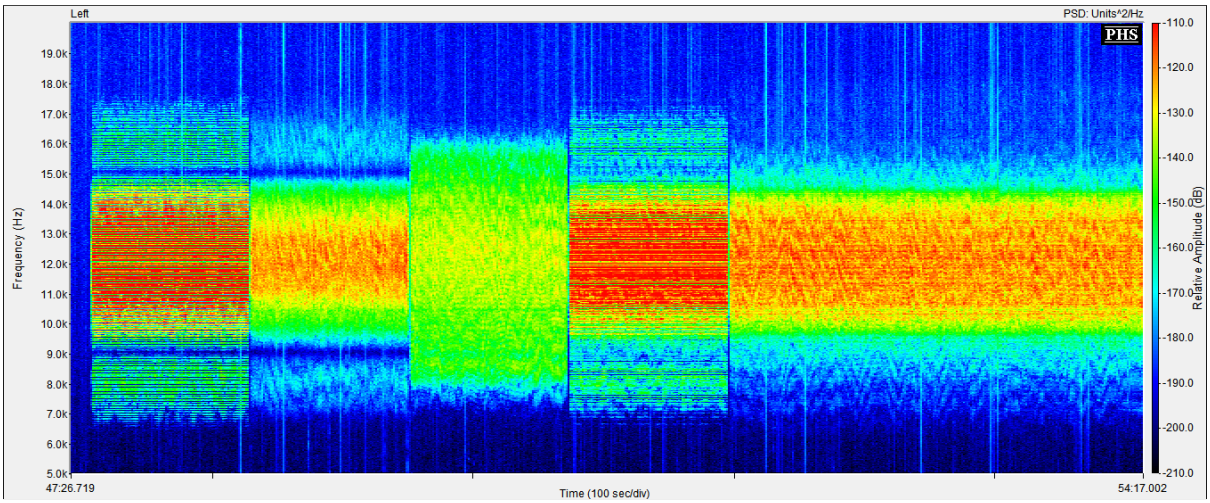

Figure B-6: T56 1000 m Rx T1996, -15 dB tx output –start ~47 mins 33 s, 58 dB SNR

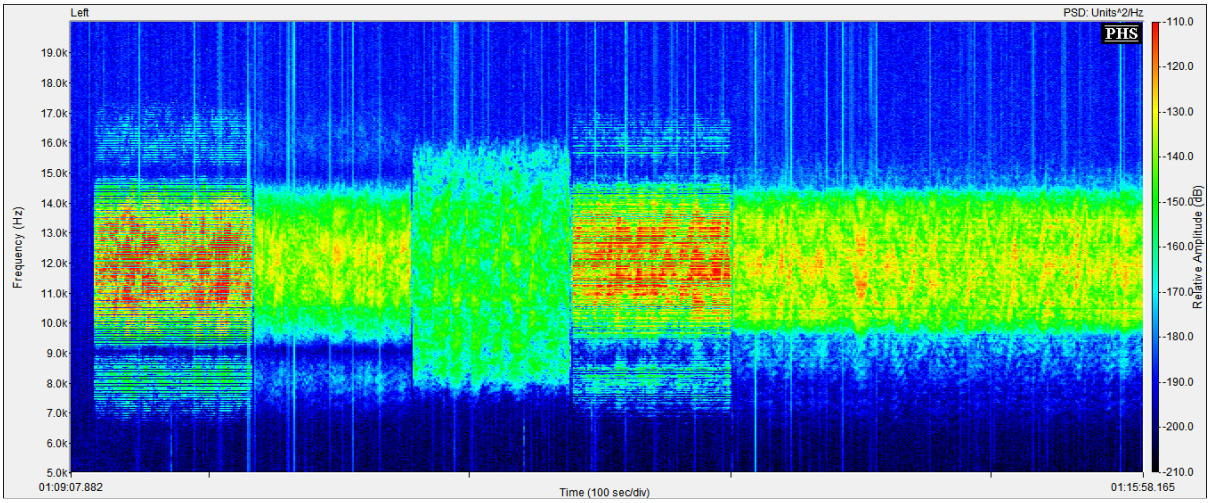

Figure B-7: T57 2000 m Rx T1996, -15 dB tx output –start ~1:09:15 s, 44 dB SNR

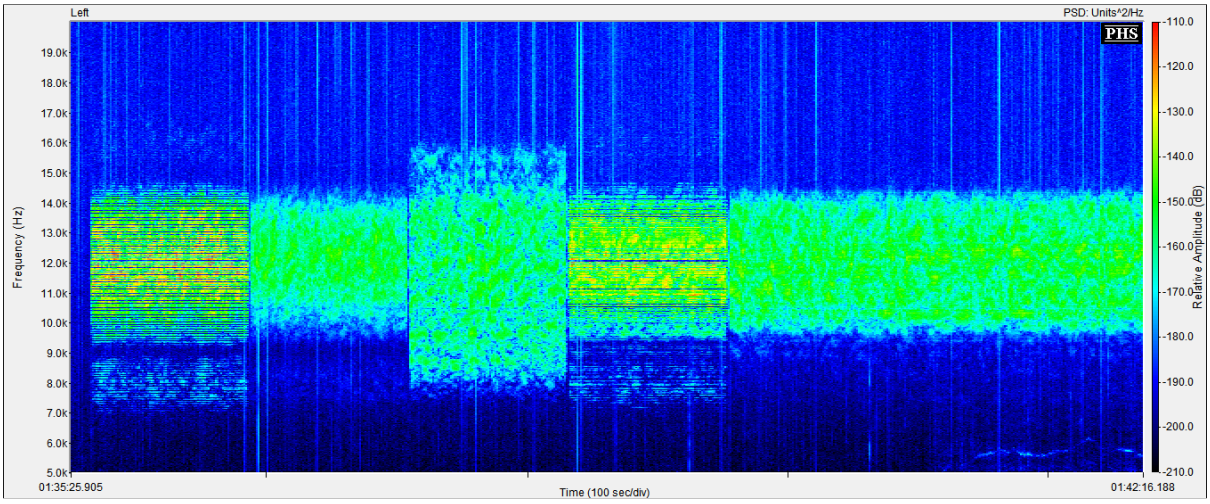

Figure B-8: T58 4000 m Rx T1996,-15 dB tx output - start ~1:43:45s,~23 dB SNR

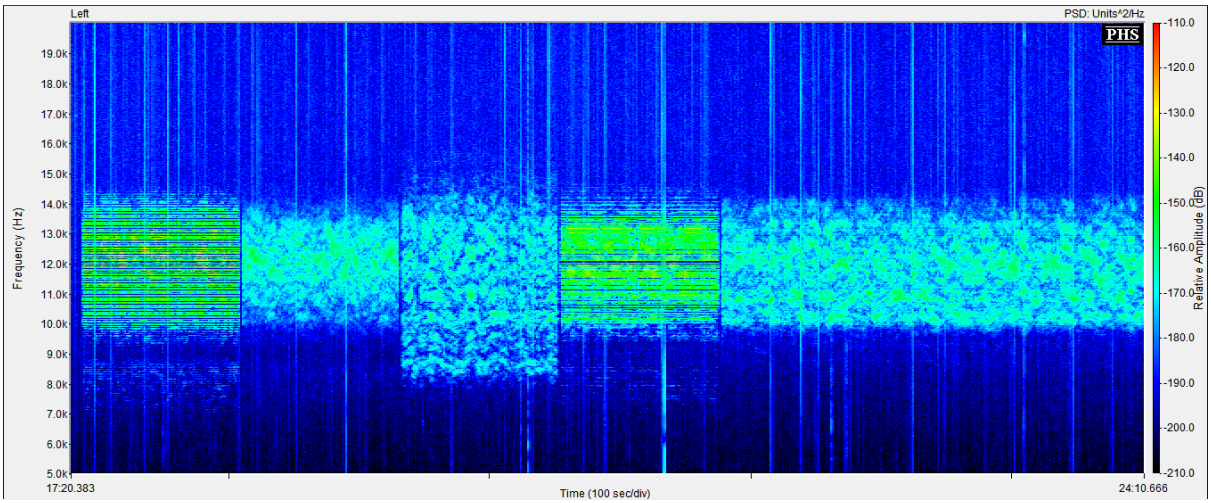

Figure B-9: T59 6000 m Rx T1997, -15 dB tx output –start ~0:17:23 s,~13 dB SNR

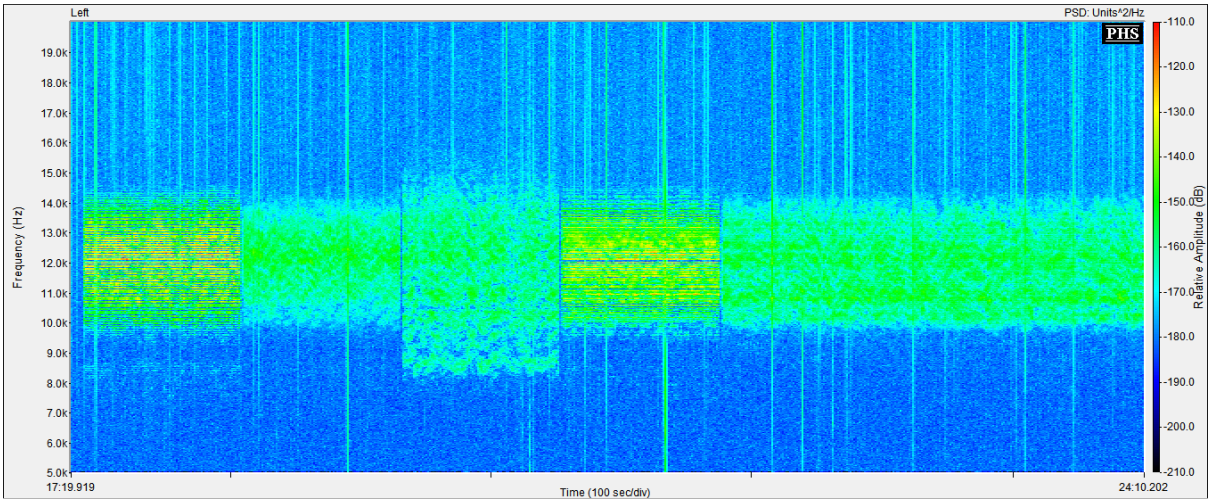

Figure B-10: T59 as above for 6000 m Rx T1997, but Channel 2 TC 4034 hydrophone

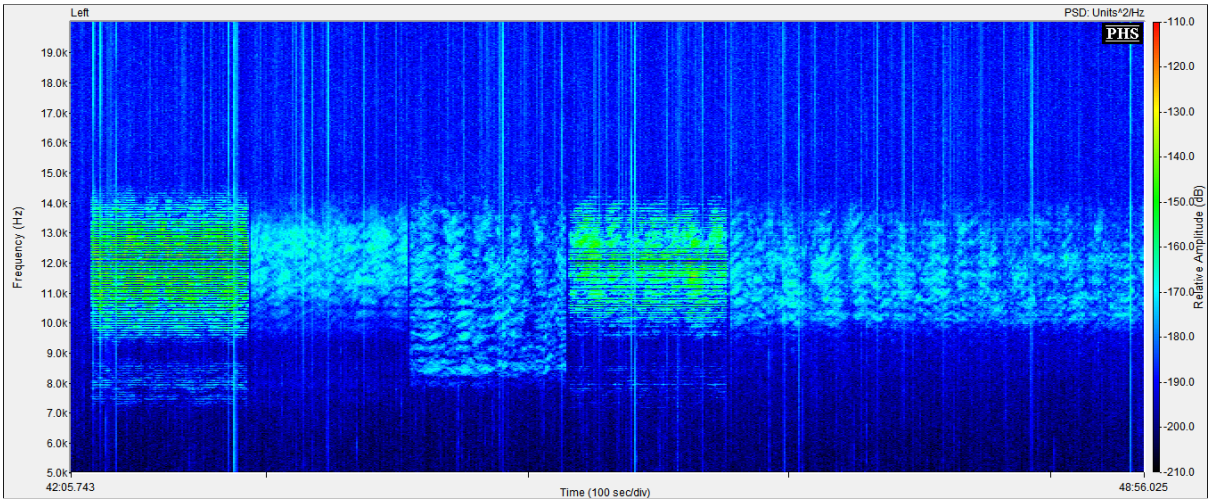

Figure B-11: T60 8000 m Rx T1997, -10 dB tx output –start ~0:42:10 s,~3 dB SNR

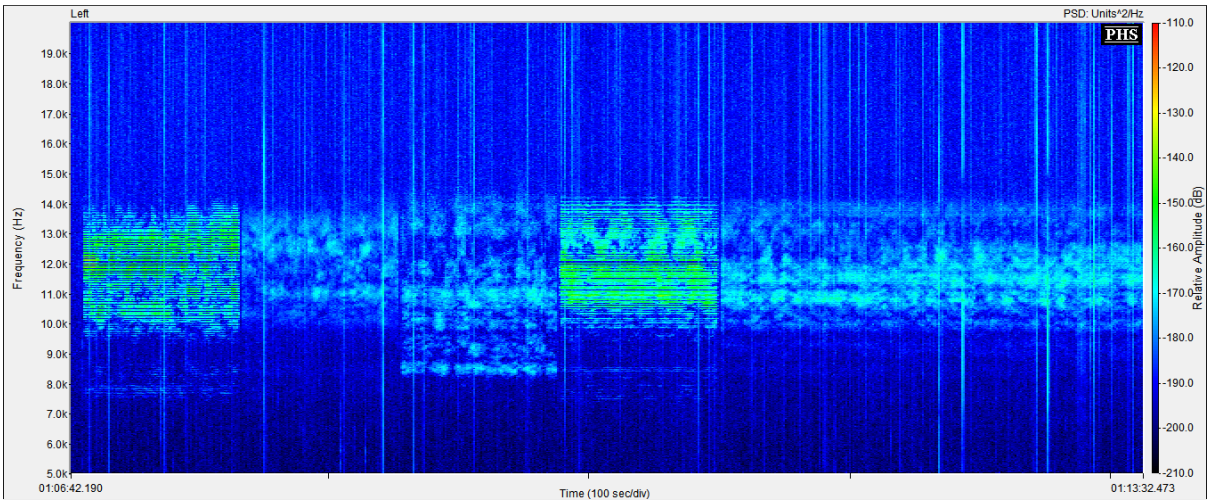

Figure B-12: T61 10,000 m Rx T1997, -10 dB tx output –start ~1:06:46 s,~3 dB SNR

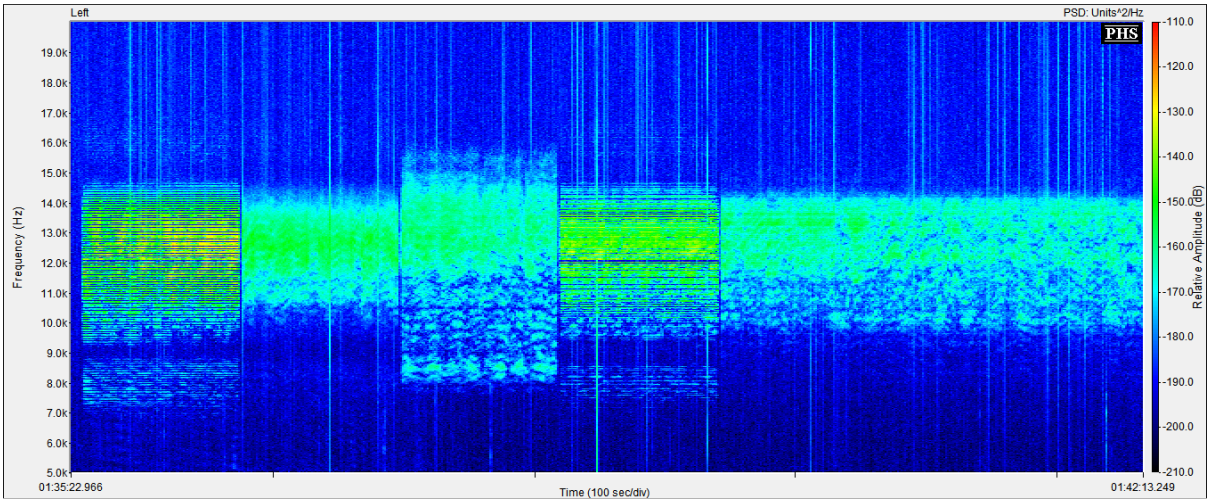

Figure B-13: T62 6000 m Rx T1997, -10 dB tx output –start ~1:35:26 s

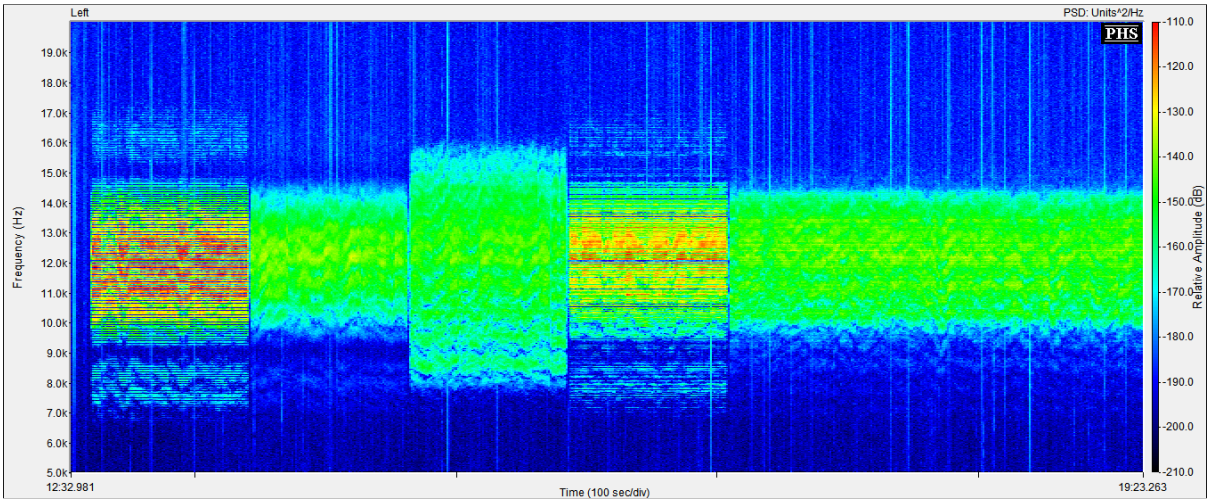

Figure B-14: T63 4000 m Rx T1998, -10 dB tx output –start ~0:12:39 s

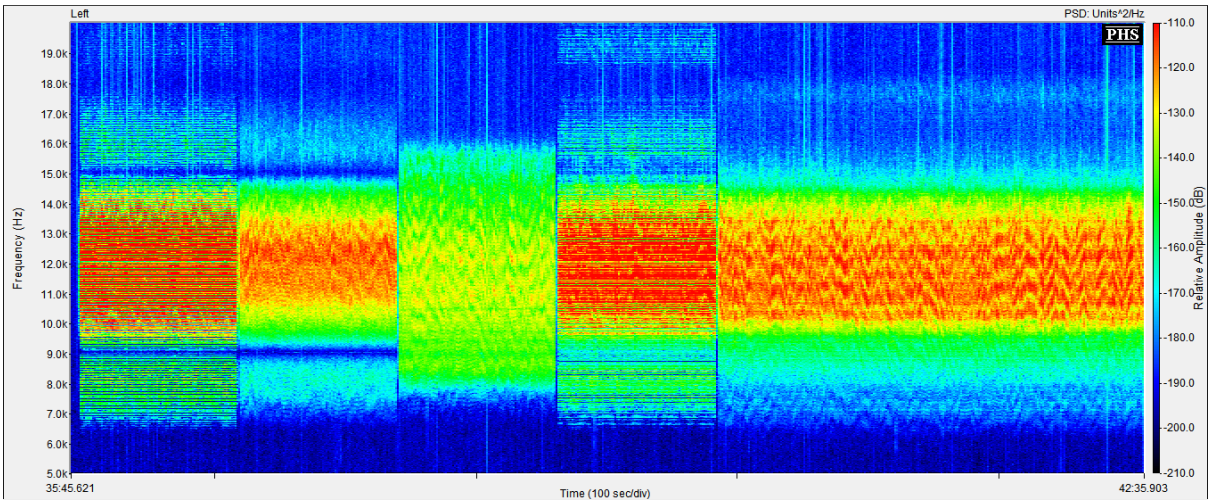

Figure B-15: T64 1000 m Rx T1998, -10 dB tx output –start ~0:37:04 s

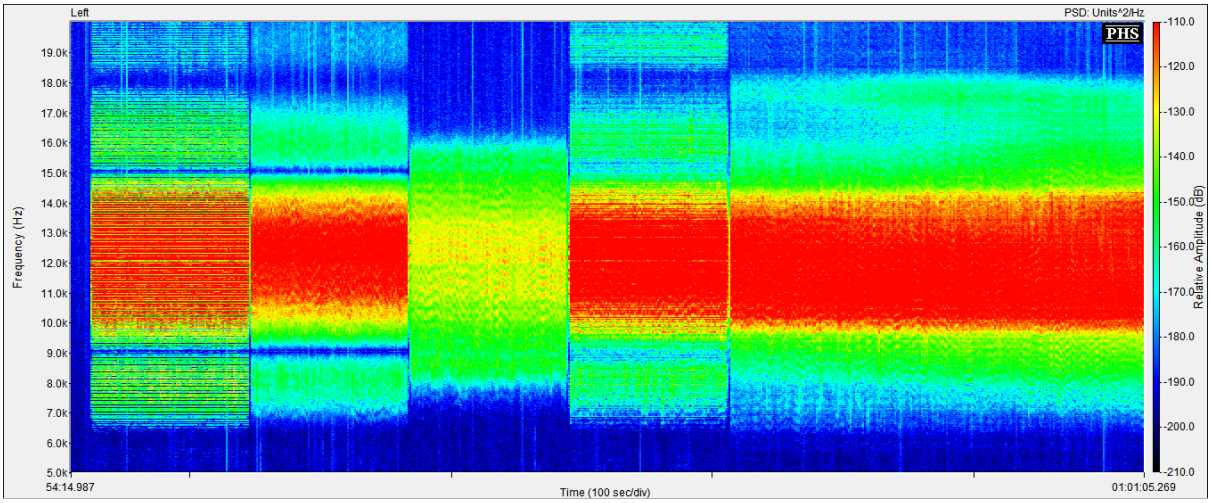

Figure B-16: T65 500 m Rx T1998, -10 dB tx output –start ~0:54:21 s

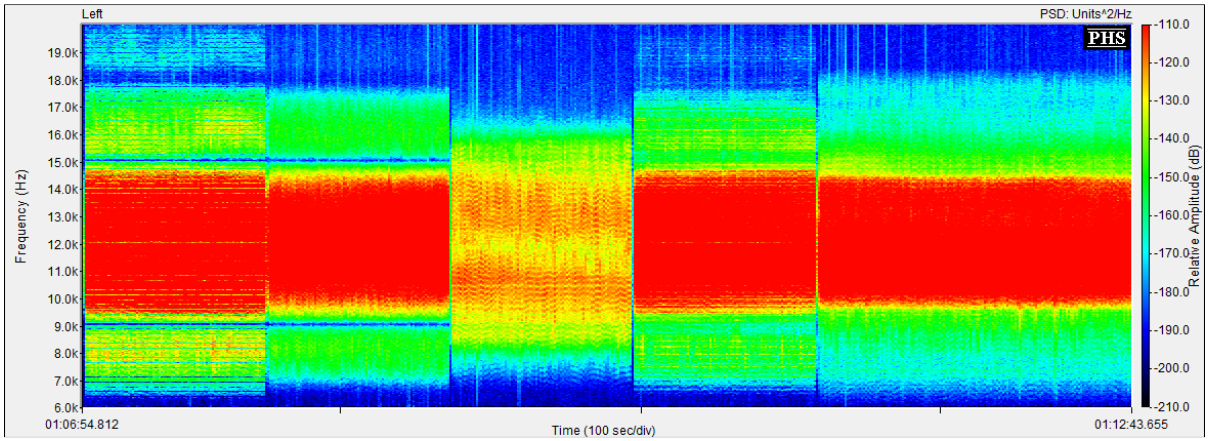

Figure B-17: T66 200 m Rx T1998, -10 dB tx output –start ~1:06:54 s

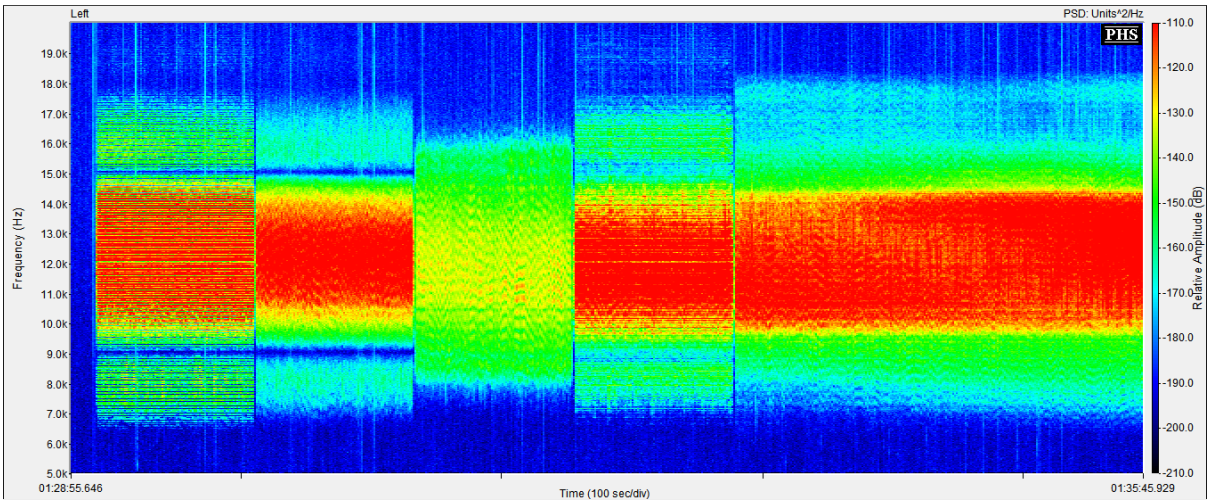

Figure B-18: T67 500 m Rx T1998, -10 dB tx output –start ~1:29:03 s, inverted transmitter

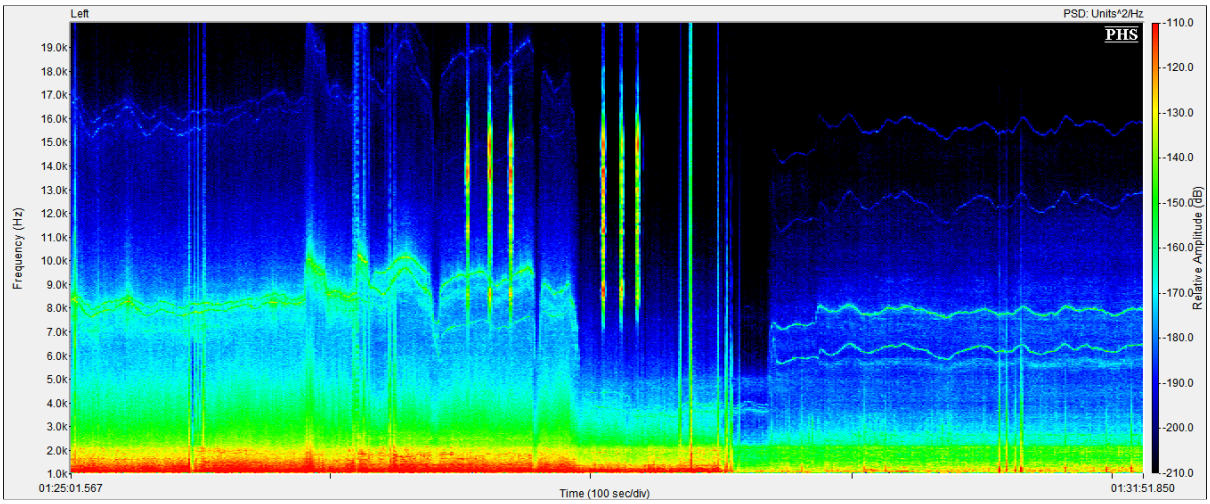

Figure B-19: T71 Synchronisation chirps on deck T1999 ~1:28:23 s second set of chirps with lower engine noise

B.5 **CTD probe sound speed profiles**

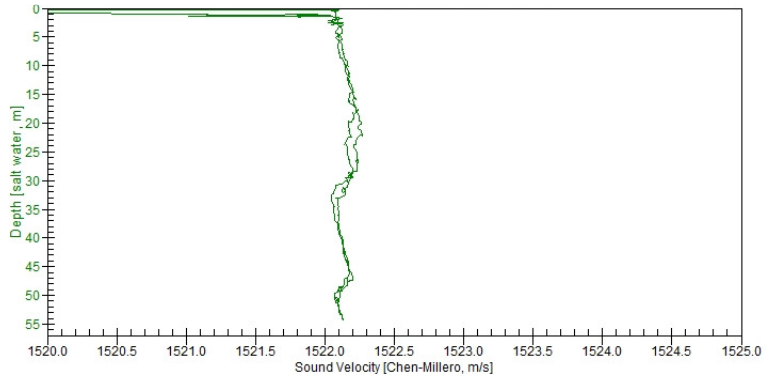

Figure B-20: Sound speed profile CTD Cast 1 – 9:38 am – 125 m range

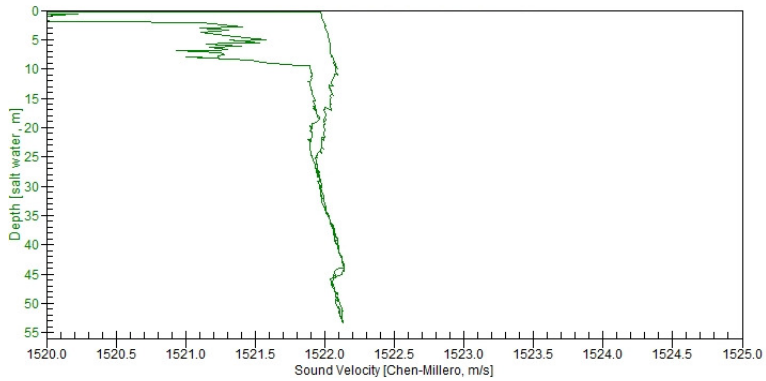

Figure B-21: Sound speed profile CTD Cast 2 – 9:58 am – 250 m range

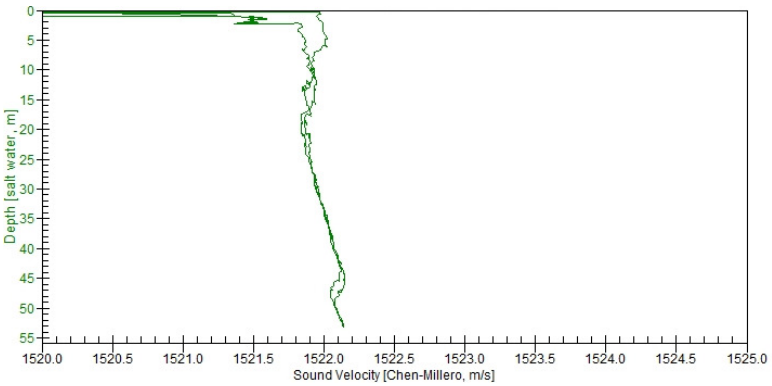

Figure B-22: Sound speed profile CTD Cast 3 – 10:37 am – 1 km range

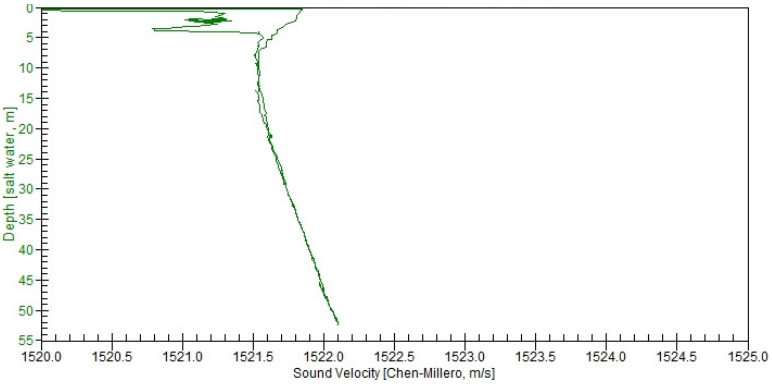

Figure B-23: Sound speed profile CTD Cast 4 – 11:25 am – 4 km range

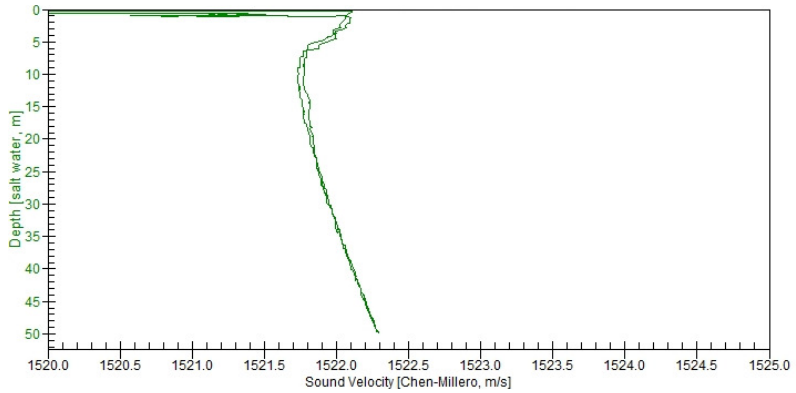

Figure B-24: Sound speed profile CTD Cast 5 – 12:15 pm – 8 km range

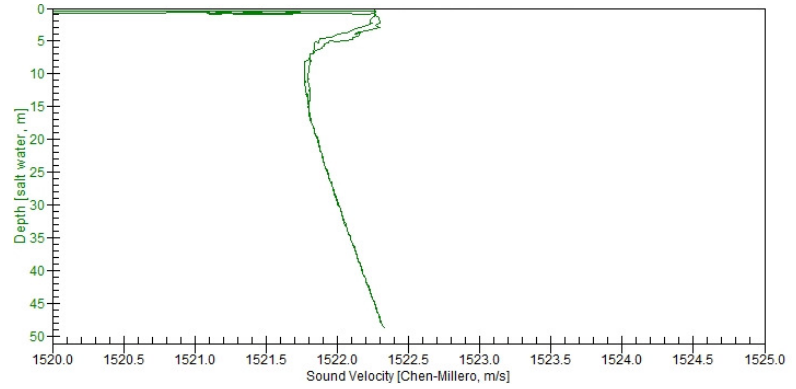

Figure B-25: Sound speed profile CTD Cast 6 –12:40 pm – 10 km range

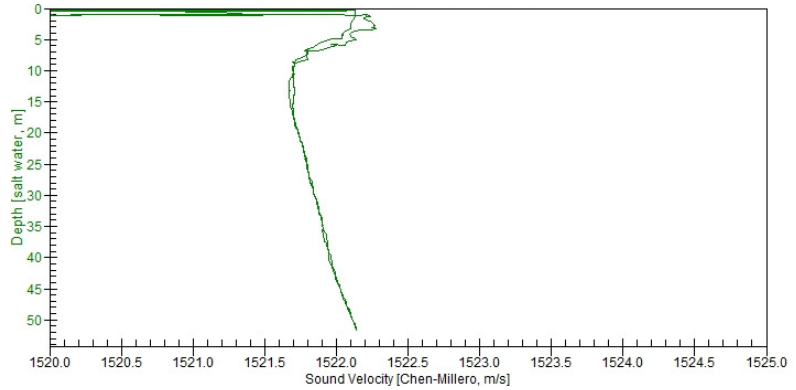

Figure B-26: Sound speed profile CTD Cast 7 – 1:10 pm – 6 km range

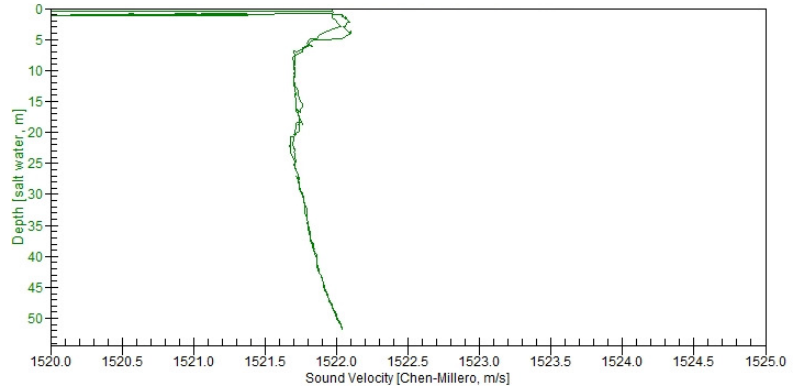

Figure B-27: Sound speed profile CTD Cast 8 – 1:30 pm – 4 km range

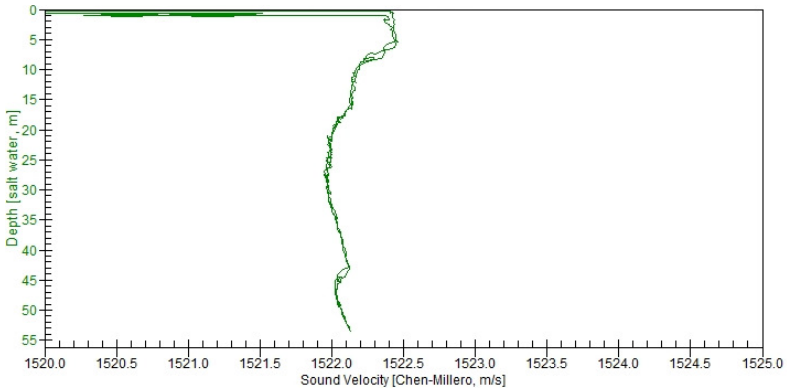

Figure B-28: Sound speed profile CTD Cast 9 – 1:53 pm – 1 km range

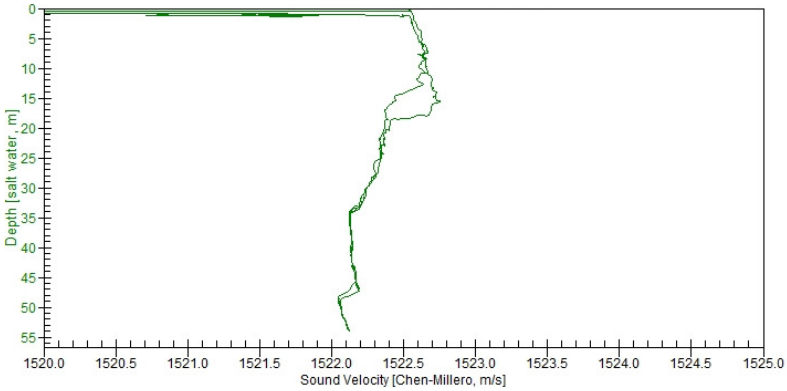

Figure B-29: Sound speed profile CTD Cast 10 – 2:12 pm – 500 m range

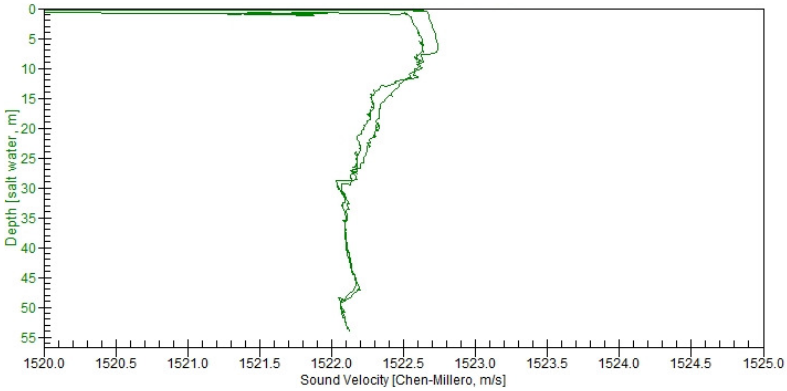

Figure B-30: Sound speed profile CTD Cast 11 – 2:46 pm - 500 m range

B.6 **Vessel pitch roll and heave notes**

(notes courtesy of Dr Tim Gourlay)

SENSOR POSITIONS:

LBP 16.535m

Bulkhead from stern 11.85m

Bulkhead 3.58m fwd of midships

TSS and Schaevitzes 0.37m fwd of BH, =3.95m fwd of midships

Crossbow 0.09m fwd of BH, 3.67m fwd of midships, lead aft

TSS 0.87m to port of CL, facing aft

Schaevitzes 1.44m to port and stbd of CL

Crossbow 0.10m to port of CL

Transmitter deployed 2m aft of BH, 1.6m fwd of midships, on port beam every time, 2.25m from CL

Hydrophone 32d06.457S, 115d23.516E

Dump weight 32d06.396S, 115d23.480E

RUN TIMES:

Times WST measured from Tim's watch, which was synchronized to internet time just before trial.

Run 1 0642 - 0712, near harbour test run

Run 2 0729.11 - , into swell near Rottnest, slamming

Dep01 = Run 3 0914.45 - 0954.48, first transmitter deployment. This run continued well after deployment finished, as did run 15.

All other runs were started and stopped just before and after deployment. One run for each deployment.

Dep02 = Run 4 0956.10 - ,

.. Run 5 1016.55 - 1028.56

Run 6 1035.32 - 1048.38

Run 7 1057.45 - 1111.00

Run 8 1123.23 - 1138.00

Run 9 1148.57 - 1202.27

Run 10 1214.18 - 1227.37

Run 11 1238.36 - 1252.41

Run 12 1307.28 - 1321.24

Run 13 1328.27 - 1341.56

Run 14 1351.22 - 1404.32

Run 15 1409.57 - 1439.40

Dep14 = Run 16 1445.36 - 1500.48

WIND:

Swell 2m SW

Wind SE 10kn at 0900, SE 5kn at 1100, sea breeze arrived 1230, SW 12kn at 1300, SW 20kn at 1500

Dep01 stbd beam-on to wind. All port beam-on thereafter.

OUTPUT FILES:

have 4 columns: Pitch (deg, +ve bow-down), Roll (deg, +ve to stbd), Heave midships (m, +ve up), Heave deployment location (m, +ve up)

all synchronized at 100Hz, starting at times shown above.

all mean-subtracted for each run.

RMS VALUES:

	Roll (deg)	Pitch (deg)	Heave midships (m)	Heave deployment location (m)	
dep01	3.6487	1.7127	0.5713	0.5693	note first run continued well after deployment finished
dep02	3.7563	1.7987	0.5299	0.5318	
dep03	3.7466	1.7812	0.5441	0.5551	
dep04	3.6163	1.8031	0.5565	0.5674	
dep05	3.7648	1.8235	0.6025	0.6236	
dep06	3.2853	1.8234	0.6262	0.6442	
dep07	3.5159	1.5725	0.5421	0.5642	
dep08	3.1594	1.3885	0.5377	0.5547	
dep09	3.2198	1.4466	0.5244	0.5436	
dep10	3.4648	1.3432	0.5420	0.5619	
dep11	3.8067	1.4310	0.5820	0.6023	
dep12	4.3340	1.3212	0.4830	0.5006	
dep13	4.0770	1.2022	0.4064	0.4355	
dep14	4.1290	1.3278	0.4500	0.4719	

Appendix C Synthetic channel simulation results

C.1 Cottesloe 120 m synthetic channel responses

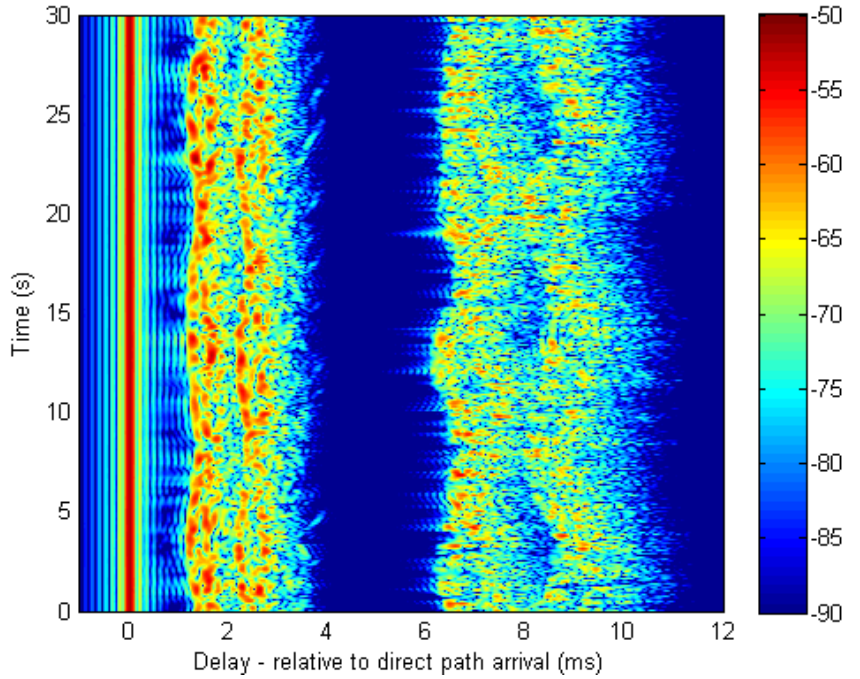

Figure C-1: Simulated whole channel response $|h(\tau,t)|^2$(dB–120 m range 13.5 m depth, surface H_s = 0.5 m, 10 base ray-paths, 3 bistatic response calculation angles, dx = 12 cm

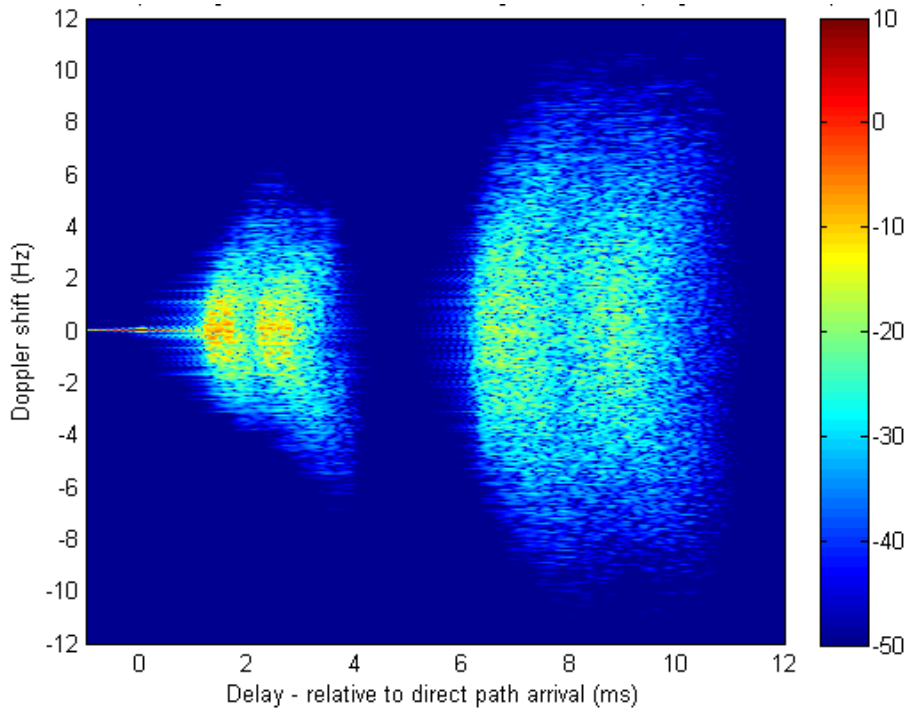

Figure C-2: Simulated whole channel spreading function $|S(\nu,\tau)|^2$(dB)– 120 m range 13.5 m depth, surface H_s = 0.5 m, 10 base ray-paths, 3 bistatic response calculation angles, dx = 12 cm

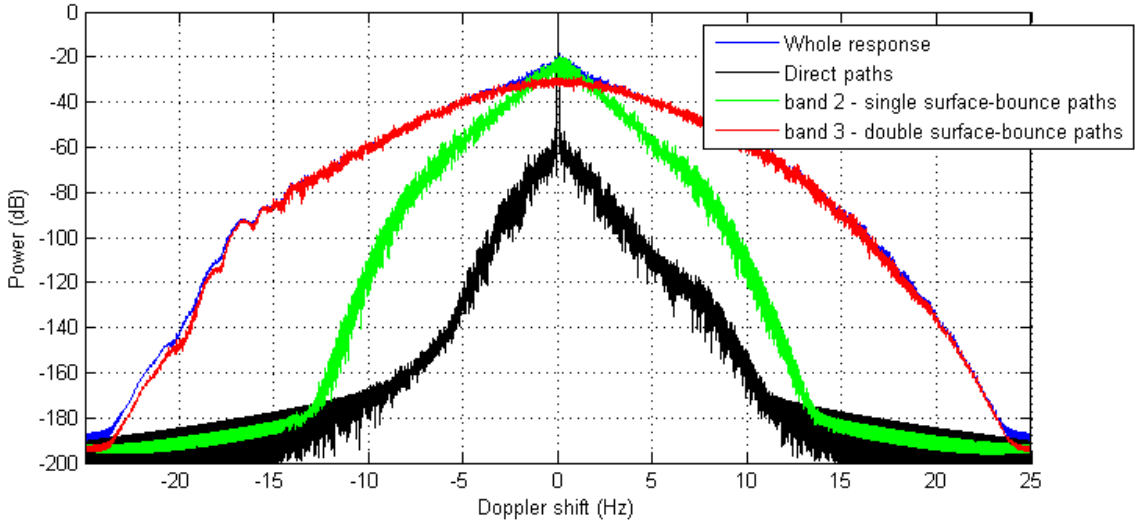

Figure C-3: Simulated channel power versus Doppler for whole response and first three arrival bands $|P(\nu,\tau)|$(dB), - 120 m range 13.5 m depth, surface H_s = 2 m, dx = 12 cm

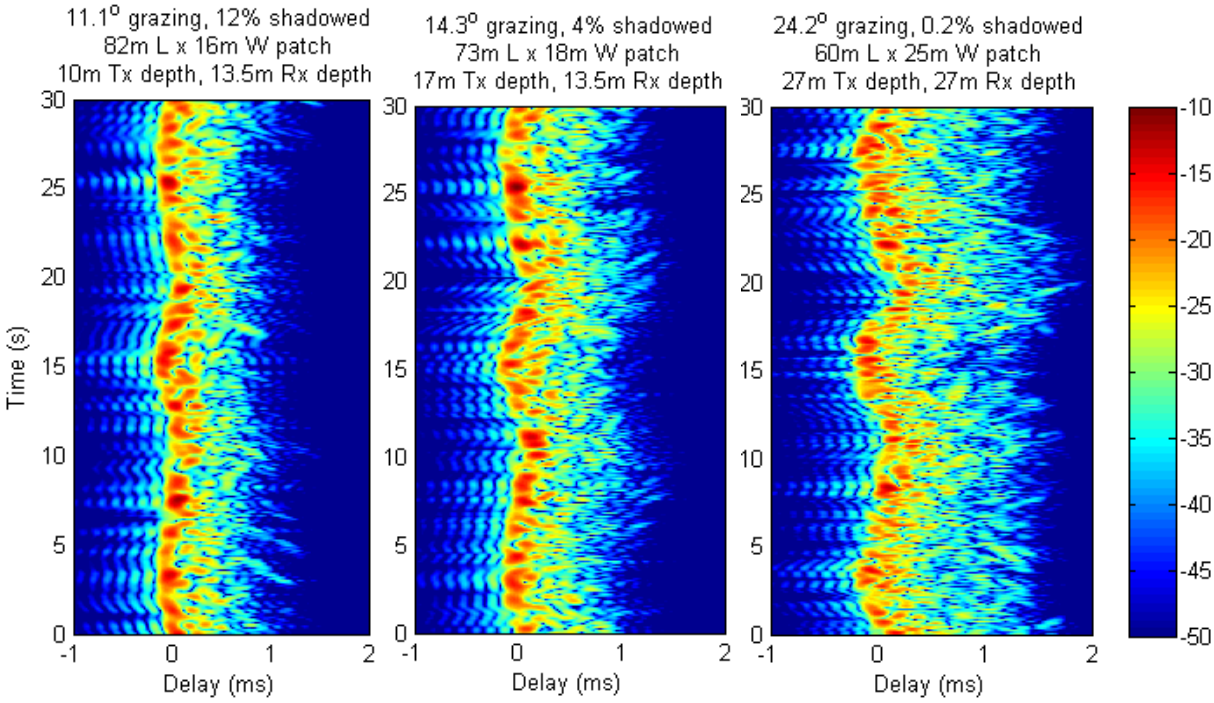

Figure C-4: Component range-normalised rationalised bistatic responses $|h(\tau,t)|^2$(dB) - 120 m range 13.5 m depth, surface H_s = 0.5 m, dx = 12 cm

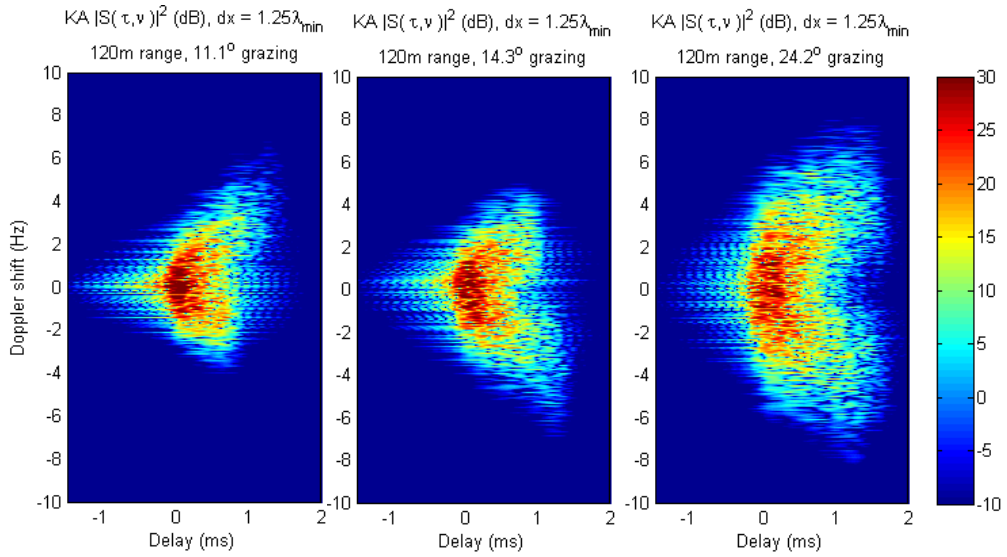

Figure C-5: Component range-normalised bistatic spreading functions$|S(\nu,\tau)|^2$(dB) relative to 12 kHz – 120 m range 13.5 m depth, surface H_s = 0.5 m, dx = 12 cm

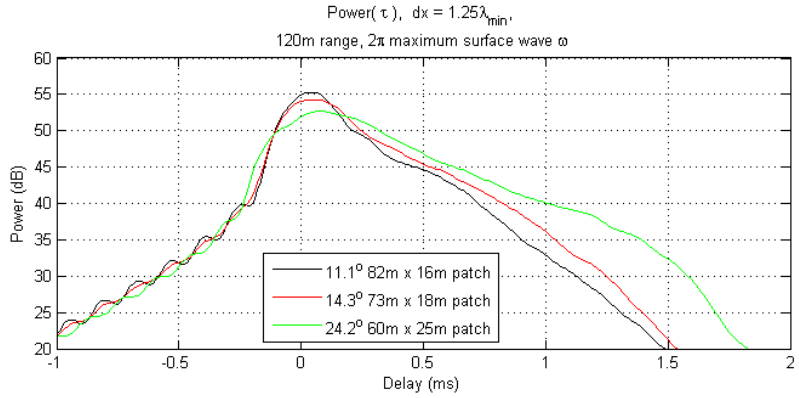

Figure C-6: Bistatic power profile versus delay and grazing angle $|P(\nu,\tau)|$ (dB) –120 m range 13.5 m depth, surface H_s = 0.5 m, dx = 12 cm

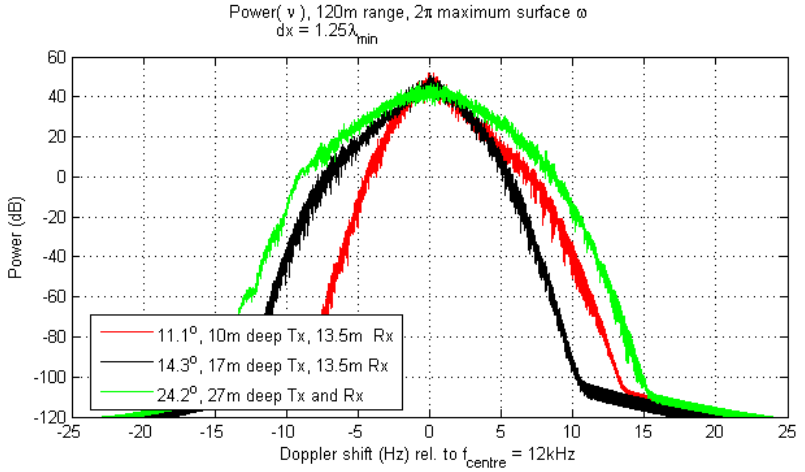

Figure C-7: Bistatic power profile versus Doppler and grazing angle $|P(\nu,\theta)|$ (dB) – 120 m range 13.5 m depth, surface H_s = 0.5 m, dx = 12 cm

C.2 **Cottesloe 500 m synthetic channel responses**

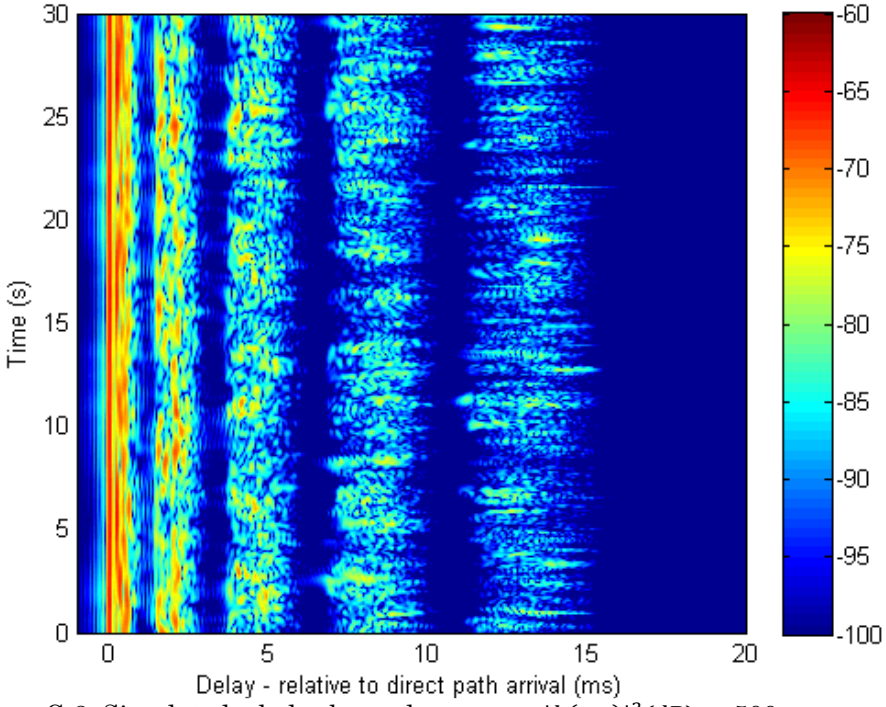

Figure C-8: Simulated whole channel response $|h(\tau,t)|^2$(dB), – 500 m range 13.5 m depth, surface H_s = 0.5 m, 22 base ray-paths, 7 bistatic response calculation angles, dx = 24 cm

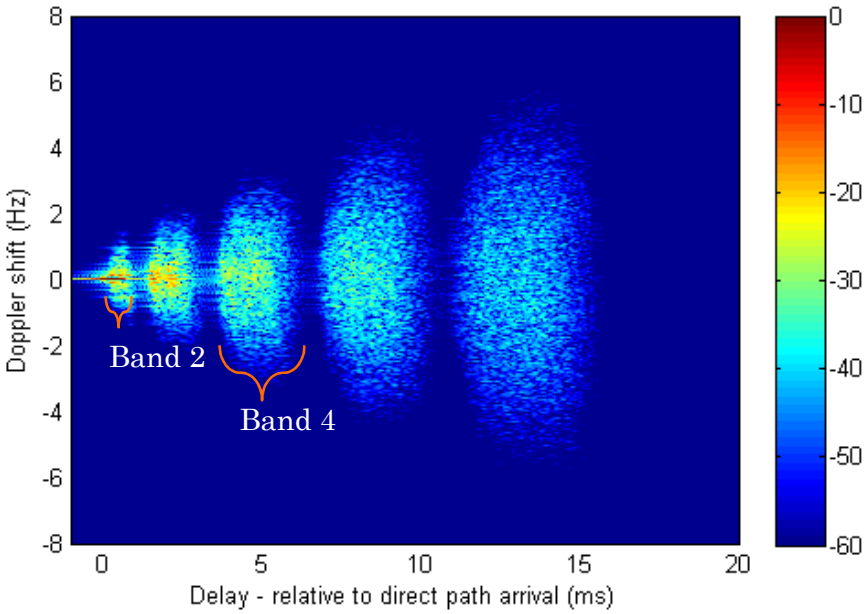

Figure C-9: Simulated whole channel spreading function $|S(\nu,\tau)|^2$(dB) – 500 m range 13.5 m depth, surface H_s = 0.5 m, 22 base ray-paths, 7 bistatic response calculation angles, dx = 24 cm

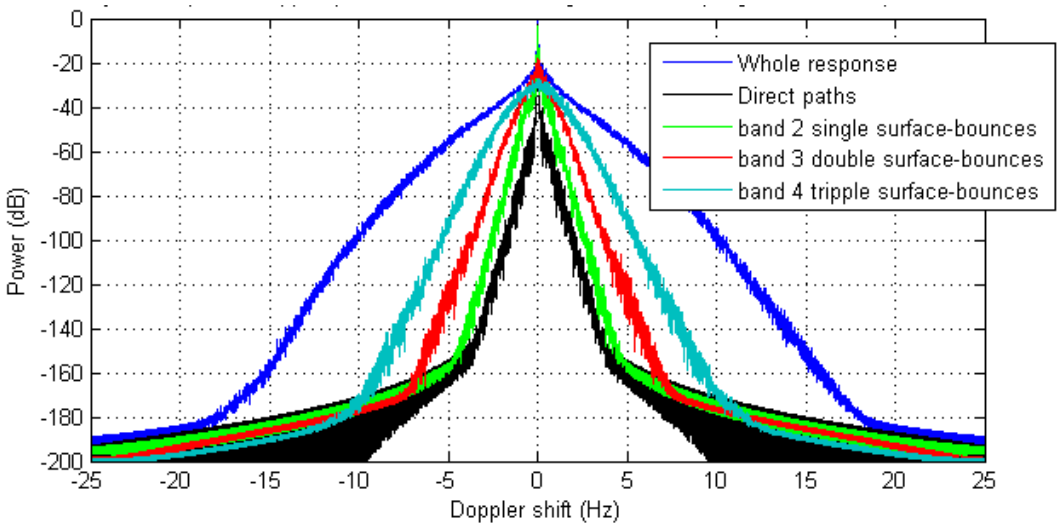

Figure C-10: Simulated channel power versus Doppler for whole response and first four arrival bands $|P(\nu,\tau)|$ (dB), - 500 m range 13.5 m depth, surface $H_s = 2$ m, dx = 24 cm

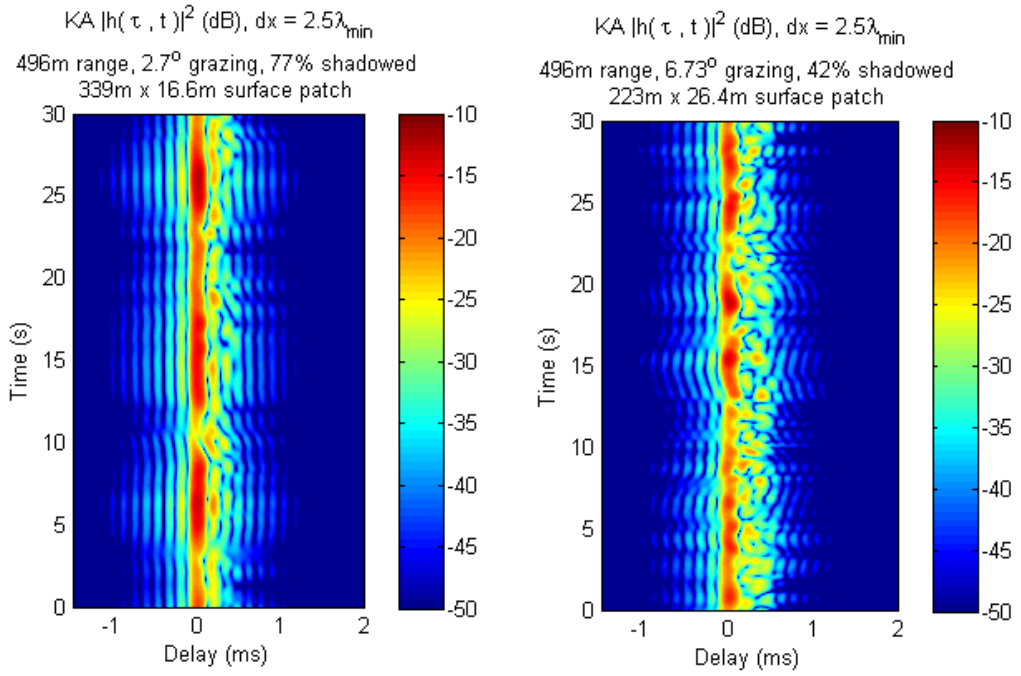

Figure C-11: Example component range-normalised bistatic responses $|h(\tau,t)|^2$(dB)- 500 m range 13.5 m depth, surface $H_s = 0.5$ m, dx = 24 cm

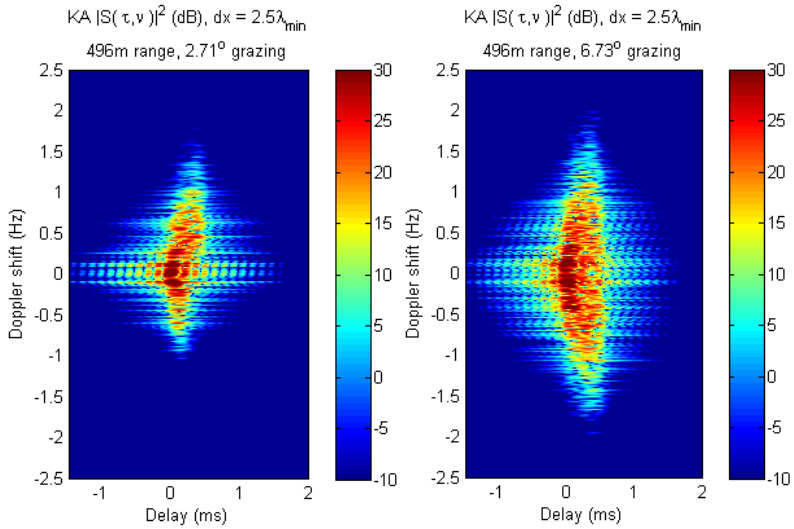

Figure C-12: Example component range-normalised bistatic spreading functions$|S(\nu,\tau)|^2$(dB) relative to 12 kHz – 500 m range 13.5 m depth, surface $H_s = 0.5$ m, dx = 24 cm

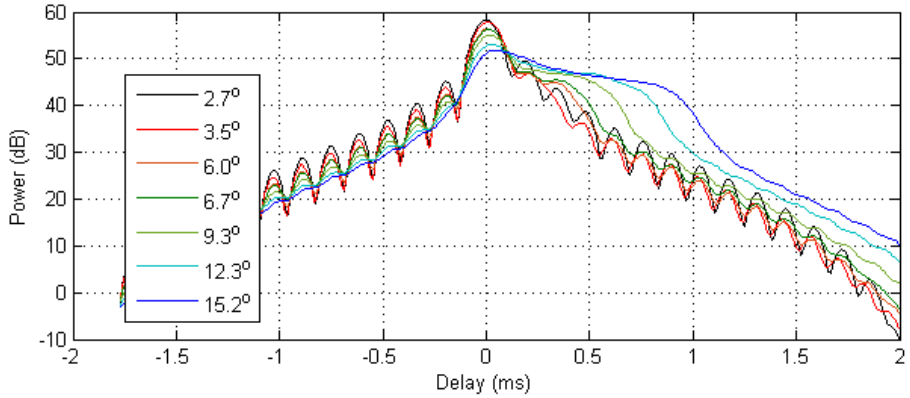

Figure C-13: Bistatic power profile versus delay and grazing angle $|P(\tau,\theta)|$ (dB) –500 m range 13.5 m depth, surface $H_s = 0.5$ m, dx = 24 cm

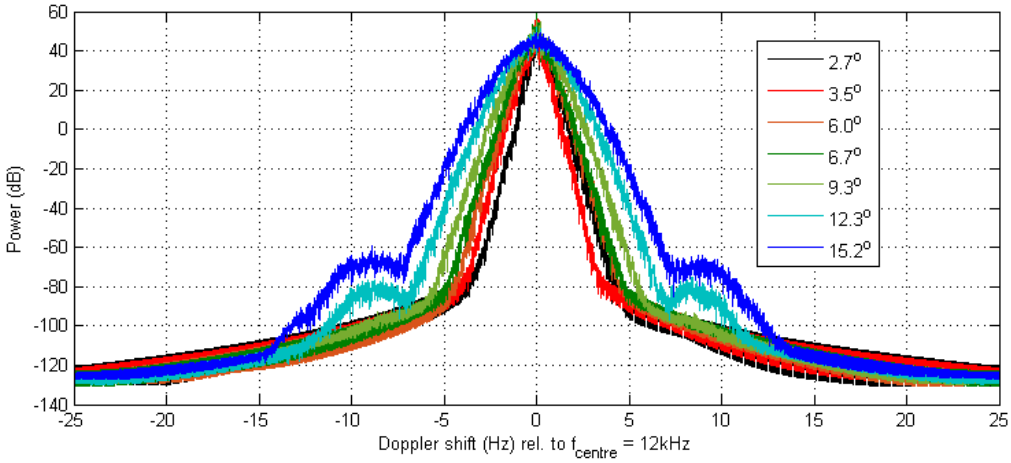

Figure C-14: Bistatic power profile versus Doppler and grazing angle $|P(\nu,\theta)|$ (dB) – 500 m range 13.5 m depth, surface $H_s = 0.5$ m, dx = 24 cm

C.3 **Cottesloe 1000 m synthetic channel responses**

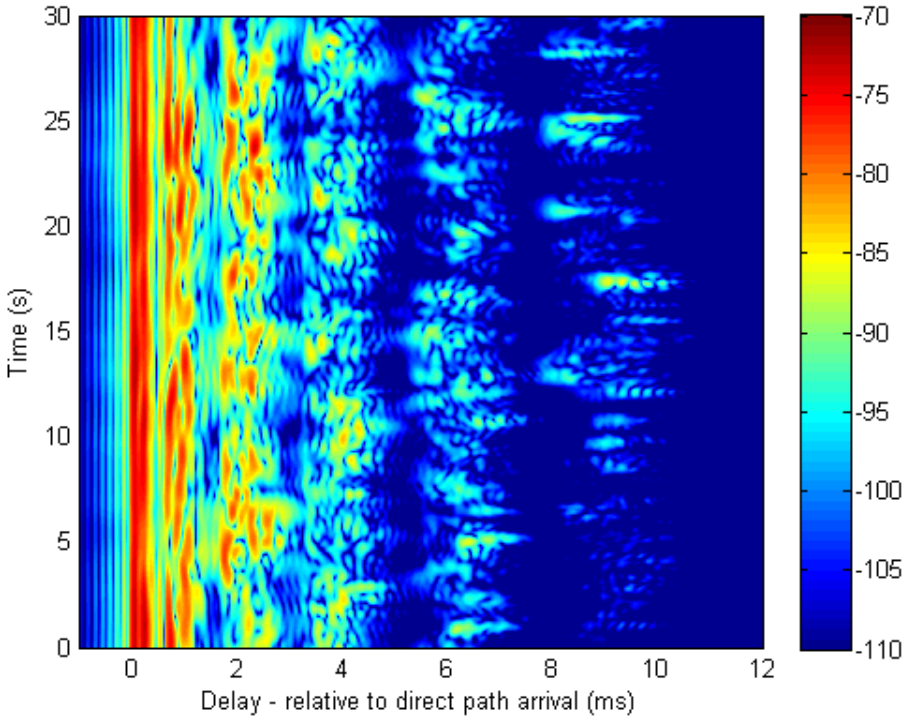

Figure C-15: Simulated whole channel response $|h(\tau,t)|^2$(dB) – 1000 m range 13.5 m depth, surface H_s = 0.5 m, 26 base ray-paths, 7 bistatic response calculation angles, dx = 48 cm

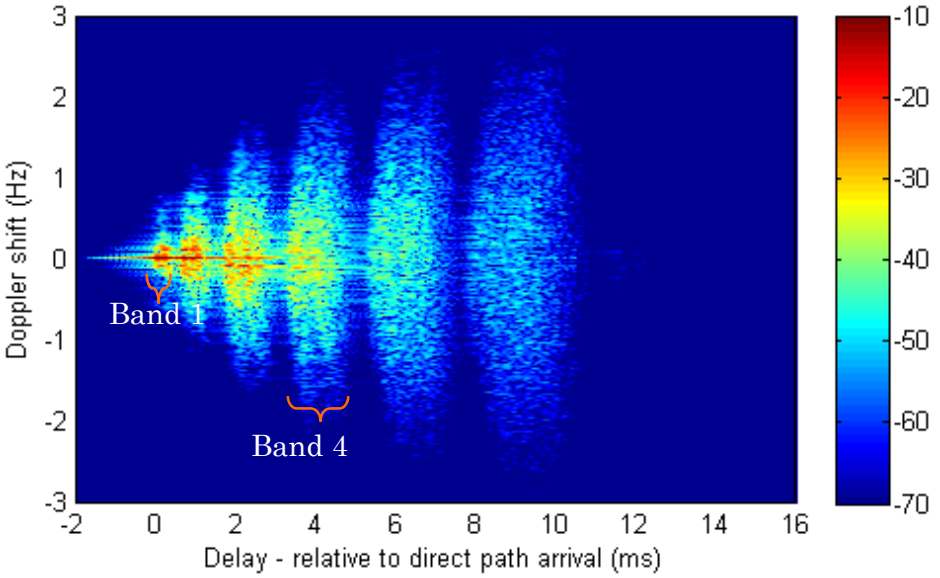

Figure C-16: Simulated spreading function $|S(\nu,\tau)|^2$(dB)- 1000m range 13.5 m depth, surface Hs = 0.5 m, 26 base ray-paths, 7 bistatic response calculation angles, dx = 48 cm

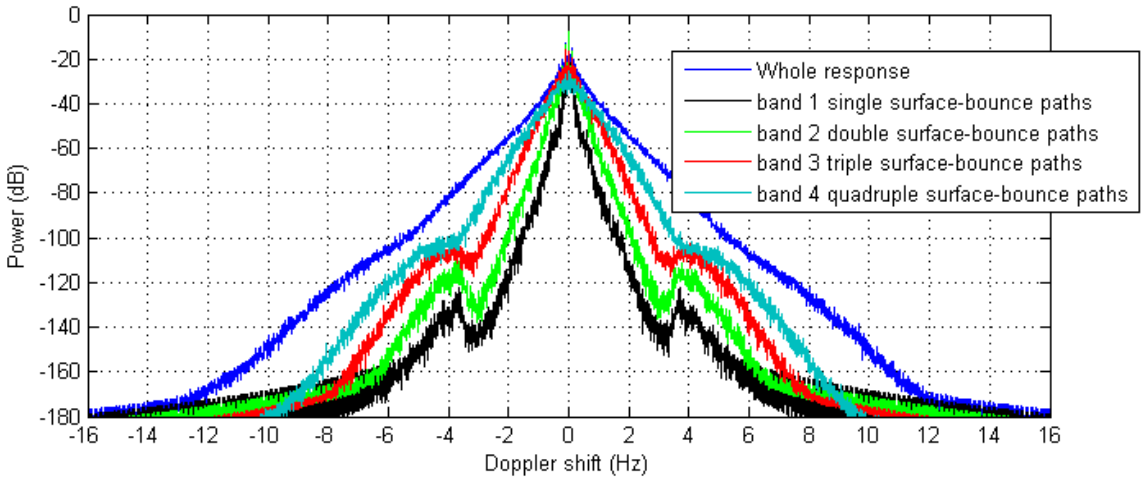

Figure C-17: Simulated channel power versus Doppler for whole response and first four arrival bands $|P(\nu,\tau)|$ (dB), - 1000 m range 13.5 m depth, surface $H_s = 2$ m, dx = 48 cm

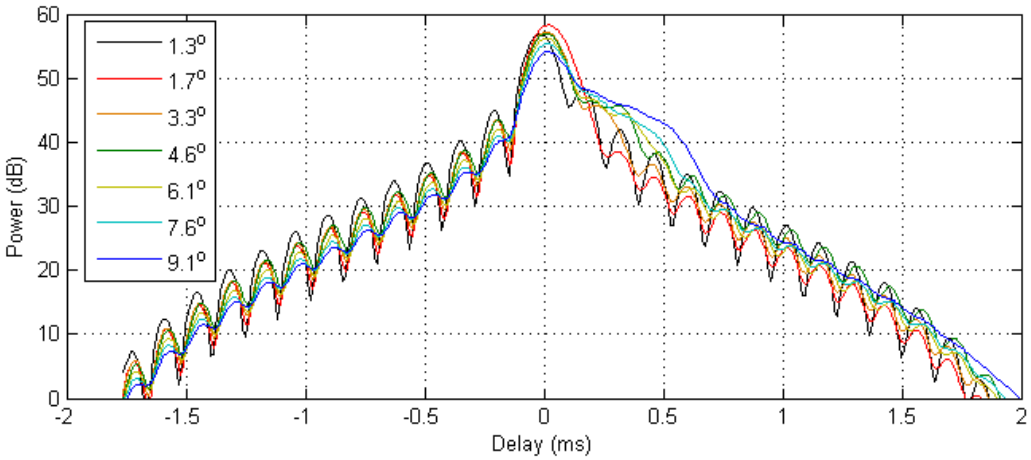

Figure C-18: Bistatic power profile versus delay and grazing angle $|P(\tau,\theta)|$ (dB) – 1000 m range 13.5 m depth, surface $H_s = 0.5$ m, dx = 48 cm

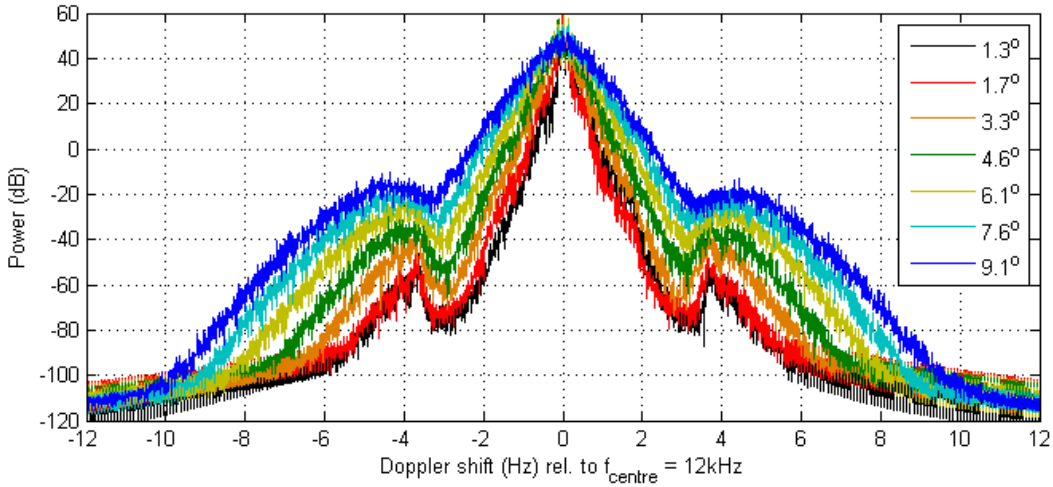

Figure C-19: Bistatic power profile versus Doppler and grazing angle $|P(\nu,\theta)|$ (dB) – 1000 m range 13.5 m depth, surface $H_s = 0.5$ m, dx = 48 cm

C.4 **Rottnest 120 m synthetic channel responses**

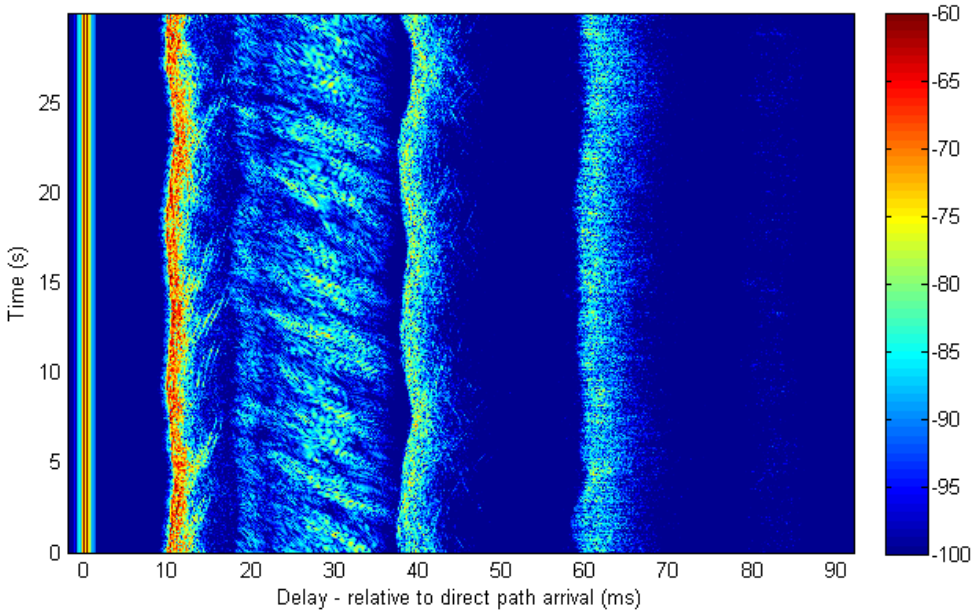

Figure C-20: Simulated whole channel response $|h(\tau,t)|^2$(dB– 120 m range 53 m depth, surface H_s = 2 m, 8 base ray-paths, 2 bistatic response calculation angles, dx = 24 cm

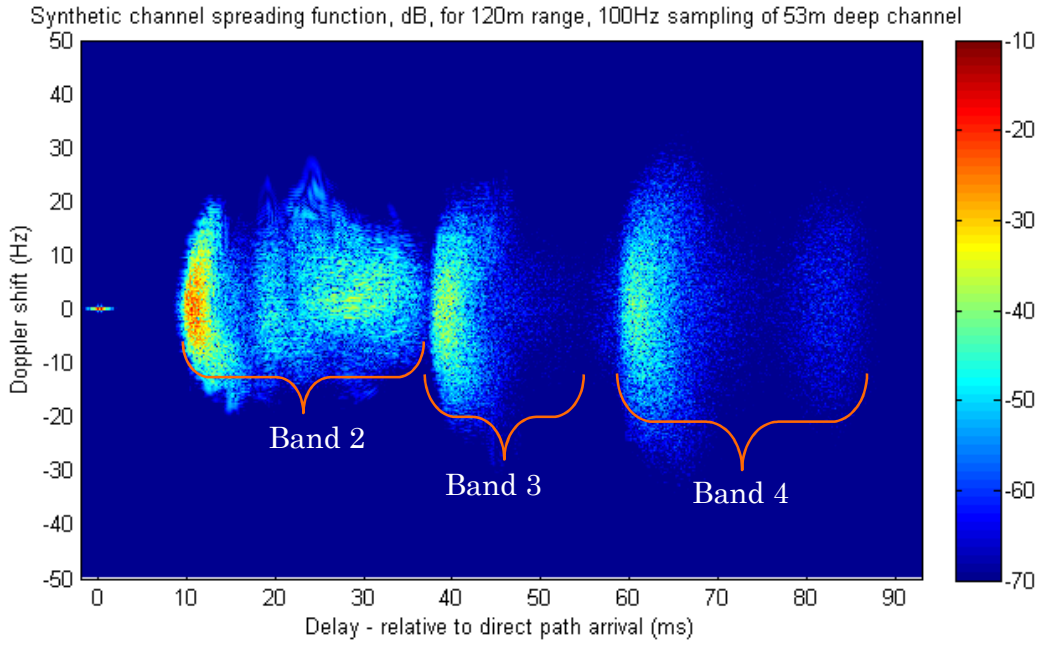

Figure C-21: Simulated whole channel spreading function $|S(\nu,\tau)|^2$(dB) – 120 m range 53 m depth, surface H_s = 2 m, 8 base ray-paths, 2 bistatic response calculation angles, dx = 24 cm

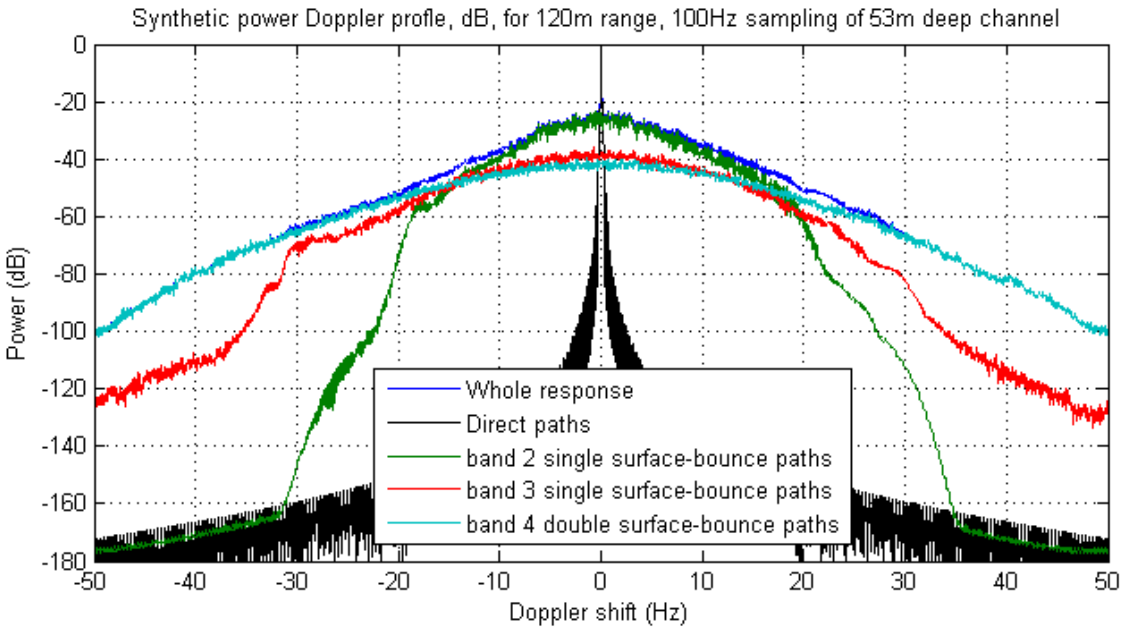

Figure C-22: Simulated channel power versus Doppler for whole response and first four arrival bands $|P(\nu,\theta)|$ (dB), - 120 m range 53 m depth, surface $H_s = 2$ m, dx = 24 cm

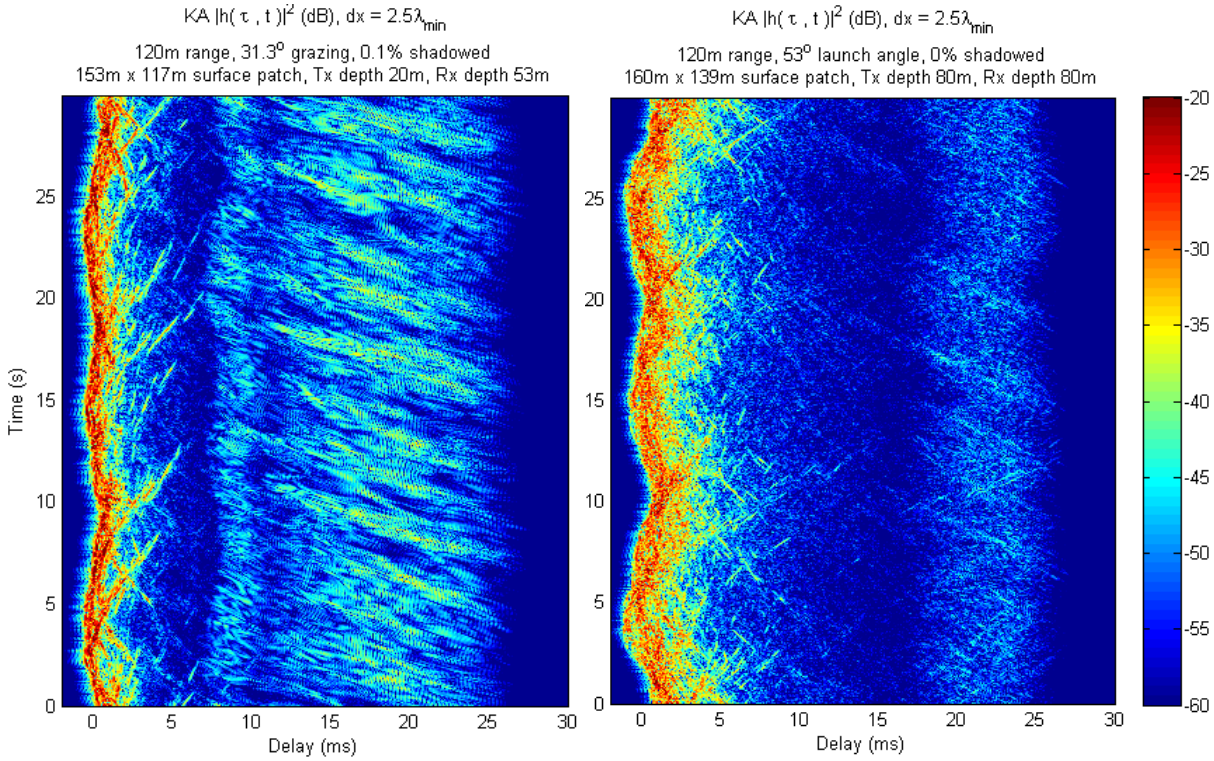

Figure C-23: Component range-normalised bistatic responses $|h(\tau,t)|^2$(dB)- 120 m range 53 m depth, surface $H_s = 2$ m, dx = 24 cm

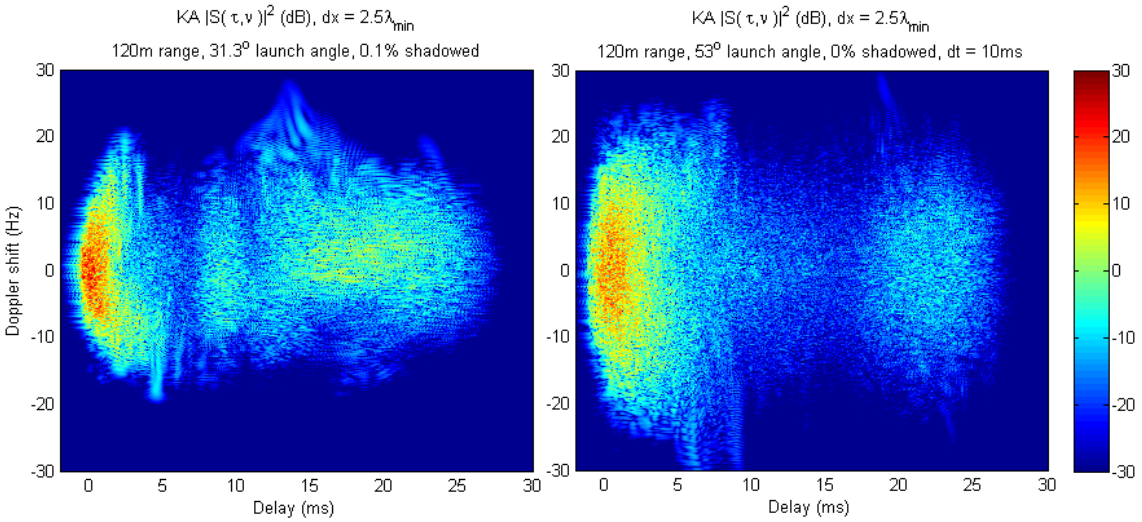

Figure C-24: Component range-normalised bistatic spreading functions$|S(\nu,\tau)|^2$(dB) relative to 12 kHz – 120 m range 53 m depth, surface H_s = 2 m, dx = 24 cm

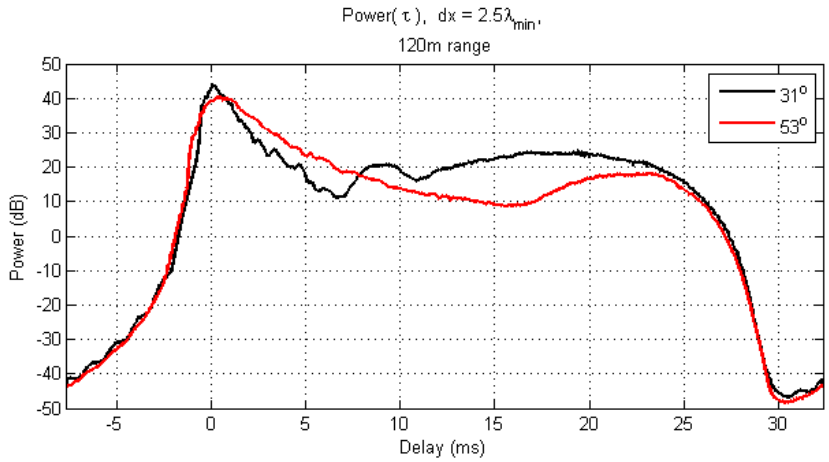

Figure C-25: Bistatic power profile versus delay and grazing angle $|P(\tau,\theta)|$ (dB) –120 m range 53 m depth, surface H_s = 2 m, patch sizing by 30 ms delay tolerance, dx = 24 cm

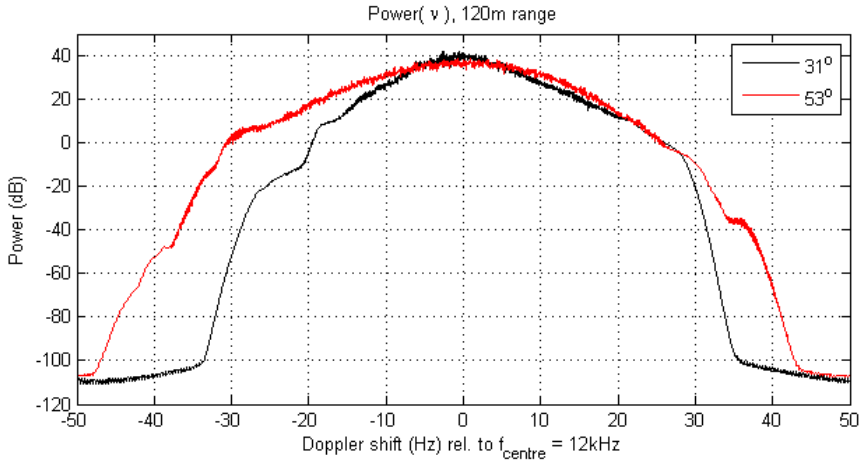

Figure C-26: Bistatic power profile versus Doppler and grazing angle $|P(\nu,\theta)|$ (dB) – 120 m range 53 m depth, surface H_s = 2 m, dx = 24 cm

C.5 **Rottnest 1100 m synthetic channel responses**

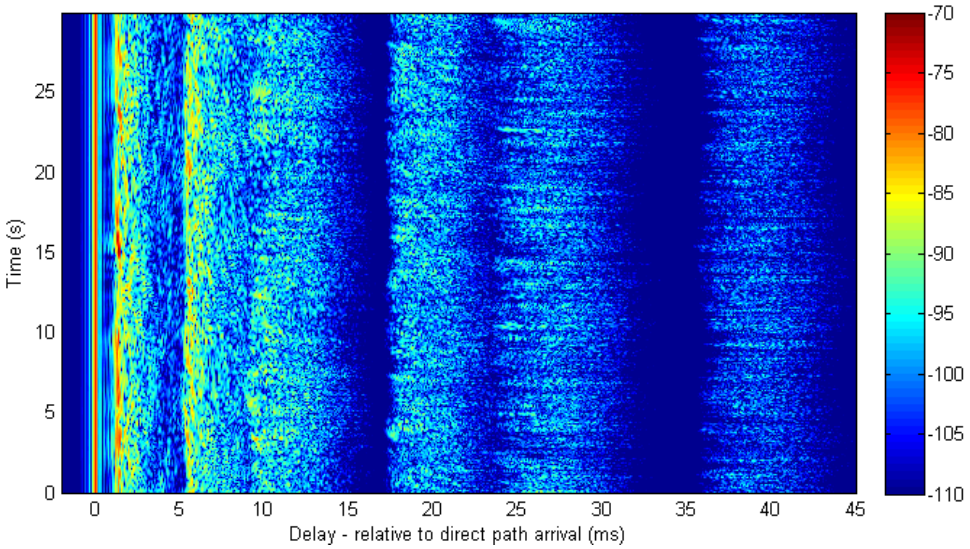

Figure C-27: Simulated whole channel response $|h(\tau,t)|^2$(dB- 1100 m range 53 m depth, surface H_s = 2 m, 14 base ray-paths, 5 bistatic response calculation angles, dx = 48 cm

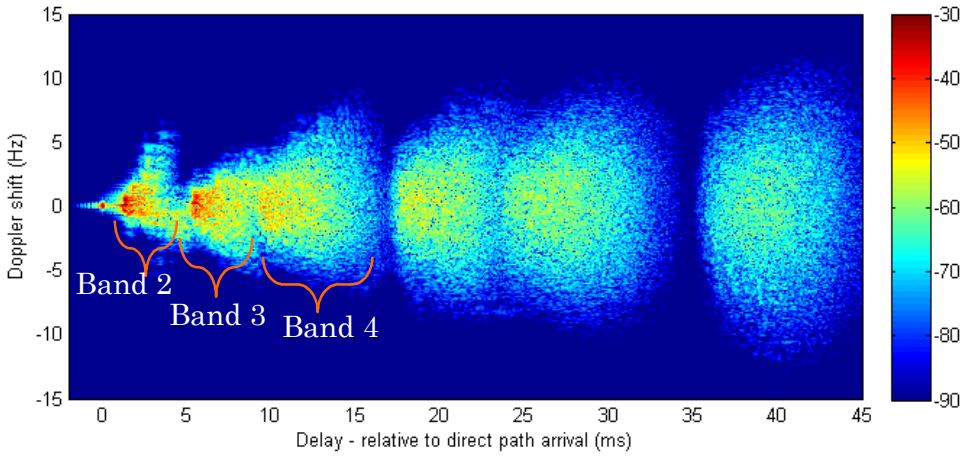

Figure C-28: Simulated whole channel spreading function $|S(\nu,\tau)|^2$(dB)- 1100 m range 53 m depth, surface H_s = 2 m, 14 base ray-paths, 5 bistatic response calculation angles, dx = 48 cm

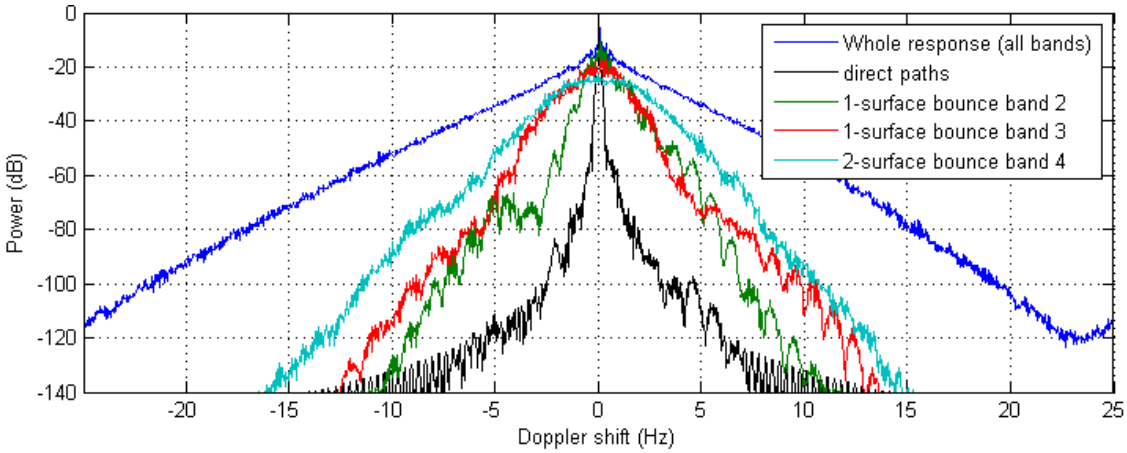

Figure C-29: Simulated channel power versus Doppler for whole response and first four arrival bands $|P(\nu,\theta)|$ (dB), - 1100 m range 53 m depth, surface H_s = 2 m, dx = 48 cm

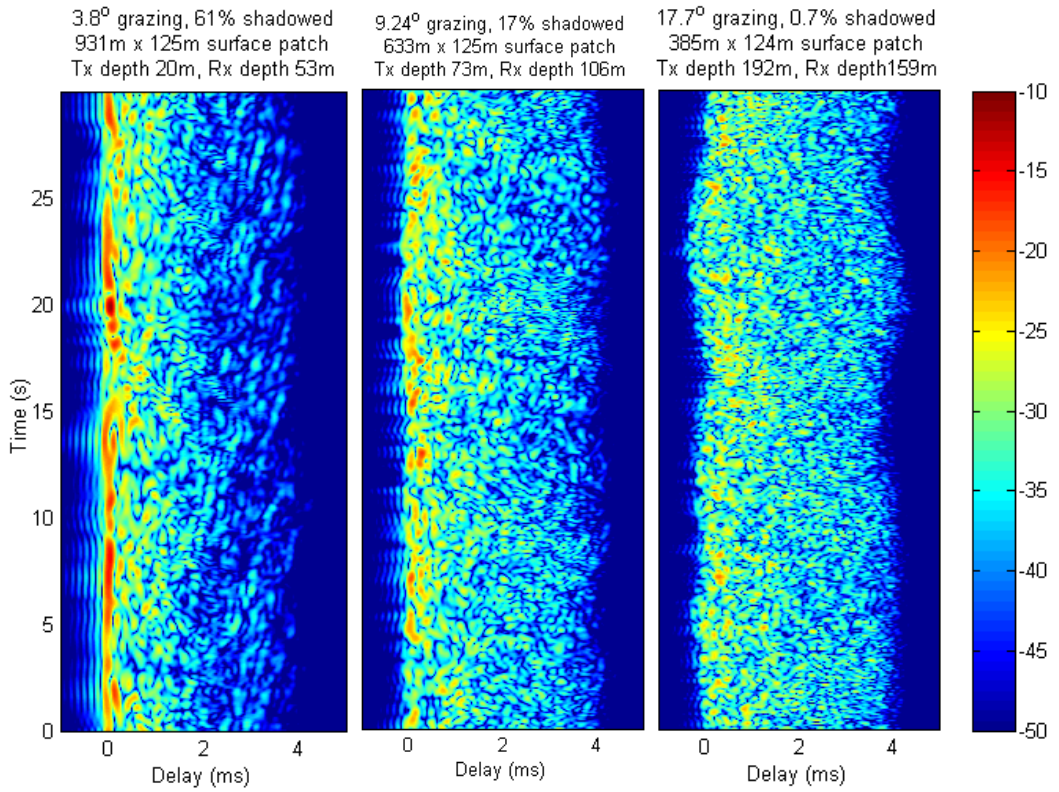

Figure C-30: Example component range-normalised bistatic responses $|h(\tau,t)|^2$(dB)- 1100 m range 53 m depth, surface H_s = 2 m, dx = 48 cm

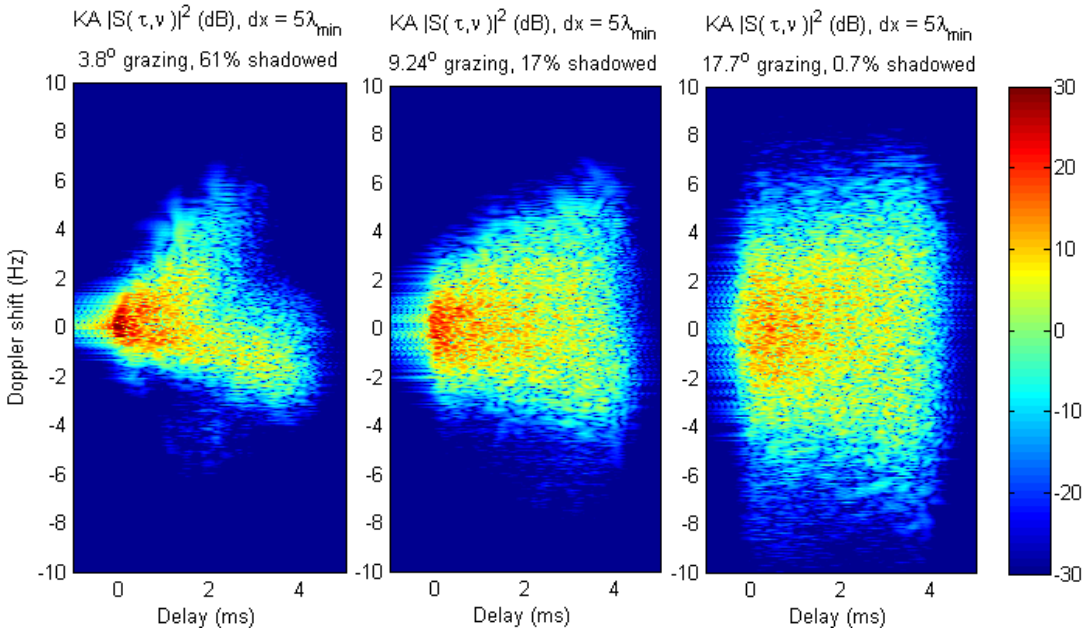

Figure C-31: Example component range-normalised bistatic spreading functions$|S(\nu,\tau)|^2$(dB) relative to 12 kHz – 1100 m range 53 m depth, surface H_s = 2 m, dx = 48 cm

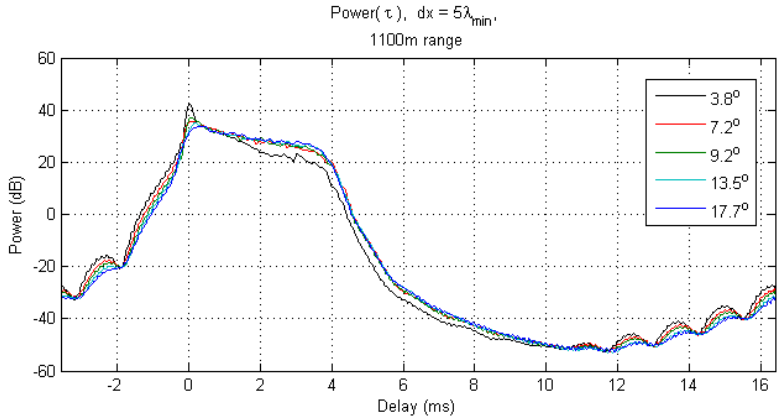

Figure C-32: Bistatic power profile versus delay and grazing angle $|P(\tau,\theta)|$ (dB) – 1100 m range 53 m depth, surface H_s = 2 m, dx = 48 cm

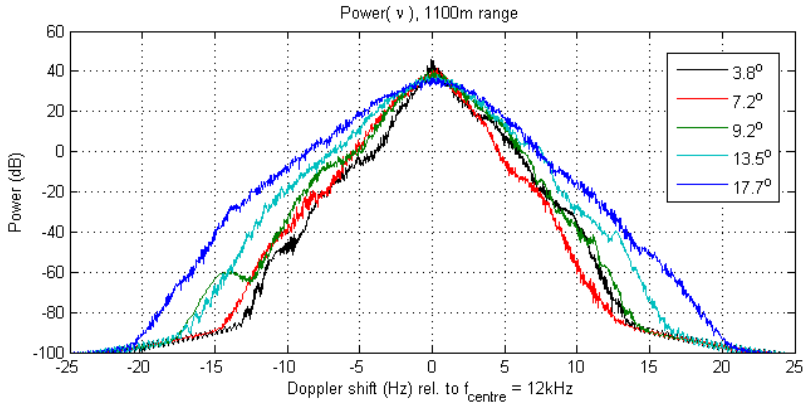

Figure C-33: Bistatic power profile Doppler and grazing angle $|P(\nu,\theta)|$ (dB) –1100 m range 53 m depth, surface H_s = 2m, dx = 48 cm

C.6 **Rottnest 7827 m synthetic channel responses**

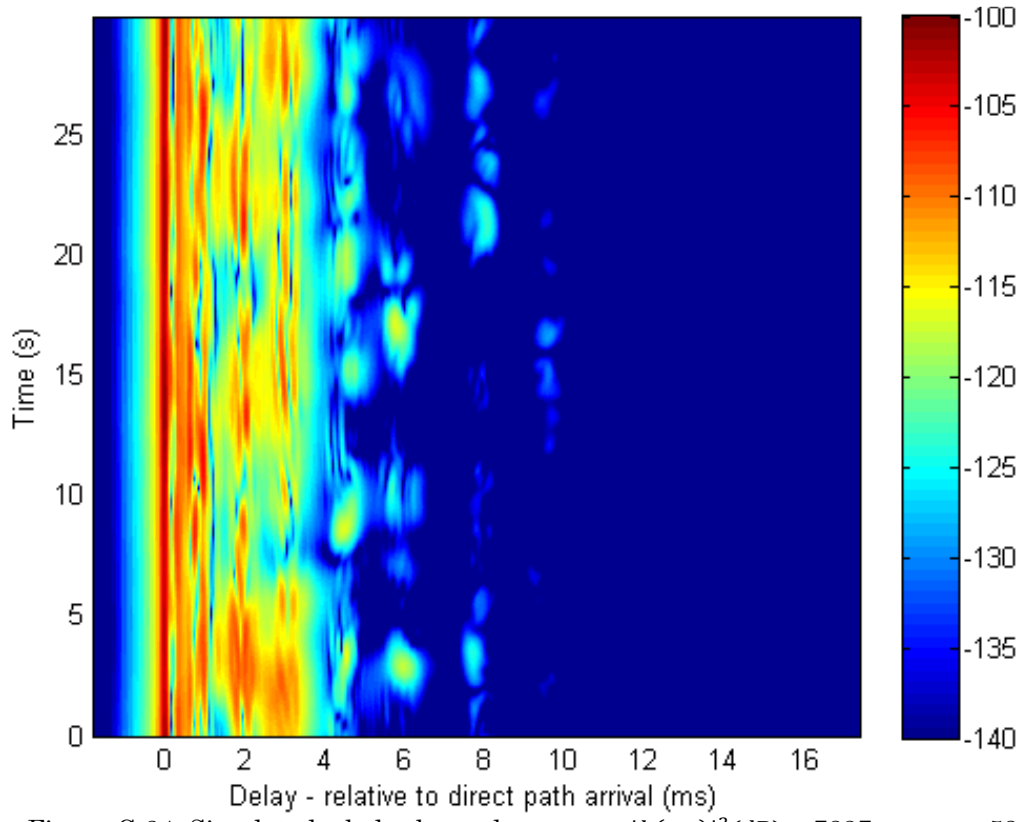

Figure C-34: Simulated whole channel response $|h(\tau,t)|^2$(dB) – 7827 m range 53 m depth, surface H_s = 2 m, 20 base ray-paths, 5 bistatic response calculation angles, dx = 95 cm

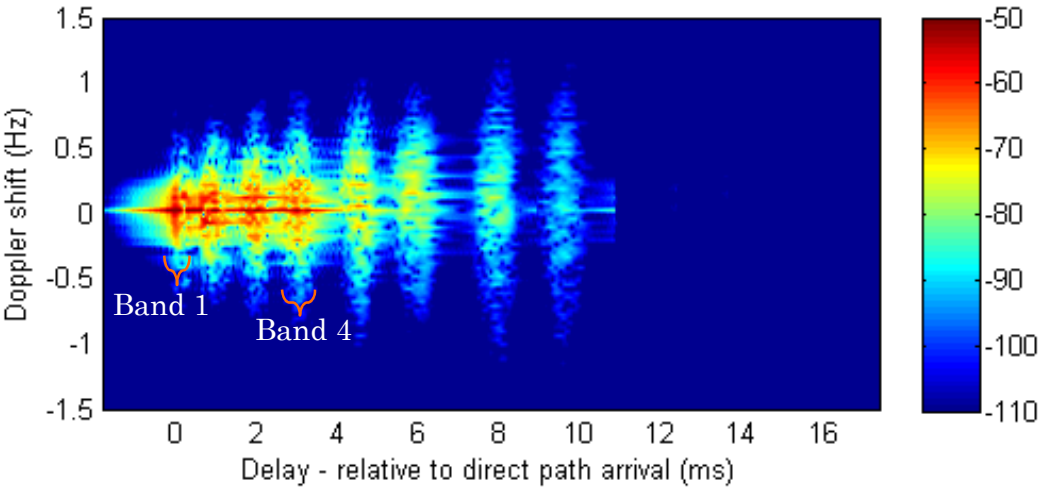

Figure C-35: Simulated whole channel spreading function $|S(\nu,\tau)|^2$(dB) -7827 m range 53 m depth, surface H_s = 2 m, 20 base ray-paths, 5 bistatic response calculation angles, dx = 95 cm

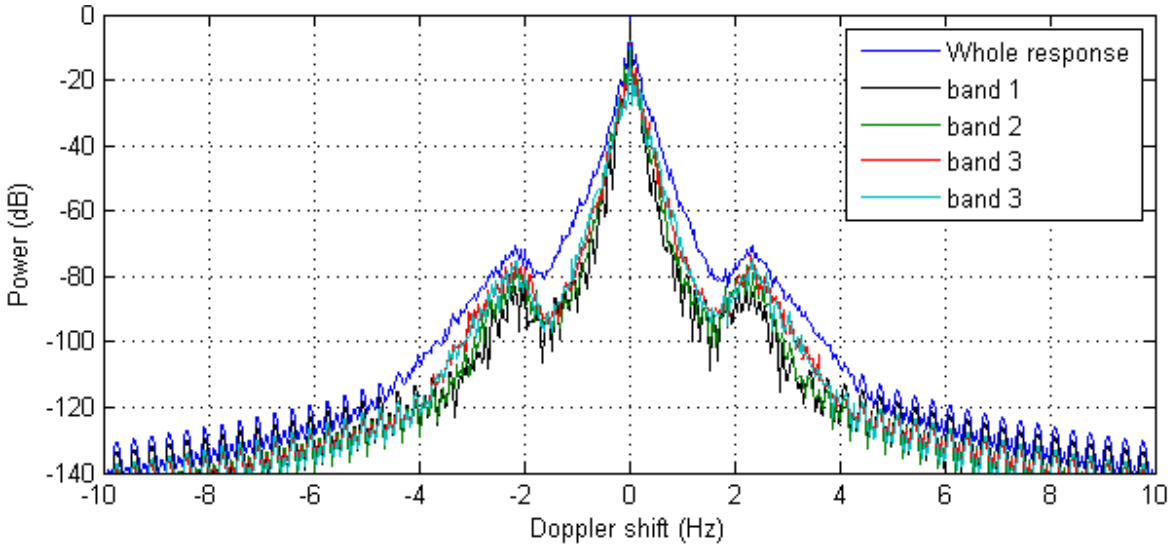

Figure C-36: Simulated channel power versus Doppler for whole response and first four arrival bands $|P(\nu,\theta)|$ (dB), - 7827 m range 53 m depth, surface H_s = 2 m, dx = 95 cm

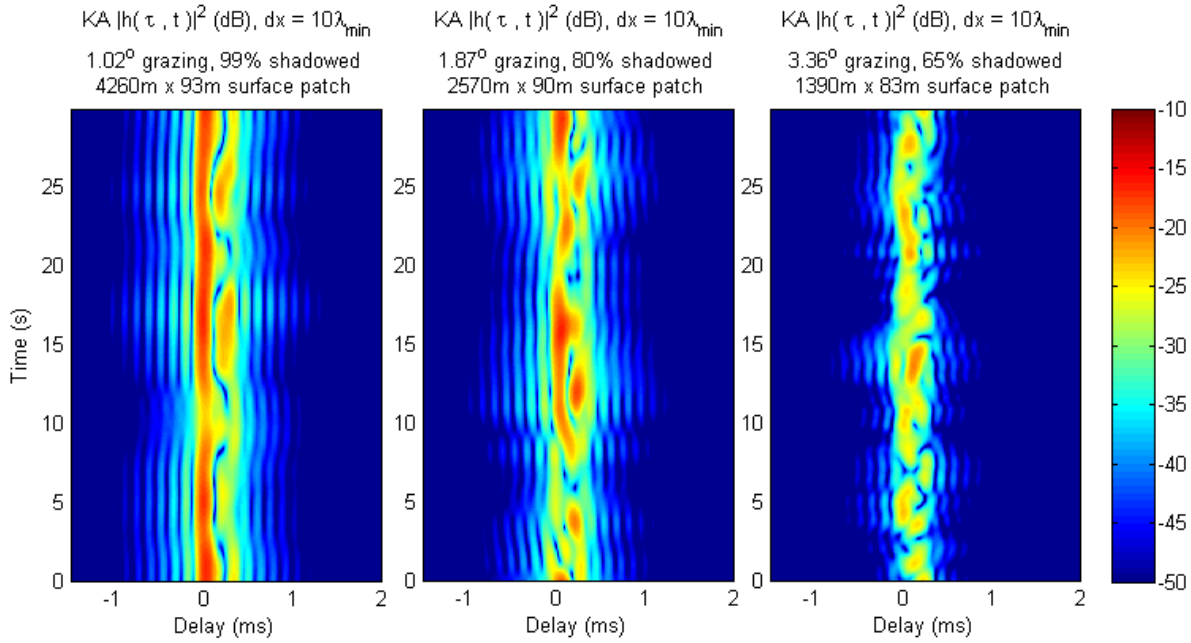

Figure C-37: Component range-normalised bistatic responses $|h(\tau,t)|^2$(dB)- 7827 m range 53 m depth, surface H_s = 2 m, dx = 95 cm

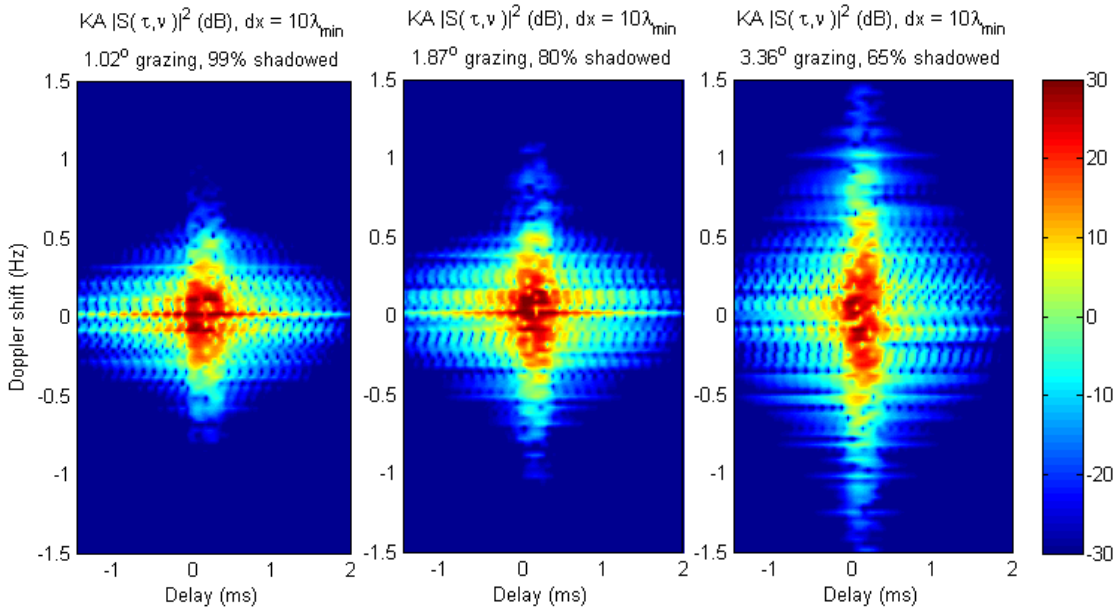

Figure C-38: Example component range-normalised bistatic spreading functions$|S(\nu,\tau)|^2$(dB) relative to 12 kHz – 7827 m range 53 m depth, surface H_s = 2 m, dx = 95 cm

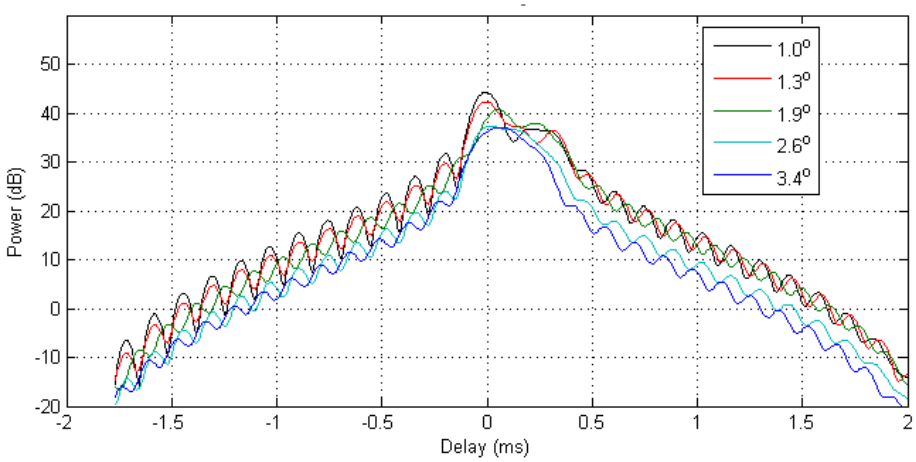

Figure C-39: Bistatic power profile versus delay and grazing angle $|P(\tau,\theta)|$ (dB) – 7827 m range 53 m depth, surface H_s = 2 m, dx = 95 cm

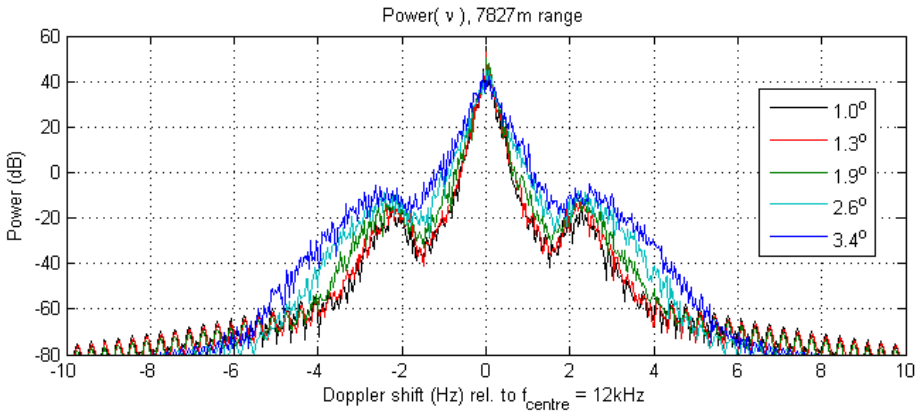

Figure C-40: Bistatic power profile versus Doppler and grazing angle $|P(\nu,\theta)|$ (dB) – 7827 m range 53 m depth, surface H_s = 2 m, dx = 95 cm

Appendix D **Matlab code and data files**

Matlab code created by the author in the preparation of this thesis remains the intellectual property of the author. Inquiries about use of this code should be directed to michael.caley@westnet.com.au.

Data used in the preparation of this thesis is the property of Curtin University Centre for Marine Science and Technology, Perth. Inquiries about the use of this data can be directed by email to Dr Alec Duncan at a.duncan@cmst.curtin.edu.au .